Metal Oxides Series

Series Editor
Ghenadii Korotcenkov

Metal Oxide Powder Technologies

Fundamentals, Processing Methods and Applications

Edited by
Yarub Al-Douri

ELSEVIER

Metal Oxide Powder Technologies

The Metal Oxides Book Series Edited by Ghenadii Korotcenkov

Forthcoming Titles

- Metal Oxide Powder Technologies, Yarub Al-Douri, 9780128175057
- Palladium Oxides Material Properties, Synthesis and Processing Methods, and Applications, Alexander M. Samoylov, Vasily N. Popov, 9780128192238
- Solution Processed Metal Oxide Thin Films for Electronic Applications, Zheng Cui, 9780128149300
- Metal Oxides for Non-volatile Memory, Panagiotis Dimitrakis, Ilia Valov, 9780128146293
- Metal Oxide Nanostructured Phosphors, H. Nagabhushana, Daruka Prasad, S.C. Sharma, 9780128118528
- Nanostructured Zinc Oxide, Kamlendra Awasthi, 9780128189009
- Metal Oxide-Based Nanostructured Electrocatalysts for Fuel Cells, Electrolyzers, and Metal-Air Batteries, Teko Napporn, Yaovi Holade, 9780128184967
- Multifunctional Piezoelectric Oxide Nanostructures, Sang-Jae Kim, Nagamalleswara Rao Alluri, Yuvasree Purusothaman, 9780128193327
- Titanium Dioxide (TiO2) and its applications, Leonardo Palmisano, Francesco Parrino, 9780128199602
- Transparent Conductive Oxides, Mirela Petruta Suchea, Petronela Pascariu, Emmanouel Koudoumas, 9780128206317
- Metal oxide-based nanofibers and their applications, Vincenzo Esposito, Debora Marani, 9780128206294
- Metal Oxides in Nanocomposite-Based Electrochemical Sensors for Toxic Chemicals, Alagarsamy Pandikumar, Perumal Rameshkumar, 9780128207277
- Metal-oxides for Biomedical and Biosensor Applications, Kunal Mondal, 9780128230336
- Metal Oxide-Carbon Hybrid Materials, Muhammad Akram, Rafaqat Hussain, Faheem K Butt, 9780128226940

Published Titles

- Colloidal Metal Oxide Nanoparticles, Sabu Thomas, Anu Tresa Sunny, Prajitha V, 9780128133576
- Cerium Oxide, Salvatore Scire, Leonardo Palmisano, 9780128156612
- Tin Oxide Materials, Marcelo Ornaghi Orlandi, 9780128159248
- Metal Oxide Glass Nanocomposites, Sanjib Bhattacharya, 9780128174586
- Gas Sensors Based on Conducting Metal Oxides, Nicolae Barsan, Klaus Schierbaum, 9780128112243
- Metal Oxides in Energy Technologies, Yuping Wu, 9780128111673
- Metal Oxide Nanostructures, Daniela Nunes, Lidia Santos, Ana Pimentel, Pedro Barquinha, Luis Pereira, Elvira Fortunato, Rodrigo Martins, 9780128115121
- Gallium Oxide, Stephen Pearton, Fan Ren, Michael Mastro, 9780128145210
- Metal Oxide-Based Photocatalysis, Adriana Zaleska-Medynska, 9780128116340
- Metal Oxides in Heterogeneous Catalysis, Jacques C. Vedrine, 9780128116319
- Magnetic, Ferroelectric, and Multiferroic Metal Oxides, Biljana Stojanovic, 9780128111802
- Iron Oxide Nanoparticles for Biomedical Applications, Sophie Laurent, Morteza Mahmoudi, 9780081019252
- The Future of Semiconductor Oxides in Next-Generation Solar Cells, Monica Lira-Cantu, 9780128111659
- Metal Oxide-Based Thin Film Structures, Nini Pryds, Vincenzo Esposito, 9780128111666
- Metal Oxides in Supercapacitors, Deepak Dubal, Pedro Gomez-Romero, 9780128111697
- Transition Metal Oxide Thin Film-Based Chromogenics and Devices, Pandurang Ashrit, 9780081018996

Metal Oxides Series

Metal Oxide Powder Technologies

Fundamentals, Processing Methods and Applications

Edited by

Yarub Al-Douri
Nanotechnology and Catalysis Research Center (NANOCAT), University of Malaya, Kuala Lumpur, Malaysia
University Research Center, Cihan University Sulaimaniya, Sulaimaniya, Iraq
Department of Mechatronics Engineering, Faculty of Engineering and Natural Sciences, Bahcesehir University, Istanbul, Turkey

Series Editor

Ghenadii Korotcenkov

Elsevier
Radarweg 29, PO Box 211, 1000 AE Amsterdam, Netherlands
The Boulevard, Langford Lane, Kidlington, Oxford OX5 1GB, United Kingdom
50 Hampshire Street, 5th Floor, Cambridge, MA 02139, United States

Notices
Knowledge and best practice in this field are constantly changing. As new research and experience broaden our understanding, changes in research methods, professional practices, or medical treatment may become necessary.

Practitioners and researchers must always rely on their own experience and knowledge in evaluating and using any information, methods, compounds, or experiments described herein. In using such information or methods they should be mindful of their own safety and the safety of others, including parties for whom they have a professional responsibility.

To the fullest extent of the law, neither the Publisher nor the authors, contributors, or editors, assume any liability for any injury and/or damage to persons or property as a matter of products liability, negligence or otherwise, or from any use or operation of any methods, products, instructions, or ideas contained in the material herein.

British Library Cataloguing-in-Publication Data
A catalogue record for this book is available from the British Library

Library of Congress Cataloging-in-Publication Data
A catalog record for this book is available from the Library of Congress

ISBN: 978-0-12-817505-7

Publisher: Matthew Dean
Acquisitions Editor: Kayla Dos Santos
Editorial Project Manager: Rachel Pomery
Production Project Manager: Vignesh Tamil
Cover Designer: Miles Hitchen

Typeset by MPS Limited, Chennai, India

Contents

This page intentionally left blank

List of contributors

Nur Azimah Abd Samad Nanotechnology & Catalysis Research Centre (NANOCAT), Institute for Advanced Studies (IAS), Universiti Malaya, Kuala Lumpur, Malaysia

Faisal Ahmad Iris Worldwide, Gurugram, India

S. Ahmad JC Bose University of Science & Technology, YMCA, Faridabad, India

Waleed K. Ahmed ERU and Mechanical Engineering Department, College of Engineering, United Arab Emirates University, Al Ain, United Arab Emirates

Omid Akbarzadeh Nanotechnology & Catalysis Research Centre, Deputy Vice Chancellor (Research & Innovation) Office, University of Malaya, Kuala Lumpur, Malaysia

Y. Al-Douri University Research Center, Cihan University Sulaimaniya, Sulaimaniya, Iraq; Nanotechnology and Catalysis Research Center (NANOCAT), University of Malaya, Kuala Lumpur, Malaysia; Department of Mechatronics Engineering, Faculty of Engineering and Natural Sciences, Bahcesehir University, Istanbul, Turkey; Nanotechnology & Catalysis Research Centre, Deputy Vice Chancellor (Research & Innovation) Office, University of Malaya, Kuala Lumpur, Malaysia

Nurhaswani Alias School of Materials and Mineral Resources, Universiti Sains Malaysia, George Town, Malaysia

Riyadh A. Al-Samarai Electromechanical Engineering Department, College of Engineering, University of Samarra, Samarra, Iraq

Sarasijah Arivalakan School of Materials and Mineral Resources, Universiti Sains Malaysia, George Town, Malaysia

Said M. Al Azar Department of Research and Development, Ontario-Academy, Amman, Jordan; Department of Basic Sciences, Middle East University, Amman, Jordan

Elmi Abu Bakar School of Aerospace Engineering, Universiti Sains Malaysia, George Town, Malaysia

Alfarooq O. Basheer Department for Earth Sciences and Environment, Faculty of Science and Technology, Universiti Kebangsaan Malaysia, Bangi, Malaysia

Zaira Zaman Chowdhury Nanotechnology & Catalysis Research Centre, Deputy Vice Chancellor (Research & Innovation) Office, University of Malaya, Kuala Lumpur, Malaysia

A. Jegatha Christy Department of Physics, Jayaraj Annapackiam College for Women, Periyakulam, India

Paul Effiong Faculty of Applied Sciences, UCSI University, Kuala Lumpur, Malaysia

Said Eray Patnos Vocational School, Ağrı İbrahim Çeçen University, Ağrı, Turkey

Sharifah Fatmadiana Department of Electrical Engineering, Faculty of Engineering, University of Malaya, Kuala Lumpur, Malaysia

Chee Chin Fei Nanotechnology and Catalysis Research Centre, University of Malaya, Kuala Lumpur, Malaysia

K.L. Foo Institute of Nano Electronic Engineering (INEE), University of Malaysia Perlis, Kangar, Malaysia

S.C.B. Gopinath Institute of Nano Electronic Engineering (INEE), University of Malaysia Perlis, Kangar, Malaysia; School of Bioprocess Engineering, University of Malaysia Perlis, Arau, Malaysia

Haslinda Abdul Hamid School of Materials and Mineral Resources, Universiti Sains Malaysia, George Town, Malaysia; Faculty of Applied Sciences, Universiti Teknologi MARA, Permatang Pauh, Malaysia

Nor Aliya Hamizi Nanotechnology & Catalysis Research Centre, Deputy Vice Chancellor (Research & Innovation) Office, University of Malaya, Kuala Lumpur, Malaysia; Nanotechnology and Catalysis Research Center (NANOCAT), University of Malaya, Kuala Lumpur, Malaysia

Yanet Rodriguez Herrero Department of Agricultural, Food & Nutritional Science, University of Alberta, Edmonton, AB, Canada

Zuhailawati Hussain School of Materials and Mineral Resources, Universiti Sains Malaysia, George Town, Malaysia

Tao Jiang School of Minerals Processing & Bioengineering, Central South University, Changsha, P.R. China

Mohd Rafie Johan Nanotechnology & Catalysis Research Centre, Deputy Vice Chancellor (Research & Innovation) Office, University of Malaya, Kuala Lumpur, Malaysia; Nanotechnology & Catalysis Research Centre (NANOCAT), Institute for Advanced Studies (IAS), Universiti Malaya, Kuala Lumpur, Malaysia

Noor Fazreena Kamaruddin School of Aerospace Engineering, Universiti Sains Malaysia, George Town, Malaysia

Go Kawamura Department of Electrical and Electronic Information Engineering, Toyohashi University of Technology, Toyohashi, Japan

Yeoh Kar Keat School of Materials and Mineral Resources, Universiti Sains Malaysia, George Town, Malaysia

Beh Khi Khim Collabrative Microelectronic Design Excellence Centre (CEDEC), Universiti Sains Malaysia, George Town, Malaysia

Tan Wai Kian Center for International Education, Toyohashi University of Technology, Toyohashi, Japan

D. Kumar JC Bose University of Science & Technology, YMCA, Faridabad, India

Chin Wei Lai Nanotechnology & Catalysis Research Centre (NANOCAT), Institute for Advanced Studies (IAS), Universiti Malaya, Kuala Lumpur, Malaysia

B.Y. Lim School of Materials Engineering, University of Malaysia Perlis, Arau, Malaysia

Jicheng Liu School of Minerals Processing & Bioengineering, Central South University, Changsha, P.R. China

Zainovia Lockman School of Materials and Mineral Resources, Universiti Sains Malaysia, George Town, Malaysia

K.V. Madhuri Vignan's Foundation for Science, Technology & Research University, Vadlamudi, Guntur, India

Amjed Saleh Mahmood Electromechanical Engineering Department, College of Engineering, University of Samarra, Samarra, Iraq

Asrulnizam Abd. Manaf Collabrative Microelectronic Design Excellence Centre (CEDEC), Universiti Sains Malaysia, George Town, Malaysia

Atsunori Matsuda Center for International Education, Toyohashi University of Technology, Toyohashi, Japan

Akihiko Matsumoto Department of Applied Chemistry and Life Science, Toyohashi University of Technology, Toyohashi, Japan

Ahmad A. Mousa Department of Basic Sciences, Middle East University, Amman, Jordan

Sudtha Murthy Department of Chemistry, University of Malaya, Kuala Lumpur, Malaysia

Muhammad Nihal Naseer Department of Mechanical Engineering, National University of Sciences and Technology, Islamabad, Pakistan

Ali Abu Odeh Khawarizmi International College, Al Ain, United Arab Emirates

Khairunisak Abdul Razak School of Materials and Mineral Resources, Universiti Sains Malaysia, George Town, Malaysia

Siti Azlina Rosli School of Materials and Mineral Resources, Universiti Sains Malaysia, George Town, Malaysia

Thennarasan Sabapathy Bioelectromagnetics Research Group, School of Computer and Communication Engineering, Universiti Malaysia Perlis (UniMAP), Kampus Pauh Putra, Arau, Malaysia

Suresh Sagadevan Nanotechnology & Catalysis Research Centre, Deputy Vice Chancellor (Research & Innovation) Office, University of Malaya, Kuala Lumpur, Malaysia; Nanotechnology and Catalysis Research Centre, University of Malaya, Kuala Lumpur, Malaysia

Kazuaki Sawada Department of Electrical and Electronic Information Engineering, Toyohashi University of Technology, Toyohashi, Japan

Nurliyana Abu Hasan Sazalli School of Materials and Mineral Resources, Universiti Sains Malaysia, George Town, Malaysia

Zijian Su School of Minerals Processing & Bioengineering, Central South University, Changsha, P.R. China

Bibi Nadia Taib Collabrative Microelectronic Design Excellence Centre (CEDEC), Universiti Sains Malaysia, George Town, Malaysia

Naoki Uchiyama Department of Mechanical Engineering, Toyohashi University of Technology, Toyohashi, Japan

Aman Ullah Department of Agricultural, Food & Nutritional Science, University of Alberta, Edmonton, AB, Canada

M. Umadevi Department of Physics, Mother Teresa Women's University, Kodaikanal, India

Siti Nur Hanisah Umar School of Aerospace Engineering, Universiti Sains Malaysia, George Town, Malaysia

C.H. Voon Institute of Nano Electronic Engineering (INEE), University of Malaysia Perlis, Kangar, Malaysia

Yasmin Abdul Wahab Nanotechnology & Catalysis Research Centre, Deputy Vice Chancellor (Research & Innovation) Office, University of Malaya, Kuala Lumpur, Malaysia; Nanotechnology and Catalysis Research Center (NANOCAT), University of Malaya, Kuala Lumpur, Malaysia

Yeoh Fei Yee School of Materials and Mineral Resources, Universiti Sains Malaysia, George Town, Malaysia

Yuanbo Zhang School of Minerals Processing & Bioengineering, Central South University, Changsha, P.R. China

This page intentionally left blank

About the author

Ghenadii Korotcenkov earned his PhD in material sciences in 1976 and his doctor of science degree (doctor habilitate) in physics in 1990. He has more than 45 years of experience as a scientific researcher. For a long time, he has been the leader of the gas sensor group and manager of various national and international scientific and engineering projects carried out in the Laboratory of Micro- and Optoelectronics, Technical University of Moldova and supported from international foundations and programs such as the CRDF, the MRDA, the ICTP, the INTAS, the INCO-COPERNICUS, the COST, and the NATO. From 2007 to 2008, he was an invited scientist in Korean Institute of Energy Research, Daejeon, South Korea. Then, until the end of 2017 Dr. G. Korotcenkov was a research professor at the School of Materials Science and Engineering at Gwangju Institute of Science and Technology, Gwangju, South Korea. Currently he is the chief scientific researcher (research professor) at the Department of Physics and Engineering at the Moldova State University, Chisinau, the Republic of Moldova.

Dr. G. Korotcenkov is either the author or editor of 39 books, including the 11-volume *Chemical Sensors* series published by the Momentum Press (United States), 15-volume *Chemical Sensors* series published by Harbin Institute of Technology Press (China), 3-volume *Porous Silicon*: *From Formation to Application* published by CRC Press (United States), 2-volume *Handbook of Gas Sensor Materials* published by Springer (United States), and 3-volume *Handbook of Humidity Measurements* published by CRC Press (United States). In addition, at present, Dr. G. Korotcenkov is an editor of *Metal Oxides* series, which is being published by Elsevier. Starting from 2017, already 16 volumes have been published within the framework of that series.

Dr. G. Korotcenkov is the author and coauthor of more than 600 scientific publications, including 30 review papers, 38 book chapters, and more than 200 articles published in peer-reviewed scientific journals [h-factor = 42 (Scopus) and h-factor = 51 (Google Scholar citation)]. In the majority of publications, he is the first author. Besides, Dr. G. Korotcenkov is a holder of 17 patents. He has presented more than 250 reports at national and international conferences, including 17 invited talks. Dr. G. Korotcenkov was coorganizer of more than 10 international scientific conferences.

Research activities of Dr. G. Korotcenkov are honored by the Prize of the Academy of Sciences of Moldova (2019), an Award of the Supreme Council of Science and Advanced Technology of the Republic of Moldova (2004); Prize of the Presidents of the Ukrainian, Belarus, and Moldovan Academies of Sciences (2003); and National Youth Prize of the Republic of Moldova in the field of science and technology (1980), among others. Dr. G. Korotcenkov also received a fellowship from the International Research Exchange Board (IREX, United States, 1998), Brain Korea 21 Program (2008−12), and Brainpool Program (Korea, 2007−08 and 2015−17).

About the author

Yarub Al-Douri has gained Doctorat D'etat in Materials Science in 2000. He was appointed full professor, visiting professor, adjunct professor, consultant expert, associate professor, assistant professor, research fellow (A), scientific collaborator, and postdoc in Malaysia, Iraq, Turkey, Algeria, Yemen, Singapore, Germany, and France, respectively. He has initiated Nanotechnology Engineering MSc Program and Nano Computing Laboratory, the first in Malaysia. He has received numerous accolades, including OeAD Award, Austria 2020, Japan Society for the Promotion of Science (JSPS) Award 2019, Asian Universities Alliance (AUA) Award 2019, Iraqi Forum for Intellectuals and Academics Award 2019, Best Researcher Award at Cihan University of Sulaimaniya 2019, Best Paper at Global Conference on Energy and Sustainable Development, Coventry, United Kingdom 2015, Distinguished Researcher Award at Universiti Malaysia Perlis 2011−15, Gold Award at ITEX Kuala Lumpur 2013, and TWAS-UNESCO Associateship 2009−12 and 2012−15. He has more than quarter century experience of research, teaching; administrative and editorial board works; and organizing events, research grants, and consultations, in addition to more than 640 publications currently, including patents, books, chapters review, papers, articles, and conferences, and US$ 4.2M research grants. He has citations = 5394, h-index = 33, and i10-index = 155 for the moment. He has graduated under his supervision many of PhD and MSc students. He is Editor-in-Chief of Experimental and Theoretical NANOTECHNOLOGY, Editor-in-Chief of World Journal of Nano Science and Engineering, Associate Editor of Nano-Micro Letters (Q1), and editor and peer reviewer of different international journals, member of different international scientific associations. His research field focuses on nanomaterials, nanoelectronics, optical studies, semiconductors, renewable energy, modeling and simulation.

This page intentionally left blank

Preface to the series

The field of synthesis, study, and application of metal oxides is one of the most rapidly progressing areas of science and technology. Metal oxides are one of the most ubiquitous compound groups on earth, which have a large variety of chemical compositions, atomic structures, and crystalline shapes. In addition, metal oxides are known to possess unique functionalities that are absent or inferior in other solid materials. In particular, metal oxides represent an assorted and appealing class of materials, properties of which exhibit a full spectrum of electronic properties—from insulating to semiconducting, metallic, and superconducting. Moreover, almost all the known effects, including superconductivity, thermoelectric effects, photoelectrical effects, luminescence, and magnetism, can be observed in metal oxides. Therefore metal oxides have emerged as an important class of multifunctional materials with a rich collection of properties, which have great potential for numerous device applications. Specific properties of the metal oxides, such as the wide variety of materials with different electrophysical, optical, and chemical characteristics, their high thermal and temporal stability, and their abilities to function in harsh environments, make metal oxides very suitable materials for designing transparent electrodes, high-mobility transistors, gas sensors, actuators, acoustical transducers, photovoltaic and photonic devices, photo- and heterogeneous catalysts, solid-state coolers, high-frequency and micromechanical devices, energy harvesting and storage devices, nonvolatile memories, and many others in the electronics, energy, and health sectors. In these devices, metal oxides can be successfully used as sensing or active layers, substrates, electrodes, promoters, structure modifiers, membranes, and fibers, which can be used as active and passive components.

Among other advantages of metal oxides are the low fabrication cost and robustness in practical applications. Furthermore, the metal oxides can be prepared in various forms such as ceramics, thick and thin films. At that for thin-film deposition can be used deposition techniques that are compatible with standard microelectronic technology. The last factor is very important for large-scale production, because the microelectronic approach promotes low cost for mass production, offers the possibility of manufacturing devices on a chip, and guarantees good reproducibility. Various metal oxide nanostructures, including nanowires, nanotubes, nanofibers, core−shell structures, and hollow nanostructures, can also be synthesized. As is known, the field of metal oxide nanostructured morphologies (e.g., nanowires, nanorods, and nanotubes) has become one of the most active research areas within the nanoscience community.

The abilities to create a variety of metal oxide−based composites and to synthesize various multicomponent compounds significantly expand the range of

properties that metal oxide–based materials can have, making metal oxides by a truly versatile multifunctional material for widespread use. As is known, small changes in their chemical composition and atomic structure can be accompanied by the spectacular variation in properties and behavior of metal oxides. Even now, advances in synthesizing and characterizing techniques are revealing numerous new functions of metal oxides.

Taking into account the importance of metal oxides for progress in microelectronics, optoelectronics, photonics, energy conversion, sensor, and catalysis, a large number of various books devoted to this class of materials have been published. However, one should note that some books from this list are too general, some books are collections of various original works without any generalizations, and the other ones were published many years ago. But, during the past decade a great progress has been made on the synthesis as well as on the structural, physical, and chemical characterization and application of metal oxides in various devices, and a large number of papers have been published on metal oxides. In addition, till now many important topics related to metal oxides study and application have not been discussed. To remedy the situation in this area, we decided to generalize and systematize the results of research in this direction and to publish a series of books devoted to metal oxides.

One should note that the proposed book series "Metal Oxides" is the first one, devoted to the consideration of metal oxides only. We believe that combining books on metal oxides in a series could help readers in searching required information on the subject. In particular, we plan that the books from our series, which have a clear specialization by its content, will provide interdisciplinary discussion for various oxide materials with a wide range of topics, from material synthesis and deposition to characterizations, processing and then to device fabrications and applications. This book series is prepared by a team of highly qualified experts, which guarantees its high quality.

I hope that our books will be useful and comfortable in use. I would also like to hope that readers will consider this "Metal Oxides" book series like an encyclopedia of metal oxides that enables one to understand the present status of metal oxides, to estimate the role of multifunctional metal oxides in the design of advanced devices, and then based on observed knowledge to formulate new goals for the further research.

The intended audience of the present book series is scientists and researchers, working or planning to work in the field of materials related to metal oxides, that is, those whose activities are related to electronics, optoelectronics, energy, catalysis, sensors, electrical engineering, ceramics, biomedical designs, etc. I believe that this "Metal Oxides" book series will also be interesting for practicing engineers or project managers in industries and national laboratories, who would like to design metal oxide–based devices but do not know how to do it, and how to select optimal metal oxide for specific applications. With many references to the vast resource of recently published literature on the subject, this book series will be serving as a significant and insightful source of valuable information, providing scientists and engineers with new insights for understanding and improving existing metal

oxide−based devices and for designing new metal oxide−based materials with new and unexpected properties

I believe that this "Metal Oxides" book series would be very helpful for university students, postdocs, and professors. The structure of these books offers a basis for courses in the field of materials science, chemical engineering, electronics, electrical engineering, optoelectronics, energy technologies, environmental control, and many others. Graduate students could also find the book series to be very useful in their research and understanding features of metal oxides' synthesis, study, and application of this multifunctional material in various devices. We are sure that all of them will find information useful for their activity.

Finally, I thank all the contributing authors and book editors who have been involved in the creation of these books. I am thankful to them because they have agreed to participate in this project and put their efforts in the preparation of these books. Without their participation, this project would have not been successful. I also express my gratitude to Elsevier for giving us the opportunity to publish this series. I especially thank the whole team of editorial office at Elsevier for showing their patience during the development of this project and for encouraging us during the various stages of preparation.

Ghenadii Korotcenkov

This page intentionally left blank

Preface

The synthesis, analysis, characterization, and application of metal oxide powder technologies are one of the rapidly progressing areas of science and technology. Metal oxides are one of the most ubiquitous compounds on the globe and have a variety of chemical compositions, atomic structures, and crystalline shapes. In addition, metal oxides are known to possess unique functionalities that are absent or less in other solid materials. Metal oxides give an assorted and appealing class of materials, where their properties exhibit a full spectrum of electronic, structural, elastic, optical, thermal, and other properties from insulating to semiconducting, metallic, and superconducting. Moreover, it could notice all phenomena of superconductivity, thermoelectric effects, photoelectrical effects, luminescence, and magnetism. Therefore metal oxides have an eminent importance of multifunctional materials with a rich collection of properties that have great potential in numerous device applications.

Specific properties—electrophysical, optical, chemical characteristics, high thermal and temporal stability, and abilities to function in harsh environments—make metal oxides very suitable materials for designing transparent electrodes, high-mobility transistors, gas sensors, actuators, acoustical transducers, photovoltaic and photonic devices, photo- and heterogeneous catalysts, solid-state coolers, high-frequency and micromechanical devices, energy harvesting and storage devices, nonvolatile memories, and many others in electronics, energy, and health sectors. For applications, metal oxides can be successfully used as sensing or active layers, substrates, electrodes, promoters, structure modifiers, membranes, and fibers, in which they can be used as active and passive compounds.

Among advantages, metal oxides are cost-effective and robust in practical applications. Furthermore, they can be used in various forms such as ceramics and thin films. For thin-film deposition, those techniques can be used which are compatible with standard microelectronic technology that is very important for large-scale production as the microelectronic approach promotes cost-effectiveness for mass production, offers the possibility of manufacturing devices on a chip, and guarantees good reproducibility. Different metal oxide nanostructures of nanowires, nanotubes, nanofibers, core−shell structures, and hollow nanostructures can be formed. It is known that the field of metal oxide nanostructures (e.g., nanowires, nanorods, and nanotubes) has become one of the most active research areas within nanoscience community.

The abilities to create different metal oxide−based composites and to synthesize various multicomponent compounds significantly expand the range of properties that metal oxide−based materials can truly have as versatile multifunctional

materials for widespread uses. A small change in their chemical composition and atomic structure can be accompanied by spectacular variations of properties and behavior of metal oxides. Even now, advances in synthesizing and characterizing techniques are revealing numerous new functions of metal oxides.

Taking into account the importance of metal oxides for progress in microelectronics, optoelectronics, photonics, energy conversion, sensors, and catalysis, many books devoted to this class of materials have been released. However, during the past decade, great progress has been achieved on the synthesis, structural, elastic, electronic, optical, thermal, and other properties as well as metal oxides' application in many devices, and a large number of published papers have been disseminated on metal oxides. To remedy this situation, it has been decided to generalize and systematize the results of research in this direction and to publish this book that is devoted to metal oxides.

One should notice that the proposed book "Metal Oxide Powder Technologies: Fundamentals, Processing Methods and Applications" is the first one devoted to the consideration of metal oxide powder technologies only. It is believed that this book could help readers and specialists in searching required information on the mentioned subject. It is planned that this book has a clear specialization by its content and will provide interdisciplinary discussion for various oxide materials with a wide range of topics, from material synthesis and deposition to characterizations and processing and then to device fabrications and applications. This book is edited by a team of highly qualified experts, which guarantee its high quality.

I hope this book will be useful and will provide ease. I would hope that readers and specialists will consider it as an encyclopedia of metal oxides that enables one to understand the present status of metal oxide powder technologies, estimate the role of multifunctional metal oxides in the design of advanced devices, and, based on observed knowledge, formulate new goals for further research. The intended audience of the present book is scientists, academics, and researchers in the field of materials, semiconductors, ceramics, and metal oxides, who have activities related to electronics, optoelectronics, energy, catalysis, sensors, electrical engineering, ceramics, biomedical designs, and others.

I believe that the book "Metal Oxide Powder Technologies: Fundamentals, Processing Methods and Applications" will be interesting for practicing engineers or project managers in industries and laboratories, who would like to design metal oxide−based devices but do not know how to do it and how to select optimal metal oxides for specific applications. With many references to the vast resource of recently published literature on the subject, this book will serve as a significant and insightful source of valuable information, provide scientists and engineers with new insights for understanding, and improve existing metal oxide−based devices for designing new metal oxide-based materials with new and unexpected properties. I believe that it would be very helpful for university students, researchers, and academics. The structure of these books offers a basis for courses in the field of materials science, semiconductors, ceramics, chemical engineering, electronics, electrical engineering, optoelectronics, energy technologies, environmental control, and others. It will definitely help one to find useful information.

The first chapter is devoted to the preparation of colloidal GaO nanoparticles in ethanol by pulsed laser ablation method. Optical and structural analyses were performed on samples generated under different laser fluences. It is shown that laser fluence has a significant effect on nanoparticles' size properties. Also, it is proven that the ablation process affects the nanoparticles' size and size distribution. The results show that higher laser fluence produces larger mean sizes of nanoparticles with a broader size distribution, followed by making metal oxides more visible and widely using an active catalyst or supporting material. Metal oxides made from an inorganic material are driven by the surface chemistry and quantum confining effect, along with a reduction in size and nano-sizing. The surface chemistry such as nucleation and crystallization of metal oxide is discussed in the determination of metal oxide sizes. In addition, changes to metal oxide will improve the transportation of charge carriers and lower the rate of recombination as elaborated in Chapter 2, Chemical Studies of Metal Oxide Powders. Chapter 3, Synthesis and Preparation of Metal Oxide Powders, has studied metal oxide in the form of powders owing to their unique and novel properties. A thorough description of current advances on the synthesis and preparation of metal oxide powders is available in the chapter. Several important methods were described. Chapter 4, Sintering Behaviors of Fe_3O_4 and CaO Powders Roasted Under $CO-CO_2-N_2$ Atmosphere, has considered calcium ferrite phases as a wonderful bonding phase in iron ore sinters. The local sintering zone where the coke breeze is combusted is not oxidizing atmosphere, but weakly reducing atmosphere, which inevitably affects the formation of calcium ferrites. Followed by introducing tribological performances of surface modification, including polymerization, nano-coating, and microencapsulation, Chapter 5, Surface Modification, Including Polymerization, Nanocoating, and Microencapsulation, starts with the classification of surface treatment, including polymerization and rapid development of nanotechnology and nanomaterials, that leads to the need of modifying the surface of nanoparticles for a number of applications to explain the surface treatments for improving the mechanical properties of tribolayers and their long-term stability under boundary lubricated conditions.

Chapter 6, Application of Metal Oxides in Composites, meets the designed and manufactured composite materials for higher performance that are required by today's advanced technology. They combine characteristic properties of ceramics, metals, and polymers in a single material, the properties of which are superior to those of each monolithic material. On the other hand, Chapter 7, Metal Oxide Powder Technology in Biomedicine, describes numerous combinations of hybrid nanomaterials of inorganic, organic, and biomolecular origins that have been synthesized with programmable physico−chemico−biological properties via their surface modifications and chemical conjugation. These hybrid nanomaterials undergo through fast emerging applications in various fields, including biomedicines. Given the current status of the developments in this context, a more comprehensive growth is anticipated in deploying the aforementioned programmable features, especially, involving stoichiometric changes during their syntheses guided by simultaneously ongoing analytical/simulation studies. From a larger family of such nanomaterials, the transition metal oxide−based complexes, including the

perovskites, are expected to offer unique possibilities of compound formations involving their d-electron interactions that are yet to be explored in depth. Also, the functional and advanced materials and their production techniques have received more attention in materials science and engineering over the past several decades as presented in Chapter 8, Mechanical and Physical Methods for the Metal Oxide Powder Production. The metal oxide powders and nanopowders and their mixtures require further intensive research. They have many applications and usages in various industrial fields. An overview of the mechanical and physical techniques for the production of metal oxide powders with a focus on processes and devices is provided. On the other hand, Chapter 9, Chemical Processes of Metal Oxide Powders, has attracted metal oxide macro-, micro-, and nanostructures studies due to its great potential in magnetic, electronic, and optical applications. Metal oxide powders are typically produced in laboratories and planned using several methods such as catalysis, physical, algae extraction, and chemical. It is reviewed on existing chemical methods in the production of metal oxide powder. Moreover, elaborated studies of metal oxide powders are put in Chapter 10, Thermal Protection Coatings of Metal Oxide Powders, for their useful industry and societal applications. Continuous development in finding out newer materials and composites is essential to meet the challenges that are posed and necessary thermal protection coating on various metal oxide powders by various physical and chemical deposition techniques that are discussed in this chapter.

Chapter 11, Metal Oxide Nanoparticles in Biomedical Applications, has archived the tremendous advancement in the past technologies and continued to become an important method that creates useful materials with designed features. Application of nanotechnology in the synthesis of metal oxides has provided a new set of materials in nano-sizes with unique features. These metal oxide nanoparticles exhibit distinct physical and chemical properties due to their smaller sizes than their bulk-sized counterparts. The unique physicochemical properties of metal oxide nanoparticles make it possible to create a wide variety of new biomedical applications. Followed by that, Chapter 12, Metal Oxide Powder Technology in Energy Technologies, will be a good guide for scientists, engineers, and academic researchers in this field to present a broad range of energy uses of metal oxide powder technology. The chapter covers the materials, manufactured by metal oxide powder technology, and their uses in different kinds of energy applications such as fuel cells, solar cells, super capacitor, and many more. On the other hand, the investigation of possibility of developing new materials and even new methods in building electronics devices is described by Chapter 13, Metal Oxides in Electronics. Metal oxides are deemed a major element in the development and building of nanoelectronics due to their extraordinary electrical, physical, and chemical properties that are different from metals, semiconductors, and insulators. The rapid evolutions in synthesizing metal oxides and using them in electronic devices open new horizons in improving the performance and functionality of these devices. But metal oxides are used in important industrial processes as catalysts, either as an active phase or as supports for highly dispersed metals, described in Chapter 14, Metal Oxide Powder Technology in Catalysis. It has described useful properties for participating in a

wide range of reactions such as oxidation, hydrogenation, polymerization, and many more. They are available from nature or obtained by synthetic methods. It has provided a description of molecular structures of metal oxides that are used as catalysts. Moreover, Chapter 15, Metal Oxide for Heavy Metal Detection and Removal, has introduced excessive quantities to different environmental matrices, imposing severe threats to the ecosystem. It is focused on the occurrence of heavy metals in Malaysia, reviewing their potential sources, existence in water, sediment, and aquatic life. However, despite the existence of contents of heavy metals in water, sediment, and aquatic life, they remain within the permissible limit. Heavy metals are known to be nondegradable and hence can lead to bioaccumulation in humans or animals. Therefore treating wastewater is essential to ensure that no heavy-metal ions are released into the environment. Next, Chapter 16, Metal Oxide Powder Technology in Membranes, has proposed powder of metal oxide nanoparticles for membrane applications such as microfiltration devices. The produced powder was analyzed and characterized. A study on the factors influencing the antimicrobial activities of metal oxide nanoparticles was taken up. Further studies have to be done on the small-sized different-shaped nanoparticles that could exhibit excellent antimicrobial activities than the present study. 3D Printing technology is developed rapidly, which plays an important role in many areas such as industrial, medical aerospace as well as automotive, as discussed in Chapter 17, 3D Printing of Ceramic Powder Technology 3D Printing of Ceramic Powder Technology. There was a huge demand for the 3D printing technology especially for the ceramic products that opened horizons for a new era of application and industrial levels. A comprehensive review for the applications of 3D printing in ceramics as well as technology associated was covered. Chapter 18, Metal Oxide Powder Technology in Dielectric Materials, has discussed the fundamentals of dielectric materials and nanostructured metal oxide powder. These nanostructured metal oxides are very vital for novel devices after a gracious controlled care of composition, structure, and surface properties. These metal oxides are the treasure for their applications in versatile scopes of industries such as water purification and medical applications. As metal oxide powder exhibits abovementioned special properties, its consideration can be advantageous especially to cosmetics industry and personal care products. Along with described benefits, these oxides may also have hazardous effects on people, amphibian, and environment.

Finally, I thank all the contributing authors. I am thankful to them because they have agreed to participate in this book to prepare it. Without their efforts, this book would have not been completed. I also express my gratitude to Elsevier for giving us the opportunity to publish this series. I especially thank the Elsevier's team for keeping their patience during the whole process of production and for encouraging us during the various stages of preparation.

Yarub Al-Douri
University of Malaya, Kuala Lumpur, Malaysia,
Cihan University Sulaimaniya, Sulaimaniy, Iraq,
Bahcesehir University, Istanbul, Turkey

This page intentionally left blank

Physical studies of metal oxide powders

1

Y. Al-Douri[1,2,3], Yasmin Abdul Wahab[1] and Nor Aliya Hamizi[1]
[1]Nanotechnology and Catalysis Research Center (NANOCAT), University of Malaya, Kuala Lumpur, Malaysia, [2]University Research Center, Cihan University of Sulaymaniyah, Sulaymaniyah, Iraq, [3]Department of Mechatronics Engineering, Faculty of Engineering and Natural Sciences, Bahcesehir University, Istanbul, Turkey

1.1 Introduction

Nanoparticles are highly interesting for biological, medical, energy conversion, storage, and electronic applications [1–4]. Nanoparticles have a large surface energy and surface-to-volume ratio. The metal nanoparticles have distinguished electrical, magnetic, optical, and chemical properties with marvelous new applications [5–8]. The last decade has seen the development of nanoparticles with controlled sizes, shapes, and phases. Different techniques, such as thermal evaporation, milling, chemical method, condensation, and sputtering [9–13], have also been reported. However, these techniques are either expensive or may produce toxic, impure, harmful, and/or low-quality nanoparticles which tend to agglomerate towards bigger size. There has been a lot of attention and interest paid to synthesizing nanoparticles by pulsed laser ablation (PLA) [14–16]. PLA has offered promising nanoparticles for nanofertilizers, surface-enhanced Raman scattering detection and biotechnology applications [17–20]. The main feature of PLA is its capability to produce stable colloidal nanoparticles. It is safe, clean, and effective for metals nanoparticles synthesis with controllable size [21–25]. For instance, the formation of both gold and nickel nanoparticles under ablation of corresponding solids by pulsed Nd:YAG laser has been reported [26–32]. The influence of liquid on the chemical composition of generated nanoparticles has also been reported [33], as well as CdS and ZnSe quantum dots formation [34]. It is demonstrated that mean size and size distribution of colloidal nanoparticles produced by PLA depend significantly on laser fluence, wavelength and pulse duration characteristics, liquid environment, and target material [35–39]. Laser radiation of a moderate fluence is shown to be capable of heating a single nanoparticle to elevated temperatures (close to the melting point of 1000°C for Au), thus explaining the high chemical reaction rate with the surrounding liquid.

It is expected by immersing nanoparticles into a liquid, the nanoparticles formation by laser ablation will be accompanied by their splitting during exposure. The resulting distribution of nanoparticles is the result of both processes, namely, ablation and further splitting. This effect seems to be negligible in experiments on laser

Metal Oxide Powder Technologies. DOI: https://doi.org/10.1016/B978-0-12-817505-7.00001-4

ablation in vacuum or in diluted gases, whereas in liquid-phase ablation with a high density of nanophase material it plays a significant role.

In this chapter, we investigate the synthesis of colloidal nanoparticles by PLA of GaO target immersed in ethanol, which to our knowledge has not been previously reported in the literature. Optical and structural analyses were performed on samples generated under different laser fluence by using tunneling electron microscopy (TEM), ultraviolet−visible (UV−Vis) absorption, and X-ray diffraction (XRD) techniques. The effects of laser fluence and liquid environment on colloidal nanoparticles size were studied in innovative research.

1.2 Metal oxides

Metals available on Earth are generally not very stable, and they form metal oxides mostly with unique functionalities and higher stability than pure metals. The metal and oxygen ions play a key role in displaying various interesting properties for industrial purposes and also form the basis to develop various theories of condensed matter physics. Metal oxides are generally in solid (powder) form with metal as the cation and oxygen as the anion. These oxides, available as abundant compounds with a large variety of properties, such as high stability, various crystal structures, phase transitions, composition, physical, optical, electrical, and chemical properties with high strength, are suitable for energy storage devices, gas sensors, solid-state microbatteries, catalysts, transistors, electronic components, transducers, optoelectronic devices, membrane reactors, and bioapplications. In general, the metal oxides are brittle in nature at room temperature [40]. However, the electrical properties of these oxides cover the entire range from insulators to superconductors through semiconductors and conductors making them economically competitive. Even then, their use has been largely confined to applications as insulating materials. The reason for this might be their brittleness, their crystalline transformation, and the difficulty in maintaining the desired oxygen levels in the compound. These crystalline transformations and phase changes may be seen as disadvantages, but at the same time they are of great advantage because the unexpected variety of properties that can be drawn from the phase transformations make them useful in electrochromic, photochromic, thermochromic devices, and microbatteries, etc. In addition to this, at certain pressures or temperatures the metal insulator transition takes place, which has drawn the attention of researchers and became a widespread research theme even before the high-temperature superconductivity sprang into center stage. Due to the availability of localized electrons, these oxides are frequently utilized as ferromagnetic and ferroelectric materials and also exhibit photo- and thermoelectric effects.

Based on the physical properties metal oxides can be classified into two categories, namely, nontransition metal oxides and transition metal oxides [41,42]. The filled valence band and empty conduction band are separated by a large bandgap in nontransition metal oxides. Hence in ordinary conditions they will act as

diamagnetic insulators. General examples of nontransition metal oxides are magnesium oxide (MgO) and silicon dioxide (SiO_2). At high temperatures, the intrinsic activation energy is higher than the energy required for the creation and migration of defects, hence ionic conduction is more predominant than electronic conduction.

In the case of transition metal oxides, they exhibit unusual electronic structures, based on the transition metal and how it bonds with oxygen [43,44]. They are an enormous and interesting group of solids exhibiting a wide variety of structural, optical, electrical, and magnetic properties. They in turn can be broadly divided into two classes:

1. Those in which the metal ion has a *d*0 electronic configuration
   Examples are vanadium pentoxide (V_2O_5), molybdenum trioxide (MoO_3), tungsten trioxide (WO_3), chromium trioxide (CrO_3), zirconium dioxide (ZrO_2), niobium oxide (Nb_2O_5), and tantalum oxide (Ta_2O_5).
2. Those in which the *d* shell is partially filled

Examples are molybdenum dioxide (MoO_2), tungsten dioxide (WO_2), osmium dioxide (OsO_2), titanium monoxide (TiO), niobium monoxide (NbO), chromium dioxide (CrO_2), rhenium dioxide (ReO_2), ruthenium oxide (RuO_2), rhodium oxide (RhO_2), and rhenium trioxide (ReO_3).

Metal oxides with *d*0 cations at octahedral sites exhibit spontaneous ferroelectric and antiferroelectric distortions. Many of them lose oxygen at high temperatures becoming nonstoichiometric. Oxygen loss or insertion of electropositive metal atoms into these oxides place electrons in the conduction band. The nature of electronic conduction in such materials depends on the strength of electron−phonon coupling and the width of the conduction band derived from metal *d* states.

Transition metal oxides containing partially filled d states show unusual interesting properties and may behave as metallic or semiconducting [45]. In recent years, the field of metal oxides and powders, as well as their composites, both in bulk and thin-film form, has become a subject of intensive study by materials scientists because of their novel characteristics and applications. This area gives a wide scope to researchers to explore challenging problems in theoretical and experimental investigations [46]. In addition, one can also have challenges in protecting these oxides from the environment, that is, protection from heat, chemical reaction with other environmental gases, so on [47,48].

The thin layer of material deposited on the surface of the metal oxide or any other material serves to protect it from the environment or any other exposure. In other words, these coatings protect the materials and devices as a shield from degradation of structures by creating a physical barrier in between the material and environment. Metals, nonmetals, and ceramics can be used as protective coatings. In addition to the protection, sometimes these functional coatings are used to change the surface properties of metal oxides, such as morphology, structure, etc. Various methods have been employed to deposit a layer which will be necessary to avoid corrosion etc. Nowadays the study of synthesis and characterization of various metal oxides has assumed more importance owing to the fact that they are increasingly being used in various industrial and scientific fields for device applications of

the emerging technologies. Moreover, these oxides can be used in the above applications either in bulk or thin-film form which increases the surface area to volume ratio. Metal oxide thin films or nanoforms of metal oxide powders are chosen to be used in various applications due to their significant enhancement in chemical, physical, and electrical properties compared with the bulk materials.

The thin-film form of metal oxide, which can be synthesized by various chemical and physical deposition techniques, is important for the enhancement of their properties in the nanoscale region with widespread use in the fabrication and development of miniaturized devices, and hence research in the fields of nanoscience and nanotechnology have taken the center stage in materials science. The ability to develop various versatile materials that exhibit various interesting properties with a small change in composition or structure resulted in their extensive use in microoptoelectronic devices, sensors, catalysis, energy storage devices, photonics, drug delivery, etc. The metal oxide powders or thin films are very sensitive to the environment, especially temperature. One of the methods to protect the films is the use of thermal barrier coatings. Due to these thermal barrier coatings, one can protect the components from destruction even at high temperatures and these coatings can act as insulators as well as oxidation- resistant layers. Hence the efficiency of the systems and devices can be improved. In addition to this, the thermal barrier also needs to be resistant to corrosion when it is exposed to higher temperatures. For example, AlTiN coating is used to increase the surface hardness, oxidation resistance, etc. A few materials have the capacity of thermal absorption which is needed for nuclear fusion applications and a few more materials are used for thermal conduction which transfers heat to the surfaces evenly. Depending on the purpose of utilization in the devices one can select the material and deposition method to coat on the surface of the metal oxide thin film. The thermal barrier coating materials, especially for protection applications, need to have a porous structure which changes with the thermal expansion during the heating and cooling process. In a few cases, the phase stability is also necessary or else cracks will damage the device.

Considering all these aspects, one can list a few effective qualities of thermal protective coatings for long service and sustainable over a large number of cycles as follows:

1. The material should be chemically inert and thermally stable
2. No phase changes in between the operating temperature and room temperature
3. Metallic surface and the material should have same thermal expansion nature
4. Protective material should be strongly adherent to the substrate
5. Should have oxidation- and corrosion-resistant properties
6. Should possess optimum range of hardness

The oxidation-resistant metallic layer is serving as a bond coat which is directly deposited on the metal substrate with a thickness of about 100 μm. Thermally grown oxide is the next layer and the ceramic thermal barrier is coated on top. This layer produces a high thermal gradient and retains the bottom layers at lower temperatures. The degradations that may occur in the coatings are due to the voids and porosity of grown oxides, open interfaces, failure in bond coats, etc.

The most widely used materials for protection coatings are mullite (compound of alumina and silica), alumina, zirconates of rare earth metals ($BaO \cdot ZrO_2$, $SrO \cdot ZrO_2$, etc.), yttria-stabilized zirconia, glass ceramics, and metal glass composites (mixture of metal and glass). Thermal protection coatings are more useful in automotive applications, gas turbines, diesel engines, and to enhance the bond strength. This chapter attempts to give an idea about the importance of metal oxides and the thermal protection coatings of the materials. It also aims to be helpful to the reader to estimate the role of multifunctional metal oxides in advanced technology and how one can protect these oxide powders by using various coatings deposited by several techniques. In this context, it is very important to know about the surface property of the layers of metal oxide powders and how to control the properties with a discussion of protection coating technologies, especially with regards to the environment and in particular temperature. The coatings with high thermal stability, which protect the metal oxide powders, either in bulk, thin-film, thick-film, or nanomaterial form, from temperature variance and help them to maintain their properties are known as thermal protection coatings or thermal barrier coatings. These coatings, in general with advanced materials, are grown on the surfaces of the metallic and oxide powders with an appropriate thickness of 200 μm to 1 mm to insulate the components from high amounts of heat. The materials used in thermal coatings should be stable and sustain a considerable amount of heat. The protection coating thus may allow higher operating temperatures without altering the composition, structure, oxidation states, fatigue strength, and thermal stability of the component. As the world has more demand for high-efficiency engines at higher temperatures, there is a significant need to develop new thermal protection coatings with better lifetime, response, durability, cyclability, and less thickness. As the abovesaid qualities are totally dependent on the physical, chemical, and electrical properties, which in turn depend on the deposition technique to develop a thin film as a surface coating to protect the oxide layer, it is important to discuss the various growth processes.

1.3 Metal oxides powder in dielectric materials

Zinc oxide (ZnO) powder is a widely used compound in many household, electrical, and industrial products. Though naturally occurring in the mineral zincite, most production originates from anthropogenic sources. Nanosized ZnO (nano-ZnO) can be produced by the grinding of bulk ZnO, where it takes on a wurtzite crystalline structure that can then be utilized for a number of applications. Nano-ZnO power can be prepared by various methods. Some of them are as follows:

- Polyol medium hydrolysis method
- Gas condensation method
- Polymeric precursor method
- Pyrolysis (aerosol spray) method
- Hydrothermal method

- Sol−gel method
- Solid-state microwave decomposition method

All the above mentioned methods are conventional methods as they require a high rate of energy consumption that make them uneconomical. The most sustainable and economical method for ZnO powder synthesis is a precipitation method [49]. Nano-ZnO serves as an n-type semiconductor due to its wide bandwidth (∼3.37 eV) [50]. Based on electric, thermal, and chemical stability, piezoelectric and superconductive properties, nano-ZnO has many applications in devices, such as piezoelectric cells [51], cholesterol and glucose biosensing [52], solar cells [53], and photovoltaic transducers [54]. When in a powder form, nano-ZnO can be mixed into foods, paints, pigments, adhesives [55], medical disinfection, and environmental remediation [56]. Due to UV−Vis luminescence and UV blocking properties, nano-ZnO is used in personal care products, such as sunscreens and cosmetics [57]. The production of nano-ZnO and other metal oxides has been found to be popular for cosmetic applications with an estimated 1000 t produced per year during 2005−10 [58].

1.4 Physical properties

Gallium oxide can form several different polymorphs, designated as α-, β-, γ-, δ-, and ε- [59]. Polymorphs are different not only in their crystal space group but also in the coordination number of Ga ions. All of these phases of gallium oxide can be prepared under specific conditions [59,60]. The first polymorph, α-Ga_2O_3 is a rhombohedral, space group $R\bar{3}c$ analogous to corundum (α-Al_2O_3). This polymorph can be synthesized by heating GaO(OH) in air between 450°C and 550°C [59]. The second form, β-Ga_2O_3 has a monoclinic structure and belongs to space group C2/m. This form of Ga_2O_3 can be obtained by baking any other polymorph of Ga_2O_3 in air at a sufficiently high temperature. When it comes to other polymorphs, little data is available because structural characterization has been hampered by their typically poorly crystalline nature. It is commonly agreed that the third form, γ-Ga_2O_3 has a defective cubic spinel-type structure ($MgAl_2O_4$-type) with $Fd\bar{3}m$ space group. The fourth and fifth polymorphs, called δ-Ga_2O_3 and ε-Ga_2O_3 were first synthesized and described by Roy et al. [59]. The authors proposed that δ-Ga_2O_3 form has a C-type rare-earth structure analogous to Mn_2O_3 and In_2O_3. As for the ε-Ga_2O_3 polymorph, Roy et al. were able to measure the powder's XRD pattern which was distinct from all other known polymorphs, but could not determine the structure of the ε-polymorph. A more recent publication by Playford et al. [61] shows that the original assumption was not correct as δ-Ga_2O_3 is merely a nanocrystalline form of ε-Ga_2O_3 and not a distinct polymorph. The structure of ε-Ga_2O_3 was simulated using density functional theory, and shown to be in the space group $Pna2_1$, the same as for κ-Al_2O_4 and ε-Fe_2O_3 by Yoshioka et al. [62]. In contrast, the experimental results presented by Playford et al. do not support that assumption as ε-Ga_2O_3 was found to belong to the $P6_3mc$ group of symmetry. The structure is

similar to that of a disordered hexagonal ε-Fe_2O_3 [63]. Playford et al. also observed the formation of a transient polymorph κ-Ga_2O_3 which is an analogue of orthorhombic κ-Al_2O_3.

1.5 Properties of GaO

The β-form is the most common and well-studied polymorph of gallium oxide. β-Ga_2O_3 is the only stable polymorph through the whole temperature range up to the melting point, whilst all other polymorphs are metastable and transform into the β-Ga_2O_3 at temperatures above 750°C−900°C [64]. The thermal stability of β-Ga_2O_3 makes it possible to produce bulk single crystals and epitaxial films via high-temperature processes such as crystallization from a melt or vapor phase epitaxy. Among the other polymorphs of gallium oxide, β-Ga_2O_3 has attracted more attention from researchers because of its availability and outstanding properties. Although β-Ga_2O_3 is well-characterized compared to other Ga_2O_3 polymorphs, there are still some discrepancies in the published data on material properties.

1.6 Characterization and analysis

The colloidal nanoparticles have significant features depending on laser fluence, as shown in our results. These colloidal nanoparticles prepared by PLA depend on the liquid medium. To produce oxide-based nanoparticles [65], the ablation method in ethanol has been used. The characterizations of GaO nanoparticles produced by the PLA technique in ethanol were performed. The synthesized nanoparticles from GaO target were irradiated by a laser beam with 360 pulses for 1 minute, as shown in Fig. 1.1. The produced nanoparticles were almost spherical or quasispherical at laser peak fluence of 160, 95, 60, and 30 J/cm^2. The nature of interaction in ethanol results in nanoparticles with different sizes.

Fig. 1.1 shows the histograms of the GaO nanoparticles obtained in an ethanol environment. It is noticed that nanoparticles of size 2 nm are produced during laser ablation. Actually, GaO in ethanol results in a narrow size distribution and it is also observed that colloidal nanoparticles size varies up to a few tens of nanometers. The formation of nanoparticles has different mechanisms, which leads to different mean size and size distribution of GaO nanoparticles in an ethanol environment.

These differences are attributed to various optical features, such as optical absorption, and other physical properties listed in Table 1.1, that is, thermal conductivity, electron−phonon coupling constant, melting and boiling points, and surface energy, that influence the nanoparticles evolution [39,67]. It is well-known that the formation of smaller nanoparticles' sizes is attributed to the interaction of GaO in ethanol that affects the material's bonds. The formation of larger nanoparticles is attributed to the agglomeration tendency of the nanoparticles, which is more prominent in the ablation process. The colloidal GaO nanoparticles produced in ethanol

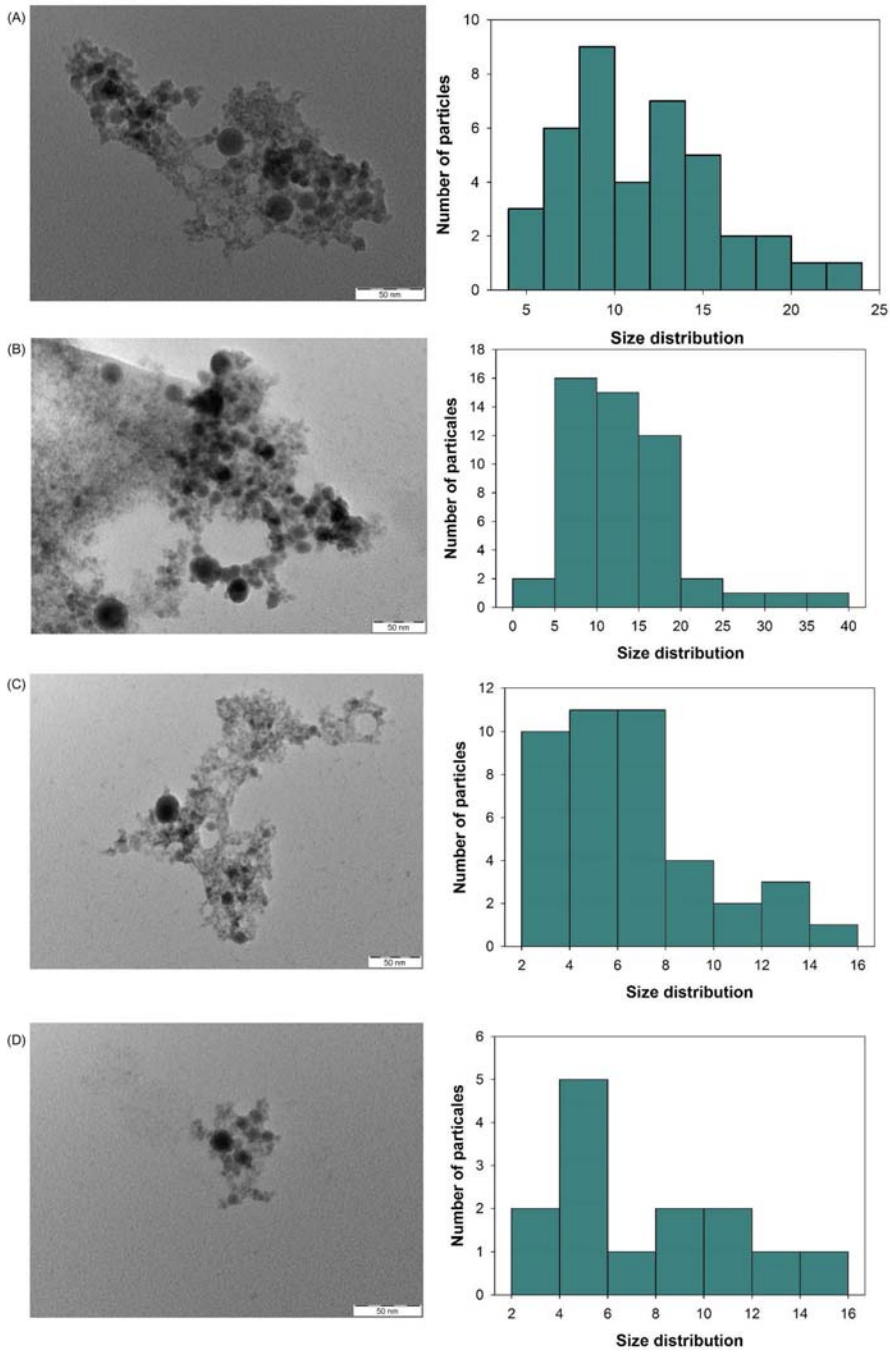

Figure 1.1 TEM images corresponding to histograms: (A) 160 J/cm^2; (B) 95 J/cm^2; (C) 60 J/cm^2; and (D) 30 J/cm^2 [66]. *TEM*, Tunneling electron microscopy.

Table 1.1 Some physical properties of GaO [39].

Physical properties	Target GaO
Lattice constant (Å)	$a = 5.120$, $c = 8.792$
Thermal conductivity (W/m K)	10.9
Specific heat (J/g/K)	0.56
Dielectric constant	9.9−10.2
Refractive index	1.9523
Density at 300K (g/cm^3)	5.88
Molar mass (g/mol)	187.44
Bulk modulus (GPa)	199[a]

[a]Ref. [65].

Table 1.2 Structural properties of GaO colloidal nanoparticles in ethanol for different laser fluences [66].

Laser fluence (J/cm^2)	2θ	Average particle size (nm)	Miller indices ($h\ k\ l$)	Interplanar distance (d) (Å)	Lattice constants (a and c) (Å)
160	43.96	22.5	2 0 2	2.057	$a = 5.82$ $c = 7.11$
95	44.00	15.4	2 0 2	2.0562	$a = 5.815$ $c = 7.98$
60	43.91	10.2	2 0 2	2.0617	$a = 5.83$ $c = 7.12$
30	44.00	10	2 0 2	2.0561	$a = 5.81$ $c = 7.1$

have a narrow distribution and a small size, as revealed by TEM images. Furthermore, the nanoparticles mean size increases as laser fluence increases. Colloidal nanoparticles sizes for different laser fluences are given in Table 1.2. The absorption spectra of colloidal nanoparticles are measured within a range of 200−900 nm, as shown in Fig. 1.2. It is evident that ns laser radiation at fluences of tens of J/cm^2 can be effectively coupled to an ensemble of metallic nanoparticles. The coupling efficiency of radiation to nanoparticles depends on the proximity of the laser wavelength to the plasmon frequency of charge carriers. The energy is transferred from electrons to lattice within 3−5 ps. This coupling results in modification of their absorption spectrum and has a direct effect on the control of both size and shape of nanoparticles [68,69].

The intensity of absorbed light varies with wavelength, as shown in Fig. 1.2, due to surface plasmon resonance that depends on nanoparticles concentration and dimensions [70]. The production of colloidal nanoparticles depends on both the

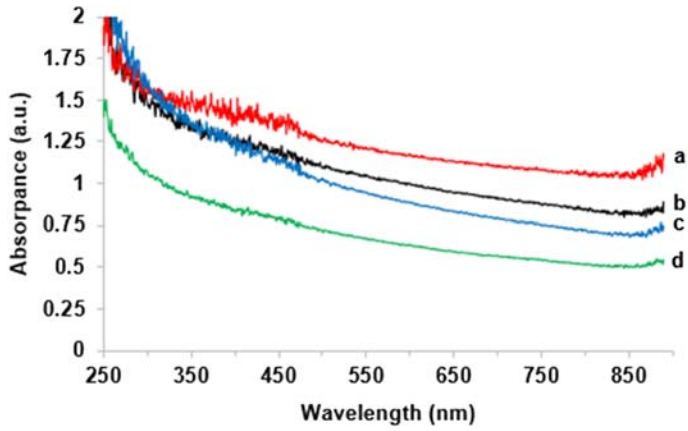

Figure 1.2 UV−Vis absorption for (a) 160 J/cm^2; (b) 95 J/cm^2; (c) 60 J/cm^2; and (d) 30 J/cm^2 [66]. *UV−Vis*, Ultraviolet−visible.

target material and liquid environment. The ablation process clearly depends on the optical absorption. As laser fluence increases, the absorption increases due to increasing production of colloidal nanoparticles. When the laser intensity increases, the optical breakdown occurs which reduces the laser energy absorption at the surface of target. The threshold intensity depends on the liquid environment. It is observed that the liquid medium is initially pure, while the ablation process makes it impure. For a GaO target in ethanol, the optical breakdown occurs at laser fluence of 160 J/cm^2.

The GaO colloidal nanoparticles produced by PLA have been investigated for different laser fluences by XRD, as shown in Fig. 1.3. XRD patterns have provided information about the structural properties of colloidal nanoparticles. The GaO colloidal nanoparticles have seven major diffraction peaks depending on laser fluence. Table 1.3 summarizes the major diffraction peaks which appear at their respective values of 2θ, along with attributed crystal diffraction planes for laser fluence of 30, 60, 95, and 160 J/cm^2. All mentioned peaks are exactly matched with the hexagonal structure of GaO colloidal nanoparticles.

We noticed that the highest peak at (2 0 2) plane is obtained at laser fluence of 160 J/cm^2. The lattice constants (a and c) were investigated from XRD patterns of (2 0 2) plane, using the given Eqs. (1.1)−(1.3) according to the hexagonal system. Table 1.2 displays the values (a and c) along with other structural properties at different laser fluence. The interplanar distance (d) was calculated using Bragg's law [71]

$$d = \frac{n\lambda}{2\sin(\theta)} \tag{1.1}$$

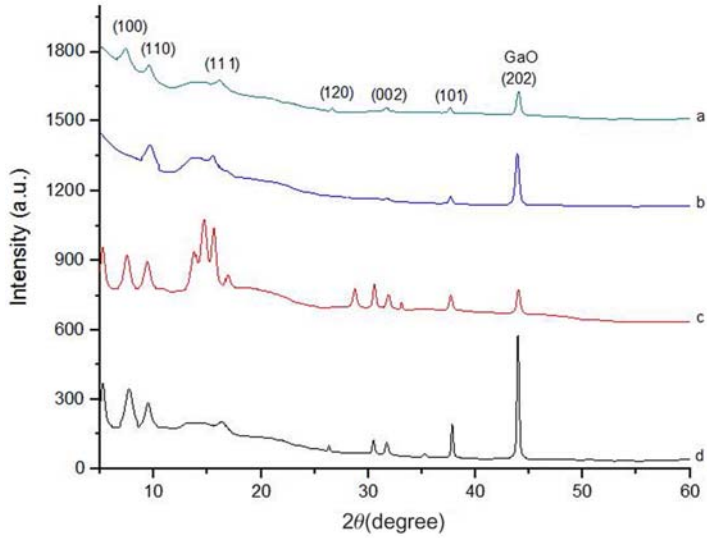

Figure 1.3 XRD patterns for (a) 160 J/cm^2; (b) 95 J/cm^2; (c) 60 J/cm^2; and (d) 30 J/cm^2 [66]. *XRD*, X-ray diffraction.

Table 1.3 Major diffraction peaks at 2θ along with attributed crystal diffraction planes [66].

Laser fluence (J/cm^2)	2θ (degree)	Attributed diffraction planes
30	8.254, 9.952, 17.000, 26.850, 32.015, 38.014, 44.800	(1 0 0), (1 1 0), (1 1 1), (1 2 0), (0 0 2), (1 0 1), (2 0 2)
60	8.154, 9.964, 15.785, 29.000, 30.015, 38.014, 44.800	(1 0 0), (1 1 0), (1 1 1), (1 2 0), (0 0 2), (1 0 1), (2 0 2)
95	9.987, 16.025, 32.015, 38.014, 44.800	(1 1 0), (1 1 1), (0 0 2), (1 0 1), (2 0 2)
160	7.689, 9.952, 16.000, 26.000, 32.015, 38.014, 44.800	(1 0 0), (1 1 0), (1 1 1), (1 2 0), (0 0 2), (1 0 1), (2 0 2)

where λ is wavelength of XRD using ($\lambda = 1.5406$ Å) and θ is Bragg's angle. Lattice constants (a and c) for tetragonal system were calculated from XRD patterns

$$\frac{1}{d^2} = \frac{h^2 + k^2}{a^2} + \frac{l^2}{c^2} \tag{1.2}$$

where $h\,k\,l$ is Miller indices, a and c are the lattice constants. By combining Eqs. (1.1) and (1.2), a and c can be calculated in terms of $\sin\theta$.

$$\sin^2\theta = \frac{\lambda^2}{4a^2}\left(h^2 + k^2\right) + \frac{\lambda^2}{4c^2}\left(l^2\right) \tag{1.3}$$

1.7 Conclusion

GaO nanoparticles prepared by the PLA technique in an ethanol environment were investigated for the first time in the literature. According to the obtained results, it is concluded that the ethanol environment plays an important role in affecting the nanoparticles' size and size distributions. The results showed that as laser fluence increases, the nanoparticles' size increases along with wider size distribution, followed by an increase in the optical absorption. The different sizes of nanoparticles are attributed to different laser-induced fragmentation and agglomeration of nanoparticles. The generation of GaO nanoparticles with different size distribution using a laser ablation technique in a liquid environment is a very promising approach for nanotechnological applications.

References

[1] G. Arun Kumar, H.S. Bhojya Naik, R. Viswanath, I.K. Suresh Gowda, K.N. Santhosh, Tunable emission property of biotin capped Gd:ZnS nanoparticles and their antibacterial activity, Mater. Sci. Semicond. Process. 58 (2017) 22–29.

[2] A.P.M. Tavares, C.G. Silva, G. Dražić, A.M.T. Silva, J.M. Loureiro, J.L. Faria, Laccase immobilization over multi-walled carbon nanotubes: kinetic, thermodynamic and stability studies, J. Colloid Interface Sci. 454 (2015) 52–60.

[3] W. Chen, Y. Lu, W. Dong, Z. Chen, M. Shen, Plasmon mediated visible light photocurrent and photoelectrochemical hydrogen generation using Au nanoparticles/TiO_2 electrode, Mater. Res. Bull. 50 (2014) 31–35.

[4] A.V. Manole, M. Dobromir, R. Apetrei, V. Nica, D. Luca, Surface characterization of sputtered N:TiO_2 thin films within a wide range of dopant concentration, Ceram. Int. 40 (2014) 9989–9995.

[5] Z.Y. Juan, H. Rao, Z.X. Fang, W.L. Zhou, W.C. Xu, Synthesis, properties, and optical applications of noble metal nanoparticle-biomolecule conjugates, Chin. Sci. Bull. 57 (2012) 238–246.

[6] K. Bagga, R. McCann, M. Wang, A. Stalcup, M. Vázquez, D. Brabazon, Laser assisted synthesis of carbon nanoparticles with controlled viscosities for printing applications, J. Colloid Interface Sci. 447 (2015) 263–268.

[7] Z. Hu, D. Chen, S. Wang, N. Zhang, L. Qin, Y. Huang, Facile synthesis of Sm-doped $BiFeO_3$ nanoparticles for enhanced visible light photocatalytic performance, Mater. Sci. Eng. B 220 (2017) 1–12.

[8] H. Su, Y. Li, X. Li, K.S. Wong, Optical and electrical properties of Au nanoparticles in two-dimensional networks: an effective cluster model, Opt. Express 17 (2009) 22223–22229.

[9] Y. Li, R. Peng, X. Xiu, X. Zheng, X. Zhang, G. Zhai, Growth of SnO_2 nanoparticles via thermal evaporation method, Superlattices Microstruct. 50 (2011) 511–516.
[10] Z. Khan, S.A. Al-Thabaiti, A.Y. Obaid, A.O. Al-Youbi, Preparation and characterization of silver nanoparticles by chemical reduction method, Colloids Surf. B Biointerfaces 82 (2011) 513–517.
[11] E. Moncada, R. Quijada, J. Retuert, Nanoparticles prepared by the sol–gel method and their use in the formation of nanocomposites with polypropylene, Nanotechnology 18 (2007) 335606–335611.
[12] J.F. de Carvalho, S.N. de Medeiros, M.A. Morales, A.L. Dantas, A.S. Carrico, Synthesis of magnetite nanoparticles by high energy ball milling, Appl. Surf. Sci. 275 (2013) 84–87.
[13] B. Chung, C. Liu, Synthesis of cobalt nanoparticles by DC magnetron sputtering and the effects of electron bombardment, Mater. Lett. 58 (2004) 1437–1440.
[14] H. Zeng, X. Du, S.C. Singh, S.A. Kulinich, S. Yang, J. He, et al., Nanomaterials via laser ablation/irradiation in liquid: a review, Adv. Funct. Mater. 22 (2012) 1333–1353.
[15] H. Wang, O. Odawara, H. Wada, One-step preparation of YVO4:Eu^{3+} nanoparticles by pulsed laser ablation, J. Alloy Compd. 683 (2016) 1–6.
[16] Y. Al-Douri, S.A. Abdulateef, A.A. Odeh, C.H. Voon, N. Badi, GaNO colloidal nanoparticles synthesis by nanosecond pulsed laser ablation: laser fluence dependent optical absorption and structural properties, Powder Technol. 320 (2017) 457–461.
[17] S. Petersen, S. Barcikowski, In situ bioconjugation: single step approach to tailored nanoparticle-bioconjugates by ultrashort pulsed laser ablation, Adv. Funct. Mater. 19 (2009) 1167–1172.
[18] H. Zeng, G. Duan, Y. Li, S. Yang, X. Xu, W. Cai, Blue luminescence of ZnO nanoparticles based on non-equilibrium processes: defect origins and emission controls, Adv. Funct. Mater. 20 (2010) 561–572.
[19] M. Prochazka, P. Mojzes, J. Stepanek, B. Vlckova, P. Turpin, Probing applications of laser-ablated Ag colloids in SERS spectroscopy: improvement of ablation procedure and SERS spectral testing, Anal. Chem. 69 (1997) 5103–5108.
[20] A.A. Derakhshan, L. Rajabi, Review on applications of carboxylate–alumoxane nanostructures, Powder Technol. 226 (2012) 117–129.
[21] V. Amendola, M. Meneghetti, Laser ablation synthesis in solution and size manipulation of noble metal nanoparticles, Phys. Chem. Chem. Phys. 11 (2009) 3805–3821.
[22] N.G. Semaltianos, S. Logothetidis, W. Perrie, S. Romani, R.J. Potter, M. Sharp, et al., II–VI semiconductor nanoparticles synthesized by laser ablation, Appl. Phys. A 94 (2009) 641–647.
[23] S. Petersen, J. Jakobi, A. Hörtinger, S. Barcikowski, In-situ conjugation-tailored nanoparticle-conjugates by laser ablation in liquids, J. Laser Micro Nanoen. 4 (2009) 71–74.
[24] Z. Wang, X. Li, M. Gao, X. Zeng, One-step preparation of amorphous iron nanoparticles by laser ablation, Powder Technol. 215–216 (2012) 147–150.
[25] R. Intartaglia, K. Bagga, M. Scotto, A. Diaspro, F. Brandi, Luminescent silicon nanoparticles prepared by ultra-short pulsed laser ablation in liquid for imaging applications, Opt. Mater. Express 2 (2012) 510–518.
[26] J. Nedersen, G. Chumanov, T.M. Cotton, Appl. Spectrosc. 47 (1993) 1959.
[27] M.S. Sibbald, G. Chumanov, T.M. Cotton, J. Phys. Chem. 100 (1996) 4672.
[28] M.-S. Yeh, Y.-S. Yang, Y.-P. Lee, H.-F. Lee, Y.-H. Yeh, C.-S. Yeh, J. Phys. Chem. B 103 (1999) 6851.
[29] P.V. Kamat, M. Flumiani, G.V. Hartland, J. Phys. Chem. B 102 (1998) 3123.

[30] A. Takami, H. Kurita, S. Koda, J. Phys. Chem. B 103 (1999) 1226.
[31] S. Link, C. Burda, B. Nikoobakht, M.A. El-Sayed, J. Phys. Chem. B104 (2000) 6152.
[32] A.V. Simakin, V.V. Voronov, G.A. Shafeev, R. Brayner, F. Bozon-Verduraz, Chem. Phys. Lett. 348 (2001) 182.
[33] S.I. Dolgaev, A.V. Simakin, V.V. Voronov, G.A. Shafeev, F. Bozon-Verduraz, Appl. Surf. Sci. 186 (2002) 546.
[34] (a) K.V. Anikin, N.N. Melnik, A.V. Simakin, G.A. Shafeev, A.G. Vitukhnovsky, Chem. Phys. Lett. 366 (2002) 357–360.
(b) J.B. Wang, G.W. Yang, C.Y. Zhang, X.L. Zhong, Z.A. Ren, Chem. Phys. Lett. 367 (2003) 10–14.
[35] P. Chewchinda, T. Tsuge, H. Funakubo, O. Odawara, H. Wada, Laser wavelength effect on size and morphology of silicon nanoparticles prepared by laser ablation in liquid, Jpn. J. Appl. Phys. 52 (2013) 025001–025011.
[36] N. Haram, N. Ahmad, Effect of laser fluence on the size of copper oxide nanoparticles produced by the ablation of Cu target in double distilled water, Appl. Phys. A 111 (2013) 1131–1137.
[37] D. Riabinina, M. Chaker, J. Margot, Dependence of gold nanoparticle production on pulse duration by laser ablation in liquid media, Nanotechnology 23 (2012) 135603–135607.
[38] G. Bajaj, R.K. Soni, Effect of liquid medium on size and shape of nanoparticles prepared by pulsed laser ablation of tin, Appl. Phys. A 97 (2009) 481–487.
[39] N. Sun, L.P.H. Jeurgens, Z. Burghard, J. Bill, Ionic liquid assisted fabrication of high performance SWNTs reinforced ceramic matrix nano-composites, Ceram. Int. 43 (2017) 2297–2304.
[40] N. Tsuda, K. Nasu, A. Yanase, K. Siratori, Electronic Conduction in Oxides, 94, Springer Series in Solid-State Sciences, 1991.
[41] C.N.R. Rao, J. Gopalakrishnan, New Directions in Solid State Chemistry, Cambridge University Press, UK, 1997.
[42] D. Adler, in: N.B. Hanny) (Ed.), Treatise on Solid State Chemistry, Vol. 2, Plenum Press, New York, 1975.
[43] C.N.R. Rao, G.V. Subba Rao, Transitional Metal Oxides, Crystal Chemistry, Phase Transition and Related Aspects, NSRDS-NBS Monograph, vol. 49, National Bureau of Standards, Washington, DC, 1974.
[44] J.B. Goodenough, "Prog. Solid State Chem. 5 (1971) 149.
[45] C.N.R. Rao, Solid State Chemistry, Marcel Dekker, New York, 1974.
[46] R.F. Bunshah, Deposition Technologies for Films and Coatings, Noyes Publications, NJ, 1982.
[47] D.R. Clarke, S.R. Phillpot, Thermal barrier coating materials, Mater. Today 8 (2005) 22–29.
[48] P.K. Wright, A.G. Evans, Current opinion in solid state, Mater. Sci. 4 (1999) 255–265.
[49] Z.M. Dang, L.Z. Fan, S.J. Zhao, C.W. Nan, Preparation of nanosized ZnO and dielectric properties of composites filled with nanosized ZnO, Mater. Sci. Eng. B 99 (2003).
[50] S.B. Khan, M. Faisal, M.M. Rahman, A. Jamal, Low-temperature growth of ZnO nanoparticles: photocatalyst and acetone sensor, Talanta 85 (2011) 943–949.
[51] S.C. Minne, S.R. Manalis, C.F. Quate, Parallel atomic force microscopy using cantilevers with integrated piezoresistive sensors and integrated piezoelectric actuators, Appl. Phys. Lett. 67 (1995) 3918–3920.
[52] A. Umar, M.M. Rahman, M. Vaseem, Y.-B. Hahn, Ultra-sensitive cholesterol biosensor based on low-temperature grown ZnO nanoparticles, Electrochem. Commun. 11 (2009) 118–121.

[53] K. Keis, E. Magnusson, H. Lindström, S.-E. Lindquist, A. Hagfeldt, A 5% efficient photoelectrochemical solar cell based on nanostructured ZnO electrodes, Sol. Energy Mater. Sol. Cells 73 (2002) 51–58.
[54] P.M. Martin, M.S. Good, J.W. Johnston, G.J. Posakony, L.J. Bond, S.L. Crawford, Piezoelectric films for 100-MHz ultrasonic transducers, Thin Solid Films 379 (2000) 253–258.
[55] R.S. Morris, M.A. Walsh, Zinc Oxide Photoactive Material, US Patent No. 6,063,849, 2000.
[56] U. Thurian, P. Kaczmarczyk, G. Siegle, H. Heitz, R. Hoffmann, A. Broser, et al., Local Vibration Modes of 3d Elements in Wurtzite Type ZnO and GaN Crystals, 1995.
[57] N.M. Franklin, N.J. Rogers, S.C. Apte, G.E. Batley, G.E. Gadd, P.S. Casey, Comparative toxicity of nanoparticulate ZnO, bulk ZnO, and $ZnCl_2$ to a freshwater microalga (*Pseudokirchneriella subcapitata*): the importance of particle solubility, Environ. Sci. Technol. 41 (2007) 8484–8490.
[58] M.J. Pitkethly, Nanomaterials – the driving force, Mater. Today 7 (2004) 20–29.
[59] R. Roy, V.G. Hill, E.F. Osborn, Polymorphism of Ga_2O_3 and the system Ga_2O_3-H_2O, J. Am. Chem. Soc. 74 (1952) 719–722.
[60] L. Li, W. Wei, M. Behrens, Synthesis and characterization of α-, β-, and γ-Ga_2O_3 prepared from aqueous solutions by controlled precipitation, Solid State Sci. 14 (2012) 971–981.
[61] H.Y. Playford, A.C. Hannon, E.R. Barney, R.I. Walton, Structures of uncharacterised polymorphs of gallium oxide from total neutron diffraction, Chem. Eur. J. 19 (2013) 2803–2813.
[62] S. Yoshioka, H. Hayashi, A. Kuwabara, F. Oba, K. Matsunaga, I. Tanaka, Structures and energetics of Ga_2O_3 polymorphs, J. Phys. Condens. Matter. 19 (2007) 346211–346219.
[63] E. Tronc, C. Chanéac, J.P. Jolivet, Structural and magnetic characterization of ε-Fe_2O_3, J. Solid State Chem. 139 (1998) 93–104.
[64] S.-D. Lee, K. Akaiwa, S. Fujita, Thermal stability of single crystalline alpha gallium oxide films on sapphire substrates, Phys. Status Solidi 10 (2013) 1592–1604.
[65] J.S. Golightly, A. Castleman, Analysis of titanium nanoparticles created by laser irradiation under liquid environments, J. Phys. Chem. B 110 (2006) 19979–19984.
[66] Y. Al-Douri, R.A. Al-Samarai, S.A. Abdulateef, A.A. Odeh, N. Badi, C.H. Voon, Nanosecond pulsed laser ablation to synthesize GaO colloidal nanoparticles: optical and structural properties, Optik 178 (2019) 337–342.
[67] N. Haustrup, G.M. O'Connor, Nanoparticle generation during laser ablation and laser-induced liquefaction, Phys. Proc. 12 (2011) 46–53.
[68] N. Badi, A. Bensaoula, A.V. Simakin, G.A. Shafeev, Laser engineered core-shell nanodielectrics with giant electrical permittivity, Mater. Lett. 108 (2013) 225–229.
[69] S.I. Stepanov, V.I. Nikolaev, V.E. Bougrouv, A.E. Romanov, Gallium oxide: properties and applications – a review, Rev. Adv. Mater. Sci. 44 (2016) 63–86.
[70] S. Maier, Plasmonics: Fundamentals and Application, Springer, 2007.
[71] S. Lee, H.J. Jung, J.H. Shin, M.Y. Choi, Production of size controlled aluminum and alumina nanoparticles via pulsed laser ablation in water, J. Nanosci. Nanotechnol. 12 (2012) 8900–8903.

This page intentionally left blank

Chemical studies of metal oxide powders

2

Nur Azimah Abd Samad, Chin Wei Lai and Mohd Rafie Johan
Nanotechnology & Catalysis Research Centre (NANOCAT), Institute for Advanced Studies (IAS), Universiti Malaya, Kuala Lumpur, Malaysia

2.1 Introduction

The discoveries of science have been tremendously successful in making our metal oxides become more visible in many applications and widely used as active catalysts or supporting materials [1]. Metal oxide can be classified as a chemical compound that is formed from metal ions (cations; Na^{+}, Li^{+}, Zn^{2+}, Ti^{3+}, W^{3+}, Mo^{3+}, V^{5+}, etc.) and oxygen (as anion with an oxidation state of -2). Typically, metal oxides are formed in some basic properties and usually form as solid at room temperature. Metal oxides are insoluble in water and produce salts with acids. But still there are metal oxides that are acidic or amphoteric in nature and form salts with bases in the neutralization reaction. Metal oxides make up of a class of inorganic materials and their surface chemistry and quantum effects in tandem will dominate their properties as they are reduced to nanosize. The oxygen anion will terminate the oxide surfaces because its size is larger than the metal cations [2,3]. In the context of semiconductors, the defect, diffusion, and reaction kinetics in metal oxides surface and interface also become important features in determining the properties, that is, catalytic, magnetic, mechanical, electronic and electrical, and many other properties. The nature of metal oxides chemical bonds is rather similar even in different electronic states. In a subsequent section, we will discuss in general the chemical bonds present in metal oxide, the defects and diffusion in metal oxide, and consider titanium dioxide (TiO_2) and zinc oxide (ZnO) in order to study the chemical properties of metal oxide powder.

2.1.1 Chemical bond present in metal oxide

An effective chemical bond in metal oxides produces a stable interface, and it affects the nanoscale behavior and its properties. The electron configuration determines the bonds that are present in metal oxides, which can be ionic, metallic, or covalent bond. The valence electrons that occupy the outermost shell in the element will participate in bonding to form aggregates. In this context, we consider the aggregates as metal oxides. Ionic bonding consists of both metal−nonmetal elements. Covalent bonding occurs by sharing of electrons between adjacent atoms to form a stable electron configuration. Meanwhile, metallic bonding occurs in

Metal Oxide Powder Technologies. DOI: https://doi.org/10.1016/B978-0-12-817505-7.00002-6

metal−metal and its alloys. However, it is difficult to determine the bonding present due to the dissimilar electronic atomic configuration in materials [4]. To understand the interface bonding, the differences in lattice parameters and the elastic constant of metal oxides need to be taken into consideration. High-resolution transmission electron microscopy can be used to study both the lattice parameter and elastic constant [5,6]. In addition, the image charge theory (ICT) helps in understanding the metal oxides' interfacial bonding [4,7−9]. Theoretically, ICT investigates the charge response of a metal surface or imperfect conductive surface [10,11]. In this context, the metal oxide is a semiconductor. This approach presents the physics of the image theory taken into account for the charges contained in the metal oxide interface. ICT focused on the geometry that existed between the charged particles and the surface ground [10,11]. Electrostatic or dipole moment curve responses from the reflection of the conducting plane can describe the atomic character of the metal oxide surface and whether it has ionic, covalent, or metallic bonding. Specifically, there are two methods to calculate the electrostatic potential, whether it comes from a point charge or a perfectly conducting surface [11,12].

Generally, the metal oxide chemical bond is determined from a few techniques such as ab initio self-consistent field wave functions. Ab initio quantum chemistry is different from other computational methods as it applies a solely quantum mechanics nature law in the determination of metal oxide chemical bond. Additionally, it is calculated from the multireference configuration interaction expansions [13]. Also, the determination of metal oxide interaction or chemical bond is calculated by considering the first principle calculations (the atomic bonding and electrical potential) [14]. Also, there are a few researchers who have stated that metal oxide interface bonding can be defined from local-potential and kinetic-energy densities [15].

2.1.2 Defects and diffusion in metal oxides

Thus far it has been tacitly assumed that perfect order exists at the atomic level in crystalline materials. However, such an idea does not exist in solids, and all contain defects or imperfections. Defects are classified as lattice irregularities on the order of an atom's diameter. Additionally, defects-influenced properties depend on the oxides themselves, the temperature, and the activities of the component. In general, defects are categorized as point defects (vacancies and self-interstitial, impurities in solids, composition specification) and other imperfections (dislocations−linear defects, interfacial defects, bulk or volume defects, and atomic vibrations) [16]. Point defects in metal oxides have limiting groups as follows (Fig. 2.1):

1. Metal deficient oxides (metal vacancies)
2. Metal excess oxides (metal interstitials)
3. Oxygen deficient oxides (oxygen vacancies)
4. Oxygen excess oxides (oxygen interstitials) [17,18]

Important features to distinguish point defects and extended defects (line defects−dislocations and planar defects−grain boundaries) are the atomic

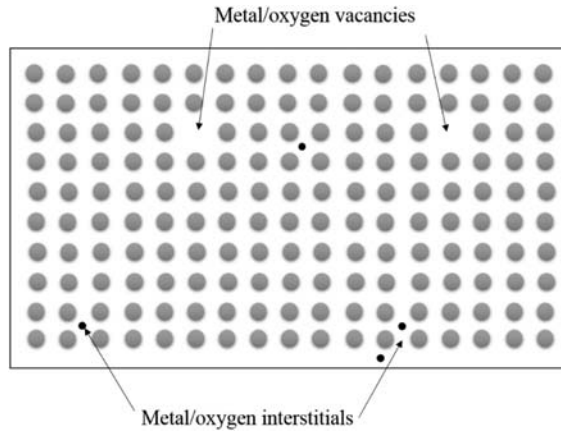

Figure 2.1 General schematic diagram of defects consisting of metal deficient oxides (metal vacancies), metal excess oxides (metal interstitials), oxygen deficient oxides (oxygen vacancies), and oxygen excess oxides (oxygen interstitials).

composition, the crystalline phase structure, and the electronic defects (the probability of an electron occupying energy states). Electronic defects are sometimes called thermodynamic defects since they are temperature-dependent defects. For an intrinsic semiconductor, the number of the electrons in the conduction band is equal to the number of holes in the valence band (Eq. 2.1), given by:

$$n = n_e = n_h = n_0 \exp\left(\frac{-E_G}{2kT}\right) \tag{2.1}$$

where n_0 is the constant and E_G is the energy gap.

For extrinsic semiconductors, carriers in the electrically active bandgap are integrated into localized energy levels. In this context, the electronic defects are considered as donor state (give electrons to the conduction band and increase n-type conductivity) on certain semiconductor energy bands which are just below the conduction band. Furthermore, it can also create an acceptor state to accept an electron from the valence band. Therefore the conductivity for p-type semiconductors will increase. The total number of charge carriers is given by (Eq. 2.2)

$$\begin{aligned} n_{\text{total}} &= n_e(\text{dopant}) + n_e(\text{intrinsic}) + n_h(\text{intrinsic}) \\ &= n_0 \exp\left(-\frac{E_D}{2kT}\right) + 2n_0 \exp\left(-\frac{E_G}{2kT}\right) \end{aligned} \tag{2.2}$$

where n_0 is the constant, E_G is the energy gap, and E_D is the donor energy level.

Since most metal oxides have a wide bandgap and often a high content of impurities, most electronic defects are the extrinsic type [2,19].

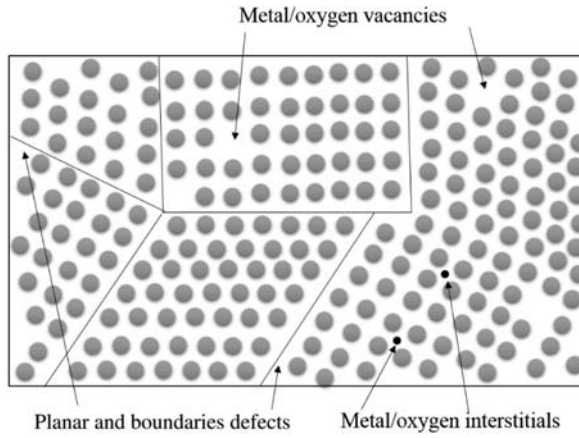

Figure 2.2 Combination of point defects and planar and boundaries defects.

Defect-influenced properties are the physical and chemical properties of a metal oxide that are affected or determined by defects. Lattice diffusion is affected by point defects and mechanical properties are greatly affected by dislocation and grain boundaries. Nevertheless, dislocation and grain boundaries are responsible for diffusion transportation and solid-state reactions (Fig. 2.2) [17,20]. In summary for defects and diffusion in metal oxides, electronic conductivity is proportional to the concentration of electronic defects while lattice diffusion is proportional to point defects and their mobility.

2.2 Titanium dioxide chemical studies

Titanium dioxide (TiO_2) is a unique material that is widely used in many high-end applications, such as medical instruments and supplies, houses (interior and exterior), vehicles, electrical products, roads, agriculture, air treatment, and water and soil treatment. All of these applications use TiO_2 in the presence of light. TiO_2 nanostructures consist of zero-dimensional TiO_2 nanoparticles; one-dimensional (1D) TiO_2 nanotubes, nanorods, nanowires, and nanobelts; two-dimensional (2D) TiO_2 nanosheets; and three-dimensional (3D) TiO_2. Nanoporous [21] TiO_2 contains a series of TiO_2 polymorphs (crystal structures) such as anatase, brookite, and rutile. These TiO_2 polymorphs can be produced by controlling experimental condition, such as synthesis method, pH, annealing temperature, and duration, and these polymorphs affect the end performance [22,23]. Certain conditions play roles in influencing the formation of TiO_2.

The synthesis temperature influenced nucleation and crystal development by regulating solution solubility and supersaturation. A rise in the temperature generated a greater solubility, which resulted in smaller particle size and a greater supersaturation index. Moreover, the amount, size, and quality of crystals were affected

by temperature. The rate of diffusion was lower, and equilibrium was slower at low temperatures than at elevated ones. Crystallization happened more slowly at low temperature. These relationships can also affect the packing of crystals and the terminating of crystal growth. Thus the temperature has a major impact on crystal nucleation, growth, packing, and termination [24,25].

Kinetic control (agitation rate) affected the chemical composition ratio of TiO_2, as it was directly proportionate to the rate of evaporation. Due to the introduction of heat, solvent evaporation happened. Consequently, the mixture is rich in O ions (including the water content) and have produced O atom-rich structure when the rates of agitation increased. The mechanical energy of agitation can trigger collisions among particles and therefore increase in the surface area. The agitation process also controlled nanoparticle seeding of TiO_2 (nucleation and crystal growth). The rate of agitation is directly proportional to the rate of evaporation [26–28]. The solvent (including water and alcohol) evaporated in that case due to the increase in temperature. The solubility of precipitation–peptization solution was affected by the solvent content. An increased agitation speed resulted in a high evaporation rate and a low solubility and supersaturation index. Thus instead of nucleating a new crystal, the crystal grew. Increased stirring therefore generated a larger crystallite size.

Many arguments have arisen in the determination of O–Ti–O bonding. But, many researchers acknowledge that TiO_2 has ionic–covalent bonding. B. Jiang and his team revealed several features in Ti–O bonding for the rutile phase. In TiO_2, the Ti $3d$ electrons play a big role in Ti–O bonding. First, the charge defects at the Ti-atomic site and the excess charge at the O-atomic site show a charge transfer between Ti and O atoms (ionic bonding). Second, in the Ti-atom site, the greater charge deficit region along with the crystal in the c direction are similar to an orbital hole type d_x^2. Third, both O and Ti atoms show a nonspherical distribution of the valence-shell load representing covalent bonding. Therefore Jiang et al. claimed that TiO_2 has ionic–covalent bonding in the rutile phase [29]. In addition, C. Sousa and her team also agreed that TiO_2 possessed an ionic–covalent bonding. Their ab initio cluster model approach showed that the degree of ionicity in TiO_2 is far below the degree of the fully ionic situation and henceforth TiO_2 presents a considerable covalent character. C. Sousa found that in the determination of ionicity, the energy associated with V(O;O) decreased and contributed to the reduction of the initial Pauli repulsion (approximately 0.6 eV). At the same time, energy larger than 10 eV was obtained after $[O_6]^{12-}$ was allowed to mix with the empty cation orbitals and hence allowed the charge transfer from $[O_6]^{12-}$ to Ti cation. This situation is called covalent mixing [30]. K.M. Glassford and his team also stated that TiO_2 has ionic–covalent bonding. He used ab initio pseudopotentials constructed within the local density approximation and plane–wave basis techniques in the determination of bonding in TiO_2. Based on the independent-atom model, the formation of charge density showed that $(\bar{1}\,1\,0)$ plane has a threefold-coordinated oxygen atom with C_{2v} site symmetry and a Ti atom with D_{2h} site symmetry, causing the lobes distortion of negative deformation of [0 0 1] direction. Thus these are the prominent

features of covalent character with a small amount of ionic character in the Ti−O bonds [31].

Another chemical study on TiO_2 surface looked at the formation of hydrogen bonds during the interaction of TiO_2 with an organic solvent, water, carbon dioxide, and oxygen with the association of oxygen vacancies. The creation of two OH groups at the TiO_2/water interface can efficiently dissociate water from oxygen vacancies [32−36]. According to Žerjav et al. and Braun and Hauser, the interaction of TiO_2 with water molecules leads to another surface chemistry of the various hydration layer chemistry, formed at the surfaces of (1 0 1) and (0 0 1) anatases nanocrystals facets, where molecules adsorbed water and titanols, respectively [37,38]. Žerjav et al. also agreed that the weak hydrogen binding on both (1 0 1) facets is equivalent to bulk water, while strong hydrogen bonds with hydroxyl surfaces at (0 0 1) facets form a layer comprising acidic protons and serve as hydrogen bonding sources [37]. Chen et al. and Yamamoto et al. supported the above statement with hydroxyls on the surface acting as the anchor for water adsorption, forming hydrogen bonds with water molecules which caused water adsorption in multiple layers [32,39].

Meanwhile, S. Huygh stated that the interaction of TiO_2 with carbon dioxide (CO_2), associated with oxygen vacancy defects leads to a new highly stable adsorption with a stronger C−O activation. This leads to a possibility for the exothermic dissociation of carbon dioxide from barriers up to 22.2 kcal/mol with a chemical lifetime less than 4 s at 300K. These reactions produce a CO molecule that easily desorbs and oxidizes the reduced surface. Oxygen vacancy defects play a key role in the catalytic activity of the surface of anatase (0 0 1) [40]. H. Zhao showed that TiO_2 surface defects affected the CO_2 photoreduction with water. First, surface defects of TiO_2 can improve dissociative adsorption of carbon dioxide and H_2O molecules. Second, the change in the structure of the TiO_2 electronic band caused by the defect can help improve the efficiency of absorption by sunlight; and third, the defect charge carrier traps can impede recombination of the charge and defects can contribute to electrons' surface migration [41]. On the other hand, Ok et al. claimed the thermal conductivity of TiO_{2-x} was considerably reduced by planar defects owing to strong phonon scattering caused by planar defects, and was 22% lower than in point defects [42]. The planar and boundaries studies are still lacking in TiO_2 for the determination of end properties.

2.3 Zinc oxide chemical studies

Zinc oxide (ZnO) is complex and has a variety of 1D (nanorod, nanotube, and nanowire), 2D (nanodisk and nanosheet), and 3D (nanodendritic) forms. Each ZnO nanostructure possesses its unique characteristics, such as the capability of electron mobility and electron scattering that will influence the final performance of any future application [43]. The most famous ZnO crystal structure is wurtzite (hexagonal close-packed sublattices) due to its thermodynamically stable phase as

compared to zinc blende, which has a face-centered facet and is metastable [44,45]. Meanwhile, another rock salt structure can only be obtained after application with high pressure. ZnO possesses ionic bonding because the total charge density retains a large amount of ionicity with no or less degree of covalency [44]. A large amount of ionicity in ZnO occurs because it has a high difference of electronegativity between the zinc and oxygen atoms, and thus causes an intense repulsion among the clouds of nearby atoms with comparable electric charge, making their crystalline structure more stable in the form of the hexagonal crystal structure (wurtzite) [46].

The surface chemistry of ZnO shows the existence of a dipole moment (in the case of zincite) which leads to the two different polar surfaces with the (0 0 0 1) being zinc-terminated and the (0 0 0 $\bar{1}$) terminated by an oxygen atom. These polar surfaces are unstable, and to achieve the phase stability, the Zn and O atoms at the ZnO surface will perform the geometrical rearrangement or metallization (charge transfer) [47,48]. The process used in the formation of ZnO nanostructures influences the surface tension, particle size, and surface energy. Thus these characteristics will affect ZnO properties and performance. In particular, the difference in surface energies from two different planes ($\{1\ 0\ \bar{1}\ 0\}$ and $\{0\ 0\ 0\ 1\}$) of ZnO crystal growth facilitates the kinetically controlled anisotropic crystal growth along the *c*-axis. Thus rod-like ZnO nanoparticles are often observed [47,49].

Meanwhile, the classical theory of the nucleation, crystal growth, and ripening of ZnO nanostructures show that large supersaturation will increase the nucleation rate and reduce the crystal growth, thus producing small ZnO particles. On the other hand, an increase in surface tension or interfacial tension will increase the dielectric constant (referred to as the liquid phase synthesis procedure), and then it will increase the solubility of the solution, and proceed with low supersaturation and a decrease in nucleation rate. Therefore the increase in surface tension will produce a bigger particle size [50]. This intrinsic polarity of the crystal structure that arises from surface tension and surface energy encourages crystal growth and leads to spontaneous polarization, plasticity, and piezoelectricity properties [51]. The particle size and morphology of ZnO nanostructures are highly affected by the electronic and electrical properties, and these characteristics are controlled by the electron mobility and electron scattering, thus differentiating the electronic performance from one structure to another.

Meanwhile, the adsorbed oxygen and zinc interstitial at the ZnO surface also will influence the electrical and photoconductivity properties of ZnO nanostructures [52]. It has been proven by past research that the surface charge density is highly influenced by the size of ZnO nanostructures; with size smaller than 10 nm the nanostructures will produce a high surface charge density [53,54]. In addition to the size of reduced nanostructures, the surface area and the number of edges, kinks, and defect site density will increase, resulting in “hot spots” of dissolution. The dissolution property is important in long-term stability, especially in environmental and health application [53].

In the ZnO research of photoluminescence, some defects such as zinc vacancies, interstitial zinc, oxygen vacancies, interstitial oxygen, and oxygen antisites

were primarily associated. The exciton recombination process in the region of 350−450 nm is determined and caused by a recombination of free excitons, which indicates the good crystalline nature of the ZnO [55,56]. ZnO nanorods had the highest arrangements for crystallinity as their minimum emissions were in the 50−450 nm region (UV area), but low emissions were found in the 600−700 nm region (orange−red region). Small intrinsic defects were caused by the presence of excess oxygen, such as the oxygen interstitial [57]. But the ZnO synthesized from the higher voltage of the electrodeposition technique showed combinations of more than one defect in its atomic structure. This combination of defects can be oxygen vacancies and zinc interstitials based on the literature, V_oZn_i [58]. Green emissions of photoluminescence were typically due to oxygen-based defects [58−61]. Also, ZnO had a broad peak covering the green, yellow, and orange region generated by a mixture of both defects, that is, oxygen vacancies and the zinc interstitials defects [58,62]. Nevertheless, few researchers have suggested that ZnO containing large $Zn(OH)_2$ quantities may generate a wide green, yellow, and orange area [57,63]. A reason, in this case, could be due to insufficient annealing.

For dense structures of ZnO with fewer defects, the photoluminescence of the 500−800 nm region showed superlative performance, but with a high recombination rate of the 350−450 nm region [43]. Bulky ZnO always possesses a dense structure of ZnO. In addition, due to the presence of high oxygen vacancies within the ZnO bulk, the electronic performance for amorphous ZnO was poorly demonstrated, indicating the increasing number of recombination centers [64]. The recombination centers, which were the main cause of enhanced trap states, significantly led to the reduction of photoinduced charge carrier mobility back into contact with the Zn itself. Moreover, the ZnO amorphous phase comprised high concentrations of other material defects, including impurities, dangling bonds, and microvoids, which also functioned as a center for charge carrier recombination and eventually led to lower electronic performance [65]. K.Dai's team and K.A. Alim's team claimed the shift of the Raman peak occurred due to the defects or impurities in the nanocrystals, optical phonon confinement, laser irradiation heating, and the tensile strain effect [66,67].

2.4 Modification of metal oxide

Great scientific interest was drawn by the dynamics in the metal oxide structure and the promising functional characteristics. It has an immense nanoarchitecture, and yet it has limited visible light absorption and fast recombination charge carriers prevent further practices in electronic applications. The use of visible light from solar energy and the reduction of the recombination of charge carriers are therefore crucial to increase the effectiveness of electronic properties. The modification of the metal oxide is thus necessary to improve the performance of its properties.

Many possible modification techniques have been recently studied and actively reported worldwide in order to improve metal oxides, such as metal-modified metal oxide, nonmetal-modified metal oxide, polymer-modified metal oxide, and semiconductor-modified metal oxide.

In the context of defects, Y. Ding and Z.L. Wang studied the planar defects in ZnO nanobelt and nanowire formed from impurity doping, and it showed $(0\,1\,\bar{1}\,1)$, $(0\,\bar{1}\,1\,2)$, $(0\,1\,\bar{1}\,3)$, and $(\bar{2}\,1\,1\,2)$ twins, I_1, I_2 basal plane stacking faults, and 1/6 $(2\,0\,\bar{2}\,3)$ prismatic plane stacking faults and provided unique semiconducting properties, piezoelectric properties, and was biosafe [68]. In addition, R. Deng and team claimed that the introduction of Sn metal in ZnO crystal structures produced an improvement in near-band edge emission at 3.24 eV by which the peak became broader and slightly shifted to a lower energy, therefore resulting in a minimization of structural strain. It is due to the rearrangement of the order of surface energies among $\{0\,0\,0\,1\}$, $\{0\,1\,\bar{1}\,0\}$, and $\{2\,\bar{1}\,\bar{1}\,0\}$ surfaces, causing the nanobelts to grow along the $\langle 0\,1\,\bar{1}\,0\rangle$ direction [69]. A lack of information for planar defects in metal oxide was found.

Meanwhile, N.A. Abd Samad and her team have shown a number of defects, such as zinc vacancies, zinc interstitials, oxygen vacancies, oxygen interstitials, and oxygen antisites, in the photoluminescence studies for the hybrid TiO_2−ZnO film. The ZnO PL spectrum shows a UV emission band that is centralized at 380 nm and a width (determined in the intrinsic defects) of the large-visible emission band [55]. With the increasing TiO_2−ZnO dipping cycles, the PL intensity continued to decrease. This is due to the rise of the TiO_2 layer and is assigned to the charge carrier separation impact of ZnO and TiO_2 (heterojunction) type-II band alignment [70]. In order to achieve an excitonic charge separation state, the photogenerated charge carriers in the staggered-band offset are separated and connected mainly into the TiO_2 and ZnO. The efficient separation of the charge carrier decreases the electron/hole recombination rate while also decreasing the PL intensity of the TiO_2−ZnO hybrid film [70−72]. Therefore the combination of semiconductor-modified metal oxide may contribute to the improvement of charge carriers transportation and reduce the recombination rate.

2.5 Conclusion

In conclusion, metal oxide possesses a variety of chemical bondings, for example, TiO_2 has ionic−covalent bonding and ZnO has a majority of ionic bonding within its crystal structure. This is because different metals interact differently with oxygen to form metal oxides. Therefore different bonding will appear and it will result in exceptional end properties. In addition, point defects and planar and boundaries defects affect the transportation of charge carriers and provide recombination centers. Therefore modification of metal oxide would improve its end properties by prolonging the transportation of charge carriers and reducing the recombination rate.

Acknowledgments

This work was financially supported by Impact-Oriented Interdisciplinary Research Grant No. IIRG018A-2019, and Global Collaborative Programme-SATU Joint Research Scheme (No. ST012-2019).

References

[1] R. Velmurugan, A. Incharoensakdi, Nanoparticles and organic matter: process and impact, Nanomaterials in Plants, Algae, and Microorganisms, Elsevier, 2018, pp. 407–428.
[2] J. Védrine, Heterogeneous catalysis on metal oxides, Catalysts 7 (11) (2017) 341.
[3] B. Pawelec, Surface processes and composition of metal oxide surfaces, Metal Oxides, CRC Press, 2005, pp. 133–154.
[4] K. Matsunaga, et al., Bonding nature of metal/oxide incoherent interfaces by first-principles calculations, Phys. Rev. B 74 (12) (2006) 125423.
[5] K. Edagawa, T. Kamimura, Y.-G. So, Evaluation of phason elastic constants from HRTEM image of a dislocation in icosahedral quasicrystal, Z. Kristallogr. Cryst. Mater. 224 (1–2) (2009) 71–74.
[6] P.M. Kibasomba, et al., Strain and grain size of TiO_2 nanoparticles from TEM, Raman spectroscopy and XRD: the revisiting of the Williamson-Hall plot method, Results Phys. 9 (2018) 628–635.
[7] F. Ernst, Metal-oxide interfaces, Mater. Sci. Eng. R. Rep. 14 (3) (1995) 97–156.
[8] M. Finnis, The theory of metal-ceramic interfaces, J. Phys. Condens. Matter. 8 (32) (1996) 5811.
[9] Y. Ikuhara, et al., Structure of V–Al_2, O_3 interfaces grown by molecular beam epitaxy, Phil. Mag. A 70 (1) (1994) 75–97.
[10] S.L. Meredith, S.K. Earles, N.E. Turner, A New Method to Describe Image Theory for an Imperfect Conductor, 2010.
[11] M. García-Hernández, P.S. Bagus, F. Illas, A new analysis of image charge theory, Surf. Sci. 409 (1) (1998) 69–80.
[12] J. Jackson, Classical Electrodynamics, Wiley, New York, 1975.
[13] N. López, F. Illas, The nature of metal-oxide chemical bond: electronic structure of PdMgO and PdOMg molecules, J. Chem. Phys. 107 (18) (1997) 7345–7349.
[14] E. Tea, et al., Atomic bonding and electrical potential at metal/oxide interfaces, a first principle study, J. Chem. Phys. 146 (12) (2017) 124706.
[15] G.V. Gibbs, et al., Classification of metal-oxide bonded interactions based on local potential- and kinetic-energy densities, J. Chem. Phys. 124 (8) (2006) 084704.
[16] W.D. Callister, D.G. Rethwisch, Materials Science and Engineering: An Introduction, Vol. 7, John Wiley & Sons, New York, 2007.
[17] P. Kofstad, Defect chemistry in metal oxides, Phase Transit. 58 (1–3) (1996) 75–93.
[18] D.M. Smyth, The defect chemistry of metal oxides, The Defect Chemistry of Metal Oxides, Oxford University Press, 2000, p. 304. Foreword by D.M. Smyth. ISBN-10:0195110145; ISBN-13:9780195110142.
[19] A. Thursfield, et al., Defect chemistry and transport in metal oxides, Chemical Industries, vol. 108, Marcel Dekker, New York, 2006, p. 55.

[20] T. Zhang, et al., A homogeneous metal oxide catalyst enhanced solid−solid reaction in the hydrogen desorption of a lithium−hydrogen−nitrogen system, ChemCatChem 6 (3) (2014) 724−727.
[21] X. Chen, A. Selloni, Introduction: Titanium Dioxide (TiO_2) Nanomaterials, ACS Publications, 2014.
[22] Y. Yu, et al., The design of TiO_2 nanostructures (nanoparticle, nanotube, and nanosheet) and their photocatalytic activity, J. Phys. Chem. C 118 (24) (2014) 12727−12733.
[23] M. Ge, et al., A review of one-dimensional TiO_2 nanostructured materials for environmental and energy applications, J. Mater. Chem. A 4 (18) (2016) 6772−6801.
[24] M. Giulietti, et al., Industrial crystallization and precipitation from solutions: state of the technique, Braz. J. Chem. Eng. 18 (4) (2001) 423−440.
[25] S. Rohani, N. Tavare, J. Garside, Control of crystal size distribution in a batch cooling crystallizer, Can. J. Chem. Eng. 68 (2) (1990) 260−267.
[26] S.C. Gad, Pharmaceutical Manufacturing Handbook: Production and Processes, vol. 5, John Wiley & Sons, 2008.
[27] S. Lascelles, et al., Effect of synthesis parameters on the particle size, composition and colloid stability of polypyrrole−silica nanocomposite particles, Colloid Polym. Sci. 276 (10) (1998) 893−902.
[28] A. Erdoğdu, et al., The effect of stirring rate on dissolution of colemanite and particle size of gypsum crystals during the boric acid production in a batch reactor, in: U. Uluslararası Bor Sempozyumu, Eskişehir, 2004, pp. 23−25.
[29] B. Jiang, et al., Charge density and chemical bonding in rutile, TiO_2, Acta Crystallogr. A 59 (4) (2003) 341−350.
[30] C. Sousa, F. Illas, Ionic-covalent transition in titanium oxides, Phys. Rev. B 50 (19) (1994) 13974.
[31] K.M. Glassford, J.R. Chelikowsky, Structural and electronic properties of titanium dioxide, Phys. Rev. B 46 (3) (1992) 1284.
[32] H. Chen, C.E. Nanayakkara, V.H. Grassian, Titanium dioxide photocatalysis in atmospheric chemistry, Chem. Rev. 112 (11) (2012) 5919−5948.
[33] B. Hammer, S. Wendt, F. Besenbacher, Water adsorption on TiO_2, Top. Catal. 53 (5−6) (2010) 423−430.
[34] S. Wendt, et al., Oxygen vacancies on TiO_2 (1 1 0) and their interaction with H_2O and O_2: a combined high-resolution STM and DFT study, Surf. Sci. 598 (1−3) (2005) 226−245.
[35] R. Schaub, et al., Oxygen vacancies as active sites for water dissociation on rutile TiO_2 (110), Phys. Rev. Lett. 87 (26) (2001) 266104.
[36] S. Wendt, et al., Formation and splitting of paired hydroxyl groups on reduced TiO_2 (110), Phys. Rev. Lett. 96 (6) (2006) 066107.
[37] G. Žerjav, et al., Effect of surface chemistry and crystallographic parameters of TiO_2 anatase nanocrystals on photocatalytic degradation of bisphenol A, Catalysts 9 (5) (2019) 447.
[38] J.M. Braun, R. Hauser, Bisphenol A and children's health, Curr. Opin. Pediatr. 23 (2) (2011) 233.
[39] S. Yamamoto, et al., In situ x-ray photoelectron spectroscopy studies of water on metals and oxides at ambient conditions, J. Phys. Condens. Matter 20 (18) (2008) 184025.
[40] S. Huygh, A. Bogaerts, E.C. Neyts, How oxygen vacancies activate CO_2 dissociation on TiO_2 anatase (001), J. Phys. Chem. C 120 (38) (2016) 21659−21669.

[41] H. Zhao, F. Pan, Y. Li, A review on the effects of TiO_2 surface point defects on CO_2 photoreduction with H_2O, J. Materiomics 3 (1) (2017) 17–32.
[42] K.M. Ok, et al., Effect of point and planar defects on thermal conductivity of TiO_{2-x}, J. Am. Ceram. Soc. 101 (1) (2018) 334–346.
[43] N.A. Abd Samad, C.W. Lai, S.B. Abd Hamid, Influence applied potential on the formation of self-organized ZnO nanorod film and its photoelectrochemical response, Int. J. Photoenergy 2016 (2016).
[44] G.S. Alghamdi, A.Z. Alzahrani, Bonding formation and orbitals nature of ZnO structure, Middle East J. Sci. Res. 13 (9) (2013) 1144–1149.
[45] H. Morkoç, Ü. Özgür, Zinc Oxide: Fundamentals, Materials and Device Technology, John Wiley & Sons, 2008.
[46] G.V. Aguilar, et al., Photoluminescence studies on ZnO thin films obtained by sol-gel method, in: Recent Applications in Sol-Gel Synthesis, 2017, p. 195.
[47] B. Ludi, M. Niederberger, Zinc oxide nanoparticles: chemical mechanisms and classical and non-classical crystallization, Dalton Trans. 42 (35) (2013) 12554–12568.
[48] C. Wöll, The chemistry and physics of zinc oxide surfaces, Prog. Surf. Sci. 82 (2–3) (2007) 55–120.
[49] R. Laudise, A. Ballman, Hydrothermal synthesis of zinc oxide and zinc sulfide, J. Phys. Chem. 64 (5) (1960) 688–691.
[50] C. Lizandara-Pueyo, et al., Nucleation and growth of ZnO in organic solvents—an in situ study, J. Am. Chem. Soc. 130 (49) (2008) 16601–16610.
[51] Ü. Özgür, et al., A comprehensive review of ZnO materials and devices, J. Appl. Phys. 98 (4) (2005) 11.
[52] S. Morrison, P. Miller Jr, Adsorption of oxygen on zinc oxide, J. Chem. Phys. 25 (5) (1956) 1064–1065.
[53] I.A. Mudunkotuwa, et al., Dissolution of ZnO nanoparticles at circumneutral pH: a study of size effects in the presence and absence of citric acid, Langmuir 28 (1) (2011) 396–403.
[54] Z. Abbas, et al., Size-dependent surface charging of nanoparticles, J. Phys. Chem. C 112 (15) (2008) 5715–5723.
[55] C. Chandrinou, et al., PL study of oxygen defect formation in ZnO nanorods, Microelectron. J. 40 (2) (2009) 296–298.
[56] X.-Y. Shen, Y.-C. Zhai, Y.-H. Zhang, Preparation and characterization of ultrafine zinc oxide powder by hydrothermal method, Trans. Nonferrous Met. Soc. China 20 (2010) s236–s239.
[57] A. Djurišić, et al., Defect emissions in ZnO nanostructures, Nanotechnology 18 (9) (2007) 095702.
[58] N.H. Alvi, Luminescence Properties of ZnO Nanostructures and Their Implementation as White Light Emitting Diodes (LEDs), Linköping University, 2011.
[59] F. Kröger, H. Vink, The origin of the fluorescence in self-activated ZnS, CdS, and ZnO, J. Chem. Phys. 22 (2) (1954) 250–252.
[60] S. Studenikin, N. Golego, M. Cocivera, Fabrication of green and orange photoluminescent, undoped ZnO films using spray pyrolysis, J. Appl. Phys. 84 (4) (1998) 2287–2294.
[61] S. Yamauchi, Y. Goto, T. Hariu, Photoluminescence studies of undoped and nitrogen-doped ZnO layers grown by plasma-assisted epitaxy, J. Cryst. Growth 260 (1) (2004) 1–6.
[62] A. Janotti, C.G. Van de Walle, Native point defects in ZnO, Phys. Rev. B 76 (16) (2007) 165202.

[63] H. Zhou, et al., Behind the weak excitonic emission of ZnO quantum dots: ZnO/Zn $(OH)_2$ core-shell structure, Appl. Phys. Lett. 80 (2) (2002) 210−212.
[64] N.A. Abd Samad, C.W. Lai, S.B. Abd Hamid, Easy formation of nanodisk-dendritic ZnO film via controlled electrodeposition process, J. Nanomater. 2015 (2015).
[65] C.W. Lai, S. Sreekantan, Photoelectrochemical properties of TiO_2 nanotube arrays: effect of electrolyte pH and annealing temperature, J. Exp. Nanosci. 9 (3) (2014) 230−239.
[66] K. Dai, et al., Photocatalytic degradation and mineralization of commercial methamidophos in aqueous Titania suspension, Environ. Sci. Technol. 42 (5) (2008) 1505−1510.
[67] K.A. Alim, V.A. Fonoberov, A.A. Balandin, Origin of the optical phonon frequency shifts in ZnO quantum dots, Appl. Phys. Lett. 86 (5) (2005) 53103.
[68] Y. Ding, Z.L. Wang, Structures of planar defects in ZnO nanobelts and nanowires, Micron 40 (3) (2009) 335−342.
[69] R. Deng, et al., Planar defects in Sn-doped single-crystal ZnO nanobelts, J. Phys. Chem. C 111 (35) (2007) 13013−13015.
[70] D. Shao, et al., High quality ZnO−TiO_2 core−shell nanowires for efficient ultraviolet sensing, Appl. Surf. Sci. 314 (2014) 872−876.
[71] L.E. Greene, et al., ZnO-TiO_2 core-shell nanorod/P3HT solar cells, J. Phys. Chem. C 111 (50) (2007) 18451−18456.
[72] S. Panigrahi, D. Basak, Core−shell TiO_2@ZnO nanorods for efficient ultraviolet photodetection, Nanoscale 3 (5) (2011) 2336−2341.

This page intentionally left blank

Synthesis and preparation of metal oxide powders

3

C.H. Voon[1], K.L. Foo[1], B.Y. Lim[2], S.C.B. Gopinath[1,3] and Y. Al-Douri[4,5,6]
[1]Institute of Nano Electronic Engineering (INEE), University of Malaysia Perlis, Kangar, Malaysia, [2]School of Materials Engineering, University of Malaysia Perlis, Arau, Malaysia, [3]School of Bioprocess Engineering, University of Malaysia Perlis, Arau, Malaysia, [4]University Research Center, Cihan University Sulaimaniya, Sulaymaniyah, Iraq, [5]Nanotechnology and Catalysis Research Center (NANOCAT), University of Malaya, Kuala Lumpur, Malaysia, [6]Department of Mechatronics Engineering, Faculty of Engineering and Natural Sciences, Bahcesehir University, Istanbul, Turkey

3.1 Introduction

Metal oxide, particularly in the powder form, has attracted much interest due to their tailorable electrical, magnetic, mechanical, and optical properties that can be used in wide range of applications. Until recently, various metal oxide, such as TiO_2, ZnO, SnO_2, CuO, and so on, were synthesized and studied for practical applications. The synthesis and preparation of metal oxide powders can be dated back to 100 years ago. Since then, many new methods and techniques have been reported for the preparation of high-quality metal oxide powders. The motivation of these efforts is the irreplaceable roles of these synthetic metal oxide powders in current and future industrial applications due to the absence of natural equivalents. Although some of the metal oxide can be obtained naturally from minerals, however, these metal oxides are not easily available for applications due to some reasons. Naturally occurring metal oxides were formed by the crystallization of multicomponent dry or aqueous melts into rocks followed by weathering action of the natural agencies on the formed rocks during the old geological times through millions of years involving prolonged interaction of a large number of ionic constituents [1]. For this reason, naturally occurring metal oxides are generally impure, and the variation of the composition of the minerals from different origins is unacceptably large. Therefore the direct application of naturally occurring metal oxides in the industry is almost impossible.

The efforts to enhance the purity of naturally occurring metal oxides to certain specifications are often uneconomical. Although the size distribution of metal oxide powders obtained by the milling of natural minerals can be controlled to a certain extent, the size distribution of synthetic metal oxides powders can be optimized to obtain desired size range, down to unagglomerated nanoparticles, or even nearly monosized powders by recently reported processes in different scales of operation [2,3]. Besides, some of the solution and vapor-based process can control the shape of the synthetic

Metal Oxide Powder Technologies. DOI: https://doi.org/10.1016/B978-0-12-817505-7.00003-8

metal oxide particles [4], while natural metal oxide powders are generally angular in shape due to the milling process. Generally, for most processing and applications which require homogeneous microstructure for enhanced and uniform densification, the ideal shape of the powder should be an equiaxed shape. The simplest equiaxed shape is that of sphere. In this aspect, synthetic metal oxide powders of controlled size and shape have advantages over the crushed and milled irregular powders from natural minerals. For this reason, synthetic metal oxide powders that have controlled purity, size, and shape are in favor of natural metal oxide powders from minerals.

In this chapter, recent progress on the synthesis and preparation of metal oxide powders is highlighted. This chapter will present most widely reported processes of metal oxide powder preparation, with relatively few descriptions about less reported, new processes as and when felt necessary. This chapter is organized into three sections. After a brief introduction of metal oxide powders in Section 3.1, Section 3.2 focuses on the various approaches for rational synthesis and preparation of various metal oxide powders, which can be divided into chemical methods, physical methods, and biological methods. This chapter ends in Section 3.3 with a concluding remark on the recent progress and future challenges in this field.

3.2 Synthesis and preparation of metal oxide powders

Significant progress of synthesis and preparation of various metal oxide powders has been achieved. The methods for the preparation and synthesis of metal oxide powders can be broadly categorized into physical and chemical method. The physical methods are mostly based on thermally and mechanically induced chemical reactions, while chemical methods are based on the precipitation or decomposition of precursors to form new compound [5]. Besides, biological methods that involved the fungi-mediated, bacteria-mediated, and plant-mediated synthesis were also explored. For these methods, two approaches are employed for the synthesis and preparation of metal oxide powders, namely, bottom-up approach and top-down approach. A bottom-up approach is also known as the self-assembly process, which involves the assembly of smaller building blocks to form the desired structure, such as coprecipitation, sol−gel, hydrothermal, solvothermal, microemulsion, and chemical vapor reactions [5]. On the contrary, the top-down approach involves the removal or etching of bulk matter for the formation of the smaller desired structure, including mechanical crushing, pulverization, grinding, milling, mechanical activation, and mechanochemical reaction [5]. Both of these approaches were used in the physical and chemical method for the preparation and synthesis of metal oxide powders. In this section, recent progress in the synthesis and preparation of metal oxide powders using chemical, physical, and biological methods are addressed.

3.2.1 Chemical methods

This section focuses on various chemical synthesis methods that are gaining rapid popularity for large-scale production of metal oxide powders. Most of the metal

oxide powders prepared through chemical methods are based on liquid processing. The chemical pathways for the preparation of metal oxides powders are mainly based on metal compounds, such as hydrothermal method and sol−gel method.

These methods normally involve the synthesis of a precursor gel of metal and decomposition of precursor or gel to the desired structure and crystalline of metal oxide powders under a certain temperature. In this session an effort has been made to summarize, with suitable examples, the methods developed by the researchers for the synthesis of metal oxide powders, especially nanopowders. Therefore five most widely used chemical-based methods that have been developed are discussed in this section, which are sol−gel method, hydrothermal method, chemical vapor deposition (CVD) method, thermal decomposition method, and sonochemical method.

3.2.1.1 Sol−gel method

Sol−gel process, which is also called soft-chemistry or wet-chemical, is widely used in metal oxide, materials science, glassy, and ceramic engineering. This method might obtain functional material through low-temperature process. Sol−gel can be briefly defined as the preparation of metal oxide material by preparing the sol (mostly colloidal), gelation of the sol, and removal of the solvent [6]. An overview of the sol−gel process is shown in Fig. 3.1. Fig. 3.1 shows that sol−gel method allows the preparation of solid from solution by using a sol or a gel as an intermediate step at much lower temperatures than other methods. Plenty of metal oxide has been synthesized using this method, such as ZnO [7−12], TiO_2 [13−16], and SnO_2 [17−21]. Sol−gel method is a well-known process in synthesizing metal oxide nanopowders due to its low temperature and low-cost process, using less amount of precursor material for preparing sol solution, can be evenly spread on the substrate, high purity process lead to high homogeneity, possibility of synthesizing highly volatile substances, and high melting temperature, and possibility of producing various forms of structures. However, this attractive process still has its disadvantages. One of them is the shrinkage of the product once it is dried. Besides that, due to the different reactivity of the alkoxide precursors, the precipitation of specific oxides during sol formation is possible. Third, it is difficult to avoid hydroxyl group or residual porosity.

Commonly, the sol−gel process involves the use of a precursor in which the solid material is mixed with a liquid solution (solvent). A colloidal solution (sol) is formed after the mixture is undergoing hydrolysis and polycondensation reactions. Metal alkoxides (alcoholates and propoxides) and metal salts, such as nitrates, acetates, perchlorates, and chlorides, are precursors that normally used in the preparation of "sols." Furthermore, the dielectric constant of a solvent is the main factor for determining the polarity and solubility of the precursor in solution. Generally, solvents with higher polarity have higher dielectric constants. Apart from that, metal salts give high solubility in highly polar solvents. Thus the solvent used must have a high dielectric constant to dissolve the metal salt [22,23].

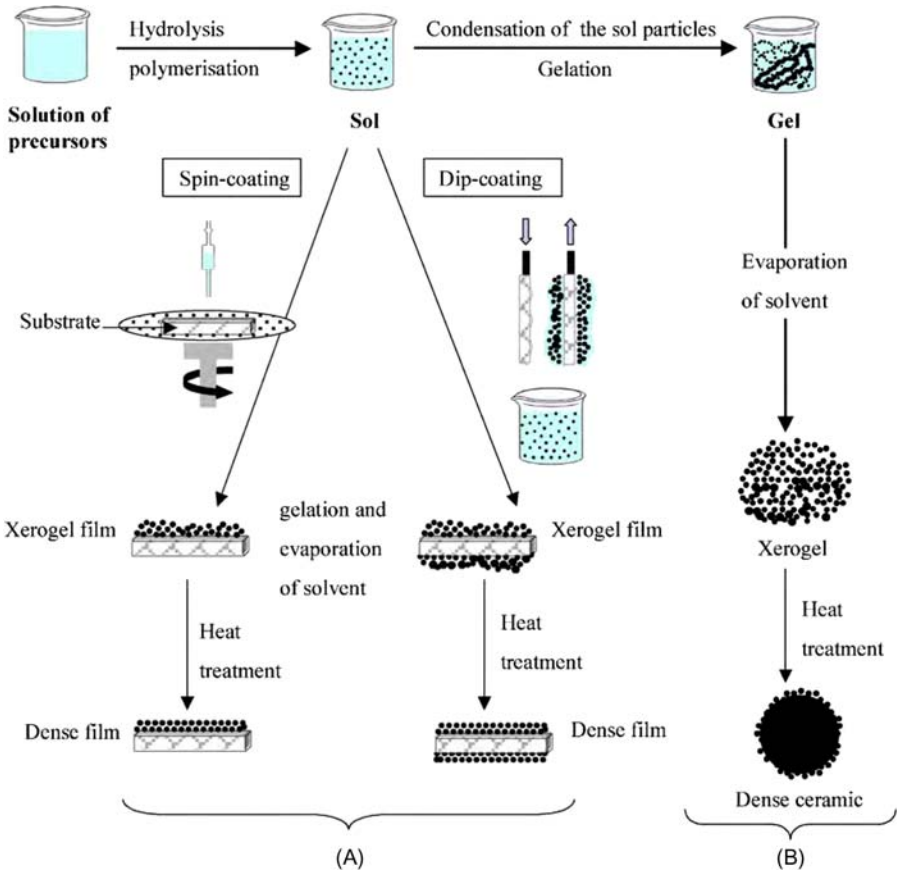

Figure 3.1 Overview of two synthesis process from sol−gel method; (A) films from a colloidal sol; (B) powder from a colloidal sol transformed into a gel.

Shojaie-Bahaabad and Taheri-Nassaj [24] prepared alumina (Al_2O_3) powder through simple aqueous sol−gel method. They used aluminum chloride hexahydrate ($AlCl_3 \cdot 6H_2O$), aluminum (Al) powder, and HCl as raw materials. In this method, $AlCl_3 \cdot 6H_2O$ was first mixed with HCl then Al powder was added gradually into the solution. The mixed solution was stirred for 4 hours at 95°C then dried for 48 hours at 85°C. The obtained dried gel was ground and calcined in a furnace with varies temperatures (600°C−1400°C). Finally, the dried powder was ball milled in ethanol media using a high dense alumina jar and highly pure alumina balls. The obtained results showed that α-Al_2O_3 is hardly formed with gel heat treated below 1100°C. Besides that, Al_2O_3 sample heat treated at 1200°C showed the particles were spherical in shape and in the range of 32−100 nm.

Omanwar et al. [25] synthesized inorganic Al_2O_3 nanopowders using citric acid sol−gel, stearic acid sol−gel, and aldo-keto gel method. All these three methods

used $Al(NO_3)_3 \cdot 9H_2O$. Among these three methods, stearic acid and acetic acid were used in stearic acid sol−gel method, citric acid and ethylene glycol ($C_2H_6O_2$) were used in citric acid sol−gel method, while aldo-keto gel method used acetone and benzaldehyde. It was found that sample prepared using stearic acid sol−gel method gave the highest crystallite size but lowest bandgap, which are 33.1149 nm and 4.2 eV, respectively. On the other hand, citric acid sol−gel prepared Al_2O_3 nanopowders showed the lowest crystallite size (29.3247 nm) but highest bandgap (5.08 eV). Under fluorescence analysis, Al_2O_3 nanopowders showed an intense blue luminescence at 224 nm irradiation. Besides that, blue emission peaks for stearic acid sol−gel, aldo-keto gel, and citric acid sol−gel method were observed at 397, 399, and 401 nm, respectively. Omanwar et al. suggested that these materials may be suitable for ceramic, sensing, and biocompatible materials application.

Jeyarani et al. [26] produced CuO nanopowders using sol−gel route with varies concentration of glucose (0.1, 0.5, and 1 M), which acted as a capping agent. CuO powder has been prepared by dissolving copper nitrate [$Cu(NO_3)_2 \cdot 3H_2O$] in ethanol and stirred for 1 hour at room temperature. Then, glucose was added into the solution and stirred for another 40 minutes. The prepared solution has to undergo gel formation by keeping it for 24 hours. Finally, the gel was dried, calcined, and annealed at 200°C, 300°C, and 500°C, respectively. X-ray diffraction analysis (XRD) results indicated that crystallite size of CuO nanoparticles decreased with the increasing glucose concentration. This result was in good agreement with the SEM image shows in Fig. 3.2, which shows the high tendency of agglomeration for uncapped CuO nanoparticles. Besides that, the SEM image also shows that CuO nanopowders became more homogeneous with the increase of glucose concentration. The Tauc's plots indicated that CuO nanopowder without capping agent (glucose) gave the lowest bandgap (1.7 eV) and the bandgap increased with increasing capping agent concentration. This phenomenon might be due to the reduction of particle size, which leads to the increase of bandgap.

By using sol−gel method, Wang et al. [27] successfully produced rutile TiO_2 from anatase phase of TiO_2. In this process, two solutions have been first prepared separately, which were mixture of titanium tetraisopropoxide (TTIP, 20 mL) and ethanol (30 mL) and mixture of acetone (7.5 mL) with ethanol (15 mL). Both solutions were then mixed and stirred for 90 minutes at room temperature. The gel product was then aged at room temperature for 72 hours and dried at 50°C for another 72 hours. They successfully transformed anatase phase of TiO_2 to rutile phase after calcining at 1000°C for 1 hour. Besides that, they also reported that calcination duration can affect the crystallinity of TiO_2. According to Wang et al., crystallinity of rutile TiO_2 increased with the increasing calcination duration while the intensities of anatase TiO_2 decreased with increasing calcination duration. Besides TiO_2, many doped TiO_2 powder were also synthesized through sol−gel method [28−31].

3.2.1.2 Hydrothermal method

Hydrothermal method, a promising approach in fabricating low dimensional hierarchical structure metal oxide, is an important and popular synthesis method, which

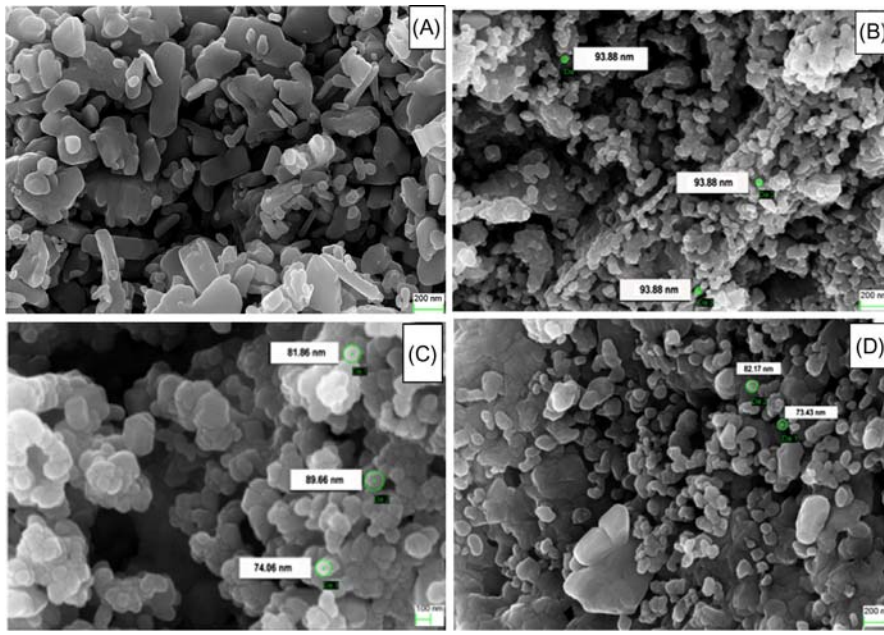

Figure 3.2 SEM images of (A) CuO and glucose-capped, (B) CuO/0.1 M, (C) CuO/0.5 M and (D) CuO/1 M nanopowder.

gathered interest from scientist and technology, especially in the last 15 years. This method was firstly used by a British geologist, named Sir Roderick Murchison. Hydrothermal method, generally defined as crystal synthesis or crystal growth of particles, involves heterogeneous reaction with the presence of aqueous solvent or mineralizes and recrystallize material that are relatively insoluble [32]. This method is usually conducted below critical temperature and the pressure of water, which are 374°C and 22.1 MPa, respectively [33]. This process can be used to synthesis materials with different types of geometry or morphology, such as thin film, single crystal, nanocrystals, and bulk powder [32].

Compared to vapor-phase and other solution-based method, hydrothermal approach has the advantages of energy saving, good in controlling the size and morphology, easy on manipulation, and good capability and flexibility. There are many factors that can affect the outcome of the synthesized product, such as solution pH value, concentrations of the reactants, presence of surfactants, nature of the substrate, deposition temperature, and time [34]. Many metal oxides have been successfully synthesized by this method, such as ZnO [35–38], TiO_2 [39–43], and CuO [44–46]. A setup to synthesize nanopowders using hydrothermal approach generally has a tubular reactor and consists of two parts. This setup consists of syringe pump, two piston pumps, back pressure valve, flow mixer, electric furnace with fluidized sand bed, cooler, pressure gauges, and manometers [47]. Another type of hydrothermal setup is normally named as autoclaves or hydrothermal bomb.

This kind of setup is usually used for synthesizing powder or nanostructure under harsh chemical condition, where the synthesis is conducted at high temperature, high pressure, and/or with the presence of corrosive liquid. Therefore stainless steel, tantalum, hastelloy, or titanium is normally used to manufacture this autoclave. Besides that, inner wall of the autoclaves is coated with Teflon, which is inert with most of the chemical.

Fang et al. [48] successfully synthesized spherical ZnO and flower-like ZnO powders through facile hydrothermal method. For flower-like ZnO, they dissolved 0.25 g of zinc acetate dihydrate [$Zn(CH_3COO)_2 \cdot 2H_2O$] in 10 mL of deionized water. Then, 2.1 g of sodium hydroxide (NaOH) mixed with 30 mL of deionized water was added dropwise into the previously prepared solution. Next, 0.12 g surfactant cetyltrimethyl ammonium bromide (CTAB) was dissolved into the prepared solution and subjected to 30 minutes sonic oscillation and heating in autoclave for 12 hours at 160°C. The precipitate was then dried in vacuum oven for 6 hours at 60°C. On the other hand, Fang et al. also used zinc acetate (4.4 g) and deionized water (200 mL) to produce spherical ZnO by adding 7.9 g of glucose in the mixed solution and autoclaved for 12 hours at 180°C and calcined at 600°C for 3 hours. They successfully prepared one-dimension ZnO with hexagonal wurtzite structure with the diameter of about 100−400 nm. Besides, Raman and photoluminescence analysis also suggested that as-prepared ZnO exhibited excellent optical properties, whereby Raman spectrum showed the ZnO hexagonal wurtzite structure contained four atoms and this unit cell belonged to the space group of C_6v^4 (P6_m mc) [49]. On the other hand, photoluminescence analysis showed a sharp peak and a broad peak at 392 and 520 nm, respectively. The sharp peak was associated with the UV emission eigen peak, while the broad peak might be due to defect-state luminescence which was related to the electron acceptors or defects such as Zn vacancy or O interstitials in ZnO. Besides that, this might also be related to the oxygen adsorbed in ZnO grain boundaries [50,51].

In another study, Wang et al. [52] synthesized dumbbell-shaped ZnO powders using facile hydrothermal method. In a typical procedure, 1.8 g of zinc nitrate hexahydrate [$Zn(NO_3)_2 \cdot 6H_2O$], 20 mL of deionized water and ammonium hydroxide ($NH_3 \cdot H_2O$) were mixed and stirred for 20 minutes. Then, the mixture solution was poured into a Teflon-lined stainless-steel autoclave and heated for 10 hours in an oven. Finally, obtained product was kept dry at 80°C for 12 hours. The obtained ZnO powders were in hexagonal wurtzite with calculated lattice constants of $a = 3.21$ Å and $c = 5.19$ Å. This result was in good agreement with bulk hexagonal wurtzite ZnO, which are $a = 3.25$ Å and $c = 5.21$ Å (JCPDS No. 36-1451) [53,54]. Aside from that, SEM images shows in Fig. 3.3 confirmed that synthesized ZnO showed dumbbell shaped with hexagonal wurtzite structure. The measured dumbbell-shaped ZnO length was about 5−20 μm and diameter of the middle part and two ends were about 1−5 and 0.5−3 μm, respectively. Wang et al. claimed that they successfully produced dumbbell-shaped ZnO powders that were not reported previously [55−57]. In another study, Baranwal et al. [58] successfully synthesized dumbbell-shaped ZnO powders using zinc acetate dihydrate, potassium hydroxide (KOH), and starch. SEM images indicated that ZnO powders synthesized by using

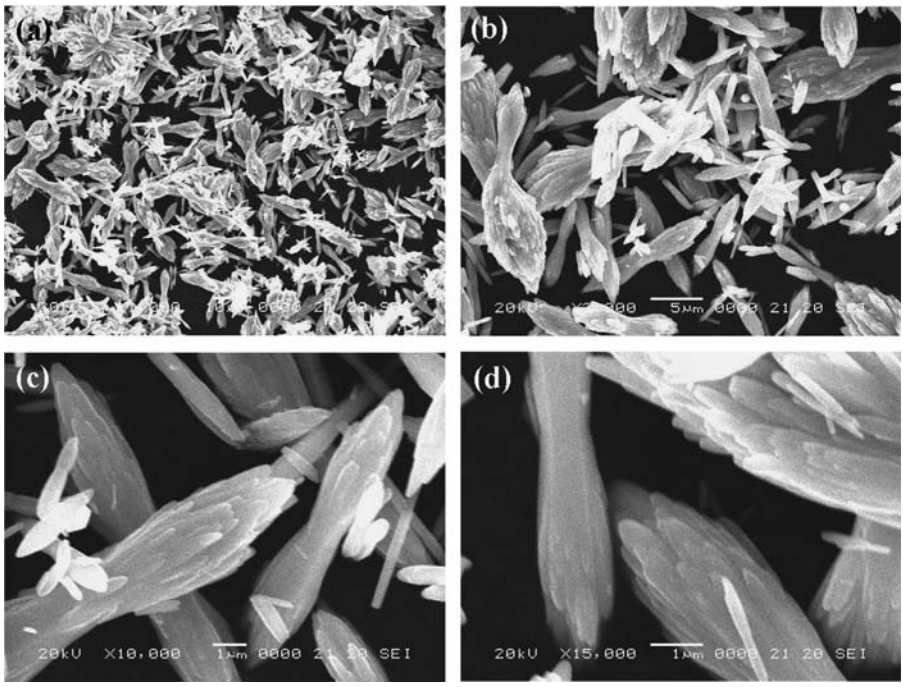

Figure 3.3 SEM images of the dumbbell-shaped ZnO microstructures with different magnification: (A and B) low magnification; (C and D) high magnification.

these chemicals also have dumbbell-shaped microstructures with the length of 5−13 μm. The diameter of the middle part and the end of the rods are 1.5−6 and 2−5 μm, respectively. Besides that, the surface of the dumbbell-shaped ZnO powders is rough and these dumbbell-shaped ZnO powders have spherical shape at both ends.

3.2.1.3 Chemical vapor deposition

There are many definitions of CVD in the published literature. However, there is a common definition to the CVD process—due to the chemical reaction, a solid material is deposited through a complex process. A typical material is formed under this deposition method or is commonly referred to as vapor ordered crystal growth. This method is good for forming a high-purity and high-quality solid materials. This is the method usually used in the semiconductor industry for depositing thin films. In this method, raw materials in gaseous state are flown into the reaction chamber. This process is actually just like physical vapor deposition (PVD). However, the raw materials used in PVD is in the form of solid powder. CVD process for metal oxide powder preparation involves the delivery of precursor in gas state (vapor) into the reaction chamber. Once the precursor gas contacts with the heated

substrate's surface, a chemical reaction occurs and decomposes and forms a solid state which then deposits onto the substrate.

There are several types of CVD, such as low-pressure CVD (LPCVD), atmospheric pressure CVD (APCVD), metalorganic CVD (MOCVD), and plasma-enhanced CVD (PECVD). The deposition process of LPCVD process occurs at sub-atmospheric pressures, while APCVD occurs at atmospheric pressure. PECVD increases the rate of chemical reaction through plasma, and this process allows to carry out at room temperature. MOCVD uses metallo-organics (types of chemical compound that contain metal and organic materials) as a precursor. Due to unnecessary gas-phase which could be reduced in the deposition chamber, low pressures deposition usually might increase the uniformity of the products. The advantages of CVD method are CVD can be operated at a wide range of temperatures, different orientations of substrate are possible, simple to operate, can accommodate several substrates, and able to provide uniform substrate temperature. However, this method has it disadvantages—deposition occurs not only at the substrate but also on reactor walls and the consumption of precursor is large and difficult to control which may result in feed-rate-limited deposition. Even so, there are researchers using CVD method to synthesize metal oxide powders, such as TiO_x [59,60], ZnO [61–64], and In_2O_3 [65–67].

Singh et al. [68] produced ZnO nanocrystalline powder through ultrasonic mist-CVD (UM-CVD). This UM-CVD setup consisted of three zones—ultrasonic spray zone (composed of a liquid source atomization system with an ultrasonic atomizer and an ultrasonic atomized droplet carrying system with air carrier gas), evaporation zone (heating zone, where the atomized droplets were pyrolyzed in a preheated reactor maintained at 400°C and deposition zone (used to capture the produced powder). In their study, 0.1 M of zinc nitrate $[Zn(NO_3)_2 \cdot 6H_2O]$ was used as the precursor. Then, liquid atomization was used to deliver the zinc nitrate solution to the reactor. Then, atomized droplets that contained precursor passed through the reactor and finally collected on a special geometry. Singh et al. reported that the obtained ZnO particles have hexagonal wurtzite structure with the crystallinity of ZnO powder increased with the increase of temperature. In addition, Singh et al. also observed that as the temperature rose from 100°C to 1000°C, the lattice parameters ("a" and "c") and particle size increased.

Lukić et al. [69] produced alumina (Al_2O_3) nanopowders through chemical vapor synthesis method. In their study, aluminum-tri-sec-butoxide (ATSB) and oxygen gas were used as the starting materials. A bubbler filled with liquid ATSB was placed in an oil bath. The temperature was controlled at 165°C. Then, helium gas (carrier gas for ASTB) was flowed at 200 and 300 sccm and the oxygen gas was controlled at 1500 sccm. Besides that, alumina tube was heated at 900°C. The entire process was done at low pressure of 20 and 30 mbar. Their XRD results confirmed the formation of η- and γ-alumina, respectively. They also reported that the crystallinity and crystallite size of Al_2O_3 increased from the entrance, in the tube and after the collector. This is due to the presence of noncrystalline phase in the powder which might contain more residual organic and unreacted precursor. The synthesized nanopowders composed of very fine primary particles with loose agglomeration.

Other than η- and γ-alumina phases, other phases of alumina such as δ-, θ-, κ-, and χ- alumina were also produced. For example, Dhonge et al. [70] produced γ- and θ-alumina using combustion CVD. In their experiment, 0.005 M of aluminum acetylacetonate dissolved in ethanol was used as the precursor. Aluminum acetylacetonate was atomized through static ultrasonic nebulizer using 1.7 MHz resonator and the deposition temperature was set at the range of 600°C to 900°C. The XRD results indicated that γ- and θ- alumina phase exist in the sample deposited at 600°C to 800°C while high intensity and sharp peaks of θ-alumina phase were observed at 900°C.

3.2.1.4 Thermal decomposition processing

Thermal decomposition (also called thermolysis) is caused by the chemical decomposition of a material under high temperature, in which the decomposition temperature of a material is the temperature at which the material chemically decomposes. Technically, it is a subcategory of solvothermal. However, it is also considered as a separate subcategory of solution-phase synthesis. Typically, this decomposition and consolidation of the precursor (usually an organometallic compound) is carried out at a high boiling point, coordinating or noncoordinating solvent under high temperature and normal ambient pressure [71–73].

The components that normally used in thermal decomposition process are precursor, solvent, and ligands. The precursor is referring to the source of the metal in producing metal oxide and normally is metal acetylacetonates or acetates. The solvent is used to provide the environment for the reaction to occur, and usually it is a high boiling point organic solvent, such as benzyl ether, 1-octadecene, and phenyl ether. Ligands (the term comes from coordination chemistry) refers to the molecular moieties or molecules that are capable of binding to the center ion or metal atom with accessible orbits. Coordination of ligands to surface atoms has the function of controls or limits growth of metal oxide, stabilizes the nanocrystals, and alters the properties of the metal oxide. The ligand is normally referring as surfactant in the context of thermal decomposition. Recently, number of high-quality metal oxide nanopowders have been produced using thermal decomposition method [74–80].

Alp et al. [80] synthesized nanocrystalline ZnO through ethylene glycol-mediated thermal decomposition. In a typical procedure, mixed solution of zinc acetate dihydrate (2 g) and ethylene glycol (15 mL) was heated at different duration (3, 6, 12, and 36 hours) at 250°C with heating rate of 4°C/min. This method produced about 0.73 g of ZnO powder, which consider a very efficient method ($>98\%$). They reported that ZnO powders produced at 250°C and 12 hours are in the form of broken spheres with a hollow microsphere (average size of 3.01 ± 0.52 μm). The ZnO powder was wurtzite ZnO phase with lattice parameters of $a = 0.3298$ nm and $c = 0.5206$ nm. They also reported that the longer the heating duration (up to 36 hours), the more ZnO microspheres were produced and finally sample heated for 12 hours showed all ZnO was composed of hollow microspheres (3.84 ± 0.81 μm). In their study, ethylene glycol acted both as a solvent and a soft template/surfactant, creating spherical-like nanocrystallites by hindering the diffusion for the formation of commonly obtained ZnO

nanowires, then these spherical nanoparticles assemble to become mesoporous hollow microspheres [81].

The same materials and methods were used by Dong and Feldmann [82] in which in their study, the amount of glycerol, heating temperature, and refluxed duration were changed, which were 50 mL, 160°C, and 1 hour, respectively. Besides that, the authors synthesized porous ZnO platelets through different thermal procedures (fast, medium, and slow thermal decomposition). Their experiment results showed that the diameter of the produced porous ZnO platelets under fast thermal decomposition was about 200−300 nm while porous ZnO platelets synthesized under medium thermal decomposition produced smaller particles with the diameter of about 10−30 nm. In contrast, due to irregular agglomeration of ZnO nanoparticles, the diameter of porous ZnO platelets prepared under slow thermal decomposition was increased (100−200 nm).

Besides ethylene glycol, ZnO spherical porous powders can also be produced using thermal decomposition of zinc palmitate (ZnP). In the study conducted by Kontopoulou et al. [83], 150 mg analytical grade of ZnP was heated in porcelain crucibles at different temperature (500°C, 650°C, and 800°C) with heating rate of 10°C/min for 6 hours. Then, the sample was cooled down under regular cooling procedures. In addition, in the case of heating at 800°C, quenching of the sample in air at room temperature was performed. ZnO powders in the hexagonal wurtzite-type of ZnO structure were obtained. However, SEM image in Fig. 3.4 shows that ZnO calcinated at 500°C (Fig. 3.4A) yielded well-dispersed grain with an average crystallite size of 96 ± 29 nm, while ZnO calcinated at 800°C (Fig. 3.4C and D) yielded spherical porous particles composed of many sintered ZnO nanocrystals. Besides, quenching in air after calcination at 800°C also led to the formation of products with few spherical particles and consisted mainly of sintered grains with a mean diameter of 189 ± 65 nm as in Fig. 3.4E and F.

3.2.1.5 Sonochemical method

Sonochemical method, a method using high-intensity ultrasonic irradiation, has been widely used to produce novel materials with unusual properties and to obtain highly crystalline nanomaterials. Due to the powerful ultrasound radiation (20 kHz to 10 MHz), molecules undergone several chemical reactions. The supplied ultrasound attributes to the generation, growth, and collapse of bubbles in the liquid phase [84−86].

There are two kinds of sonochemical reaction, which are homogeneous (produced by the formation of free radicals) and heterogeneous sonochemistry (resulting from the mechanical effects of cavitation) [86,84]. The cavitations are generated from the liquid phase expansion and compression cycle. When the cavitation occurred very close to the electrode surface, a liquid jet passes through inside the bubble, which is perpendicular to the surface of the electrode, resulting in the formation of a high-velocity microjet toward the surface [87]. The collapse of bubbles due to the ultrasound intensity is higher than the threshold intensity is also related to the shock wave [88] and the microstreaming [89]. This phenomenon causes a decrease in the thickness of the diffusion layer [90,91]. Moreover, this situation

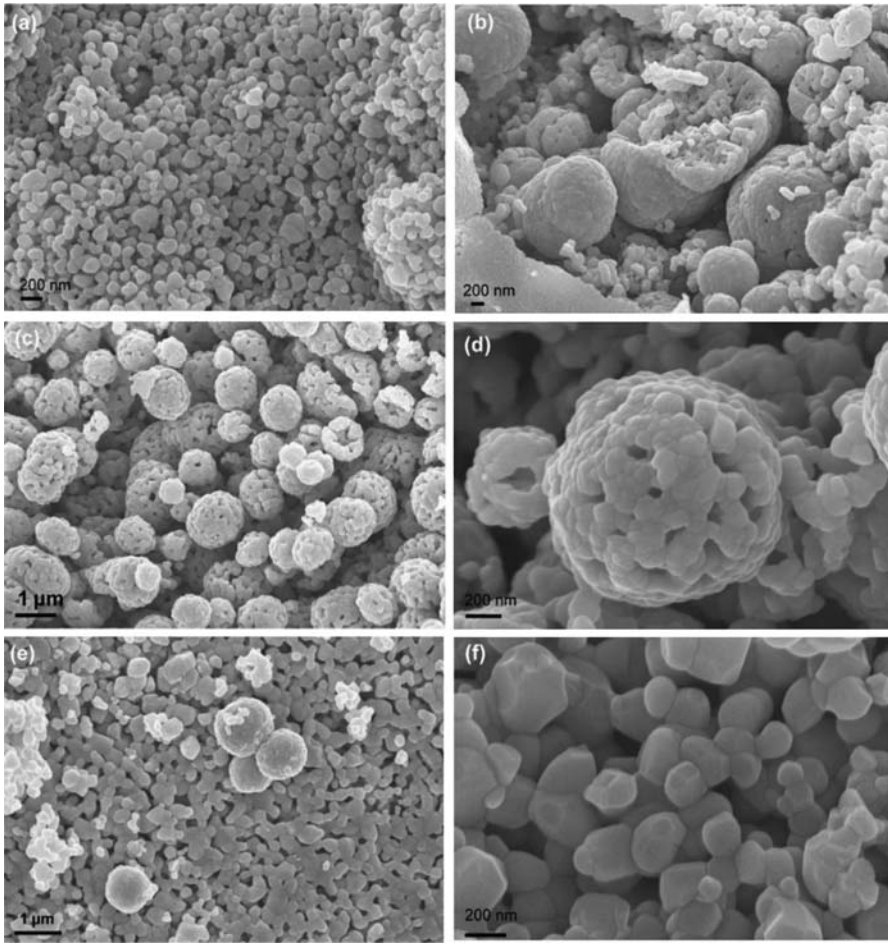

Figure 3.4 SEM images of ZnO nanoparticles and nanostructures synthesized at: (A) 500°C, (B) 650°C, (C) and (D) 850°C, (E) and (F) 850°C after quenching.

improves the overall mass transfer and increases the reaction rate, which is actually the cleaning and degassing of the electrode surface [84,87,92]. This method was first used to produce iron nanoparticles. Since then, it has been used to synthesize various metal oxide, such as CuO [93–95], TiO_2 [96,97], and NiO [98–100].

The advantages of using sonochemical method to produce metal oxide powders are this method can be operated under ambient conditions, crystalline phase can be obtained by annealing at a relatively low temperature, and the mixing of the constituent ions in the amorphous phase is at the atomic level [5]. However, sonochemical method also consists of some drawbacks—this method has to be conducted under argon atmosphere and irregular/random morphology of nanoparticles are normally obtained and long processing time and heating duration are required [101].

Bhosale and Bhanage [101] developed a simple, simple, economical, additive free, and capping agent-free approach for the synthesis of Cu_2O nanoparticles via sonochemical method using only two reagents, that is, copper acetate as a precursor and glycerol as a green solvent. In this study the mixture 0.5 g of copper acetate and 15 mL of glycerol underwent sonochemical irradiation through ultrasonic horn with 20 kHz frequency and 750 W for 0.5, 1.0, and 1.5 hours, respectively. Then the product was centrifuged at 8000 rpm for 10 min and rinsed with deionized water and ethanol for several times and then dried in oven. They reported that Cu_2O nanoparticles did not appear in sample sonicated for 0.5 hour, while 1.0 hour sonicate time was the sufficient time for the formation of Cu_2O nanoparticles. The particle size of Cu_2O nanoparticles measured from TEM was in the range of 80−150 nm in Fig. 3.5. Fig. 3.5 also shows spherical Cu_2O nanoparticles are in good dispersion. HRTEM analysis shown in Fig. 3.6 indicated that the interplanar distance was about 0.279 nm and corresponds to the *d* spacing of the (1 1 1) plane. Brunauer−Emmett−Teller (BET) result showed that the Cu_2O nanoparticles have higher BET surface area than commercial Cu_2O, which leads to the high catalytic activity.

Instead of copper acetate, Kaviyarasan et al. [102] used copper sulfate pentahydrate ($CuSO_4 \cdot 5H_2O$) as a precursor. In their work, 50 mL of copper sulfate pentahydrate was brought into a sonication container followed by purging nitrogen gas for 30 minutes. A quantity of 52.8 mg ascorbic acid was then dissolved in 15 mL of

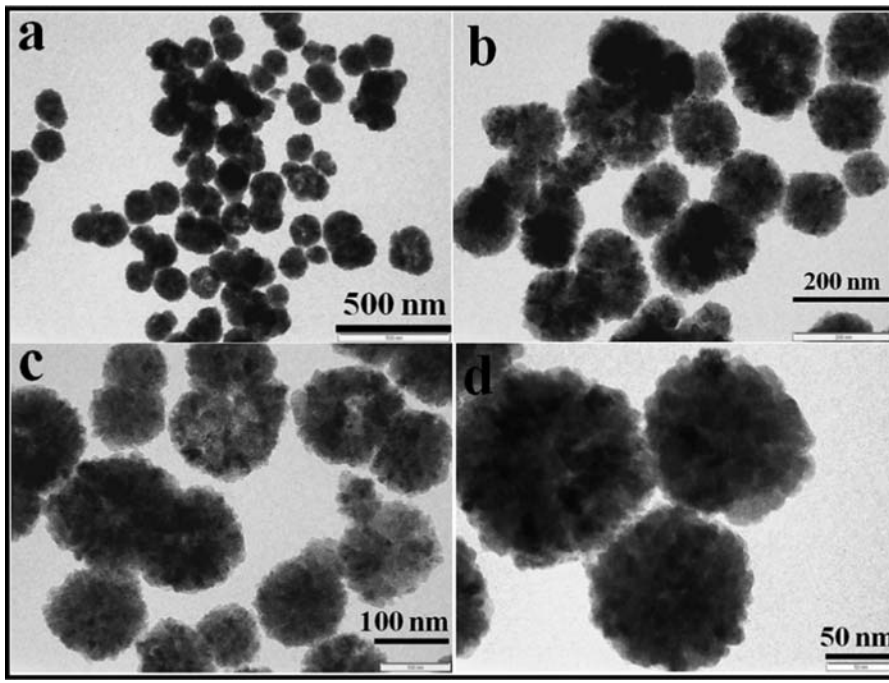

Figure 3.5 TEM images of Cu_2O nanoparticles.

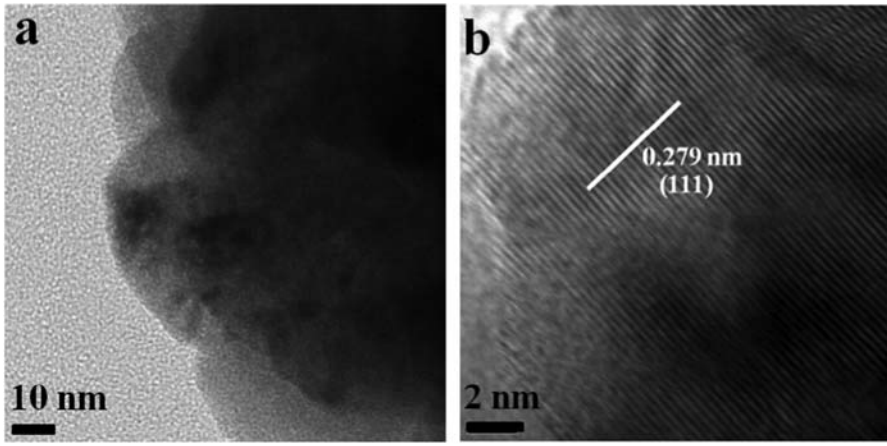

Figure 3.6 (A) and (B) HRTEM images of Cu_2O nanoparticles.

ethylene glycol. The mixed solution was then slowly added into the copper sulfate pentahydrate solution under vigorous stirring. After 20 minutes, 0.036 g of polyvinylpyrrolidone and 20 mL sodium hydroxide (NaOH) were added into the mixture. The pH of the solution was controlled at about 11. The mixture was continually stirring until deep orange color was obtained indicating Cu_2O nanocubes were formed. The length of Cu_2O nanocubes prepared using this parameter was about 400 ± 20 nm, which indicated that the nanocubes were monodisperse in size.

In order to produce homogeneous and nanosized lanthanum manganite ($LaMnO_3$) powders, sonochemical has been used by Das et al. [103]. In this method, 0.1 M of lanthanum nitrate, 0.1 M manganese acetate, small amount of decalin, and 0.1 mmol/L of sodium dodecyl sulfate (SDS) surfactant were mixed together. SDS was added to prevent agglomeration of the nanopowders. Then, the mixture was subjected to sonication using direct immersion of Ti horn (20 kHz, 1500 W) at room temperature for 2 hours. Next, oxalic acid was added to the solution and sonication was continued for another 4 hours. After sonication completed the product was washed with alcohol and acetone and dried at 40°C. Finally, the produced powder was calcined at various temperatures (700°C−800°C) and duration (2−10 hours). They reported that the particle size was uniformly distributed with higher calcination temperature and longer heating duration produced nanopowders with larger particle size. A uniform and homogeneous $LaMnO_3$ powder can be easily produced using sonochemical method.

Barium titanate ($BaTiO_3$) that has been widely used in multilayer ceramic capacitors, embedded capacitance in printed circuit boards, and thermistors with positive temperature coefficient of resistivity [104] can be synthesized through sonochemical process. One of the examples is monosized spherical $BaTiO_3$ particles, which has been prepared by Xu et al. [105]. In this study, chemometrics amounts of barium chloride dihydrate ($BaCl_2 \cdot 2H_2O$) and titanium tetrachloride ($TiCl_4$) were mixed in 100 mL of deionized water, whereby the Ba/Ti molar ratio (R) was set to 0.90, 0.95, 1.1, 1.2, 1.5 with a constant titanium concentration (0.2 mol/L). Then,

sodium hydroxide (NaOH) was added under stirring. Then, the solution was subjected to ultrasound irradiation (20 kHz and 150 W/cm^2) for 40 minutes. After sonication the solution was washed with ammonia and dried in an oven at 100°C. This experiment revealed that Ba/Ti ratio may influence the product of $BaTiO_3$. As pointed out by Lencka and Riman [106], the ratio of Ba/Ti less than 1 would cause the contamination of $BaTiO_3$. However, complete reaction occurred if the Ba/Ti ratio was more than 1. Xu et al. reported that when Ba/Ti ratio is less than 1 (0.9 and 0.95), the prepared $BaTiO_3$ powders contained an amorphous unidentified phase. This result was almost same as reported by Testino et al. [107]. From the average particle size measured using laser particle size analyzer, Xu et al. also pointed out that the $BaTiO_3$ particle size decreased with the increasing Ba/Ti ratio.

3.2.2 Physical methods

3.2.2.1 Comminution

Comminution is a mechanical processing for the production of metal oxide powders, involving the reduction of larger size solids into smaller size powders, by crushing, grinding, and milling. The basic mechanisms of this method for the preparation of metal oxide powders are the compression, mechanical impact, and particle attrition at high velocities. Different types of milling process with different operating mechanism, advantages, and drawbacks are used in the preparation of metal oxide powders, including ball milling, vibratory milling, and attrition milling. All these milling processes require milling media and can be conducted in dry or wet conditions. The most widely used milling process for the preparation of various powders is the high energy ball mill. Depending on the grinding conditions, high energy ball milling can produce metal oxide powders ranged from micron-sized to nanosized, although obtaining nanosized powders may require extensive milling time. Besides, the microstructures of the metal oxide powders are highly dependent on the grinding conditions. For example, the milling time can significantly affect the size, size distribution, chemical composition, and morphology of metal oxide powders. Therefore the properties of the metal oxide powders can be tailored accordingly by varying the grinding conditions. Yadav reported the preparation of nanosized cerium oxide powders in oxygen ambient using cerium powder by high energy ball milling [108]. They successfully synthesized cerium oxide nanopowder of 10 nm in diameter using milling time of 30 hours. Other researchers also reported the preparation of nanosized B_2O_3 [109] and TiO powders [110] by ball milling of microsize powders of the same composition.

Other than simple oxide powders, complex oxide powders can also be prepared by using ball milling. Lee et al. reported the rapid preparation of perovskite oxides of (Bi, Na)TiO_3, (K, Na)NbO_3 and their modified complex compositions with low contamination using high energy ball milling process with a milling time of 40 minutes [111]. França et al. also reported the preparation of Fe_2TiO_5 nanopowders from $-Fe_2O_3$ and TiO_2-anatase by combining ball-milling and postannealing [112]. They successfully produced Fe_2TiO_5 nanopowders in pseudobrookite phase with

crystallite size of 38.43 nm. Stoyanova also reported the preparation of $CaTiO_3$ nanosized powders by combining ball milling and hydrothermal process [113]. They first prepared ethanolic solution of titanium *n*-butoxide, stabilized with acetylacetone and mixed with aqueous solution of calcium chloride anhydrous ($CaCl_2$). To prepare the $CaTiO_3$ precipitate, aqueous solution of sodium hydroxide (1.8 M) was added dropwise to the prepared mixture until reaching pH value 12 and sealed into autoclave at 180°C for 36 hours, followed by natural cooling down to room temperature. The obtained precipitates were dried up in an oven at 180°C for 24 hours. The precipitates were subjected to ball milling for 15, 30, and 45 minutes, respectively. They found that as the ball milling time was increased from 15 to 45 minutes, the shape of the particles changes from prisms to globular, while the size of particles was reduced from 130 nm for as prepared precipitate to 87 nm for ball milling of 15 minutes and finally to 53 nm for balling milling of 45 minutes. They also reported the bandgap of $CaTiO_3$ powder decreases with the increasing milling time. Pedro-García et al. reported the synthesis of $BiFeO_3$ particles by high energy ball milling and annealing [114]. In their study, stoichiometric mixtures of Bi_2O_3 and Fe_2O_3 were mixed and milled for 5 hours using high-energy ball milling and annealed at 650°C. The As-synthesized $BiFeO_3$ particles before subjecting to ball milling have homogeneous particle size distribution around 300−400 nm with polyhedral shape. The As-synthesized particles were then subjected to crystallite size reduction by milling-process (CSRM) up to 60 minutes to obtain $BiFeO_3$ nanoparticles with average size of 23.778 nm. They also found that CSRM promotes a change in the magnetic order of the $BiFeO_3$ nanoparticles from antiferromagnetic to ferromagnetic.

Other than the reduction of particle size, mechanochemical synthesis can occur if chemical reaction involves during the high energy ball milling which results in a product with a new composition. Cuprous oxide nanopowders with the average size of 11 nm, for example, were synthesized through mechanochemical synthesis using copper powder in high energy planetary ball mill in oxygen atmosphere by Khayati et al. [115]. It is, however, difficult to produce high purity metal oxide powders by using comminution. The major concern of producing metal oxide powders of high purity is the impurity pickup from the milling media and atmosphere during the process, and this can be reduced by using chamber and the media of the same composition as that of the feedstock material.

3.2.2.2 Spray drying

The spray drying process involves the atomization of a solution, slurry, or emulsion containing one or more components of the desired product into droplets by spraying followed by the rapid evaporation of the sprayed droplets into solid powder by hot air at a certain temperature and pressure. The solid powders comprising salts or hydroxides are then subjected to calcination to obtain metal oxide powders. The atomization, drying, and calcination process are very crucial to obtain metal oxide powders with desired composition, crystallinity, size distribution, shape, and other properties. Many techniques have been developed for the formation of finely

atomized droplets, such as centrifugal atomization, pressure nozzle atomization, ultrasonic atomization, electrostatic atomization, and pneumatic atomization. The nature of the feedstock used in the atomization process can affect significantly the spray drying process and the quality of the metal oxide powders. Feedstock for spray drying process should have an optimized solid content, viscosity, and density with good dispersion of agglomerate-free particles. The drying process also plays an important role in determining the yield and quality of the metal oxide powders and can occur in cocurrent, counter-current, or mixed flow method. Depending on the method and the spray dryer system, the drying process can have many complex and critical parameters. Yıldız and Soydan, for example, synthesized ZnO nanopowders by dry spraying process [116]. In their study the effect of solid−liquid ratio of the feedstock suspension and the parameters for spray dryer system, namely, inlet temperature of hot air, flow rate of the hot air, feeding rate of the suspension, spray air pressure and outlet temperature of drying chamber on the particle size, shape, crystallinity, morphology, and specific surface area of the powders were studied. They revealed that these parameters have significant influence on the properties of powders including the size, morphology, crystallinity, and specific surface area. Powders with size ranged from 5 to 200 nm specific surface area of 21−114 m^2/g can be obtained depending on the drying process parameters. They reported that hard agglomeration did not occur up to 180°C. ZnO nanopowders in a spherical granule formed with high specific surface area can be prepared without grinding the powders.

Preparation of metal oxide-containing composite nanopowders by spray drying was also reported. Loghman-Estarki et al. reported the preparation of $MgAl_2O_4$−Si_3N_4 composite powders of 5 μm by spray drying process [117]. The suspension of $MgAl_2O_4$−2.5 vol.% Si_3N_4 suspension was first prepared with ultrasonic irradiation of $MgAl_2O_4$−Si_3N_4 nanoparticles in distilled water with the assistance of binder followed by the spray drying of the suspension into powders. The powders are composed of particles with size ranging from 50 to 100 nm. In another study, Yıldız and Ali reported direct synthesis of zirconia toughened alumina nanopowders as soft spherical granules by combining coprecipitation with spray drying [118]. They first obtain zirconia toughened alumina precipitate by coprecipitation of alumina (Al_2O_3) and yttria-stabilized zirconia (YSZ). The As-synthesized zirconia toughened alumina precipitate was then subjected to spray drying to atomize, dry, and granulate the suspension to form zirconia toughened alumina nanopowders. They found that the zirconia toughened alumina nanopowders containing 4−20 wt.%. YSZ have alumina crystalline structure with the average nanoparticle size between 26.64 and 46.70 nm. These nanopowders also have very high specific surface area between 77.43 and 112.41 m^2/g. Yıldız and Ali also revealed that the crystallinity, morphology, particle size, SSA, and granule form of the synthesized ZTA nanopowders are significantly influenced by the preparation and drying conditions of the synthesized precipitate, the solid−liquid ratio of the suspension, and the molar mass ratio of YSZ in Al_2O_3 matrix.

Ehrhart et al. also reported the use of spray drying for the production of hercynite ($FeAl_2O_4$) complex oxide particles using pH-modification of a charge-stabilized sol [119]. Other researchers also reported the successful preparation of

cerium oxide [76], hydroxyapatite-coated iron oxide [120], and complex oxide $(Y_xGd_{(3-x)})_3Al_5O_{12}$ [121] powders by using spray drying method. Although spray drying is a widely used and scalable method for the preparation of metal oxide powders in industry, this method generally produces powders with density lower than the bulk density due to the presence of hollow particles.

3.2.2.3 Spray pyrolysis

Gas different from spray drying which only involves the drying of the atomized droplets into solids, in spray pyrolysis, atomized precursor droplets undergo decomposition, and conversion to final metal oxide powders. Spray pyrolysis generally consists of three steps, namely, atomization of the liquid feedstock, evaporation, and drying of the sprayed droplets into spherical solid particles, and pyrolysis and sintering of the dried precursor spheres into final metal oxide powders. Spray pyrolysis is a relatively convenient method due to the fact the mixing process can be simplified and the properties of the powder prepared by this method can be easily controlled by changing the conditions of the pyrolysis reaction. Besides, spray pyrolysis can also be scaled up for large-scale and continuous production of metal oxide powders. Currently, this method is actively studied for the preparation of various metal oxide powders, especially the nanopowders, and for this reason, applications of this method are expanding quickly. Yu and Kim reported the preparation of nickel oxide nanopowders with an average particle size below 50 nm from nickel chloride solution by spray pyrolysis process [122]. They revealed that the average particle size and particle size distribution increased significantly with the concentration of raw material solution while the average particle size and particle size distribution of the powder decrease with the air pressure. Hwangbo et al. also reported the preparation of zirconium oxide powders using ultrasonic spray pyrolysis with citrate precursor method [123]. They successfully controlled the morphology and size of the zirconium oxide powders from hollow submicron particles to minute nanoparticles by varying the diffusion rate of zirconium cations in a pyrolysis step through a chelating reaction. Spray pyrolysis also enables the production of doped metal oxide powders. For example, Raju and Bhattacharya reported the preparation of nanocrystalline pure and indium doped tin oxide powders by flame spray pyrolysis [124]. Other simple metal oxide powders produced by spray pyrolysis are zinc oxide powder and magnesia powder [125].

Other than simple metal oxide, spray pyrolysis is also widely used in the preparation of metal oxide powders with complex compositions. This is because during the pyrolysis process, microscale reactions can take place in the droplets. Choi and Kang reported the preparation of $ZnMn_2O_4$ nanopowders from aqueous spray solution containing Zn and Mn components by flame spray pyrolysis [126]. They managed to prepare $ZnMn_2O_4$ powders with a mean size of 65 nm and nonaggregation characteristics by subjecting the precursor particles to posttreatment at 500°C. Granados et al. reported the preparation of $CoAl_2O_4$ nanopowders by flame spray pyrolysis method using metallorganic precursors of cobalt propionate and alumatrane [127]. The nanoparticles showed spherical morphology with average particle

size of 27 nm. Krasnikova et al. also reported the use of ultrasonic spray pyrolysis for the preparation of uniform-sized NiO−CuO−MgO fine powders [128]. By studying the effects of process conditions, namely, solvent nature, precursor concentration, and temperature, they successfully obtain spherical NiO−CuO−MgO particles with the diameters ranged in the nanometer scale ($d = 170-300$ nm) at relatively low temperatures (400°C−600°C). It is, however, similar to spray drying, very often hollow particles are obtained, render the powders not suitable for further processing due to the precipitation at the surface of the droplets during the process.

3.2.2.4 Freeze drying

Comparing to techniques, such as spray drying, spray pyrolysis, and vaporization−condensation, that use heat to remove the solvent, freeze drying does not involve heating to remove the solvent. Instead, sublimation is used to remove the solvent. Schnettler et al. first reported the use of this method to prepare Al_2O_3, MgO, and $MgAl_2O_4$ spinel in 1968. Since then, the freeze drying process has been studied extensively for the preparation of other metal oxide powders. Freeze drying normally involves three steps. First, the salt solution containing the desired cation or cations is atomized into a liquid of low freezing point, normally in liquid nitrogen or liquid hexane. Freezing is accomplished rapidly to preserve the solution homogeneity. The atomized droplets freeze to ice and the salt precipitates out from the ice. Sublimation of frozen solvent occurs in vacuum or lowered pressure condition and produces porous salt particles in soft agglomerates, resembling the initially frozen droplets. Metal oxide powders are obtained by subjecting these salt particles to calcination. Free drying is capable of producing metal oxide particles with uniformly distributed particle size. Besides, sudden quenching of the precursor solution during the freezing process immobilizes the ions within the droplets and thus metal oxide powder with homogenous concentration can be produced. In addition, the sintering of such powders can be conducted at a much lower temperature. Tallón et al. reported the preparation of ZrO_2 nanopowders by freeze drying using $ZrOCl_2$ solutions [129]. ZrO_2 powders with nonspherical shape made up of soft agglomerates were produced. They also reported that post thermal treatment determined the crystalline phase formed, such that t-ZrO_2 with an acicular shape was obtained at temperature below 400°C while monoclinic phase with increased agglomeration was produced at higher temperature. ZnO nanopowder was prepared by Liu et al. using polyvinyl alcohol (PVA)−assisted freeze drying process [130]. In their study, PVA was applied as a polymeric carrier and the presence of PVA as carbonaceous residue that results by its thermal decomposition served as a surfactant for the oxides particles, thus improving the dispersivity of ZnO nanopowders. Other metal oxide powders that were successfully prepared by freeze drying methods include SiO_2 nanopowders [131], CeO_2 nanopowders [132], and MgO nanopowders [133].

Freeze drying can also be used together with other methods for the preparation of metal oxide powders. Chiriac et al., for example, reported the use of freeze-drying assisted sol−gel method to synthesize silica-based particles embedding iron [134]. In their study the gels were prepared by sol−gel route and were rapidly

frozen in liquid nitrogen for 15 minutes, and the frozen gels were lyophilized for 2 weeks at a temperature ranging from −50°C to −54°C and vacuum pressure of 0.04−0.024 mbar. Iron incorporating silica-based powders of $x\mathrm{Fe_2O_3}\cdot(100-x)[0.7\mathrm{SiO_2}0.3\mathrm{Na_2O}]$ were successfully produced in their study. However, freeze drying is known for its slow drying rate, high operating cost, and low energy efficiency in comparison with other powder preparation method and, therefore, limits the large-scale industrial applications of this method.

3.2.2.5 Pulsed laser ablation

Pulsed laser ablation (PLA) is a process in which a pulsed laser beam is focused on a solid target material to remove material from the target surface. It is an eco-friendly way of powders preparation due to minimal chemical usage. PLA can be conducted in vacuum or in ambient media (gas or liquid). Typically, laser ablation device consists of a pulsed laser and an ablation chamber. During the operation the temperature of the laser-irradiated surface of a solid target material increases rapidly, thus vaporizing the target material. The collisions between the evaporated species (atom and clusters) and the surrounding molecules result in excitation of the electron state coupled with light emission and generation of electrons and ions, forming a laser-induced plasma plume [135]. Under suitable conditions (depending on the target material, ambient media, ambient pressure, and laser conditions), the vaporized materials condensate into clusters and particles. In some other cases, new materials maybe formed from the reaction between the vaporized materials and other reactants. PLA has been employed for the atomization of targets to obtain thin film and ultrafine powders. PLA was first used by Neddersen et al. in 1993 to obtain the dispersions of Ag, Au, Pt, Pd, and Cu nanoparticles in water and organic solvents [136]. Since then, PLA been extensively studied for the preparation of various powders in nanoscale and thousands of research papers have been published on the synthesis, properties, and applications of metal oxide powders. The PLA offers the advantage of producing highly pure powders without additional chemicals or by-products and, therefore, no further purification is needed. Besides, the experimental setup for PLA is relatively low cost and simple with easily controlled parameters. For PLA in liquid, due to the extreme confined conditions, unusual metastable phase can be formed. This is because the plasma plume experiences additional compression by the liquid that may result in the formation of metastable phase that is difficult to be achieved by other methods. Svetlichnyi et al. prepared iron oxide nanocrystalline powder by PLA [137]. In their study, metallic iron target was ablated using PLA in water, and $\mathrm{Fe_3O_4}$ nanocrystalline powder with average size of about 5 nm and is obtained after the solution was dried in vacuum. Henley et al. synthesized iron oxide nanopowders with different morphologies, from nanoparticles to nanowires and nanosheets by nanosecond PLA with different laser wavelength and growth time of fine iron powder in different liquid media of water, methanol, ethanol, and isopropanol [138]. They found that hematite α-$\mathrm{Fe_2O_3}$ nanopowder was formed when water was used, while iron oxyhydroxide nanopowder was formed when alcohol was used. Iron oxyhydroxide nanowires and two-dimensional nanosheets were also obtained by employing different laser wavelengths of 248 and 532 μm for PLA in methanol. In

another study, Al-Nassar et al. prepared zinc oxide nanoparticles using PLA process from a pure zinc metal placed inside liquid environment containing cetyltrimethyl ammonium bromide (CTAB) of 10^{-3} molarity and distilled water [139]. The author used Ti:Sapphire laser of 800 nm wavelength, 1 kHz pulse repetition rate, 130 fs pulse duration at three values of pulse energies of 0.05, 1.11, and 1.15 mJ in their process. They found that in the presence of CTAB, the decrease in the laser pulse energy yielded smaller size of nanoparticles with narrow size distributions. Besides, they also revealed that ZnO nanoparticles with larger particle sizes, more spherical, homogeneous, and broad size distribution can be obtained by increasing the value of pulse energy.

Other than in liquid media, PLA in gaseous media and vacuum can also be employed for the preparation of high purity metal oxide powder. Siraj et al., for example, reported the preparation of cadmium oxide (CdO) and yttrium Oxide (Y_2O_3) powders by ablation of CdO and Y_2O_3 target in vacuum using pulsed KrF Excimer laser [140]. The metal oxide powders were reported to range from 71 nm to 1.1 μm. However, in spite of its advantages comparing to other preparation methods of metal oxide powder, PLA presents some drawbacks. Powders, especially nanopowders, synthesized by PLA method tend to agglomerate. Besides, relatively low amount of powders can be produced by using PLA, which limits the large-scale industrial applications of this method.

3.2.2.6 Vaporization–condensation

Vaporization–condensation method has been used for the preparation of various thin film and particles on substrates. Particularly, vaporization–condensation method has also been employed for the preparation of metal oxide nanopowders. In this process the target material is heated and vaporization occurs, and powders are formed by rapid condensation of the vapor. Depending whether the chemical reaction is involved in the process, this method can be categorized into chemical or physical method. Physical vapor condensation occurs when the resultant powder has the same composition as the target material, indicating no chemical reaction takes place during the process. Vodopyanov et al. reported that the preparation of WO_3 and ZnO nanopowders range from 20 to 500 nm by local heating of the initially pressed powder using a focused beam of microwave radiation of a subterahertz gyrotron [141]. Zhan et al. reported the preparation of lead oxide nanopowders from waste electric and electronic equipment by high-temperature oxidation–evaporation and condensation [142]. They revealed that the condensation temperature and distance significantly affected the morphology and size of the lead oxide nanopowders, respectively. Vaporization–condensation method can also be employed for the preparation of composite powder. Stötzel et al. reported the preparation of iron oxide–silica composite nanopowders with diameters ranging from 20 to 50 nm by vaporization–condensation method [143]. In their study, the mixture of hematite powder (α-Fe_2O_3) and quartz sand (SiO_2) was subjected to CO_2 laser covaporization (CoLAVA). Evaporation and plasma generation occurred in a continuously flowing process gas at normal pressure, the vapor was then rapidly quenched and nanopowder was formed by gas-phase condensation. They revealed that with increasing iron

oxide content, the mean size of the maghemite domains increases, while the number of maghemite domains in each NP decreases until Janus particles with one γ-Fe_2O_3- and one SiO_2-hemisphere are obtained [143].

However, since most metal oxide has high-melting point and low vapor pressure, this method has limited success for the preparation of metal oxide powders with high melting points. Besides, the drawback of this method also include possible occurrence of reactions between metal vapors and oven materials, inhomogeneous heating which impose limitations for the control of particle size and distribution, and difficulties in controlling the composition of the mixed metal particles due to the difference in composition between the alloys and the mixed vapors [144].

3.2.3 Biological methods

Growing environmental awareness has led to the development of various environment-friendly processes for the nontoxic synthesis of metal oxide powders. Biological methods that lead to the green synthesis of metal oxide powders, especially nanopowders can be generally divided into protein-mediated, microorganism-mediated (fungi, bacteria, and yeast) and plant-mediated methods. Besides nontoxic process, biological-mediated methods have the advantages of high selectivity and precision, good reproducibility in production, easy scaling-up, and well-defined morphology of metal oxide powders. Kashyap, for example, synthesized biomimetic iron oxide nanoparticles mediated by an acidic bacterial recombinant protein, Mms6 by the controlled addition of sodium hydroxide to solution-phase Mms6 protein micelles incubated with ferric chloride [145]. He proposed that protein self-assembly and micellar surface iron binding lower the energy barrier to subsequent nucleation, thus facilitating the process of synthesis of iron oxide nanoparticles. Microorganisms such as fungi, bacteria, and yeast have the ability to accumulate and detoxify heavy metals which can be utilized to produce metal and metal oxide nanoparticles. Bharde et al. reported the bacteria-mediated precursor-dependent biosynthesis of superparamagnetic iron oxide nanoparticles [146]. They revealed that bacterium *Actinobacter* sp. can yield iron oxide nanoparticles when reacted with ferric chloride under aerobic condition. Jayaseelan et al. reported the use of *Aeromonas hydrophila* as eco-friendly reducing and capping agent in biosynthesis for the simple production of ZnO nanoparticles. They proposed that the synthesis of ZnO nanoparticles was resulted from the variation in the level of rH2 or pH, which activates the pH sensitive oxidoreductases enzymes. Compared with bacteria, the use of fungi in mycosynthesis of metal oxide powder is a straightforward approach because most fungi containing important metabolites with higher bioaccumulation ability and simple downstream processing are easy to culture for the efficient production of nanopowders [147]. Besides, fungi have higher tolerances to, and uptake competences for, metals, particularly in terms of the high wall-binding capability of metal salts with fungal biomass for the high-yield production of nanoparticles [148]. Salvadori et al. used dead biomass of the fungus *Hypocrea lixii* as a biological system for the production of nickel oxide nanoparticles [149]. In their process, nickel ions were

converted into nickel oxide nanoparticles in aqueous solution and were accumulated intracellularly and extracellularly on the cell wall surface through biosorption. The dead fungus biomass played an important role by acting as a reducing agent and stabilizer to form metallic nanoparticles, which were then oxidized to nickel oxide in the medium. Kalpana also reported extracellular synthesis of ZnO nanoparticles using culture filtrates of *Aspergillus niger* [150]. They successfully synthesized ZnO nanoparticles with diameter ranging from 53 to 69 nm with an average size of 61 ± 0.65 nm.

Recently, extract from plants are used in the preparation of metal oxide powders. Compared with using bacteria and fungi, plants are easily available and the procedure of biogenic synthesis is cost-effective and less tedious. The active biological compound present in plant parts such as enzyme, flavonoids, terpenoids, glycosides, alkaloids, inositols, resins, saponins, terpenes, volatile oil, tannins, steroids, and quinine can act as a reducing and capping agent for the preparation of metal oxide powders [151]. Chaudhuri and Malodia prepared ZnO nanoparticles using *Calotropis gigantea* leaf extract with zinc acetate salt in the presence of 2 M NaOH [151]. Highly monodisperse crystalline ZnO nanoparticles with 20 nm size was successfully produced by their process. Zahir et al. reported the synthesis of titanium dioxide nanoparticles with size 83.22 ± 1.50 nm using green synthesis from aqueous leaf extract of *Euphorbia prostrata* as antileishmanial agents [152]. In another study, Geetha et al. reported the synthesis of ZnO nanoparticles using *Euphorbia Jatropha* plant latex as a reducing agent by the combustion method [153].

3.3 Concluding remarks

Due to the importance of the metal oxide powders in current and future industrial applications, various methods for the synthesis and preparation of metal oxide powders were studied and developed. This chapter has reviewed the current progress on the synthesis and preparation of various metal oxide powders. These methods, in the process media of vapor, liquid, and solid, can be categorized into chemical, physical, and biological methods. The current trend in the synthesis and preparation of metal oxide powders is emphasized on the preparation of various nanoscale powders of metal oxide. Significant breakthroughs were made with the introduction of these nanoscale metal oxide powders into various applications. From the published literatures which were included in this chapter, it can be clearly seen that the researches on the synthesis and preparation of metal oxide powders were mainly focused on chemical methods.

The preparation of metal oxide powders by various currently used chemical methods was presented, such as sol−gel, hydrothermal, CVD, thermal decomposition, and sonochemical method. Physical methods of preparation of metal oxide powders includes comminution, spray drying, spray pyrolysis, freeze drying, PLA, and vaporization−condensation method in which comminution is the most widely used method for the bulk synthesis of metal oxide powders, although the

metal oxide powders produced by this method are generally large in size and have wide size distribution. Synthesis and preparation of metal oxide powders by biological methods, including protein-mediated, microorganism-mediated, and plant-mediated methods, is gaining immense attention amongst scientific community although these methods are scarcely reported due to several serious factors that may influence them. Many of these new methods are actually the combination or variants of and/or improvements over the well-established procedures used by the industry. There are still processing challenges for the synthesis of metal oxide powders with controllable parameters at high yield and low cost that can be integrated into the current manufacturing process. Although these methods can successfully synthesize metal oxide powders, their drawbacks are numerous. These new methods claimed the successful developments in the control of the particle size; however, the control of agglomeration, during or after synthesis, still remained an unsolved key issue. Stringent storage and handling conditions, especially in a humid atmosphere, are required to prevent the unagglomerated fine powders obtained from these methods to become agglomerated. Besides, these reported new methods that are able to produce high-quality powders, in terms of composition, size distribution, and shape, cannot produce gram-quantities metal oxide powders, particularly methods that involve vapor-phase reactions and, therefore, has a very slow production rate of metal oxide powders. The upscaling of these methods is not possible at the present stage to meet the high demand from the industry. More experimental and theoretical works are needed to close the gap between research outcomes and industrial expectations to integrate these methods to current manufacturing process and open new avenues for metal oxide powders.

References

[1] D. Ganguli, M. Chatterjee, Ceramic Powder Preparation: A Handbook, Springer US, 2013.

[2] B. Saravanakumar, R. Shobana, G. Ravi, V. Ganesh, R. Yuvakkumar, Preparation and electrochemical characterization of Mo_9O_{26} nanopowders for supercapacitors applications, Nano-Struct. Nano-Objects 19 (2019) 100340. Available from: https://doi.org/10.1016/j.nanoso.2019.100340.

[3] Musyarofah, N.D. Lestari, R. Nurlaila, N.F. Muwwaqor, Triwikantoro, S. Pratapa, Synthesis of high-purity zircon, zirconia, and silica nanopowders from local zircon sand, Ceram. Int. 45 (6) (2019) 6639−6647. Available from: https://doi.org/10.1016/j.ceramint.2018.12.152.

[4] L. Ghasemi, H. Jafari, Morphological characterization of tungsten trioxide nanopowders synthesized by sol-gel modified Pechini's method, Mater. Res. 20 (2017) 1713−1721.

[5] B.D. Stojanovic, A.S. Dzunuzovic, N.I. Ilic, Review of methods for the preparation of magnetic metal oxides, in: B.D. Stojanovic (Ed.), Magnetic, Ferroelectric, and Multiferroic Metal Oxides, Elsevier, 2018, pp. 333−359.

[6] C.J. Brinker, G.W. Scherer, Chapter 1 − Introduction, in: C.J. Brinker, G.W. Scherer (Eds.), Sol-Gel Science, Academic Press, San Diego, CA, 1990 (pp. xvi-18).

[7] R. Peña-Garcia, Y. Guerra, B.V.M. Farias, D.M. Buitrago, A. Franco, E. Padrón-Hernández, Effects of temperature and atomic disorder on the magnetic phase transitions in ZnO nanoparticles obtained by sol–gel method, Mater. Lett. 233 (2018) 146–148. Available from: https://doi.org/10.1016/j.matlet.2018.08.148.
[8] M. Taheri, H. Abdizadeh, M.R. Golobostanfard, Hierarchical ZnO nanoflowers and urchin-like shapes synthesized via sol-gel electrophoretic deposition with enhanced photocatalytic performance, Mater. Chem. Phys. 220 (2018) 118–127. Available from: https://doi.org/10.1016/j.matchemphys.2018.08.043.
[9] J.N. Hasnidawani, H.N. Azlina, H. Norita, N.N. Bonnia, S. Ratim, E.S. Ali, Synthesis of ZnO nanostructures using sol-gel method, Procedia Chem. 19 (2016) 211–216. Available from: https://doi.org/10.1016/j.proche.2016.03.095.
[10] Z.N. Kayani, M. Anwar, Z. Saddiqe, S. Riaz, S. Naseem, Biological and optical properties of sol–gel derived ZnO using different percentages of silver contents, Colloids Surf. B: Biointerfaces 171 (2018) 383–390. Available from: https://doi.org/10.1016/j.colsurfb.2018.07.055.
[11] K. Mahendraprabhu, A. Selva Sharma, P. Elumalai, CO sensing performances of YSZ-based sensor attached with sol-gel derived ZnO nanospheres, Sens. Actuators B: Chem. 283 (2019) 842–847. Available from: https://doi.org/10.1016/j.snb.2018.11.164.
[12] R.-X. Ou, C.-H. Lin, T.-F. Guo, T.-C. Wen, Improvement in inverted polymer solar cells via 1-benzoyl-2-thiourea as surface modifier on sol-gel ZnO, J. Taiwan Inst. Chem. Eng. (2018). Available from: https://doi.org/10.1016/j.jtice.2018.10.017.
[13] S. Javed, M. Islam, M. Mujahid, Synthesis and characterization of TiO_2 quantum dots by sol gel reflux condensation method, Ceram. Int. 45 (2, Part A) (2019) 2676–2679. Available from: https://doi.org/10.1016/j.ceramint.2018.10.163.
[14] O. Jongprateep, R. Puranasamriddhi, Effects of reagents on the formation of nanoparticulate titanium dioxide synthesized by sol-gel technique, Mater. Today: Proc. 5 (5, Part 1) (2018) 10925–10931. Available from: https://doi.org/10.1016/j.matpr.2018.01.005.
[15] M. Kinoshita, T. Kamizato, Y. Shimoyama, Effect of precursor structure on mixed-crystal phase titanium oxide synthesized by sol-gel reaction in supercritical carbon dioxide, J. Supercrit. Fluids 138 (2018) 193–199. Available from: https://doi.org/10.1016/j.supflu.2018.04.017.
[16] M. Kinoshita, Y. Shimoyama, Photocatalytic activity of mixed-phase titanium oxide synthesized by supercritical sol-gel reaction, J. Supercrit. Fluids 138 (2018) 29–35. Available from: https://doi.org/10.1016/j.supflu.2018.03.023.
[17] K. Sakthiraj, M. Hema, K. Balachandra Kumar, The effect of reaction temperature on the room temperature ferromagnetic property of sol-gel derived tin oxide nanocrystal, Phys. B. Condens. Matter 538 (2018) 109–115. Available from: https://doi.org/10.1016/j.physb.2018.03.023.
[18] C.R. da Cunha, G.H. Toffolo, C.E.I. dos Santos, R.P. Pezzi, Structural, optical and chemical characterizations of sol–gel grown tin oxide aerogels, J. Non-Crystalline Solids 380 (2013) 48–52. Available from: https://doi.org/10.1016/j.jnoncrysol.2013.08.028.
[19] S. Gul, A. Azam, N. Imrose, S. Riaz, S. Naseem, Tin oxide thin films prepared by sol-gel for PV applications, Mater. Today: Proc. 2 (10, Part B) (2015) 5793–5798. Available from: https://doi.org/10.1016/j.matpr.2015.11.129.
[20] H.J. Kim, M.-J. Maeng, J.H. Park, M.G. Kang, C.Y. Kang, Y. Park, et al., Chemical and structural analysis of low-temperature excimer-laser annealing in indium-tin oxide

sol-gel films, Curr. Appl. Phys. 19 (2) (2019) 168−173. Available from: https://doi.org/10.1016/j.cap.2018.12.005.
[21] K. Banjerdteerakul, P. Vas-Umnuay, V. Pavarajarn, Synthesis of mesoporous tin dioxide via sol-gel process assisted by resorcinol−formaldehyde gel, Particuology 37 (2018) 26−32. Available from: https://doi.org/10.1016/j.partic.2017.07.006.
[22] D. Sun, M. Wong, L. Sun, Y. Li, N. Miyatake, H.-J. Sue, Purification and stabilization of colloidal ZnO nanoparticles in methanol, J. Sol-Gel Sci. Technol. 43 (2) (2007) 237−243. Available from: https://doi.org/10.1007/s10971-007-1569-z.
[23] E. Hosono, S. Fujihara, T. Kimura, H. Imai, Non-basic solution routes to prepare ZnO nanoparticles, J. Sol-Gel Sci. Technol. 29 (2) (2004) 71−79. Available from: https://doi.org/10.1023/B:JSST.0000023008.14883.1e.
[24] M. Shojaie-Bahaabad, E. Taheri-Nassaj, Economical synthesis of nano alumina powder using an aqueous sol−gel method, Mater. Lett. 62 (19) (2008) 3364−3366. Available from: https://doi.org/10.1016/j.matlet.2008.03.012.
[25] S.K. Omanwar, S.R. Jaiswal, V.B. Bhatkar, K.A. Koparkar, Comparative study of nano-sized Al_2O_3 powder synthesized by sol-gel (citric and stearic acid) and aldo-keto gel method, Optik 158 (2018) 1248−1254. Available from: https://doi.org/10.1016/j.ijleo.2017.12.068.
[26] W.J. Jeyarani, T. Tenkyong, N. Bachan, D.A. Kumar, J.M. Shyla, An investigation on the tuning effect of glucose-capping on the size and bandgap of CuO nanoparticles, Adv. Powder Technol. 27 (2) (2016) 338−346. Available from: https://doi.org/10.1016/j.apt.2016.01.006.
[27] C.-L. Wang, W.-S. Hwang, H.-L. Chu, H.-J. Lin, H.-H. Ko, M.-C. Wang, Kinetics of anatase transition to rutile TiO_2 from titanium dioxide precursor powders synthesized by a sol-gel process, Ceram. Int. 42 (11) (2016) 13136−13143. Available from: https://doi.org/10.1016/j.ceramint.2016.05.101.
[28] E. Ovodok, H. Maltanava, S. Poznyak, M. Ivanovskaya, A. Kudlash, N. Scharnagl, et al., Sol-gel template synthesis of mesoporous carbon-doped TiO_2 with photocatalytic activity under visible light, Mater. Today: Proceedings 5 (9, Part. 2) (2018) 17422−17430. Available from: https://doi.org/10.1016/j.matpr.2018.06.044.
[29] I. Singh, R. Kumar, B.I. Birajdar, Zirconium doped TiO_2 nano-powder via halide free non-aqueous solvent controlled sol-gel route, J. Environ. Chem. Eng. 5 (3) (2017) 2955−2963. Available from: https://doi.org/10.1016/j.jece.2017.05.046.
[30] I. Ganesh, Surface, structural, energy band-gap, and photocatalytic features of an emulsion-derived B-doped TiO_2 nano-powder, Mol. Catal. 451 (2018) 51−65. Available from: https://doi.org/10.1016/j.mcat.2017.10.024.
[31] O. Jongprateep, K. Meesombad, R. Techapiesancharoenkij, K. Surawathanawises, Chemical composition, microstructure, bandgap energy and electrocatalytic activities of TiO_2 and Ag-doped TiO_2 powder synthesized by solution combustion technique, Ceram. Int. 44 (2018) S228−S232. Available from: https://doi.org/10.1016/j.ceramint.2018.08.108.
[32] G.W. Morey, P. Niggli, The hydrothermal formation of silicates, a review, J. Am. Chem. Soc. 35 (9) (1913) 1086−1130. Available from: https://doi.org/10.1021/ja02198a600.
[33] H. Hayashi, Y. Hakuta, Hydrothermal synthesis of metal oxide nanoparticles in supercritical water, Materials 3 (7) (2010) 3794.
[34] Q. Yang, Z. Lu, J. Liu, X. Lei, Z. Chang, L. Luo, et al., Metal oxide and hydroxide nanoarrays: hydrothermal synthesis and applications as supercapacitors and nanocatalysts, Prog. Nat. Sci.: Mater. Int. 23 (4) (2013) 351−366. Available from: https://doi.org/10.1016/j.pnsc.2013.06.015.

[35] S.M. Saleh, ZnO nanospheres based simple hydrothermal route for photocatalytic degradation of azo dye, Spectrochim. Acta, A: Mol. Biomol. Spectrosc. 211 (2019) 141−147. Available from: https://doi.org/10.1016/j.saa.2018.11.065.
[36] P. Shubha, M.L. Gowda, K. Namratha, H.B. Manjunatha, K. Byrappa, In vitro and In vivo evaluation of green-hydrothermal synthesized ZnO nanoparticles, J. Drug. Deliv. Sci. Technol. 49 (2019) 692−699. Available from: https://doi.org/10.1016/j.jddst.2018.12.017.
[37] J. Wang, S. Yu, H. Zhang, Effect of surfactants on photoluminescence properties of ZnO synthesized by hydrothermal method, Optik 180 (2019) 20−26. Available from: https://doi.org/10.1016/j.ijleo.2018.11.062.
[38] P. Obreja, D. Cristea, A. Dinescu, C. Romaniţan, Influence of surface substrates on the properties of ZnO nanowires synthesized by hydrothermal method, Appl. Surf. Sci. 463 (2019) 1117−1123. Available from: https://doi.org/10.1016/j.apsusc.2018.08.191.
[39] M.R. Alfaro Cruz, D. Sanchez-Martinez, L.M. Torres-Martínez, TiO_2 nanorods grown by hydrothermal method and their photocatalytic activity for hydrogen production, Mater. Lett. 237 (2019) 310−313. Available from: https://doi.org/10.1016/j.matlet.2018.11.040.
[40] M. Machida, M. Kobayashi, Y. Suzuki, H. Abe, Facile synthesis of >99% phase-pure brookite TiO_2 by hydrothermal conversion from Mg_2TiO_4, Ceram. Int. 44 (14) (2018) 17562−17565. Available from: https://doi.org/10.1016/j.ceramint.2018.06.170.
[41] A.H. Mamaghani, F. Haghighat, C.-S. Lee, Hydrothermal/solvothermal synthesis and treatment of TiO_2 for photocatalytic degradation of air pollutants: preparation, characterization, properties, and performance, Chemosphere 219 (2019) 804−825. Available from: https://doi.org/10.1016/j.chemosphere.2018.12.029.
[42] M. Marandi, S. Bayat, M. Naeimi Sani Sabet, Hydrothermal growth of a composite TiO_2 hollow spheres/TiO_2 nanorods powder and its application in high performance dye-sensitized solar cells, J. Electroanal. Chem. 833 (2019) 143−150. Available from: https://doi.org/10.1016/j.jelechem.2018.11.023.
[43] S. Mehraz, P. Kongsong, A. Taleb, N. Dokhane, L. Sikong, Large scale and facile synthesis of Sn doped TiO_2 aggregates using hydrothermal synthesis, Sol. Energy Mater. Sol. Cell 189 (2019) 254−262. Available from: https://doi.org/10.1016/j.solmat.2017.06.048.
[44] S. Bhuvaneshwari, N. Gopalakrishnan, Hydrothermally synthesized copper oxide (CuO) superstructures for ammonia sensing, J. Colloid Interface Sci. 480 (2016) 76−84. Available from: https://doi.org/10.1016/j.jcis.2016.07.004.
[45] T. Jiang, Y. Wang, D. Meng, X. Wu, J. Wang, J. Chen, Controllable fabrication of CuO nanostructure by hydrothermal method and its properties, Appl. Surf. Sci. 311 (2014) 602−608. Available from: https://doi.org/10.1016/j.apsusc.2014.05.116.
[46] Z. Li, J. Wang, N. Wang, S. Yan, W. Liu, Y.Q. Fu, et al., Hydrothermal synthesis of hierarchically flower-like CuO nanostructures with porous nanosheets for excellent H_2S sensing, J. Alloy. Compd. 725 (2017) 1136−1143. Available from: https://doi.org/10.1016/j.jallcom.2017.07.218.
[47] V.I. Anikeev,. Hydrothermal synthesis metal oxide nanoparticles, Russian Federation: GOUVPO Ivan Gos Khim-Tekhnol Un-t, 2010.
[48] Y. Fang, Z. Li, S. Xu, D. Han, D. Lu, Optical properties and photocatalytic activities of spherical ZnO and flower-like ZnO structures synthesized by facile hydrothermal method, J. Alloy. Compd. 575 (2013) 359−363. Available from: https://doi.org/10.1016/j.jallcom.2013.05.183.
[49] D. Shuang, J.B. Wang, X.L. Zhong, H.L. Yan, Raman scattering and cathodoluminescence properties of flower-like manganese doped ZnO nanorods, Mater. Sci.

Semicond. Process. 10 (2) (2007) 97–102. Available from: https://doi.org/10.1016/j.mssp.2007.04.002.

[50] M.H. Huang, Y. Wu, H. Feick, N. Tran, E. Weber, P. Yang, Catalytic growth of zinc oxide nanowires by vapor transport, Adv. Mater. 13 (2) (2001) 113–116. doi:10.1002/1521-4095(200101)13:2 < 113::AID-ADMA113 > 3.0.CO;2-H.

[51] D.C. Look, Recent advances in ZnO materials and devices, Mater. Sci. Eng.: B 80 (1) (2001) 383–387. Available from: https://doi.org/10.1016/S0921-5107(00)00604-8.

[52] F. Wang, X. Qin, Z. Guo, Y. Meng, L. Yang, Y. Ming, Hydrothermal synthesis of dumbbell-shaped ZnO microstructures, Ceram. Int. 39 (8) (2013) 8969–8973. Available from: https://doi.org/10.1016/j.ceramint.2013.04.096.

[53] W. Wang, L. Wang, L. Liu, C. He, J. Tan, Y. Liang, Morphology-controlled synthesis and growth mechanism of ZnO nanostructures via the NaCl nonaqueous ionic liquid route, CrystEngComm 14 (15) (2012) 4997–5004. Available from: https://doi.org/10.1039/C2CE25232E.

[54] J. Lian, Z. Ding, F.-l Kwong, D.H.L. Ng, Template-free hydrothermal synthesis of hexagonal ZnO micro-cups and micro-rings assembled by nanoparticles, CrystEngComm 13 (15) (2011) 4820–4822. Available from: https://doi.org/10.1039/C1CE05301A.

[55] Y. Liu, H. Lv, S. Li, G. Xi, X. Xing, Synthesis and characterization of ZnO with hexagonal dumbbell-like bipods microstructures, Adv. Powder Technol. 22 (6) (2011) 784–788. Available from: https://doi.org/10.1016/j.apt.2011.05.011.

[56] J.-H. Sun, S.-Y. Dong, Y.-K. Wang, S.-P. Sun, Preparation and photocatalytic property of a novel dumbbell-shaped ZnO microcrystal photocatalyst, J. Hazard. Mater. 172 (2) (2009) 1520–1526. Available from: https://doi.org/10.1016/j.jhazmat.2009.08.022.

[57] L. Wang, Y. Fan, H. Bala, G. Sun, Controllable synthesis of hierarchical ZnO microstructures via a hydrothermal route, Micro Nano Lett. 6 (9) (2011) 741–744. Available from: https://doi.org/10.1049/mnl.2011.0149.

[58] V. Baranwal, A. Zahra, P.K. Singh, A.C. Pandey, Starch assisted growth of dumbbell-shaped ZnO microstructures, J. Alloy. Compd. 646 (2015) 238–242. Available from: https://doi.org/10.1016/j.jallcom.2015.06.007.

[59] J. Sung, M. Shin, P.R. Deshmukh, H.S. Hyun, Y. Sohn, W.G. Shin, Preparation of ultrathin TiO_2 coating on boron particles by thermal chemical vapor deposition and their oxidation-resistance performance, J. Alloy. Compd. 767 (2018) 924–931. Available from: https://doi.org/10.1016/j.jallcom.2018.07.152.

[60] E. Fredriksson, J.-O. Carlsson, Chemical vapour deposition of TiO and Ti_2O_3 from $TiCl_4/H_2/CO_2$ gas mixtures, Surf. Coat. Technol. 73 (3) (1995) 160–169. Available from: https://doi.org/10.1016/0257-8972(94)02378-6.

[61] J. Tatebayashi, G. Yoshii, T. Nakajima, M. Mishina, Y. Fujiwara, Formation and optical properties of Tm, Yb-codoped ZnO nanowires grown by sputtering-assisted metalorganic chemical vapor deposition, J. Cryst. Growth 503 (2018) 13–19. Available from: https://doi.org/10.1016/j.jcrysgro.2018.09.006.

[62] Z. Ye, T. Wang, S. Wu, X. Ji, Q. Zhang, Na-doped ZnO nanorods fabricated by chemical vapor deposition and their optoelectrical properties, J. Alloy. Compd. 690 (2017) 189–194. Available from: https://doi.org/10.1016/j.jallcom.2016.08.100.

[63] Y. Zhao, C. Li, M. Chen, X. Yu, Y. Chang, A. Chen, et al., Growth of aligned ZnO nanowires via modified atmospheric pressure chemical vapor deposition, Phys. Lett. A 380 (47) (2016) 3993–3997. Available from: https://doi.org/10.1016/j.physleta.2016.06.030.

[64] S. Iwan, J.L. Zhao, S.T. Tan, X.W. Sun, Enhancement of UV photoluminescence in ZnO tubes grown by metal organic chemical vapour deposition (MOCVD), Vacuum 155 (2018) 408−411. Available from: https://doi.org/10.1016/j.vacuum.2018.06.035.
[65] D.W. Sheel, J.M. Gaskell, Deposition of fluorine doped indium oxide by atmospheric pressure chemical vapour deposition, Thin Solid Films 520 (4) (2011) 1242−1245. Available from: https://doi.org/10.1016/j.tsf.2011.04.206.
[66] C. Feng, X. Liu, S. Wen, Y. An, Controlled growth and characterization of In_2O_3 nanowires by chemical vapor deposition, Vacuum 161 (2019) 328−332. Available from: https://doi.org/10.1016/j.vacuum.2018.12.055.
[67] J.M. Gaskell, D.W. Sheel, Deposition of indium tin oxide by atmospheric pressure chemical vapour deposition, Thin Solid. Films 520 (12) (2012) 4110−4113. Available from: https://doi.org/10.1016/j.tsf.2011.04.191.
[68] P. Singh, A. Kumar, Deepak, D. Kaur, ZnO nanocrystalline powder synthesized by ultrasonic mist-chemical vapour deposition, Optical Mater. 30 (8) (2008) 1316−1322. Available from: https://doi.org/10.1016/j.optmat.2007.06.012.
[69] S. Lukić, I. Stijepović, S. Ognjanović, V.V. Srdić, Chemical vapour synthesis and characterisation of Al_2O_3 nanopowders, Ceram. Int. 41 (3, Part A) (2015) 3653−3658. Available from: https://doi.org/10.1016/j.ceramint.2014.11.034.
[70] B.P. Dhonge, T. Mathews, S.T. Sundari, M. Kamruddin, S. Dash, A.K. Tyagi, Combustion chemical vapour deposition of Al2O3 films: effect of temperature on structure, morphology and adhesion, Surf. Coat. Technol. 205 (7) (2010) 1838−1842. Available from: https://doi.org/10.1016/j.surfcoat.2010.08.026.
[71] M.V. Reddy, G.V. Subba Rao, B.V.R. Chowdari, Metal oxides and oxysalts as anode materials for li ion batteries, Chem. Rev. 113 (7) (2013) 5364−5457. Available from: https://doi.org/10.1021/cr3001884.
[72] Y. Yin, A.P. Alivisatos, Colloidal nanocrystal synthesis and the organic−inorganic interface, Nature 437 (2004) 664. Available from: https://doi.org/10.1038/nature04165.
[73] C. Burda, X. Chen, R. Narayanan, M.A. El-Sayed, Chemistry and properties of nanocrystals of different shapes, Chem. Rev. 105 (4) (2005) 1025−1102. Available from: https://doi.org/10.1021/cr030063a.
[74] R. Al-Gaashani, B. Aïssa, M. Anower Hossain, S. Radiman, Catalyst-free synthesis of ZnO-CuO-$ZnFe_2O_4$ nanocomposites by a rapid one-step thermal decomposition approach, Mater. Sci. Semicond. Process. 90 (2019) 41−49. Available from: https://doi.org/10.1016/j.mssp.2018.10.004.
[75] K. Rahimi, A. Yazdani, Improving photocatalytic activity of ZnO nanorods: a comparison between thermal decomposition of zinc acetate under vacuum and in ambient air, Mater. Sci. Semicond. Process. 80 (2018) 38−43. Available from: https://doi.org/10.1016/j.mssp.2018.02.018.
[76] V. Sharma, K.M. Eberhardt, R. Sharma, J.B. Adams, P.A. Crozier, A spray drying system for synthesis of rare-earth doped cerium oxide nanoparticles, Chem. Phys. Lett. 495 (4) (2010) 280−286. Available from: https://doi.org/10.1016/j.cplett.2010.06.060.
[77] S. Sohrabnezhad, M.J. Mehdipour Moghaddam, T. Salavatiyan, Synthesis and characterization of CuO−montmorillonite nanocomposite by thermal decomposition method and antibacterial activity of nanocomposite, Spectrochim. Acta, A: Mol. Biomol. Spectrosc. 125 (2014) 73−78. Available from: https://doi.org/10.1016/j.saa.2014.01.080.

[78] Y. Bo, B. Huang, Y. Zhang, J. Wang, W.M. Lau, Z. Zheng, Controlled growth of biomorphic CuO via an one-step thermal decomposition on biotemplates, Powder Technol. 264 (2014) 396–400. Available from: https://doi.org/10.1016/j.powtec.2014.05.064.
[79] X. Bu, F. Liu, Z. Zhang, Z. Wang, J. Liu, W. Liu, Facile synthesis of flower-like ZnO@Fe_2O_3 hierarchical nanostructures with enhanced catalytic activity on the thermal decomposition of ammonium perchlorate, Mater. Lett. 219 (2018) 33–36. Available from: https://doi.org/10.1016/j.matlet.2018.02.066.
[80] E. Alp, E.C. Araz, A.F. Buluç, Y. Güner, Y. Değer, H. Eşgin, et al., Mesoporous nanocrystalline ZnO microspheres by ethylene glycol mediated thermal decomposition, Adv. Powder Technol. 29 (12) (2018) 3455–3461. Available from: https://doi.org/10.1016/j.apt.2018.09.028.
[81] J. Rao, A. Yu, C. Shao, X. Zhou, Construction of hollow and mesoporous ZnO microsphere: a facile synthesis and sensing property, ACS Appl. Mater. Interfaces 4 (10) (2012) 5346–5352. Available from: https://doi.org/10.1021/am3012966.
[82] H. Dong, C. Feldmann, Porous ZnO platelets via controlled thermal decomposition of zinc glycerolate, J. Alloy. Compd. 513 (2012) 125–129. Available from: https://doi.org/10.1016/j.jallcom.2011.10.004.
[83] I. Kontopoulou, A. Angelopoulou, N. Bouropoulos, ZnO spherical porous nanostructures obtained by thermal decomposition of zinc palmitate, Mater. Lett. 165 (2016) 87–90. Available from: https://doi.org/10.1016/j.matlet.2015.11.110.
[84] H. Xu, B.W. Zeiger, K.S. Suslick, Sonochemical synthesis of nanomaterials, Chem. Soc. Rev. 42 (7) (2013) 2555–2567. Available from: https://doi.org/10.1039/C2CS35282F.
[85] R.G. Compton, J.C. Eklund, F. Marken, Sonoelectrochemical processes: a review, Electroanalysis 9 (7) (1997) 509–522. Available from: https://doi.org/10.1002/elan.1140090702.
[86] P.J. Jodłowski, R.J. Jędrzejczyk, D.K. Chlebda, A. Dziedzicka, Ł. Kuterasiński, A. Gancarczyk, et al., Non-noble metal oxide catalysts for methane catalytic combustion: sonochemical synthesis and characterisation, Nanomaterials 7 (7) (2017) 174.
[87] T.J. Mason, Sonochemistry: uses of ultrasound in chemistry and related disciplines, in: R.J. Siegel (Ed.), Ultrasound Angioplasty, Springer US, Boston, MA, 1996, pp. 25–54.
[88] P.R. Birkin, D.G. Offin, P.F. Joseph, T.G. Leighton, Cavitation, shock waves and the invasive nature of sonoelectrochemistry, J. Phys. Chem. B 109 (35) (2005) 16997–17005. Available from: https://doi.org/10.1021/jp051619w.
[89] J. Klíma, C. Bernard, Sonoassisted electrooxidative polymerisation of salicylic acid: role of acoustic streaming and microjetting, J. Electroanal. Chem. 462 (2) (1999) 181–186. Available from: https://doi.org/10.1016/S0022-0728(98)00407-0.
[90] R.G. Compton, J.C. Eklund, F. Marken, T.O. Rebbitt, R.P. Akkermans, D.N. Waller, Dual activation: coupling ultrasound to electrochemistry—an overview, Electrochim. Acta 42 (19) (1997) 2919–2927. Available from: https://doi.org/10.1016/S0013-4686(97)00113-8.
[91] J.P. Lorimer, B. Pollet, S.S. Phull, T.J. Mason, D.J. Walton, The effect upon limiting currents and potentials of coupling a rotating disc and cylindrical electrode with ultrasound, Electrochim. Acta 43 (5) (1998) 449–455. Available from: https://doi.org/10.1016/S0013-4686(97)00126-6.
[92] T.J. Mason, J.P. Lorimer, D.J. Walton, Sonoelectrochemistry, Ultrasonics 28 (5) (1990) 333–337. Available from: https://doi.org/10.1016/0041-624X(90)90041-L.
[93] D.-S. Kim, J.-C. Kim, B.-K. Kim, D.-W. Kim, One-pot low-temperature sonochemical synthesis of CuO nanostructures and their electrochemical properties, Ceram.

Int. 42 (16) (2016) 19454–19460. Available from: https://doi.org/10.1016/j.ceramint.2016.09.044.

[94] N.F. Andrade Neto, P.M. Oliveira, R.M. Nascimento, C.A. Paskocimas, M.R.D. Bomio, F.V. Motta, Influence of pH on the morphology and photocatalytic activity of CuO obtained by the sonochemical method using different surfactants, Ceram. Int. 45 (1) (2019) 651–658. Available from: https://doi.org/10.1016/j.ceramint.2018.09.224.

[95] D.N. Oosthuizen, D.E. Motaung, H.C. Swart, In depth study on the notable room-temperature NO_2 gas sensor based on CuO nanoplatelets prepared by sonochemical method: comparison of various bases, Sens. Actuators B: Chem. 266 (2018) 761–772. Available from: https://doi.org/10.1016/j.snb.2018.03.106.

[96] U.O. Bhagwat, J.J. Wu, A.M. Asiri, S. Anandan, Sonochemical synthesis of Mg-TiO_2 nanoparticles for persistent Congo red dye degradation, J. Photochem. Photobiol. A: Chem. 346 (2017) 559–569. Available from: https://doi.org/10.1016/j.jphotochem.2017.06.043.

[97] S.A. Mansour, Non-isothermal crystallization kinetics of nano-sized amorphous TiO_2 prepared by facile sonochemical hydrolysis route, Ceram. Int. 45 (2, Part B) (2019) 2893–2898. Available from: https://doi.org/10.1016/j.ceramint.2018.07.273.

[98] W. Zhu, A. Shui, L. Xu, X. Cheng, P. Liu, H. Wang, Template-free sonochemical synthesis of hierarchically porous NiO microsphere, Ultrason. Sonochem. 21 (5) (2014) 1707–1713. Available from: https://doi.org/10.1016/j.ultsonch.2014.02.026.

[99] N. Duraisamy, A. Numan, S.O. Fatin, K. Ramesh, S. Ramesh, Facile sonochemical synthesis of nanostructured NiO with different particle sizes and its electrochemical properties for supercapacitor application, J. Colloid Interface Sci. 471 (2016) 136–144. Available from: https://doi.org/10.1016/j.jcis.2016.03.013.

[100] Y. Hanifehpour, A. Morsali, B. Mirtamizdoust, S.W. Joo, B. Soltani, Thermolysis synthesis of pure phase NiO from novel sonochemical synthesized Ni(II) nano metal-organic supramolecular architecture, Ultrason. Sonochem. 37 (2017) 430–435. Available from: https://doi.org/10.1016/j.ultsonch.2017.02.003.

[101] M.A. Bhosale, B.M. Bhanage, A simple approach for sonochemical synthesis of Cu_2O nanoparticles with high catalytic properties, Adv. Powder Technol. 27 (1) (2016) 238–244. Available from: https://doi.org/10.1016/j.apt.2015.12.008.

[102] K. Kaviyarasan, S. Anandan, R.V. Mangalaraja, T. Sivasankar, M. Ashokkumar, Sonochemical synthesis of Cu_2O nanocubes for enhanced chemiluminescence applications, Ultrason. Sonochem. 29 (2016) 388–393. Available from: https://doi.org/10.1016/j.ultsonch.2015.10.018.

[103] N. Das, D. Bhattacharya, A. Sen, H.S. Maiti, Sonochemical synthesis of $LaMnO_3$ nano-powder, Ceram. Int. 35 (1) (2009) 21–24. Available from: https://doi.org/10.1016/j.ceramint.2007.09.002.

[104] J.-F. Chen, Z.-G. Shen, F.-T. Liu, X.-L. Liu, J. Yun, Preparation and properties of barium titanate nanopowder by conventional and high-gravity reactive precipitation methods, Scr. Mater. 49 (6) (2003) 509–514. Available from: https://doi.org/10.1016/S1359-6462(03)00361-0.

[105] M. Xu, Y.-n Lu, Y.-f Liu, S.-z Shi, T.-s Qian, D.-y Lu, Sonochemical synthesis of monosized spherical $BaTiO_3$ particles, Powder Technol. 161 (3) (2006) 185–189. Available from: https://doi.org/10.1016/j.powtec.2005.10.001.

[106] M.M. Lencka, R.E. Riman, Thermodynamic modeling of hydrothermal synthesis of ceramic powders, Chem. Mater. 5 (1) (1993) 61–70. Available from: https://doi.org/10.1021/cm00025a014.

[107] A. Testinon, M.T. Buscaglia, M. Viviani, V. Buscaglia, P. Nanni, Synthesis of $BaTiO_3$ particles with tailored size by precipitation from aqueous solutions, J. Am. Ceram. Soc. 87 (1) (2004) 79−83. Available from: https://doi.org/10.1111/j.1551-2916.2004.00079.x.

[108] T.P. Yadav, O.N. Srivastava, Synthesis of nanocrystalline cerium oxide by high energy ball milling, Ceram. Int. 38 (7) (2012) 5783−5789. Available from: https://doi.org/10.1016/j.ceramint.2012.04.025.

[109] M. Alizadeh, F. Sharifianjazi, E. Haghshenasjazi, M. Aghakhani, L. Rajabi, Production of nanosized boron oxide powder by high-energy ball milling, Synth. React. Inorg. Met.-Org. Nano-Met. Chem. 45 (1) (2015) 11−14. Available from: https://doi.org/10.1080/15533174.2013.797438.

[110] T.-T.-N. Nguyen, J.-L. He, Preparation of titanium monoxide nanopowder by low-energy wet ball-milling, Adv. Powder Technol. 27 (4) (2016) 1868−1873. Available from: https://doi.org/10.1016/j.apt.2016.04.022.

[111] G.-J. Lee, E.-K. Park, S.-A. Yang, J.-J. Park, S.-D. Bu, M.-K. Lee, Rapid and direct synthesis of complex perovskite oxides through a highly energetic planetary milling, Sci. Rep. 7 (2017) 46241. Available from: https://doi.org/10.1038/srep46241.

[112] D.T. França, B.F. Amorim, A.M. de Morais Araújo, M.A. Morales, F. Bohn, S.N. de Medeiros, Structural and magnetic properties of Fe_2TiO_5 nanopowders prepared by ball-milling and post annealing, Mater. Lett. 236 (2019) 526−529. Available from: https://doi.org/10.1016/j.matlet.2018.10.149.

[113] D. Stoyanova, I. Stambolova, V. Blaskov, K. Zaharieva, I. Avramova, O. Dimitrov, et al., Mechanical milling of hydrothermally obtained $CaTiO_3$ powders—morphology and photocatalytic activity, Nano-Struct. Nano-Objects 18 (2019) 100301. Available from: https://doi.org/10.1016/j.nanoso.2019.100301.

[114] F. Pedro-García, F. Sánchez-De Jesús, C.A. Cortés-Escobedo, J.A. Patiño-Pineda, A. M. Bolarín-Miró, Multiferroic properties of nanostructured $BiFeO_3$ tailored by milling and sintering by SPS, J. Alloy. Compd. 792 (2019) 694−701. Available from: https://doi.org/10.1016/j.jallcom.2019.04.106.

[115] G.R. Khayati, E. Nourafkan, G. Karimi, J. Moradgholi, Synthesis of cuprous oxide nanoparticles by mechanochemical oxidation of copper in high planetary energy ball mill, Adv. Powder Technol. 24 (1) (2013) 301−305. Available from: https://doi.org/10.1016/j.apt.2012.07.006.

[116] Ö. Yıldız, A.M. Soydan, Parameters for spray drying ZnO nanopowders as spherical granules, J. Am. Ceram. Soc. 101 (1) (2018) 103−115. Available from: https://doi.org/10.1111/jace.15191.

[117] M.R. Loghman-Estarki, H. Sheikh, E. Mohammad sharifi, M.H. Babaee, M. Kharraziha, A. Alhaji, From sub-microsized $MgAl_2O_4$ powder to $MgAl_2O_4$−Si_3N_4 nanocomposite powder by spray drying of ultrasonicated suspensions, Ceram. Int. 43 (15) (2017) 12781−12788. Available from: https://doi.org/10.1016/j.ceramint.2017.06.165.

[118] Ö. Yıldız, A.M. Soydan, Synthesis of zirconia toughened alumina nanopowders as soft spherical granules by combining co-precipitation with spray drying, Ceram. Int. 45 (14) (2019) 17521−17528. Available from: https://doi.org/10.1016/j.ceramint.2019.05.314.

[119] B.D. Ehrhart, B.J. Ward, B.M. Richardson, K.S. Anseth, A.W. Weimer, Partial flocculation for spray drying of spherical mixed metal oxide particles, J. Am. Ceram. Soc. 101 (10) (2018) 4452−4457. Available from: https://doi.org/10.1111/jace.15727.

[120] k Donadel, M.D.V. Felisberto, M.C.M. Laranjeira, Preparation and characterization of hydroxyapatite-coated iron oxide particles by spray-drying technique, An. da Acad. Bras. Ciências 81 (2009) 179−186.

[121] A.V. Makeenko, T.V. Larionova, O.G. Klimova-Korsmik, R.V. Starykh, V.V. Galkin, O.V. Tolochko, Synthesis of complex oxides with garnet structure by spray drying of an aqueous salt solution, Tech. Phys. 62 (4) (2017) 613–618. Available from: https://doi.org/10.1134/s1063784217040168.

[122] J. Yu, D. Kim, The preparation of nano size nickel oxide powder by spray pyrolysis process, Powder Technol. 235 (2013) 1030–1037. Available from: https://doi.org/10.1016/j.powtec.2012.11.031.

[123] Y. Hwangbo, Y.-I. Lee, Facile synthesis of zirconia nanoparticles using a salt-assisted ultrasonic spray pyrolysis combined with a citrate precursor method, J. Alloy. Compd. 771 (2019) 821–826. Available from: https://doi.org/10.1016/j.jallcom.2018.08.308.

[124] M.J.S. Raju, S.S. Bhattacharya, Structural and optical properties of nanocrystalline pure and indium doped tin oxide powders synthesized in a single step by flame spray pyrolysis, Mater. Res. Exp. 4 (7) (2017) 075034.

[125] T. Tani, A. Kato, H. Morisaka, Effects of solvent on powder characteristics of zinc oxide and magnesia prepared by flame spray pyrolysis, J. Ceram. Soc. Jpn. 113 (1315) (2005) 255–258. Available from: https://doi.org/10.2109/jcersj.113.255.

[126] S.H. Choi, Y.C. Kang, Characteristics of $ZnMn_2O_4$ nanopowders prepared by flame spray pyrolysis for use as anode material in lithium ion batteries, Int. J. Electrochem. Sci. 8 (2013) 6281–6290.

[127] N.B. Granados, E. Yi, R. Laine, O.J.R. Baena, $CoAl_2O_4$ blue nanopigments prepared by liquid-feed flame spray pyrolysis method, Matéria (Rio de. Jan.) 20 (2015) 580–587.

[128] I.V. Krasnikova, I.V. Mishakov, Y.I. Bauman, T.M. Karnaukhov, A.A. Vedyagin, Preparation of NiO-CuO-MgO fine powders by ultrasonic spray pyrolysis for carbon nanofibers synthesis, Chem. Phys. Lett. 684 (2017) 36–38. Available from: https://doi.org/10.1016/j.cplett.2017.06.036.

[129] C. Tallón, R. Moreno, M.I. Nieto, Synthesis of ZrO_2 nanoparticles by freeze drying, Int. J. Appl. Ceram. Technol. 6 (2) (2009) 324–334. Available from: https://doi.org/10.1111/j.1744-7402.2008.02279.x.

[130] B. Liu, Y. You, H. Zhang, H. Wu, J. Jin, H. Liu, Synthesis of ZnO nano-powders via a novel PVA-assisted freeze-drying process, RSC Adv. 6 (111) (2016) 110349–110355. Available from: https://doi.org/10.1039/C6RA24154A.

[131] A.S. Picco, L.F. Ferreira, M.S. Liberato, G.B. Mondo, M.B. Cardoso, Freeze-drying of silica nanoparticles: redispersibility toward nanomedicine applications, Nanomedicine 13 (2) (2018) 179–190. Available from: https://doi.org/10.2217/nnm-2017-0280.

[132] V.K. Ivanov, O.S. Polezhaeva, A.E. Baranchikov, A.B. Shcherbakov, Thermal stability of nanocrystalline CeO_2 prepared through freeze drying, Inorg. Mater. 46 (1) (2010) 43–46. Available from: https://doi.org/10.1134/s0020168510010103.

[133] L.K.H. Pallon, R.T. Olsson, D. Liu, A.M. Pourrahimi, M.S. Hedenqvist, A.T. Hoang, et al., Formation and the structure of freeze-dried MgO nanoparticle foams and their electrical behaviour in polyethylene, J. Mater. Chem. A 3 (14) (2015) 7523–7534. Available from: https://doi.org/10.1039/C4TA06362G.

[134] L.B. Chiriac, M. Todea, A. Vulpoi, M. Muresan-Pop, R.V.F. Turcu, S. Simon, Freeze-drying assisted sol–gel-derived silica-based particles embedding iron: synthesis and characterization, J. Sol-Gel Sci. Technol. 87 (1) (2018) 195–203. Available from: https://doi.org/10.1007/s10971-018-4702-2.

[135] M. Kim, S. Osone, T. Kim, H. Higashi, T. Seto, Synthesis of nanoparticles by laser ablation: a review, KONA Powder Part J. 34 (2017) 80–90. Available from: https://doi.org/10.14356/kona.2017009.

[136] J. Neddersen, G. Chumanov, T.M. Cotton, Laser ablation of metals: a new method for preparing SERS active colloids, Appl. Spectrosc. 47 (12) (1993) 1959–1964.
[137] V.A. Svetlichnyi, A.V. Shabalina, I.N. Lapin, Structure and properties of nanocrystalline iron oxide powder prepared by the method of pulsed laser ablation, Russian Phys. J. 59 (12) (2017) 2012–2016. Available from: https://doi.org/10.1007/s11182-017-1008-8.
[138] S.J. Henley, S. Mollah, C.E. Giusca, S.R.P. Silva, Laser-induced self-assembly of iron oxide nanostructures with controllable dimensionality, J. Appl. Phys. 106 (6) (2009) 064309. Available from: https://doi.org/10.1063/1.3224854.
[139] S.I. Al-Nassar, F.I. Hussein, K.M. Adel, The effect of laser pulse energy on ZnO nanoparticles formation by liquid phase pulsed laser ablation, J. Mater. Res. Technol. (2019). Available from: https://doi.org/10.1016/j.jmrt.2019.07.012.
[140] K. Siraj, Y. Sohail, A. Tabassum, Metals and metal oxides particles produced by pulsed laser ablation under high vacuum, Turkish J. Phys. 35 (2) (2011) 179–183.
[141] A.V. Vodopyanov, A.V. Samokhin, N.V. Alexeev, M.A. Sinayskiy, A.I. Tsvetkov, M. Y. Glyavin, et al., Application of the 263 GHz/1 kW gyrotron setup to produce a metal oxide nanopowder by the evaporation-condensation technique, Vacuum 145 (2017) 340–346. Available from: https://doi.org/10.1016/j.vacuum.2017.09.018.
[142] L. Zhan, X. Xiang, B. Xie, B. Gao, Preparing lead oxide nanoparticles from waste electric and electronic equipment by high temperature oxidation-evaporation and condensation, Powder Technol. 308 (2017) 30–36. Available from: https://doi.org/10.1016/j.powtec.2016.12.005.
[143] C. Stötzel, H.D. Kurland, J. Grabow, F.A. Müller, Gas phase condensation of superparamagnetic iron oxide–silica nanoparticles–control of the intraparticle phase distribution, Nanoscale 7 (17) (2015) 7734–7744. Available from: https://doi.org/10.1039/C5NR00845J.
[144] M.S. El-Shall, W. Slack, W. Vann, D. Kane, D. Hanley, Synthesis of nanoscale metal oxide particles using laser vaporization/condensation in a diffusion cloud chamber, J. Phys. Chem. 98 (12) (1994) 3067–3070. Available from: https://doi.org/10.1021/j100063a001.
[145] S. Kashyap, T.J. Woehl, X. Liu, S.K. Mallapragada, T. Prozorov, Nucleation of iron oxide nanoparticles mediated by Mms6 protein in situ, ACS Nano 8 (9) (2014) 9097–9106. Available from: https://doi.org/10.1021/nn502551y.
[146] A.A. Bharde, R.Y. Parikh, M. Baidakova, S. Jouen, B. Hannoyer, T. Enoki, et al., Bacteria-mediated precursor-dependent biosynthesis of superparamagnetic iron oxide and iron sulfide nanoparticles, Langmuir 24 (11) (2008) 5787–5794. Available from: https://doi.org/10.1021/la704019p.
[147] H. Almoammar, M. Rai, E. Said-Galiev, K.A. Abd-Elsalam, Myconanoparticles: synthesis and their role in phytopathogens management, Biotechnol. Biotechnol. Equip. 29 (2) (2015) 221–236. Available from: https://doi.org/10.1080/13102818.2015.1008194.
[148] P. Singh, Y.-J. Kim, D. Zhang, D.-C. Yang, Biological synthesis of nanoparticles from plants and microorganisms, Trends Biotechnol. 34 (7) (2016) 588–599. Available from: https://doi.org/10.1016/j.tibtech.2016.02.006.
[149] M.R. Salvadori, R.A. Ando, C.A. Oller Nascimento, B. Corrêa, Extra and intracellular synthesis of nickel oxide nanoparticles mediated by dead fungal biomass, PLoS One 10 (6) (2015) e0129799. Available from: https://doi.org/10.1371/journal.pone.0129799.
[150] V.N. Kalpana, B.A.S. Kataru, N. Sravani, T. Vigneshwari, A. Panneerselvam, V. Devi Rajeswari, Biosynthesis of zinc oxide nanoparticles using culture filtrates of *Aspergillus niger*: antimicrobial textiles and dye degradation studies, OpenNano 3 (2018) 48–55. Available from: https://doi.org/10.1016/j.onano.2018.06.001.

[151] S.K. Chaudhuri, L. Malodia, Biosynthesis of zinc oxide nanoparticles using leaf extract of *Calotropis gigantea*: characterization and its evaluation on tree seedling growth in nursery stage, Appl. Nanosci. 7 (8) (2017) 501−512. Available from: https://doi.org/10.1007/s13204-017-0586-7.

[152] A.A. Zahir, I.S. Chauhan, A. Bagavan, C. Kamaraj, G. Elango, J. Shankar, et al., Green synthesis of silver and titanium dioxide nanoparticles using *Euphorbia prostrata* extract shows shift from apoptosis to G0/G1 arrest followed by necrotic cell death in *Leishmania donovani*, Antimicrobial. Agents Chemother. 59 (8) (2015) 4782−4799. Available from: https://doi.org/10.1128/aac.00098-15.

[153] M.S. Geetha, H. Nagabhushana, H.N. Shivananjaiah, Green mediated synthesis and characterization of ZnO nanoparticles using *Euphorbia Jatropha* latex as reducing agent, J. Sci.: Adv. Mater. Dev. 1 (3) (2016) 301−310. Available from: https://doi.org/10.1016/j.jsamd.2016.06.015.

This page intentionally left blank

Sintering behaviors of Fe_3O_4 and CaO powders roasted under $CO-CO_2-N_2$ atmosphere

4

Yuanbo Zhang, Zijian Su, Tao Jiang and Jicheng Liu
School of Minerals Processing & Bioengineering, Central South University, Changsha, P.R. China

4.1 Introduction

Iron ore sintering and pelletizing are the predominant processes in the iron-making industry [1,2]. During the iron ore sintering process, calcium ferrite phase is believed to be the most desirable bonding phase because it has high reducibility and sufficient mechanical strength [3–5]. The sintering process can be divided into three procedures: (1) heating-up period. Calcium ferrites are formed from iron oxides and basic fluxes (lime or calcite), and then a small quantity of calcium ferrites react with gangue components via solid-state reaction; (2) high-temperature period. Calcium ferrites become liquid phases and gangue components fast dissolve into them; and (3) cooling period. The solidification and precipitation of the liquid phases take place [6]. The generation of calcium ferrites and sintering atmosphere during the sintering process are closely related to the combustion of coke breeze, which not only provide the heat energy but also produce CO and CO_2 gases [7,8]. A considerable amount of researchers have reported the formation behavior of calcium ferrites related to the iron ore sintering process [9–18]. However, most of previous investigations mainly focused on the formation of calcium ferrites under different oxidizing atmosphere (or O_2 partial pressures).

It is well known that the combustion reaction of coke breeze takes place at temperatures higher than 600°C to supply the necessary heat for the mineralization reactions during the sintering process. In addition, CO_2 and CO gases emit during the combustion of coke breeze. Some studies reported that the $CO/(CO + CO_2)$ values during the sintering process were in the range of 12–35 vol.% as the coke breeze dosage increased from 5 to 15 wt.% [19–25]. Hence, during iron ore sintering process, the actual sintering atmosphere where the coke breeze is combusted is not entirely oxidizing atmosphere but weakly reducing atmosphere, which inevitably affects the formation of calcium ferrites. Therefore it is necessary to investigate the formation behaviors of calcium ferrites under certain $CO-CO_2$ atmosphere.

In this study the reaction behaviors of CaO and Fe_3O_4 roasted under $CO-CO_2$ atmosphere at 800°C–1250°C were investigated to determine the formation mechanism of calcium ferrites under a reducing atmosphere by using x-ray diffraction

Metal Oxide Powder Technologies. DOI: https://doi.org/10.1016/B978-0-12-817505-7.00004-X

(XRD), thermogravimetric analysis (TG)−differential scanning calorimetry (DSC), scanning electron microscope (SEM)−energy dispersive spectrometer (EDS), Factsage, etc.

4.2 Experimental

4.2.1 Materials

The materials used in this study were analytical reagents of Fe_3O_4 and CaO powders (Aladdin, Shanghai, with purities of beyond 99.95 wt.%). All the reagents were preground until the particle size passed through a 0.074 mm sieve. The briquette (10 mm diameter and 10 mm height) was prepared by pressing 2.5−3.0 g of the ground mixtures into a cylindrical mold for 2 minutes with 10 MPa pressure. Then, the briquettes were dried at 100°C for 4 hours. The gases included CO, CO_2, and N_2 with the purity of 99.99 vol.%.

4.2.2 Methods

4.2.2.1 Roasting tests

The roasting tests were conducted in a horizontal resistance furnace, and the schematic apparatus for the roasting experiment is shown in Fig. 4.1.

During the sintering process the atmosphere was controlled by passing various gas mixtures into the reaction tube. The roasting temperature was measured by a Pt−Rh thermocouple and controlled by a KSY intelligent temperature controller (accuracy ±0.1°C). The total inlet gas flow rate was fixed at 5.0 L/min and the rate flow of the gas was measured by a flow meter.

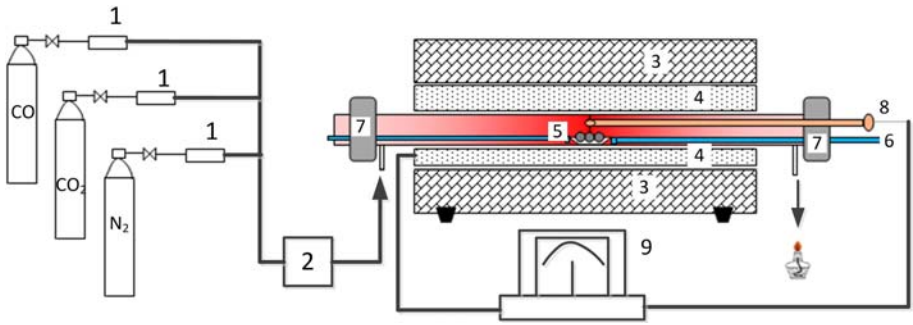

Figure 4.1 Schematic apparatus of the roasting experiment (1—flowmeter; 2—mixing chamber; 3—tube furnace; 4—SiC heating component; 5—sample boat; 6—pushbeam; 7—sealing ring; 8—thermocouple; 9—KSY intelligent temperature controller).

The detailed procedures were as follows: first of all, pure N_2 gas was led into the tube until the temperature reached a given value, then, the dried samples were placed in a corundum crucible (size: 80 mm × 10 mm) and loaded into a heat-resisting quartz tube. Second, the quartz tube carrying with the samples was pushed into the roasting zone; after that the $CO-CO_2-N_2$ mixed gas immediately took the place of N_2 gas, and then the samples were roasted at given temperatures for a certain period. Third, the roasted samples were taken out rapidly and quenched in liquid nitrogen. Finally, some cooled samples were ground to 100 wt.% passing through 0.074 mm for XRD analyses, and some other samples were used for microstructure analyses.

4.2.2.2 Fusion temperature measurement

The external shape of the roasted samples and the roasting temperature were recorded by a camera every 2 seconds according to the previous report [8].

The fusion temperature−measurement equipment was shown in Fig. 4.2A. CaO and Fe_3O_4 mixtures were shaped into a pyramid sample with a bottom side length of 12 mm and vertical height of 35 mm. The sample was then placed on a corundum plate and heated in the horizontal tube furnace with a heating rate of 10°C/min in air and $CO-CO_2-N_2$ atmosphere from 20°C to 1600°C, respectively. The external shape change of each specimen was recorded by a camera every 2 seconds and characterized by the standard as described in the literature [26]. Three characteristic temperatures were identified (Fig. 4.2B): (1) deformation temperature (T_d), determined by the temperature at which the tip of the pyramid becomes spherical; (2) sphere temperature (T_s), determined by the temperature at which the whole pyramid becomes hemispheric; and (3) flow temperature (T_f), determined by the temperature at which the pyramid melts until the vertical height is less than 1.5 mm.

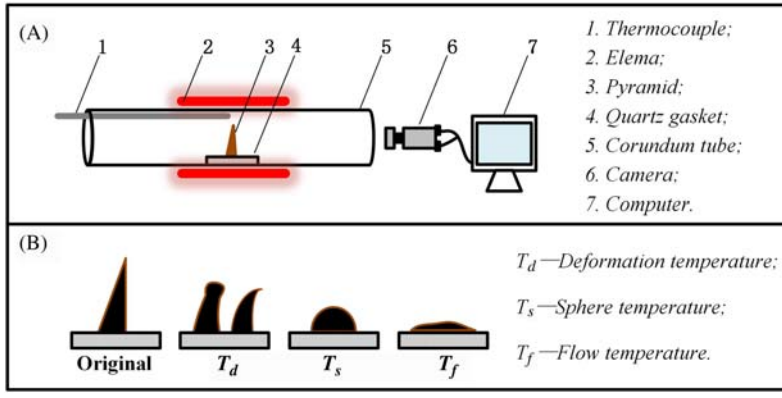

Figure 4.2 Schematic diagram of horizontal tube furnace (A) and the external shape of the sample at different temperatures (B).

4.2.2.3 Characterization

TG−derivative thermogravimetry (DTG) analyses of the samples were performed using a thermal analyzer (Netzsch STA 449C, Germany) in the temperature range of 20°C−1200°C with a heating rate of 10°C/min under $CO-CO_2-N_2$ atmosphere. Phase compositions of the samples were determined by XRD with a diffractometer (Rigaku D/Max 2500; Rigaku Corporation, Tokyo, Japan) under the conditions of radiation: Cu *K*a, tube current and voltage: 250 mA, 40 kV, scanning range: 10−80 degrees (2θ), step size: 0.02 degree (2θ), and scanning speed: 8 degrees/min. The microstructural images of the samples were conducted by an optical microscopy (LEICA DM RXP, Germany) and scanning electron microscope equipped with an energy diffraction spectrum (SEM−EDS, JEOL, JSM-6490LV, Japan).

4.3 Results and discussion

4.3.1 Phase diagrams of $CaO-Fe_3O_4$ system under $CO-CO_2-N_2$ and air atmosphere

The phase diagrams of $CaO-Fe_3O_4$ system under $3\%CO-22\%CO_2-75\%N_2$ and air atmosphere were first performed using FactSage software and shown in Fig. 4.3. It was seen that calcium ferrite ($Ca_2Fe_2O_5$) was the most stable phase under air and $3\%CO-22\%CO_2-75\%N_2$ atmosphere, and the final phase constitutions were determined by the mole ratio of $Fe_3O_4/(Fe_3O_4 + CaO)$. However, it was found that different liquidus lines existed under various atmospheres, and the liquidus temperature was 1110°C as shown in Fig. 4.3A, while the value was 1205°C in Fig. 4.3B. It is well-known that the melting points of binary calcium ferrites ($CaO \cdot Fe_2O_3$, $CaO \cdot 2Fe_2O_3$, $2CaO \cdot Fe_2O_3$) and FeO_x (FeO, Fe_3O_4, Fe_2O_3) were higher than 1200°C. However, some liquid phases with low-melting point (1110°C) were observed under $3\%CO-22\%CO_2-75\%N_2$ atmosphere. Then, further study was carried out to determine the liquid phases.

4.3.2 Phase transformation of CaO and Fe_3O_4 mixtures in $CO-CO_2-N_2$ atmosphere

The effect of roasting temperature and CO content on the phase transformation were examined. The CO content refers to the CO volume concentration in the $CO-CO_2-N_2$ mixed gas [i.e., $CO/(CO + CO_2 + N_2)$, N_2 content was fixed at 75 vol.%].

4.3.2.1 Effect of temperature

The effect of roasting temperature varying from 700°C to 1250°C on the phase transformation was first investigated and the XRD patterns of the roasted samples were presented in Fig. 4.4.

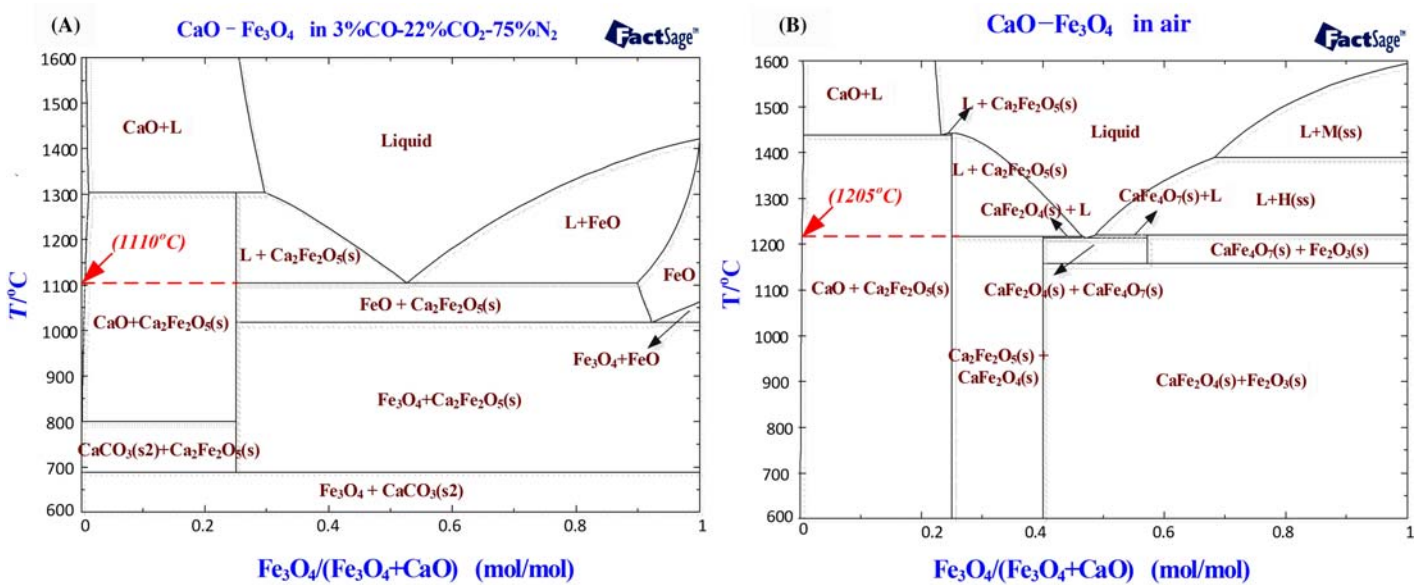

Figure 4.3 Phase diagrams of $CaO-Fe_3O_4$ system under (A) $3\%CO-22\%CO_2-75\%N_2$ and (B) air atmospheres.

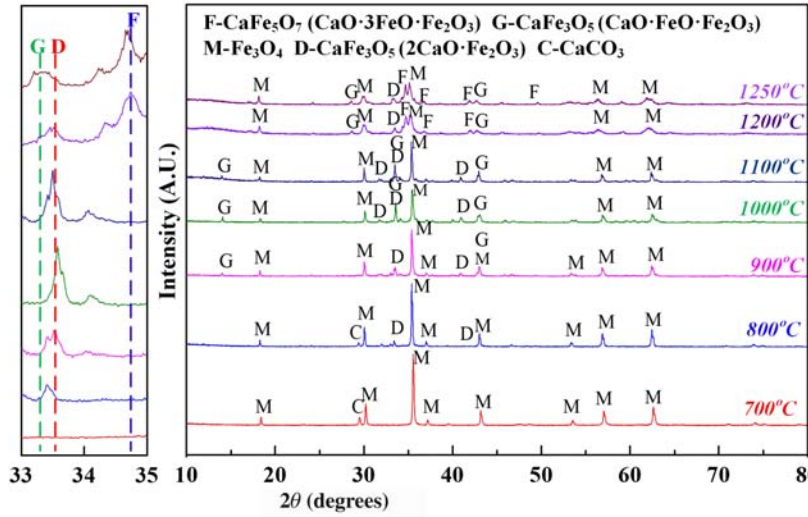

Figure 4.4 XRD patterns of samples roasted at different roasting temperatures. (CO content of 3 vol.%, roasting time of 5 min, Fe_3O_4:CaO mass ratio = 90:10).

It was seen from Fig. 4.4 that the major phases in the roasted samples were $Ca_2Fe_2O_5$, Fe_3O_4, and the ternary calcium ferrites ($CaO \cdot FeO \cdot Fe_2O_3$ and $CaO \cdot 3FeO \cdot Fe_2O_3$). It was found by careful observation that $Ca_2Fe_2O_5$ (PDF#71−2108, at $2\theta = 33.515$ degrees) was first formed at 800°C, and the diffraction peak intensity of $Ca_2Fe_2O_5$ increased as the temperature increased to 1000°C. The results indicated that $Ca_2Fe_2O_5$ was the most stable phase and easily formed under $CO-CO_2-N_2$ atmosphere, which was consistent with the phase diagram shown in Fig. 4.3. However, the diffraction peak of $Ca_2Fe_2O_5$ decreased obviously when roasting temperature was higher than 1100°C, meanwhile, ternary calcium ferrites ($CaO \cdot FeO \cdot Fe_2O_3$ and $CaO \cdot 3FeO \cdot Fe_2O_3$) were found. As the roasting temperature further increased to 1250°C, the diffraction peak intensity of $CaO \cdot 3FeO \cdot Fe_2O_3$ increased and $CaO \cdot 3FeO \cdot Fe_2O_3$ became the main Ca−Fe−O phases in the roasted samples, indicating that higher roasting temperature promoted FeO dissolving into binary calcium ferrite ($Ca_2Fe_2O_5$).

Previous studies reported the phase diagram of $CaO-FeO-Fe_2O_3$ system under nitrogen atmosphere, and the results shown in Fig. 4.5 indicated that ternary calcium ferrites ($CaO \cdot FeO \cdot Fe_2O_3$ and $CaO \cdot 3FeO \cdot Fe_2O_3$) had much lower melting points (<1150°C) than that of binary calcium ferrite [27,28]. The formation of ternary calcium ferrites is beneficial to the formation of liquid phases (such as $Ca_2Fe_2O_5$) during the iron ore sintering process.

The microstructural images of the roasted samples were shown in Fig. 4.6, and it was seen that $Ca_2Fe_2O_5$ and Fe_3O_4 were the main phases when the roasting temperature was lower than 1100°C, while a new phase appeared as roasting temperature increased to 1200°C and 1250°C. Then, SEM−EDS analysis was conducted to

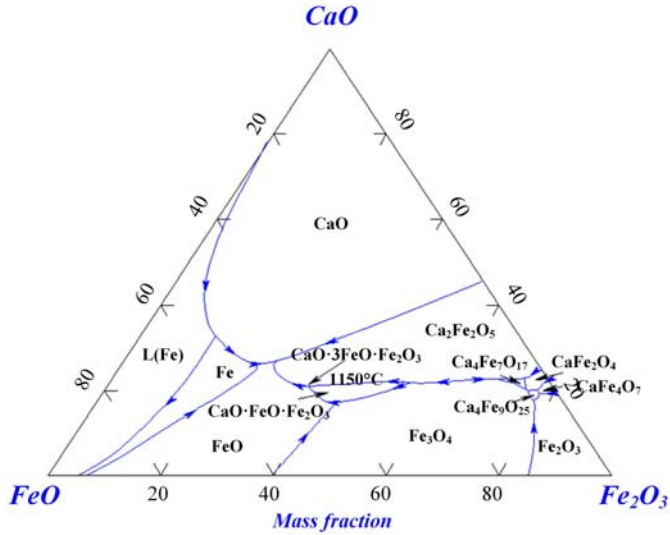

Figure 4.5 Phase diagram of the $CaO-FeO-Fe_2O_3$ system [27,28].

confirm the phase compositions of the new phase, and the results were shown in Fig. 4.7. It was shown that Ca/Fe atom ratio of Spots A, B, and C was approaching to 1:5, which was close to $CaO \cdot 3FeO \cdot Fe_2O_3$. The results were in accordance with the XRD results in Fig. 4.4.

4.3.2.2 Effect of CO content

Fig. 4.8 demonstrates the XRD patterns of the roasted samples under different CO content varying from 1 to 10 vol.%. As seen from Fig. 4.8, the predominant phases in the samples were Fe_3O_4, binary calcium ferrite ($Ca_2Fe_2O_5$), and the ternary calcium ferrite ($CaO \cdot FeO \cdot Fe_2O_3$ and $CaO \cdot 3FeO \cdot Fe_2O_3$). The diffraction peaks of $Ca_2Fe_2O_5$ decreased obviously when the CO content increased from 1 to 5 vol.%. The peaks of $CaO \cdot 3FeO \cdot Fe_2O_3$ increased sharply as the increase of CO content, which indicated that higher CO content promoted the reduction of iron oxides to FeO, then FeO was dissolved into $Ca_2Fe_2O_5$ to generate ternary calcium ferrite ($CaO \cdot xFeO \cdot Fe_2O_3$, $x = 1, 3$).

4.3.3 Liquid phase formation of $CaO-Fe_3O_4$ system in $CO-CO_2-N_2$ atmosphere

To identify the formation of low-melting-point calcium ferrite phases, $CaO \cdot FeO \cdot Fe_2O_3$ and $CaO \cdot 3FeO \cdot Fe_2O_3$, the amount of liquid phases in $CaO-Fe_3O_4$ system was calculated using FactSage 7.0. Then, the fusion temperature of CaO and Fe_3O_4 mixtures was tested.

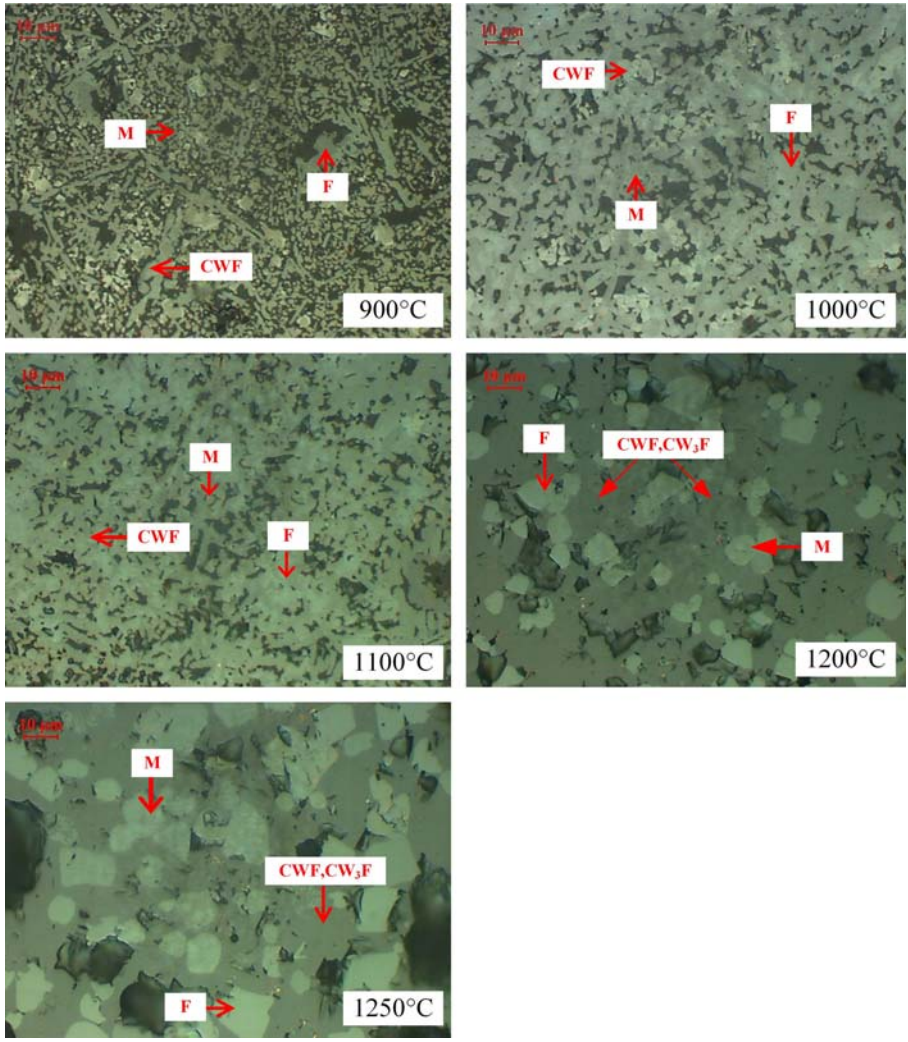

Figure 4.6 Microstructural images of the roasted samples.
(CO content of 3 vol.%, roasting time of 5 min). (M—Fe_3O_4; F—$Ca_2Fe_2O_5$; CWF—$CaO \cdot FeO \cdot Fe_2O_3$; CW_3F—$CaO \cdot 3FeO \cdot Fe_2O_3$)

The effect of temperature on the liquid phase formation of $CaO-Fe_3O_4$ system in air and $CO-CO_2-N_2$ atmosphere was shown in Fig. 4.9. In $CO-CO_2-N_2$ atmosphere the liquid phase started to form at 1100°C, which was about 100°C lower than that in air. When the temperature was in the range of 1200°C−1300°C, the mass fraction of liquid phase reached 50−70 wt.% in air, while it was 70−90 wt.% in $CO-CO_2-N_2$ atmosphere. It was known that the melting temperature of binary calcium ferrites was about 1205°C; hence, the significant difference of the liquid

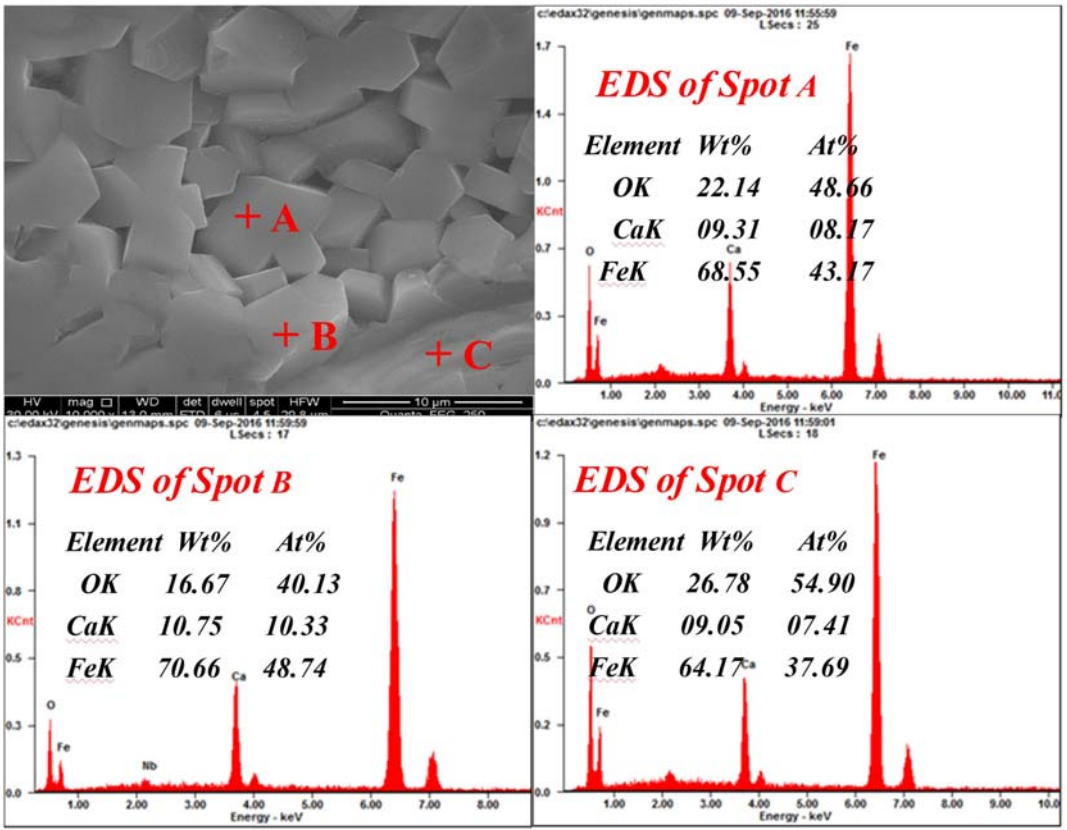

Figure 4.7 SEM−EDS results of the roasted samples.
(CO content of 3 vol.%, roasting temperature of 1200°C, roasting time of 5 min).

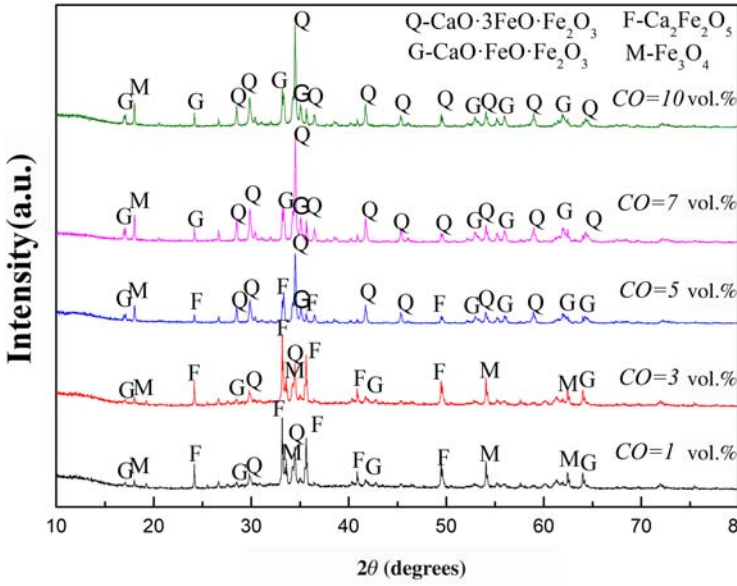

Figure 4.8 XRD patterns of the samples roasted at different CO contents (temperature of 1200°C, roasting time of 5 min, Fe_3O_4:CaO mass ratio = 90:10).

phase mass fractions was attributed to the formation of ternary calcium ferrite under $CO-CO_2-N_2$ atmosphere.

The fusion temperatures of $CaO-Fe_3O_4$ mixtures in air and $CO-CO_2-N_2$ atmosphere were measured as the method in Section 4.2.2.2, and the results were shown in Table 4.1. It was seen from Table 4.1 that T_d, T_s, and T_f were decreased as increasing CaO/Fe_3O_4 mole ratio. Compared with those in air, the T_d, T_s, and T_f values in $CO-CO_2-N_2$ atmosphere showed a decreasing trend, which attributed to the formation of the low-melting-point ternary calcium ferrites, $CaO \cdot FeO \cdot Fe_2O_3$ and $CaO \cdot 3FeO \cdot Fe_2O_3$.

4.3.4 Reaction mechanism between CaO and Fe_3O_4 under $CO-CO_2-N_2$ atmosphere

TG–DTG analysis was conducted to study the reaction behavior of CaO and Fe_3O_4 under $3\%CO-22\%CO_2-75\%N_2$ atmosphere. Fig. 4.10 showed that the TG curve decreased obviously when the temperature was higher than 700°C, which was attributed to the decomposition of $CaCO_3$ ($CaCO_3 = CaO + CO_2$). After the temperature was over 820°C, the TG curve decreased slowly, and the reason would be investigated further.

The CaO and Fe_3O_4 mixed powders were roasted under N_2 atmosphere to investigate the formation mechanism of ternary calcium ferrites, and the XRD patterns

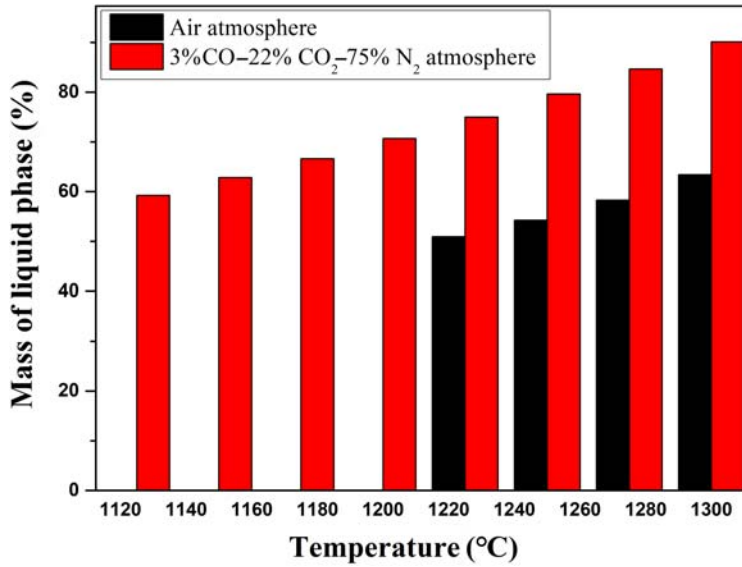

Figure 4.9 Mass fraction of liquid phase of $CaO-Fe_3O_4$ mixtures under different atmospheres (Fe_3O_4:CaO mass ratio = 90:10).

Table 4.1 The melting features of $CaO-Fe_3O_4$ mixtures in different atmospheres.

Samples	Air atmosphere			$3\%CO-22\%CO_2-75\%N_2$ atmosphere		
	T_d (°C)	T_s (°C)	T_f (°C)	T_d (°C)	T_s (°C)	T_f (°C)
CaO/Fe_3O_4 = 5:95	1353	1491	>1500	1163	1289	>1500
CaO/Fe_3O_4 = 10:90	1297	1398	1482	1056	1179	1258
CaO/Fe_3O_4 = 20:80	1159	1219	1224	987	1098	1169

of the roasted samples were shown in Fig. 4.11. It was found that $Ca_2Fe_2O_5$ was first formed at a relatively lower temperature of 1000°C, and the diffraction peaks of $CaO \cdot FeO \cdot Fe_2O_3$ and $CaO \cdot 3FeO \cdot Fe_2O_3$ were observed at 1100°C−1200°C. However, the peaks of $CaO \cdot FeO \cdot Fe_2O_3$ was much stronger than that of $CaO \cdot 3FeO \cdot Fe_2O_3$, which indicated that FeO just came from Fe_3O_4 ($FeO \cdot Fe_2O_3$). Compared with the results shown in Fig. 4.8, more FeO could be produced under reduction atmosphere, which promoted the formation of $CaO \cdot 3FeO \cdot Fe_2O_3$.

The formation process of calcium ferrites between CaO and Fe_3O_4 in $CO-CO_2-N_2$ atmosphere could be regarded as the process of CaO substitute for FeO in Fe_3O_4 ($FeO \cdot Fe_2O_3$). Due to the similar ionic radius ($r_{Ca^{2+}} = 0.099$ nm, $r_{Fe^{2+}} = 0.078$ nm) and valence of Ca^{2+} and Fe^{2+}, CaO and FeO were easily

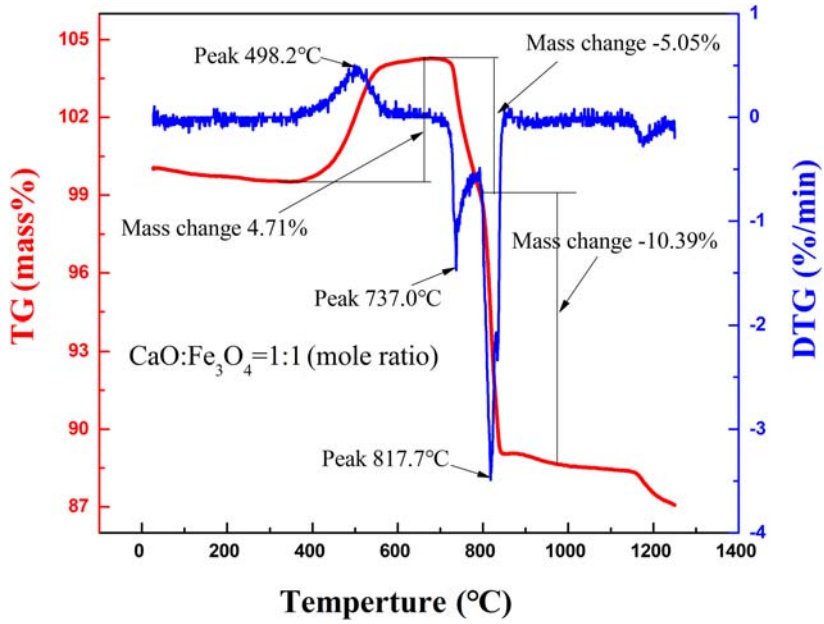

Figure 4.10 TG−DTG curve of the CaO and Fe_3O_4 mixed powders under 3%CO−22% CO_2−75%N_2 atmosphere.

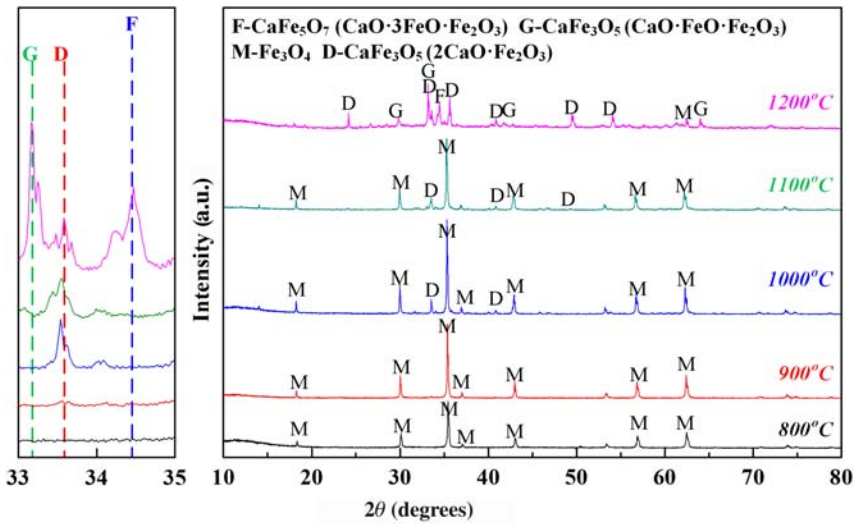

Figure 4.11 XRD patterns of samples roasted under N_2 atmosphere (roasting time of 5 min, Fe_3O_4:CaO mass ratio = 90:10).

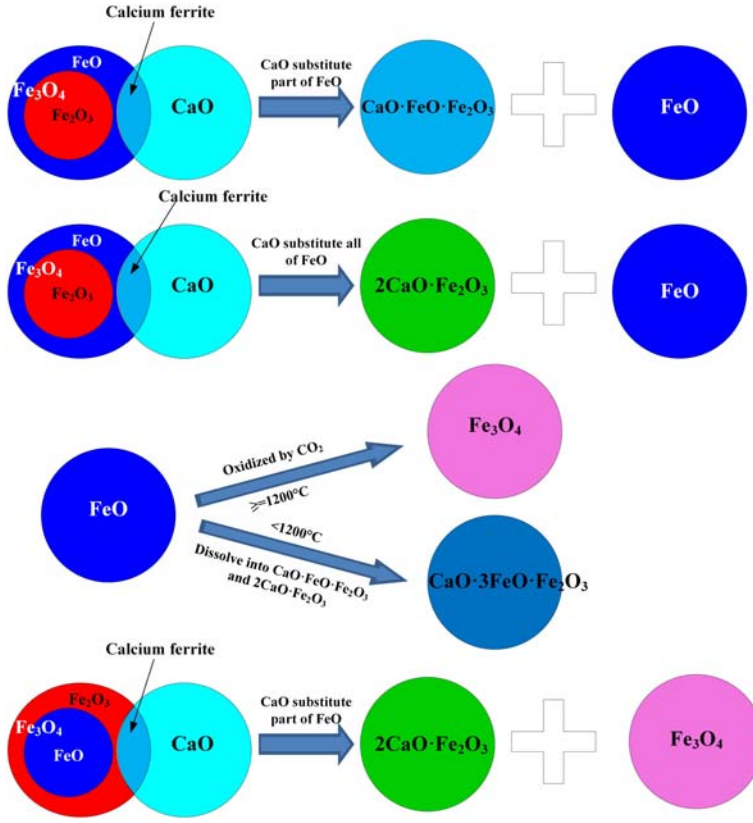

Figure 4.12 The reaction model between CaO and Fe_3O_4 in $CO-CO_2-N_2$ atmosphere.

substitute with each other. The reaction model between CaO and Fe_3O_4 under $CO-CO_2-N_2$ atmosphere was shown in Fig. 4.12.

When the temperature was lower than 1200°C, $CaO \cdot 2Fe_2O_3$ and FeO were easily formed because CaO was substitute for part of FeO in Fe_3O_4. The shadow area was the stable existence zone of Fe_3O_4 ($CO/(CO + CO_2) = 12$ vol.%, temperature $<1200°C$) which was given in Fig. 4.13 (*point b*). Then, the newly formed FeO could be again oxidized into Fe_3O_4 under this condition, and the oxidation process was promoted by the formation of $CaO \cdot xFeO \cdot Fe_2O_3$. Finally, $Ca_2Fe_2O_5$ was observed in the roasted products as all the FeO in Fe_3O_4 were substituted by CaO.

It was the stable existence zone of FeO under 12 vol.% $CO/(CO + CO_2)$ content above 1200°C as shown in Fig. 4.13 (*points a and c*), then the newly formed FeO was steady and easily dissolved into $Ca_2Fe_2O_5$, and more ternary calcium ferrites ($CaO \cdot xFeO \cdot Fe_2O_3$) were generated under those conditions, as shown in Figs. 4.4, 4.8, and 4.11. In the present study the mass ratio of CaO/Fe_3O_4 was 10%:90%. Thus FeO in Fe_3O_4 ($FeO \cdot Fe_2O_3$) could not be fully substituted by CaO. The newly formed FeO was either oxidized to Fe_3O_4 or dissolved into $Ca_2Fe_2O_5$ and

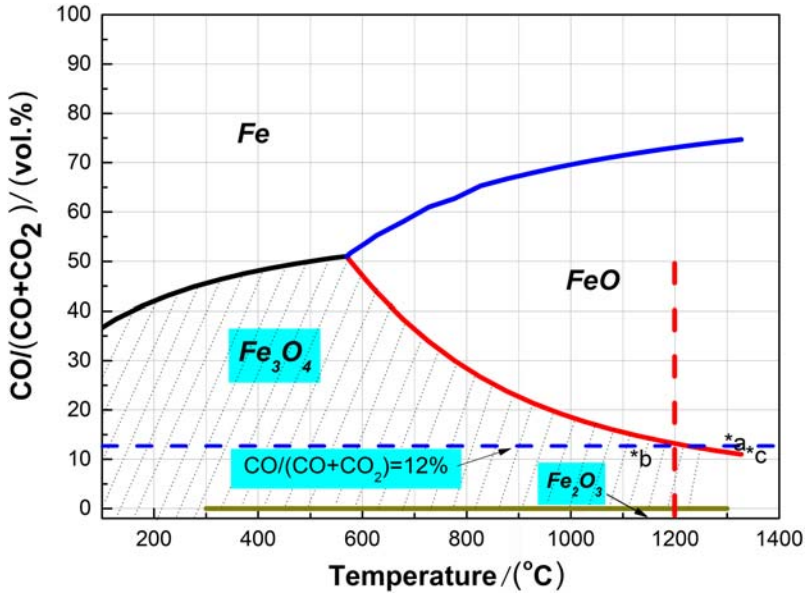

Figure 4.13 Gas-phase equilibrium diagram of Fe_xO under $CO-CO_2$ atmospheres.

$CaO \cdot FeO \cdot Fe_2O_3$ to form $CaO \cdot 3FeO \cdot Fe_2O_3$, which was affected by the temperature and CO concentration. Fe_2O_3 in Fe_3O_4 ($FeO \cdot Fe_2O_3$) could directly react with CaO to form $Ca_2Fe_2O_5$ when they were connected with each other. The main reactions during the roasting process between CaO and Fe_3O_4 in $CO-CO_2-N_2$ atmosphere were represented as follows:

$$CaO + Fe_3O_4 = CaO \cdot FeO \cdot Fe_2O_3 \tag{4.1}$$

$$2CaO + Fe_3O_4 = 2CaO \cdot Fe_2O_3 + FeO \tag{4.2}$$

$$3FeO + CO_2 = Fe_3O_4 + CO \tag{4.3}$$

$$CaO \cdot FeO \cdot Fe_2O_3 + 2FeO = CaO \cdot 3FeO \cdot Fe_2O_3 \tag{4.4}$$

$$2CaO \cdot Fe_2O_3 + xFeO \rightarrow CaO \cdot xFeO \cdot Fe_2O_3 \tag{4.5}$$

4.4 Conclusions

1. The binary calcium ferrite ($Ca_2Fe_2O_5$) and the ternary calcium ferrite ($CaO \cdot FeO \cdot Fe_2O_3$ and $CaO \cdot 3FeO \cdot Fe_2O_3$) could be easily formed from CaO and Fe_3O_4 roasted under 1−10 vol.% $CO/(CO + CO_2 + N_2)$ atmosphere.

2. The melting point of $CaO-Fe_3O_4$ mixtures under $CO-CO_2-N_2$ atmosphere was about 100°C lower than that under air, which was attributed to the formation of $CaO \cdot xFeO \cdot Fe_2O_3$. The formation reactions of calcium ferrites were promoted by increasing the roasting temperature and CO content of the mixed gas.
3. The formation of calcium ferrites under $CO-CO_2-N_2$ atmosphere can be regarded as CaO substitute for FeO in Fe_3O_4 ($FeO \cdot Fe_2O_3$). During the sintering process, the newly formed FeO can be oxidized by CO_2 to Fe_3O_4. The main reactions included: $2CaO + Fe_3O_4 = 2CaO \cdot Fe_2O_3 + FeO$ and $3FeO + CO_2 = Fe_3O_4 + CO$. FeO was dissolved into $CaO \cdot Fe_2O_3$ to form the ternary calcium ferrites ($CaO \cdot xFeO \cdot Fe_2O_3$).

Acknowledgments

The authors would express their hearty thanks to National Natural Science Foundation of China (No. U1960114 & 51574283).

References

[1] G. Gustafsson, H.Å. Häggblad, P. Jonsén, P. Marklund, Determination of bulk properties and fracture data for iron ore pellets using instrumented confined compression experiments, Powder Technol. 241 (2013) 19–27.
[2] S.P.E. Forsmo, S.E. Forsmo, P.O. Samskog, B.M.T. Björkman, Mechanisms in oxidation and sintering of magnetite iron ore green pellets, Powder Technol. 183 (2008) 247–259.
[3] S. Machida, H. Sato, K. Takeda, Development of the process for producing pre-reduced agglomerates, JFE Tech. Rep. 5 (2009) 7–13.
[4] N.V. Scarlett, M.I. Pownceby, I.C. Madsen, A.N. Christensen, Reaction sequences in the formation of silico-ferrites of calcium and aluminum in iron ore sinter, Metall. Mater. Trans. B 35 (2004) 929–936.
[5] J.M.F. Clout, J.R. Manuel, Fundamental investigations of differences in bonding mechanisms in iron ore sinter formed from magnetite concentrates and hematite ores, Powder Technol. 130 (2003) 393–399.
[6] L.H. Hsieh, J.A. Whiteman, Effect of oxygen potential on mineral formation in lime-fluxed iron ore sinter, ISIJ Int. 29 (1989) 625–634.
[7] H. Kang, S. Choi, W. Yang, B. Cho, Influence of oxygen supply in an iron ore sintering process, ISIJ Int. 51 (2011) 1065–1071.
[8] G.O. Egundebi, J.A. Whiteman, Evolution of microstructure in iron-ore sinters, Ironmak. Steelmak. 16 (1989) 379–385.
[9] N.A. Webster, M.I. Pownceby, I.C. Madsen, J.A. Kimpton, Effect of oxygen partial pressure on the formation mechanisms of complex Ca-rich ferrites, ISIJ Int. 53 (2013) 774–781.
[10] X.M. Mao, Z.X. You, Y.B. Zhang, Z.Y. Fan, G.H. Li, T. Jiang, Calcium ferrite formation characteristic during iron ore sintering with different oxygen atmospheres, J. Cent. South Univ. 21 (2014) 3043–3048.
[11] X.W. Lv, C.G. Bai, Q.Y. Deng, X.B. Huang, G.B. Qiu, Behavior of liquid phase formation during iron ores sintering, ISIJ Int. 51 (2011) 722–727.

[12] S. Sukenaga, Y. Gonda, S. Yoshimura, N. Saito, K. Nakashima, Viscosity measurement of calcium ferrite based slags during structural relaxation process, ISIJ Int. 50 (2010) 195−199.
[13] T. van den Berg, J.P.R. de Villiers, An assessment of the production of fine material in iron ore sinter, Miner. Process. Extr. Metall. 118 (2009) 214−221.
[14] X. Ding, X.M. Guo, Study of SiO_2 involved in the formation process of silico-ferrite of calcium (SFC) by solid-state reactions, Int. J. Miner. Process. 149 (2016) 69−77.
[15] X. Ding, X.M. Guo, C.Y. Ma, K. Tang, Y.D. Zhao, Effect of SiO_2 on the crystal structure stability of SFC at 1473 K (1200°C), Metall. Mater. Trans. B. 46 (2015) 1146−1153.
[16] X. Ding, X.M. Guo, The formation process of silico-ferrite of calcium (SFC) from binary calcium ferrite, Metall. Mater. Trans. B. 45 (2014) 1221−1231.
[17] M.I. Pownceby, T.R. Patrick, Stability of SFC (silico-ferrite of calcium), Eur. J. Mineral. 12 (2000) 455−468.
[18] T. Miki, Y. Fujita, Reaction between iron oxide and gangue minerals at 1373 K under Ar atmosphere, ISIJ Int. 55 (2015) 1206−1209.
[19] L.X. Yang, E. Matthews, Sintering reactions of magnetite concentrates under various atmospheres, ISIJ Int. 37 (1997) 1057−1065.
[20] Q.D. Zhou, L.T. Kong, Theory and Process of Iron Ore Agglomeration, Metallurgical Industry Publish, Beijing, 1992 (in Chinese).
[21] Y.B. Zhang, B.B. Liu, Z.J. Su, G.H. Li, Z.Y. Fan, T. Jiang, Effect of CO and CO_2 content in suction gas on sintering process for iron ores, ISIJ Int. 54 (2014) 1991−1993.
[22] C.E. Loo, Role of coke size in sintering of a hematite ore blend, Ironmak. Steelmak. 18 (1991) 33−40.
[23] Z.J. Su, Y.B. Zhang, B.B. Liu, J. Chen, G.H. Li, T. Jiang, Behavior of SnO_2 in the tin-bearing iron concentrate during a reducing sintering process, J. Min. Metall. B 53 (2017) 67−74.
[24] Y.B. Zhang, Z.J. Su, B.B. Liu, J. Chen, G.H. Li, T. Jiang, Phase evolution of tin, iron and calcium oxides roasted in a simulative sintering atmosphere, Powder Technol. 311 (2017) 303−312.
[25] Z.J. Su, Y.B. Zhang, Y.M. Chen, G.H. Li, T. Jiang, Reaction between CaO and Fe_3O_4 under CO-CO_2 atmosphere at 800°C-1100°C, ISIJ Int. 57 (2017) 62−67.
[26] National Standards of the People's Republic of China, GB/T 219-2008, Determination of Fusibility of Coal Ash, National Standards of the People's Republic of China, 2008 (in Chinese).
[27] X.M. Guo, Generation and Mineralogy of the Calcium Ferrites During Sintering, Metallurgical Industry Press, Beijing, 1999 (in Chinese).
[28] M. Hillert, M. Selleby, B. Sundman, An assessment of the Ca-Fe-O system, Metall. Mater. Trans. A 21 (1990) 2759−2776.

Surface modification, including polymerization, nanocoating, and microencapsulation

5

Riyadh A. Al-Samarai[1], *Amjed Saleh Mahmood*[1] *and Y. Al-Douri*[2,3,4]
[1]Electromechanical Engineering Department, College of Engineering, University of Samarra, Samarra, Iraq, [2]University Research Center, Cihan University Sulaimaniya, Sulaymaniyah, Iraq, [3]Nanotechnology and Catalysis Research Center (NANOCAT), University of Malaya, Kuala Lumpur, Malaysia, [4]Department of Mechatronics Engineering, Faculty of Engineering and Natural Sciences, Bahcesehir University, Istanbul, Turkey

5.1 Introduction

The rapid development of nanotechnology and nanomaterials led to the need to modify the surface of nanoparticles (NPs) for various applications [1]. The surface may be adapted to specific physical, optical, electronic, chemical, and medical−biological properties by depositing a thin film material of NPs on the surface. Coating or encapsulation of NPs is a serious problem because of the extremely small size, high surface energy, and high NP surface area [2−5]. There is a new method using supercritical CO_2 (SC CO_2) as an antisolvent (SAS) for NPs coating/encapsulation. The system model, using silica NPs as the particles of the polymer for the coating material, of the SAS process leads to the heterogeneous nucleation of the polymer NPs acting as nuclei and the subsequent growth of the polymer on the surface of the NPs which induced mass transfer and phase's transition.

The polymeric matrix structure is formed by the encapsulated agglomeration of coated NPs. Conventional methods for coating the NP are divided into dry and wet approaches. Dry methods include (1) physical vapor deposition, (2) plasma-treating [6−8], (3) precipitation (with) chemical vapor deposition [9], and (4) pyrolysis of polymeric or nonpolymeric. Furthermore, organic materials can be used in place of the NPs in a matrix [10]. The wet coating methods of NPs include (1) sol−gel processes and (2) emulsifying and solvent evaporation methods [11,12]. Coating or encapsulating the NPs of active substances has been found to be of particular interest. Controlled release systems provide the advantage of protection against rapid degradation and delivery orientations. However, to develop a new technique for coating or encapsulating ultrafine (nanoparticles) for modifying properties of supercritical CO2 (SC CO2) in the SAS process, CO_2 environment is ideal treatment [13].

Metal Oxide Powder Technologies. DOI: https://doi.org/10.1016/B978-0-12-817505-7.00005-1

Rong et al. [14] studied the process for applying polymer that dissolved in CO_2. A solution is released from the nozzle, generating microparticles that coat the surface. The supercritical solution causes a significant reduction in CO_2 dissolving ability which leads to very high supersaturation and particle growth. However, a strict application of the method is limited by the fact that the polymers generally have CO_2 solubility at temperatures below 80°C [15]. In addition, the operating pressure of the soil settlement gauge is usually above 200 bar, which is less attractive economically. The use of the RESS combination process and the fluidized particles in the solution of the coating material in the SC CO_2, rather than in organic solvents, are sprayed onto the fluidized particles. These methods are used to coat entirely the ultrafine particles and others [16]. The coating particles use a supercritical fluid process medium [17]. However, these methods are less attractive in terms of safety and cost, and probably cannot be applied to the industry, since high temperatures may adversely affect or even destroy the majority of powders. Using the SAS process, however, it can usually be carried out at a pressure below 10 MPa and at a temperature just above the critical temperature (304, 1K). Moreover, the SAS process is quite flexible in terms of solvent choice. Thus the synthesis of ultrafine particles using SAS has been reported in several studies [18–20] along with the production of composite microspheres in SAS. A homogeneous solution of various solutes and the polymer was sprayed into solvent SC CO_2. Coprecipitation of solutes and polymers occurred, and composite microspheres or microcapsules were formed [21]. The surface properties such as roughness, morphology, charge, chemical composition, surface energy, and wettability all affect biomaterial interaction with biological compounds. These surface properties can be modified in various ways, which include, but are not limited to, laser treatment, ion implantation, or plasma and NPs grafting. Each method provides a unique route to the surface modulation with its pros and cons [22].

5.2 Classification of surface treatment

Surface modification and heat treatment are available to improve the use of the material and in order to save energy and natural resources. In addition, they can achieve the desired properties of the alloys and components that are used in the automotive industry [23]. Today, a variety of commercial techniques are available in the industry. A flowchart of possible steps involved in surface treatment is shown in Fig. 5.1.

Heat treatment does not dramatically change the morphology but does harden the matrix, which leads to an increase in alloy strength. Increased hardness of composite materials can be achieved by heat treatment in an electric furnace [24]. Table 5.1 shows the test conditions and the materials of the investigations.

There are two steps involved in the heat treatment of the material: (1) solution for processing: alloy or composite powder is heated for 3 hours at a temperature of

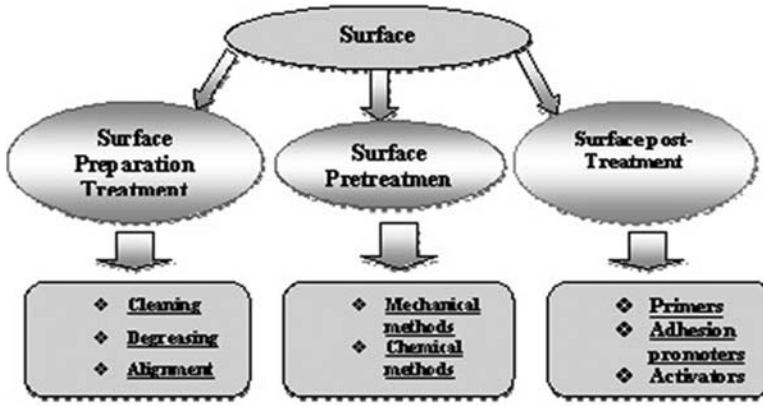

Figure 5.1 Flow chart of possible steps involved in surface treatment.

Table 5.1 Test conditions and the materials of the investigations based on the effect of heat treatment of polymer and alloys.

Reference	Apparatus	Matrix type	Test conditions
Gupta and Ling [25]	DMD technique	Hypo/hyper-eutectic Al−Si	Specimens were solutionized for 1 h at 529°C
Ardakan et al. [26]	DSRW	Hypereutectic A390 (Al−17Si)	500°C for 1 h, followed by immediate quenching in normal water before aging at 175°C for 8 h
Eshaghi et al. [24]	Pin-on-disk	Hypoeutectic Al−Si alloys	520°C for 12 h followed by quenching in water at 60°C
Vencl [30]	Pin-on-disc	Hypoeutectic Al−Si alloy A356	Solution annealing at 548°C for 6 h, followed by water quenching

DMD, dynamic mode decomposition; DSRW, Dry sand rubber wheel.

400°C; and (2) hardening: the treated material is quenched in water or in air [24]. Gupta and Ling [25] investigated Al−7%Si, Al−10%Si, and Al−19%Si alloys. The results show that the microstructural characteristics and mechanical properties of Al−Si alloys were correlated with silicon, aluminum, and recycling methods.

The selection of the method of heat treatment is very important to produce parts of reliable quality. Other factors affect the quality and reliability of the final components: refining, casting, and rolling. In addition, the wear resistance, stiffness, fatigue strength, hardness, and microstructure of the heat conditions and treatment outcomes are major factors. It is very important to make sure that an appropriate method is used for these factors. Types of heat treatment to produce automobile parts are shown in Table 5.2.

Table 5.2 Types of heat treatment and surface hardening for automotive components.

Types of heat treatment	Purpose	Typical components
Solution treatment and aging	Optimize hardness and strength of Al and age hardening metallic materials	Aluminum casting: T/M and Dif. casings In. and Ex. valves
Thermal spraying (plasma) posttreatment	Obtain the desired spray molten particles compensation for wear, etc.	Piston ring, lifter periphery, synchronizer ring
Quench coating	Improving the surface properties of the molded protective film on quenching	Fasteners, V.S. retainer
Low temperature processing	Deep cooling at the end of the conversion rate	Gears, dies
Shot peening (0.8−1.4C steel or cast iron)	Spray particles to increase fatigue strength and residual stress	Leaf and coil springs
Hard, twice shot hardening	Spray large and small hard particles to increase residual stress for higher fatigue force	T/M and differential gears
Hardening solids (fine particles)	Spray small particles to clean, remove the surface layer and the formation of dimples shot	Piston skirts, continuously variable transmission drums

Eshaghi et al. [24] investigated the microstructure and wear behavior of hypoeutectic Al−Si alloys with iron contents of 0.15, 0.7, and 1.2 wt.%. Dry sliding wear tests were performed on a pin-on-disk tribometer under normal loads of 20, 30, and 40 N. The results showed that the highest wear resistance was before the heat treatment under the loads tested. T6 heat treatment improved the wear resistance of the alloys with different iron contents compared to the nonheat treated 0.7 wt.% iron alloy under all applied loads. The change in the morphology of the phase particles reduced the probability of nucleation and propagation of subsurface cracks and increased the wear resistance in the samples [25,26].

The wear properties of A390 (Al−17Si−4.5Cu−0.5Mg, wt.%) hypereutectic Al−Si alloy were compared to new alloys containing 6 and 10 wt.% Mg. The wear test results showed an improvement in wear resistance for alloys with high Mg content. The microstructure of the worn surface indicated that the intermetallic Mg_2Si particles in alloys with 6% and 10% Mg addition are more solidly bonded to the matrix compared with the coarse primary silicon particles in A390 alloy, which can be pulled out from the matrix. The worn surface of the A390 alloy exhibits deep and nonuniform grooves compared with shallow and uniform grooves for the high Mg content alloys, resulting in the improved resistance to wear.

Gomez de Salazar and Barrena [27] investigated the effects of high wear resistance. Maximum hardness of the matrix is obtained when the composite was

heated at 560°C for 3 hours, cooled in an ice water at 0°C, and aged at 175°C for 7 hours. It is found that T6 heat treatment increased the hardness of the matrix, and so it was admitted to metal matrix composites. A356 alloy meets or exceeds all requirements for mechanical strength, flexibility, strength, fatigue, tightness of pressure, and efficiency. While Basavakumar et al. [28] studied the microstructure and dry sliding wear behavior of Al and Al−7%Si−2.5%Cu cast alloys with different melt after treatment, as a refinement of the grain, and showed that the combined grain refined and modified Al−7%Si−2.5Cu cast alloys' microstructure, with Al grains evenly distributed, and a fine network of eutectic Al−Si and fine particles in the $CuAl_2$ region. These alloys exhibited improved wear resistance in the as-cast condition compared with those in the untreated alloy. Das et al. [29] investigated the effect of reinforcement and heat treatment on two-body abrasive wear of Al−Si alloys, and their study showed that the alloy and composites have a minimum speed of wear after heat treatment due to the improved hardness.

Vencl [30] studied the effect of casting alloys. They found that the value of the constant wear was higher than in the heat-treated alloys and composites. In the process of wear, cracks mostly originated in the matrix and reinforcement interfaces. Heat-treated alloys and composites showed high strength and hardness, which reduced the tendency to crack and showed improved strength. Both alloys require liners or surface treatment of the cylinder walls of sufficient strength to operate [31−33]. Hegde and Prabhu [34] showed that these alloys are used for the modification of the melt treatment, which converts the needle morphology of silicon fiber and shows improvement in strength and elongation. Rao et al. [35] studied the effect of heat treatment for various loads, sliding speed, wear, high temperature, pressure, and friction coefficient. The maximum hardness of the material is maintained for 6 hours. The aging time is increased from 4 to 10 hours. Li et al., [36] show that in Al-7.5%Si the mechanical properties improved by the addition of Y heat treatment T6, and a good combination of strength (353 MPa), the yield point (287 MPa), the strength and elongation (12.1%), by adding 0.3%. In the foundry 10 different thermal treatments (Table 5.3) are generally practiced with many additional variations.

5.3 Surface treatment including polymerization

Polymers come from natural or synthetic sources, and can be relatively easily formed into structures which range from simple foil to various complex shapes. They offer a wide range of physical and chemical properties due to the large diversity in their chemical composition, which makes them interesting candidates for biomedical applications. Their use is limited by their mechanical properties, such as tensile strength and Young's modulus, which are irregular in comparison to other materials in traditional medicine, such as metals or ceramic composites. On the other hand, the polymers are very flexible and capable of withstanding heavy loads because of the high degree of freedom in the movement of the individual polymer

Table 5.3 Temperature designation of polymer and alloys [37].

T1	Cooled from an elevated temperature shaping process (such as extrusion or casting) and strengthened by naturally aging to a substantially stable condition. These products are not cold-worked
T2	Annealed to improve ductility and dimensional stability of a product. These products are cold-worked
T3	Solution heat-treated (quenched), cold-worked by a flattening or straightening operation to strengthen the product, and naturally aged to a substantially stable condition
T4	Solution heat-treated (quenched) and strengthened by naturally aging to a substantially stable condition
T5	Partially solution heat-treated (quenched), then artificially aged. These products are not cold-worked
T6	Solution heat-treated (quenched) and artificially aged. These products are not cold-worked
T7	Solution heat-treated (quenched), then overaged/stabilized. These products are artificially aged to carry them beyond a point of maximum strength to provide control of some significant characteristic other than mechanical properties
T8	Solution heat-treated (quenched), cold-worked, then artificially aged
T9	Solution heat-treated (quenched), artificially aged, then cold-worked to strengthen the product
T10	Partially solution heat-treated (quenched), artificially aged, and then cold-worked to strengthen the product

chains. The polymers are crystalline materials and the degree of crystallinity affects their stress−strain behavior which can vary from stiff to high elasticity [38−40]. Due to their versatility, polymers are widely used materials for scientific and industrial applications. Various polymer substrates offer a wide range of physicochemical properties which may be further modified by various methods of surface treatment to achieve characteristics suitable for each individual application. Methods of surface treatment can be varied from large, such as chemical modification or treatment of the UV lamp, changing properties of a few square nanometers of surface, while the have accurate affecting simple square nanometers, changing only a few atomic layers of the substrate such as laser treatment [41,42]. Any type of surface modification will lead to a change in surface chemistry and morphology, which in turn is more or less significant, influencing the optical, mechanical, tribological, and various other electrical properties of the modified substrate. Such changes should occur only in a small depth from the surface, while the bulk of the modified polymer and hence its properties should remain unchanged [43]. While polymers are promising materials for many biomedical applications, they are rarely used in their original form. Polymers in their native state typically are biologically inert, and thus surface treatment is necessary to turn them into more advanced materials that induce a specific response to different biological molecules or when they come in contact with the surface. Modulation properties of polymeric substrates, such as morphology and roughness, as well as physicochemical composition are necessary to achieve the

desired interaction between the polymer and the biological agent. Appropriate surface modification can lead to changes in the morphology of the polymer surface, which leads to various nanoscale structures that serve as reference points for specific proteins of the cell membrane, thus improving cell adhesion to the surface [44]. Cell adhesion to the substrate is a two-stage process. First, a cell adheres to the surface via noncovalent interactions (van der Waals forces, hydrogen bonding, and electrostatic, polar, and ionic interactions) between specific molecules in the cell membrane and the polar groups on the substrate surface. The second step consists of the adhesion of molecules, such as fibronectin, vitronectin, collagen, and laminin, to the extracellular matrix receptors under control. Cells attach via integrin receptors located in the cytoplasmic membrane of the amino acid sequences [45,46]. The polymer depends on all the physicochemical and morphological properties of the polymer surface, as above, which gives us the ability to modulate the surface as required to improve cytocompatibility.

5.4 Effects of coating process on tribological properties of polymer and alloys

One of the most important goals in the automotive industry is to improve fuel economy in order to reduce emissions and thus lower the use of natural resources. By reducing vehicle weight and reducing friction in the engine and transmission systems, this goal is achievable. For example, one-third of the fuel energy in cars is consumed to overcome friction in the engine including the transmission, tires, and brakes [47]. Possible measures to reduce friction in the car are the use of advanced coatings and surface modifications on the engine and drivetrain components. There is growing global demand for energy saving, and with the help of modern technology various energy efficiency and performance of operations improvements can be achieved. The use of advanced surface treatment and functional coatings can reduce the cost of repair of rotating equipment and can offer several options for improving the sliding properties of metal surfaces [48].

Today more than 60% of the engines produced for vehicles use Al−Si alloys. However, these alloys require surface treatments.

Many surface modification approaches have been examined, in order to improve the properties of Al−Si alloys for the needs of the automotive industry. These processes include microarc beam oxidation, remelting high power pulsed electron beam treatment, plasma electrolytic oxidation, and plasma spraying [49]. Plasma spraying is a more appropriate surface modification technology for a wide range of applications in the automotive industry, and is particularly noted for its use for piston rings, generator covers, and the ceramic coating for oxygen sensor protection [50]. Plasma spraying has clear advantages for fuel consumption and energy saving by increasing the surface hardness and reducing the coefficient of friction (COF) of the drive components in the car. Various factors influence the friction behavior of coated tribological contacts [51].

5.5 Surface treatment including nanocoating and microencapsulation

Recently, the potential for expanding the use of Cr_2O_3 coatings has focused considerable attention on the use of these materials as wear-resistant coatings in different aerospace and automotive industries [52]. Plasma spraying has become the most commonly used for a wide range of Cr_2O_3-based ceramic coatings, which show favorable tribological behavior, that is, high antiwear and easy oil lubrication [53]. However, the plasma processing parameters and process characteristics strongly affect the quality of coatings, such as the microstructure and chemical distribution structure, hardness, adhesion, and strength properties [54]. The surface coatings can be divided into the following application fields [55]:

- Coatings to increase wear resistance
- Coatings to improve thermal properties
- Coatings to increase the knock resistance
- Coatings to improve sliding characteristics

The tribological properties of the coatings of Cr_2O_3 at high temperatures were studied. However, the tribological properties of ceramic Cr_2O_3 coatings with a low COF and wear obtained in dry sliding conditions are still unacceptable in many high-temperature applications. Thus it is important to find effective lubrication for Cr_2O_3 ceramic coatings when they are used in applications in extreme temperatures [56]. However, only a limited number of experiments have used grease to cover Cr_2O_3 ceramics. There are many methods to remove the surface sediments and pollution that affect significantly the rate of wear negatively on the surface layer during the process of sliding. Table 5.4 shows test conditions and materials of investigations.

Hieman [57] used chromium oxide (Cr_2O_3) and found that these coatings have good wear resistance and corrosion resistance. In addition, the very high hardness HV 0.5 kg of chromium coatings was useful in marine and other diesel engines, water pumps, and pressure rollers. Ouyang and Sasaki [58] examined the

Table 5.4 Test conditions and the materials of the investigations based on the effect of coating material.

Reference	Apparatus	Matrix type	Test conditions
Hieman [57]	Chromium oxide (Cr_2O_3)	Al−Si alloy	Plasma spraying
Ouyang and Sasaki [58]	Pure Cr_2O_3 coating	Al−Si alloy	Plasma spraying with additives, CaF_2, Ag_2O, and ZrO_2
Bakshi and Wang [69]	Composite coatings containing aluminum	Al−11.6% Si alloy	Cold spraying

microstructure and tribological properties of high-temperature low-pressure plasma spray Cr_2O_3 ceramic coatings on composites. ZrO_2 and Cr_2O_3 components were observed in the form of small lamellar structures; Ag_2O was observed in the form of individual particles with different levels. Some crystal structures of ZrO_2 grains or dendritics were clearly observed in the ZrO_2 strip on polished friction composite coatings with high levels of additives at room temperature and the wear rate gradually decreased with the increase of Cr_2O_3 coatings. An intrinsic property of the surface cleaning method can be so aggressive that it can smooth the surface of the material excessively [59]. Kitsunai et al. [60] investigated Cr_2O_3 coatings on stainless steel, analyzing the microscopic wear modes for Cr_2 coatings. The sliding wear processes for 100 cycles were subsequently observed in a scanning electron microscope and they were also compared with stainless steel SUS304. It was found that regimes fall into the crack and powder form, scale, and plowing and powder formation. These modes of wear are mainly due to the fracture.

Voevodin et al. [61] found that the application of the coating could reduce wear of components made of Al alloys by several orders of magnitude. Wang and Tung [62] found that the DLC, Ni−P−SiC, and Si_3N4 Ni coatings allowed less severe wear to 390 Al than a TiN coating. Gui et al. [63] showed that some Al/SiC interfaces were very clean. Wang et al. [64] researched tribological coatings and the compatibility between the piston skirt and of aluminum or cast iron bore counter surfaces. The results show that the aluminum piston skirt coatings composites Ni P BN coating internal resistance and friction durability without oil. CDS anodized surface coatings with good resistance to seizure showed significant improvements in power.

Gary and Luan [65] discussed in detail the use of magnesium-based substrates for surface modification technology of the coatings, conversion coatings, anodizing, chemical vapor deposition processes, laser surface alloying, and organic coatings. With growing global demand for energy, and with the use of advanced technology and a variety of energy efficiency, processing capacity, operation, and maintenance should be increased.

Nakata and Ushio [66] improved the wear resistance of Al−17%Si with different iron content and showed good wear resistance—about four times the substrate and a low COF and interaction between the coating. Vetter et al. [67] reported that the improved methods of deposition of PVD, PECVD, and thermochemical treatment of heat and thermal spraying have been developed. Transmission and engine applications of these new techniques are becoming more and more widespread. A variety of substrates (e.g., aluminum alloys, hardened steels, etc.) are optimized to create surfaces, geometry influences (e.g., holes), and operating costs.

Vissutipitukul and Aizawa [68] used the microstructure in the course of formation of uniform hardness. Dry wear test method was used to prove the degree of wear and friction under the protective layer. The results showed the low specific volume of less wear proved the ongoing process of the nitriding surface treatment of aluminum alloy. Functional coatings offer several options for improving the sliding properties of metal surfaces.

Bakshi and Wang [69] investigated composite, aluminum and 11.6% by weight of silicon eutectic alloy coatings containing different stages. The compositions were

Table 5.5 Some applications of ceramics as coating material [72].

Ceramic materials	Application areas
Cr_2O_3, Al_2O_3, TiO_2, $Al_2O_3-TiO_2$, $Cr_2O_3-TiO_2$, carbides	Wear-resistant coating on textile machinery, automobile parts, pistons, jet engine and, pump components, etc.
$ZrO_2-Y_2O_3$, magnesium zirconate	Thermal barrier coatings on diesel engines, aircraft parts, gas turbine engine parts
$Al_2O_3-TiO_2$, Al_2O_3	Electrical insulation coatings on computer systems, high voltage components, etc.
Al_2O_3, hydroxy apatite	Bioceramics (coating on implants)

prepared using cold spraying. Two coatings containing the same width and height distribution Al−Si particles showed more signs of the particles. Dry tests showed the wear plate sliding volume loss of the ball and Al/C, despite the increase in the microhardness of composite coatings. Friction coating aluminum has decreased execution time. The composite coatings containing aluminum and aluminum−11.6 wt.% silicon eutectic alloy phases of varying compositions were fabricated using cold spraying. The results showed the hardness of the coatings increased as the volume fraction of Al−Si in the coating increased. The COF of aluminum coating reduced on increasing Al−Si [69].

Bao et al. [70] used Al−Si composite coatings reinforced 0%, 0.5%, and 2% by volume. Nanodiamonds were synthesized by plasma spraying. The effect on microstructure, hardness, and tribological performance of nanodiamonds composite coatings were examined. Plasma spray-coated nanodiamonds have excellent potential as wear-resistant coatings in the automotive industry. In an internal combustion engine, coatings and surface treatments are often used for one or more elements of pistons, piston rings, and cylinder liners used by the system. In recent years, nanotechnology has gained popularity among manufacturers and researchers because of the excellent results obtained by controlling the composition of the material. The term nanotechnology was first presented by a professor of literature at Tokyo University of Science in 1974, Norio Taniguchi. He defines it as follows: "Nanotechnology in the department of general treatment consists of two consolidation and deformation of materials by one atom or molecule" [71]. Powder which is used for thermal spraying contains many powdered metals, metal alloys, and ceramic powders. In addition to the above, there is a growing demand for oxide ceramics, such as TiO_2, Al_2O_3, Cr_2O_3, ZrO_2, and on the industrial scale for thermal spray coatings, as shown in Table 5.5.

5.6 Effects of WS_2 nanoparticles lubricants on polymer and alloys

Recently, it was discovered that the WS_2 and MoS_2 NPs (inorganic fullerene-like) when mixed with the oil and impregnated porous matrix of powder materials, seem

to improve the tribological properties of the contact surfaces in a certain range of loads compared with typical metal lubricants. Layered solid materials, such as graphite, MoS_2, and WS_2, are used as solid lubricant and as additives in liquid lubricant. Minimum tangential resistance is often associated with the weak interaction between layers [73]. The recent years have proved that the use of different types of NPs on a large scale in order to reduce friction and wear under conditions of high-speed loading and lubricants could achieve the objective [74]. These NPs have been added to metal surfaces to prevent direct contact between the surfaces during operation [25]. Where most additives phosphorus, sulfur, chlorine, and other types that are more environmentally friendly materials and played an active role in the improvement of the industrial technology [75]. These additives react with metals to produce film produced by a chemical reaction at the contact between the surfaces [76].

In some cases, the friction coefficient of the composite is lower than that of the matrix material. Kao et al. [77] prepared and tested friction in a car brake master cylinder. They studied the behavior of elastomeric seals and found that a brake fluid of nonaluminum oxide with its spherical shape can greatly reduce friction in order to prevent excessive wear on the seals, and reduce slippage in the spot braking [78]. The main favorable benefit of the WS_2 NPs was attributed previously to the following three effects: (1) rolling friction; (2) the WS_2 NPs serve as spacer, which eliminate metal to metal contact between the asperities of the two mating metal surfaces; and (3) third body material transfer [79]. Nonmetric tungsten disulfide (WS_2) NPs appear to have excellent tribological properties within a definite load range ($PV \approx 150$ Nm/s) in comparison with typical metal dichalcogenides. Reshak and Auluck [80] studied the electronic properties of $2H-WSe_2$ intercalated with Cu. They concluded that there is a weak hybridization between the Cu states and W and Se states. They have prepared the new materials WS_xSe_{2-x} ($x = 0.5$ and 1.5) that possess second harmonic generation. It has been shown that these materials can be used as nonlinear crystals. Gu et al. [81] have studied the application of CeO_2 and $CaCO_3$ NPs in lubricating oils and found tribological chemical reactions in the friction surface of the metal calcium, cerium, and metal oxide films.

To reduce the shear stress, Chang et al. [82] have studied the tribological properties of TiO_2 nanolubricant on piston and cylinder surfaces. They concluded that the lubricant with added TiO_2 NPs can protect the piston ring surface. Zhang et al. investigated the effect of Cu NPs on the tribological behaviors of serpentine powders (SPs) suspended in diesel oil. They determined that there is an optimum mass ratio of Cu NPs to SPs of 7.5:92.5. With the addition of the above mixture to oil, the tribological properties can be significantly improved compared with those of the oil containing SPs alone.

In recent years, many researchers have been devoted to the study of friction and wear of polymer and alloys behavior. However, most of these studies were conducted under conditions of dry friction. Many studies on lubricant friction have been conducted mainly on polymer and alloy morphology and the effects of friction and wear resistance of these alloys. In addition, studies of friction and wear tests

have been conducted mainly in the air [83]. Al−Si alloys are widely used, especially in automotive parts, such as in piston and engine blocks for internal combustion engines, automotive air-conditioning compressors, and inclined plates.

5.7 Conclusion

It is known that the environment around contacts have a significant impact on the tribological performance. Thus this chapter is summarized below:

- Most researchers agree that the sliding surface topography has an important role in understanding the nature of the surface. As a result, microtopography, the contact between two moving surfaces, is an important basis for the development of basic concepts. In recent years, modern technologies and the size and the availability of digital computers have allowed us to describe and measure the surface shape of polymer and alloys [84].
- In the literature, although many studies have been conducted on the dry sliding of polymer and alloys, some researchers have studied the lubricating effect of the alloys in piston engines. The study of alloys has received the most attention. This is due to the fact that in alloys corrosion resistance is high and there is a low coefficient of thermal expansion [85].
- Researchers agree that the wear depends on the silicon content in the polymer and alloys and the minimum volume. Their strength and durability of other alloying elements,and the higher Si (for example, 17% Si) are the most popular. 17% Si alloy and alloy 390 are necessary for many applications where there is high durability of Al−Si alloys. The difference in the light wear (<5 μm), characterized by the formation of a particle mode and are mainly composed of aluminum oxide. Thus, generated soft modes of wear, oxidation, wear mechanism of wear particles of regime of large ($>$ 15 μm), some of the wear on the surface of metal , but its depends on the sliding speed and load , changes in behavior of wear that occur at high temperature [88].
- In recent years, most researchers agree that copper increases the wear resistance of polymer and alloys. The use of up to 1% magnesium is also helpful in reducing the wear . Sodium works well as a modifier in the absence of phosphorus (P), since it has a tendency to react with P. Na is working as an effective modifier in all crystallization conditions, copper−tin bronze tin is used as a material carrying properties of high wear resistance and friction of the material. Reducing high concentrations of Pb reduces wear aluminum alloy and the strength of the alloy at high temperatures on the surface. Other elements are usually made of titanium, sodium, useful for reducing wear [85,88].
- mechanisms of polymer and alloys at room temperature were divided into three stages. In the first stage, particles are removed in the matrix in ultra mild wear , and In the second stage, UMW- II started to increase wear aluminum by increase load and sliding speed. In stage (UMW-III). Laboratory tests and dynamometer studies have shown that the hypereutectic Al−Si alloys can be a potential substitute for the expensive hypereutectic Al−Si alloys and cast iron liners. However, some unresolved issues require further study [88].
- .To optimum properties, several studies, including the effect of heat treatment, coating hypereutectic and hypoeutectic Al - Si alloys, such as high ambient temperature to simulate the effect of surface treatment, the benefits of thermal spraying on the piston, the cylinder block made of cast iron. Researchers agree that the treatment of the surface is used to increase the life of components and structures, especially in the surface. Plasma

deposition of Cr_2O_3 and Ni/Cr, Al_2O_3, TiO_2, and $Al_2O_3-TiO_2$ coatings are wear-resistant coatings which are widely used in the automotive industry. They have several key advantages that will help in the further implementation of the technology in mass production. However, no comprehensive studies have shown a comparative assessment of NPs. Thermal spray processes are combined to provide raw materials that can be found in the literature. In addition, some studies in the open literature on microstructures and mechanical and tribological properties of NPs show conflicting results. Some researchers agree that the rheological properties of nanometer NP oil lubricants and their tribological performance indicate that they can be used to reduce wear and friction. Oils without NPs reveal the level of friction and loss that the NPs dispersed oil lubricants can reduce, thus improving the mechanism. The NPs used, such as CeO_2, $CaCO_3$, WS_2, and MoS_2, as well as the promotion of the contact surface in the form of a combined, reduce wear on the surface of the film. Thus the lubricant which is added to the NPs can protect the surface of the piston [89]. However, the tribological performance of polymer and alloys requires a careful assessment. The ability of nanopowder coatings surface and nanolubrication to reduce wear, improve the mechanism, microhardness, impact strength, and durability depends on the properties of the raw materials and the process parameters, as well as the different methods used for the study of friction and wear of alloy behavior. There is a need to continue the development of environmentally sound technologies to meet the needs of the industry in better fuel economy, comfort, safety, durability, and cost and emissions standards. International collaborative efforts on the line really need solutions for the automotive industry [88,89].

Acknowledgment

This work has been performed at College of Engineering, Samarra University, Iraq. We are very thankful to College of Engineering, for their help in carrying out surface modification, including polymerization, nanocoating, and microencapsulation.

References

[1] J.W.H. Wennink, Y. Liu, P.I. Mäkinen, et al., Macrophage selective photodynamic therapy by meta-tetra (hydroxyphenyl) chlorin loaded polymeric micelles: a possible treatment for cardiovascular diseases, Eur. J. Pharm. Sci. 107 (2017) 112−125.
[2] Y.-J. Wang, M. Larsson, W.-T. Huang, et al., The use of polymer-based nanoparticles and nanostructured materials in treatment and diagnosis of cardiovascular diseases: recent advances and emerging designs, Prog. Polym. Sci. 57 (2016) 153−178.
[3] V. Bakola, V. Karagkiozaki, F. Pappa, et al., Drug delivery nanosystems for cardiovascular stents, Mater. Today Proc. 4 (7) (2017) 6869−6879.
[4] Y. Fan, Q. Yang, H. Han, et al., Clinical characteristics and causes analysis of atrial fibrillation in elderly patients, J. Cardiovasc. Pulm. Dis. 35 (9) (2016) 715−718.
[5] Y. Fan, Q. Yang, J. Lv, X. Pang, X. Chen, Clinical characteristics analysis of heart failure in elderly patients, J. Cardiovasc. Pulm. Dis. 34 (6) (2015) 444−451.
[6] V.E. Bosio, J. Brown, M.J. Rodriguez, D.L. Kaplan, Biodegradable porous silk microtubes for tissue vascularization, J. Mater. Chem. B 5 (6) (2017) 1227−1235.

[7] World Health Organization, Global Status Report on Noncommunicable Diseases, vol. 1, World Health Organization, Geneva, Switzerland, 2014.
[8] M.J. Fabra, P. Pardo, M. Martinez-Sanz, A. Lopez-Rubio, J.M. Lagaron, Combining polyhydroxyalkanoates with nanokeratin to develop novel biopackaging structures, J. Appl. Polym. Sci. 133 (2016).
[9] E. Bugnicourt, T. Kehoe, M. Latorre, C. Serrano, S. Philippe, M. Schmid, Recent prospects in the inline monitoring of nanocomposites and nanocoatings by optical technologies, Nanomaterials 6 (2016) 150.
[10] J. Zink, T. Wyrobnik, T. Prinz, M. Schmid, Physical, chemical and biochemical modifications of protein-based films and coatings: an extensive review, Int. J. Mol. Sci. 17 (2016) 1376.
[11] W. Lu, J. Sun, X. Jiang, Recent advances in electrospinning technology and biomedical applications of electrospun fibers, J. Mater. Chem. B 2 (17) (2014) 2369−2380.
[12] H. Chen, Y. Zhao, K. Xiong, et al., Multifunctional coating based on EPC-specific peptide and phospholipid polymers for potential applications in cardiovascular implants fate, J. Mater. Chem. B 4 (48) (2016) 7870−7881.
[13] M. Schmid, K. Reichert, F. Hammann, A. Stäbler, Storage time-dependent alteration of molecular interaction-property relationships of whey protein isolate-based films and coatings, J. Mater. Sci. 50 (2015) 4396−4404.
[14] M.Z. Rong, M.Q. Zhang, K. Friedrich, Eur. Polym. J. 38 (2002) 1573−1582.
[15] Q. Li, Z. Wang, S. Zhang, et al., Functionalization of the surface of electrospun poly (epsilon-caprolactone) mats using zwitterionic poly(carboxybetaine methacrylate) and cell-specific peptide for endothelial progenitor cells capture, Mater. Sci. Eng. C 33 (3) (2013) 1646−1653.
[16] V. Karagkiozaki, P.G. Karagiannidis, N. Kalfagiannis, et al., Novel nanostructured biomaterials: implications for coronary stent thrombosis, Int. J. Nanomed. 7 (2012) 6063−6076.
[17] S. McGinty, A decade of modelling drug release from arterial stents, Math. Biosci. 257 (2014) 80−90.
[18] D.E. Heath, Promoting endothelialization of polymeric cardiovascular biomaterials, Macromol. Chem. Phys. 218 (8) (2017). article 1600574.
[19] D. Williams, Essential Biomaterials Science, first ed., Cambridge University Press, Cambridge, 2014.
[20] D.E. Heath, S.L. Cooper, Design and characterization of sulfobetaine-containing terpolymer biomaterials, Acta Biomater. 8 (8) (2012) 2899−2910.
[21] D. Shemesh, I. Goldin, J. Hijazi, et al., A prospective randomized study of heparin-bonded graft (Propaten) versus standard graft in prosthetic arteriovenous access, J. Vasc. Surg. 62 (1) (2015) 115−122.
[22] X. Gu, Z. Mao, S.-H. Ye, et al., Biodegradable, elastomeric coatings with controlled anti-proliferative agent release for magnesium-based cardiovascular stents, Colloids Surf. B Biointerfaces 144 (2016) 170−179.
[23] T.S.N. Sankara Narayanan, I.S. Park, M.H. Lee, Strategies to improve the corrosion resistance of microarc oxidation (MAO) coated magnesium alloys for degradable implants: prospects and challenges, Prog. Mater. Sci. 60 (2014) 1−71.
[24] A. Eshaghi, H. Ghasemi, J. Rassizadehghani, Effect of heat treatment on microstructure and wear behavior of Al−Si alloys with various iron contents, Mater. Des. 32 (2011) 1520−1525.
[25] M. Gupta, S. Ling, Microstructure and mechanical properties of hypo/hypereutectic Al−Si alloys synthesized using a near-net shape forming technique, J. Alloys. Comp. 287 (1999) 284−294. 4.

[26] A.H. Ardakan, et al., Wear behaviour of hypereutectic Al−Si−Cu−Mg casting alloys with variable Mg contents, Wear 269 (2010) 684−692.
[27] J. Gomez de Salazar, M. Barrena, Influence of heat treatments on the wear behaviour of an AA6092/SiC.25p, composite, Wear 256 (3) (2004) 286−293.
[28] K.G. Basavakumar, et al., Influence of grain refinement and modification on dry sliding wear behaviour of Al−7Si and Al−7Si−2.5Cu cast alloys, J. Mater. Process. Technol. 186 (2007) 236−245.
[29] S. Das, D. Mondal, S. Sawla, et al., Synergic effect of reinforcement and heat treatment on the two body abrasive wear of an Al−Si alloy under varying loads and abrasive sizes, Wear 264 (2008) 47−59.
[30] A. Vencl, Tribological properties of thixocasted and heat-treated hypoeutectic Al-Si alloy A356, Ekoinżynieria 15 (2009).
[31] H. Yao, J. Li, N. Li, K. Wang, X. Li, J. Wang, Surface modification of cardiovascular stent material 316L SS with estradiol-loaded poly(trimethylene carbonate) film for better biocompatibility, Polymer 9 (11) (2017) 598.
[32] J.-L. Wang, B.-C. Li, Z.-J. Li, et al., Electropolymerization of dopamine for surface modification of complex-shaped cardiovascular stents, Biomaterials 35 (27) (2014) 7679−7689.
[33] P. Li, L. Li, W. Wang, et al., Enhanced corrosion resistance and hemocompatibility of biomedical NiTi alloy by atmospheric-pressure plasma polymerized fluorine-rich coating, Appl. Surf. Sci. 297 (2014) 109−115.
[34] S. Hegde, K.N. Prabhu, Modification of eutectic silicon in Al−Si alloys, J. Mater. Sci. 43 (2008) 3009−3027.
[35] R.N. Rao, S. Das, et al., Effect of heat treatment on the sliding wear behaviour of aluminum alloy (Al−Zn−Mg) hard particle composite, Tribol. Intern. 43 (2010) 330−339. 198.
[36] Y. Li, D. Zhang, et al., Rapidly solidified hypereutectic Al-Si alloys prepared by powder hot extrusion, Trans. Nonferrous Met. Soc. China 12 (5) (2002) 878−881.
[37] R.D. Howard, Aluminum Heat Treatment Processes—Applications and Equipment, 2009, <www.industrialheating.com>.
[38] M. Santos, E.C. Filipe, P.L. Michael, J. Hung, S.G. Wise, M.M.M. Bilek, Mechanically robust plasma-activated interfaces optimized for vascular stent applications, ACS Appl. Mater. Interfaces 8 (15) (2016) 9635−9650.
[39] M. Jurak, A.E. Wiącek, R. Mroczka, R. Łopucki, Chitosan/phospholipid coated polyethylene terephthalate (PET) polymer surfaces activated by air plasma, Colloids Surf. A Physicochem. Eng. Asp. 532 (2017) 155−164.
[40] Z. Yang, X. Lei, J. Wang, et al., A novel technique toward bipolar films containing alternating nano−layers of allylamine and acrylic acid plasma polymers for biomedical application, Plasma Process. Polym. 8 (3) (2011) 208−214.
[41] M.Q. Zhang, M.Z. Rong, K. Friedrich:, in: H.S. Nalwa (Ed.), 'Handbook of Organic-Inorganic Hybrid Materials and Nanocomposites', 2, American Science Publishers, CA, 2003.
[42] G. Jagadeesh, P. Balakumar, K. Maung-U (Eds.), Pathophysiology and Pharmacotherapy of Cardiovascular Disease, Springer International Publishing AG, Switzerland, 2015.
[43] T. Govindarajan, R. Shandas, A survey of surface modification techniques for next-generation shape memory polymer stent devices, Polymers 6 (9) (2014) 2309−2331.
[44] A. Abdal-Hay, N.A.M. Barakat, J.K. Lim, Influence of electrospinning and dip-coating techniques on the degradation and cytocompatibility of Mg-based alloy, Colloids Surf. A Physicochem. Eng. Asp. 420 (2013) 37−45.

[45] A.S. Avishan, Formulation and Testing of Biodegradable Polymeric Coating on Zinc Wires in Cardiovascular Stent Application (Tech. Rep., open access master's thesis), Michigan Technological University, 2017.
[46] D.G. Ahn, K.W. Byun, M.C. Kang, Thermal characteristics in the cutting of inconel 718 super alloy using Nd:YAG laser, J. Mater. Sci. Technol. 26 (2009).
[47] C.H.R. Vikram Kumar, P. Keasvan Nair, B. Ramamoorthy, Characterization of Multilayer PVD Nanocoatings Deposited on Tungsten Carbide Tools, 2007.
[48] K. Matsui, M. Ohgai, Formation mechanism of hydrous zirconia particle produced by hydrolysis of ZrCL2 solution, kinetics study for nucleation and crystal growth processes of primary particle, J. Am. Ceram. Soc. 84 (2001) 2203−2313.
[49] M. Hasegawa, K. Arai, S. Saito, J. Polym. Sci. Polym. Chem. 25 (1987) 3117−3125.
[50] V.M. Gunko, E.F. Voronin, E.M. Pakhlov, V.I. Zarko, V.V. Turov, N.V. Guzenko, et al., Colloid Surf. A 166 (2000) 187−201.
[51] E. Leidich, A. Maiwald, J. Vidner, A proposal for a fretting wear criterion for coated systems with complete contact based on accumulated friction energy density, Wear 297 (1−2) (2013) 903−910.
[52] P. Espiard, A. Guyot, Polymer 36 (1995) 4391−4395.
[53] M.L.C.M. Oosterling, A. Sein, A.J. Schouten, Polymer 33 (1992) 4394−4400.
[54] Q.L. Ji, M.Z. Rong, M.Q. Zhang, K. Friedrich, Polym. Polym. Compos. 10 (2002) 531−539.
[55] B. Li, H. Wang, J. Jie, et al., Effects of yttrium and heat treatment on the microstructure and tensile properties of Al−7.5 Si−0.5 Mg alloy, Mater. Des. 32 (2011) 1617−1622.
[56] Y. Luo, M.Z. Rong, M.Q. Zhang, K. Friedrich, J. Polym. Sci. Polym. Chem. 42 (2004) 3842−3852.
[57] R.B. Hieman, Plasma Spray Coating-Principles and Applications, VCH Publishers Inc., New York, 1996.
[58] J.H. Ouyang, S. Sasaki, Effects of different additives on microstructure and high-temperature tribological properties of plasma-sprayed Cr_2O_3 ceramic coatings, Wear 249 (2001) 56−67.
[59] S. Dinesh, F.M. Ahmad, S. Vijanth, Computation of Scale Independent Surface Roughness Via the Generation of Multistage Digital Elevation Models Sabayon and Technology 1 (2008). 4244-1692.
[60] H. Kitsunai, K. Hokkirigawa, et al., Transitions of microscopic wear mechanism for Cr_2O_3 ceramic coatings during repeated sliding observed in a scanning electron microscope tribosystem, Wear 151 (1991) 279−289.
[61] A. Voevodin, A. Yerokhin, V. Lyubimov, et al., Characterization of wear protective Al-Si-O coatings formed on Al-based alloys by micro-arc discharge treatment, Surf. Coat. Technol. 86 (1996) 516−521.
[62] Y. Wang, S.C. Tung, Scuffing and wear behavior of aluminum piston skirt coatings against aluminum cylinder bore, Wear 225−229 (1999) 1100−1108.
[63] M.-C. Gui, D.B. Wang, et al., Microstructure and mechanical properties of cast (Al−Si)/SiCp composites produced by liquid and semisolid double stirring process, J. Mater. Sci. Technol. 16 (5) (2000) 556−563.
[64] Y. Wang, K. Brogan, S.C. Tung, Wear and scuffing characteristics of composite polymer and nickel/ceramic composite coated piston skirts against aluminum and cast iron cylinder bores, Wear 250 (2001) 706−717.
[65] J. Gary, B. Luan, Protective coatings on magnesium and its alloys a critical review, J. Alloy. Compd. 336 (1) (2002) 88−113.

[66] K. Nakata, M. Ushio, Effect of Fe content on wear resistance of thermal-sprayed Al-17Si, Fe alloy coating on A6063 Al alloy substrate, Surf. Coat. Technol. 169 (2003) 443–446.
[67] J. Vetter, G. Barbezat, et al., Surface treatment selections for automotive applications, Surf. Coat. Technol. 200 (5) (2005) 1962–1968.
[68] P. Vissutipitukul, T. Aizawa, Wear of plasma-nitrided aluminum alloys, Wear 259 (2005) 482–489.
[69] S.R. Bakshi, D. Wang, Microstructure and wear properties of aluminum/aluminum–silicon composite coatings prepared by cold spraying, Surf. Coat. Technol. 204 (2009) 503–510.
[70] M. Bao, C. Zhang, et al., The tribological behavior of plasma-sprayed Al-Si composite coatings reinforced with nanodiamond, JOM 64 (6) (2012) 702–708.
[71] O. Prucker, J. Ruhe, Langmuir 14 (1998) 6893–6898.
[72] K. Funatani, Heat treatment of the automobile components: current status and future trends, Trans. Indian Inst. Met. 57 (4) (2004) 381–396.
[73] G.D. Enrico, Improving tribological properties of steels by surface texturing and coating, in: Ricerca in Nano & Physical Sciences, Ph.D. Course in Physics, 2009.
[74] R. Jordan, A. Ulman, J. Am. Chem. Soc. 120 (1998) 243–247.
[75] H. Yu, Y. Xu, et al., Tribological behaviours of surface-coated serpentine ultrafine powders as lubricant additive, Tribol. Int. 43 (3) (2010) 667–675.
[76] L. Rapoport, V. Leshchinsky, I. Lapsker, et al., Tribological properties of WS nanoparticles under mixed lubrication, Wear 255 (2003) 785–793.
[77] M. Kao, H. Chang, et al., The Friction of Vehicle Brake Tandem Master Cylinder, IOP Publishing, 2006.
[78] M. Weck, J.J. Jackiw, R.R. Rossi, P.S. Weiss, R.H. Grubbs, J. Am. Chem. Soc. 121 (1999) 4088–4089.
[79] M. Ejaz, S. Yamamoto, Y. Tsujii, T.M. Fukuda, Macromolecules 35 (2002) 1412–1418.
[80] A.H. Reshak, S. Auluck, The linear and nonlinear optical properties of WS = 0.5, 1.5, and 2.0, Phys. B: Condens. Matter 393 (1) (2007) 88–93.
[81] C. Gu, Q. Li, Z. Gu, et al., Study on application of CeO and CaCO, nanoparticles in lubricating oils, J. Rare Earths 26 (2008) 163–167.
[82] H. Chang, Z.Y. Li, et al., Tribological property of TiO_2 nanolubricant, J. Alloy. Comp. 495 (2010) 481–484.
[83] M. Cantarella, R. Sanz, M.A. Buccheri, F. Ruffino, G. Rappazzo, S. Scalese, et al., Immobilization of nanomaterials in PMMA composites for photocatalytic removal of dyes, phenols and bacteria from water, J. Photochem. Photobiol. A 321 (2016) 1–11.
[84] Merck. Merck Presents Organic Photovoltaic Materials at EXPO 2015 in Milan, Merck KGaA, Darmstadt, Germany, 2015.
[85] L. Schlagenhauf, B. Kianfar, T. Buerki-Thurnherr, Y.Y. Kuo, A. Wichser, F. Nüesch, et al., Weathering of a carbon nanotube/epoxy nanocomposite under UV light and in water bath: impact on abraded particles, Nanoscale 7 (2015) 18524–18536.
[86] C. Serrano, E. Bugnicourt, C. Niculescu, C. Ghituleasa, I. Dumitrescu, A. Sobetkii, et al., Manucoat, Integrated manufacturing process of active textiles by deposition of doped TiO_2, in: Proceedings of the ANNIC 2015 Applied Nanotechnology and Nanoscience International Conference, Paris, France, 5–7 November 2015.
[87] A. Störmer, J. Bott, D. Kemmer, R. Franz, Critical review of the migration potential of nanoparticles in food contact plastics, Trends Food Sci. Technol. 63 (2017) 39–50.

This page intentionally left blank

Application of metal oxides in composites

6

Said Eray
Patnos Vocational School, Ağrı İbrahim Çeçen University, Ağrı, Turkey

6.1 Introduction

Today's modern and rapidly growing technology along with the need to make a better use of available resources necessitates the development of high-performance materials. In most cases, modern and high-tech engineering applications demand advanced materials with a range of properties such as light weight, high strength, high thermal stability, low thermal expansion and superior wear and corrosion resistance. It is challenging to develop a monolithic material that provides a combination of these properties. Composite materials have been widely investigated and developed over the last decades, in an attempt to reach the abovementioned property combinations.

Composites, in its general meaning, are material composed of two or more components which are insoluble in one another. The main concern is to use the desired characteristics of each component in order to obtain a new material whose properties are superior to those of monolithic components each. Commonly, one of the components, that is, matrix, is continuous and bind the other components together. The other component, that is, reinforcement, is embedded within the matrix to improve its weaknesses.

Composite materials can be classified based on either reinforcement type or matrix material. Reinforcement phase can be dispersed within the matrix in the form of particles or continuous/discontinuous fibers which are called particulate composites and fibrous (fiber-reinforced) composites, respectively. The last member of this classification is laminate composites that are composed of several layers of particulate or fibrous composites. Reinforcement properties such as type, concentration, or fiber orientation differ within the layers.

Composites are commonly classified into three categories based on matrix material:

- ceramic matrix composites (CMCs);
- metal matrix composites (MMCs); and
- polymer matrix composites (PMCs).

Matrix material determines the major properties of the composites and is selected according to the requirements of the design. It is difficult to make a full comparison of advantages and disadvantages of these three groups of matrix

Metal Oxide Powder Technologies. DOI: https://doi.org/10.1016/B978-0-12-817505-7.00006-3

materials, since each group offer a wide range of properties. However, some basic characteristic properties can be identified as summarized in Table 6.1.

A variety of nitride, boride, carbide, oxide, and glassy ceramic materials in form of powders, whiskers, or fibers are used in the production of composites. However, in this chapter, as indicated by the scopes of this book, the subject is confined into only metal oxide powders and their applications in each composite category. Particle size, amount, and distribution of the reinforcing phase and, processing method play major roles in determining composite properties. So, it is challenging to make a comprehensive comparison of the data available in the literature. However, in this chapter, some examples of very common composites are given and their important properties are discussed.

6.1.1 Application of metal oxide powders in ceramic matrix composites

Ceramic materials intrinsically offer advantages over metals in high-temperature applications. However, they suffer from low fracture toughness. Several methods have been used to make ceramics tougher, of which the addition of suitable reinforcement especially fibrous reinforcement is the most successful one.

Table 6.1 Basic characteristic properties of different materials.

Property	**Matrix material**		
	Ceramics	**Metals**	**Polymers**
Density	Low	Medium to high	Low
Thermal stability	High	Medium	Low
Mechanical properties	High shear and compressive strength, low impact strength, very hard but brittle	High tensile strength, good impact strength, moderately hard and ductile	Poor
Conductivity	Low thermal and electrical conductivity to insulating	Conductive	Low conductivity to insulating[a]
Corrosion resistance	Great	Vulnerable but can be improved via alloying	Great
Shaping	Difficult	Capable of shaping, cutting and joining without breaking	Easy to shape into complex forms
Cost	Less costly	More costly	Less costly

[a]There exists some organic polymers with high electrical conductivity.

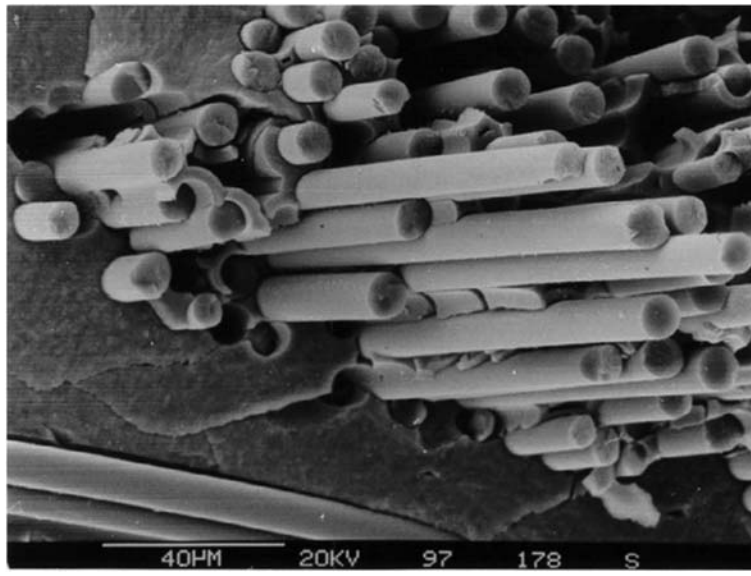

Figure 6.1 The SEM micrograph of fibrous reinforcement embedded in a ceramic matrix [1].

Fig. 6.1 shows the SEM micrograph of fibrous reinforcement embedded in a ceramic matrix. Embedded reinforcement improves fracture toughness by bridging the cracks that may form and also by carrying part of the applied stress, thereby increasing the energy required for crack propagation.

Unlike most metals, ceramic materials are seldom processed by liquid-state methods like foundry because of their high melting point and their lack of success in resisting thermal shocks. To overcome these limitations, a number of processing techniques such as chemical vapor infiltration, sol−gel, and polymer precursor have been developed. However, as far as metal oxide powders are concerned, the main processing method is sintering of the powdery substance. Some common methods are explained in the next section.

6.1.1.1 Processing of oxide-based ceramic matrix composites

Cold pressing followed by sintering

Cold pressing is a common method to fabricate oxide-based CMCs. In this method, a mixture of matrix oxide powder and particulate or short fiber reinforcements is prepared. The mixture is compacted into the desired form by either uniaxial or isostatic pressing. Generally some water and organic binder are added to the mixture so as to get enough strength for carrying the green compact. The binder is burned out at low temperatures. The final composite product is obtained by consequent heating of the green compact at a high enough temperature. The process is illustrated in Fig. 6.2.

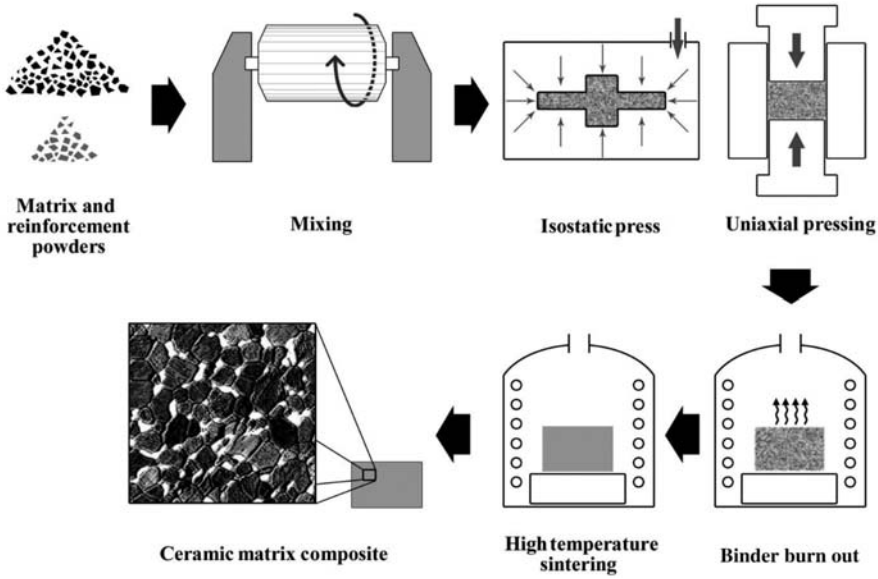

Figure 6.2 Cold pressing followed by sintering method for processing of CMCs. *CMCs*, Ceramic matrix composites.

This method suffers from high amounts of shrinkage (10%−20%) and resultant problems of distortion, residual stress, and even cracking. In addition, this method is not suitable for long fiber-reinforced composites as the reinforcements are damaged during pressing.

Hot pressing

Hot pressing is alike to cold pressing but it combines pressing and sintering in a single step. The simultaneous usage of pressure and high temperature helps to overcome the problems associated with cold pressing and allows rapid consolidation of the product at a considerably lower pressure. Hot pressing also serves to produce composite parts with more complex shape.

Slurry infiltration

Slurry infiltration is the major process for producing long fiber-reinforced composites. In this technique, continuous fibers are immersed in a slurry of matrix material (metal oxide powder). In addition to the matrix material, the slurry generally involves water or alcohol as the liquid carrier, organic binders, and plasticizers. A thin layer of matrix powder covers the surface of the immersed fibers which are spooled around a drum. This allows these fibers to be shaped into the form of large sheets of unidirectional fibers. These sheets are cut into the sizes and shapes needed to the specific part being produced. The cutout layers are stacked onto each other

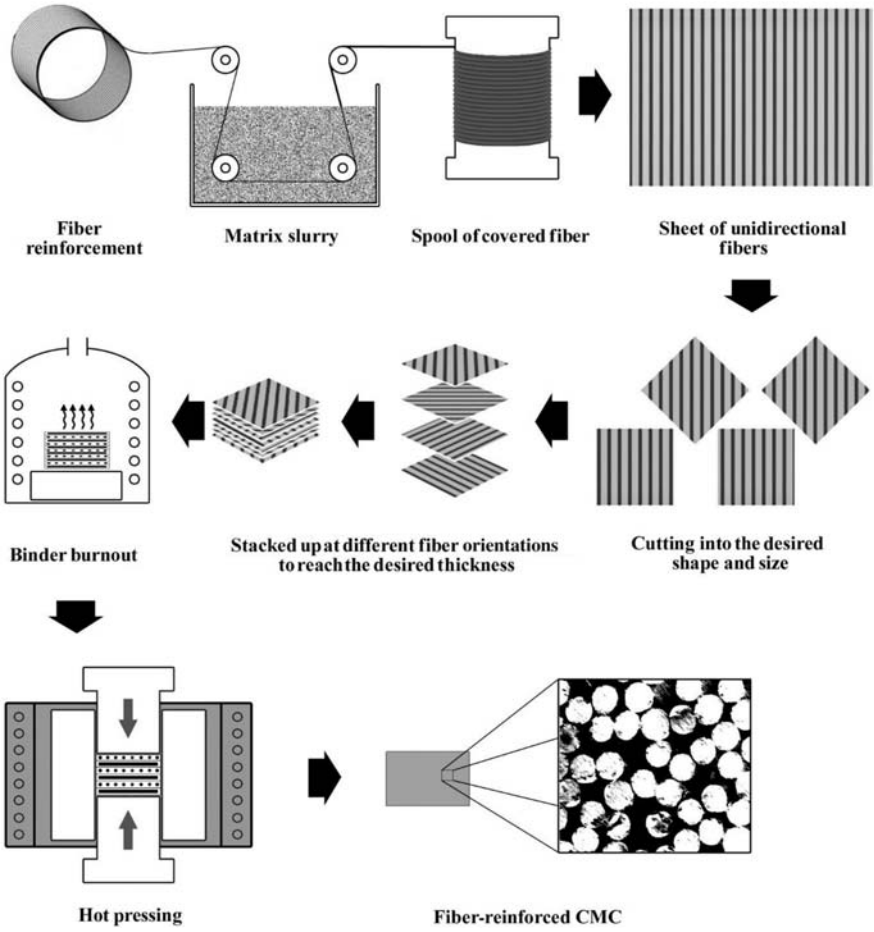

Figure 6.3 Slurry infiltration method for processing of fiber-reinforced CMCs. *CMCs*, Ceramic matrix composites.

generally at different fiber orientations and hot pressed to obtain CMCs. The process is schematically shown in Fig. 6.3.

Lamination process

Lamination process is used for textile-based CMCs. In these composites, the reinforcing phase is fabrics of woven ceramic fibers. The slurry of matrix material is infiltrated into the ceramic fabrics manually by a trowel. Infiltrated fabrics are stacked onto each other until the desired thickness is achieved. This stack is then cold or hot pressed in a mold. It also can be shaped by covering the stack with a peel foil, putting it into a plastic bag and evacuating the bag. Lamination process is a slow process and is suitable only individual items.

6.1.1.2 Some examples of oxide-based ceramic matrix composites

The most frequently used oxides in the ceramic matrix are those of aluminum, silicon, titanium, and zirconium. Some basic properties of these oxides are given in Table 6.2. Owing to its low density, low cost, high melting point, high hardness, good chemical and thermal stability, and wear resistance, alumina (Al_2O_3) is the mostly used matrix in CMCs. Some common examples of metal oxide powders application in CMCs are given in following section.

Alumina–titanium carbide composites

Alumina–titanium carbide composites were first introduced as cutting tools for ferrous alloys in the early 1970s. They offered a high dimensional accuracy and fine finish. These composites have high thermal shock resistance, high hardness, and high fracture toughness. They maintain their hardness at high temperatures up to 800°C.

Commercially produced composites consist about 30%–40% of TiC. They are produced by hot isostatic pressing of uniformly blended high-purity aluminum oxide and titanium carbide powders. Generally, powders finer than 1 μm are treated. Hot isostatic pressing provides minimal porosity level and high performance. A typical microstructure of Al_2O_3–TiC composites is shown in Fig. 6.4.

Alumina–silicon carbide composites

Being accepted as the most important nonoxide ceramic material, silicon carbide (SiC) is widely used as either matrix or reinforcement in CMCs. It shows excellent thermal and mechanical properties.

Silicon carbide is normally added, as the reinforcement, to the alumina matrix in the form of whiskers. One of the most popular applications of Al_2O_3–SiC_w composites is cutting tools. These oxide-based CMCs are used for machining of Inconel, nickel-based superalloys, and other nonferrous alloys. Addition of up to 25 wt.% SiC_W to the alumina matrix results in low density product with considerable improvement in fracture toughness, bend strength, and Young's modulus. At the same time, SiC whiskers decrease the coefficient of thermal expansion of the resulting composite and increase its thermal conductivity, thereby increasing its thermal shock resistance. Al_2O_3–SiC_W composites are fabricated by slip cast, cold pressing followed by sintering or hot pressing routes.

Table 6.2 Properties of some oxide ceramics.

	Density (g/cm^3)	**Melting point (°C)**	**Young's modulus, *E* (GPa)**	**Coefficient of thermal expansion at RT, α ($10^{-6}K^{-1}$)**	**Mohs' hardness**
Al_2O_3	3.96	2072	380–410	5.5	9
SiO_2	2.65	1723	80–100	8.1	7
TiO_2	4.23	1855	230–290	7.1	6.5
ZrO_2	5.68	2715	180–220	7	8

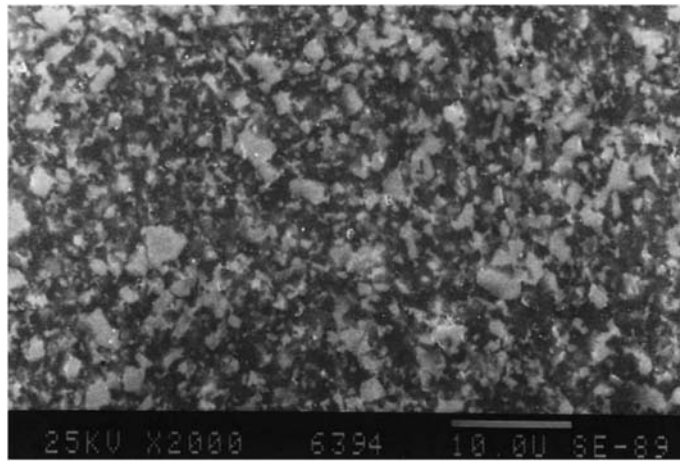

Figure 6.4 A typical SEM micrograph of Al_2O_3/TiC composite cutting tools [2].

Silicon carbide is also added to the alumina matrix in the form of fibers. Silicon carbide fibers (SiC_f) provide much better durability, strength, and creep resistance compared with other ceramic fibers such as carbon and alumina fibers. One commercial use of $Al_2O_3-SiC_f$ is CMC shrouds of turbofan LEAP engine.

Alumina–zirconia composites

Alumina–zirconia composites are advanced materials which combine the high hardness of alumina with excellent fracture toughness of zirconia. These composites have increasingly being used in arthroplasty as a load bearing material, for example, hip prosthesis (Fig. 6.5). Superior mechanical and tribological properties of $Al_2O_3-ZrO_2$ composites accompanied by their long-standing biocompatibility enable the production of prostheses with relatively long lifetime. A typical SEM micrograph of these composites is shown in Fig. 6.6. Either alumina or zirconia can

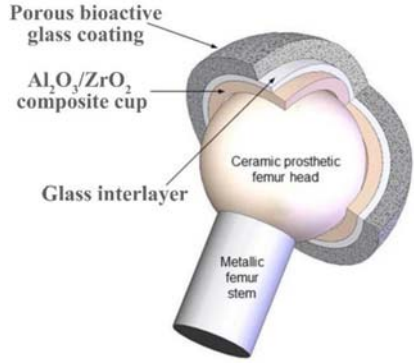

Figure 6.5 Usage of $Al_2O_3-ZrO_2$ composites in hip prosthesis [3].

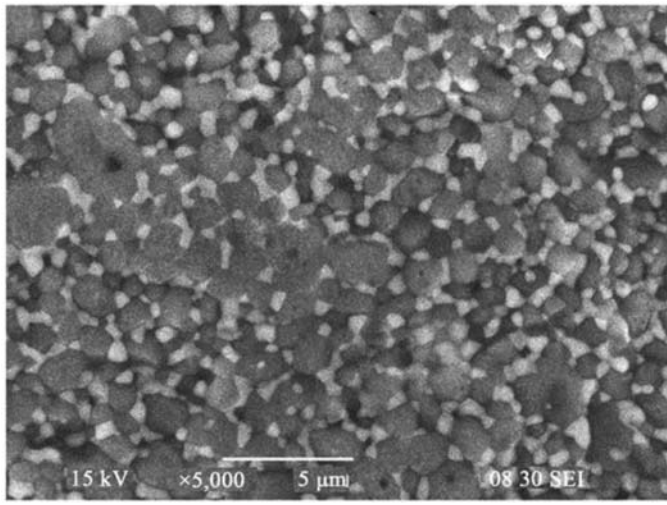

Figure 6.6 A typical SEM micrograph of $Al_2O_3-ZrO_2$ composites [4].

be used as the matrix material. One example where ZrO_2 is used as the matrix is alumina-toughened zirconia implants.

The other commercial application of $Al_2O_3-ZrO_2$ composites is cutting tools. Usage of SiC_W as reinforcement in the cutting tools entails the problem of dissolution in steels and other ferrous alloys. SiC interacts with iron and is chemically incompatible. Zirconia-reinforced alumina or zirconia-toughened alumina has been developed to overcome this difficulty.

Zirconia can also be used as the matrix material while alumina plays the reinforcement role. Monolithic zirconia undergoes two phase transformations (cubic to tetragonal at 2370°C and tetragonal to cubic at 1173°C) during cooling from high temperatures that are accompanied by significant volume contraction. Yttria (Y_2O_3) is added to zirconia to avoid these transformations at high temperatures and make tetragonal or cubic structure stable at room temperature. This material is called yttria-stabilized zirconia (YSZ). As an advanced ceramic material, YSZ has use in oxide fuel cells as electrolyte and biomedical implants. It is reported [5] that the addition of up to 30 mol.% of particulate or platelet alumina has decreased its density and improved its mechanical properties such as hardness, fracture toughness, and elastic modulus.

Alumina–alumina composites

Alumina fiber–reinforced alumina or simply alumina–alumina composites are lightweight high-temperature materials (their densities are about one-third of the high-temperature steel alloys) with good thermal shock resistance and acceptable stability in oxidizing atmospheres. These composites are being used for high-temperature (up to 1150°C) applications such as flame tubes, hot gas

distributors, and furnace components [6]. Alumina−silica or alumina−zirconia mixtures can also be used as the matrix material.

Other oxide-based ceramic matrix composites

Silica matrix composites such as SiO_2−CNT (carbon nanotube) and SiO_2−AlN are other examples for the use of metal oxides in the CMCs. However, they are commonly studied in laboratory scale researches with no commercial success. Other example is TiO_2−Al_2O_3 composites which are generally used as wear and corrosion resistant coatings on metals such as steels.

6.1.2 Application of metal oxide powders in metal matrix composites

MMCs combine characteristic properties of metals such as ductility, formability, toughness, electrical conductivity, and thermal conductivity with those of ceramic materials such as thermal durability, low density, high hardness, high modulus, and low coefficient of thermal expansion.

Ceramic materials are used in the form of particulate, whiskers, short, and long fibers to reinforce the matrix metal. Discontinuously reinforced composites, that is, particulate-, whiskers-, and short fiber-reinforced composites, are cost-effective and are suitable for mass production. In addition, they are isotropic material and can be subjected to deformation and cutting to produce complex parts.

A wide range of carbides, oxides, borides, and nitrides can be used as the reinforcing phase. In the following section, we will confine ourselves to only particulate-reinforced composites and also to metal oxide powders as the reinforcing phase.

6.1.2.1 Processing methods of particulate-reinforced metal matrix composites

Standard powder metallurgy

Standard powder metallurgy or powder metallurgy (PM) is a versatile method for producing various discontinuously reinforced composites. This method includes blending of matrix and reinforcement powders followed by consolidation of the mixture to obtain composite. It is very similar to the cold and hot pressing methods as previously explained for CMCs. The main difference is that microstructure of the matrix alloy can be refined, and reinforcement distribution can be better controlled by ball milling the mixture prior to consolidation. In addition, secondary processing methods such as extrusion and rolling can be applied to improve mechanical properties and achieve full consolidation.

In situ powder metallurgy

Standard PM methods prevent problems associated with the liquid phase methods such as unwanted reactions at reinforcement-matrix interface and inhomogeneous particle distribution. However, they are relatively expensive due to the high cost of alloy powders and the relatively long mixing times required to obtain a

homogeneous mixture. In situ PM (IPM) overcomes these challenges by using alloy ingots as raw materials and producing homogeneous powder mixture during the process.

In this method, matrix alloy is melted and then stirred vigorously in the presence of a sufficient amount of nonwettable particles (Fig. 6.7). The melt is disintegrated by the collision of high energy particles and, upon cooling, results in a homogeneous mixture of matrix alloy and reinforcing particles. The process is schematically shown in Fig. 6.8. The mixture can be further processed via routine consolidation methods. IPM has successfully been used for the production of $Al-Al_2O_3$ and Al−SiC composites. The main disadvantage of the process is its being batch-wise. Furthermore, the properties of the alloy powder are interrelated to the type, particle size, and amount of the reinforcing particles which, in turn, make it difficult to control the process and properties of the resultant composites.

Stir casting

Stir casting is the simplest liquid-state processing method for fabrication of particulate-reinforced MMCs. In this method, particulate reinforcement is gradually added to the molten matrix metal which is stirred mechanically. Schematic diagram of the process is shown in Fig. 6.9. A graphite impeller is generally used for stirring. A vigorous stirring is required to ensure a good distribution of the reinforcements. The reinforcement-molten matrix slurry is subsequently cast by conventional methods. The composite product is obtained upon cooling.

The main disadvantage of this method is the agglomeration of particles. This situation can become even worse when suspended particles are repelled by the solidification front. Particle repulsion can be largely overcome by rapid solidification. Care must be taken to avoid gas entrapment in the melt during stirring which can result in porosities and unwanted reactions with the melt.

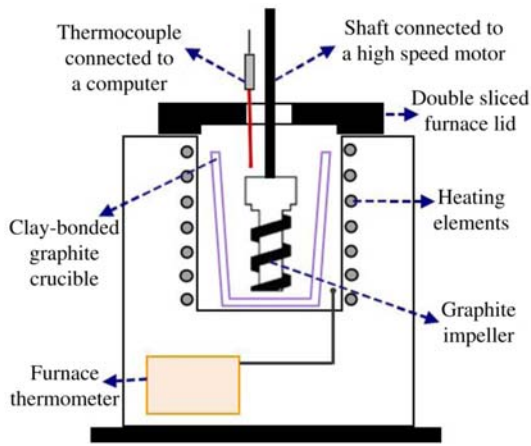

Figure 6.7 Schematic diagram of IPM setup [7]. *IPM*, In situ powder metallurgy.

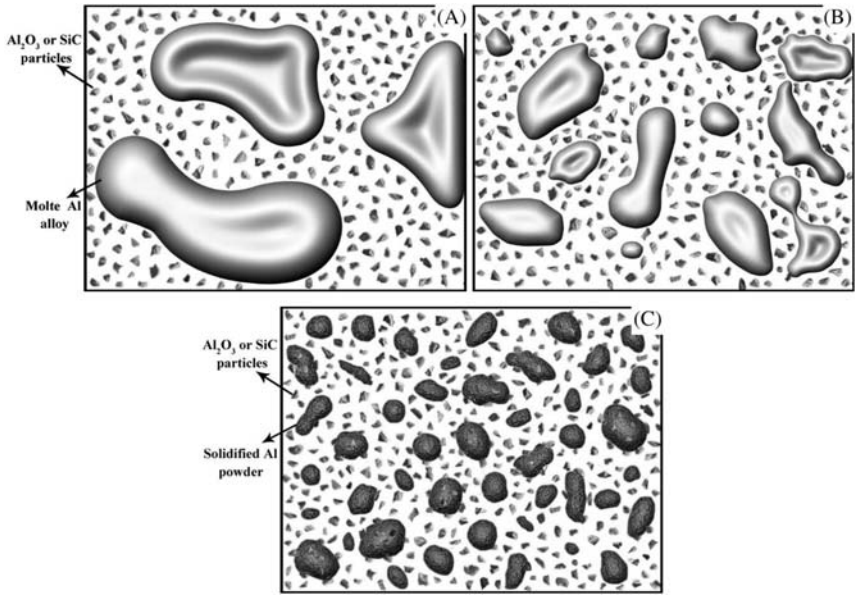

Figure 6.8 Schematic snapshots of the mixture (A) at the beginning of stirring, (B) at longer stirring times, and (C) after solidification [7].

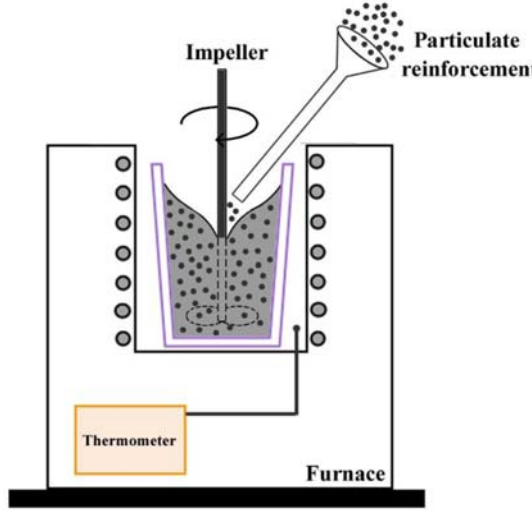

Figure 6.9 Schematic diagram of stir casting method.

When compared to PM methods, stir casting is a simple and economical method, offers better matrix−reinforcement bonding and allows fabrication of large parts.

Infiltration method

In this method, a molten metal percolates through and fills the pores of a preform of compacted reinforcing particles, fibers etc. Synthesis of the preform with acceptable mechanical strength and permeability is the key step in this process. The driving force for the percolation process can be capillary forces (spontaneous or pressureless infiltration), gas or mechanical pressure, centrifugal forces, vacuum, etc. Some commonly used infiltration methods are schematically shown in

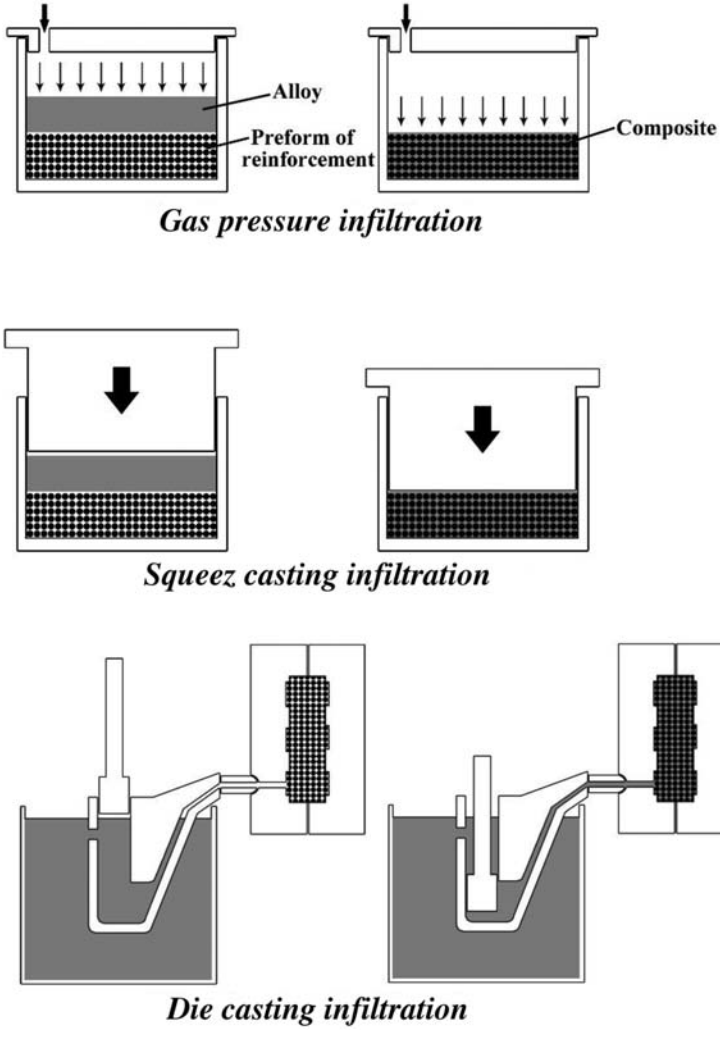

Figure 6.10 Some commonly used infiltration methods.

Fig. 6.10. This method produces near net shape composites with intimate control over the distribution of the reinforcement. However, it is not suitable for composites with low percentages of reinforcing particles. It is applicable when a high volume fraction of reinforcement is desirable.

6.1.2.2 Some examples of metal matrix composites reinforced with metal oxide powders

Aluminum matrix composites

A sort of metals such as iron, nickel, copper, titanium, and their alloys can be used as the matrix material but for many researchers MMCs refer to those of aluminum and its alloys. A combination of properties, such as low price, low density, good corrosion resistance, high conductivity and being amenable to precipitation hardening, has created a great demand for aluminum alloys as matrix material. They are used in such an extent that forms its own classification of aluminum-based MMCs or simply aluminum matrix composites (AMCs).

They are processed by both liquid-state processes and PM. Liquid-state processes are suitable for mass production and provide low cost and high-processing rates. However, generally they are not suitable for composites containing higher than 20 vol.% of reinforcements due to agglomeration. Higher percentages (up to 50 vol. % in some cases) can be homogeneously distributed in the matrix by PM route.

The most commonly used metal oxide reinforcement is alumina. Alumina has greater stability in Al matrix compared to the most commonly used nonoxide reinforcement, that is, SiC. Addition of micron-sized alumina improves wear resistance and compressive strength of the composites. Addition of nanosized alumina can also improve tensile and yield strength of aluminum alloy. It is reported [8] that 10 vol.% of 50 nm alumina powder to Al 319 alloy can increase its yield strength to 515 MPa which is 1.5 times greater than that of AISI 304 steel. This makes it a good choice for connecting rods, brake rotors, brake calipers, and drive shafts, where high strength is required. Other applications of $Al-Al_2O_3$ composites in the automotive industry are piston rings and brake disks, where high wear resistance is essential. Addition of graphite gives self-lubricating property to these composites which are used in pistons and cylinder liners. As an example, Honda fabricated engine cylinder liner (Fig. 6.11) from an AMC (12% Al_2O_3 powder + 9% carbon fiber). The cylinder liners were fabricated by squeeze casting.

Other metal oxide reinforcements are SiO_2, TiO_2, MgO, and ZrO_2. Mechanical and tribological properties of the composites reinforced with these oxides have been studied by many researchers. Nonetheless, unlike $Al-Al_2O_3$ composites, they are not yet commercially available.

Magnesium matrix composites

Although the mechanical and thermal properties of magnesium and its alloys are inferior to those of aluminum alloys, they are of interest to engineers as the lightest construction materials. Magnesium alloys are, therefore, a natural choice for the aerospace and automotive industries, where fuel consumption is required to be

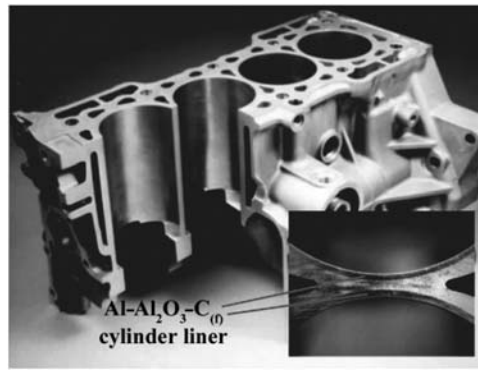

Figure 6.11 Honda Prelude engine with AMC cylinder liner [9]. *AMC*, Aluminum matrix composite.

minimized. Magnesium alloys are also extensively used in sports equipment. Many researches have been conducted to enhance the mechanical properties of magnesium alloys using an appropriate reinforcing agent. The most commonly used oxide reinforcement is that of aluminum, that is, Al_2O_3. The addition of nano- and submicron alumina has been reported [10,11] to significantly increase tensile strength, yield strength, and hardness of the magnesium and decrease their coefficient of thermal expansion. However, ductility was adversely affected.

Other metal oxides used as the reinforcement are ZrO_2, SiO_2, and Y_2O_3. In a study [12] to compare the effects of ZrO_2 and SiO_2 as a reinforcement, it is reported that ZrO_2 results in higher hardness and yield strength, whereas SiO_2 gives higher ultimate tensile strength. Although not as good as Al_2O_3, ZrO_2, and Y_2O_3 have comparable beneficial effects on the mechanical properties of Mg composites.

Titanium matrix composites

Compared to aluminum, titanium proposes higher stiffness, much better corrosion resistance, higher Young's modulus and better high-temperature durability. Although titanium is more expensive, the abovementioned properties make it a good choice for the aerospace industry and medical uses, where attaining the desired properties are far more important than the cost. However, the high reactivity of titanium in both liquid and solid states imposes limitations on the processing method of titanium-based composites and on the type of the reinforcement. This problem has led to little success in production of Ti-matrix composites using oxide reinforcements. In most of the cases, a compound of Ti such as TiC and TiB_2 are used as the reinforcement.

Copper matrix composites

Copper is of interest for its excellent electrical and thermal conductivities. Nevertheless, pure copper is soft and has poor mechanical properties and low wear resistance. When alloyed, its characteristic properties, that is, electrical and thermal conductivities, are adversely affected. This problem can be overcome to a large

extent by the use of copper-based composite materials. A variety of metal oxides such as Al_2O_3, ZrO_2, SiO_2, Y_2O_3, and TiO_2 are used to reinforce the copper matrix. Although not as worse as alloying, the addition of electrically insulating oxide particles to the matrix decreases the conductivity of the resultant composites. Some additives such as silver [13] have been used to improve the conductivity of oxide-based composites, but the major focus has been on the use of conductive reinforcements such as graphene and CNT.

Iron matrix composites

Iron alloys, especially steels, are the most important construction materials due to their high mechanical properties, abundance, and reasonable prices. Steel-based composites are of little importance when improvement in mechanical properties such as tensile strength is concerned. However, in some cases, density reduction, improved wear resistance and enhanced high-temperature properties have become the major motivation for the processing of this group of composite materials. Zirconia-reinforced steel has been produced by infiltration method [14]. Lower friction coefficient and better wear behavior of the composite has been reported. Similar effects are reported [15] for the addition of Al_2O_3 particulates to steels.

Oxide dispersion strengthened (ODS) steels are the most significant and industrially used steel-based composites. Nanosized dispersed oxide particles, for example, Y_2O_3 and Al_2O_3, considerably increases high temperature properties of steels (creep resistance in particular). In fact, nickel alloys were the first alloys which were strengthened by dispersion of nanosized oxide particles for high-temperature applications. Nickel alloys have been preferred to a greater extent because of their excellent corrosion resistance at high temperatures. However, the high price of nickel alloys has shifted researches toward the use of cost-effective steel materials. ODS steels are used in turbine blades, heat exchanger tubes, nuclear reactors, and the outer protecting layer of space crafts.

6.1.3 Application of metal oxides in polymer matrix composites

Properties such as low density, low cost, and ease of fabrication make polymers attractive as a group of engineering material. However, they are of low thermal resistance and low mechanical and electrical properties. Thermal properties of polymers cannot be improved significantly but their mechanical and electrical properties are enhanced via PMCs. For this purpose, either natural (sisal, kenaf, flax, etc.) or synthetic (glass, carbon, aramid, boron, alumina, etc.) fiber reinforcements are widely used by engineers. A car door trim fabricated from hemp fiber−reinforced polyethylene is shown in Fig. 6.12. Fiber-reinforced PMCs have found many applications in the automotive, aerospace, and marine industries.

Generally, particulate inorganic materials are added to the fiber-reinforced PMCs to enhance their properties. However, the major limitation is the mismatch between the polymeric matrix and most of the inorganic reinforcements. In contrast to metals and ceramics, which are crystalline materials, polymers are composed of large molecules in long chains. This situation results in a weak

Figure 6.12 Car door trim fabricated from hemp fiber−reinforced polyethylene [16].

matrix−reinforcement bond arising from intermolecular forces only. This problem can be overcome by functionalization along with a dispersion on a molecular scale, that is, nanoscale. This can lead to chemical bonding and substantial improvements in mechanical properties. Polymer-based composites reinforced with inorganic nanoparticle (NP) have progressively attracted attention due to their unique properties. The effect of metal oxide powders, which are most commonly added to PMCs, is described later.

6.1.3.1 Alumina-reinforced polymer matrix composites

Aluminum oxide is one of the promising inorganic reinforcements (also referred to as fillers in the case of PMCs) used in PMCs. Provided proper dispersion and suitable interfacial bonding, addition of small amounts of nanosized alumina particles to the polymeric matrix can result in tremendous improvement in mechanical properties such as tensile strength and Young's modulus [17]. Alumina is also added to improve thermal and electrical conductivity of the polymeric matrix [18]. In addition to the abovementioned applications, alumina may be used where optical transparency is also important. Fig. 6.13 shows the fairly transparent composite obtained by the addition of 1 wt.% nanosized alumina to polycarbonate (PC) polymers.

6.1.3.2 SiO_2-reinforced polymer matrix composites

Silicon dioxide NPs have properties, such as abrasion resistance, optical ultraviolate filtering, luminescent, and biocompatibility. They also have low refractive index and high mechanical and thermal stability. The surface of SiO_2 NPs have a

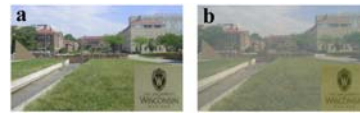

Figure 6.13 Transparencies of (A) PC neat resin, (B) 1 wt.% alumina-PC composite [19]. *PC*, Polycarbonate.

high concentration of hydroxyl groups which makes them to be easily functionalized. Provided good dispersion in the matrix, they can share these characteristic properties with polymers.

One of the most noticeable effects of the SiO_2 NPs is improving mechanical and tribological properties of PMCs. These properties along with their excellent chemical durability make these composites a suitable choice as a protective coatings where wear resistance and/or corrosion resistance are needed.

Unique electrical properties of SiO_2 NPs also attracted the attention of researchers to introduce a new generation of dielectrics, that is, electrically insulators. In the recent years, conventional oil paper and ceramics insulators have been replaced by different kinds of polymeric ones. It was reported by many researchers [20] that the addition of SiO_2 NPs to these polymers improves their electrical breakdown property.

Another use of SiO_2 NPs is optical fibers. Polymer optical fibers are of advantages over the glass fibers due to their flexibility, low cost, and ease of production. Resistance of these fibers to abrasion and scratching can be improved by addition of ceramic NPs such as silica, alumina, and zirconia. At the same time, it makes it possible to adjust the refractive index of the fiber over the required range [21].

SiO_2 NPs are also utilized in the production of mixed matrix membranes. These membranes are used for gas separation. Addition of SiO_2 NPs into the polymer matrix enhances the gas permeability especially for low-permeable polymers. However, in most of the cases the selectivity of the separation process is adversely affected.

6.1.3.3 TiO_2-reinforced polymer matrix composites

Titanium dioxide is the other commonly used reinforcement in PMCs. In addition to the improvements in mechanical properties, TiO_2 decreases water absorption [22] by the polymeric matrix, thereby hindering composite degradation.

6.1.3.4 ZnO-reinforced polymer matrix composites

Zinc oxide (ZnO) is used as piezoelectric, sensing, dielectric, and electromagnetic shielding constituent in PMCs [23]. However, it has been reported that its addition decreased mechanical properties because of weak interfacial adhesion between the nano-particles and the matrix [24].

Silica (SiO_2) is also used in PMCs. It is reported [20] SiO_2 NPs can be used in PMCs to enhance mechanical and tribological properties, impose flame retardancy, and control optical properties.

6.2 Conclusion

Unique mechanical, thermal, electrical, and chemical properties, together with abundance and low cost, have made metal oxides an attractive material for engineers. However, monolithic metal oxides show low tolerance to crack propagation and have low fracture toughness. This problem can be overcome via making composites. Appropriate reinforcing materials can be added to ceramics to produce CMCs with enhanced fracture toughness. Some examples are alumina−titanium carbide and alumina−silicon carbide composites which have applications in cutting tools and shrouds of turbofan LEAP engines. The other method to use the beneficial properties of metal oxides is to use them as the reinforcing materials in the metallic or polymeric matrices to obtain metal matrix and PMCs. Powders of aluminum oxide, titanium dioxide, silicon dioxide, zirconium oxide, and yttrium oxide are widely used as the reinforcing materials. MMCs have been increasingly used in different industries, particularly in the automotive and aerospace industries. PMCs reinforced by metal oxide powders are the least developed group of composites due to the mismatch between inorganic reinforcement and polymeric matrix. However, many researches are being conducted to enhance the properties of these composites. It is reported that the addition of functionalized and nanoscale metal oxides can solve the mismatch problem, thereby improving the properties of PMCs.

References

[1] Wikipedia contributors, "Ceramic matrix composite," Wikipedia, The Free Encyclopedia, [Online]. Available from: <https://en.wikipedia.org/w/index.php?title = Ceramic_matrix_composite&oldid = 945949321> (accessed 15.03.20).
[2] E.D. Whitney, Ceramic Cutting Tools: Materials, Development, and Performance, Noyes Publications, NJ, 1994.
[3] F. Baino, J. Minguella-Canela, F. Korkusuz, P. Korkusuz, B. Kankılıç, M.Á. Montealegre, et al., In vitro assessment of bioactive glass coatings on alumina/zirconia composite implants for potential use in prosthetic applications, Int. J. Mol. Sci. 20 (3) (2019) 1−15.
[4] M. Gafur, M. Sarker, M. Alam, M. Qadir, Effect of 3 mol% yttria stabilized zirconia addition on structural and mechanical properties of alumina-zirconia composites, Mater. Sci. Appl. 8 (7) (2017) 584−602.
[5] S.R. Choi, N.P. Bansal, Alumina-reinforced zirconia composites, in: N.P. Bansal (Ed.), Handbook of Ceramic Composites, Springer, Boston, MA, 2005, pp. 437−457.
[6] W. Pritzkow, A. Nöth, A. Rüdinger, Oxide ceramic matrix composites − manufacturing, machining, properties and industrial applications, Ceram. Appl. 3 (2) (2015) 48−54.

[7] S. Pournaderi, Mahdavi, F. Akhlaghi, Fabrication of Al/Al2O3 composites by in-situ powder metallurgy (IPM), Powder Technol. 229 (2012) 276–284.
[8] J. Qu, L. An, P.J. Blau, Sliding friction and wear characteristics of Al2O3-Al nanocomposites, in: STLE/ASME 2006 International Joint Tribology Conference, San Antonio, TX, 2006.
[9] B. Stojanović, L. Ivanović, Application of aluminium hybrid composites in automotive industry, Tehnički Vjesn. 22 (1) (2015) 247–251.
[10] M. Habibnejad-Korayem, R. Mahmudi, W. Poole, Enhanced properties of Mg-based nano-composites reinforced with Al2O3 nano-particles, Mater. Sci. Eng. A 519 (2009) 198–203.
[11] W.L.E. Wong, S. Karthik, M. Gupta, Development of high performance Mg–Al2O3 composites containing Al2O3 in submicron length scale using microwave assisted rapid sintering, Mater. Sci. Technol. 21 (9) (2005) 1063–1070.
[12] C.I. Chang, Y.N. Wang, H.R. Pei, C.J. Lee, J.C. Huang, On the hardening of friction stir processed Mg-AZ31 based composites with 5–20% nano-ZrO2 and nano-SiO2 particles, Mater. Trans. 47 (12) (2006) 2942–2949.
[13] X. Zhou, Z. Hu, D. Yi, Enhancing the oxidation resistance and electrical conductivity of alumina reinforced copper-based composites via introducing Ag and annealing treatment, J. Alloy. Compd. 787 (2019) 786–793.
[14] D. Wittig, A. Glauche, C. Aneziris, T. Minghetti, C. Schelle, T. Graule, et al., Activated pressureless melt infiltration of zirconia-based metal matrix composites, Mater. Sci. Eng. A 488 (2008) 580–585.
[15] C. Kuforiji, M. Nganbe, Powder metallurgy fabrication, characterisation and wear assessment of SS316L-Al2O3 composites, Tribol. Int. 130 (2019) 339–351.
[16] Wikipedia contributors, "Natural fiber reinforced plastic," Wikipedia, The Free Encyclopedia, [Online]. Available from: <https://de.wikipedia.org/w/index.php?title = Naturfaserverst%C3%A4rkter_Kunststoff&oldid = 194194275> (accessed 17.03.20).
[17] Z. Guo, T. Pereira, O. Choi, Y. Wang, H.T. Hahn, Surface functionalized alumina nanoparticle filled polymeric nanocomposites with enhanced mechanical properties, J. Mater. Chem. 16 (28) (2006) 2800–2808.
[18] S. Mallakpour, E. Khadem, Recent development in the synthesis of polymer nanocomposites based on nano-alumina, Prog. Polym. Sci. 51 (2015) 74–93.
[19] A. Chandra, L.-S. Turng, P. Gopalan, R.M. Rowell, S. Gong, Study of utilizing thin polymer surface coating on the nanoparticles for melt compounding of polycarbonate/alumina nanocomposites and their optical properties, Compos. Sci. Technol. 68 (3–4) (2008) 768–776.
[20] S. Mallakpour, M. Naghdi, Polymer/SiO_2 nanocomposites: production and applications, Prog. Mater. Sci. 97 (2018) 409–447.
[21] J. Böhm, J. Haußelt, P. Henzi, K. Litfin, T. Hanemann, Tuning the refractive index of polymers for polymer waveguides using nanoscaled ceramics or organic dyes, Adv. Eng. Mater. 6 (1–2) (2004) 52–57.
[22] V. Prasad, M. Joseph, K. Sekar, Investigation of mechanical, thermal and water absorption properties of flax fibre reinforced epoxy composite with nano TiO_2 addition, Compos., A 115 (2018) 360–370.
[23] D. Ponnamma, J.-J. Cabibihan, M. Rajan, S.S. Pethaiah, K. Deshmukh, J.P. Gogoi, et al., Synthesis, optimization and applications of ZnO/polymer nanocomposites, Mater. Sci. Eng. C 98 (2019) 1210–1240.
[24] D.W. Chae, B.C. Kim, Characterization on polystyrene/zinc oxide nanocomposites prepared from solution mixing, Polym. Adv. Technol. 16 (2005) 846–850.

This page intentionally left blank

Metal-oxide powder technology in biomedicine

7

Faisal Ahmad[1], *Y. Al-Douri*[2,3,4], *D. Kumar*[5] *and S. Ahmad*[5]
[1]Iris Worldwide, Gurugram, India, [2]University Research Center, Cihan University Sulaimaniya, Sulaymaniyah, Iraq, [3]Nanotechnology and Catalysis Research Center (NANOCAT), University of Malaya, Kuala Lumpur, Malaysia, [4]Department of Mechatronics Engineering, Faculty of Engineering and Natural Sciences, Bahcesehir University, Istanbul, Turkey, [5]JC Bose University of Science & Technology, YMCA, Faridabad, India

7.1 Introduction

Metals reacting with oxygen form the corresponding metal oxides (MOs) that are generally water insoluble solids at room temperature produce salts after interacting with acids. Some MOs are acidic/amphoteric and produce salts after reacting with a base, as noted in the case of aluminum oxide producing sodium aluminate in sodium hydroxide [1].

The transition MOs (TMOs) are unique among the known MOs because of the loosely bound and unpaired *d-electrons* that enable compound formations with different stoichiometries and variable oxidation states. Consequently, lower ionization potentials of these compounds, arising out of the hybridizations of their atomic orbitals, offer possibilities of synthesizing the engineered MO-complexes with programmable features. The resultant properties of these TMOs are currently invoking special interests for applications in designing complexes with known features using theoretical models. Interactions involving TMO and nanomaterials (NMs) of lower dimensions (i.e., 0, 1, and 2D), including organic and inorganic species, are currently being used in preparing compounds useful in human healthcare and environment. The special features of these compounds are worth examining further for their yet unexplored applications. Especially, those comprising of MO species as nanoparticles (NPs), nanorods (NRs), nanoclusters (NCs), nanosheets (NSs), and hierarchical supramolecular structures of inorganic/organic species are reviewed here with special reference to their biomedical applications. Numerous possibilities are currently under study because of the atomic and molecular level changes that are possible to introduce during their chemical syntheses [2–6].

The micro- and nanostructured MO species comprising atomic/molecular-thin 2D-NSs are evoking interests for using them in catalysis, sensing, and energy storage applications. A large number of inorganic 2D-NMs have been synthesized (top-down or bottom-up methods), producing mono/multiple-layered NS-structures for

Metal Oxide Powder Technologies. DOI: https://doi.org/10.1016/B978-0-12-817505-7.00007-5

their uses in sensors, theranostics, drug delivery, wound management, a variety of nanobiomedical devices that are examined as important constituents of the MO-technology as discussed in Refs. [7−11].

Conventionally exfoliated NSs from naturally occurring oxide crystals of Mo, W, Ga, and V were found stable under ambient conditions due to oxygen-terminated unit-cells forming single or multiple-layered planar sheets. There are several other substoichiometric noncrystalline compounds of Ti and Zn oxides, which were also exfoliated either from their stratified-compounds or layer-by-layer (LbL) deposited samples followed by postgrowth stabilizations using charged-motifs or functional groups. The family of perovskite-NSs offer a good example of ABO_3 stoichiometry having A and B-ions at the corners and center of a cubic unit cell, respectively, prepared by LbL depositions and stabilizations. The layered-perovskites of ABO_3 stoichiometry contain interleaved thin-sheets of A and B-cations of varying motif-layer thickness and lateral off-setts of the perovskite layers with reference to each other. There are three types of "Aurivillius" (AU), "Dion−Jacobson" (DJ) and "Ruddlesden−Popper" (RP) phases, in which, the AU-phase $[Bi_2O_2]$-$[A_{(n-1)}B_nO_{3n+1}]$ with Bi_2O_2 separating motif produces stable Bi_2WO_6 and $SrBi_2Ta_2O_9$-layers. Similarly, the DJ-phase $[MA_{(n-1)}B_nO_{(3n+1)}]$ with a separating motif layer of alkali metal or lanthanide ions (M) produce $LaNb_2O_7$, $(Ca, Sr)_2Nb_3O_{10}$, $CaLaNb_2TiO_{10}$, and $La_2\ Ti_2\ NbO_{10}$ sheets. The RP-phase with separating motif layer produces the compounds such as $SrLaTi_2\ TaO_{10}$ and $Ca_2\ Ta_2\ TiO_{10}$. The polarized phases of these perovskites could thus be put to use in preparing a number of dielectric and ferroelectric materials. Likewise, superconducting oxides were formed involving planar cuprates and CoO_2. These quasi-2D-TMOs were stabilized using La, Ba, and Sr-ion dopings as discussed already [12,13].

Robust physicochemical properties of the planar sheets of MnO_2, MoS_2, and Co_3O_4 were easily modified and used in preparing nanoplatforms of biomedicines. The redox behavior of MnO_2-NSs with three atomic layers, where each Mn is coordinated to six O-atoms, form edge-sharing MnO_6 octahedra and Mn-vacancies make them negatively charged. Moreover, the d−d transitions of Mn-ions exhibit a broad absorption spectrum (200−600 nm) with large extinction coefficient @380 nm. The associated properties of these NMs are found structure sensitive as discussed in the cited literature [14].

The MnO_2-NSs were found decomposing organic pollutants, dyes, and heavy metal ions with environment-friendly behavior due to their octahedral crystal structure. The broad-spectrum optical absorption of MnO_2-NSs overlapping with fluorescence excitation and/or emission spectra of the organic dyes, QDs, fluorescent-NPs, and metal-NCs, helped in quenching of fluorescence resulting in Förster resonance energy transfer (FRET) type of interactions between MnO_2-NSs and the organic dyes/fluorescent NMs. A new class of biosensing platform was, subsequently, developed for probing DNA-hybridizations and aptamer-target interactions leading to the adsorption of the single-stranded DNAs on the MnO_2-platelets due to van der Waals (vdW) interactions between the nucleobases and the basal plane that produced negatively charged double-stranded DNAs (dsDNAs). The presence of Mn^{4+}

imparted strong oxidizability and catalytic activity causing faster decompositions. Most of these features associated with various forms of the MnO_2-NMs were already discussed in Ref. [15].

MnO generated from MnO_2 was used for detecting the reducing biological species besides using Mn^{2+} as MRI contrast agent for bioimaging along with higher drug-loading capability. The MnO_2-NSs could penetrate across the cell membranes resulting in cancer drug delivery. Of late, MnO_2-NSs, have also been used in biosensing, drug delivery, bioimaging, and cancer therapy using them in varying topologies as reported [12,15].

7.2 Syntheses

Principles of "top-down" and "bottom-up" methods syntheses of the 2D-mateials in general are outlined in Fig. 7.1A and B with brief descriptions. The specific techniques for preparing MO-NSs are highlighted in the following text.

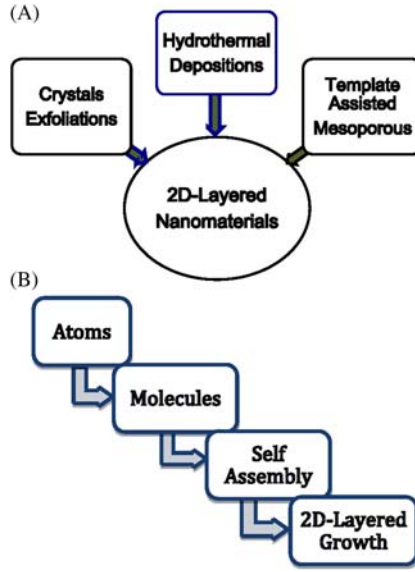

Figure 7.1 Basic schemes of 2D-materials syntheses for several applications including biomedicine. Part (A) describes the "top-down" approach of preparing the 2D-nanomaterials of inorganic, organic, polymeric, and biomolecular origin involving surface modifications of the basic building blocks before conjugating them with appropriate chemical moieties for preparing nanocomposites with designed physico-chemico-biological properties. Part (B) describes the "bottom-up" route, where the basic material building blocks are prepared using atomic and molecular species that are subjected to the process of self-assembly of monolayers, which are further deployed in synthesizing heterostructures and superlattices for numerous useful design of supramolecular hierarchical structures with intelligent properties.

Commercially viable syntheses of 2D-NSs should, in principle, not only be cost-effective but also green in nature. For reaching this stage, it will be necessary to examine various routes already explored in this context in the recent past and the understandings gathered therefrom. Some of the salient features of these developments are discussed later.

Hydrothermal depositions of 2D-MOs using soft/hard-template-scaffolds were carried out successfully. In soft-templated techniques the surfactants of flexible organic molecules, bioprotein, and block-copolymers were used for preparing micellar-morphologies. Using the electrostatic attraction, hydrogen bonding, and vdW forces among the surfactant molecules and NMs, the conversion of the precursors into nanostructures could be realized. In one-step synthesis, sodium dodecyl sulfate (SDS) templates could produce MnO_2-NSs involving redox reaction between $KMnO_4$ and SDS through hydrolysis. Water-dispersed MnO_2-NSs were prepared using cetyltrimethylammonium bromide, 2-(*N*-morpholino) ethanesulfonic acid (MES), and $KMnO_4$ as cationic surfactant, reducing agent, and precursor, respectively, leading to self-assembly of a stable oil/water emulsion enabling faster reactions between $KMnO_4$ and MES at the interfaces. Protein-directed-syntheses are now emerging fast as low cost, simple, and environment-friendly green processes, involving biotemplates to produce NSs, NPs, and NCs. Using the capsid proteins, MnO_2-NSs were prepared, for the first time, via the oxidation of Mn^{2+} in alkaline solution showing peroxidase-like activity and antioxidant behaviors. Likewise, MnO_2-NSs were also formed on hard-templates including graphene oxide (GO), montmorillonite, SiO_2-NPs, Fe_3O_4-NPs using $KMnO_4$ precursor. MnO_2 and graphene nanocomposites were prepared by adding $MnSO_4$ into GO-suspension resulting in Mn^{2+} attached to graphene. During hydrothermal reaction at 140°C, GO was not only reduced forming MnO_2-NSs but also attached radicals like ketones, quinines, carboxylic, hydroxyl, and others, forming negatively charged NSs. Requirement of high temperature, and pressure over a long duration was generally considered as a disadvantage of the hard-template methods asking for replacement with low-cost and simpler techniques. Having done all these, still it is difficult to control the size, shape, and uniformity of the final products besides the presence of residual surfactants, organic substances, macromolecules besides cost of the biotemplates. With these limitations of the soft-template processes, further investigations are still needed. Moreover, several template-less techniques were also reported to synthesize MnO_2-NSs using $MnCl_2 \cdot 4H_2O$ and H_2O_2 as precursor and oxidizing agents, respectively, to produce MnO_2-NSs within a day. In the presence of H_2O_2 and tetramethylammonium cations (TMA), Mn^{2+} ions were oxidized to MnO_2 in an aqueous solution at room temperature, in which, the cations inhibited the flocculations producing good dispersion.

Room-temperature metal−insulator transitions were observed in a double-exchange process of MnO_2-NSs involving double-exchange of Mn (III)-O-Mn (IV) structures followed by a low-oxygen-pressure thermal anneal of the pristine MnO_2-NSs. Subsequently, a 30 minute process of one-step redox reaction involving aqueous $KMnO_4$ + MES buffer at pH 6 could produce MnO_2-NSs at room temperature.

In situ synthesis of MnO_2-CQDs-nanocomposites was reported using $KMnO_4$ and MES along with the fluorescence reporter-CQDs for fluorescence quenching-based detections. A template-free direct synthesis of MnO_2-NSs was accordingly performed on the surface of the core−shell NaYF:Yb/Tm@NaYF-NPs.

Recently, a composite of graphitic-phase C_3N_4(g-C_3N_4) and MnO_2-NSs was reported using one-step facile production of MnO_2-NPs with a broad absorption band (250−500 nm wavelenghts), which matched well with the optical characteristic of MnO_2-NSs. The absorption spectrum of MnO_2-NPs, overlapping well with the fluorescence-emission of g-C_3N_4-NSs, could thus be used in FRET system. The fluorescence was restored after adding GSH due to reduction reactions. This could be put to use in cancer cell detection by monitoring the fluorescence signal change of UCNPs as a function of GSH in aqueous solutions with a minimum detection limit of ∼0.9 mM. This principle of fluorescence-based detections involving carbon dot-MnO_2-NSs, quantum dot-MnO_2-NSs, organic dye-MnO_2-NSs, metal-NCs-MnO_2-NSs, and polymer fluorescence-NPs were developed, accordingly, for the detection of GSH and other substances subsequently as reported elsewhere. One-step based rapid and selective FRET sensing of GSH was reported using C-dots-MnO_2 nanocomposite. For example, a novel FRET platform was reported using C-dots and MnO_2-NSs as the energy donor−acceptor pairs for GSH sensing in human whole blood samples and intracellular fluids, respectively. For the further study of GSH in living cells a fluorescence "turn-on" nanosensor using graphene quantum dots-MnO_2-NSs composite was reported for selective GSH detection in the living cells (minimum detection limit of ∼150 nM). Cost-effective, fast, and user-friendly biosensors for GSH detection using QDs-MnO_2 nanocomposites have currently been in more demand with user friendly, fast, and accurate point-of-care testing capabilities involving lateral flow test-strip assay that is convenient to use as reported. MnO_2-NSs-CuNCs−based nanoprobes were reported involving easier decomposition of MnO_2-NSs by being easily H_2O_2.

The oxides of Zn, Ti, Fe, Mn, Mo, and W were found better for biosensors, drug delivery, and bioimaging with enhanced contrast, photo/electro-luminescence, and surface functionalizations. A variety of polymeric composites with higher stability in liquid media, and directional charge-transfer properties along the planes were discussed in detail in several publications [16−18].

7.3 Cytotoxicity

Compared to most of the TMOs with lower toxicity, the oxides of V and Mo were found slightly genotoxic. Even with the limited data available till date on 2D-TMOs regarding their overall biological impacts, the preliminary toxicity studies of these materials were particularly found influenced by the exposed crystal facets at their edges, defect density, and chemical compositions, with trends similar to those of 2D-transition metal dichalcogenides (TMDCs). There are reports available on in vitro cell viability assays for determining their toxicity, including MoO_3 and

MnO_2, which clarified that MoO_3-NSs could induce toxicity in breast cancer cell-line MCF-7 and activate the caspase pathway, but not in the HaCAT cells. 2D-MoO_3 platelets were also found toxic to bacteria after noting a significant decrease of cell viability reported in the breast cancer cell-line MCF-7. An in vivo toxicity test of 2D-TiO_2 in a mice model exhibited low toxicity following intraperitoneal injection causing particle accumulation in the liver, which led to minor abnormalities after prolonged exposure as discussed separately [19].

7.4 Applications

A variety of applications of 2D-NMs are getting added to the list of their uses with continuous improvement in syntheses of better materials along with the improved understanding of the atomic-level changes explored through more advanced theoretical modeling and characterization. Their electronic transport properties were especially found influenced by the changes taking place during their conjugation with a large variety of lower dimensional chemical species, which are foreseen to open newer ways of using them. Some of the recent advances made in this context are summarized later.

7.4.1 Bioimaging and theranostics

Nanoparticulate iron oxides were widely used as a negative or positive magnetic resonance imaging (MRI) contrast agents, depending on their lateral dimensions that showed improved performances in the case of the sizes >10 nm. However, other 2D-paramagnetic-TMOs, such as MnO_2-NSs, demonstrated lower efficiencies in MRI, as the Mn-ions in MnO_2 lattice were shielded from water and hence did not contribute to the spin−lattice or spin−spin relaxation of the protons. Instead, paramagnetic Mn^{2+} ions in MnO-NSs were found as stronger MRI contrast agents allowing an efficient interaction with water molecules. MnO_2-NSs undergoing dissolutions due to reduction could produce Mn^{2+} in the presence of intracellular glutathione after endocytosis triggering the activation of the T1-MRI. Because of the d−d transitions of Mn-ions in the MnO_6 octahedral configuration, MnO_2-NSs exhibited intense light absorption resulting in luminescence quenching in the compounds. The reduction of MnO_2-NSs into Mn^{2+}-ions in the presence of glutathione led to the reemergence of the luminescence and hence could be used in fluorescent imaging of the cancer cells.

It was also reported that the weight ratios between the drug and the carrier for PEGylated 2D-MnO_2 was $\sim$90%, which is comparable to those of the other 2D-materials such as 2D-TMD and graphene. MnO-NSs could thus be used for concurrent ultrasensitive pH-responsive MRI and drug release/delivery. The fast break-up of MnO_2-NSs in a mildly acidic environment enabled such theranostic applications. Several-layered MnO_2-NSs were found rapidly dissociating in the low-pH environment of the cancer cells ensuring that the drug-induced apoptosis of the target

cancer cells after the NSs were endocytosed. MnO_2-NSs were also used as protective materials for complexation with a DNAzyme (a therapeutic gene-silencing agent) against enzymatic protein digestions, resulting in the smooth delivery of the therapeutic agent to the target cells.

The 2D-substoichiometric-MoO_x is another material with remarkable drug-loading capability of 230% for SN38 and 80% for Ce_6 due to the presence of large adsorption sites. The 2D-MoO_x possessing a strong plasmonic absorption peak in the near infrared (NIR), based on its substoichiometry and free charge carrier concentrations, could efficiently be used in photothermal therapy when PEGylated. A rapid heating of the target cancer cells (e.g., up to 55°C) was observed in just 10 minutes upon irradiation with 808-nm laser. The pH-dependent decomposition of 2D-MoO_x also facilitated their excretion out of the body after injection. Similarly, 2D-substoichiometric-WO_x demonstrated excellent photothermal efficiency, with which the temperature of the target cells could be raised to 44°C via 980 nm laser irradiation.

Because of the low absorbance of most of the 2D-TMOs in the NIR, the investigation of photothermal therapy has still not been advanced much. Through the induction of doping and oxygen vacancies in 2D TMOs, their free charge carrier concentration were increased to higher values ($10^{20}-10^{21}/cm^3$), leading to the generation of plasmonic absorption peaks in the NIR region and that could possibly be put to use in efficient PTT as described elsewhere [19–21].

MnO_2-NSs have widely been used as the fluorescence quencher. The controlled degradation of MnO_2 inside the tumor with low-pH and high-GSH concentrations leading to MnO_2 induced fluorescence quenching could be restored once MnO_2 was reduced to Mn^{2+} offering controlled imaging capability. Recently, several MnO_2 nanostructure–based bioimaging platforms were reported for intracellular or in vivo imaging. For instance, urchin-shaped MnO_2-NMs were found pH-responsive contrast agents for in vivo MRI imaging in mice tumors. The degradation of MnO_2-NSs was explored under the conditions of low pH in tumor cells and observed that the Mn^{2+} ions so produced had MRI properties. When DOX-PEG-MnO_2 composite species were taken inside the cells through endocytosis, low pH-responsive MnO_2 could decompose into Mn^{2+}, which acted as a highly efficient T1-MRI CAs for the in vivo nude mice tumor imaging. Meanwhile, the conjugated DOX was released in the tumor tissues that induced apoptosis offering successful cancer theranostics in intelligent form. In order to improve the quality of single MIR imaging, a novel dual fluorescence/MRI platform was also developed for imaging cancer cells using MnO_2-Cy5-labeled aptamer-based nanoprobes, which could target, recognize, and enter tumor cells, wherein, the overexpressed GSH could dissociate MnO_2 and release Cy5-labeled aptamers as well as $Mn_2{}^+$. These Cy5-labeled aptamers could, thus, be used for fluorescence imaging along with $Mn_2{}^+$ contrast agent for MRI in a dual fluorescence/MRI platform for cancer cell imaging. The feasibility of an NS–sgc8 nanoprobe for cellular MRI was also evaluated by examining CCRF-CEM cells (e.g., human T-cell acute lymphoblastic leukemia cell-line cells) and Ramos cells incubated with nanoprobes at different concentrations. These observations made in connection with various imaging

modalities and image-enhancing methods based on MnO_2-NSs were developed to provide help in cancer detection in its early stages and their applications in cancer management subsequently as discussed in the recent publications [22].

7.4.2 Biosensing

"Optical Biosensing Platforms" required for detecting a variety of biomolecular species are currently being investigated using MO-NSs with significant light absorptions that quench the luminescence of the fluorophores when conjugated mainly via FRET. However, upon optical irradiation of the analyte, the phenomenon of luminescence is restored either due to structural changes or reduction in binding affinity between the target luminescent material and 2D-TMOs. Luminescent materials including organic fluorophores, C-based materials, and upconversion NPs employed along with the different biomolecular species, including H_2O_2, glucose, ascorbic acid, ochratoxin A, ascorbic acid, cathepsin D, DNA, adenosine, glutathione, microRNA, thrombin, and aflatoxinB1 (AFB1), have been examined exhibiting the minimum detection limit over a wide range of concentrations (pM to M). The electrochemical intercalations of the ionized species with the oxides of W, Mo, and Nb could increase the electron concentrations via band-structure changes. Consequently, the resultant plasmonic properties were put to use in detecting the associated species, as reported by several groups. Consequently, the properties of MO-NSs in the planar form were used in biomedical applications involving sensing, molecular adsorption, biological imaging, drug delivery, and cancer therapy, especially, in the light of their lower cytotoxicity and higher biocompatibility in the case of the lamellar MnO_2-NSs. Highly oxidizing MnO_2-NSs, possessing strong catalytic activity, have also been used in realizing three broad categories of nanobiosensors involving the phenomenon of fluorescence, in addition to their significant electrochemical, and colorimetric interactions examined very recently and discussed in detail in the referred publications [15,23−27].

7.4.3 Therapeutic applications

Sufficient indications are already there for deploying nanostructured materials and their conjugates with biomedically active species providing better alternate therapies against diseases that are otherwise turning resistant to the antibiotic treatments. How does it happen in these formulations that are prepared from the combinations of lower dimensional materials of organic, inorganic, and biomolecular species would certainly require further investigations to understand the basic mechanisms involved before using those. Some of the developments reported in this context are summarized for highlighting the current status.

7.4.3.1 Cancer therapy

MnO_2-NSs decompose due to overexpressed GSH in cancer cells as effective therapy involving a core−shell-based magnetic upconversion (MSU) composite probe.

Amino modified Fe_3O_4@SiO_2-NPs and carboxyl functionalized NaYF4:Yb, Er-NPs, and MnO_2-NSs layer deposition onto MSU provided drug loading and release. Targeted delivery of Fe_3O_4 to tumor cells was achieved at the lesion sites followed by fluorescence recovery and upconversion-based luminescence. These MnO_2-NSs carriers could detect intracellular glutathione and trigger DOX release. Subsequently, some more molecular target species involving folic acid (FA) and hyaluronic acid (HA) were also examined for tumor targeting by incorporating them in extracellular matrix (ECM), cell surface, and intracellular matrix of various body tissues besides their specific receptor bindings that were highly expressed on the tumor cell surface [28].

A multifunctional theranostic system was reported for tumor targeting and MRI using FA as targeting agent and MnO_2-NSs as drug carrier and potential MRI agent. The MnO_2-PEG-FA/DOX-NSs were found efficient in delivering DOX to tumors in vitro and in vivo because of the folate receptors. Quick MnO_2 dissociation into Mn^{2+} enabled MRI with a high-GSH concentration. Biodegradable NS−based platforms were used in tumor-targeted theranostics involving the active targeting and efficient MRI capability causing pH-responsive multiple reductions. Similarly, BSA-MnO_2-DOX NMs (BMDN) were fabricated for cancer MRI and reversing multidrug resistance in the tumors. BMDN delivered drug into the MDR tumors with enhanced cellular uptake, reduced drug efflux, and decreased hypoxic tumor environment besides acting as an effective in vitro/vivo MRI agent. Consequently, different research groups could develop targeted delivery platforms of HA-modified mannan-conjugated MnO_2-NPs (Man-HA-MnO_2-NPs) for alleviating the tumor hypoxia with better chemotherapy responses by reacting with H_2O_2. The tumor treatment with Man-HA-MnO_2-NPs and DOX could increase the diffusion coefficient of breast tumors, inhibiting tumor growth and proliferations along with better MRI contrast. Coordination-polymer-shelled-MnO_2 composites in the form of multistage redox/pH/H_2O_2-responsive nanoplatform were used in cancer treatment by broadening their applications in MRI and cancer treatment. A series of drug delivery platforms based on MnO_2 composites were also reported for GSH bioimaging in CEM cells and tissues using two-photon mesoporous silica (TP-MSNs) coated with MnO_2-NSs fluorescence. DOX-loaded MSNs with photo-sensitizer Chlorin e6 (Ce6) were used in which aptamer of cancer cell (Sgc8) was adsorbed on the surface of MnO_2-NSs and acted as gatekeeper for TP-MSNs and quencher for TP-fluorescence and MRI contrast agent. This scheme was used in intracellular GSH-imaging, as well as targeting the CEM cells for releasing DOX and Ce6 in the cancer cells, besides synergizing chemotherapy and PDT. Knowing the relation between GSH concentration and SOR generation, a multifunctional chlorin e6 (Ce6)-MnO_2 based system could inhibit extracellular SOR by Ce6 with fewer side effects and enhanced cellular uptake of the photosensitizers for efficient PDT. The MnO_2-NSs could deliver Ce6 into cells in PDT showing higher promises in monitoring various types of cancers. Chemical conjugation of MnO_2-NSs with PEG-NH_2 could improve its water solubility/physiological stability and reactivity toward H_2O_2 within the tumor. Multifunctional Ce6@MnO_2-PEG could provide enhanced tumor-specific PDT and MRI in solid tumors as reported in the recent publications [11,20,29−36].

While examining ZnO and Fe_3O_4-NPs, it was observed that the size, dispersion, and light affected antibacterial properties of ZnO-NPs were found useful in wound dressings and coatings for various medical devices preventing biofilm formations. Magnetic Fe_3O_4-NPs was found appropriate for MRI contrast agents, hyperthermia tumor therapy, bioseparations, and targeted drug delivery. In addition, coated Fe_3O_4-NPs loaded with drugs have been finding their uses in antibacterial and antifungal applications as reviewed recently [37].

Engineered organic/inorganic-NPs have been recognized for deep tissue noninvasive imaging using superparamagnetic NPs/QDs as image contrast agents. Fast responding aerosol-based pulmonary drug deliveries have been explored in this context. PTT for cancer treatment using Au-NPs responded well. MSPs and lipid-NPs were found to be alternate carriers explored currently for targeted gene/drug deliveries and aerosol-assisted thin films for sensor applications. Well-known syntheses routes and surface functionalization schemes have been found critical in imparting biocompatible features. However, several aspects like long-term stability, toxicological impacts, site-specific internalization, and metabolism of NP-based drug/drug vehicles still require better evaluations and deeper understanding. Techniques for controlling structure and composition of NP, for instance, have been found critical in drug delivery, imaging, and sensing applications in improving the human health. It might be easier to control the functionalities of such smart materials that are responsive to light, magnetic field, pH, or heat, in targeted deliveries, controlled release, medical implants, tissue scaffoldings, and wound dressings, to name a few. Raliya et al. were skeptical in treating human ailments despite the fast-growing applications of NPs with benefits by raising concerns about the unknown toxic issues related to deploying them as drug carriers that would also deliver the toxic species into the human body. For example, though the aerosol drug delivery has been found effective in taking the drugs to the blood stream in noninvasive manner, the same route might also take the toxic species as well to the brain via olfactory system after bypassing the blood−brain barrier. The potential inadvertent impacts on the human health must be evaluated more carefully and exhaustively before deploying NPs in biomedical applications as emphasized [38].

Protein absorptions of PEGylated NPs in the cultured cells were studied by linking polymer to the maximal grafting density achievable. Changes in effective hydrodynamic radii of the NPs upon adsorption of human serum albumin (HSA) and fibrinogen (FIB) were measured in situ using fluorescence correlation spectroscopy. An increase in thickness ($\sim$3 nm) was noted due to HSA monolayer adsorption at higher HSA concentration in bare NPs and 50% of this value was found in PEGylated NPs. The detailed characterization of PEGylated NPs involving fluorescence lifetime and quenching experiments suggested that the HSA molecules were buried within the PEG shell. In vitro uptakes of the NPs by 3T3 fibroblasts were reduced by $\sim$10% upon PEGylation with 10 kDa chains. Pelaz et al. noted in their studies that the PEGylation, though did not completely prevent protein adsorption, still showed the reduction of cellular uptakes with respect to the bare NPs [39].

PEGylation has been used in improving the efficiency of drug and gene deliveries to the target cells/tissues. With improved systemic circulation time and decreasing

immunogenicity, the influence of PEGylation on the administered formulations have been studied till date as it protects the surface from aggregation, opsonization, and phagocytosis in prolonging the systemic circulation time. Suk et al. examined the influence of PEG-coatings on NPs in overcoming various biological barriers required in the efficient drug and gene deliveries associated with other modes of administration, ranging from gastrointestinal to ocular ones as reported [40].

Despite assessing the cytotoxicity of the nanoparticulate material species, the associated environmental risk remained still difficult to estimate as uptake mechanisms are not known. In one of the studies of cellular uptakes, parameter examined included their material properties, experimental conditions, and the cell types. Important uptake mechanisms for eukaryotic cells were found involving macropinocytosis, receptor-mediated endocytosis, and phagocytosis in mammalian cells. It was demonstrated that the uptakes into nonphagocytic cells were strongly dependent on the size that was optimum around 50 nm. More surface charges could increase the particle uptakes in comparison to those of the neutral ones. Results regarding the influence of shapes have been rather ambiguous. Facing challenges in producing NPs by changing exclusively one property at a time especially calls for more exhaustive characterization before coming to conclusions as to which property affected the uptakes and up to what extent.

The capability of low-cost, biocompatible, and low-toxic ZnO-NPs to trigger excess ROS production, to release zinc ions, and to induce cell apoptosis has been considered for anticancer and antibacterial applications. ZnO-NPs are found effective in antidiabetic treatment as they do not affect the structural integrity of insulin. ZnO-NPs with excellent luminescent properties were found suited for bioimaging. Recent nanomedicines involving ZnO-NPs were found more effective by Sharma et al., and Martinez-Carmona et al., in destroying the cancer cells against those achieved in conventional therapies such as chemo, radio, and surgery, by offering potentials to eliminate the side effects with better biocompatibility, easy surface functionalization, better targeting, and drug delivery capabilities. Zn^{2+} being an essential nutrient for the adults, nanoparticulate-ZnO species are expected to be in vivo safe. ZnO-NPs–based biocompatible and biodegradable nanoplatforms were developed due to these advantages with reference to cancer treatments [41,42].

While tracing the pathways of anticancer agent's entry into the cancer cells by destroying electron transport chain and releasing ROS through the mitochondrial electron transport, Moghimipour et al. observed that the intracellular ROS generation caused mitochondrial damage resulting in the loss of protein activity balance led to the cell apoptosis ultimately. ZnO-NPs were noted offering cytotoxicity to cancer cells mainly by themselves based on a higher intracellular release of dissolved zinc ions, followed by increased ROS induction and induced cell death via the apoptosis signaling pathway [43].

During the cytotoxic study of ZnO-NPs on liver cancer cells (HepG2), Moghaddam et al. noted higher cytotoxicity and genotoxicity, which were associated with cell apoptosis mediated by the ROS-triggered mitochondrial pathways. The loss of the mitochondrial membrane potential could open pores to release of

apoptotic proteins including cytochrome into the cytosol and caspase activation. Besides, p38 and JNK were also activated inducing and attracting p53 ser15 phosphorylation independent of JNK and p38 pathways. These results provided better insights into the mechanism of ZnO-NPs-induced apoptosis in human liver HepG2 cells. These ZnO-NPs were synthesized using a new strain of yeast (Pichia kudriavzevii GY1) for evaluating their anticancer activity in breast cancer MCF-7 cells. ZnO-NPs were noted to show powerful cytotoxicity against MCF-7 cells that led to apoptosis. The ZnO-NPs-induced apoptosis was mainly through both extrinsic and intrinsic apoptotic pathways, and some antiapoptotic genes of Bcl-2, AKT1, and JERK/2 were downregulated involving proapoptotic genes of p21, p53, JNK, and upregulated Bax as reported [44].

The cytotoxicity of ZnO-NPs was studied in cocultured C2C12 myoblastoma cancer cells and 3T3-L1 adipocytes confirming their stronger influence on C2C12 myoblastoma cancer cells compared to those in 3T3-L1 cells while inhibiting C2C12 cell proliferations causing apoptosis via ROS-mediated mitochondrial apoptotic pathways [45]. Autophagy could be triggered by different kinds of stresses, including damaged organelles, ROS generation, anticancer agents, and protein aggregation. Excessive cellular damage could result into cell death by autophagy and cellular self-consumption resulting in cancer cell apoptosis. ZnO-NPs ($\sim$20 nm) as observed in concentration-dependent loss of ovarian cancer SKOV3 cell viability. Examination of LC3 showed a remarkable fluorescence after exposure of SKOV3 cells at higher concentration of ZnO-NPs. In addition, ZnO-NPs-treated SKOV3 cells exhibited an upregulation of LC3-I/II and p53 expression, which could induce further autophagic cell deaths [46].

While studying size-dependent inhibition of HT1080 cell proliferations by ZnO_2-NPs autophagy was confirmed being related to ROS generation as dye stained cells displayed orange and red fluorescence upon ZnO-NPs treatment, which indicated the autophagic cells having excessive DNA-damages. The regulatory mechanism of autophagy and relation between autophagy and ROS in ZnO-NPs-treated lung epithelial cells could clarify better about the accumulation of autophagosomes and impairment of autophagic flux in A549 cells. Impaired autophagic flux resulted in the accumulation of damaged mitochondria, which led to cell death due to excessive ROS. Compared to other nanospecies, the ZnO-NPs were found attractive due to their lower toxicity and biodegradable nature besides lower cost. Different types of drugs such as doxorubicin, paclitaxel, curcumin, and baicalin and DNA fragments were successfully loaded onto the ZnO-NPs to show better solubility, higher toxicity to cancer cells compared with individual agents, and effective delivery into cancer cells [47–50].

A number of research groups have, of late, recognized the target-specific deliveries of NP-composites offering more therapeutic-benefits besides site-specific localization, enhanced delivery of drug/multidrug conjugations, easy modification of release kinetics, and bypassing the multidrug-resistance mechanisms. For enhancing the selective targeting against cancer cells, several functionalization schemes were reported. Surface-modified ZnO-NPs, for instance, had improved stability promoting their specificity toward cancer cells. Efforts were made to functionalize ZnO-

NPs surfaces with different biomolecules, including different types of proteins, peptides, nucleic acids, FA, and hyaluronan. Such biocompatible coatings could enhance the cancer cell targeting with improved safety against normal cells [51,52].

The problems of solubility and bioavailability of curcumin was addressed to by deploying two-copolymer-encapsulated ZnO-NPs forming combinations of Cur/PMMA-PEG/ZnO-NPs and Cur/PMMA-AA/ZnO-NPs composites for releasing curcumin@pH5.8 with largest inhibition of human gastric cancer AGS cell viability and induced cell cycle arrest at the S phase. PEGylated-ZnO-NPs were tested positive against breast cancer cells by generating ROS and triggering p53-dependent apoptosis leading to cell death. Green synthesis of hyaluronan/ZnO composites for cancer treatment caused morphological changes inhibiting proliferations of pancreatic adenocarcinoma PANC-1, ovarian adenocarcinoma CaOV-3, colonic adenocarcinoma COLO205, and acute promyelocytic leukemia HL-60 cells. HA-ZnO-composite treatment for 72 hours did not cause toxicity to the normal human lung fibroblast (MRC-5) cells by increasing the toxicity of the ZnO-NPs to breast cancer MCF-7 and MDA-MB-231 cells at lower doses as reported elsewhere [52,53].

PEGylated-ZnO-NP-DOX-nanocomposites did enhance the intracellular DOX-accumulation by offering a concentration-dependent inhibition of cervical cancer HeLa proliferations. ZnO-NR-DOX-complex when tested against the cultured SMMC-7721 hepatocarcinoma cells acted as DOX delivery system with enhanced cellular uptakes. DOX-ZnO-nanocomplexes along with UV irradiation caused more cell deaths through photocatalytic effects by synergistically triggering the caspase-led apoptosis. A new ZnO-hollow-nanocarrier engineered with biocompatible substrates by surface conjugation with FA and loaded with paclitaxel (PAC) nanocomplex showed preferential bioaccumulation, and cancer cell uptakes in the folate receptors overexpressed breast cancer MDA-MB-231 cells. FA-mediated endocytosis combined with the releases within the endolysosomes led the FCP-ZnO complexes to exhibit higher cytotoxicity to in vitro MDA-MB-231 cells as well as reduced MDA-MB-231 xenograft tumors in nude mice [54].

Antibacterial properties of ZnO-NPs turned out to be superior in blocking the growth of a wide range of pathogenic agents. The antibacterial mechanism involved was primarily to ROS generation in the form of superoxide anions, hydroxyl radicals, and hydrogen peroxide. The accumulation of ZnO-NPs in the outer membrane of bacterial cells could trigger release of Zn^{2+} causing the disintegration of bacterial cell membranes via membrane-protein damage, and genomic instability leading to cell deaths [54]. Presently, Gram-negative/positive bacteria such as *Escherichia coli* and *Staphylococcus aureus* have been used in evaluating the antibacterial properties of ZnO-NPs along with many others, including *Pseudomonas aeruginosa*, *Proteus vulgaris*, *Vibrio cholerae*, *Bacillus subtilis*, and *Enterococcus faecalis*. The antibacterial effect of ZnO-NPs against different species are already reported in the cited references by many [55–59]. ZnO-NPs caused cell deaths in *E. coli* by triggering the destruction of the phospholipid bilayer membrane. Jiang et al. concluded in their studies that ROS production was necessary for their antibacterial properties after noting the influences of the additional scavenger-radicals such as mannitol, vitamin E, and glutathione in blocking the antibacterial effects of ZnO-NPs. For

instance, 13 nm ZnO-NPs could completely suppress *E. coli* growth at a concentration of 3.4 mM although started inhibiting *S. aureus* growth at much lower concentrations (≥1 mM). The smaller ZnO-NPs were found more effective in contrast to the larger ones. From ICP-AES measurement the amount of Zn^{2+} released from smaller size ZnO-NP was much higher than those due to larger ones while *E. coli* were more sensitive to Zn^{2+} than *S. aureus*. Zn^{2+} ions released from ZnO-NPs were crucial for their antibacterial behavior [54]. Subsequently, Ishwarya et al. could improve ZnO-NP after coating with Phβ-GBP from the extract of β-1,3-glucan molecules and binding protein (Phβ-GBP) from the hemolymph of Paratelphusa hydrodromus, that could inhibit the growth of *S. aureus* and *P. vulgaris* by altering the cell membrane permeability and triggering ROS formation and was thus considered as one of the significantly potent antibacterial NMs [60].

7.4.3.2 Other therapies

Cholera, an epidemic disease caused by the intestinal infection of Gram-negative bacterium *V. cholerae*, has been found affecting the populations in the developing countries. Aiming at the development of nanomedicine against cholera, a detailed study was carried out using ZnO-NPs against *V. cholerae* (two biotypes of cholera bacteria: classical and El Tor). ZnO-NPs were found more effective in hindering the growth of El Tor biotype of *V. cholerae*, which was associated with ROS production that resulted in increased bacterial membrane damage, causing higher permeations, and substantial morphological modifications. The antibacterial activity of the ZnO-NPs was detected in cholera toxin (CT) mouse models by inducing the gradual CT secondary structure collapses while interacting with CT by interrupting CT binding with the GM1 ganglioside receptor [61,62].

Although ZnO-NPs are promising antibacterial agents due to their wider activities against both the Gram-positive and -negative bacteria, the exact antibacterial mechanism of ZnO-NPs has not yet been understood properly. Therefore studying it deeply has a lot of important theoretical and realistic values. In the future, it is believed that ZnO-NPs could be explored as antibacterial agents in the form of ointments, lotions, and mouthwashes. In addition, it could be coated on various substrates to prevent bacteria from adhering, spreading, and breeding in medical devices.

Zn is a well-known element playing an active role in the secretion of insulin from pancreatic cells that are important in the case of metabolic disease as diabetes mellitus resulting in the body's incapacity to produce insulin or by the ineffective use of the insulin produced. The trace element Zn abundantly found in all human tissues and fluids also participates in insulin synthesis, storage, and secretion. Therefore for making specific uses of antibacterial properties via targeted delivery of ZnO-NPs has been explored in detail for their applications in treating diabetes as discussed by several groups [63,64]. In another study a natural extract of red sandalwood (RSW) was noted as an effective antidiabetic agent in conjugation with ZnO-NPs assessed with the help of α-amylase and α-glucosidase inhibition assays with murine pancreatic and small intestinal extracts. Results showed that ZnO-RSW

conjugates possessed moderately higher percentage of inhibition (20%) against porcine pancreatic α-amylase and were more effective against the crude murine pancreatic glucosidase than any of the two elements (RSW and ZnO-NPs). The conjugated ZnO-RSW displayed 61.93% inhibition in glucosidase, while the bare ZnO-NPs and RSW showed only 21.48% and 5.90%, respectively [64].

Subsequent detailed studies compared the antidiabetic activity and oxidative stress of ZnO-NPs and $ZnSO_4$ in diabetic rats by noting that the smaller size ZnO-NPs at higher doses (3 and 10 mg/kg) exhibited a much stronger antidiabetic effect compared to $ZnSO_4$. It exhibited an outstanding reduction of blood glucose and increasing insulin levels as well as improving serum zinc status in a time and dose-dependent manner. However, severely elicited oxidative stresses particularly at higher doses were also observed by the altered erythrocyte antioxidant enzyme activities, increased in malondialdehyde (MDA) production, and marked the reduction of serum total antioxidant capacity [63].

The direct enhancement of an inflammatory state in hyperglycemic conditions by regulating C-reactive protein (CRP) and cytokines like interleukins were found involved in developing the cardiovascular diseases. ZnO-NPs were prepared using hydroxyl ethyl cellulose as a stabilizing agent to alleviate the abovementioned diabetic complications after noting significant decreases in MDA and fast blood sugar, and asymmetric dimethylarginine (ADMA) levels. The inflammatory markers, interleukin-1 (IL-1α) and CRP, were also notably reduced after ZnO-NPs treatment, concomitant with an increase in nitric oxide (NO) and serum antioxidant enzyme (PON-1) levels in diabetic rats [42].

The antiinflammatory effects of ZnO-NPs were found very attractive in treating inflammations due to the complex biological response of the body tissues to harmful stimuli, such as, pathogens, damaged cells, or irritants. Atopic dermatitis (AD), for instance, is a chronic inflammatory skin disease characterized by the impairment of the skin-barrier functions, which was involved with complex interaction between genetic and environmental factors. ZnO-functionalized textile fibers were used for controlling the oxidative stress in AD in vitro and in vivo since textiles have the longest and most intense contact with the human skin. When AD patients wore the ZnO-coated textiles overnight for 3 consecutive days in a study, an obvious improvement was noted in AD pruritus and subjective sleep quality. This could possibly be due to the high antioxidative and strong antibacterial capacity of the ZnO-textile, which needs further study.

The size-dependent penetrations of ZnO-NPs were examined in injured and allergic skin in the mouse AD model, which clearly proved that only nanosized ZnO was able to reach into the deep layers of the allergic skin, but bulk-sized ZnO stayed in the upper layers of both damaged and allergic skin. Compared with bulk ZnO, nano-ZnO exerted higher antiinflammatory properties by decreasing drastically on proinflammatory cytokines in the mouse model. These results demonstrated that ZnO-NPs with a small size had great effects on reducing skin inflammations in animal models [65]. The antiinflammatory activity of ZnO-NPs was also found very effective against other inflammatory diseases. Given the antiinflammatory activity of ZnO-NPs already, a straightforward, inexpensive, and

ecofriendly synthesis using the root extract of *Paeonia tenuifolia* was employed in investigating the antiinflammatory activities in LPS-stimulated RAW 264.7 macrophages. ZnO-NPs were found possessing remarkable antiinflammatory activity via dose-dependent suppressions of NO production as well as the related protein expressions of iNOS, COX-2, IL-1β, IL-6, and TNF-α. The ZnO-NPs, prepared under photocondition using the aqueous extracts of two mangrove plants, *Heritiera fomes* and *Sonneratia apetala*, showed higher antiinflammatory activity (79%) in comparison with Ag-NPs (69.1%). ZnO-NPs exhibited efficient blue and near-UV emissions, which have green or yellow luminescence related to oxygen vacancies, therefore further extending its application in bioimaging as discussed by several groups [32,33,66,67].

Highly stable aqueous ZnO@polymer core−shell NP-based composite ZnO@poly(MAA-*co*-PEGMEMA) was reported, for the first time, using a sol−gel method exhibiting high quantum yield and very stable broad photoluminescence in aqueous solutions. ZnO^{-} and ZnO^{2-} derived from LiOH and NaOH (i.e., with 3, and 4 nm average size, respectively) showed green and yellow fluorescence in human hepatoma cells. These NPs in <0.2 mg/mL concentration were found nontoxic to human hepatoma cells. However, their stable luminescence during cell culture and capability, to live up to 45 minutes of exposure, could offer them as safe and cheap luminescent labels in fluorescent probes for in vitro cell imaging. ZnO-NSs were synthesized for cultured cell imaging, in which, yellow-orange light emission was observed around or inside the cells under UV irradiation (365 nm) at room temperature in leukemia cells K562. ZnO-nanostructures could thus easily get attached onto or penetrated into the cells suggesting their utility in bioimaging.

Chemical precipitation−based synthesis of ZnO-NPs exhibited blue, green, yellow, and orange color emissions in which the emission colors were changed via adjusting the pH of the solution precipitation. To stabilize ZnO-NPs in water, these ZnO-NPs were stabilized with silica to form ZnO@silica core−shell nanostructures exhibiting excellent water stability, and retaining the visible emissions. These NPs were attached to the NIH/3T3 cells displaying different fluorescent colors.

Based on its intrinsic fluorescence properties, ZnO NMs were employed as a promising candidate for cell imaging and pathological studies. ZnO-NPs, for instance, exhibited promising biomedical properties based on its anticancer, antibacterial, antidiabetic, antiinflammatory, drug delivery, as well as bioimaging activities. Due to inherent toxicity of ZnO-NPs, they possess strong inhibition effects against cancerous cell and bacteria, by inducing intracellular ROS generation and activating apoptotic pathways that made them usable as anticancer and antibacterial agents. In addition, ZnO-NPs are also well known to promote the bioavailability of therapeutic drug or biomolecules, when used as drug carriers to achieve enhanced therapeutic efficiency. Moreover, with the ability to decrease blood glucose and increase insulin levels, ZnO-NPs have shown promising efficacies in treating diabetes and attenuating its complications that were evaluated further by several groups [54].

FDA, United States, has already approved ZnO-NPs as a safe substance in various applications. However, some critical issues of ZnO-NPs still remain there to be

further explored. This included the lack of examining various aspects such as the comparison of its biological advantages with those of the other M-NPs; the controversies attached to their toxicity toward the biological systems studied recently; evidence-based randomized research efforts exploring their therapeutic influences in improving anticancer, antibacterial, antiinflammatory, and antidiabetic activities; and the insight into corresponding animals studies related to its anticancer, antibacterial, antiinflammatory, and antidiabetic properties. Subsequent studies were, thus, focused on the abovementioned issues to further elucidate and comprehend the potential uses of ZnO-NPs in biomedical diagnostic and therapeutic fields. These NMs are believed to accelerate the development of medicines involving ZnO-NPs that would be more exciting contributions as reported very recently [54].

Functionalized iron oxide NPs (IONPs) were found useful due to their wide range of uses in nanomedicines. However, their further applications were found hampered due to their fast agglomeration, and oxidation, for which, adequate surface modifications involving small organic molecules, polymers, and inorganic materials became imperative to take care of these problems with improved physicochemical properties.

Synthesis of smaller size superparamagnetic iron oxide and its nanocomposites was reported using a supersonic thermal-plasma process by examining the influence of oxygen flow rates, gas injection position, and carrier gas types, and the phase composition of the product material estimated by refined techniques. The smallest iron oxide NP samples (i.e., 10 nm average size) were synthesized at 19 SLPM flow of O_2 with the largest contribution from the magnetite/maghemite phases (i.e., @88%). The saturation magnetization and magnetic coercivity of these samples were $\sim$28 emu/g and $\sim$6 Oe, respectively, demonstrating satisfactory biocompatibility that made them suitable for advanced biomedical and environmental applications. A superparamagnetic nanocomposite of iron oxide, carbon-encapsulated iron NPs, along with SWCNTs was also prepared ($\sim$5 nm average size) having saturation magnetization $\sim$52 emu/g, coercivity $\sim$10 Oe and were more toxic possibly due to the presence of the SWCNTs. Higher reduction rates of production and single step processing are the inherent advantages of this technique for producing the nanocomposite materials in quantity [68].

The synthesis of MgO-NPs was reported using *Aspergillus niger* process in agar wells diffusion method for evaluating the antibacterial activity against Gram-positive *S. aureus*, and Gram-negative *P. aeruginosa* bacteria isolated from urinary tracts infection. These results confirmed the antibacterial activities of the biosynthesized MgO-NPs (i.e., 43−91 nm) against *S. aureus*, with a zone inhibition diameter of 27 mm. However, the zone inhibition diameter against *P. aeruginosa* bacteria was 24 mm, compared with inhibition effects of ciprofloxacin antibiotics at 24 and 20 mm, respectively [69]. The systematic investigations of the antibacterial mechanisms of MgO-NPs against the phytopathogen *Ralstonia solanacearum* were made, for the first time, due to catastrophic bacterial wilt that resulted in the worldwide reduction of tobacco production. MgO-NPs possessed statistically significant concentration-dependent antibacterial activity, and the minimum inhibitory concentration (MIC) and minimum bactericidal concentration were measured as 200 and

250 μg/mL, respectively. Additional studies confirmed that they inflicted cell membrane injuries along with decreased motility and biofilm formation ability of *R. solanacearum*, due to the direct attachment of MgO-NPs to the bacterial cell surfaces. SEM and TEM studies confirmed the abovementioned observation. ROS accumulation could also be a factor for their antibacterial behavior inducing DNA damage. The toxicity assessment assays carried out under greenhouse conditions demonstrated that the MgO-NPs exerted a large effect on tobacco bacterial wilt, reducing the bacterial wilt index as reported elsewhere [70].

In another recent study of assessing the antibacterial features of MgO-NPs, broth dilution method was adopted followed by colony count in agar medium, in which the antibacterial activity was found increasing with size reductions of the MgO-NPs in the case of *B. subtilis* ATCC 9372. Weaker and stronger size-dependent bactericidal efficacies were shown in two size ranges, namely, $\sim 45-70$ and <45 nm, respectively. Smaller MgO-NPs possessed efficient antibacterial activity toward *E. coli* and *S. aureus* as well. During further investigations, it was suspected that the MgO-NPs, when inside through the cell membranes, could facilitate restructuring using the individual MgO-NPs. The antibacterial activity of the MgO-NPs was found stronger toward Gram-positive compared to the Gram-negative bacteria. Further, the antibacterial activity was also found to be dosage-dependent after observing the enhanced activity against *E. coli* with the increasing concentrations. For instance, approximately seven order of magnitude reductions in *E. coli* O157:H7 was observed in an 8 mg/mL MgO-NP treatment after 24 hours. The concentration-dependent anti-*E. coli* O157:H7 activity of MgO-NPs (≥ 3 mg/mL) could significantly reduce the cell concentrations to undetectable limits after 24 hours at room temperature, indicating complete cell killing. The cell walls of Gram-positive and negative bacteria strains, comprising thin layers of lipid A, lipopolysaccharide, and peptidoglycan, and only peptidoglycan, respectively, could possibly be the cause of different efficacies, in which, *E. coli* showed a stronger resistance to MgO-NPs compared to *S. aureus*. The lower sensitivities of *E. coli* could be due to tightly packed lipopolysaccharide molecules providing an effective barrier. ZnO doping of MgO-NPs in solid solutions showed reductions in the antibacterial activity against *E. coli* and *S. aureus*, in which, the pH of lower concentration of physiological saline (e.g., 2.5 mg/mL) showed an alkaline region above 10.0 and decreased with the increase of ZnO amount in MgO-ZnO solution. The reason for the decrease in antibacterial activity might be assigned to the decreasing stability of O_2^- generated at the surface of the solid solution and decreasing of the medium pH. The antibacterial activity of MgO-GeO composite powder was studied showing good activity toward both Gram-negative as well as Gram-positive bacteria though more efficient against Gram-positive ones, and the nanocomposite powders were noted to be more effective against *S. aureus* than *E. coli* at lower concentrations. At higher concentrations (>5 mg/mL) the bacterial growth was almost completely inhibited ($>95\%$) in both the cases. The minimal inhibitory concentration (MIC) for *S. aureus* was found to be ~ 0.05 mg/mL, whereas that of *E. coli* was 0.25 mg/mL as summarized in an earlier publication [71].

With the possibility of finding synergetic influence a combination of Ag/MgO-NPs was examined showing broad-spectrum antibacterial activities against infectious pathogens. However, the use of such nanosynthesized biomedical materials has been a major concern due to their high cost, toxic nature, and production of non−−ecofriendly by-products and nonbiodegradable stabilizing agents causing health hazards. Consequently, green synthesis of a bilayered Ag-MgO-nanocomposite was attempted using aqueous peel extract of grapefruit red under an accelerated uniform heating for testing its antibacterial efficacy against *E. coli*. Parameters such as surface modifications and compositions were also explored using conventional methods along with estimating the efficacy of As-synthesized Ag-MgO-nanocomposite against *E. coli*. In this experiment, dispersed nanocomposite comprising cubical crystal lattice network comprising Ag-NPs (20−100 nm) embedded within MgO-NPs was noted to produce stronger antibacterial activity against *E. coli* as compared to MgO-NPs alone, indicating a synergy between Ag and MgO-ions. Although the exact antibacterial mechanism of MgO-NPs is not yet very clear, nevertheless, three main mechanisms were proposed, such as the formation of ROS, the interaction of NPs with bacteria, subsequently damaging the bacterial cells, and an alkaline effect as reported recently [72].

Out of several MO-NPs explored for their antibacterial properties, ZnO-NPs were found as "generally recognized as safe" compound according to US FDA (vide ref: US FDA: 21CFR182.8991) with minimal toxicity to humans and high photocatalytic activity besides being more biocompatible than TiO_2. ZnO-NPs with pronounced antimicrobial activity could be assigned to their high surface-to-volume ratios and surface abrasiveness in inhibiting the growth of both Gram-positive/negative bacteria, including *S. aureus*, *Streptococcus pyogenes*, and *E. faecalis* that experienced 95% growth inhibition in the presence of ZnO-NPs. These NPs showed activity against common food pathogens such as *Campylobacter jejuni*, *E. coli O157:H7*, *Shigella* spp., *Listeria monocytogenes*, and *S. aureus*, indicating their usefulness in the form of food preservatives besides in antibacterial creams, lotions, ointments, and deodorants. ZnO-NPs imparted self-cleaning features to glass and ceramics surfaces as well. The antimicrobial properties of ZnO-NPs were attributed to the intracellular accumulations causing damage to the cell walls and disrupting the DNA replications. While inside the cells, the NPs released metal ions generating ROS and accumulating in the bacterial membranes. Strong ROS generating potential of ZnO-NPs was found causing massive bacterial killings, including cell wall damages, increasing membrane permeabilities, internalizations due to the loss of proton motive forces and the uptake of toxic-dissolved zinc ions. Similarly, wide spectrum antimicrobial and antibiofilm activities were observed in TiO_2-NPs against a wide range of pathogenic microorganisms, including bacteria, fungi, parasites, and viruses. Subsequently, FDA approved the use of TiO_2 in human food, drugs, and cosmetics applications. The unique photocatalytic property of TiO_2-NPs and the quantum size effects made them as ideal antimicrobial agents, including other applications such as air, water purifications, and antimicrobial coatings on biomedical devices. Further modification of TiO_2-NPs with plant extracts like *Garcinia zeylanica* resulted in enhanced bactericidal activity in combination with

antimicrobial activity of the plant extracts and photocatalytic activity that could destroy the microorganisms under light illumination. ROS generated by TiO_2-NPs could oxidize the components of the cell membrane leading to their fast destructions. In the absence of light irradiation, direct contact and adsorption of the cells onto TiO_2-NPs could damage the membrane integrity. CaO and MgO-NPs also exhibited strong antibacterial activity, mediated by the generation of superoxide and also increasing pH due to hydration of CaO and MgO with water. Al_2O_3-NPs exhibited strong binding to the bacterial cell walls increasing their permeability. Some of these abovementioned features of the MO-NPs species were discussed in detail in recent publications included in Refs. [73,74].

The toxicity of chronic exposure of ZnO-NPs having lower than the minimum inhibitory concentration (MIC) was also studied by repeatedly treating the *E. coli* strain culture exhibiting higher toxicity than the single exposure of higher concentrations. The observed growth inhibition (57%) corresponding to the chronic exposure of 0.06 mg/mL of ZnO-NPs was found almost two times stronger than that from the single exposure of 0.30 mg/mL concentration. The toxicity of ZnO-NPs in *E. coli* was studied in the light of ROS formations measured as MDA equivalent by thiobarbituric acid-ROS (TBARS) assay, and the effect of Zn-dissolution from ZnO-NPs. Higher growth inhibitions of chronic exposures were correlated with higher ROS generations, which contributed toward membrane lipid peroxidation, confirmed from the observations of the cell wall deformations measured by SEM and EDAX analyses showing adherence on the cell walls [75].

7.5 Antibacterial behavior

Various kinds of NPs were found effective against the antibiotic resistances by combatting the microbes employing multiple mechanisms simultaneously in addition to being effective drug delivery carriers. These NPs, in general, are noted to damage the bacterial membranes and discourage biofilm formations due to their physicochemical properties. These sub-100 nm NPs were found exhibiting enhanced cell interactions due to larger surface-to-volume ratios. Owing to compact nature of the bacterial cell membranes, it is not easy to change them through only a few genetic mutations. The hindrances encountered during biofilm formations is another important issue, as biofilms facilitate the bacterial resistance by providing protection to the embedded microorganisms while facilitating their escape from the antibiotics. The bacterial biofilms provide effective breeding grounds for frequent resistant mutations via exchanges and alterations among different bacterial cells. The NPs of Au, Ag, Mg, NO, ZnO, CuO, Fe_3O_4, and YF have been found effective in preventing biofilm formations. In contrast to the traditional antibiotics, NPs have shown ability to combat microbes via simultaneously active multiple mechanisms that do not allow the microbes having the mutated genes, and accordingly it is more difficult to develop resistance to NPs as observed elsewhere [76–78].

NPs are also known as effective "medium/carrier" of antibiotics as observed in several cases currently reported in drug delivery applications, namely, liposomal NPs, solid lipid-NPs, polymer-based NPs, polymer micelles, inorganic nanodrug carriers (including magnetic NPs, mesoporous silica-NPs, carbon NMs, and quantum dots), terpenoid-based NPs, and dendrimer NPs. The main advantages of these NPs against the conventional delivery systems include their ultrasmall and controllable sizes that are suitable for conducting antimicrobial operations and combating intracellular bacteria [8,79–82].

A modified treatment strategy of infections using drug-loaded NPs as alternative was proposed to overcome the limitations posed by the drug-resistant intracellular pathogen strains owing to the antibiotics' poor membrane transport. The ultrasmall sizes of the NPs enable them to be phagocytosed by the host. Furthermore, the NPs are suitable drug carriers with the flexible entry to the host cells via endocytosis for most of the drugs to be released intracellularly. NP carriers could also help in increasing the serum levels of antibiotics and protect the drugs from resistance by target bacteria. Within the NP carriers, drugs are protected from detrimental chemical reactions; thus the potency of the drugs could be maintained easily. The protection from the resistance mechanisms of the target bacteria is an important mechanism. The common reasons for acquiring resistance to the traditional antibiotics is via increased efflux and decreased uptake of antibiotics in bacterial cells. However, many NPs are known to overcome these limitations by inhibiting the drug resistance. For example, in the gastrointestinal tract, dendrimers could inhibit *P*-glycoprotein-mediated efflux as reported [83].

NP carriers targeted to an infection site could deliver the drugs and thereby minimize the associated side effects. It is difficult to deliver high-dose drug absorption at the desired sites while preventing side effects (including drug toxicity) when using conventional antibiotics without a carrier. NP-based antibacterial drug delivery systems, being site specific, give rise to minimum side effects. The undesired adverse effects of antibiotics on the body are specifically minimized because of the higher drug doses delivered to the infection sites. The targeted delivery has been achieved through enhanced permeation and site-specific retention of the drug molecules that are loaded with the surface-modified NP carriers that carry the drug and release the same by selectively recognizing the characteristic ligand on the cells at the infection sites. Targeting could be of various kinds such as receptor targeting, magnetic targeting, and temperature targeting. Vancomycin, although, known as strong inhibitor of the Gram-positive bacteria, is otherwise highly toxic to ear and kidney. One way to improve vancomycin treatment could be to enhance the drug delivery to the desired locations for limiting the amount of drug reaching other organs, where it is not needed. With the help of NP carriers, vancomycin-modified mesoporous silica-NPs were designed for detecting and killing the Gram-positive bacteria selectively over macrophage-like cells. The strategy, therefore, frequently employed in affecting "target therapy" could be designed to first target macrophages with NPs because most active bacteria at infection sites could be targeted and swallowed by the macrophages. The drug in the NPs is then released in the macrophages, in which, the bacteria are present. It is also feasible to minimize the

severe side effects by repeated administrations of lower dosages in the drug delivery. With the appropriate NP carriers, possessing controllable drug release mechanisms, the blood concentration of the medicine at the infection site can be sustained at the required level for a longer duration, resulting in good stability, reduced frequency of medication, improved patient compliance, and reduced pain. Compared to the free drug at the same concentration, drug delivered via NP carriers has a more prominent inhibitory effect on cellular growth, along with prolonged drug release. Moreover, different types of controllable stimulatory factors are also possible to incorporate, including chemical agents, magnetic field, light, pH, and heat to activate the NPs for the required drug release. In ocular formulations using an appropriate NP-carrier could prolong the retention time in the precorneal area, the release of levofloxacin and other drugs was controllably sustained, producing a better recovery compared to those from the conventional ophthalmic solutions. Some of these details are described in the cited literature [84−88].

Multiple drugs/antimicrobials were combined together within the single or multiple species of the NPs that could conjugate with other constructs to improve the antibacterial properties. In the case of a single type of NP containing multiple antibacterial agents, it is difficult for the bacteria to develop resistance because the probability of a cell containing multiple resistance mutations is rather small. In addition, the simultaneous combination of different drugs possesses higher efficacy due to the joint action of multiple mechanisms. In addition, two or more types of NPs could also be used for enhanced antibacterial effects with the prevention of resistance. When used alone, different types of NPs might show disadvantages as noted in the case of liposomes having shorter shelf life, poor stability, low encapsulation efficacy, rapid removal by the reticuloendothelial system, cell interactions or adsorption, and intermembrane transfers. Thus using hybrid NPs could very well maximize the strengths while minimizing the weaknesses of the individual types of NPs. For example, superior efficacy of in vivo cellular deliveries was achieved by lipid−polymer hybrid-NPs compared to the delivery without polymeric-NPs or by liposomes alone. In addition, a prolonged effective time could be achieved through the “combinatorial” method, which could effectively and significantly reduce the possibility of developing resistant strains of bacteria as discussed by various groups [89].

The appearance of drug-resistant bacterial strains and the increasing rate of hospital infection outbreaks encouraged the researchers to reexamine the NPs afresh due to their novel antimicrobial resistance properties. The influences of NP’s features such as the average particle size, shape, specific surface area, and surface curvature on its antibacterial activities were consequently explored further in detail for killing the bacteria to reduce the bacterial infections significantly as highlighted in the following observations extracted from the recent publications in this context [47].

Considering multiple interactions with the bacterial membranes using theoretical as well as experimental methods was found essential for understanding the mechanisms involved in the observed antibacterial properties of 2D-NMs. MD simulations, for instance, were found useful in clarifying the issues related to the rupturing of

the lipid membrane by denting on their surfaces and extracting phospholipid molecules that ultimately reduced the membrane integrity due to the interactions of the lipid tails with S atoms and electrostatic interactions of lipid head groups with the Mo and S atoms in the lateral edges of the MoS_2-NS, resulting in the cytoplasm loss and bacterial death. MoS_2-NS created more severe dents compared to the direct insertion of graphene-based NMs, possibly due to thicker and stiffer structure of MoS_2 as concluded recently [90].

The metallic conductivity, hydrophilicity, and other unique physiochemical properties of the emerging 2D-MXene-NSs−based ceramics were found usable in biomedicines after meeting the requirements of their unique structural, physicochemical, and compositional properties spanning over different aspects such as mechanical, optical, chemical, and electronic considerations. Examining their design/synthesis strategies, therapeutic modalities, diagnostic imaging, biosensing, antimicrobial, and biosafety issues recently indicated that these engineered MXenes NSs would finally emerge as one of the most useful biocompatible inorganic nanoplatforms for multiple and extensive applications in the clinical translations of the nanomedicine. Facile surface functionalizations of the Mxene-NSs were found better due to their reduced toxicity, enhanced colloidal stability, and extended circulation during in vivo applications. Synthesizing state-of-the-art Mxene-NSs for biomedical applications, including structural and dose-dependent antimicrobial activity, photothermal therapy, drug delivery, and implants, were discussed recently along with their sensor applications, including photoacoustic, MRI, computed tomography, and optical imagings. The challenges and future opportunities of applying Mxene-NSs in biomedicine were also considered [91,92].

The cytocompatibility and physicochemical properties of the NSs of TMDCs and graphene-based materials were found helpful in facilitating their immobilization onto the bacterial surfaces, when in contact, particularly, with their basal planes in contrast to the sharp edges. A transparent substrate coated with GO/MoS_2-NSs was deployed in studying the antimicrobial properties against *E. coli*. These GO−MoS_2-NSs exhibited enhanced antimicrobial activities with increased glutathione oxidation capacity and partial conductivity. Measuring variations in refractive index of each voxel in bacterial cell using holotomographic microscopy could reconstruct the 3D-images of morphological disruptions in the individual cells having contacts with the GO−MoS_2 nanocomposite surfaces. This also provided the quantitative estimations of the reductions in both the volume (67.2%) and the dry mass (78.8%) of the cells in contact for 80 minutes resulting in the release of intracellular components mediated by membrane and oxidative stress [93].

The antimicrobial properties of MnO_2 and MoS_2 toward Gram-positive and negative bacteria were examined by treating *B. subtilis* and *E. coli* bacteria individually with 100 μg/mL of randomly oriented and vertically aligned NMs for ∼3 hours in the dark. These kinds of antibacterial NMs are finding applications in biomedicine and environmental remediations. Flow cytometry and fluorescence imaging were used in determining the bacterial viability in the presence of the vertically aligned 2D-MnO_2 and MoS_2 grown on 2D-GO-NSs, rGO-NSs, and Ti_3C_2 Mxene. In the presence of both MnO_2 and MoS_2-NSs, Gram-positive bacteria showed a higher

loss in membrane integrity due to detrimental effect on viability via compromising the cell wall leading to significant morphological changes. Vertically aligned 2D-MnO_2-NSs showed the highest antimicrobial activity, suggesting that their edges were likely compromising the cell walls upon contact [94].

7.5.1 Replacing antibiotics

The antimicrobial coatings of Ca, Si, P, and Ag-NP enriched TiO_2 films on fully implantable devices such as heart valves and dental implants were found compatible to prevent thrombosis by inhibiting the adhesion and growth of bacteria such as *Streptococcus mutans*, *Staphylococcus epidermidis*, and *E. coli* causing inflammations around the implants. In the case of partially implantable devices such as catheters, intravenous, and neurosurgical catheters, which are more prone to bacterial colonization causing enhanced infections in clinical applications, were suggested to deploy nanopolymers as antibacterial materials to retard the growth of catheter biofilms. NP-coatings on invasive neurosurgical catheters could reduce the bacterial infections and complications, with sustained release of NPs over 6 days that resulted in retarded growth of *S. aureus* [95].

A number of medical devices were developed using IONPs in theranostics applications, including contrast agents for MRI, magnetic particle imaging, and magneto-motive ultrasound, photoacoustic imaging, and magnetic particle hyperthermia. Fluorescent ZnO-NPs have been used in cancer cell imaging in which the surface functionalization could enhance their water solubility and biocompatibility along with reduced cellular toxicity. The ZnO-NPs functionalized with specific biomolecules were explored for photosensitive biosensors. The feature such as high surface-to-volume ratios of these NPs favored the adsorption of the plasma proteins as discussed by several authors [85,96,97].

By tuning surface roughness of the implanted devices for better responses of osteogenic cells and causing effective mechanical contacts between the tissues and the implant, it has been possible to use the recent nanotechnological developments in tissue and implant engineering. Titanium and its alloys were found quite suitable for bone replacements. For taking care of the failures in such applications owing to the presence of thin fibrous layers separating the metallic implant and the bone in osteointegration, surface modification became necessary to create a stronger bone-implant bonding. Changing the morphology along with the addition of bioactive compounds and rough surfaces gave promising results in biomedical applications as discussed in the cited references.

In connection with modifying the metallic implant surfaces to produce very intimate contacts between the implant and the live tissues in bone substitutions, processes such as interaction with water and protein adsorption, and cell attachments that started operating just after the tissues came in contact with the implants, in which, the functionalized surfaces facilitated better cell attachments. These processes are governed by the surface topography, wettability, charge distributions, and chemical compositions. Consequently, the implant surfaces could be engineered for realizing the optimized surfaces for maximizing the anchorage of the implant to

the tissues. The clinical observations of the differential bone growth rates in opposite directions in the direction away from and toward the implant surfaces confirmed the importance of such surface functionalizations as reported extensively [98].

In the context of bone substitutions the topographical features are found promoting the cell anchorage and protein adsorptions leading to better adhesion of osteoblasts improving the metabolism of these cells to regulate gene expression, collagen synthesis, and activation of integrins. The phenomenon of osteogenesis occurs faster on the surfaces modified at the nanometer levels than those on the smoother surfaces. Therefore the manipulation of the nanotopography could stimulate and control cellular behavior, including attachment, migration, spreading, gene expression, proliferation, differentiation, and secretion of matrix components. Creating such NMs organized at the nano levels could be considered an important step toward targeting the specific cells via recognition for affecting the interaction of solvent molecules with the surface, impacting the interfacial energy as discussed separately [99].

The surface free energy (SFE) of biomaterial decides whether the polar or the nonpolar portions of the proteins and cell membranes would interact with the surfaces. The protein layers absorbed onto the implant surfaces determine how are the cells attached and spread resulting into cell maturations. Albumin blocks the cell-implant interactions by turning the surface hydrophobic that inhibits replacement by other ECM proteins. On the contrary, adsorbed albumin onto the hydrophilic surface enables replacement with ECM proteins. Consequently, the type of protein and its binding decide the cellular adhesion and migration. Cells could also nonspecifically adhere to the surfaces through ionic and vdW forces or via adsorbed protein clusters. The integrin receptors in osteoblasts recognize Arg-Gly-Asp (RGD) motifs on proteins such as fibronectin and vitronectin to form local adhesions that activate a cascade of signaling pathways affecting the cell behavior. Integrin-mediated cell attachment mechanism modifies the metallic surfaces by immobilizing sequences of RGD-peptides. This is how by altering the chemistry of the bioactive coating, topographic changes are realized. Recognizing the importance of SFE in stimulating the cell adhesion, hydroxyapatite (HAp) was used for adsorbing more ECM proteins, binding more integrins and osteoblast precursor cells than simple metal. The addition of polar bioactive compounds to the metallic surfaces could, thus, be an alternative approach to tailor SFE. On the hydrophobic surfaces, human fetal osteoblasts are found expressing significantly lower levels of the $\alpha 5$ and $\beta 3$ integrins than those on the cells cultured on the hydrophilic surfaces. Surfaces with COOH and NH_2 groups display an enhanced activity of integrins leading to higher adhesion and spreading of the fibroblast cells. Using macrophage cultures, it was observed that materials with higher surface wettability produce an antiinflammatory microenvironment through the activation of macrophages and cytokine productions. This highlights the importance of controlling the wettability when attempting to improve the healing responses to the biomaterials [100].

The metallic implant surfaces are possible to modify using bioactive minerals required in bone-structure formation. The manufacture of calcium phosphates

coatings is quite common in bone-regeneration implants. HAp resembles the biological apatite found in bone tissues, where HAp crystals are hierarchically organized into the array of collagen fibers. Plasma spray and sputter-coating techniques produce the apatite coatings commercially. These methods are not only complex and expensive but also have drawbacks of nonuniform thicknesses and crystallinity resulting in lower coating adhesions, besides particles released from the surface during phase changes in CaP during processing [101].

Human skins damaged by trauma, burns, and chronic ulcers start healing after dressings applied for facilitating wound healing and rebuilding their barrier properties of protection from the pathogens and foreign bodies, maintaining the equilibrium of water and electrolytes, promoting wound healing by reducing the infections. An ideal dressing must, therefore, promote the proliferation and migration of fibroblasts, accelerate the epithelial tissue formations, reduce the scars, and have antibacterial/antiinflammatory properties. Gram-positive/negative bacteria infect the wounds whereas the chronic infections are caused by the multiple bacterial species. Yu et al., could identify NPs with broad-spectrum antimicrobial properties inhibiting the bacterial growth and reproduction. The combination of Ag-NPs + PVA + CS, when applied using a fiber-mat dressing, was found effective in wound healing in which silver-NPs facilitated good contact with bacteria resulting in growth inhibition and improved wound healing [102]. The antibacterial properties of ZnO-NPs were better exploited in several hydrogel-based dressings because of their fewer toxic effects on the mammalian cells than Ag-NPs. In a recent study, *n*-ZnO-NPs were introduced into a microporous CS hydrogel bandage with high swelling ability, enabling the absorption of wound exudates, besides activating the platelets and blood clotting. Such bandages were cytocompatible and antibacterial for promoting reepithelialization and collagen deposition during in vivo studies. In another study, ZnO-nano flowers exhibited proangiogenic activity, which was confirmed by in vivo/vitro assays. However, despite the higher potentials of the M-NPs in treating drug-resistant bacteria, these materials possess higher toxicity, thus limiting their uses in wound healings [103].

Low-cost and UV blocking ZnO-NPs−based hydrogels were used in developing ZnO-NPs/polymer composites useful for several applications. For example, β-chitin/ZnO-NPs composite hydrogels were used in wound dressing by mixing ZnO-NPs into the solution of β-chitin and then freeze-drying to form porous hydrogel with controlled swelling and degradation properties exhibiting higher blood clotting and platelet activations while acting against *S. aureus* and *E. coli.* The associated cytocompatibility was evaluated on human dermal fibroblast cells. At higher and lower concentrations of ZnO-NPs, the cells' viabilities were noted to be around 50%−60%, and 80%−90%, respectively. Faster healing and collagen depositions were observed in rat models. Similarly, collagen−dextran−ZnO-NPs composites were reported as promising formulations for future applications in wound dressing and skin regenerations. In another study, CMC was cross-linked to maleic, succinic, and citric acids, followed by ZnO-NPs loading through in situ synthesis of NPs in the hydrogel that exhibited excellent swelling by cross-linking with succinic acid. The loading of ZnO-NPs into hydrogel provided antibacterial activity against both

Gram-positive/negative bacteria. CMC cross-linking with epichlorohydrin followed by ZnO-NPs loading in the hydrogel matrix resulted in improved swelling of the hydrogel when tested at different pH and salt solutions confirming its pH and salt-sensitive swelling behavior while testing against *S. aureus* and *E. coli*. More recently, a flexible nanocomposite hydrogel was reported using a combination of ZnO-NPs impregnated with mesoporous silica (ZnO-MCM-41) as a nanodrug carrier with CMC hydrogel, in which, the citric acid cross-linker could reduce its cytotoxicity besides exhibiting higher tensile strength, swelling ability, and gas permeability. The drug delivery and bactericidal properties of the nanocomposite hydrogel films were examined using sustained releasing tetracycline with excellent antibacterial properties against *S. aureus* and *E. coli*. The nanocomposite hydrogels showed cytocompatibility against adipose tissue-derived stem cells. Considering these properties, CMC/ZnO/MCM-41 could serve as promising wound dressing material with sustained drug-delivery properties. Another formulation of CMCh/ZnO nanocomposite hydrogels was reported by cross-linking CMCh with epichlorohydrin followed by ZnO-NPs loading via in situ synthesis in the hydrogel-network resulting in pH-dependent swelling properties exhibiting maximum swelling at 7 pH. The antibacterial activity was found concentration dependent of ZnO-NPs increasing with higher concentrations. The experimental results showed a 100% reduction of bacterial population within 4 hours of treatment with this nanocomposite hydrogel as reviewed recently [104].

The wound healing capability of poly (vinyl alcohol)/ZnO-NPs composite hydrogel was proven using a synthetic polymers/ZnO-NPs nanocomposite possessing antimicrobial properties after assessing its biocompatibility via bovine serum albumin adsorption, antihemolytic activity, and in vitro cytotoxicity tests. Yet another formulation of poly(*N*-isopropylacrylamide) (PNIPAAm) hydrogel loaded with ZnO-NPs was found better in antibacterial surface coating applications. The nanocomposite films showed antibacterial properties against *E. coli* for a ZnO-NP concentration as low as 1.33 mmol/cm^3, which was determined by inductively coupled plasma optical emission spectrometry showing nontoxicity toward a mammalian cell line (NIH/3T3) at bactericidal loading of ZnO over an extended period of 7 days as reported [105–109].

A number of research groups have been investigating the antimicrobial properties of CuO-NPs against a range of pathogens, including MRSA and *E. coli*. The mechanism of antimicrobial activity of CuO-NPs was supported by contact killing of bacterial cells via two-stage lysis. In the first stage, CuO-NPs were found damaging the bacterial cells, while in the second stage, they produced free radicals capable of toxicating the inner cell complexes. The ROS production by CuO-NPs adhering to the bacterial cells was found causing enhanced intracellular oxidative stress as confirmed experimentally. The wound dressing material was prepared by incorporating CuO microparticles into the polymer that prevented infections leading to increased wound healing rates, compared to standard treatments. Recently, a Cu-based nanocomposite involving polymers such as cellulose, chitosan, polyacrylic acid, and polypropylene was found producing an attractive antimicrobial nanocomposite hydrogel. CMC-based hydrogels along with CuO-NPs were reported

effective antibacterial agents by various research groups along with another formulation of copolymeric hydrogel nanocomposite for wound dressing by employing diallyldimethylammonium chloride (DADMAC) monomer and *N*,*N*′-methylenebisacrylamide (MBA) cross-linking agent on water-soluble CMC to produce in situ CuO-NPs within the matrix of the CMC-DADMAC hydrogel nanocomposite attached to cotton fabric were found effective against Gram-positive/negative bacteria with excellent response. Furthermore, they also loaded Ag-NPs to CMC-DADMAC hydrogel, which showed better antibacterial results than the CMC-DADMAC/CuO nanocomposite hydrogel. Another study confirmed the antibacterial properties of carboxymethylcellulose (CMC) hydrogel loaded with CuO-NPs, with epichlorohydrin as the cross-linker. The swelling behavior of the hydrogel nanocomposite was studied at different pH and salt solutions while testing them against *S. aureus* and *E. coli*. In addition to CMC, chitosan-based antibacterial hydrogels loaded with CuO-NPs were also reported recently employing chitosan/CuO nanocomposite hydrogel beads in which the chitosan was cross-linked by sodium tripolyphosphate, while CuO-NPs were formed in situ during the formation of hydrogel beads involving 10−25 nm CuO-NPs showing pH-sensitive swelling behavior and being effective against *S. aureus* and *E. coli*. Recently, CMCh/CuO-NPs nanocomposite hydrogels were produced by the cross-linking of CMCh and CuO-NPs by using epichlorohydrin to produce 20−50 nm NPs that showed antibacterial activity against *S. aureus* and *E. coli* [110,111].

Besides using well-known Ag and Au-NPs, there are a number of other antimicrobial M-NPs, but only few of them are used in hydrogel form. For instance, ZnO-NPs are extensively used in cosmetics due to their antibacterial and noncytotoxic nature at appropriate concentrations, in which their conjugations with bacterial cell membranes destroys the lipids and proteins creating enhanced membrane permeability and cell lysis. Formations of Zn^{2+} ions, ROS, and H_2O_2 damage the bacterial cells. ZnO-NPs are effective against Gram-positive/negative bacteria because of their high temperature/pressure-resistant spores. The antibacterial performance of CMC/ZnO nanocomposite coatings against *E. coli* and *S. aureus* was further enhanced with hydrogel involving PEG methyl ether methacrylate-modified ZnO (ZnO-PEGMA) and 4-azidobenzoic agarose (AG-N3). ZnO-NP-hydrogels were found useful as drug carriers and wound healing materials as observed in some recent studies. CMC and CS-hydrogels were found effective against Gram-positive/-negative bacteria and wound healing, respectively. Lower cytotoxicity of ZnO-NPs makes them preferred in numerous clinical applications along with their positive effect on bone regeneration in orthopedic surgery despite their poorer antibacterial ability as discussed in the cited literature. Hydrogels of Ni-NPs + chitin, and Co exchanged natural zeolite/PVA were found effective against *S. aureus* and *E. coli*. Cu/CuO-NPs possessing a wider range of microbicidal features against *S. cerevisiae*, *E. coli*, *S. aureus*, and *L. monocytogenes* and preferred against Ag-NPs. CMC/CuO and CS-based hydrogels loaded with Cu-NPs were found effective against *E. coli* and *S. aureus* without causing any toxicity in the recent studies. NPs of magnesium, and their oxides and halides were found effective in combating

microbes. MgO-NPs loaded hydrogels derived from hydroxyalkyl κ-carrageenan derivatives controlled the drug delivery in gastrointestinal tract studies. All these experimental investigations indicated about the necessity of studying NPs derived from the other metals and their alloys that are foreseen more appropriate in designing and fabricating biomaterials as good substitutes replacing antibiotics with rarely reported bacterial resistance. The ultrasmall M-NPs enable them to pass through the peptidoglycan cell walls and cell membranes before entering into the cell cytoplasm. Moreover, highly stable M-NPs implied that they would further continue killing other microbial cells after being released from the dead cells resulting in sustainable antimicrobial effects. Using hydrogels as drug delivery system for local applications, the antibacterial property could be improved further with increasing concentration of M-NPs providing them in enhanced concentration at the infection sites.

The swelling behavior and mechanical properties along with antibacterial features of carrageenan loaded with ZnO and CuO-NPs separately, as well as collectively in hydrogel form were studied. The swelling ratio of carrageenan hydrogel (e.g., 2980%) was found improved to 3535% after the introduction of ZnO-NPs. The carrageenan-based hydrogel exhibited strong antibacterial activity against foodborne *E. coli* and *L. monocytogenes*. The ZnO-NP-incorporated hydrogel exhibited higher water holding capacity, better mechanical strength, UV-screening, thermal stability, and antibacterial properties compared to CuO-NP-incorporated ones. The nanocomposite hydrogels could have higher potentials for biomedical, cosmetic, and active food-packaging applications. The TiO_2-NPs exhibited morphology-dependent antimicrobial properties by creating oxidative stress via ROS generation for imparting antibacterial features in TiO_2-NPs. ROS generation could cause site-specific DNA-damage of the bacterial cells. The effect of TiO_2-NPs was studied with different antibiotics against MRSA, in which, improved effects were noted in cephalosporins, aminoglycosides, macrolides, beta lactams, glycopeptides, lincosamides, and tetracycline against MRSA. The photocatalytic TiO_2-NPs could completely eradicate bacteria by producing ROS under UV light, which was accompanied by lipid peroxidation causing membrane fluidity interrupting the cell integrity. The usage of TiO_2-NPs under UV light is limited because of the damage to other human cells and tissues, which could possibly be reduced by doping them with metal ions. These doped TiO_2-NPs could shift the light-absorption range to visible region without using UV light. Another solution to this problem was proposed using nontoxic polymer conjugations. TiO_2-NPs embedded in ethylene vinyl alcohol copolymer, polypropylene, and poly[2-(*tert*-butylamino) ethyl methacrylate-*co*-ethylene glycol dimethacrylate] and employed in producing nanocomposites were found effective against Gram-positive and negative strains. Zhang et al. reported methacrylated gelatin hydrogel films with homogenously dispersed TiO_2-NPs (from 85 to 130 nm) showing absorption capabilities in the range of 471%–758%, which could prevent the accumulation of wound exudates. The antibacterial activity of the nanocomposite hydrogel films was evaluated against *S. aureus* and *E. coli* by the shake flask test that demonstrated superior performance of nanocomposite hydrogel films. Cytotoxicity tests showed that all films were nontoxic with favorable adherence in the presence of L929 cells.

Photo-active antibacterial properties of TiO_2-NPs/CMCh/PVA ternary nanocomposite hydrogels were reported by going through freeze−thaw cycles and electron beam radiation with PVA, CMCh, and TiO_2-NPs exhibiting a porous structure of TiO_2/CMCh/PVA hydrogel. In addition, the nanocomposite hydrogel showed significant antibacterial activity against *E. coli* and *S. aureus* bacteria. The cytotoxicity test of these hydrogels was carried out against L929 cells that suggested no obvious cytotoxicity. These materials find numerous applications in cosmetics, medical dressings, and environmental protection [8,112−114].

The formations of superoxide on the surface of MgO-NPs and high pH resulting from hydration could impart antibacterial features causing cell membrane damage leading to bacterial cell death. Low cost, biocompatible, and easily available MgO-NPs make them favorable for antibacterial applications besides using them in environmental protection, food processing, and medical treatment. For instance, a polyacrylamide/MgO-nanocomposite hydrogel was synthesized using sodium carboxymethylcellulose (NaCMC); *N*,*N*′-methylenebisacrylamide (MBA) along with ammonium persulfate (APS) and *N*,*N*,*N*′,*N*′-tetramethylethylenediamine (TEMED) as the initiator. MgO-NPs embedded hydrogel revealed that the presence of NaCMC into the hydrogel enhanced its swelling capacity, mechanical strength, and flexibility. The antibacterial tests of composite hydrogel (i.e., 0.3 g MgO-NP) against *E. coli* showed 3-times enhanced antibacterial activity. Various aspects of antibacterial properties of metals, their alloys, and other chemical compounds have been discussed in detail in Refs. [19,115−117].

A bone disease called osteomyelitis is microorganism-induced progressive bone destruction involving staphylococci, with *S. aureus* and *S. epidermidis* in most of the cases. Such infections are found antibiotic resistant by evading the host immune system and antibiotics and are known as a major clinical challenge, with recurrent and persistent infections occurring in ∼40% of the patients. A number of metals including Ag, Fe, Hg, Te, Cu, Zn, and Pb are known to possess antimicrobial properties without the risk of decomposition. Although less known, some metals kill the microbes by ion penetration leading to enzyme inactivation's, while others impair membrane functions or produce ROS. These species are now foreseen as potential antimicrobial agents against drug-resistant bacteria, including MRSA and MRSE. CS, for instance, a positively charged linear polysaccharide is biodegradable, biocompatible, and nontoxic displaying antimicrobial activity and exhibiting metal binding properties and is often combined with metal ions for enhancing its antimicrobial activity against bacteria, including *S. aureus* (including MRSA) and *S. epidermidis*.

Similarly, antimicrobial peptides (AMPs) that are secreted by leukocytes in the epithelial skin layers, and mucosal membranes, demonstrated a broad antimicrobial activity along with the promotion of bone regeneration by using LL-37 that inhibited both the binding and biofilm-forming abilities of *S. epidermidis* and found effective against extra/intracellular *S. aureus* isolates. There are currently 2707 peptides in the "Antimicrobial Peptide Database" reported to have antimicrobial activity derived from a variety of sources, including bacteria, archaea, protists, fungi, plants, and animals, as discussed elsewhere [118].

7.5.2 Orthopedic and dental formulations

Room temperature curing bone-cements (i.e., of PMMA or modified PMMA with MMA) commonly used in knee or hip replacement surgery were found effective against higher infection rates of the total joint replacement surgery after antibiotic-loaded PMMA treatment. In other studies, however, the abovementioned antibiotic mixed bone-cements were found almost ineffective. Therefore it is still not clear whether the traditional method of loading bone cement with antibiotics effectively reduces the infection in arthroplasty. However, the number of resistant bacterial strains is currently increasing, and if effective measures are not taken, incurable infections and small wounds might turn to be fatal. NPs have a strong killing effect on certain types of antibiotic-resistant bacteria, and this effect is being examined extensively. A PMMA-bone-cement with Ag-NPs was found reducing the surface biofilm formations effective in preventing the bacterial surface colonizations. A low-concentration nano-silver (i.e., 0.05%) could similarly reduce the number of arthroplasty surgery-related infections significantly, including methicillin-resistant *S. aureus* (MRSA), *S. aureus*, *S. epidermidis*, and *Acinetobacter baumannii* infections. Ag-NPs have also been used to replace antibiotics in the development of promising antibacterial bone-cements.

Acrylic bone-cements (ACB) as polymer-ceramic composites with PMMA are widely used in orthopedics as suture materials and fixation devices that are biocompatible while supporting new bone growth (osteoconductive) and form a calcium phosphate layer on its surface by serving as interfacial phase between the high modulus metallic implant and the bone. Cemented prosthesis with ABC demonstrated a good primary fixation and load distribution between implant and bone, along with the advantage of fast recovery of the patient. However, problems are still there, as the orthopedic ABCs must be curable at low temperature in order to avoid thermal necrosis of the bone tissues during the setting-time of the appropriate formulation that neither cures too fast nor too slow with higher compressive strength in order to withstand the compressive loads involved in daily activities. The improved mechanical properties could be realized in three possible directions, including finding an alternative to PMMA, chemical modification of PMMA, and further reinforcement of PMMA by adding different bioactive particles, antimicrobials, and vitamins.

New types of PMMA-composite cements with improved fracture and fatigue strengths were reported accordingly using the concept of incorporating a low-volume fraction of fibers or bioactive particles/NPs (e.g., $\sim 1\%-2\%$) like carbon nanofibers, titanium dioxide, zirconia oxide, silver oxide, or silver-NPs. While these composites have displayed improved fatigue failure properties, biocompatibility concerns and possible complications of processing did prevent their implementations in manufacturing these PMMA bone-cements. Cavalu suggested using silver-NPs with strong antibacterial activity and no significant reduction in mechanical strength [119]. A novel SrO modified TiO_2-NTs were incorporated into the PMMA matrix to enhance its mechanical, physical, and biological properties with enhanced radiopacity and osteoblast cell viability attributed to the modification of the n-TiO_2-NTs with SrO showing a novel pathway to develop an alternate radiopacifier for bone cements, which could also act as a reinforcing agent.

The MO-NPs of Cu, Fe, Ta, V, and Co are currently being examined as promising constituents of dental formulations in addition to those including TiO_2 and ZnO that have produced most of the experimental results so far from in vitro experiments with positive activity against a wide range of oral cavity pathogens like *S. mutans*, *Streptococcus sanguis*, Lactobacillus, *Prevotella intermedia*, *Porphyromonas gingivalis*, *Fusobacterium nucleatum*, and *Aggregatibacter actinomycetemcomitans*. In vitro assessment of the antibacterial formulations based on TiO_2-NPs + CS mixed in glass-ionomer cement, and nano-TiO_2 containing films showed strong efficacies against *S. mutans* biofilms, *S. mutans*, and A. viscosus, respectively. In another work, solutions of 40−60 nm TiO_2-NPs showed significant efficacies against *S. mutans*, and *S. sanguis* offering almost equivalent replacement of chlorhexidine or sodium fluoride mouthwashes. TiO_2-NT-coatings onto the surface of Ti-biocomposite−based dental implants showed significant in vitro results in taking care of *S. mutans*. The antibacterial activities of these nano formulations are based on enhanced SOR generation causing damage to membranes, DNAs, other macromolecules, as well as the functions of the bacterial cells via photocatalytic effects in the presence of visible and near-UV/UV-radiations. A colloidal solution of TiO_2-NPs could, for instance, destroy the spores' membranes of B. cereus releasing the organelles into the surrounding environment as reported in detail elsewhere [120,121].

Several observations were made in using dental preparations of ZnO-NP-coated orthodontic wires possessing antibacterial properties, whereas ZnO-NPs covering on anodized TiO_2-NTs exhibited 45%−85% reductions in the growth of S. mutants and *P. gingivalis*. ZnO-NPs (∼35 nm) in a homogeneous suspension demonstrated a strong in vitro influence on controlling the growth of *Rothia* isolates in planktonic and biofilm forms. In vitro experiments using ZnO-NPs containing pastes promoted the antibacterial properties of chlorhexidine against *E. faecalis*. One of the studies of bactericidal effects of very dilute concentrations (e.g., 10^{-7}−10^{-6}mg/L) of the colloidal solutions of the MO-NPs of Ti, Fe, Ta, V, Co, Ta, Zn, and Cu showed positive effects against *E. coli*. The influence of composite coatings of titanium surfaces was also noted against species, including *P. intermedia*, *P. gingivalis*, *F. nucleatum*, and *A. actinomycetemcomitans*; in descending order as nanosilver (Ag) > nano-(Ag + CuO) > nanocupric oxide (CuO) > nanocuprous oxide (Cu_2O) > nano-(Ag + ZnO) > nano-ZnO > nanotitanium dioxide (TiO_2) > nano−tungsten oxide (WO_3). Thus antibacterial activity of Ag + ZnO and Ag + CuO-NPs composite was found stronger than that of Ag and ZnO-NPs, but lower than that of CuO-NPs [47,122].

The novelty of antibacterial properties of various materials containing MO-NPs investigated in vitro has primarily been assigned to their highly reactive surfaces. Moreover, materials, which are inert in their bulk forms, might also possess different new antibacterial properties when produced in nanoparticulate forms. A comparison of the antibacterial activities of the varying sizes (i.e., 18, 22, and 28 nm) of the NPs of the oxides of Zn, Cu, and Fe was made using *E. coli*, *P. aeruginosa*, *S. aureus*, and *B. subtilis* bacteria species with significant variations but still confirming that the antimicrobial activities were, in general, enhanced by reducing the particle size. More recent studies demonstrated the long-term antibacterial effects

(i.e., up to 9 days) of silver and iron oxide against dental pathogenic germs favoring the introduction of their nanoparticulate forms in preparing dental formulations [123].

Dental plaque offers an environment that allows microbes to settle on the teeth and initiate common mouth diseases. Many dental materials showed improved performance after their conversions in nanocrystal forms as noted in the case of nanodiamond-functionalized amoxicillin in combination with gutta-percha for root canal treatment. In addition, due to the proliferation of bacteria and the reduction in pH in the course of treatment, the orthodontic treatments often lead to the formation of dental plaque chalk and brackets coated with CuO and ZnO-NPs that checks the growth of *S. mutans*. While using maxillofacial prostheses in an external environment containing a variety of flora, it caused biofilm formations that increased the incidence of tissue inflammations. Adding nano-TiO_2 to such prostheses resulted in antibacterial effects following light exposure. MO-NPs, in general, are emerging as promising constituents in the dental formulations with antibacterial properties to overcome the resistance to conventional antibacterial drugs as can be seen from the reported observations [124].

7.6 The antibacterial pathways

Biomedical applications of nanoparticulate material species have continuously been growing based on their antibacterial properties. For example, changing the metabolic processes of bacteria due to the metal-NPs could advantageously be used in eliminating the bacterial infections and curing the related diseases. Ability of the NPs to enter biofilms also provides a practical method to inhibit biofilm formation based on the Ag-inhibited gene expressions [47]. The nanoparticulate species are attracted to bacteria before making contacts with them involving mechanisms like electrostatic attraction, vdW forces, receptor-ligand, and hydrophobic interactions to facilitate them in crossing the membrane and gather along the metabolic pathways besides influencing the shape and function of the membrane. Thereafter, these are found interacting with DNAs, lysosomes, ribosomes, and enzymes, leading to oxidative stresses, heterogeneous alterations including changes in cell membrane permeability, electrolyte balance disorders, enzyme inhibition, protein deactivation, and changes in gene expressions that have quite often been proposed in current studies of oxidative stresses, metal ion releases, and nonoxidative mechanisms [125,126].

In ROS-caused oxidative stresses, NPs are found interacting with generic molecules that have strong positive redox potentials leading to different types of ROS generations by reducing oxygen as superoxide radical (O^{2-}), the hydroxyl radical ($\cdot OH$), hydrogen peroxide (H_2O_2), and singlet oxygen (O_2), creating different levels of activity. For example, calcium and magnesium oxide-NPs could generate O^{2-}, whereas ZnO-NPs generated H_2O_2 and OH but not O^{2-}. Although, CuO-NPs are capable of producing all four types of ROS's. Studies have also confirmed that

O^{2-} and H_2O_2 cause less acute stresses and are neutralized by superoxide enzymes and catalase, whereas $\cdot OH$ and O_2 could result in acute microbial death. The main causes of ROS production involve restructuring by creating defect sites, and oxygen vacancies in the crystal. Under normal circumstances the production and clearance of ROS in bacterial cells are balanced. In contrast, with the excessive production of ROS, the redox balance of the cell favors oxidation producing oxidative stresses, which damage the individual components of the bacterial cells.

Oxidative stress has been confirmed as main contributor to the changing permeability of the cell membrane creating damages in bacterial cell membranes. It was confirmed in one of the studies that Al_2O_3-NPs crossed the cell membrane to become intracellular, and their interactions with the cell membrane eventually triggered the loss of membrane integrity, most likely due to intracellular oxidative stress. Similarly, nano-silver ions were used as catalysts to activate the oxygen in air or water, leading to the production of hydroxyl radicals and reactive oxygen ions, which prevented the proliferation by killing the bacteria. A number of studies have also shown that ROS play a key role in the interaction between DNA and bacterial cells. ROSs are beneficial to increasing the gene expression levels of oxidative proteins, which is a key mechanism in bacterial cell apoptosis. Furthermore, ROS can attack proteins and reduce the activity of periplasmic enzymes that are essential to maintain normal morphology and physiological processes in bacterial cells. NPs could produce ROS by different mechanisms. The photocatalytic hypothesis is the latest explanation, in which, oxide-NPs of Zn and Ti absorbing light irradiation allow the transition of electrons from the valence to the conduction band creating a hole in the valence band and produce highly reactive states on the surface and inside the catalytic material. The holes adhere to the surface of ZnO after interaction with H_2O or OH^- producing the hydroxyl radical ($\cdot OH$). Similarly, the OH-radicals are reduced to the superoxide radicals (O^{2-}) after electronic interaction with O_2 that stay onto ZnO surface. The active constituents that maintain the normal morphological and physiological functions of the microorganism are degraded due to ROS generation. In particular, the photo-generated electron-hole pairs in TiO_2-NPs react with water and air on the surface producing highly active ROS's that attack intracellular organic matters in the bacteria. In another example, Zn produces highly reactive ROSs in presence of UV and visible light radiations. While the negatively charged O^{2-} and OH-radicals remain confined to ell surface without penetrating inside the bacteria, H_2O_2 species could penetrate the cell membrane. ZnO-NPs were found transformed from the spiral *C. jejuni* cells into spherical ones, causing cell damage and leakage as revealed by SEM. Quantitative real-time polymerase chain reaction (RT-PCR) confirmed that the expressions of the oxidative stress-genes (Kat A and Ahp C) and general stress responding gene (Dna K) were enhanced by 52, 7, and 17 times, respectively, due to ROS. Ultrasonic activation was also found causing ROS formation. ZnO-NPs splitting H_2O into H^+ could react with dissolved oxygen to generate H_2O_2 in the environment having water and oxygen and then penetrated the cell membrane to kill bacteria. Ultrasonic treatment of polymer-NPs and colony-forming units could dissociate the NPs and promote their penetration through the cell membrane. In addition, antimicrobial metal ions are

released from the surface fast to inhibit the proliferation of bacteria under ultrasonic treatments, which may be due to the increased rates of transport of bacterial oxygen, nutrients, and wastes produced. A previous study, however, noted the antibacterial activities of the NPs even in the dark. Photo-stimulated ZnO could produce minimal amounts of OH-radicals. Oxygen vacancies situated on the ZnO-surface were found facilitating significant production of H_2O_2. In heterogeneous catalysts the catalytic activity of MO is dependent on the density of the active sites. The parameters such as size, lattice constant, and orientation of the ZnO-crystallites decide the associated antibacterial activity.

The metal ions, released from the MO, are absorbed through the cell membrane before interacting with the functional groups of proteins and nucleic acids comprising −SH, −NH, and −COOH groups and damaging the enzyme activity, changing the cell structure, affecting the normal physiological processes, and ultimately inhibiting the microorganism. However, the impact of metal ions on the pH inside lipid vesicles is not strong during the antibacterial process of MO-suspensions with weak antimicrobial activity. Therefore dissolved metal ions do not produce the antimicrobial effects in MO-NPs. Similarly, it was confirmed that superparamagnetic IONPs interact with microbial cells by penetrating the cell membrane and interfering with transmembrane electron transfers. In addition, heavy metal ions were found acting indirectly as carriers of antimicrobial substances as discussed in detail in Ref. [127].

The antibacterial activities of MgO-NPs found affecting *E. coli* under UV, natural light, or darkness were considered unrelated to the membrane lipid peroxidation caused by oxidative stress. MgO-NPs are not observed in the cells even after the bacterial cell membranes are damaged showing the surface pores clearly. Even energy-dispersive X-ray spectroscopy could not detect the presence of Mg-ions. Only one type of MgO-NP interaction could produce small amounts of ROS, whereas it is absent in other two cases. Lipopolysaccharide (LPS) and phosphatidylethanolamine (PE) in the cell wall were not significantly changed by MgO-NP treatment indicating that they did not cause lipid peroxidation while the amount of ROS-associated proteins in the cells are not increased, but many critical cellular metabolic processes related to proteins, including amino acid metabolism, carbohydrate metabolism, energy metabolism, and nucleotide metabolism, are significantly reduced [47,128].

Examining the structural details of the bacterial cell-walls and membranes that act as barrier for protecting them from the external environment was found necessary to identify the viable NP-adsorption pathways to the cells. For example, a negatively charged region in the cell wall of Gram-negative bacteria was noted to attract NPs in contrast to the teichoic acid that was only expressed in the cell wall of Gram-positive bacteria facilitating the NP-distributions along the molecular chain of phosphate preventing their aggregations. NPs were consequently found more active against Gram-positive bacteria than the Gram-negative ones because of the presence of LPS, lipoproteins, and phospholipids, which only permitted the entry of macromolecules. In contrast, the cell-walls of the Gram-positive bacteria, including a thin layer of peptidoglycan and teichoic acid along with abundant pores,

allowed foreign molecules to penetrate the cells resulting in cell death. In addition, the enhanced presence of negative charges on the cell-wall surfaces of the Gram-positive bacteria could attract NPs as observed in the case of a hydroxyapatite whisker/nano-ZnO composites exhibiting improved antimicrobial influence against *S. mutans*, *Candida albicans*, and *S. aureus* than on *E. coli*. These observations suggested that NPs could destroy bacteria with specific components and structures of the bacterial cells. The antimicrobial behavior of ZnO-NPs was found dependent on the bacterial cell compositions that were more favorable in Gram-positive species. Certain components such as LPS in the Gram-negative bacteria prevented the adhesion of ZnO-NPs to the bacterial cell barrier regulating the in/out-flow of ions across the cell membrane. The phospholipid head groups of the LPS membranes in *E. coli* interacting with ε-poly-L-lysine through electrostatic attraction could damage the cell membranes. However, the amphoteric *Listeria innocua* film containing lysine-derived phospholipids having insufficiently strong negative charges to attract cationic peptides; the cell membrane of *L. innocua* had lower permeability than those of *E. coli*. The important enzymes and proteins coupling with the intracellular components were further restrained in causing a bacterial metabolism-disorder leading to cell deaths. Various aspects of antibacterial properties of nanoparticulate species were discussed in detail in Ref. [129].

The antibacterial efficacies of the nanoparticulate material species were found dependent on their morphologies, charge distributions, zeta potentials, and crystal structures, along with the biofilms formed onto the bacteria surfaces that could be responsible for antibiotic resistances. Moreover, other factors such as environmental conditions, the bacterial strain, and the exposure time were also noted affecting the overall antibacterial effects of the NPs in addition to their large specific surface areas, higher surface energies, and atomic ligand deficiencies causing their aggregations. The current studies found that for better understanding of the antibacterial activities of the metal-NPs as function of their size and shape, it needed more detailed examination of the NP-characteristics. For instance, the morphology of the TiO_2-NTs in a composite film of TiO_2-NTs + silica-NPs was found deciding the extent and mechanism of its antibacterial activity. Although, smaller NPs with larger specific surface areas imparted higher probability of making contact and entering through the cell membrane than the larger ones, however, the analysis of the size-dependent antibacterial activities of the three different types of $Mg(OH)_2$-NPs clarified that the smallest $Mg(OH)_2$-NPs had the weakest antibacterial effect. This particular observation confirmed that the size alone was not a dominant factor. It, therefore, required still more detailed examinations of the other physicochemical properties while exploring their antibacterial activities. However, NPs with different shapes could inflict varying degrees of cell damages through interactions with periplasmic enzymes as noted in a comparative study of three different types of ZnO-NPs (i.e., pyramidal, plate-like, and spherically shaped morphologies). In a combined influence of β-galactosidase and shape-specific photocatalytic ZnO-NPs could obstruct and restructure the enzymes, in which, the pyramid-shaped n-ZnO-NPs prevented the enzyme degradations resulting in stronger antibacterial activity against *Pseudomonas desmolyticum* and *S. aureus*, which might rupture membranes.

Similarly, in another study of the sustained-release of Ag-NPs as bactericidal agents, better efficacy of the cuboid-NPs was observed compared to the spherical ones indicating toward the significance of shape effect on the antibacterial activity derived from combined effect of specific surface area and facet reactivity. In addition, with increasing surface roughness of the NPs, the size and the surface area-to-volume ratio promoted the adsorption of the bacterial proteins, followed by a reduction in bacterial adhesion. Recent studies have also shown that the zeta potential of NPs influenced the bacterial adhesion strongly due to the electrostatic attraction between positively charged NPs and negatively charged bacterial cell membranes. For example, $Mg(OH)_2$-MgCl and $Mg(OH)_2$-$MgSO_4$-NPs were found getting adsorbed onto the bacterial surfaces, in contrast to their negatively charged counterparts. The potential of the NPs to selectively gather at the sites of bacterial infection could enhance the vascular permeability. Accumulation of the cationic NPs was found beneficial to inhibiting bacterial growth by limiting bacterial attachment. Slight penetration of NPs into the outer regions of the *S. aureus* envelopes somehow provided higher germicidal efficacy, possibly because the NPs could reach key structures through ion-exchange. Compared to the negatively charged and neutral NPs, positively charged counterparts were believed to enhance ROS productions, whereas the negatively charged NPs did not adhere to bacteria due to repulsions. However, at higher concentrations, negatively charged NPs could also exhibit a certain level of antibacterial activity due to molecular crowding, which led to interactions between the NPs and the bacterial surfaces as discussed by various authors [130].

Doping of the NPs is one of the most effective ways of regulating and controlling the interactions of the NPs and bacteria besides stabilizing their dispersions. Of late, the combination of ZnO-NPs + Au forming ZnO/Au nanocomposites was used in improving the photocatalytic activity and enhancing the ROS generation as a result of the factors such as improved light absorption due to the surface plasmon resonance of Au, altered bandgap of ZnO-NPs enhancing the reactivity of photo-induced charge carriers, and increasing the efficiency of electron transport and charge carrier separations. For instance, F-doped ZnO-NPs generated more ROS than undoped ones, resulting in greater damage to the bacterial cells. The O-content at the surface of the ZnO-NPs was found regulating antimicrobial efficacy against both Gram-negative and positive bacteria. Nano-TiO_2, being widely used in orthopedic and dental implants, exhibited antibacterial activity by reducing the formation of the biofilms. Compared to the unmodified nano-TiO_2, which could improve photocatalytic activity, the doped ones extended the active spectrum to the visible light region due to bandgap reductions as noted in various studies [131].

Another interesting class of NM species, known as ZnO nano−sea urchins and tetrapods, were reported blocking the viral entries (HSV-1 and HSV-2) into the cells as they got attached to the receptors at the viral surfaces resulting in restricted viral entry. These reductions were further accentuated after UV illumination of the ZnO-nanostructures. The interaction of heparan sulfate groups enveloping the HSV-1 virus and the gD-receptors on the cells was, for instance, found facilitating their cell entry. The UV-irradiation was found creating more oxygen vacancies than

those ZnO nano-microstructures treated with sunlight. Similar observations were made in the case of SnO_2 NW networks in blocking the entry of HSV-1. These nano-microscale ZnO-tetrapods exhibited very low level of cytotoxicity as compared to conventional spherical NPs and $ZnCl_2$ [132].

The environmental conditions were found affecting the antimicrobial activity of nanoparticulate species. For example, the influence of temperature was found correlated to the ROS generation in stimulated ZnO-NPs capturing electrons at the active sites. Afterward, the electrons interacted with oxygen (O_2) to produce ROS, thereby enhancing the antimicrobial effectiveness of ZnO-NPs. Moreover, the pH of the environment influenced in vitro antimicrobial activity by noting that decrease in the pH increased the dissolution rate of ZnO-NPs that resulted in greater antimicrobial properties as pH was specifically found improving the NP adhesion to the bacterial surfaces. In addition, the loss of efficacy of poly (lactic-*co*-glycolic acid) (PLGA)-poly (L-histidine) (PLH)-poly (ethylene glycol) (PEG)-encapsulated vancomycin decreased under acidic conditions suggesting that the selective protonation of the imidazole groups of PLH under acidic conditions strongly influenced NP surface charges. At low pH the NP's surfaces were positively charged, which is beneficial to the interaction with the negatively charged groups of the bacterial cell barriers, inducing strong multivalent electrostatic regulations. Another study proposed an oxidative dissolution mechanism for Ag-NPs through the interaction of Ag^+ with dissolved oxygen and protons. The characteristics of the medium, such as the pH and osmotic pressure, were found influencing the aggregation, surface charge, and solubility of the NPs. Antibacterial tests of ZnO-NPs in five types of media demonstrated that its antimicrobial activity was mainly due to free Zn ions and their complexes. The preparation of ZnO-NPs under different stirring conditions was found affecting their antibacterial activity against *B. subtilis* and *E. coli* and *C. albicans* as reported [133].

7.7 Discussions and conclusion

The availability of the electron states in the outermost unsaturated atomic orbitals of the constituent atomic species in a nanostructured material species decides the enhanced interaction capabilities via chemical bond formation, which has been employed in exploring their novel properties as explained in this chapter. A number of compounds formed using these basic chemical conjugation techniques have been further highlighted in Table 7.1.

This highlights some of the recent applications of 2D-NMs and their composites in biomedicines for human healthcare and environment. Theoretical studies of these interactions using simulation tools have been found useful in systematically exploring quite a few novel characteristic properties in the case of the families of perovskites briefly described earlier. The electron states corresponding to the d-orbitals, already known to offer possibilities of not only forming strong chemical bonds but also leading to chemical conjugations involving weak interactions, are noted to add

Table 7.1 Engineered graphene in biomedicine.

Test year	Material combinations	Affected bacterial strains	Inhibition (%)
2019	GO	*Staphylococcus aureus/ Pseudomonas aeruginosa*	93.7/48
2019	rGO−TiO_2	*Escherichia coli/S. aureus*	100
2019	rGO−Cu_2O	*E. coli/S. aureus*	70/65
2019	PDMS−GO−DMA	*S. aureus*	∼40
2018	rGO−Ag/Ag_2S	*E. coli*	100
2018	GO−ZnO	*E. coli*	100
2018	PVA−CS−GO	*E. coli*	1.25/ 1.4 mm[a]
2017	GO−Ag_3PO_4 NPs	*E. coli/S. aureus*	100
2017	rGO−Ag-NPs	*E. coli*	100
2017	rGO−Van−nHA	*E. coli/S. aureus*	N/A
2017	GO-cefalexin	*E. coli/S. aureus*	6.3/ 6.9 mm[a]
2015	GO−Mn−Fe_2O_4	*E. coli*	82
2015	GO−Bi_2WO_6	Mixed culture	100
2015	GO−PEG−PHGC	*E. coli*	N/A
2015	GO−Lys	*E. coli/Bacillus subtilis*	68
2015	GO−PEI−ciprofloxacin	*E. coli/S. aureus*	100
2015	rGO−PEI−Ag−NPs−Fe_2O_3	*E. coli*	99.9
2015	rGO−Ag−$CoFe_2O_4$	*E. coli/S. aureus*	97−99

Graphene-derivatives functionalized with Ag-NPs, metal ions/oxides, polymers, antibiotics, enzymes, and multicomponent composites [134].
[a]Agar Diffusion Assay (ADA).

more flexibilities in designing alternate stoichiometries that were synthesized later and used in practical applications involving their electron/phonon transports, magnetic effects, thermoelectric effects, electromagnetic interactions via photons, besides a whole host of biomolecular applications via currently ongoing studies [3,5,25,114,121,135]. Interactions based on vdW force, hydrogen bonds, and numerous polarization-based electrostatic interactions existing in these MO-NM-based hierarchical supramolecules are, therefore, foreseen extremely important in biomedical applications. Possibly, the existence of such interactions could be one of the reasons that these compounds are pharmaceutically active in those cases where conventional antibiotics are known to be ineffective after their continued uses in a number of therapies [136].

There are evidences to conclude, only partially at this point of time, about the fast emerging novel possibilities that would be explored in these MO species available in 0/1/2/3-dimensions bearing insulating, semiconducting, and semimetallic properties, for their electronic applications; quantum confinement supported electron-phonon interactions based thermoelectric applications, catalytic properties replacing cost-intensive noble metals; besides their unique interactions with

biomolecular species as discussed particularly in this chapter. Newer opportunities of synthesizing compounds possessing unusual physico-chemico-biomedical properties that would be used in many more emerging applications not yet explored, and hence it would require periodic review of this fast-growing subject of utmost importance in human healthcare as such besides other associated industrial applications.

References

[1] WP-1, **2018**, Text available @ <https://chemistry.tutorvista.com/inorganic-chemistry/metal-oxide.html>.

[2] L. Peng, P. Xiong, L. Ma, Y. Yuan, Y. Zhu, D. Chen, et al., Holey two-dimensional transition metal oxide nanosheets for efficient energy storage, Nat. Commun. 8 (2017). Article No. 15139.

[3] J. Azadmanjiri, V.K. Srivastava, P. Kumar, J. Wang, A. Yu, Graphene-supported 2D transition metal oxide heterostructures, J. Mater. Chem. A 6 (2018) 13509−13537.

[4] S.-J. Choi, I.-D. Kim, Recent developments in 2D nanomaterials for chemiresistive-type gas sensors, Electron. Mater. Lett. 14 (3) (2018) 221−260.

[5] K. Yang, Q. Han, B. Chen, Y. Zheng, K. Zhang, Q. Li, et al., Antimicrobial hydrogels: promising materials for medical application, Int. J. Nanomed. 13 (2018) 2217−2263.

[6] T. Yang, T.T. Song, M. Callsen, J. Zhou, J.W. Chai, Y.P. Feng, et al., Atomically thin 2D transition metal oxides: structural reconstruction, interaction with substrates, and potential applications, Adv. Mater. Interfaces 6 (1) (2019) 1970003.

[7] S. Anandan, J.J. Wu, D. Bahnemann, A. Emeline, M. Ashokkumar, Crumpled Cu_2O-g-C_3N_4 nanosheets for hydrogen evolution catalysis, Colloids Surf. A Physicochem. Eng. Asp. 527 (2017) 34−41.

[8] C. Liu, J. Guo, X. Yan, Y. Tang, A. Mazumder, S. Wu, et al., Antimicrobial nanomaterials against biofilms: an alternative strategy, Environ. Rev. 25 (2017) 225−244.

[9] A. Umar, A.A. Alshahrani, H. Algarni, R. Kumar, CuO nanosheets as potential scaffolds for gas sensing applications, Sens. Actuat. B—Chem. 250 (2017) 24−31.

[10] W.J. Song, Intracellular DNA and microRNA sensing based on metal-organic framework nanosheets with enzyme-free signal amplification, Talanta 170 (2017) 74−80.

[11] M. Zhang, L. Xing, H. Ke, Y.J. He, P.F. Cui, Y. Zhu, et al., MnO_2-based nanoplatform serves as drug vehicle and MRI contrast agent for cancer theranostics, ACS Appl. Mater. Interfaces 9 (2017) 11337−11344.

[12] M.M.Y.A. Alsaif, A.F. Chrimes, T. Daeneke, S. Balendhran, D.O. Bellisario, Y. Son, et al., High-performance field effect transistors using electronic inks of 2D molybdenum oxide nanoflakes, Adv. Funct. Mater. 26 (2016) 91−100.

[13] F. Haque, T. Daeneke, K. Kalantar-zadeh, J.Z. Ou, Two-dimensional transition metal oxide and chalcogenide-based photocatalysts, Nano-Micro Lett. 10 (2018) 23.

[14] Y. Dou, Atomically thin transition metal oxides for energy conversion and storage, in: A Thesis Submitted for Fulfilment of the Requirements for the Award of the Degree Doctor of Philosophy, University of Wollongong, November 16, **2016**.

[15] J. Chen, H. Meng, Y. Tian, R. Yang, D. Du, Z. Li, et al., Recent advances in functionalized MnO_2 nanosheets for biosensing and biomedicine applications, Nanoscale Horiz. 4 (2019) 321−338.

[16] M.N. Grisolia, J. Varignon, S. Sanchez-Santolino, A. Arora, S. Valencia, M. Varela, et al., Hybridization-controlled charge transfer and induced magnetism at correlated oxide interfaces, Nat. Phys. 12 (2016) 484−492.
[17] C. Zhao, H. Zhang, W. Si, H. Wu, Mass production of two-dimensional oxides by rapid heating of hydrous chlorides, Nat. Commun. 7 (2016) 12543.
[18] C. Tan, X. Cao, X.-J. Wu, Q. He, J. Yang, X. Zhang, et al., Recent advances in ultrathin two-dimensional nanomaterials, Chem. Rev. 117 (9) (2017) 6225−6231.
[19] Z. Wang, W. Zhu, Y. Qiu, X. Yi, A. von dem Bussche, A. Kane, et al., Biological and environmental interactions of emerging two-dimensional nanomaterials, Chem. Rev. 45 (2016) 1750−1780.
[20] Y. Hao, L. Wang, B. Zhang, H. Zhao, M. Niu, Y. Hu, et al., Multifunctional nanosheets based on folic acid modified manganese oxide for tumor-targeting theranostic application, Nanotechnology 27 (2016) 025101.
[21] G. Song, J. Hao, C. Liang, T. Liu, M. Gao, L. Cheng, et al., Degradable molybdenum oxide nanosheets with rapid clearance and efficient tumor homing capabilities as a therapeutic nanoplatform, Angew. Chem. Int. Ed. 55 (2016) 2122−2126.
[22] M. Wu, P. Hou, L. Dong, L. Cai, Z. Chen, M. Zhao, et al., Manganese dioxide nanosheets: from preparation to biomedical applications, Int. J. Nanomed. 14 (2019) 4781−4800.
[23] J. Li, B. Du, Y. Li, Y. Wang, D. Wu, Q. Wei, A turn-on fluorescent sensor for highly sensitive mercury (II) detection based on a carbon dot-labeled oligodeoxyribonucleotide and MnO_2 nanosheets, N. J. Chem. 42 (2018) 1228−1234.
[24] H. Ouyang, Q. Lu, W. Wang, Y. Song, X. Tu, C. Zhu, et al., Dual-readout immunochromatographic assay by utilizing MnO_2 nanoflowers as the unique colorimetric/chemiluminescent probe, Anal. Chem. 90 (2018) 5147−5152.
[25] H.-B. Wang, Y. Li, H.-Y. Bai, Y.-M. Liu, DNA-templated Au nanoclusters and MnO_2 sheets: a label-free and universal fluorescence biosensing platform, Sens. Actuat. B: Chem. 259 (2018) 204−210.
[26] T. Xiao, J. Sun, J. Zhao, S. Wang, G. Liu, X. Yang, FRET effect between fluorescent polydopamine nanoparticles and MnO_2 nanosheets and its application for sensitive sensing of alkaline phosphatase, ACS Appl. Mater. Interfaces 10 (2018) 6560−6569.
[27] X. Yan, Y. Song, C. Zhu, H. Li, D. Du, X. Su, et al., MnO_2 nanosheet-carbon dots sensing platform for sensitive detection of organophosphorus pesticides, Anal. Chem. 90 (2018) 2618−2624.
[28] D. Zeng, L. Wang, L. Tian, S. Zhao, X. Zhang, H. Li, Synergistic photothermal/photodynamic suppression of prostatic carcinoma by targeted biodegradable MnO_2 nanosheets, Drug. Deliv. 26 (1) (2019) 661−672.
[29] Q. Chen, L. Feng, J. Liu, W. Zhu, Z. Dong, Y. Wu, et al., Intelligent albumin-MnO_2 nanoparticles as pH-/H_2O_2-responsive dissociable nanocarriers to modulate tumor hypoxia for effective combination therapy, Adv. Mater. 28 (2016) 7129−7136.
[30] H. Fan, G. Yan, Z. Zhao, X. Hu, W. Zhang, H. Liu, et al., A smart photosensitizer-manganese dioxide nanosystem for enhanced photodynamic therapy by reducing glutathione levels in cancer cells, Angew. Chem. 55 (2016) 5477−5482.
[31] B.A. Othman, C. Greenwood, A.F. Abuelela, A.A. Bharath, S. Chen, I. Theodorou, et al., Correlative light-electron microscopy shows RGD-targeted ZnO nanoparticles dissolve in the intracellular environment of triple negative breast cancer cells and cause apoptosis with intratumor heterogeneity, Adv. Healthc. Mater. 5 (11) (2016) 1310−1325.

[32] P. Zhu, Z. Weng, X. Li, X. Liu, S. Wu, K.W.K. Yeung, et al., Biomedical applications of functionalized ZnO nanomaterials: from biosensors to bioimaging, Adv. Mater. Interfaces 3 (1) (2016). Article ID 1500494.
[33] W. Zhu, Z. Dong, T. Fu, J. Liu, Q. Chen, Y. Li, et al., Modulation of hypoxia in solid tumor microenvironment with MnO_2 nanoparticles to enhance photodynamic therapy, Adv. Func. Mater. 26 (2016) 5490−5498.
[34] R. Dhivya, J. Ranjani, P.K. Bowen, J. Rajendhran, J. Mayandi, J. Annaraj, "Biocompatible curcumin loaded PMMA-PEG/ZnO nanocomposite induce apoptosis and cytotoxicity in human gastric cancer cells, Mater. Sci. Eng.: C. 80 (2017) 59−68.
[35] L. Jingjing, C. Qian, Z. Wenwen, Y. Xuan, Y. Yu, D. Ziliang, et al., Nanoscale-coordination-polymer-shelled manganese dioxide composite nanoparticles: a multistage redox/pH/H_2O_2-responsive cancer theranostic nanoplatform, Adv. Func. Mater. 27 (2017) 1605926.
[36] S. Zhang, Y. Sunami, H. Hashimoto, Nanosheet technology towards biomedical application, Nanomaterials (Basel) 7 (9) (2017) 246.
[37] E.A. Gavrilenko, D.A. Goncharova, I.N. Lapin, A.L. Nemoykina, V.A. Svetlichnyi, A. A. Aljulaih, et al., Comparative study of physicochemical and antibacterial properties of ZnO nanoparticles prepared by laser ablation of Zn target in water and air, Mater. (Basel) 12 (1) (2019) 186.
[38] R. Raliya, T.S. Chadha, K. Hadad, P. Biswas, Perspective on nanoparticle technology for biomedical use, Curr. Pharm. Des. 22 (17) (2016) 2481−2490.
[39] E. Sánchez-López, M. Ettcheto, M.A. Egea, M. Espina, A. Cano, A.C. Calpena, et al., Memantine loaded PLGA PEGylated nanoparticles for Alzheimer's disease: in vitro and in vivo characterization, J. Nanobiotechnol. 16 (2018) 32.
[40] J.S. Suk, Q. Xu, N. Kim, J. Hanes, L.M. Ensign, PEGylation as a strategy for improving nanoparticle-based drug and gene delivery, Adv. Drug. Deliv. Rev. 99 (Pt A) (2016) 28−51.
[41] H. Sharma, K. Kumar, C. Choudhary, P.K. Mishra, B. Vaidya, Development and characterization of metal oxide nanoparticles for the delivery of anticancer drug, Artif. Cells, Nanomedicine, Biotechnol. 44 (2) (2016) 672−679.
[42] M. Martinez-Carmona, Y. Gun'ko, M. Vallet-Regi, ZnO nanostructures for drug delivery and theranostic applications, Nanomaterials 8 (4) (2018) 268.
[43] E. Moghimipour, M. Rezaei, Z. Ramezani, M. Kouchak, M. Amini, K.A. Angali, et al., Transferrin targeted liposomal 5-fluorouracil induced apoptosis via mitochondria signaling pathway in cancer cells, Life Sci. 194 (2017) 104−110.
[44] B. Moghaddam, M. Moniri, S. Azizi, R.A. Rahim, A. Bin Ariff, M. Navaderi, et al., Eco-friendly formulated zinc oxide nanoparticles: induction of cell cycle arrest and apoptosis in the MCF-7 cancer cell line, Genes 8 (10) (2017) 281.
[45] M. Chandrasekaran, M. Pandurangan, In vitro selective anti-proliferative effect of zinc oxide nanoparticles against co-cultured C2C12 myoblastoma cancer and 3T3-L1 normal cells, Biol. Trace Elem. Res. 172 (1) (2016) 148−154.
[46] D.P. Bai, X.F. Zhang, G.L. Zhang, Y.F. Huang, S. Gurunathan, Zinc oxide nanoparticles induce apoptosis and autophagy in human ovarian cancer cells, Int. J. Nanomed. 12 (2017) 6521−6535.
[47] L. Wang, C. Hu, L. Shao, The antimicrobial activity of nanoparticles: present situation and prospects for the future, Int. J. Nanomed. 12 (2017) 1227−1249.
[48] J. Wang, J.S. Lee, D. Kim, L. Zhu, Exploration of zinc oxide nanoparticles as a multitarget and multifunctional anticancer nanomedicine, ACS Appl. Mater. Interfaces 9 (46) (2017) 39971−39984.

[49] S.B. Ghaffari, M.H. Sarrafzadeh, Z. Fakhroueian, S. Shahriari, M.R. Khorramizadeh, Functionalization of ZnO nanoparticles by 3-mercaptopropionic acid for aqueous curcumin delivery: synthesis, characterization, and anticancer assessment, Mater. Sci. Eng.: C. 79 (2017) 465−472.
[50] Y. Li, C. Zhang, L. Liu, Y. Gong, Y. Xie, Y. Cao, The effects of baicalein or baicalin on the colloidal stability of ZnO nanoparticles (NPs) and toxicity of NPs to Caco-2 cells, Toxicol. Mech. Methods 28 (3) (2017) 167−176.
[51] K.C. Biplab, S.N. Paudel, S. Rayamajhi, D. Karna, S. Adhikari, B.G. Shrestha, et al., Enhanced preferential cytotoxicity through surface modification: synthesis, characterization and comparative in vitro evaluation of TritonX-100 modified and unmodified zinc oxide nanoparticles in human breast cancer cell (MDA-MB-231), Chem. Cent. J. 10 (1) (2016) 2016.
[52] F. Namvar, S. Azizi, H.S. Rahman, R. Mohamad, A. Rasedee, M. Soltani, et al., Green synthesis, characterization, and anticancer activity of hyaluronan/zinc oxide nanocomposite, Onco Targets Ther. 9 (2016) 4549−4559.
[53] S. Chakraborti, S. Chakraborty, S. Saha, A. Manna, S. Banerjee, A. Adhikary, et al., PEG-functionalized zinc oxide nanoparticles induce apoptosis in breast cancer cells through reactive oxygen species-dependent impairment of DNA damage repair enzyme NEIL2, Free. Radic. Biol. Med. 103 (2017) 35−47.
[54] J. Jiang, J. Pi, J. Cai, The advancing of zinc oxide nanoparticles for biomedical applications, Bioinorg. Chem. Appl. 2018 (2018) 1062562.
[55] C. Mahendra, M. Murali, G. Manasa, P. Ponnamma, M.R. Abhilash, T.R. Lakshmeesha, et al., Antibacterial and antimitotic potential of bio-fabricated zinc oxide nanoparticles of *Cochlospermum religiosum* (L.), Microb. Pathogenesis 110 (2017) 620−629.
[56] R. Ishwarya, B. Vaseeharan, S. Kalyani, B. Banumathi, M. Govindarajan, N.S. Alharbi, et al., Facile green synthesis of zinc oxide nanoparticles using *Ulva lactuca* seaweed extract and evaluation of their photocatalytic, antibiofilm and insecticidal activity, J. Photochem. Photobio. B: Biol. 178 (2018) 249−258.
[57] R. Dhivya, J. Ranjani, J. Rajendhran, J. Mayandi, J. Annaraj, Enhancing the anti-gastric cancer activity of curcumin with biocompatible and pH sensitive PMMA-AA/ZnO nanoparticles, Mater. Sci. Eng.: C. 82 (2018) 182−189.
[58] M. Divya, B. Vaseeharan, M. Abinaya, S. Vijayakumar, M. Govindarajan, N.S. Alharbi, et al., Biopolymer gelatin-coated zinc oxide nanoparticles showed high antibacterial, antibiofilm and anti-angiogenic activity, J. Photochem. Photobiol. B: Biol. 178 (2018) 211−218.
[59] P. Horky, S. Skalickova, L. Urbankova, D. Baholet, S. Kociova, Z. Bytesnikova, et al., Zinc phosphate-based nanoparticles as a novel antibacterial agent: *in vivo* study on rats after dietary exposure, J. Anim. Sci. Biotechnol. 10 (2019) 17.
[60] A. Iswarya, B. Vaseeharan, M. Anjugam, B. Ashokkumar, M. Govindarajan, N.S. Alharbi, et al., Multipurpose efficacy of ZnO nanoparticles coated by the crustacean immune molecule β-1,3-glucan binding protein: toxicity on HepG2 liver cancer cells and bacterial pathogens, Colloids Surf. B − Biointerfaces 158 (2017) 257−269.
[61] S. Sarwar, S. Chakraborti, S. Bera, I.A. Sheikh, K.M. Hoque, P. Chakrabarti, The antimicrobial activity of ZnO nanoparticles against *Vibrio cholerae*: variation in response depends on biotype, Nanomed.: Nanotechnol., Biol. Med. 12 (6) (2016) 1499−1509.
[62] S. Sarwar, A. Ali, M. Pal, P. Chakrabarti, Zinc oxide nanoparticles provide anti-cholera activity by disrupting the interaction of cholera toxin with the human GM1 receptor, J. Biol. Chem. 292 (44) (2017) 18303−18311.

[63] A. Nazarizadeh, S. Asri-Rezaie, Comparative study of antidiabetic activity and oxidative stress induced by zinc oxide nanoparticles and zinc sulfate in diabetic rats, AAPS PharmSciTech 17 (4) (2016) 834−843.
[64] S.N. Seclen, M.E. Rosas, A.J. Arias, C.A. Medina, Elevated incidence rates of diabetes in Peru: report from PERUDIAB, a national urban population-based longitudinal study, BMJ Open. Diabetes Res. Care 5 (1) (2017). Article ID e000401.
[65] J. Hussein, M. El-Banna, T.A. Razik, M.E. El-Naggar, Biocompatible zinc oxide nanocrystals stabilized via hydroxyethyl cellulose for mitigation of diabetic complications, Int. J. Biol. Macromol. 107 (2018) 748−754.
[66] R.J. Toncic, B. Marinovic, The role of impaired epidermal barrier function in atopic dermatitis, Acta Dermatovenerol. Croat. 24 (2) (2016) 95−109.
[67] P. Thatoi, R.G. Kerry, S. Gouda, G. Das, K. Pramanik, H. Thatoi, et al., Photomediated green synthesis of silver and zinc oxide nanoparticles using aqueous extracts of two mangrove plant species, *Heritiera fomes* and *Sonneratia apetala* and investigation of their biomedical applications, J. Photochem. Photobiol. B: Biol. 163 (2016) 311−318.
[68] L. Sarma, T. Sarmah, N. Aomoa, S. Sarma, U. Deshpande, H. Bhuyan, et al., Size-controlled synthesis of superparamagnetic iron-oxide and iron-oxide/iron/carbon nanotube nanocomposites by supersonic plasma expansion technique, J. Phys. D: Appl. Phys. 51 (2018) 195003.
[69] E.J. Ibrahem, K.M. Thalij, A.S. Badawy, Antibacterial potential of magnesium oxide nanoparticles synthesized by *Aspergillus niger*, Biotechnol. J. Int. 18 (1) (2017) 1−7. Article no. BJI.29534.
[70] L. Cai, J. Chen, Z. Liu, H. Wang, H. Yang, W. Ding, Magnesium oxide nanoparticles: effective agricultural antibacterial agent against *Ralstonia solanacearum*, Front. Microbiol. 9 (2018) 790.
[71] P. Singh, A. Garg, S. Pandit, V.R.S.S. Mokkapati, I. Mijakovic, Antimicrobial effects of biogenic nanoparticles, Nanomaterials 8 (2018) 1009.
[72] W.B. Ayinde, M.W. Gitari, M. Muchindu, A. Samie, Biosynthesis of ultrasonically modified Ag-MgO nanocomposite and its potential for antimicrobial activity, J. Nanotechnol. 2018 (2018). Article ID 9537454.
[73] U.L. Senarathna, S.S. Fernando, C.P. Gunasekara, M.M. Weerasekera, H.G. Hewageegana, N.D. Arachchi, et al., Enhanced antibacterial activity of TiO_2 nanoparticle surface modified with *Garcinia zeylanica* extract, Chem. Cent. J. 11 (2017) 7.
[74] S.S.N. Fernando, T.D.C.P. Gunasekara, J. Holton, Antimicrobial nanoparticles: applications and mechanisms of action, Sri Lankan J. Infect. Dis. 8 (1) (2018) 2−11.
[75] M.M. Wang, R. Cao, W.G. Jiang, Y.K. Liu, F. Yang, L.X. Yuea, et al., Long-term exposure to low doses of fresh and aged zinc oxide nanoparticles causes cell malignant progression enhanced by a tyrosine phosphatase SHP2 gain-of-function mutation, Environ. Sci.: Nano 6 (2019) 2389−2404.
[76] B. Khameneh, R. Diab, K. Ghazvini, B.S.F. Bazzaz, Breakthroughs in bacterial resistance mechanisms and the potential ways to combat them, Microb. Pathog. 95 (2016) 32−42.
[77] L. Miao, C. Wang, J. Hou, P. Wang, Y. Ao, Y. Li, et al., Aggregation and removal of copper oxide (CuO) nanoparticles in wastewater environment and their effects on the microbial activities of wastewater biofilms, Bioresour. Technol. 216 (2016) 537−544.
[78] Q. Yu, J. Li, Y. Zhang, Y. Wang, L. Liu, M. Li, Inhibition of gold nanoparticles (AuNPs) on pathogenic biofilm formation and invasion to host cells, Sci. Rep. 6 (2016) 26667.

[79] M. Daeihamed, S. Dadashzadeh, A. Haeri, M.F. Akhlaghi, Potential of liposomes for enhancement of oral drug absorption, Curr. Drug Deliv. 2016 (2016). January, 15.
[80] P.P.N.S. Garcia, M.F.B. Cardia, R.S. Francisconi, L.N. Dovigo, D.M.P. Spolidório, A. N. de Souza Rastelli, et al., Antibacterial activity of glass ionomer cement modified by zinc oxide nanoparticles, Microscopy Res. Tech. (2016). Available from: https://doi.org/10.1002/jemt.22814.
[81] M. Kachoei, A. Nourian, B. Divband, Z. Kachoei, S. Shirazi, Zinc-oxide nanocoating for improvement of the antibacterial and frictional behavior of nickel titanium alloy, Nanomed. (Lond.) 11 (2016) 2511−2527.
[82] A.-C. Burdusel, O. Gherasim, A.M. Grumezescu, L. Mogoanta, A. Ficai, E. Andronescu, Biomedical applications of silver nanoparticles: an up-to-date overview, Nanomaterials 8 (2018) 681.
[83] P.V. Baptista, M.P. McCusker, A. Carvalho, D.A. Ferreira, N.M. Mohan, M. Martins, et al., Nano-strategies to fight multidrug resistant bacteria − "a battle of the titans", Front. Microbiol. 9 (2018) 1441.
[84] M.S. Baig, A. Ahad, M. Aslam, S.S. Imam, M. Aqil, A. Ali, Application of Box-Behnken design for preparation of levofloxacin-loaded stearic acid solid lipid nanoparticles for ocular delivery: optimization, in vitro release, ocular tolerance, and antibacterial activity, Int. J. Biol. Macromol. 85 (2016) 258−270.
[85] H. Liu, J. Zhang, X. Chen, X.-S. Du, J.-L. Zhang, G. Liu, et al., Application of iron oxide nanoparticles in glioma imaging and therapy: from bench to bedside, Nanoscale 8 (2016) 7808−7826.
[86] E.K. Lim, B.H. Chung, S.J. Chung, Recent advances in pH-sensitive polymeric nanoparticles for smart drug delivery in cancer therapy, Curr. Drug. Targets (2016). June, 2.
[87] J. Wu, Y. Shen, W. Jiang, W. Jiang, Y. Shen, Magnetic targeted drug delivery carriers encapsulated with pH-sensitive polymer: synthesis, characterization and in vitro doxorubicin release studies, J. Biomater. Sci. Polym. Ed. 27 (13) (2016) 1303−1316.
[88] S. Yun, J.J. Huang, Routes for drug delivery: sustained-release devices, Dev. Ophthalmol. 55 (2016) 84−92.
[89] A. Mukherjee, A.K. Waters, P. Kalyan, A.S. Achrol, S. Kesari, V.M. Yenugonda, Lipid−polymer hybrid nanoparticles as a next-generation drug delivery platform: state of the art, emerging technologies, and perspectives, Int. J. Nanomed. 14 (2019) 1937−1952.
[90] R. Wu, X. Ou, R. Tian, J. Zhang, H. Jin, M. Dong, et al., Membrane destruction and phospholipid extraction by using two-dimensional MoS_2 nanosheets, Nanoscale 10 (43) (2018) 20162−20170.
[91] H. Lin, Y. Chen, J. Shi, Insights into 2D MXenes for versatile biomedical applications: current advances and challenges ahead, Adv. Sci. (Weinh.) 5 (10) (2018) 1800518.
[92] M. Soleymaniha, M.A. Shahbazi, A.R. Rafieerad, A. Maleki, A. Amiri, Promoting role of MXene nanosheets in biomedical sciences: therapeutic and biosensing innovations, Adv. Health Mater. 8 (1) (2019) e1801137.
[93] T.I. Kim, B. Kwon, J. Yoon, I.J. Park, G.S. Bang, Y. Park, et al., Antibacterial activities of graphene oxide-molybdenum disulfide nanocomposite films, ACS Appl. Mater. Interfaces 9 (9) (2017) 7908−7917.
[94] F. Alimohammadi, G.M. Sharifian, N.H. Attanayake, A.C. Thenuwara, Y. Gogotsi, B. Anasori, et al., Antimicrobial properties of 2D MnO_2 and MoS_2 nanomaterials vertically aligned on graphene materials and Ti_3C_2 Mxene, Langmuir 34 (24) (2018) 7192−7200.

[95] S. Zhang, L. Wang, X. Liang, J. Vorstius, R. Keatch, G. Corner, et al., Enhanced antibacterial and antiadhesive activities of silver-PTFE nanocomposite coating for urinary catheters, ACS Biomater. Sci. Eng. 56 (2019) 2804−2814.
[96] J.L. Liu, W.J. Zhang, X.D. Li, N. Yang, W.S. Pan, J. Kong, et al., Sustained-release genistein from nano-structured lipid carrier suppresses human lens epithelial cell growth, Int. J. Ophthalmol. 9 (5) (2016) 643−649.
[97] A.P. Ramos, M.A.E. Cruz, C.B. Tovani, P. Ciancaglini, Biomedical applications of nanotechnology, Biophys. Rev. 9 (2) (2017) 79−89.
[98] W. Liu, S. Liu, L. Wang, Surface modification of biomedical titanium alloy: micromorphology, microstructure evolution and biomedical applications, Coatings 9 (2019) 249.
[99] S. Huang, N. Liang, Y. Hu, X. Zhou, N. Abidi, Polydopamine-assisted surface modification for bone biosubstitutes, BioMed. Res. Int. 2016 (2016). Article ID 2389895.
[100] K.M. Hotchkiss, G.B. Reddy, S.L. Hyzy, Z. Schwartz, B.D. Boyan, R. Olivares-Navarrete, Titanium surface characteristics, including topography and wettability, alter macrophage activation, Acta Biomater. 31 (2016) 425−434.
[101] J. Jeong, J.H. Kim, J.H. Shim, N.S. Hwang, C.Y. Heo, Bioactive calcium phosphate materials and applications in bone regeneration, Biomater. Res. 23 (2019). Article No: 4.
[102] V.K.H. Bui, D. Park, Y.-C. Lee, Chitosan combined with ZnO, TiO_2 and Ag nanoparticles for antimicrobial wound healing applications: a mini review of the research trends, Polym. (Basel) 9 (1) (2017) 21.
[103] A.K. Barui, S.K. Nethi, C.R. Patra, Investigation of the role of nitric oxide driven angiogenesis by zinc oxide nanoflowers, J. Mater. Chem. B 5 (2017) 3391−3403.
[104] S.K. Nethi, S. Das, C.R. Patra, S. Mukherjee, Recent advances in inorganic nanomaterials for wound-healing applications, Biomater. Sci. 7 (2019) 2652−2674.
[105] G. Păunica-Panea, A. Ficai, M.M. Marin, S. Marin, M.G. Albu, V.D. Constantin, et al., New collagen-dextran-zinc oxide composites for wound dressing, J. Nanomaterials (2016). Article ID 5805034.
[106] F. Wahid, J.J. Yin, D.D. Xue, H. Xue, Y.S. Lu, C. Zhong, et al., Synthesis and characterization of antibacterial carboxymethyl Chitosan/ZnO nanocomposite hydrogels, Int. J. Biol. Macromol. 88 (2016) 273−279.
[107] P. Mekhail, S. Chaturvedi, S. Chaturvedi, Surgical Management of Wounds, **2016**, text @ <www.intechopen.com/books/wound-healing-new-insights-into-ancient-challenges/surgical-management-of-wounds>.
[108] S. Hamdan, I. Pastar, S. Drakulich, E. Dikici, M. Tomic-Canic, S. Deo, et al., Nanotechnology-driven therapeutic interventions in wound healing: potential uses and applications, ACS Cent. Sci. 3 (3) (2017) 163−175.
[109] R. Rakhshaei, H. Namazi, A potential bioactive wound dressing based on carboxymethyl cellulose/ZnO impregnated MCM-41 nanocomposite hydrogel, Mater. Sci. Eng. C: Mater. Biol. Appl. 73 (2017) 456−464.
[110] S. Farhoudian, M. Yadollahi, H. Namazi, Facile synthesis of antibacterial chitosan/CuO bio-nanocomposite hydrogel beads, Int. J. Biol. Macromol. 82 (2016) 837−843.
[111] F. Wahid, H.S. Wang, Y.S. Lu, C. Zhong, L.Q. Chu, Preparation, characterization and antibacterial applications of carboxymethyl chitosan/CuO nanocomposite hydrogels, Int. J. Biol. Macromol. 101 (2017) 690−695.
[112] Y.-S. Li, Y. Han, J.-T. Qin, Z.-Y. Song, H.-H. Cai, J.-F. Du, et al., Photosensitive antibacterial and cytotoxicity performances of a TiO_2/carboxymethyl chitosan/poly(vinyl

alcohol) nano composite hydrogel by in situ radiation construction, J. Appl. Polym. Sci. 133 (2016) 44150.
[113] N.U. Saqib, R. Adnan, I. Shah, A mini-review on rare earth metal-doped TiO_2 for photo catalytic remediation of wastewater, Environ. Sci. Pollut. Res. 23 (2016) 15941−15951.
[114] B. Yang, Y. Chen, J. Sh, Material chemistry of two-dimensional inorganic nanosheets in cancer theranostics, Chem 4 (6) (2018) 1284−1313.
[115] Z. Zare-Akbari, H. Farhadnejad, B. Furughi-Nia, S. Abedin, M. Yadollahi, M. Khorsand-Ghayeni, PH-sensitive bionanocomposite hydrogel beads based on carboxymethyl cellulose/ZnO nanoparticle as drug carrier, Int. J. Biol. Macromol. 93 (A) (2016) 1317−1327.
[116] M. Yadollahi, S. Farhoudian, S. Barkhordari, I. Gholamali, H. Farhadnejad, H. Motasadizadeh, Facile synthesis of chitosan/ZnO bio-nanocomposite hydrogel beads as drug delivery systems, Int. J. Biol. Macromol. 82 (2016) 273−278.
[117] Y. He, S. Ingudam, S. Reed, A. Gehring, T.P. Strobaugh Jr, P. Irwin, Study on the mechanism of antibacterial action of magnesium oxide nanoparticles against foodborne pathogens, J. Nanobiotechnol. 14 (1) (2016) 54.
[118] N. Kavanagh, E.J. Ryan, A. Widaa, G. Sexton, J. Fennell, S. O'Rourke, et al., Staphylococcal osteomyelitis: disease progression, treatment challenges, and future directions, Clin. Microbiol. Rev. 31 (2) (2018). 14, 00084-17.
[119] S. Cavalu, Acrylic bone cements: new insight and future perspective, Key Eng. Mater. 745 (2017) 39−49.
[120] C.M. Ghiciuc, O.N. Ghiciuc, L. Ochiuz, C.E. Lupuşoru, Antibacterial effects of metal oxides-containing nanomaterials in dentistry, in: The Sixth IEEE Int. Conf. E-Health and Bioengineering − EHB-2017, G. T. Popa University of Medicine and Pharmacy, Sinaia, Romania, June 22−24, **2017**.
[121] M.A. Ibrahim, B.M. Priyadarshini, J. Neo, A.S. Fawzy, Characterization of chitosan/TiO_2 nano-powder modified glass-ionomer cement for restorative dental applications, J, Esthetic Restor. Dent. (2017). Available from: https://doi.org/10.1111/jerd.12282.
[122] L. Duffy, M.J. Osmond-McLeod, J. Judy, T. King, Investigation into the antibacterial activity of silver, zinc oxide and copper oxide nanoparticles against poultry-relevant isolates of *Salmonella* and *Campylobacter*, Food Control. 92 (2018) 293−300.
[123] X. Kuang, V. Chen, X. Xu, Novel approaches to the control of oral microbial biofilms, BioMed. Res. Int. 2018 (2018). Article ID 6498932.
[124] F. Iolanda, V. Claudia, P. Antonella, Antifouling and antimicrobial biomaterials: an overview, J. Pathol. Microbiol. Immuno. Spec. Issue: Biofilm Infect. 125 (4) (2017) 392−417.
[125] V.V. Zakharova, C. Dib, Y.B. Saada, Y.S. Vassetzky, I.I. Galkin, B.V. Chernyak, et al., Uncoupling of oxidative phosphorylation and antioxidants affect fusion of primary human myoblasts in vitro, Biopolym. Cell 32 (2) (2016) 111−117.
[126] S.B. Gunnarsson, Nanostructure and biomolecule interactions characterizing the complex, in: Doctoral Dissertation Submitted to the Faculty of Science, Lund University, Sweden, **2018**.
[127] G. Cheloni, V.I. Slaveykova, Photo-oxidative stress in green algae and cyanobacteria, Reactive Oxyg. Species 5 (14) (2018) 126−133.
[128] K. Gold, B. Slay, M. Knackstedt, A.K. Gaharwar, Antimicrobial activity of metal and metal-oxide based nanoparticles, Adv. Ther. 1 (3) (2018) 1700033.

[129] B. Lallo da Silva, B.L. Caetano, B.G. Chiari-Andréo, R.C.L.R. Pietro, L.A. Chiavacci, Increased antibacterial activity of ZnO nanoparticles: influence of size and surface modification, Colloids Surf. B: Biointerf 177 (2019) 440−447.
[130] X. Hong, J. Wen, X. Xiong, Y. Hu, Shape effect on the antibacterial activity of silver nano particles synthesized via a microwave assisted method, Environ. Sci. Pollut. Res. Int. 23 (5) (2016) 4489−4497.
[131] J. Podporska-Carroll, A. Myles, B. Quilty, D.E. McCormack, R. Fagana, S.J. Hinder, et al., Antibacterial properties of F-doped ZnO visible light photocatalyst, J. Hazard. Mater. 324 (pt A) (2017) 39−47.
[132] N. Duggal, D. Jaishankar, T. Yadavalli, S. Hadigal, Y.K. Mishra, R. Adelung, et al., Zinc oxide tetrapods inhibit herpes simplex virus infection of cultured corneas, Mol. Vis. 23 (2017) 26−38.
[133] M.F. Khan, A.H. Ansari, M. Hameedullah, E. Ahmad, F.M. Husain, Q. Zia, et al., Sol-gel synthesis of thorn-like ZnO nanoparticles endorsing mechanical stirring effect and their antimicrobial activities: potential role as nano-antibiotics, Sci. Rep. 6 (2016) 27689.
[134] P. Kumar, P. Huo, R. Zhang, B. Liu, Antibacterial properties of graphene-based nanomaterials, Nanomaterials 9 (2019) 737.
[135] A. Jayakumar, A. Surendranath, M. Pv, 2D materials for next generation healthcare applications, Int. J. Pharm. 551 (1−2) (2018) 309−321.
[136] S. Kumar, C. Chen, N. Indugu, G.O. Werlang, M. Singh, W.K. Kim, et al., Effect of antibiotic withdrawal in feed on chicken gut microbial dynamics, immunity, growth performance and prevalence of foodborne pathogens, PLoS One 13 (2) (2018) e0192450.

Mechanical and physical methods for the metal oxide powders production

8

Said M. Al Azar[1,2] *and Ahmad A. Mousa*[2]
[1]Department of Research and Development, Ontario-Academy, Amman, Jordan,
[2]Department of Basic Sciences, Middle East University, Amman, Jordan

8.1 Introduction

There is still a need to design and develop new materials with unique mechanical, physical, and chemical properties by simulating the processing of materials and their applications as well as adjusting their properties using new programs and techniques. Nowadays, numerous new techniques are used to prepare high-quality powders of materials. This will help to innovate and develop many novel technological applications [1,2].

Metal oxide and metal oxide-based powders have been widely studied recently because of their unique optical, electrical, and electronic properties so that they can be used in many demanding technological applications. The industrial area where metal oxides or ceramics powders are used in huge amounts is mechanical and structural applications, electronic and electrical materials, catalysts, pigments, lubricants, and coating of metals [1].

Metal oxide materials can be categorized into two types: first one: simple metal oxides such as periclase (MgO), wustite (FeO), and ferropericlase (MgO + FeO) that have a 1:1 ratio, cuprite (Cu_2O) copper (I) oxide, rutile or anatase (TiO_2), cassiterite (SnO_2), pyrolusite (MnO_2) that have a 2:1 ratio, corundum (Al_2O_3); hematite (Fe_2O_3), that have a 2:3 ratio. The other type is multiple (or mixed) oxide such as spinels and perovskite. The general formula for spinel is AB_2O_4, while for perovskites, it is ABO_3. Examples of spinel are mineral balas ruby $MgA_{l2}O_4$, chromite $FeCr_2O_4$, magnesiochromite ($MgCo_2O_4$), hercynite ($FeA_{l2}O_4$), and magnetite (Fe_3O_4) where Fe is in two oxidation states $Fe^{2+}Fe_2{}^{3+}O_4$ [1].

It is well known that many bulk ceramics are manufactured directly by compacting and sintering their metal oxides powders such as Al_2O_3, TiO_2, ZnO, and ZrO_2. Burke and Turnbull proposed that to produce a material in nonequilibrium phase, we need a sequence to energize and quench processes such as solid-state quenching, melting-solidification, vapor−condensation, and irradiation [3]. On an industrial scale the use of the equipment and raw materials efficiently and reducing energy consumption, as well as taking into consideration environmental issues, has become more important. Therefore the choice of the specific technique for powder

Metal Oxide Powder Technologies. DOI: https://doi.org/10.1016/B978-0-12-817505-7.00008-7

production depends on particle size, shape, purity, microstructure, and chemistry of powder and also on the cost of the process. The physical and mechanical methods to produce the metal oxide powders rely on the most important methods in producing metal oxides powders because they are cheap and easy to produce a huge amount of powders.

By using external dynamic agents, for example, through melting or evaporation process (increasing the temperature), irradiation, the pressure applied, or plastic deformation for energy storing, the equilibrium state is transferred to nonequilibrium state (higher Gibbs free energy). For instance, during rapid solidification, the initial solids are melted, and during vapor deposition, the material evaporates. The active material is then "quenched" into a configurationally frozen state in ways such as rapid solidification or mechanical alloying (MA) so that the resulting phase is in a highly metastable state and has a free energy G1 [4]. Some powder preparation methods allow us to control the product morphology by changing the preparation conditions and parameters. As an example, the shapes of ZnO particles prepared by hydrothermal technique change from ellipsoidal to a long prism-like shape with increasing ammonia concentration [5].

Fig. 8.1 presents a schematic representation of various metal oxide powder production methods. Some mixed methods such as the mechanochemical method and reactive milling technique also could be used to produce powders. This chapter deals with a review of the well-known mechanical and physical techniques to produce the metal oxide powders with a focus on the processes and apparatuses.

8.2 Production of metal oxides powder by using crushing and milling

Mechanical forces such as crushing, grinding, and milling are used to transfer the bulk solids into grains or particles. To choose the specific technique for powder production, some characteristics should be taken into account such as particle size, shape, microstructure, and chemistry of the powder but also the cost of the process. The shape of the individual particles in the powder is an important parameter to prepare the homogeneous microstructure ceramics. Also, the powder particle size is an important factor in the sintering and densification processes where the densification is inversely proportional to the particle size and the volume diffusion is inversely proportional to the 1.5 power of the particle size [6]. As an example, the crushing process produces grains about 1 mm in size, whereas grinding and milling produce micro-sized powders [7].

To produce a small amount of metal oxide powder in the laboratory, we can use some simple methods such as chopping (cutting) or rubbing (abrasion). In the chopping process the material is cut up into small pieces employing a milling cutter. It is difficult and costly to make powders by this technique. The abrasion method could be performed by one of the following techniques: (1) rubbing of two surfaces where the hard surface material removes part of the material from the surface of the

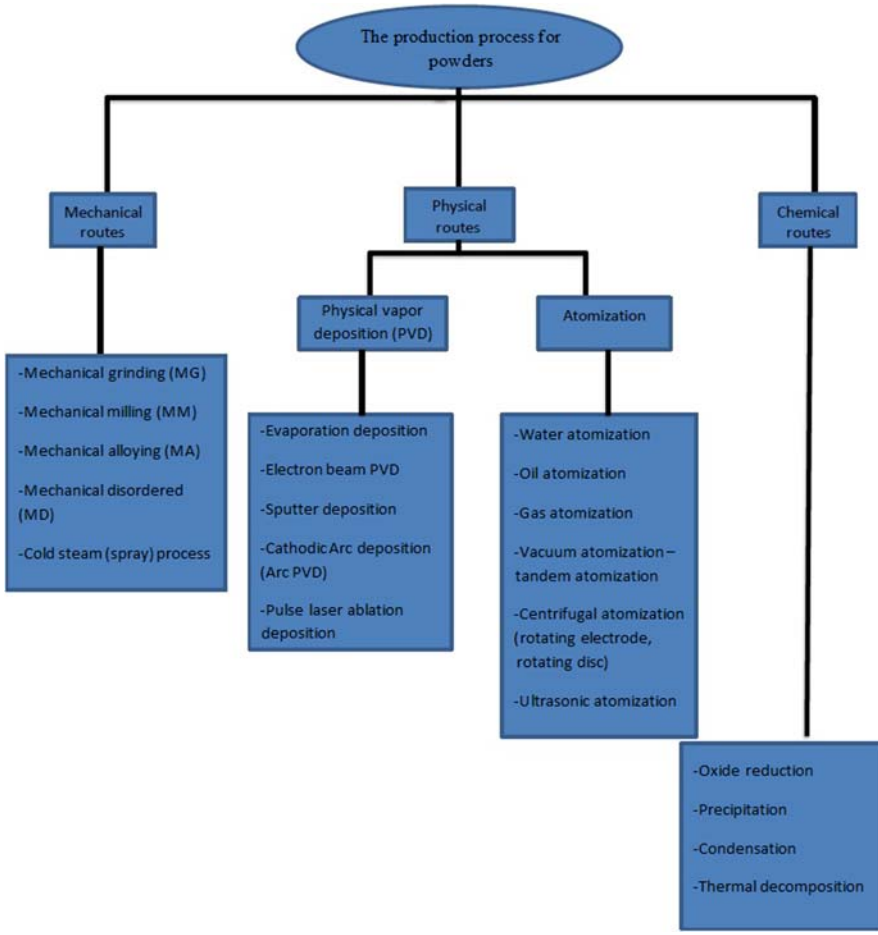

Figure 8.1 Presents schematic representation of various metal oxides powder production methods.

soft material. (2) Filling, this technique could be employed to produce alloy powders, coarse powders of dental alloys, and finer powders. This technique is not feasible commercially. (3) Scratching if a hard pin is used to rub on some soft metal oxides, the powder flakes will be produced. (4) Machining process by using a lathe or a milling cutter to get fine chips and turnings. It could then be reduced further in size by grinding. Machining has two disadvantages, one of them is the lack of control on powder characteristics such as chemical contamination (oxidation, oil, and other impurities), and the other one is irregularity and coarseness of the powder shape. The advantage of machining is consuming scrap from another process [1].

Two main parameters that determine the type of milling technique to produce metal oxides powders on a large scale are as follows: first, the product output

amounts, where the milling technique that produces more quantities of powder is preferable. Second, the contamination of the produced powder, which is affected by the initial purity of input materials, the milling equipment design, the milling processing conditions such as milling speed, the size ratio between milling ball and material powder and atmosphere [8].

The first stage of disintegration is grinding of the metal oxides or raw materials in a jaw crusher. This is performed between a fixed jaw and a moving one, where a coarse metal oxide powder is obtained. Basic disintegration procedures are pressure, shear, wear, and impact. Fig. 8.2 illustrates these procedures. The milling process is carried out under dry or wet conditions and at most used grinding media [7].

Mechanical methods applied to produce natural and synthetic oxide powders are categorized into [1]

1. ball milling is a powder mixing process,
2. attrition milling, and
3. vibration milling.

The classification of mill techniques depending on milling energy is a horizontal ball mill, attritor, planetary ball mill, and vibration ball mill. Fig. 8.3 and Table 8.1 summarized their principles and parameters [9,10].

Fig. 8.4 shows one-dimensional powder production using a high-energy ball mill. Ball milling is most suitable for brittle materials but not suitable for the materials that have ductility and cold welding characteristics. The mechanism in a high energy ball mill to produce fine powder is illustrated in Fig. 8.5. Also, it could be employed to oxidize the metal powder so we obtain metal oxide powders [1].

The limitations of using ball milling to produce metal oxide are as follows [1]:

1. Rubbing action causes contamination of powder since balls may also get rubbed.
2. Working hardening of metal powder is caused during milling.
3. The quality of the powder is poor.
4. Particle welding and agglomeration may take place.

Attrition is a high energy mill consisting of a vertical container, has impellers that rotate along its axis, which in turn agitate the balls inside the drum.

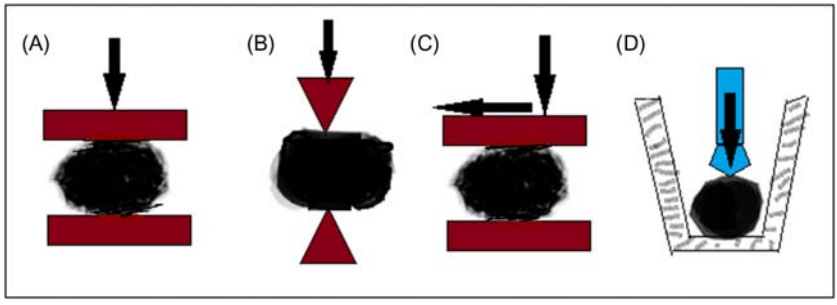

Figure 8.2 The basic disintegration procedures are (A) pressure, (B) shear, (C) wear, and (D) impact.

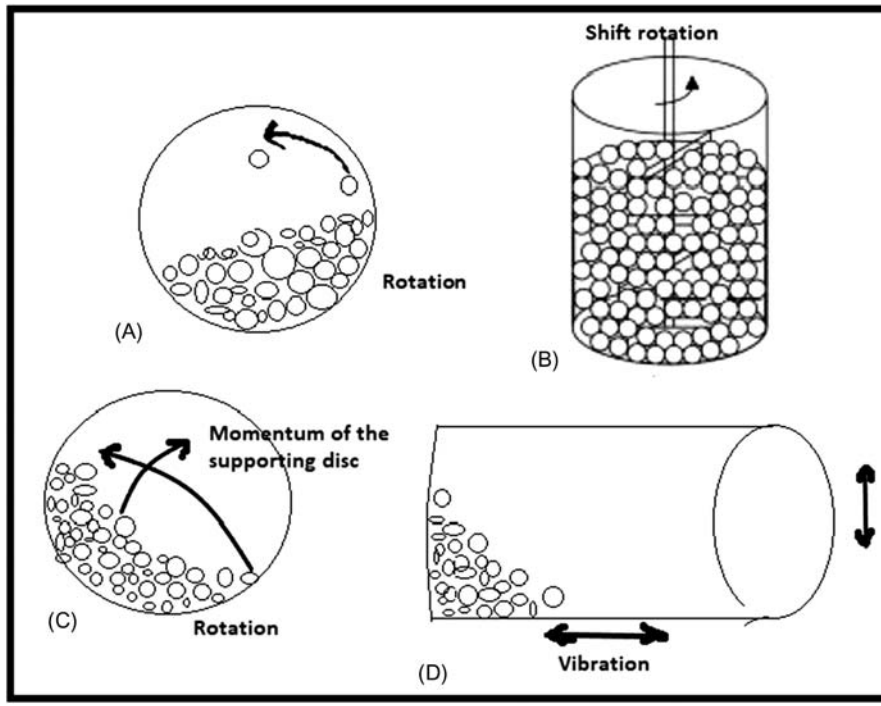

Figure 8.3 Difference milling techniques using to produced powders. (A) horizontal mills, (B) Szegvari attrition mill, (C) planetary ball mill, and (D) shaker vibrating mill.

The materials inside the attritor are affected by different forces such as impact, rotation, tumbling, pressing, and shearing. As a result, the powder starts to form and their particle size reduces with time, and the fine powders are produced. The speed of grinding in attritors is less than planetary and Shaker mills, typically 0.5 m/s this means less energy is consumed [11].

To select the suitable grinding media to use in the milling process, it should be denser than the produced powders and the grinding ball size larger than the produced powder size, but to get fine powders, the grinding ball should be small enough to reach the powder size wanted. Also, the hardness of the grinding media impacts the contamination amount in produced powders. The PH in wet milling is important also discoloration as well as the cost of the media. Lubricants and surface-active agents are used to nullify the welding forces that cause agglomeration [7].

Besides, the types or ratio of contamination in the powders is one of the most important criteria for many novel applications. Sometimes to avoid possible contamination, the balls, stirring rods, and the tank may be made from the same material as the powder produced [12].

Table 8.1 The different milling methods optimal parameters [7].

	Cycle time (h)	Powder amount	Mill speed (rpm)	Ball diameter (mm)	Ball filling level (%)	Powder filling level	Powder size (μm)
Vibrating mill	0.01−0.5	>1 kg (industry) 1 g (laboratory)	1000 (industry) 3300 (laboratory)	1−10			1−10
Planetary ball mill	1−10	10−100 g	80−400	6−30	50−70	1:10 powder to ball weight ratio	5−100
Vertical attritor	0.1−10	100 kg (industry) 100 g (laboratory)	60 (industry) 300 (laboratory)	6−10	70	1:10	5−100
Horizontal attritor	0.1−10	100 kg (industry) 100 g (laboratory)	1800	6−10	30	1:10	5−100
Horizontal ball mill	>10	>1 t	10−50	6−25	50	100% of ball interstices	10−50

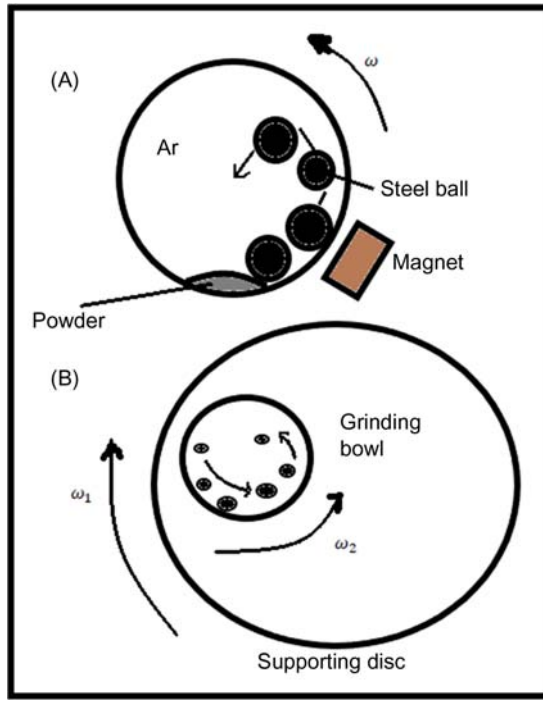

Figure 8.4 One-dimensional nanomaterials synthesized using high energy ball mill. (A) a vertical rotation ball mill and (B) a planetary ball mill.

The empirical relative energy (W) needed for milling may be utilized [13]:

$$W = g \cdot \left(D_k^{-a} - D_p^{-a} \right) \tag{8.1}$$

where g is a constant depending on the material, mill design, and milling conditions; $D_p(m)$ is an initial granularity; and $\boldsymbol{D_k}(m)$ is a final granularity size. The exponent (a) ranges from 1 to 2. As an example, by assuming that the energy rate consume is constant, if time needed to reduce the dimension of material particles, using milling process, from 300 to 110 μm is 8 hours, the time needed to reduce the resultant powder to the 75 μm particles size is 10.6 hours and the energy consumed is about 1.33 times greater.

The critical speed of a tumbling ball mill (V_c) given by

$$V_c = \frac{42.3}{\sqrt{D-d}} \text{rpm} \tag{8.2}$$

where D is the vial diameter and d is the balls diameter.

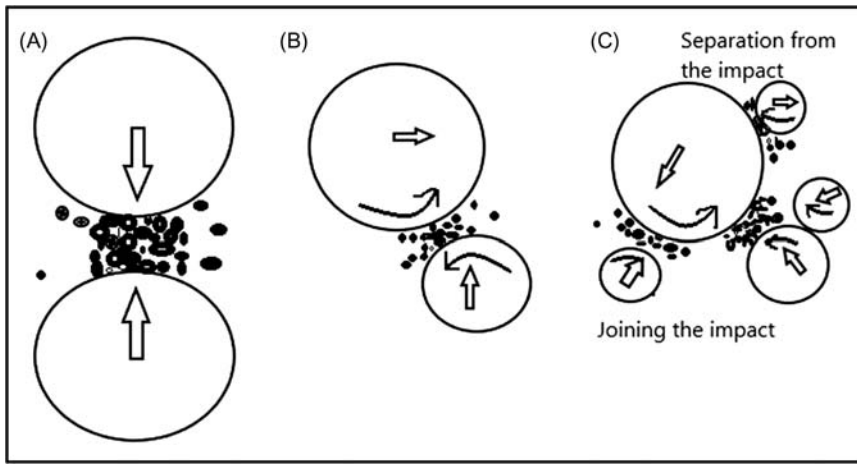

Figure 8.5 Processing of advanced materials using high energy mechanical: (A) head-on impact, (B) oblique impact, and (C) multiball impact.

The high energy ball milling method is one of the important techniques used to prepare large-scale, micro-, and nanosized powders for many applications. It is based on a mechanical energy transfer between hard ball and target materials by colliding action. High-energy ball-mills categorize into three types.

8.2.1 Mechanical alloying

MA is defined as a solid state powder preparation method. It was developed in the mid-1960s. It could be used to prepare a variety of both equilibrium and nonequilibrium alloy phase which involves repeated cold welding and fracturing of powder particles in a dry, high-energy ball milling technique. The properties of produced powders are strongly affected by the process parameters such as milling time, ball-to-powder weight ratio, milling environment, milling media, and rotation speed [14].

One of the main materials produced by MA is oxide-dispersion strengthened (ODS) materials. ODS materials have high strength at room and elevated temperatures, excellent oxidation, and hot corrosion resistance. These characteristics due to the uniform dispersion (with a spacing of around 100 nm) of very fine (5−50 nm) oxide particles (Y_2O_3, ThO_2, and La_2O_3) in superalloys based on Ni or Fe [15,16].

8.2.2 Mechanical milling (MM) or grinding

It describes the process where stoichiometric composition materials such as pure metals, intermetallics, or prealloyed are ground, without requiring for material transfer. In mechanical milling/mechanical disordered (MM/MD) the time of milling is less than in MA because the alloys already exist, where we only reduced the

particle size. Consequently, the oxidation process during the MM powder production reduces [17].

8.2.3 Mechanical disordered

It is a process of producing either disordered intermetallic materials or an amorphous phase by destruction of the long-range order [18].

The main factors that affect the MA, MD, and MM processes are

1. milling time;
2. milling speed;
3. milling media (ball or rods);
4. impurities and milling tools;
5. shape of the milling vials (the internal shape of the vial is flat-ended or concave-ended type);
6. type of mills (drum ball mills, jet ball mills, bead-mills, roller ball mills, vibration ball mills, and planetary ball mills);
7. milling temperature;
8. milling media-to-powder weight ratio;
9. milling environment (dry or wet milling); and
10. milling atmosphere (air, nitrogen, or an inert gas).

$BaTiO_3$ powder prepared by ball milling technique where equal weights of $BaTiO_3$ and KCl were added to ethanol and milled for several minutes stirred for 2 hours and dried at 70°C for 12 hours. After that it calcined in Al_2O_3 crucible at 1100°C for 5 hours with 5°C/min heating/cooling rates [19]. Fig. 8.6 shows field emission scanning electron microscope (FE-SEM) images of a spherical shape copper-doped $BiVO_4$ nanopowder with size ranging from 40 to 160 nm. Furthermore, the inset particle size distribution plots show the reduction in particle sizes for higher Cu-doped samples. The high energy ball-mill technique was used with synthesis parameter such as ball-to-powder ratio (5:1, 8:1, and 10:1) with 6 hours and 11 hours as a milling time and annealed at 450°C under air for 1 hours to prepare Cu-doped $BiVO_4$ powder [20]. Chatterjee et al. in 2003 prepared doped-$BaTiO_3$ powder in solid-state reaction route by using a ball mill of the $BaCO_3$ and TiO_2 with dopant oxides La_2O_3, Sb_2O_3, and MnO [21].

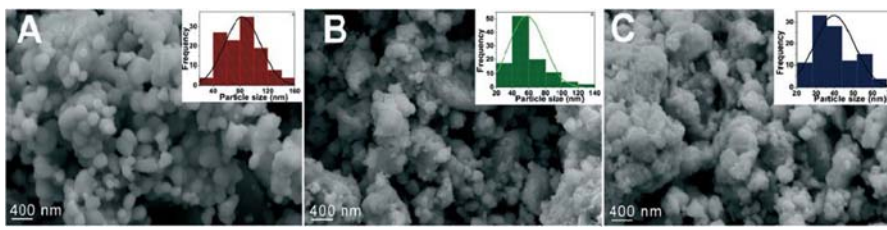

Figure 8.6 FE-SEM images of Cu-doped $BiVO_4$ nanopowders for (A) 1 at%, (B) 5 at%, and (C) 10 at%. The inset shows the particle size distribution [20].

8.3 Production of metal oxides powders using evaporation techniques

8.3.1 Simple (or thermal) evaporation technique

Simple (or thermal) evaporation or is one of the easiest methods to obtain powders from the solutions by evaporating the solvent. In this process the soluble salt solution is heated in a suitable container until the solvent molecules evaporate completely. The remaining result is the dry powdery materials that are calcined at suitable temperature ($\sim 500^{\circ}C$) to get oxide powder. The main process parameters are the temperature, pressure, atmosphere, and evaporation time period. An example of mixed metal oxide powder prepares using this method is lead lanthanum zirconate titanate [22]. One of disadvantages of this method is the lack of control on the powder during the formation. Another disadvantage is the possible segregation of the various components in the solution during transition in the supersaturation stages under heating.

8.3.2 Laser evaporation technique

In 1987 Dijkkamp et al. succeeded in depositing the first Y−Ba−Cu oxide thin films using pulsed excimer laser evaporation technique from a bulk material [23]. Williams and Coles prepared nanopowders of Al_2O_3, ZrO_2, and SnO_2 metal oxide by a laser evaporation method [24]. Popp et al. prepared ceramic nanopowders (nanocrystalline ceramic powders) of ZrO_2 and Al_2O_3 by laser evaporation and recondensation technique [25]. Schemes of the evaporation chambers for rods and coarse powders are illustrated in Fig. 8.7. They established a relationship between evaporation rate and laser power. Also, the particle size distributions were impacted by laser power, area of the laser focus, pulse length in the case of plane wave mode, streaming velocity, and type of the carrier gas. Fig. 8.8 depicts the transmission electron microscopy (TEM) image of laser-evaporated nanopowders of alumina and zirconia where the shape of the particle is spherical. Partil et al. used laser ablation in liquid media to synthesis iron oxide nanostructure using 694 nm light of ruby laser [26] also zinc oxide nanostructures have been synthesized by Singh et al. [27].

There are three types of solvent evaporation technique:

1. freeze-drying technique
2. spray-drying technique
3. spray-pyrolysis technique

8.4 Atomization for metal oxide powder production

Atomization (also called spray drying) is one of the methods used to breakdown materials, usually melting or fluid feedstock, into droplets which upon drying

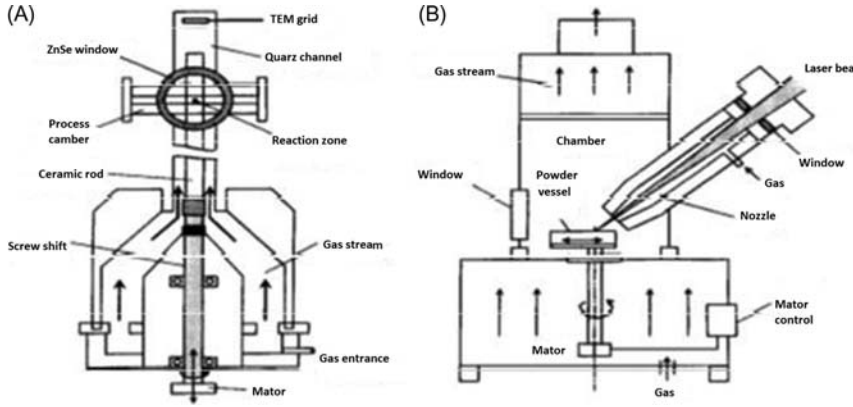

Figure 8.7 Schemes of the evaporation chambers for (A) rods and (B) coarse powders [25].

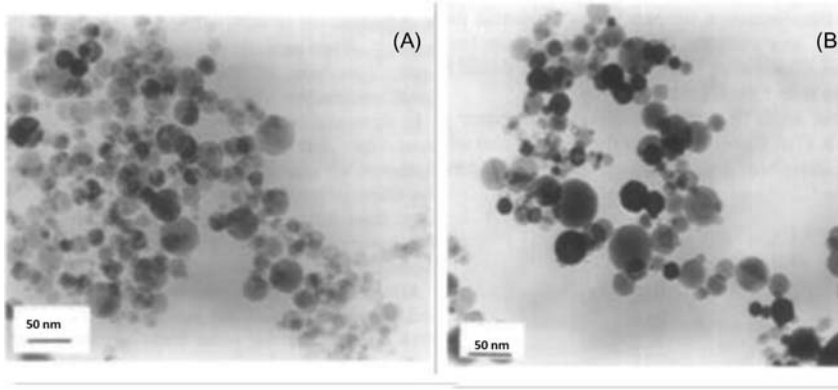

Figure 8.8 TEM image of laser-evaporated nanopowder of (A) alumina (B) zirconia [25].

become spherical powder agglomerates. It considered commercially one of the high-quality powder production methods for many metals and alloys powders. Fig. 8.9 shows a schematic representation of laboratory atomization [28,29]. The factors such as melting temperature; melting viscosity and surface stress; cooling conditions and atomization conditions impact the properties of the resulting particles. The proportion of the fine powder produced (i.e., the particle size is reduced) is increased when increasing the melt overheating and mechanical energy applied on the melt.

The type of fluid feedstock determines the product obtained. If it was a ceramic slurry or suspension, the product consists of dried agglomerates of the ceramic

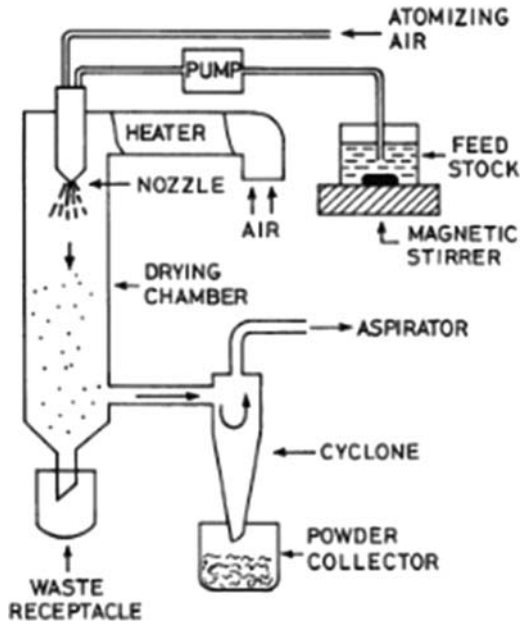

Figure 8.9 The schematic representation of the laboratory atomization.

particles. On the other hand, if the fluid feedstock is solutions or sols the obtained agglomerates are composed of salts, hydroxides, which need calcined to get the oxides [30]. The main advantage of the atomization processes of molten materials is the homogeneity and the spherical shape of the resulting powder particles as well as the narrow particle size distribution.

The main types of atomization process (as in Fig. 8.10) are [8]

1. rotary (or centrifugal) atomization,
2. pressure nozzle (or hydraulic) atomization,
3. pneumatic (or two-fluid) atomization,
4. ultrasonic atomization, where a film of liquid metal (e) or the atomizing fluid (f) is agitated by ultrasonic vibration.

Whatever the sort of atomization process, the basic steps remain the same: (1) preparation of the starting materials (solution, slurry, emulsion, and sol), (2) atomized the feedstock, (3) dry the droplets in the chamber, (4) calcined and if necessary, sintering the products [1].

8.4.1 Atomization mechanism

The mechanism of conventional atomization divided into five stages after the stream of molten material pouring through the nozzle, a high-pressure gas or water impinged the steam of molten to disintegrate into droplets: (1) formation the wavy surface of the molten liquid due to small perturbations, (2) wave fragmentation and

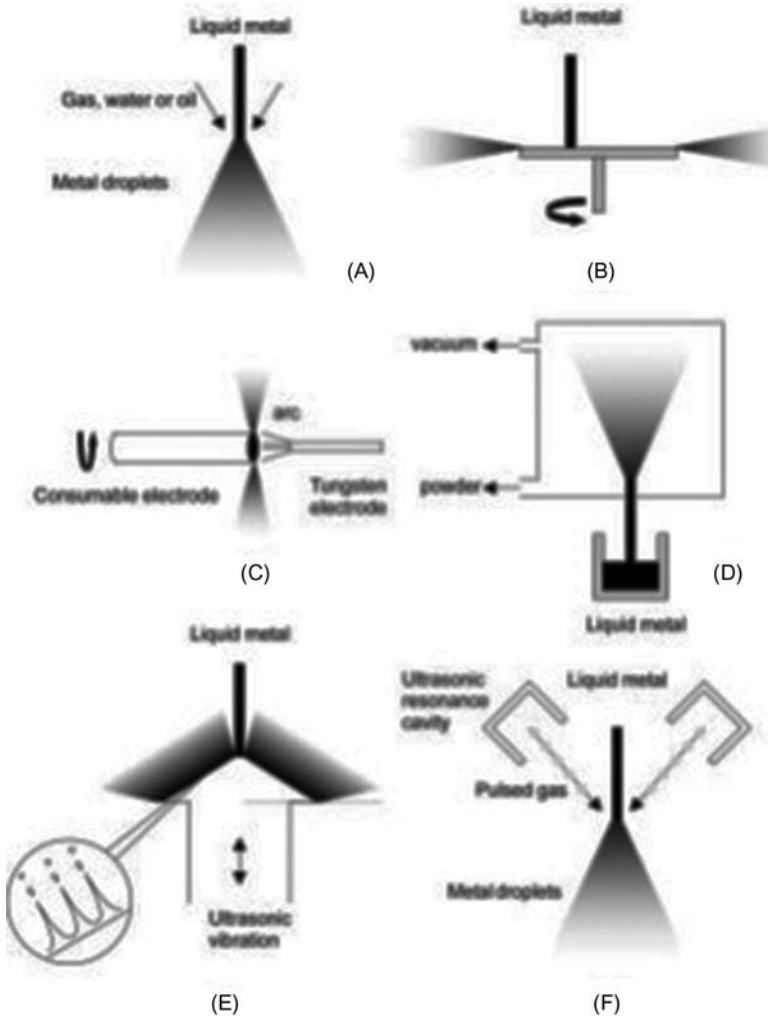

Figure 8.10 Atomization processes: (A) Gas, water, or oil atomization, (B and C) centrifugal atomization, (D) vacuum atomization, (E and F) ultrasonic atomization [8].

ligament formation, (3) the disintegration of ligament into fine droplets, (4) further breakdown of fragments into fine particles, (5) collision and coalescence of particle [30].

There is a lack of literature that talks about the preparation of metal oxides powders using atomization techniques although there are many published about metals powder production using atomization processes. Liu et al. prepared spherical ZnO powder using an ultrasonic atomizer driven spray-pyrolysis technique. They concluded that the high vapor pressure of zinc acetate is responsible for the production of ultrafine zinc oxide powder [31].

8.5 Physical vapor deposition

It is one of the vapor-phase synthetic techniques that used to prepare ultrafine powder. This method employs evaporation and condensation process of similar compositions. To evaporate the solid materials, we use arc, plasma, laser, and electrical heater. The main characteristics of physical vapor deposition (PVD) technique are high purity of the produced powder, highly discrete and nonaggregated powder particles, narrow size distribution, and many types of material can be prepared such as metals, nonoxides, and oxides powder [32]. To synthesis or deposition metal oxides powders or nanostructure a variety of PVD techniques can be employed such as thermal evaporation, electron beam PVD, the two types of sputtering magnetron and RF, cathodic arc deposition and pulsed laser ablation deposition.

Pulsed laser ablation method considers one of the fever methods because it is fast, inexpensive, easy to use, and easy to control process parameters and no need for expensive chemical reagents. Sasaki et al. used nanosecond pulsed laser ablation in liquids to prepare TiO_2 and SnO_2 nanoparticles [33]. Recently, nanocrystalline Fe_3O_4 powder prepared by vacuum drying of a colloidal solution of Fe_3O_4 nanoparticles that synthesized by nanosecond pulsed laser ablation (Nd:YAG laser, 1064 nm, 7 ns, and 180 mJ) [34].

8.6 Mixed methods

Sometimes more than one method may be employed to prepare the metal oxide powders. Furthermore, combining two different methods such as mechanochemical electrochemical or physicochemical techniques could be suitable for some powders. Also, most chemical route used milling as a part of the process. Here, we will discuss briefly the processes mechanochemical, reactive milling techniques, and cold stream (spray) [1].

8.6.1 Mechanochemical method

Within the top-down methods, mechanochemical synthesis can be used to produce nanoparticles embedded in a matrix that avoids agglomeration and is subsequently washed away; the method has been successfully applied to prepare different oxides, such as Al_2O_3, ZrO_2, Cr_2O_3, SnO, and ZnO. microemulsions have been used to prepare $SrTiO_3$, $SrZrO_3$, CeO_2, and SnO_2 as well as magnetic particles and $YBa_2Cu_3O_7$ superconductors. Domanski et al. synthesized (prepared) successfully $MgAl_2O_4$ spinel powder using a mechanochemical technique (route) where a mixture of γ-Al_2O_3−MgO, AlO(OH)−MgO, or α-Al_2O_3−MgO were grinded (milled) at room temperature under air atmosphere [35].

The MgO−CaO−TiO_2 ($MgCaO_4$) ternary system is prepared by mixing TiO_2 and 54% dolomite, after that the mixture is dry-homogenized and grinded (milled)

at high temperatures, then the produced powder is carried out in a muffle furnace under atmospheric conditions to firing [36].

Spann et al. used Y_2O_3, $BaCO_3$, and CuO as precursor materials to prepare $YBa_2Cu_3O_7$ semiconductor powder. The dry and wet ball milling of the mixture was done followed by (1) heating to 950°C under vacuum, (2) flow of pure oxygen gas for 4.0 hours, (3) cooling to 250°C before taking out to the ambient. These single steps allowed the product to calcine [37].

8.6.2 Reactive milling technique

Umbrajkar et al. prepared nanocomposite powder of MoO_3 in Al matrix by using arrested reactive milling technique. They determined the maximum Al concentration in the powder mix. A shaker mill (8000 series by Spex CertiPrep) was used to produce the powder. A steel milling ball of 5 mm diameter was used to grind the powder. The process carried out in argon atmosphere (environment) and hexane (C_6H_{14}) as a process control agent to prevent the possibility of cold welding and partial reaction to happen [38].

Gallium-doped zinc oxide powder was prepared by mixing Ga metal or Ga_2O_3 with ZnO and then ground together in an agate mortar and pestle before sealing in predried silica tubes under vacuum ($\sim 50-100$ mTorr). The SEM image of Ga-doped zinc oxide powder after being pressed at 4 t/cm^2 shows a breaking up of the agglomerates (Fig. 8.11) [39].

8.6.3 Cold stream (spray) process

Cold steam process is one of the mechanical methods, which is based on impact phenomenon caused by the collision of high-speed particles against the cemented tungsten carbide plate. It is implemented using apparatus that consists of a feed container. A compressor is operated at 7.0 MPa to produce a high-speed stream of air about 1.0 m^3/s. Also, supersonic nozzle and target plate which are made of cemented tungsten carbide (WC) [40–42].

Fig. 8.12 shows the SEM images of powders obtained by different powders methods and exhibit how its shape and size varying from one method to the others. The comparison between the different powder production methods showed the different of quality of the resultant powders [8].

8.7 Conclusion

In this chapter the mechanical and physical methods for preparing metal oxides powders have been discussed. Diverse techniques can be used to produce the metal oxides powders which depend on the composition nature of the metal oxide, the shape and size of the powder particles, purity, the amount to produce, cost, and the applications used. The milling techniques, atomization and PVD are the main

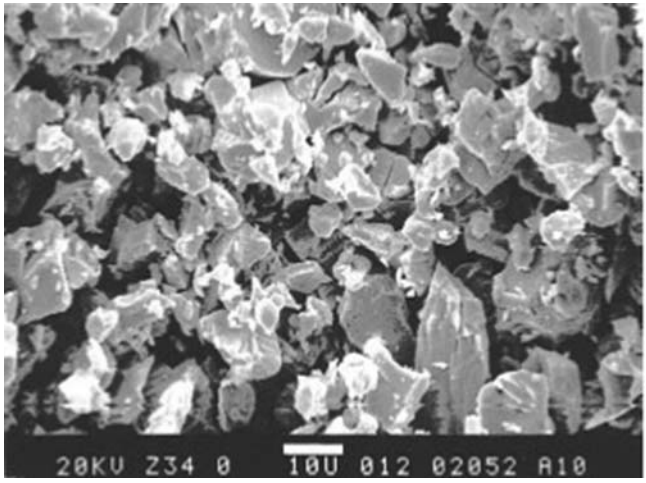

Figure 8.11 SEM image of Ga-doped ZnO.

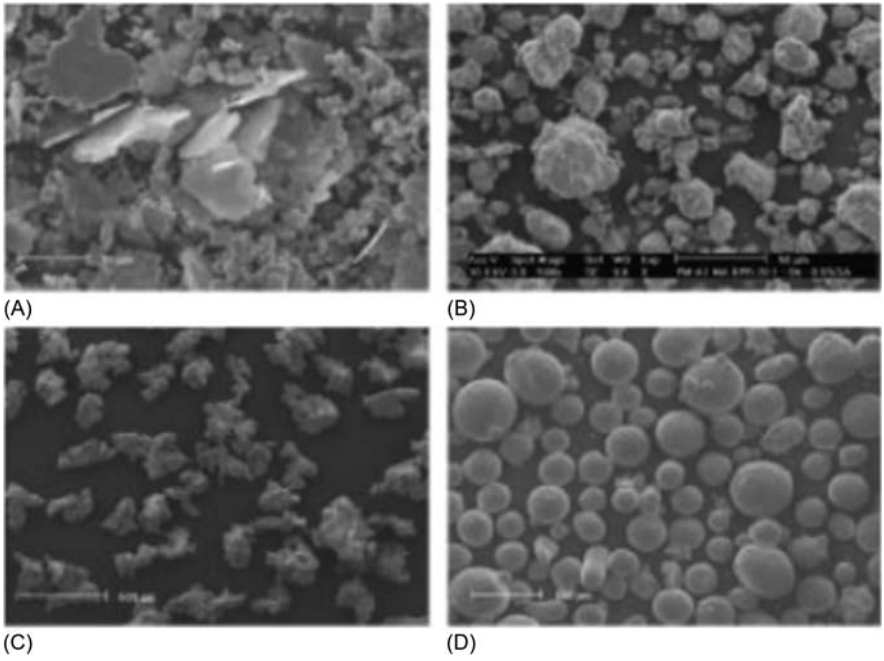

Figure 8.12 Morphology of powders obtained by (A) milling, (B) mechanical alloying, (C) water atomization, (D) gas atomization.

mechanical and physical methods used to produce metal oxides powders. The comparison between these different techniques shows that some metal oxides powders could be produced by more than one technique. The choice of the suitable method depends on the quality of the product.

Acknowledgment

We acknowledge Mr. Yaseen Solo for your discussion and explanation as well as proofreading of this chapter.

References

[1] D. Ganguli, M. Chatterjee, Techniques of powder preparation, Ceramic Powder Preparation: A Handbook, Springer, Boston, MA, 1997.
[2] W. Brian James, P. Samal, J. Newkirk (Eds.), ASM Handbook, vol. 7, Powder Metallurgy, 2015.
[3] J.E. Burke, D. Turnbull, Recrystallization and grain growth, Prog. Met. Phys. 3 (1952) 220.
[4] P. Granger, V.I. Parvulescu, S. Kaliaguine, W. Prellier, Perovskites and Related Mixed Oxides: Concepts and Applications, John Wiley & Sons, 2015.
[5] H. Xu, H. Wang, Y. Zhang, W. He, M. Zhu, B. Wang, et al., Hydrothermal synthesis of zinc oxide powders with controllable morphology, Ceram. Int. 30 (1) (2004) 93–97.
[6] I.B. Cutler, Active powders, in: G.Y. Onoda Jr, L.L. Hench (Eds.), Ceramic Processing Before Firing, John Wiley, New York, 1978, pp. 21–29.
[7] W.L. McCabe, J.C. Smith, Unit Operations of Chemical Engineering, 3rd ed., McGraw-Hill, Tokyo, 1976, pp. 818–851.
[8] S. Seetharaman (Ed.), Fundamentals of Metallurgy, Elsevier, 2005.
[9] C.C. Koch, Milling of brittle and ductile materials, ASM Handbook: Powder Metall. Technol. Appl. 7 (1998) 53–66.
[10] È.L. Lu, M.O. Lai, Mechanical Alloying, Kluwer Academic Publishers, Boston/Dordrecht/London, 1998.
[11] A. Szegvari, The fine grinding of ceramics with attritors, Interceram, 43 (1994) 97–98; Swiss Patent 132086 (1928).
[12] R.M. German, S.J. Park, Handbook of mathematical relations in particulate materials processing: ceramics, powder metals, cermets, carbides, hard materials, and minerals, second ed., R. M. Powder Metallurgy Science., vol. 3, John Wiley & Sons, German, 2009. Princeton: MPIF, 1994, 472 p.
[13] F. Thummiler, R. Oberacker, Introduction to Powder Metallurgy, first ed., The University Press, Cambridge, 1993.
[14] R.B. Schwarz, Viewpoint set on mechanical alloying, Scripta Mater. 34 (1996) 1–73.
[15] J.S. Benjamin, Mechanical alloying—a perspective, Met. Powder Rep. 45 (2) (1990) 122–127.
[16] C. Suryanarayana, Mechanical alloying, ASM Handbook: Powder Metall. Technol. Appl. 7 (1998) 80–94.
[17] M.S. El-Eskandarany, K. Aoki, K. Suzuki, J. Less-Common. Met. 167 (1990) 113–118.

[18] A.W. Weeber, H. Bakker, F.R. de Boer, Europhys. Lett. 2 (1986) 445–448.
[19] L. Li, G.S. Rohrer, P.A. Salvador, Heterostructured ceramic powders for photocatalytic hydrogen production: nanostructured TiO_2 shells surrounding microcrystalline (Ba, Sr) TiO_3 cores, J. Am. Ceram. Soc. 95 (4) (2012) 1414–1420.
[20] V.-I. Merupo, S. Velumani, K. Ordon, N. Errien, J. Szade, A.-H. Kassiba, Structural and optical characterization of ball-milled copper-doped bismuth vanadium oxide ($BiVO_4$), CrystEngComm 17 (17) (2015) 3366–3375.
[21] S. Chatterjee, B.D. Stojanovic, H.S. Maiti, Effect of additives and powder preparation techniques on PTCR properties of barium titanate, Mater. Chem. Phys. 78 (2003) 702–710.
[22] J. Thomson Jr., Chemical preparation of PLZT powders from aqueous nitrate solutions, Am. Ceram. Soc. Bull. 53 (1974) 421–424. 433.
[23] D. Dijkkamp, T. Venkatesan, X.D. Wu, S.A. Shaheen, N. Jisrawi, Y.H. Min-Lee, et al., Preparation of Y-Ba-Cu oxide superconductor thin films using pulsed laser evaporation from high Tc bulk material, Appl. Phys. Lett. 51 (8) (1987) 619–621.
[24] G. Williams, G.S. Coles, Gas sensing properties of nanocrystalline metal oxide powders produced by a laser evaporation technique, J. Mater. Chem. 8 (7) (1998) 1657–1664.
[25] U. Popp, R. Herbig, G. Michel, E. Müller, C. Oestreich, Properties of nanocrystalline ceramic powders prepared by laser evaporation and recondensation, J. Eur. Ceram. Soc. 18 (9) (1998) 1153–1160.
[26] P.P. Partil, D.M. Phase, S.A. Kulkarni, S.V. Ghaisas, S.K. Kulkarni, S.M. Kanrtkar, et al., Phys. Rev. Lett. 58 (1987) 238.
[27] S.C. Singh, J. Singh, R. Gopal, O.N. Srivastava, Chapter 16: ZnO nanostructures synthesized by laser and thermal evaporation, in: A. Umar, Y.B. Hahn (Eds.), Metal Oxide Nanostructures and Their Applications, vol. 5, 2009, ISBN No. 1-58883-170-1.
[28] L.M. Sheppard, Trends in powder processing equipments, Am. Ceram. Soc. Bull. 72 (5) (1993) 28–37.
[29] S.J. Lukasiewicz, Spray-drying ceramic powders, J. Am. Ceram. Soc. 72 (1989) 617–624.
[30] N. Ashgriz (Ed.), Handbook of Atomization and Sprays: Theory and Applications, Springer Science & Business Media, 2011.
[31] T.Q. Liu, O. Sakurai, N. Mizutani, M. Kato, Preparation of spherical fine ZnO particles by the spray pyrolysis method using ultrasonic atomization techniques, J. Mater. Sci. 21 (10) (1986) 3698–3702.
[32] D.M. Mattox, Handbook of Physical Vapor Deposition (PVD) Processing, William Andrew, 2010.
[33] T. Sasaki, Y. Shimizu, N. Koshizaki, Preparation of metal oxide-based nanomaterials using nanosecond pulsed laser ablation in liquids, J. Photochem. Photobiol. A: Chem. 182 (3) (2006) 335–341.
[34] V.A. Svetlichnyi, A.V. Shabalina, I.N. Lapin, Structure and properties of nanocrystalline iron oxide powder prepared by the method of pulsed laser ablation, Russ. Phys. J. 59 (12) (2017) 2012–2016.
[35] D. Domanski, G. Urretavizcaya, F.J. Castro, F.C. Gennari, Mechanochemical synthesis of magnesium aluminate spinel powder at room temperature, J. Am. Ceram. Soc. 87 (11) (2004) 2020–2024.
[36] A.E. Lavat, M.C. Grasselli, Synthesis and characterization of ceramic materials based on the system MgO-CaO-TiO_2 from dolomite, Procedia Mater. Sci. 8 (2015) 162–171.
[37] J.R. Spann, I.K. Lloyd, M. Kahn, M.T. Chase, Preparation of orthorhombic $Ba_2YCu_3O_7$ powder by single-step calcining, J. Am. Ceram. Soc. 73 (1990) 435–438.

[38] S.M. Umbrajkar, S. Seshadri, M. Schoenitz, V.K. Hoffmann, E.L. Dreizin, Aluminum-rich Al-MoO_3 nanocomposite powders prepared by arrested reactive milling, J. Propuls. Power 24 (2) (2008) 192−198.
[39] R. Wang, A.W. Sleight, D. Cleary, High conductivity in gallium-doped zinc oxide powders, Chem. Mater. 8 (2) (1996) 433−439.
[40] R. Lupoi, W. O'Neill, Powder stream characteristics in cold spray nozzles, Surf. Coat. Technol. 206 (6) (2011) 1069−1076.
[41] D.J. Craze, U.S. Patent No. 5,483,801, U.S. Patent and Trademark Office, Washington, DC, 1996.
[42] V.K. Champagne, The Cold Spray Materials Deposition Process, Elsevier Science, 2007.

This page intentionally left blank

Chemical processes of metal oxide powders

9

Alfarooq O. Basheer[1], *Y. Al-Douri*[2,3,4] *and Zaira Zaman Chowdhury*[2]
[1]Department for Earth Sciences and Environment, Faculty of Science and Technology, Universiti Kebangsaan Malaysia, Bangi, Malaysia, [2]Nanotechnology & Catalysis Research Centre, Deputy Vice Chancellor (Research & Innovation) Office, University of Malaya, Kuala Lumpur, Malaysia, [3]University Research Center, Cihan University of Sulaymaniyah, Sulaymaniyah, Iraq, [4]Department of Mechatronics Engineering, Faculty of Engineering and Natural Sciences, Bahcesehir University, Istanbul, Turkey

9.1 Introduction

Since 1980, efforts have been made to invent synthetic methods for nanoparticles with desired properties [1]. Synthesis of the nanomaterials is categorized in two types, top-down approach and the bottom-up approach. In the top-down approach a large piece of material is broken into nanosized entities. It requires complex, expensive, and highly energy intensive and specialized setup to maintain specific conditions such as pressure, temperature, and environment (inert and nonflammable). It has been observed that despite using high cost setup/instrumentation, top-down approach produces nanomaterial with surface defects, nonuniform shapes, which hinders applicability [2]. In the bottom-up approach, atomic or molecular species is integrated to form nanostructures. Bottom-up approach is largely based on wet chemical synthesis that is relatively simple, modular, and scalable. Wet chemical process has used to have better control over nanostructure. Wet chemical synthesis approach has achieved great success as it helps to have a kinetic and thermodynamic provision to tune size, shape, and composition that can reflect the change in optical, electronic, and surface properties. While a few interesting examples are reported in the literature, it is necessary to explore different wet chemical synthesis techniques for having an in-depth analysis of the controlling size, shape, and crystallinity. Controlled synthesis of nanoparticles is a central prerequisite for achieving the desired properties. Reaction parameters play a vital role (namely, type of precursor, heating method, heating/cooling rates, temperature, concentration, mixing, and types of ligands, solvent properties, addition of the sequence, and addition rate) that decides the size and shape of nanoparticles [3]. Therefore it is necessary to compile literature data on the controlled wet chemical synthesis of the metal oxide nanoparticles. Wet chemical synthesis approaches have been realized to produce desirable size and shape of metal oxide nanoparticles in a reproducible manner. Control over size and shape is achieved by a better understanding of elementary

Metal Oxide Powder Technologies. DOI: https://doi.org/10.1016/B978-0-12-817505-7.00009-9

events, the mechanism by conversion of the precursor, surface-stabilizing agent, and reagent in the system and its correlation with growth and nucleation rate. To realize the industrial application of the colloidal metal oxide, synthesis procedure should be scalable to meet the industrial requirement in terms of quality and quantity of the product. A typical conventional batch protocol if used for scale up can yield nanoparticles at an average production capacity of 10 mg/mL. To scale up the synthesis of metal oxide nanoparticles, most of the people would like to increase batch volume or reactor volume [4].

One of the most important applications of nanomaterials is as catalyst to be widely used in petroleum and chemical industries, which has been a hot research area attracting high attention from researchers around the world. A lot of nanomaterials that have shown highly catalytic activity are nano-sized metal oxide crystals or doped metal oxide crystals. As well known, the nature of semiconductor is one of major features for solid catalyst, especially for solid photocatalyst. The properties could exhibit or work as catalysts only when the metal oxide bears crystal structure. Therefore the crystallization of oxide or doped oxide is a key step in the preparation of catalyst. Nowadays, the current processes of preparing metal oxide nanocrystal are mainly involved in sol−gel method and some modified sol−gel methods. The products synthesized by the methods, however, are metal hydroxides that have to undergo a firing treatment (at over 350°C) in order to have them crystallized and to be endowed with semiconductive and catalytic properties. But, the formation of oxide crystals in the roasting process involves a phase transition process, in which a new grain boundary forms and expands at high temperature, leading to size increase of the particle obtained in solution synthesis or even to a new matrix element phase from which the doping element is excluded [5]. In addition, the process of phase transformation in calcination is unfavorable for the preparation of nuclear shell structure of nanomaterials such as a magnetic nuclear coated with TiO_2, SiO_2, or SnO_2, resulting in tow-phase separation and a failure of coating on magnetic nuclear. For the synthesis of nanocrystalline metal oxides with alterable valence, the calcination in the air causes the valence of metal to rise by oxidation and the original crystalline structure to change. And also, on the surface of the directly synthesized metal oxide nanocrystals without high-temperature burning, there exist a large number of hydroxyl groups, which are more conducive to water molecules, organic solvents, or organic compounds compatible and to surface modification and functionalization of nanocrystals. A modified sol−gel method, "precipitation−condensation with nonaqueous ion exchange," associating with a drying method, "azeotropic drying of isoamyl acetate," that is, in ethanol, a strongly basic anion resin was used as an exchanger to remove by-product Cl^- and as a reactant to provide OH^- for hydrolysis. The high-purity metal hydroxide tends to dehydrate in an intermolecular manner with the assistance of super water-absorbable ethanol to form crystal [6,7].

Metal oxide nanomaterials represent a growing asset in many industries, especially with their heightened chemical, physical, and electronic properties compared with their bulk counterparts. Metal oxide nanomaterials are versatile materials that can be used in applications such as environmental remediation, medical technology,

energy, water treatment, and personal care products, with their applications projected to increase. Studies show that three to four consumer products are released per week that may contain metal oxide nanomaterials. Becoming increasingly popular in their usage, exposure of metal oxide nanomaterials to people and the environment through occupational processes and consumer products is likely. Therefore it is important to investigate how these nanomaterials affect human health and the environment. The following sections will include an overview of the applications and potential toxicity to humans, aquatic organisms, and terrestrial organisms of several metal oxide nanomaterials, including two of the most widely used metal oxides—nano-ZnO and nano-TiO_2 [8–10].

9.2 Sol–gel method

As the heading implies, sol–gel processes involve both sol and gel components. The sol is a colloidal suspension of nanometer-sized solid particles in a liquid phase. When these particles attract one another, under the correct conditions, they bond together forming a three-dimensional (3D) network called a gel. This contains a continuous solid skeleton enclosing a continuous liquid phase [10,11]. If the smallest dimension of the gel is greater than a few millimeters, the material is called a monolith. If the gels have dimensions spanning from a few nanometers to a few millimeters, they are called a particulate gel. Drying the gel by evaporation under ambient pressure gives rise to capillary pressure that causes shrinkage of the network, and the resulting materials are called xerogels. These are relatively dense with low surface areas. In contrast, drying the gel under supercritical conditions eliminates the interface between the liquid and vapor phases, and the resulting materials are called aerogels. The first gel derived from a metal alkoxide was synthesized, whereas the first aerogels were prepared. A typical aerogel comprises both meso- (2–50 nm in diameter) and micropores (<2 nm in diameter). It exhibits a large surface area of hundreds of square meters per gram and has extremely low thermal conductivities and fascinating acoustic properties due to the porous structure. The high surface area of such metal oxide aerogels provides better properties for applications such as catalysis and insulation [12]. This, in turn, helps compensate for the relatively high capital cost and inconvenience of high-pressure operation. In addition, there are comprehensive textbooks available on the physics and chemistry of sol–gel science [13,14]. Recent developments in sol–gel technology are marked by the use of organic solvents or supercritical fluids (SCFs) for synthesizing a variety of metal oxides. However, it should be noted that conventional organic solvents are currently used by manufacturing and processing industries on a scale of billions of kilograms per year. The fact that they play a significant role in global environmental pollution and smog formation cannot be ignored. Alternatively, since SCFs are considered to be environmentally benign, and ecological credits are added to the sustainability of the sol–gel process, they offer a viable alternative [15–17]. Another major advantage of using SCFs as reaction media for

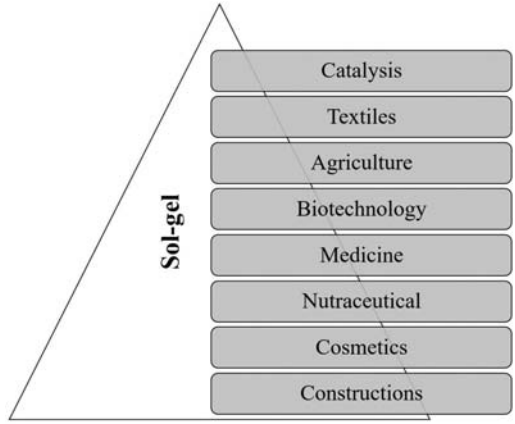

Figure 9.1 Applications of sol−gel.

sol−gel reactions lies in the fact that the resulting materials are readily dried after SCF venting. Such one-pot synthesis processes are attractive, as described later in this review. In addition, sol−gel reaction kinetics can be fine-tuned using both pressure and temperature, thus allowing some difficult sol−gel reactions to take place, for example, hydrolysis and condensation of metal nitrates in simulated cooling water (SWC). Finally, although materials prepared using conventional sol−gel reactions are often amorphous (e.g., TiO_2 and ZrO_2), many crystalline metal oxides can be readily prepared in high-temperature sol−gel SCF processes. This eliminates the heat-treatment step and further simplifies the manufacturing process [18−22]. Fig. 9.1 shows the applications of sol−gel.

9.3 Microwave-assisted synthesis

Microwave-assisted synthesis of nanomaterials has been under development for last three decades. With the technological advancements in the design of microwave generators, the synthesis of nanomaterials is becoming more and more attractive. Rapid heating in the reaction system can be achieved using microwave radiation which enhances reaction rates and reduces reaction time. Hence, microwave radiation has been used to reduce reaction time by enhancing reaction kinetics [23−25]. First publication in this area appeared where liquid phase synthesis of TiO_2 microsphere by the sol−gel process is reported using microwave heating in kerosene. Around this period, there is explored microwave heating to carry out organic reactions. Over the years the number of publications on the microwave-assisted synthesis of nanomaterial and organic compounds has rapidly increased. Earlier, synthesis of nanomaterial was carried out in a domestic microwave oven and it has no control over temperature and pressure which leads uncertainty in the product quality. Recently, microwave oven or reactors are well equipped with in situ measurement

of temperature and pressure with infrared sensors (IR) sensor. Online monitoring reaction parameters such as temperature and pressure allow us to improve quality of nanoparticles by manipulating reaction parameters. Microwave radiation can be absorbed by the solvents having high dielectric constant and produces heat during irradiation and causes uniform heating in a reaction mixture through dipole−dipole interaction with the alternating electric field generated by microwave. This property makes microwave energy more efficient for selective heating. This method requires less energy and time to obtain nanoparticles compared to conventional heating method. Conventional heating generates a thermal gradient in the reaction solution in the absence of efficient mixing which can alter the local nucleation and growth kinetics of nanomaterial and may result in poor quality of the product having significant variation in shape and size distribution [17,26]. Microwave heating induces homogeneous heating that leads to uniform nucleation and growth kinetics in entire solution and gives the better quality product, preferably under efficient mixing. Details on the effect of power density, frequency, the penetration depth of microwave and type of reactor material on the product quality will be elaborated separately. Various metal oxides that have been synthesized using microwave-assisted technique include ZnO, α-Fe_2O_3, β-Fe_2O_3, Fe_3O_4, CuO, Cu_2O, Mn_3O_4, MnO_2, TiO_2, and Co_3O_4. Iron oxides occur in different forms such as FeO, α-Fe_2O_3, β-Fe_2O_3, γ-Fe_2O_3, ε-Fe_2O_3, and Fe_3O_4. Particularly, magnetic property and color of iron oxides vary with uniformity in size, shape, crystal phase, and composition at nanoscale dimensions [27−30].

Hematite (α-Fe_2O_3), maghemite (β-Fe_2O_3), and magnetite (Fe_3O_4) are extensively investigated due to their applications in magnetic memory storage, catalysis, and biomedical and pigment industry. Iron oxide nanoparticles show well-defined properties when they are monodispersing in size and shape. Most of the synthesis processes are driven by properties of solvent, namely, boiling point and polarity. The synthesis of monodisperse spherical Fe_3O_4 nanoparticles has polydispersity index that is 3% in ionic solvent using microwave-assisted method. According to the LaMer theory, to obtain uniform size nanoparticles, instant nucleation is necessary throughout the reaction solution and to achieve this, temperature gradient should be eliminated throughout the reaction mass. Thus microwave heating mechanism under efficient mixing eliminates thermal gradients in reaction system and allows nuclei to grow homogeneously. These iron oxide nanoparticles were prepared using ionic solvent [BMIM] [BF_4] as cosolvent that acts as microwave absorber and helps to induce uniform heating into the solution and maintains thermal homogeneity by an ionic conduction mechanism that led to forming monodisperse nanoparticles. The influence of different glycols on iron oxide nanoparticles prepared by microwave-assisted synthesis is prepared [31,32]. It shows that using different glycols in reaction system affects the final phase of the iron oxide nanoparticles, as well as size or length of glycol is sensitive to particle size. Particles prepared by ethylene glycol, polyethylene glycol, and polypropylene glycol in water have crystal sizes 35, 29.9, and 28.2 nm for Fe_3O_4, α-Fe_2O_3, and γ-Fe_2O_3, respectively. The synthesis of rose-like nanocrystalline Fe_3O_4 superstructures using ethylene glycol as a solvent by a rapid microwave-assisted approach is demonstrated.

Three-step mechanism was proposed for nano-rose formation. In first step, Fe_3O_4 nuclei formed by absorption of P123. In the second step the free P123 molecules could selectively adsorb onto certain surfaces of neighboring Fe_3O_4 nanocrystal to suppress their natural anisotropic growth. These small crystalline primary particles aggregate and form interparticle porosity, resulting in the porous nature of the Fe_3O_4 nano-roses. Effect of metal precursor decides morphology, size, and final phase of nanoparticles due to anionic part of a metal complex which can act as surface-stabilizing agent or surface etchant [33–37].

The effect of the precursor on the sizes of iron oxide nanoparticles is studied. Fe $(acac)_2$, $Fe(ac)_2$, and $Fe(acac)_3$ precursors were used for the preparation of 11, 7, and 5 nm sized Fe_3O_4 nanoparticles, respectively, in benzyl alcohol. The Fe_3O_4/Fe_2O_3 nanoparticles in water using $FeCl_3$ and dextran at 100°C are synthesized. Dextran serves as a surface-stabilizing agent and confined nucleation and growth of nanoparticles in limited space that delivered a smaller size of Fe_3O_4 within 6.5 nm. The synthesis of fluorescein-labeled extremely small size iron oxide nanoparticles with 2.5 nm size using microwave in a single step is prepared, as a viable tool for cell labeling and T1-MRI agent. In their method, they have functionalized the surface of iron oxide nanoparticles with a carboxymethyl derivative of fluorescein isothiocyanate–labeled dextran as an anchoring site for further biomodification and fluorescence signal which acts as T1 contrasting agent. Lamellar nanostructures of sodium/potassium iron oxide nanosheets were obtained by heating the suspension of iron(II) sulfate, sodium thiosulfate, and sodium/potassium hydroxide in the microwave for 5 minutes [38–42]. Nanosheets were observed after 1 minutes microwave radiation and increase in reaction time up to 5 minutes gave bigger sodium iron oxide nanosheets. These results showed a rapid increase in the growth rate upon microwave irradiation. The synthesis of Fe_3O_4 and α-Fe_2O_3 nanoparticles by a fast microwave-assisted solution method is reported. The elliptical α-Fe_2O_3 nanoparticles were formed following an oriented attachment mechanism. The hexagonal Fe_3O_4 nanoplates with an average edge length of 80 nm are synthesized by microwave irradiation. Reaction time, microwave power, concentration of NaOH, and additives such as citric acid, sodium acetate, and sodium hypophosphite were used to tune morphology and size of iron oxide nanoparticles. Citric acid plays vital role in the formation of plate-like Fe_3O_4 nanoparticles, which acts as capping agent and shape-directing agent because it can form achelate with metal by carboxylate group, whereas without surfactant, iron oxide formed aggregated and undefined shape of nanoparticles [43–50].

ZnO nanoparticles have been an attractive candidate due to antibacterial, antifungal, anticorrosive, and UV-filtering properties. Various structures of ZnO have been prepared using the microwave and tested for multiple applications due to size- and shape-dependent properties. The size tuning of monodisperse ZnO colloidal nanocrystal clusters (CNCs) by a microwave polyol synthesis is measured. ZnO nanocrystal cluster prepared from $Zn(OOCCH_3)_2 \cdot 2H_2O$ in ethylene glycol by seed-mediated mechanism, where the secondary structure of ZnO CNCs obtained from smaller ZnO nuclei (7–8 nm) attached to each other to form nicely assemble spherical colloidal nanocrystal. The ZnO nanocrystal in the presence of an ionic liquid [BMIM] [NTf_2]

by the microwave assisted method is prepared. The average size of ZnO nanoparticles is 41.3 nm and it has been used in nanofluids for antibacterial material [51]. The shape-controlled growth of ZnO nano- and microstructures by microwave-assisted synthesis is done. Different basic structures of ZnO, namely, nanorods, nanocandles, nanoneedles, nanodisks, nanonuts, microstars, micro-unidentified flying object (UFOs), and microballs, are reported at a low temperature (90°C) with a low-power microwave-assisted heating and a subsequent aging process. These nanostructures are obtained by changing the metal precursor, the capping agents, and the aging times. Even more complicated ZnO structures, including ZnO bulky stars, cakes, and jellyfishes, are also reported by microwave irradiation to a mixture of the as-prepared basic ZnO structures. Evolution of variable morphology is explained by preferential growth of particular plane and suppression of a specific plane. ZnO nanorods are obtained by preferential growth along (0 0 0 1) plane that grows fast as compared to other planes. As reaction proceeds, dissolution becomes dominant owning to reduction of concentration of growth units [52].

Cobalt oxide is another important metal oxide that has played a significant role in memory storage, electronics, and catalysis due to its superior magnetic properties and surface properties [53–55]. The controlled Co_3O_4 synthesis achieved by microwave hydrothermal synthesis using Co-MPA (3-mercaptopropionic acid) within 10 minutes is fulfilled. The shape of Co_3O_4 depends upon temperature. While the low temperature favors spherical nanoparticles, high temperature favors cubic particles of 12–20 nm. However, the spherical Co_3O_4 nanoparticles have a size in the range of 3–12 nm by fast microwave-assisted synthetic route using a surfactant trioctyl phosphine octane. Mesoporous Co_3O_4 nanoflakes prepared by the microwave-assisted method and low-temperature conversion method are reported. It is observed that the formation of Co_3O_4 gone through layered intermediate cobalt carbonate hydroxide hydrate $Co(CO_3)_{0.5}(OH)_{0.11}H_2O$ with interconnected architectures. The synthesis of CoO using cobalt acetate in benzyl alcohol at 200°C in size range of 45–75 nm within a few seconds is prepared.

TiO_2 nanoparticles attracted great attention because it has been used as pigment in cosmetics, paints, food additives, and self-cleaning glass as it breaks down dust in sunlight by photocatalysis. The TiO_2 synthesis in a mixture of alcohols (ethanol + benzylalcohol) and obtained 5 and 7 nm nanocrystal by microwave-assisted route is demonstrated. The average size of TiO_2 is 295 nm when ethyl alcohol is used as solvent. Here, randomly oriented aggregation results in reduction of overall surface energy. Oriented aggregation is observed that is actually enabled by the rapid formation of nuclei and absence of a growth controlling agent. In another report the hierarchical TiO_2 nanocrystallite aggregates, composed of 10 nm nanocrystallites, are synthesized, and with a size of 500 nm by a microwave-assisted method at 150°C in a short time. Ethanol and $TiCl_4$ are selected as the solvent and titanium precursor, respectively. The rapid heating rate and superheating "hot spots" of the reaction system under microwave irradiation result in formation of larger number of nuclei instantly, which leads to the formation of a lot of clusters. This implies that it is possible to use microwave for generating a

large number of nuclei, which can be used subsequently for growing larger particles [13,56−58].

9.4 Thermal decomposition

A chemical process in which metal precursor when heated above its decomposition temperature in high-boiling solvent is known as thermal decomposition. Usually, use of an aqueous and volatile solvent for metal oxide preparation suffers from polydispersity, agglomeration, and poor crystallinity. Metal oxide nanoparticles obtained by thermal decomposition do not need postsynthesis thermal treatment and these nanoparticles are highly monocrystalline. Along with monocrystalline nature, particles are monodispersing in size and shape [59]. Nucleation and growth rate of metal oxide formation by thermal decomposition is very well understood and has shown a good control over particle size and shape by slight changes in the reaction parameters. Most of the metal oxide nanoparticles synthesized by this method use organometallic precursors dissolved in an organic solvent and a surface-stabilizing agent at a high temperature in an inert environment. During decomposition the presence of several reagents and their ionic forms actually lead to complex reactions. The separation between nucleation and growth phases is shown by adjusting reaction parameters and optimized synthesis to get tuneable-sized nanoparticles [60]. The shape of iron oxide nanoparticles can be controlled by the addition of small amounts of gadolinium oleate (Gd-oleate) complex as surface passivation agent at particular planes. Interestingly, the addition of Gd-oleate introduces shape change in iron oxide nanoparticles from sphere to cube. This shape change has been explained by DFT calculation which proved that Gd-oleate complex strongly binds to (1 0 0) plane compared to (1 1 1) plane that reduces energy by surface passivation, which results in slow growth at (1 0 0) plane. On the other hand, iron oxide nanoparticles grow along (1 1 1) plane and result into cube shape. The ultralarge-scale synthesis of monodisperse metal oxide nanocrystal. Fe_2O_3, CoO, MnO, FeO@Fe, and $MnFe_2O_4$ are synthesized using metal-oleate precursor in a high-boiling solvent. Effect of boiling point of the solvent on the size of Fe_2O_3 nanoparticles has been studied; 5 nm sized iron oxide nanoparticles were synthesized using 1-hexadecene (having boiling point 274°C) and trioctylamine (having boiling point 365°C) yields 22 nm iron oxide nanoparticles. The monodisperse MFe_2O_4 nanoparticles (M = Fe, Co, Mn) in phenyl ether (boiling point 258°C, 4 nm) and benzyl ether (boiling point 298°C, 6 nm) are synthesized. With increasing reaction temperature, particle size increases and results in much higher growth rates [61].

9.5 Solvothermal synthesis

The oldest techniques for the synthesis of metal oxides are solvothermal method. The first application of this method can be dated back to 1845 when Schafhautl

performed the first hydrothermal synthesis, which is a special type of solvothermal synthesis where the solvent is water, and obtained quartz microcrystals. Chemical process performed in closed vessels at above ambient pressure and temperature is known as solvothermal process. During solvothermal method, reaction vessels or autoclaves are operated in temperature range of 100°C−1000°C and pressure range of 1−10,000 bar. Due to high pressure and temperature, interactions between reactants are facilitated that gives single crystalline product. Products obtained with this method are highly selective and reproducible in terms of purity, crystallinity, and morphologies. Large-scale synthesis using this method is intricate due to high temperature, high pressure, and prolonged reaction time. However, depending upon the value of material, it can be adapted for scale up. It has shown transformation of iron oxide into 0D−3D structure using hydrothermal approach. Time-dependent study reveals nanocube formation of single crystalline α-Fe_2O_3 after 8 hours and it is transformed into γ-Fe_2O_3 smaller nanoparticles due to deformation of nanocubes after 10 hours [57,62]. Time-dependent TEM images show that nanocube obtained from quantum dots of α-Fe_2O_3 capped with oleate and coordinated through oleylamine that forms aggregates and transformed into nanocube due to equivalent growth rate of (0 1 2), (1 1 2), and (1 0 2) planes. The monodisperse polyhedrons of iron oxide nanoparticles without surfactants are prepared. In the course of formation, iron oxide edges and corner got etched selectively due to higher surface energy at edges and corner than (1 0 2) plane of octahedra under assistance of Cl^- and H^+ ion. After attaining equilibrium, unchanged truncated octahedra (700 nm) is observed. It has shown synthesis of monocrystalline TiO_2 in toluene in the presence of oleic acid as surfactant at 250°C for 20 hours. Shape of anatase TiO_2 nanoparticles can be tuned from spherical to elongated dumbell shape−like nanorods either by increasing the concentration of oleic acid with respect to titanium isopropoxide (TIP) or increasing concentration of TIP in toluene. The hydrothermal synthesis of rutile TiO_2 nanotubes in NaOH water ethanol solution with 20 nm diameter and length up to several microns is displayed. Despite the formation of rutile phase requiring higher temperature, with the help of hydrothermal process it is achieved at low temperature (130°C). The monodisperse TiO_2 nanoparticles and metal-ion-doped (such as Sn^{4+}, Fe^{3+}, Co^{2+}, and Ni^{2+}) TiO_2 nanocomposites by solvothermal reactions use lauryl alcohol (LA) as solvent as well as surfactant. Size, shape, dispersibility, and component of TiO_2 nanoparticles are controlled through fine tuning of the reaction parameter. When 6 mmol of LA was used, small aggregated particles were obtained. As amount of LA increased to 21 and 75 mmol, nanorods with 25 and 50 nm in length were formed, respectively. When NH_4CO_3 was introduced into the reaction mixture, the morphology of TiO_2 nanoparticles was seen to get changed. When 4 mmol of NH_4CO_3 and 21 mmol of LA concentration were used, elongated particles were obtained. On the other hand, the amount of NH_4CO_3 is more (25 mmol), so aggregated spherical particles are observed. Decomposition of NH_4CO_3 provides H_2O for hydrolysis reaction, which helps for rapid nucleation and produces smaller TiO_2 particles. In addition, LA serves as a hydrolyzing agent and also as a coordinating agent to promote anisotropic growth. Solvothermal or hydrothermal method is being used for preparation of monocrystalline metal oxide nanopowder [51,58,63].

9.6 Evaporation–condensation technique

Evaporation–condensation allows one to obtain disordered mats of nanowires, covering the area of substrates with the catalyst. Fig. 9.2 (top) shows the field emission scanning electron microscope (FE-SEM) images of NiO nanowires at different magnifications, while middle and bottom parts of Fig. 9.1 report SnO_2 nanowires and ZnO nanowires, respectively. Nanowires were directly grown on the active substrates used for functional characterization. It has been observed that the NiO nanowires were grown thin and long and they showed a dense morphology covering the whole substrate. The diameters of these nanowires were found to lie in the range of 20–60 nm. The same holds for tin oxide nanowires, even if in this case nanowires are distributed more uniformly on the substrates. ZnO nanowires exhibit a smaller average diameter (20–50 nm), but they are also shorter and form a very dense mat [14,64,65].

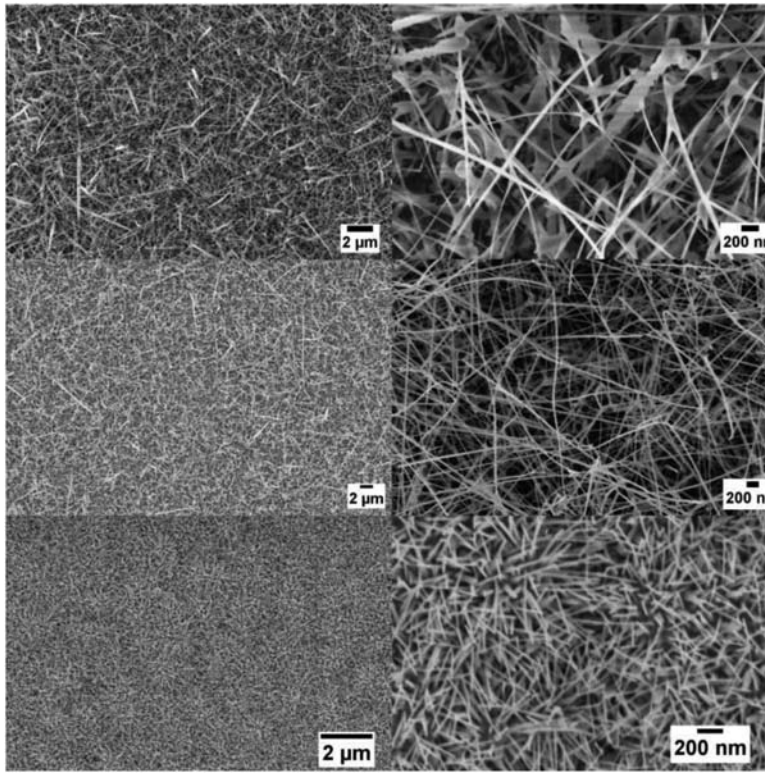

Figure 9.2 FE-SEM images of NiO nanowires at different magnifications (top), SnO_2 nanowires (middle), and ZnO nanowires (bottom) [64]. *FE-SEM*, Field emission scanning electron microscope.

9.7 Thermal oxidation technique

Thermal oxidation of metallic tungsten films resulted in a disordered mats of tungsten oxide nanowires, covering all the patterned area of the substrates. Fig. 9.3 reports a SEM picture of the nanowires, at 50k magnification, highlighting the lack of a preferred orientation on the substrate. The average diameter of the nanowires is very small (20−30 nm), while the length is approximately 1−2 μm [66,67].

9.8 Hydrothermal technique

During the preparation of niobium oxide nanostructures using a hydrothermal technique, during the first experiments, we had adhesion problems of the metal layer to the substrates. We changed the thickness of the film, working temperature, KOH molarity, and time in order to find out the best conditions to synthetize niobium oxide nanostructures directly onto the substrate. Once we achieved reproducible results, nanostructures were investigated in terms of morphology, structural features, and functional properties. By using SEM (LEO 1525), it was possible to verify the presence of the nanostructures on alumina substrates and show their morphology. During the hydrothermal treatment, Nb_2O_5 nanoflowers were formed (Fig. 9.4) [68−71].

9.9 Atomic or molecular condensation

In one type of polymerization reaction, a series of condensation steps takes place, whereby monomers or monomer chains add to each other to form longer chains. This is termed "condensation polymerization," or "step-growth polymerization," and occurs in such processes as the synthesis of polyesters or nylons. Nylon is a

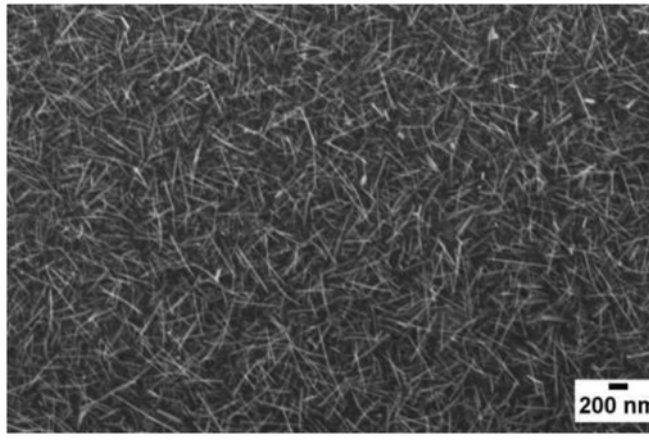

Figure 9.3 SEM picture of WO_3 nanowires on alumina substrate [66]. *SEM*, Scanning electron microscopy.

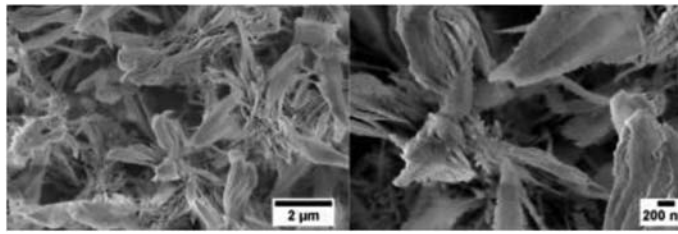

Figure 9.4 SEM images of Nb_2O_5 nanoflowers at 25k (left) and 75k (right) magnification level [68]. *SEM*, Scanning electron microscopy.
From D. Zappa, A. Bertuna, E. Comini, N. Kaur, N. Poli, V. Sberveglieri, G. Sberveglieri. Metal oxide nanostructures: preparation, characterization and functional applications as chemical sensors, Beilstein J. Nanotechnol. 2017, 8, 1205−1217. https://doi.org/10.3762/bjnano.8.122.

silky material used to make clothes made of repeating units linked by amide bonds and is frequently referred to as polyamide. This reaction may be either a homopolymerization of a single monomer A−B with two different end groups that condense, or a copolymerization of two comonomers A−A and B−B. Small molecules are usually liberated in these condensation steps, unlike polyaddition reactions [64].

Additional carbon dioxide has helped trap additional heat being radiating off the planet. Carbon dioxide, water vapor, and other greenhouse gases are adept at stopping heat from leaving the atmosphere, causing the Earth to heat up. Some greenhouse gases are beneficial—without them, Earth would be as cold as the moon—but the recent increase in carbon dioxide has upset the precise balance between too cold, too hot, and just right [70].

The atmosphere is further classified into multiple layers by temperature, which includes the thermosphere, the mesosphere, the stratosphere, and the troposphere. Both air pressure and density increase upon approaching the Earth's surface. The layer closest to the Earth, the troposphere, contains most of the water vapor and is where weather occurs. The next layer, the stratosphere, contains an ozone layer that results from the reaction of ionizing solar radiation with oxygen gas; this ozone layer is responsible for the absorption of UV light. We have damaged our ozone layer by putting chlorofluorocarbons (CFCs) into the atmosphere. The CFCs have damaged ozone, resulting in a hole in the ozone layer. In recent years, CFCs have been banned and the ozone layer hole is shrinking. Farther from the surface, the mesosphere, the thermosphere, and then the exosphere make up the top layers of our atmosphere. Planes typically fly in the stratosphere. The atmosphere performs a various beneficial function for the inhabitants of the Earth, including absorbing UV radiation, heating the Earth's surface, and buffering temperature fluctuations [60,69,72].

9.10 Cryochemical synthesis

The most widespread of such methods are cryochemical synthesis techniques with the use of aqueous solutions. In this case, solutions, suspensions, or products of

chemical coprecipitation of initial solution components containing cations of the synthesized material in a stoichiometric proportion are rapidly frozen and freeze dried in vacuum, after which thermal decomposition follows. The products of this synthesis are generally oxide powders with crystallite sizes of 40−300 nm whose degree of agglomeration depends on the choice of substances frozen in the process (solution/suspension/sludge). It is also possible to remove ice by low-temperature extraction in polar organic solvents (cryoextraction) and coprecipitation of frozen components in low-temperature precipitant solution (cryoprecipitation) [73]. When applying catalysts on porous supports, it is advisable to use the cryoimpregnation method, where substrates soaked with a solution of catalytically active components undergo rapid freezing and freeze-drying. The use of low temperatures can significantly increase the homogeneity of the micro-component distribution on the substrate's surface. According to some authors, cryochemical methods also include low-temperature mechanochemical techniques, in particular, cryomilling [74]. Deposition of metal vapors on very cold surfaces in the presence of inert gases or organic substances is an efficient method to produce nanoparticles of metals ranging from 1 to 10 nm in size (see cryocondensation, cryochemistry).

9.11 Hydrothermal synthesis

The method is based on the ability of water and aqueous solutions to dilute at high temperature (500°C) and pressure (10−80 MPa, sometimes up to 300 MPa) substances practically insoluble under normal conditions: some oxides, silicates, and sulfides. The main parameters of hydrothermal synthesis, which define both the processes kinetics and the properties of resulting products, are the initial pH of the medium, the duration and temperature of synthesis, and the pressure in the system. The synthesis is carried out in autoclaves that are sealed steel cylinders that can withstand high temperatures and pressure for a long time. Nanopowders are normally produced by means of either high-temperature hydrolysis reactions of various compounds directly in the autoclave or hydrothermal treatment of reaction products at room temperature; the latter case is based on the sharp increase in the rate of crystallization of many amorphous phases in hydrothermal conditions. In the first case the autoclave is loaded with aqueous solution of precursor salts, in the second case—with suspension of products derived from solution reactions flowing under normal conditions. There is normally no need to use special equipment and maintain a temperature gradient [75].

Advantages of the hydrothermal synthesis method include the ability to synthesize crystals of substances that are unstable near the melting point, and the ability to synthesize large crystals of high quality. Disadvantages are the high cost of equipment and the inability to monitor crystals in the process of their growth. Hydrothermal synthesis can be affected both under temperatures and pressures below the critical point for a specific solvent above which differences between liquid and vapor disappear, and under supercritical conditions. The solubility of many

oxides in hydrothermal solutions of salts is much higher than in pure water; such salts are called mineralizers. There is also a group of solvothermal synthesis methods, relational to hydrothermal methods; this group of methods is based on the use of organic solvents and supercritical CO_2. Substantial enhancement of the hydrothermal method facilitates the use of additional external factors to control the reaction medium during the synthesis process. As of now, this approach is implemented in the hydrothermal−microwave, hydrothermal−ultrasonic, hydrothermal−electrochemical, and hydrothermal−mechanochemical synthesis methods. One of the most widely known nanomaterials produced by the hydrothermal method is synthetic zeolite. A necessary condition for their production is the presence in the solution of some surface active agents that actively influence morphological evolution of oxide compounds in hydrothermal solutions. The choice of synthesis conditions and type of surfactants can ensure the production of targeted porous nanomaterials with given pore size controlled in a fairly wide range of values [76].

9.12 Coprecipitation methods

This involves dissolving a salt precursor (chloride, nitrate, etc.) in water (or other solvent) to precipitate the oxo-hydroxide form with the help of a base. Very often, control of size and chemical homogeneity in the case of mixed-metal oxides are difficult to achieve. However, the uses of surfactants, sonochemical methods, and high-gravity reactive precipitation appear as novel and viable alternatives to optimize the resulting solid morphological characteristics [77]. In the basic aqueous solution the magnetic nanoparticles take place by the following reaction:

$$M^{2+} + 2Fe^{3+} + 8OH^{-} MFe_2O_4 + 4H_2O$$

where M can be salt. The type of salt used, the reaction temperature and pH value, the ratio of salt, ionic strength of the solution affects the size, shape, and composition of magnetic nanoparticles.

Iida et al. [78] investigated the effect of iron salts, namely, sulfates and chlorides, and the ratio of ferrous ions to ferric ions on the size and magnetic properties of Fe_3O_4. The formation of larger particles (B37 nm) was observed with the use of ferrous salts only compared with the particles with the size of approximately 9 nm synthesized with both ferrous and ferric salts. The size of the Fe_3O_4 magnetic nanoparticles was mainly varied with the valence of the ions instead of the type of the counter ion of the iron salt used in the synthesis. The saturation magnetization values of the magnetic nanoparticles from ferrous sulfate and chloride were 86.6 and 81.0 emu/g, respectively, while that of nanoparticles synthesized with both ferrous and ferric sulfate and chloride, 46.7 and 55.4 emu/g, respectively. This reduction in saturation magnetization was explained as an effect of thermal fluctuation that rises near the surface of the synthesized magnetic nanoparticles or due to the much finer size of the particles.

9.13 Microemulsion technique

Microemulsion or direct/inverse micelles represent an approach based on the formation of micro-/nano-reaction vessels under a ternary mixture containing water, a surfactant, and oil. Metal precursors on water will proceed precipitation as oxo-hydroxides within the aqueous droplets, typically leading to monodispersed materials with size limited by the surfactant−hydroxide contact [79]. The surfactant in this system reduces the interfacial tension between the water and oil phases by specific interactions of its polar or ionic part and its nonpolar hydrophobic part with each phase, respectively, so that a transparent solution is established. Different types of surfactants containing branched or straight hydrocarbon chain of 8−18 carbon atoms and hydrophilic part are used in water-in-oil microemulsions.

The size of the nanoparticles synthesized via microemulsion method can be controlled by the size of water nanoreactors, which can be tuned by the water-to-surfactant molar ratio. Size of the water nanoreactors, the micelles, has a linear dependence on the water-to-surfactant molar ratio, W_0, proposed by Pileni [80] as expressed with the following equation:

$$R_w = \frac{3 \cdot V_{AQ}}{A_h} \cdot W_0 = K \cdot W_0$$

where V_{AQ} is water molecule volume and A_h is area of the surfactant polar group. It was also reported that it is necessary to use very low metal precursor concentrations (10^{-3} to 10^{-4} M) to minimize the size of the particles in dispersed phase of the microemulsion. Although the calculated and experimentally measured radii of the nanoparticles agree at low precursor concentration up to 0.08 wt.%, radius differs from the calculated value for the precursor concentration of 0.16 wt.%, indicating the significant effect of precursor concentration on the microemulsion droplet size.

9.14 Template/surface derivatized methods

Template techniques are common to some of the previously mentioned methods and use two types of tools; soft-templates (surfactants) and hard-templates (porous solids as carbon or silica). Template- and surface-mediated nanoparticles precursors have been used to synthesize self-assembly systems [53]. Gas−solid transformation methods with broad use in the context of ultrafine oxide powder synthesis are restricted to chemical vapor deposition (CVD) and pulsed laser deposition (PLD) [81].

There are a number of CVD processes used for the formation of nanoparticles among which we can highlight the classical (thermally activated/pydrolytic), metalorganic, plasma-assisted, and photo CVD methodologies. The advantages of this methodology consist of producing uniform, pure, and reproduce nanoparticles and films although require a careful initial setting up of the experimental parameters [82]. Furthermore, the CVD is a relatively uncomplicated and flexible technology,

which can accommodate many variations, and the reaction process and reactor design are simple as the reaction is easy to control and manipulate. Raw materials are abundantly available in the form of gases. With the CVD, it is possible to coat almost any shape of almost any size. Unlike other thin film, techniques such as sputtering CVD can also be used to produce vertically aligned nanotubes, fibers, monoliths, foams, and powders [83]. A typical CVD system has shown in Fig. 9.5.

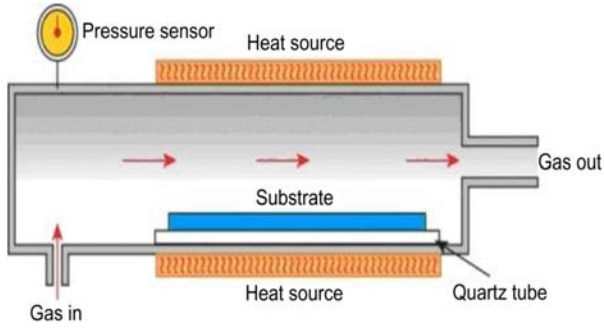

Figure 9.5 Schematic of typical CVD process.

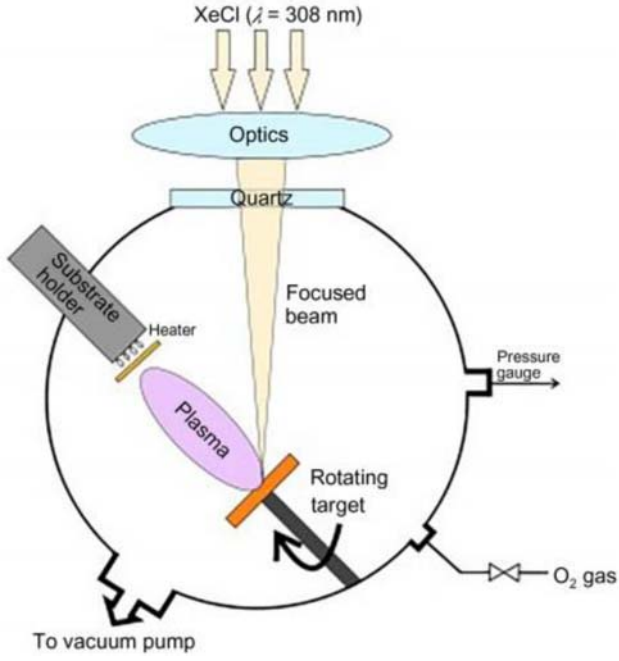

Figure 9.6 Schematic illustration PLD setup [85]. *PLD*, Pulsed laser deposition.

PLD is a relatively recent technique providing a simple, versatile, and contamination-free deposition of nanoparticles and thin films of various materials especially suited for oxide growth [84]. In PLD, material vaporized from the target using high-power pulsed laser beam is deposited on a substrate located opposite to the target. The laser beam enters a high vacuum chamber, in which the target and the substrate are located, through a window and is focused on the target of the desired composition. Depending on the background gases, for example, O_2 or Ar, used during the process, composition of the deposited materials is controlled. A schematic diagram of typical PLD setup is shown in Fig. 9.6.

9.15 Conclusion

A review of chemical methods and techniques was displayed. It was proved that the metal oxide macro-, micro-, and nanostructures are interested due to multi-application. Intensive studies were presented. Several method and techniques were detailed such as sol−gel method, microwave-assisted synthesis, thermal decomposition, solvothermal synthesis, evaporation−condensation technique, thermal oxidation technique, hydrothermal technique, atomic or molecular condensation, cryochemical synthesis, hydrothermal synthesis, coprecipitation methods, microemulsion technique and, surface-derivatized methods. It is expected that this chapter will be benefitted for the community of science and technology.

References

[1] M.E. Franke, T.J. Koplin, U. Simon, Small 2 (2006) 36−50.
[2] S. Brovelli, N. Chiodini, R. Lorenzi, A. Lauria, M. Romagnoli, A. Paleari, Nat. Commun. 3 (2012) 690.
[3] H. Zhang, X. Yu, P.V. Braun, Nat. Nanotechnol. 6 (2011) 277−281.
[4] Z. Zhang, C. Dong, C. Yang, D. Hu, J. Long, L. Wang, et al., Adv. Synth. Catal. 352 (2010) 1600−1604.
[5] S.E. Skrabalak, R.L. Brutchey, Chem. Mater. 28 (4) (2016) 1003−1005.
[6] J.M. Köhler, S. Li, A. Knauer, Chem. Eng. Technol. 36 (2013) 887−899.
[7] R.L. Hartman, J.P. McMullen, K.F. Jensen, Angew. Chem. Int. Ed. 50 (2011) 7502−7519.
[8] L. Zhang, Y. Xia, Adv. Mater. 26 (2014) 2600−2606.
[9] S. Duraiswamy, S.A. Khan, Small 5 (2009) 2828−2834.
[10] V. Sebastian, M. Arruebo, J. Santamaria, Small 10 (2014) 835−853.
[11] S. Komarneni, R. Roy, Mater. Lett. 3 (1985) 165−167.
[12] R.J. Giguere, T.L. Bray, S.M. Duncan, G. Majetich, Tetrahedron Lett. 27 (1986) 4945−4948.
[13] Q. Li, J. Wang, Y. He, W. Liu, X. Qiu, Cryst. Growth Des. 9 (2009) 3100−3103.
[14] X. Fang, L. Hu, K. Huo, B. Gao, L. Zhao, M. Liao, et al., Adv. Funct. Mater. 21 (2011) 3907−3915.

[15] M. Chaouchi, A. Loupy, S. Marque, A. Petit, Eur. J. Org. Chem. 2002 (2002) 1278–1283.
[16] D.E. Clark, W.H. Sutton, Annu. Rev. Mater. Sci. 26 (1996) 299–331.
[17] Y.J. Zhu, W.W. Wang, R.J. Qi, X.L. Hu, Angew. Chem. 116 (2004) 1434–1438.
[18] X. Hu, J. Gong, L. Zhang, J.C. Yu, Adv. Mater. 20 (2008) 4845–4850.
[19] W.-W. Wang, Y.-J. Zhu, M.-L. Ruan, J. Nanopart. Res. 9 (2007) 419–426.
[20] W.-W. Wang, Y.-J. Zhu, G.-F. Cheng, Y.-H. Huang, Mater. Lett. 60 (2006) 609–612.
[21] A.V. Nikam, A. Arulkashmir, K. Krishnamoorthy, A.A. Kulkarni, B. Prasad, Cryst. Growth Des. 14 (2014) 4329–4334.
[22] I. Bilecka, I. Djerdj, M. Niederberger, Chem. Commun. (2008) 886–888.
[23] M.I. Dar, A.K. Chandiran, M. Gratzel, M.K. Nazeeruddin, S.A. Shivashankar, J. Mater. Chem. A 2 (2014) 1662–1667.
[24] T. Hyeon, S.S. Lee, J. Park, Y. Chung, H.B. Na, J. Am. Chem. Soc. 123 (2001) 12798–12801.
[25] H. Hu, H. Yang, P. Huang, D. Cui, Y. Peng, J. Zhang, et al., Chem. Commun. 46 (2010) 3866–3868.
[26] S. Guru, D. Mishra, S.S. Amritphale, S. Joshi, Colloid Polym. Sci. 294 (2016) 207–213.
[27] Z. Ai, K. Deng, Q. Wan, L. Zhang, S. Lee, J. Phys. Chem. C. 114 (2010) 6237–6242.
[28] E.A. Osborne, T.M. Atkins, D.A. Gilbert, S.M. Kauzlarich, K. Liu, A.Y. Louie, Nanotechnology 23 (2011) 215602.
[29] L. Wu, H. Yao, B. Hu, S.-H. Yu, Chem. Mater. 23 (2011) 3946–3952.
[30] H. Zhou, R. Yi, J. Li, Y. Su, X. Liu, Solid State Sci. 12 (2010) 99–104.
[31] R. Jalal, E.K. Goharshadi, M. Abareshi, M. Moosavi, A. Yousefi, P. Nancarrow, Mater. Chem. Phys. 121 (2010) 198–201.
[32] S. Cho, S.-H. Jung, K.-H. Lee, J. Phys. Chem. C 112 (2008) 12769–12776.
[33] D. Sharma, S. Sharma, B.S. Kaith, J. Rajput, M. Kaur, Appl. Surf. Sci. 257 (2011) 9661–9672.
[34] I. Bilecka, P. Elser, M. Niederberger, ACS Nano 3 (2009) 467–477.
[35] A. Pimentel, D. Nunes, P. Duarte, J. Rodrigues, F.M. Costa, T. Monteiro, et al., J. Phys. Chem. C 118 (2014) 14629–14639.
[36] L. Li, J. Ren, Mater. Res. Bull. 41 (2006) 2286–2290.
[37] A.S. Bhatt, D.K. Bhat, C.-W. Tai, M.S. Santosh, Mater. Chem. Phys. 125 (2011) 347–350.
[38] S. Chen, Y. Zhao, B. Sun, Z. Ao, X. Xie, Y. Wei, et al., ACS Appl. Mater. Interfaces 7 (2015) 3306–3313.
[39] X. Wang, J. Tian, C. Fei, L. Lv, Y. Wang, G. Cao, RSC Adv. 5 (2015) 8622–8629.
[40] R. Bhavesh, A.V. Lechuga-Vieco, J.S. Ruiz-Cabello, F. Herranz, Nanomaterials 5 (2015) 1880–1890.
[41] S.C. Padmanabhan, D. Ledwith, S.C. Pillai, D.E. McCormack, J.M. Kelly, J. Mater. Chem. 19 (2009) 9250–9259.
[42] S. Vijayakumar, A.K. Ponnalagi, S. Nagamuthu, G. Muralidharan, Electrochim. Acta 106 (2013) 500–505.
[43] J. Park, K. An, Y. Hwang, J.-G. Park, H.-J. Noh, J.-Y. Kim, et al., Nat. Mater. 3 (2004) 891–895.
[44] H.-W. Song, N.-Y. Kim, J.-E. Park, J.-H. Ko, R.J. Hickey, Y.-H. Kim, et al., Nanoscale (2017).
[45] S. Sun, H. Zeng, D.B. Robinson, S. Raoux, P.M. Rice, S.X. Wang, et al., J. Am. Chem. Soc. 126 (2004) 273–279.

[46] J.A. Bau, P. Li, A.J. Marenco, S. Trudel, B.C. Olsen, E.J. Luber, et al., Chem. Mater. 26 (2014) 4796−4804.
[47] G. Muscas, G. Singh, W. Glomm, R. Mathieu, P.A. Kumar, G. Concas, et al., Chem. Mater. 27 (2015) 1982−1990.
[48] A.W. Jansons, J.E. Hutchison, ACS Nano 10 (2016) 6942−6951.
[49] Q. Dou, K.M. Ng, Powder Technol. 301 (2016) 949−958.
[50] J. Jeong, N. Kim, M.-G. Kim, W. Kim, Chem. Mater. 28 (1) (2016) 172−179.
[51] H. Zhang, X. Wang, C. Chen, C. An, Y. Xu, Y. Dong, et al., Inorg. Chem. Front. (2016).
[52] S. Mehra, A. Bergerud, D.J. Milliron, E. Chan, A. Salleo, Chem. Mater. (2016).
[53] J. Buha, I. Djerdj, M. Niederberger, Cryst. Growth Des. 7 (2007) 113−116.
[54] C. Cavelius, K. Moh, S. Mathur, Cryst. Growth Des. 12 (2012) 5948−5955.
[55] Z.C. Orel, A. Anzlovar, G. Drazic, M. Zigon, Cryst. Growth Des. 7 (2007) 453−458.
[56] J. Paek, C.H. Lee, J. Choi, S.-Y. Choi, A. Kim, J.W. Lee, et al., Cryst. Growth Des. 7 (2007) 1378−1380.
[57] G. Leem, S. Sarangi, S. Zhang, I. Rusakova, A. Brazdeikis, D. Litvinov, et al., Cryst. Growth Des. 9 (2008) 32−34.
[58] R.I. Walton, Chem. Soc. Rev. 31 (2002) 230−238.
[59] N.M. Abdul Rashid, C. Haw, W. Chiu, N.H. Khanis, A. Rohaizad, P. Khiew, et al., CrystEngComm 18 (2016) 4720−4732.
[60] S. Yang, Y. Xu, Y. Sun, G. Zhang, D. Gao, CrystEngComm 14 (2012) 7915−7921.
[61] C.-S. Kim, B.K. Moon, J.-H. Park, B.-C. Choi, H.-J. Seo, J. Cryst. Growth 257 (2003) 309−315.
[62] J. Yan, S. Feng, H. Lu, J. Wang, J. Zheng, J. Zhao, et al., Mater. Sci. Eng. B 172 (2010) 114−120.
[63] X.L. Li, Q. Peng, J.X. Yi, X. Wang, Y. Li, Chemistry−A Eur. J. 12 (2006) 2383−2391.
[64] D. Zappa, A. Bertuna, E. Comini, M. Molinari, N. Poli, G. Sberveglieri, Anal. Methods 7 (2015) 2203−2209.
[65] E. Núñez Carmona, V. Sberveglieri, E. Comini, D. Zappa, A. Pulvirenti, Procedia Eng. 87 (2014) 1453−1456.
[66] N. Kaur, E. Comini, D. Zappa, N. Poli, G. Sberveglieri, Nanotechnology 27 (2016) 205701.
[67] S. Steinhauer, E. Brunet, T. Maier, G.C. Mutinati, A. Köck, O. Freudenberg, et al., Sens. Actuators, B 187 (2013) 50−57.
[68] Z. Wang, Y. Hu, W. Wang, X. Zhang, B. Wang, H. Tian, et al., Int. J. Hydrogen Energy 37 (2012) 4526−4532.
[69] S.N. Mohammad, J. Chem. Phys. 131 (2009) 224702.
[70] E. Comini, C. Baratto, G. Faglia, M. Ferroni, A. Vomiero, G. Sberveglieri, Prog. Mater. Sci. 54 (2009) 1−67.
[71] H.G. Moon, H.W. Jang, J.-S. Kim, H.-H. Park, S.-J. Yoon, Sens. Actuators, B 153 (2011) 37−43.
[72] R.T. Brackmann, W.L. Fite, Condensation of atomic and molecular hydrogen at low temperatures, J. Chem. Phys. 34 (1961) 1572.
[73] Yu.D. Tretyakov, O.A. Shlyakhtin, Recent progress in the cryochemical synthesis of oxide materials, J. Mater. Chem. 9 (1999) 19−24.
[74] T.I. Shabatina, G.B. Sergeev, Low-temperature reactions in the chemistry of nanosystems (in Russian), Usp. Khim. 72 (2003) 643−663.

[75] S. Komarneni, Q. Li, K.M. Stefansson, R. Roy, Microwave-hydrothermal processing for synthesis of electroceramic powders, J. Mater. Res. 8 (1993) 3176−3183.
[76] P.E. Meskin, V.K. Ivanov, A.E. Baranchikov, B.R. Churagulov, Y.D. Tretyakov, Ultrasonically assisted hydrothermal synthesis of nanocrystalline ZrO_2, TiO_2, $NiFe_2O_4$ and $Ni_{0.5}Zn_{0.5}Fe_2O_4$ powders, Ultrason. Sonochem. 13 (2006) 47−53.
[77] K.S. Suslick, S.B. Choe, A.A. Cichowlas, M.W. Geenstaff, Nature 353 (1991) 414.
[78] H. Iida, K. Takayanagi, T. Nakanishi, T. Osaka, Synthesis of Fe_3O_4 nanoparticles with various sizes and magnetic properties by controlled hydrolysis, J. Colloid Interface Sci. 314 (1) (2007) 274−280.
[79] V. Uskokovick, M. Drofenik, Surf. Rev. Lett. 12 (2005) 239.
[80] M.P. Pileni, Reverse micelles as microreactors, J. Phys. Chem. 97 (27) (1993) 6961−6973.
[81] L. D'Souza, R. Richards, Chapter 3: Synthesis of metal-oxide nanoparticles: liquid-solid transformations, in: J.A. Rodríguez, M. Fernández-García (Eds.), Synthesis, Properties and Applications of Oxide Nanoparticles, Wiley, NJ, 2007.
[82] J. Ohring, The Material Science of Thin Films, Academic-Press, San Diego, CA, 1992.
[83] N.M. Mubarak, F. Yusof, M.F. Alkhatib, The production of carbon nanotubes using two-stage chemical vapor deposition and their potential use in protein purification, Chem. Eng. J. 168 (1) (2011) 461−469.
[84] S.H. Soytaş, O. Oğuz, Y.Z. Menceloğlu, Polymer nanocomposites with decorated metal oxides, Polymer Composites With Functionalized Nanoparticles, Elsevier, 2019, pp. 287−323.
[85] J. Huotari, V. Kekkonen, J. Puustinen, J. Liimatainen, J. Lappalainen, Pulsed laser deposition for improved metal-oxide gas sensing layers, Procedia Eng. 168 (2016) 1066−1069.

Thermal protection coatings of metal oxide powders

10

K.V. Madhuri
Vignan's Foundation for Science, Technology & Research University, Vadlamudi, Guntur, India

10.1 Metal oxides—Introduction

Metals available on the earth are not much stable, and they form metal oxides mostly with unique functionalities and higher stability than pure metals. The metal and oxygen ions play a key role to display various interesting properties for industry purposes and also form the basis to develop various theories of condensed matter physics. Metal oxides are in general solid (powder) form with cation as metal and anion as oxygen. These oxides, available as abundant compounds with large variety of properties such as high stability, various crystal structures, phase transitions, composition, physical, optical, electrical, and chemical with high strength, are suitable for energy storage devices, gas sensors, memories, solid-state microbatteries, catalysts, transistors, electronic components, transducers, optoelectronic devices, membrane reactors, and bioapplications. In general, the metal oxides are brittle in nature at room temperature [1]. However, the electrical properties of these oxides cover entire range from insulators to superconductors through semiconductors and conductors making them economically competitive. Even then, their use has been largely confined to applications as insulating materials. The reason for this might be their brittleness, crystalline transformation, and difficulty in maintaining the desired oxygen levels in the compound. These crystalline transformations and phase changes may be seen as a disadvantage, but at the same time they are of great advantage because of an unexpected variety of properties that can be drawn from the phase transformations made them useful in electrochromic photochromic, thermochromic devices, microbatteries, etc. In addition to this, at certain pressure or temperature the metal insulator transition takes place, which has drawn the attention of researchers and became widespread research theme even before the high-temperature superconductivity sprang onto the center stage. Due to the availability of localized electrons, these oxides are frequently utilized as ferromagnetic and ferroelectric materials and also exhibit photo-and thermoelectric effects.

10.1.1 Classification of metal oxides

Based on the physical properties, metal oxides can be classified into two categories: nontransition and transition [2,3].

Metal Oxide Powder Technologies. DOI: https://doi.org/10.1016/B978-0-12-817505-7.00010-5

The filled valence band and empty conduction band are separated by a large bandgap in nontransition metal oxides. Hence, in the ordinary conditions, they will act as diamagnetic insulators. General examples of nontransition metal oxides are magnesium oxide (MgO), silicon dioxide (SiO_2), etc. At high temperatures the intrinsic activation energy is higher than the energy required for the creation and migration of defects; hence, ionic conduction is predominant than electronic conduction.

In the case of transition metal oxides, they exhibit unusual electronic structure based on the transition metal and how it bonds with oxygen [4,5]. They are enormous and interesting group of solids exhibiting a wide variety of structural, optical, electrical, and magnetic properties. They in turn can be broadly divided into two classes:

1. Those in which the metal ion has a d^0 electronic configuration
   Examples: Vanadium pentoxide (V_2O_5), molybdenum trioxide (MoO_3), tungsten trioxide (WO_3), chromium trioxide (CrO_3), zirconium dioxide (ZrO_2), niobium oxide (Nb_2O_5), and tantalum oxide (Ta_2O_5).
2. Those in which the d shell is partially filled
   Examples: Molybdenum dioxide (MoO_2), tungsten dioxide (WO_2), osmium dioxide (OsO_2), titanium monoxide (TiO), niobium monoxide (NbO), chromium di oxide (CrO_2), rhenium dioxide (ReO_2), ruthenium oxide (RuO_2), rhodium oxide (RhO_2), and rhenium trioxide (ReO_3).

Metal oxides with d^0 cations at octahedral sites exhibit spontaneous ferroelectric and antiferroelectric distortions. Many of them lose oxygen at high temperatures becoming nonstoichiometric. Oxygen loss or insertion of electropositive metal atoms into these oxides place electrons in the conduction band. The nature of electronic conduction in such materials depends on the strength of electron phonon coupling and the width of the conduction band derived from metal d states.

Transition metal oxides containing partially filled d states show unusual interesting properties and may behave as metallic or semiconducting [6]. In recent years the field of metal oxides and powders as well as their composites, both in bulk and thin film form, has become a subject of intensive study by the materials scientists because of the novel characteristics and applications. This area gives a wide scope to the researchers to explore challenging problems in theoretical and experimental investigations [7–10]. In addition, one can also have challenges in protecting these oxides from environment, that is, protection from heat and chemical reaction with other environmental gases [11,12].

10.2 Necessity of protection coatings

The thin layer of material deposited on the surface of the metal oxide or any other material serves to protect it from environment or any other exposure. In other words, these coatings protect the materials and devices as a shield from degradation of structures by creating a physical barrier in between the material and

environment. Metals, nonmetals, and ceramics can be used as protective coatings. In addition to the protection, sometimes these functional coatings are used to change the surface properties of metal oxides such as morphology and structure. Various methods have been employed to deposit a layer that will be necessary to avoid corrosion, etc. Nowadays, the study of synthesis and characterization of various metal oxides has assumed more importance owing to the fact that they are increasingly being used in various industrial and scientific fields for device applications of the emerging technologies. Moreover, these oxides can be used in the abovementioned applications either in bulk or thin film form, which increases the surface-area-to-volume ratio. Metal oxide thin films or nano-form of metal oxide powders are chosen to be used in various applications due to their significant enhancement in chemical, physical, and electrical properties compared with the bulk materials.

The thin film form of metal oxide, which can be synthesized by various chemical and physical deposition technologies, is important to enhance their properties in nanoscale region with widespread use in the fabrication and development of miniaturized devices; hence, research in the fields of nanoscience and nanotechnology have taken the center stage in Materials Science. The ability to develop various versatile materials that exhibit various interesting properties with a small change in composition or structure resulted in their extensive use in microoptoelectronic devices, sensors, catalysis, energy storage devices, photonics, drug delivery, etc. The metal oxide powders or thin films are very sensitive to environment especially temperature. One of the methods a researcher can think of is to protect the films by thermal barrier coatings. Due to these thermal barrier coatings, one can protect the components from destruction even at high temperatures and these coatings can act as insulators as well as oxidation-resistant layers. Hence, the efficiency of the systems and devices can be improved. In addition to this, thermal barrier also needs to be resistant to corrosion when it is exposed to higher temperatures. For example, AlTiN coating is used to increase the surface hardness, oxidation resistance, etc. A few materials have the capacity of thermal absorption, which is needed for nuclear fusion applications, and a few more materials are used for thermal conduction that transfers heat to the surfaces evenly. Depending on the purpose of utilization in the devices, one can select the material as well as deposition method to coat on the surface of the metal oxide thin film. The thermal barrier coating materials especially for protection applications need to have porous structure that changes with the thermal expansion during heating and cooling process. In a few cases the phase stability is also necessary or else cracks will damage the device.

Considering all these aspects, one can list down a few effective qualities of thermal protective coatings for long service and sustainable to more number of cycles as following:

1. The material should be chemically inert and thermally stable.
2. No phase changes in between the operating temperature and room temperature.
3. Metallic surface and the material should have same thermal expansion nature.
4. Protective material should be strongly adherent to the substrate.

5. The material should have oxidation- and corrosion-resistant property.
6. The material should possess optimum range of hardness.

The typical structure of thermal protective coatings consists of four layers as shown in Fig. 10.1.

The bottom layer is the metal substrate that is needed to be protected. The oxidation-resistant metallic layer is serving as bond coat that is directly deposited on the metal substrate with thickness of about 100 μm. Thermally grown oxide is the next layer and on the top ceramic thermal barrier is coated. This layer produces a high thermal gradient and retains the bottom layers at lower temperatures. The degradations may occur in the coatings due to the voids and porosity of grown oxides, open interfaces, failure in bond coats, etc.

The most widely used materials for protection coatings are mullite (compound of alumina and silica), alumina, zirconates of rare earth metals ($BaO \cdot ZrO_2$, $SrO \cdot ZrO_2$, etc.), yttria-stabilized zirconia, glass ceramics, metal glass composites (mixture of metal and glass), etc. Thermal protection coatings (TPCs) are more useful in automotive applications, gas turbines, diesel engines, and enhancing the bond strength.

This chapter attempts to give an idea about the importance of metal oxides and the TPCs of the materials. It also aims to be helpful to the reader to estimate the role of multifunctional metal oxides in advanced technology and how one can protect these oxide powders by using various coatings deposited by several techniques. In this context, it is very important to know about the surface property of the layers of metal oxide powders and how to control the properties with a discussion of protection coating technologies especially with environment and in particular with temperature. The coatings with high thermal stability, which protect the metal oxide powders, either in bulk, thin film, thick film or nano-material form, from the temperature variance and help them to maintain the properties, are known as TPCs or thermal barrier coatings. These coatings, in general with advanced materials, are grown on the surfaces of the metallic and oxide powders with appropriate thickness of 200 μm to 1 mm to insulate the components from large

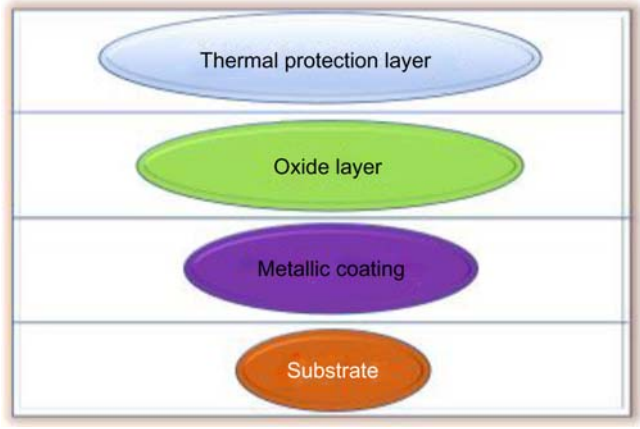

Figure 10.1 Structure of thermal protective coating.

heat. The materials used in thermal coatings should be stable and sustain a considerable amount of heat. The protection coating thus may allow higher operating temperatures without altering the composition, structure, oxidation states, fatigue strength, and thermal stability of the component. As the world has more demand for high-efficiency engines at higher temperatures, there is a significant need to develop new TPCs with better lifetime, response, durability, cyclability, and less thickness. As the abovementioned qualities are totally dependent on the physical, chemical, and electrical properties, which in turn depend on the deposition technique to develop a thin film as a surface coating to protect the oxide layer, it is important to discuss the various growth processes.

10.3 Various coating technologies

This section gives the details about the growth of protecting materials on the surfaces of metal oxides by various deposition techniques. The layers that protect the metal oxide powders from various environmental changes and heat could be deposited at various deposition parameters by using coating technologies.

Growth and structure are the key features for the thin protection coatings for their utilization in devices, which basically depend on control of deposition parameters and deposition method utilized in the process. The thin film deposition techniques may be extensively grouped into two categories based on how the atoms/species/structural components are produced in the condensation process to get deposited on the surface of the metal oxide powders and nano- or thin films. The two main categories are chemical vapor deposition (CVD) and physical vapor deposition (PVD) techniques that are clearly discussed in the following sections.

10.3.1 Chemical vapor deposition techniques

The CVD method is used to deposit thin and thick films with thickness ranging from Angstroms to fraction of a millimeter with controlled structure.

In these methods the film composition depends on precursors and the stoichiometry can be achieved by controlling the precursors and rate of deposition. The films will be produced on the surface of the substrate due to the chemical reaction of vapor-phase precursors. Since the growth of the film can be on any side based on the attainment of gas precursor, this method can coat large surface areas, which will be more useful in industries. CVD techniques are used to grow thin films at normal atmospheric conditions. Organic, inorganic insulating films and semiconductor films are deposited by this technique. Fig. 10.2 represents various CVD methods used for TPCs. Out of various chemical deposition techniques few will be discussed in detail in this chapter.

10.3.1.1 Sol–gel deposition method

Sol–gel technique is one of the oldest and popular chemical methods among chemists to prepare oxide material coatings. The advantage of this is synthesizing the

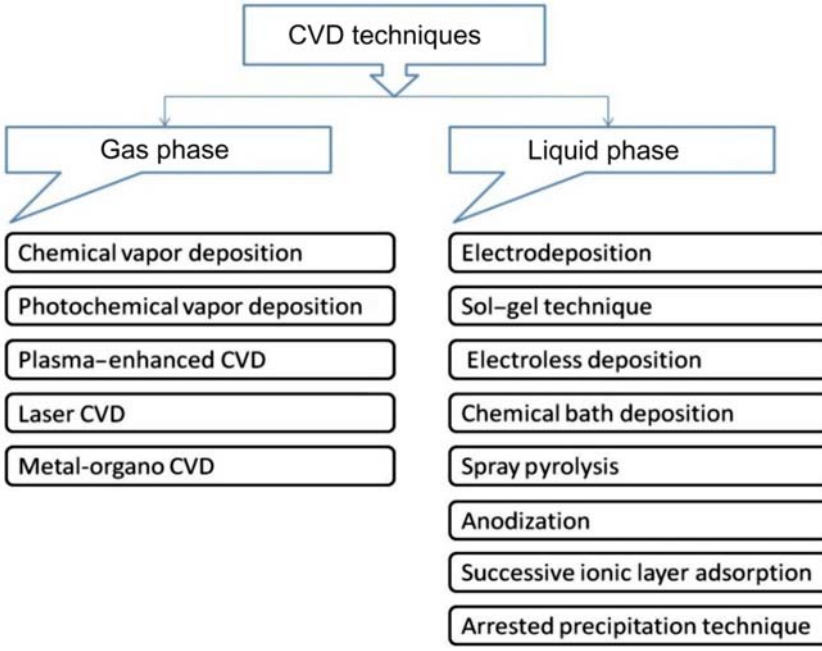

Figure 10.2 Categorization of CVD techniques. *CVD*, Chemical vapor deposition.

nonmetallic inorganic materials, ceramics, glass ceramics, etc. and it can produce large quantities of nano-materials, large areas of coatings at low cost. Moreover, by using this technique, one can synthesize two or more materials simultaneously, one upon another (three-dimensional objects) with high homogeneity and purity. The schematic representation and various steps involved in sol−gel method is shown in Fig. 10.3.

The precursor (starting material) in the form of metal alkoxides or metal chlorides is dissolved in a suitable solvent to form solution called solution (sol). The "sol" undergoes polycondensation or polyesterification to form gel by removal of solvents. Calcination of the gel at higher temperatures about 1073K stabilizes the gel. By using this method, one can easily get the porous structure that is very much important for protection coatings. Thickness of coated film and structure can be controlled by sol/gel transition.

Inorganic−organic hybrid coatings that are suitable for corrosion resistant was explained by several authors. The amount of inhibitor has a limit to be incorporated in the coating based on core material, further amount of inhibitor may lead to form defects and reduction of barrier properties [14]. The coatings are used to repel water, which forms dense films and reduces coating porosity. The film deposition conditions are optimized for attaining maximum corrosion resistance. Hybrid coatings for maximum anticorrosion of metals were proposed by Zhang and Li [15]. Strong chemical bond between organic and inorganic components improves

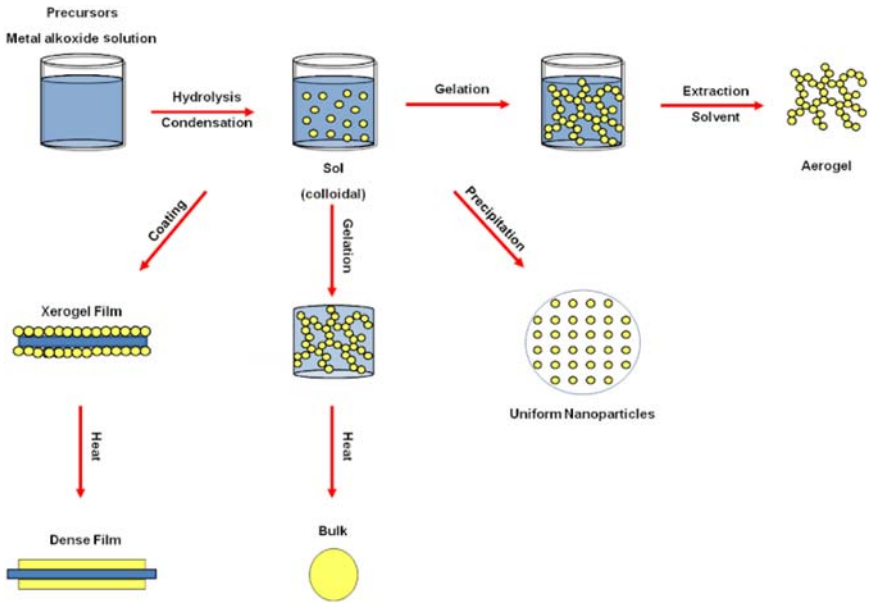

Figure 10.3 Process of sol−gel technique.
Source: From G.C. Righini, A. Chiappini, Glass optical waveguides: a review of fabrication techniques, Opt. Eng. 53 (7) (2014) 071819 [13].

anticorrosion property [16,17]. Superhydrophobic coatings are showing high resistance to fouling [18−21].

10.3.1.2 Chemical vapor deposition

CVD, one of the well-known chemical methods, used in wide range of industries for high temperature protection, erosion protection, and combinations of both. Here, the film is deposited on the surface of the substrate through chemical reaction from gas-phase or vapor-phase precursor. This technique needs activation energy. Several gases are admitted into the vacuum chamber through inlet and after dissociation between the species, the newly formed chemical molecules are deposited on the heated substrate as shown in Fig. 10.4.

The process of CVD can be covered in various processes such as atmospheric pressure CVD, low-pressure CVD (when the pressure is less than ambient), laser CVD, plasma-enhanced CVD (when plasma enhances the decomposition), photochemical vapor deposition, chemical vapor infiltration, and chemical beam epitaxy.

The operating parameters, modes, and conditions can be selected based on the base material and application. Technology was developed by researchers to form thermal barrier coating with high operational parameters in CVD process [22]. To deposit a material as thermal coatings, the mechanical, thermal properties and phase stability such as melting point, thermal conductivity plays an important role

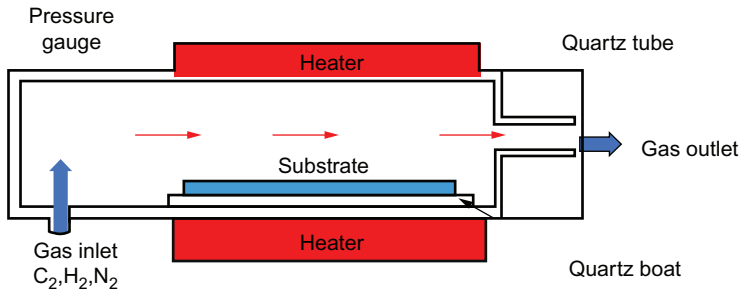

Figure 10.4 Typical set up for CVD technique. Adapted from https://www.azonano.com/article.aspx?ArticleID=3427. *CVD*, Chemical vapor deposition.

[23−25]. High-temperature protective coatings are used for lightweight with high specific strength materials such as carbon-reinforced Si C was reported by various researchers [26−32].

10.3.1.3 Spray pyrolysis

In spray pyrolysis technique, precursor solution is sprayed in the form of narrow mist by mixing it with a carrier gas. The narrow mist is deposited and condenses as a thin film on a substrate that is heated to different temperatures as shown in Fig. 10.5. This process is repeated for several cycles to obtain thin/thicker films of different thickness. This method is used for different types of oxide materials. The stoichiometry of films can be obtained by using different reactants and also by altering the particle velocities.

Different modes of spraying can be adopted. In thermal spraying the materials that are going to be sprayed as protection coating should be melt either with electrical or chemical sources and directly sprayed on the surface of the material or metal oxides. This method is preferably used for large-area applications with high thickness, porosity, hardness, roughness, and bond strength. Wire flame spray and electric arc spray can be used to any metal that is in the form of a wire. Plasma spraying is a widely used method, where the material to be deposited is in the form of powder. A wire is introduced in the plasma jet, originating from a plasma torch. As the temperature rises and at about 10,000K, the material turns to liquid and is driven to the surface of the substrate. Atmospheric plasma spraying method is used at high temperatures about 20K in which the powder is injected into plasma; hence, the powder melts and accelerated, which builds up the coating on the substrate [34,35]. Air and vacuum plasma sprays are also widely used techniques that yield fine microstructure and hence improve the mechanical properties [36−38].

10.3.1.4 Dip coating

Dip coating is a technique of depositing uniform, high-quality thin film even on bulky and complex shapes. The schematic representation of dip coating method is shown in Fig. 10.6.

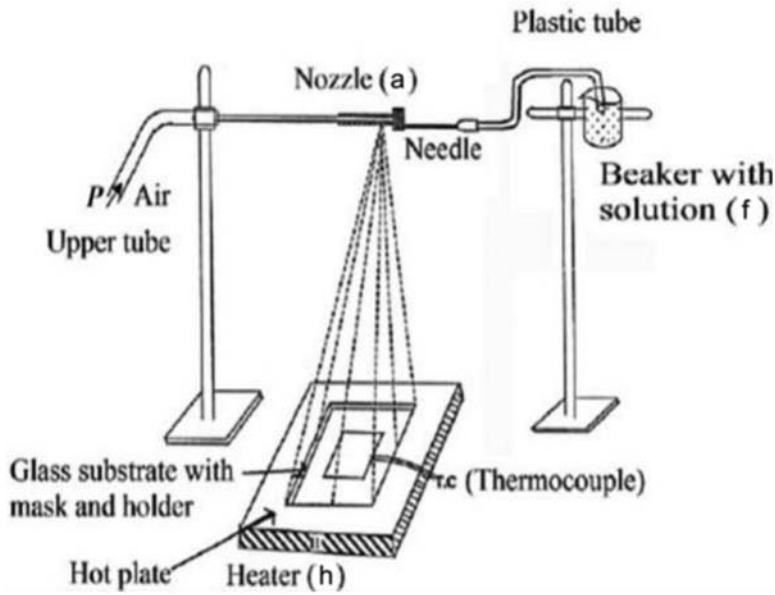

Figure 10.5 Model of spray pyrolysis.
Source: From M. Kamruzzaman, T.R. Luna, J. Podder, M.G.M. Anowar, Semicond. Sci. Technol. 27 (3) (2012) 035017 [33].

In this technique the substrate is immersed in the solution of coating material for a specific time and is withdrawn with a constant speed, which allows the thin film formation on the surface of the substrate. The withdrawal speed determines the thickness of the film. The excess liquid will be drained, and solvent evaporates forming a thin film. The structure and thickness of film depends on factors such as substrate surface immersion time and withdrawal rate. Electrodeposition technique offers more homogeneous coating than spray and dip coating methods. SiO_2 when coated on aluminum substrate by dip coating are of superior attention for protection of metals against oxidation and acid corrosion at elevated temperature. Few of the samples need protective coatings at temperature above 2600°C, which are useful in hypersonic flight vehicles [40–44].

10.3.1.5 Atomic layer deposition

Atomic layer deposition (ALD), one of the chemical methods, permits control on deposition of film growth at the scale of atomic level and provides uniform deposition rate. This technique can deposit the various materials into thin film form from vapor phase. Unlike in CVD, the gaseous chemical precursors are inserted sequentially in a series of alternating pulses. In addition to this, precursor will not be present all the time in the reactor. The individual gas species react at the surface of substrate. During the process of deposition, the precursor is pulsed into the vacuum chamber for chosen amount of time as shown in Fig. 10.7.

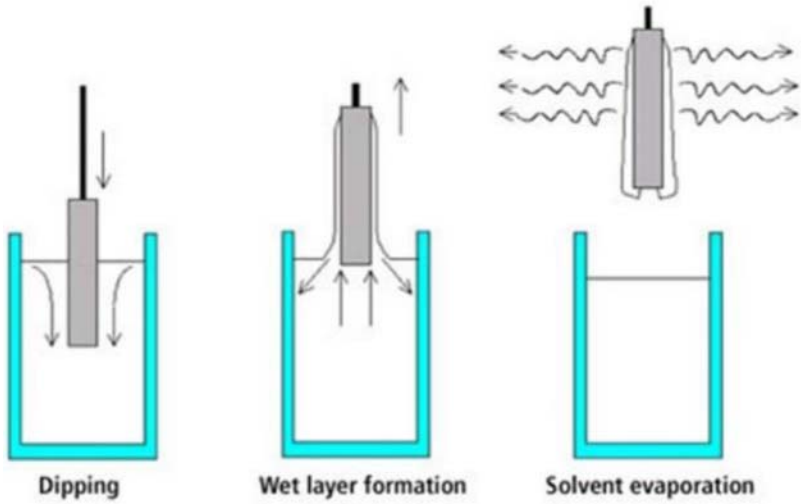

Figure 10.6 Representation of dip coating method.
Source: From F.D. Balacianu, R. Bartos, A.C. Nechifor, Organic−inorganic membrane materials, UPB Sci. Bull., Ser. B: Chem. Mater. Sci. 71 (3) (2009) 37−54 [39].

At each pulse the precursor molecules produce one monolayer on the substrate surface in a self-controlled manner. The residues of precursors left in the chamber are flushed out with noble gas. Then one layer of preferred material is created by purging through introducing the pulse of counter reactant precursor. The procedure is repeated till the required thickness is reached. The consumption of reactive sites terminates the reaction on the surface. Thus the maximum amount of material deposited on the surface after a single exposure to all the precursors can be estimated by the nature of

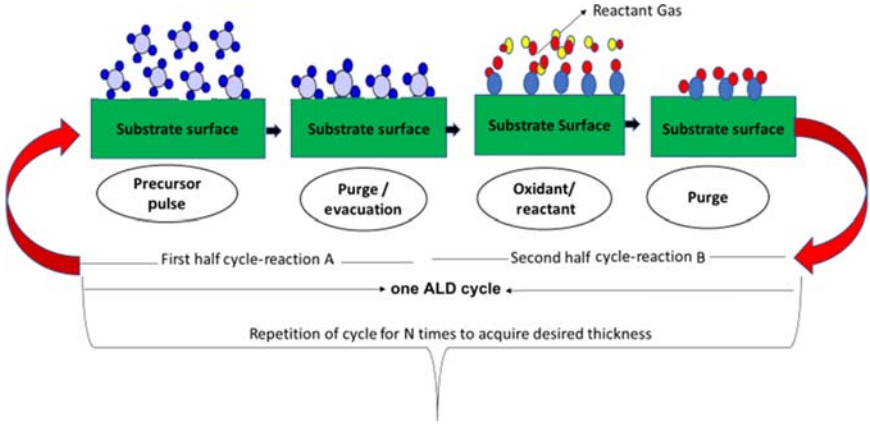

Figure 10.7 Steps involved in ALD technique. *ADL*, Atomic layer deposition.

interaction between the precursor and surface. It is possible to develop uniform layers on large substrates and complex substrates by altering the number of cycles.

In addition to the abovementioned chemical techniques, PVD techniques are also utilized to deposit TPC. Compared to the chemical methods, these have more stoichiometry and exactly desired composition. Researchers significantly improve the thermal, chemical, and mechanical stability of nanotube layers by depositing Al_2O_3, etc. coatings by ALD process [45–47].

10.3.2 Physical vapor deposition

The selected material is vaporized and is condensed on the substrate to form a desired thin film in the case of PVD, whereas in CVD techniques, thermal energy heats the gases and the constituents of vapor phase react together and form solid film. These PVD techniques involve either high-temperature evaporation or sputtering and CVD techniques involve liquid phase and gaseous phase. Fig. 10.8 represents the categorization of various PVD techniques.

10.3.2.1 Steps involved in the process of physical vapor deposition techniques

In general, all PVD methods require vacuum or reduced pressure ambient should be maintained. In PVD methods the material is transferred to substrate in the atomic

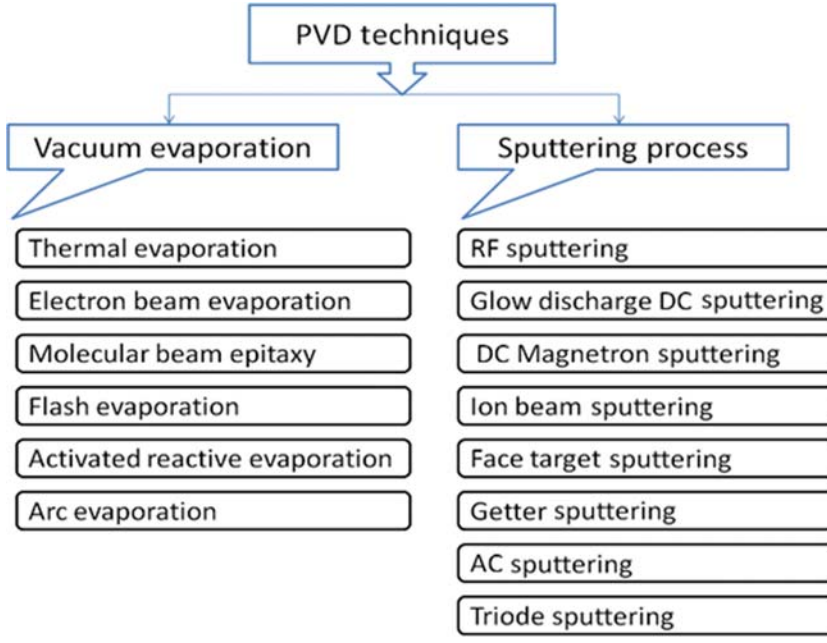

Figure 10.8 Categorization of PVD techniques. *PVD*, Physical vapor deposition.

level. In the process of deposition of thin films, PVD techniques have the following steps shown in Fig. 10.9.

1. The depositing material is placed in the boat and is transformed into vapor phase initially by evaporation. Various kinds of boats such as square boats, spiral boats, and basket boats used for physical deposition techniques are shown in Fig. 10.10.
2. The vapor phase of the given material is transported to the substrate from source.
3. Finally, the vapor condenses on the substrate to form a film.

10.3.2.2 Merits of physical vapor deposition techniques

1. All inorganic materials and a few kinds of organic materials can be deposited.
2. Effective method to deposit multicomponent compounds for device applications.
3. Environmental-friendly and safer technique.
4. Effective method to improve the surface strength and durability.
5. To deposit a film, more than one technique can be used.
6. This method is able to deposit very dense films with unique properties.
7. The prepared films are defect free and well adherent.

A variety of deposition techniques such as thermal evaporation, pulsed laser deposition (PLD), molecular beam epitaxy (MBE), plasma deposition, and DC and radio-frequency (RF) magnetron are discussed in the following sections. Each technique has specific merits and demerits with respect to process specifications, substrate materials, expected properties of thin films, and cost.

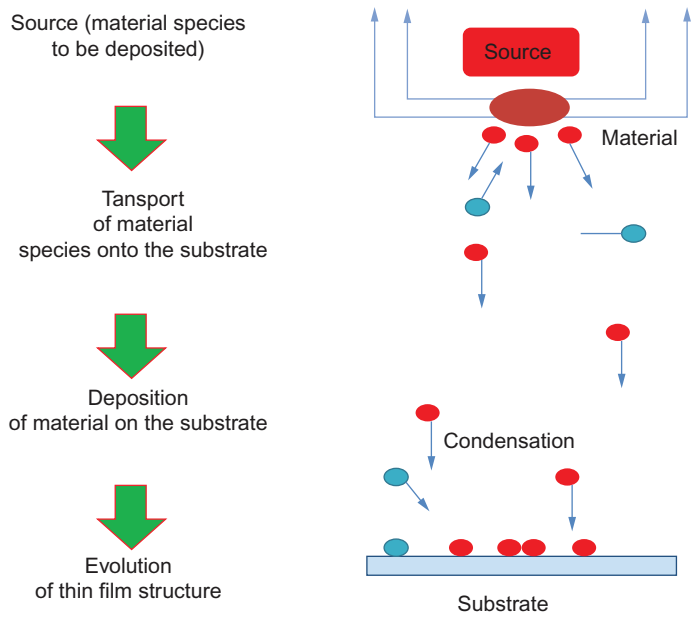

Figure 10.9 Various steps involved in PVD process. *PVD*, Physical vapor deposition.

Figure 10.10 Different shapes of boat used in PVD techniques. *PVD*, Physical vapor deposition.

10.3.2.3 Thermal evaporation

Thermal evaporation is one of the oldest techniques among PVD methods. It is still widely used both in laboratory and industry. The schematic representation of thermal evaporation is shown in Fig. 10.11.

It is a very simple and convenient technique in which the material is heated with the help of a boat or any filament that is made of refractory materials with or without ceramic coatings. In this technique, thermal energy is supplied by the suitable method (such as resistance heating and high frequency) to source material from which the atoms are evaporated for deposition. This vapor is transferred from source to substrate through reduced pressure in the vacuum chamber and condenses on the substrate to form thin solid film. The supporting boat can be chosen based on the material to be deposited and the boat should not chemically react with the evaporant. Few of the thermal evaporation sources are shown in Fig. 10.10. The deposition rate and the properties of the grown films depend on the distance between source and substrate, base vacuum, and substrate temperature. Most of the ceramic materials can be used as TPCs deposited by this technique [48,49].

10.3.2.4 Pulsed laser deposition

PLD technique is a flexible, promising, simplest, and widely exploited method for the preparation of metal oxide and complex metal oxide. This technique uses a powerful pulsed laser to evaporate the target material in ultrahigh vacuum or in the presence of gases such as oxygen. In reactive pulsed deposition the deposition is carried out in the presence of chemically reactive gas, where the gas molecules interact with the ablated material and deposit on the substrate. In this technique the

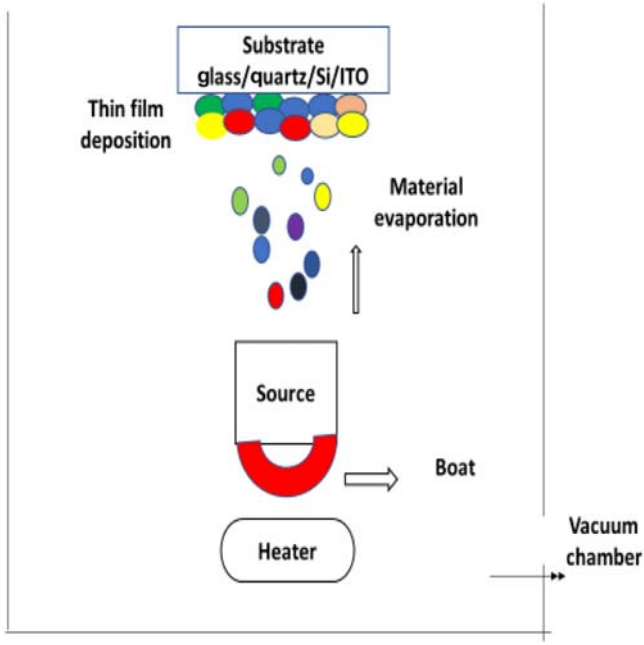

Figure 10.11 Mechanism of thermal evaporation technique.

crystallization is achieved at low deposition temperatures than other PVD techniques because the ionized species have high kinetic energy.

When laser beam interacts with source material and induces ablation, it can cause rapid heating and cooling of the source material with very high temperature. Hence, an instant evaporation is possible over small areas of the target. Power is delivered in the form of high-power pulses creating flash evaporation condition, which leads to an important advantage of congruent evaporation of compound materials.

When the high-power laser radiation falls on the surface of a solid, it will be absorbed only when the energy density is greater than the ablation threshold and converted into electronic excitation and then into thermal energy to cause evaporation, ablation, and excitation. The schematic diagram of PLD technique is shown in Fig. 10.12. Alumina protection coatings, diamond carbon coatings by PLD technique were reported by several authors [50,51].

10.3.2.5 DC sputtering

DC sputtering is one of the powerful PVD techniques for both research and production purposes in which the ejection of atoms from surface of the target material to the substrate is carried out by bombarding with high energy particles. In cathodic sputtering the ejection is due to the positive ion bombardment in the vacuum chamber where the target and substrate are placed parallel to each other. Mostly the

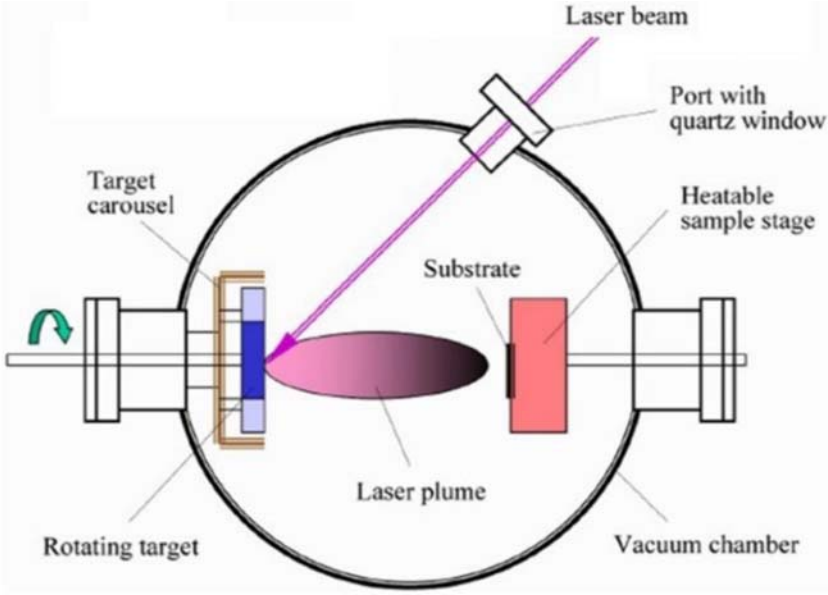

Figure 10.12 Technical details of PLD system. *PLD*, Pulsed laser deposition.
Source: Courtesy of http://groups.ist.utl.pt/rschwarz/rschwarzgroup_files/PLD_files/PLD.htm.

conducting metals are used as targets and this technique is extensively used in semiconductor industry, decorative fields, nonreflective coatings, and protective coatings for sensitive metal oxides.

Fig. 10.13 shows the process of DC sputtering that consists of one cathode for which the negative voltage is applied (target electrode) and one anode (substrate) that is generally grounded or biased.

Noble gases (argon) are used in the chamber as they do not interact with the target material. Initially, the chamber is at a pressure as high as 1 Torr and later after the glow discharge is stabilized, the pressure can be maintained at about few hundred mTorr. Positive ions in the discharge strike the cathode plate and discharge neutral atoms. The rate of material sputtered, Q, under constant conditions is inversely proportional to the gas pressure, p and anode−cathode distance, D. It can also be accepted that the amount sputtered will be proportional to the positive ion current, flowing to the cathode,

$$Q = \frac{KV_i}{\rho D^+}$$

where K is proportionality constant, which is a function of the voltage, V. However, the rate of sputtering also depends on the sputtering yield (the number of atoms ejected per incident ion), which in turn depends on the ion energy, mass of the ion, target material, and target−substrate geometry.

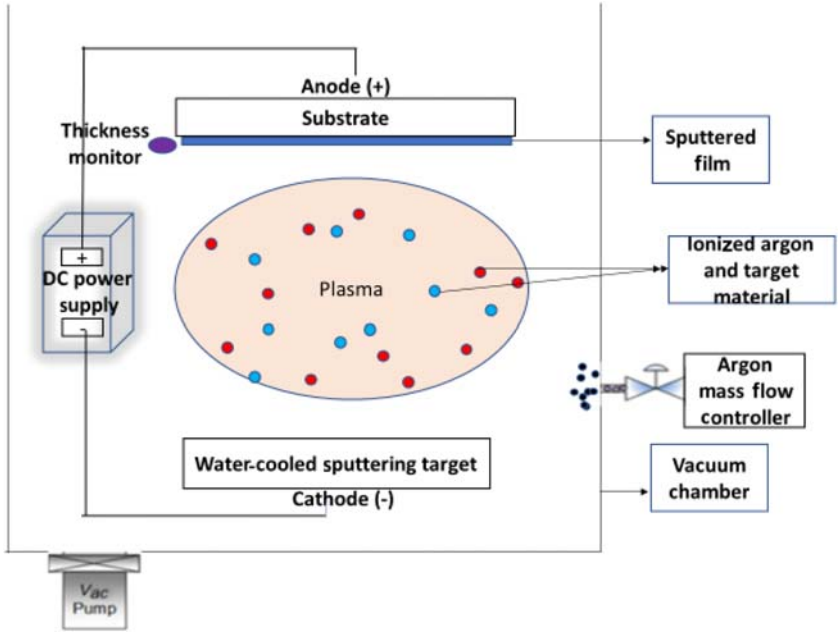

Figure 10.13 DC sputtering process.

These sputtered particles stream in the plasma and strike the substrate and get deposited on the substrate. Nowadays, the research extends to test the metallic and ceramic coatings deposited on plastics by sputtering phenomena for their effective utilization in personal protection equipment used by fire fighters [52]. The progress in the technology of magnetron sputtering toward electromagnetic shielding, thermal protection, bacterial resistance, hydrophilic and hydrophobic properties, structural color, etc. was explained by several authors [53,54].

10.3.2.6 Radio-frequency sputtering

A simple variation of the DC sputtering technique results in a solution of q fundamental faceted. In RF sputtering, alternating current (AC) is used to neutralize the charge build up on the insulating plate as shown in Fig. 10.14.

When negative potential is applied to the target, it is bombarded by positive ions and since the target is insulating, the positive charge keeps on building on the target until it repels any further positive bombardment. Later during the positive half of the cycle, it is bombarded by electrons and thus neutralizes the target. Frequencies of 1 MHz or more are required for producing continuous discharge. For the flow of AC at these frequencies to an insulating target is equivalent to a dielectric of a series capacitor. Standard RF for industry allocated by international communication authorities is 13.56 MHz, so that it does not interfere with communication.

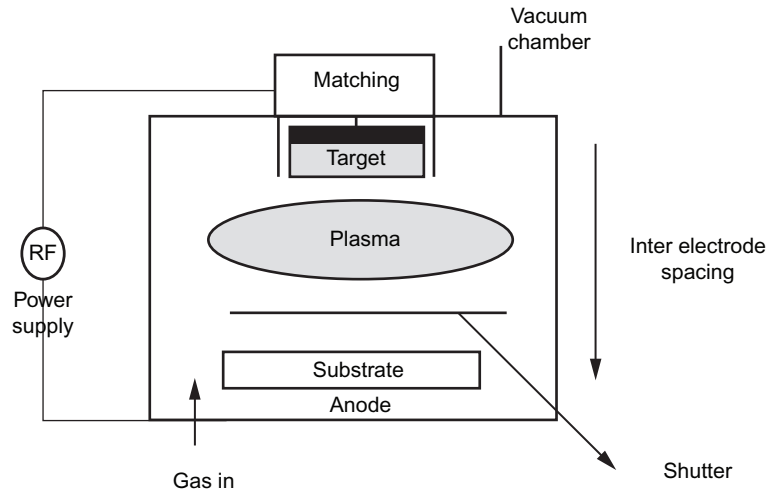

Figure 10.14 Schematic diagram of RF sputtering. *RF*, Radio-frequency.

The plasma impendence mainly depends on temperature, area, and pressure. RF plasma impedance must be matched to the standard 50 Ω impedance of RF generator. Plasma impedance changes with the process conditions. (The plasma impedance greatly depends upon the plate area, spacing, gas type, pressure, and temperature.) Therefore an impedance matching network is needed so that load inside the chamber appears as 50 Ω to the RF generator to ensure minimum power loss.

As the electrons are less massive than gas ions, they attain greater velocities due to the application of practical RF voltage. Hence, electrons can accumulate on the substrate, target, and also on the walls of the chamber. Hence, the plasma is the most effective positive potential in the system. The induced negative voltage accelerates the positive ions toward negatively charged surface. RF sputter deposition basically depends on the large difference in the mass of electrons and ions, which lead to change in mobility. The target is sputtered by controlling the relative surface area of the target and substrate. The ion current flux, J, can be calculated by the Child−Langmuir equation.

The structural materials for aircraft engine blades [55] were made up of nickel-based alloys that have to withstand to degradation process, fatigue, thermal stability, and environmental corrosion. Studies are going on aeronautical nickel-based alloys to improve the oxidation resistance by thermal barrier coatings of YSZ and iridium coatings on carbon composites and graphite [56].

10.3.2.7 Molecular beam epitaxy

MBE is a technique, used to develop epitaxial structure of high quality under an ultrahigh vacuum. The schematic diagram of MBE is shown in Fig. 10.15.

The substrates are specially cleaned after loading into the chamber by argon ion bombardment followed by annealing. Due to this one can prevent the contamination from the undesired oxides present on the surface of the substrate and annealing

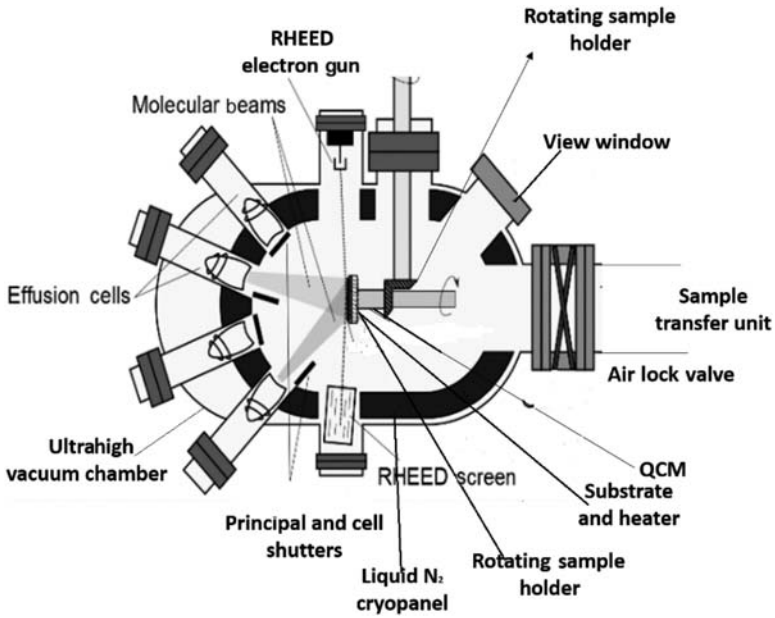

Figure 10.15 Schematic diagram of molecular beam epitaxy system.

heals the damage of the substrates by the bombardment. In this method the source materials for the films are especially from elemental sources.

The source of species is generally specially designed for evaporation to reduce the interaction of material and the source as well as the desorption of vapors by the source during functioning. This deposition system in a ultra high vacuum (UHV) chamber is complemented by various analytical methods (mass spectrometer for analyzing the vapor impinging to the substrate, refection high- and/or low-energy electron diffraction, Auger electron spectroscopy (AES) and X-ray photoelectron spectroscopy (XPS) analysis system, etc.). Even though, it has the conceptual simplicity, a great technological effort is required to produce desired quality films with high purity, uniformity, and interface control [57,58].

10.3.2.8 Flash evaporation method

Flash evaporation is one of the widely used PVD techniques to deposit stoichiometric semiconducting compounds and alloys. Fig. 10.16 represents the schematic diagram of flash evaporation technique.

Alloys and intermetallic compounds consist of different melting points and when resistively heated, the elements are deposited on the substrate based on their melting points. This problem can be rectified by this flash evaporation technique. In this a fine powder of compound can fall on the heated boat by means of mechanical, vibrating, or electromagnetic method. Hence, the instantaneous and complete evaporation of component elements take place irrespective of their melting point.

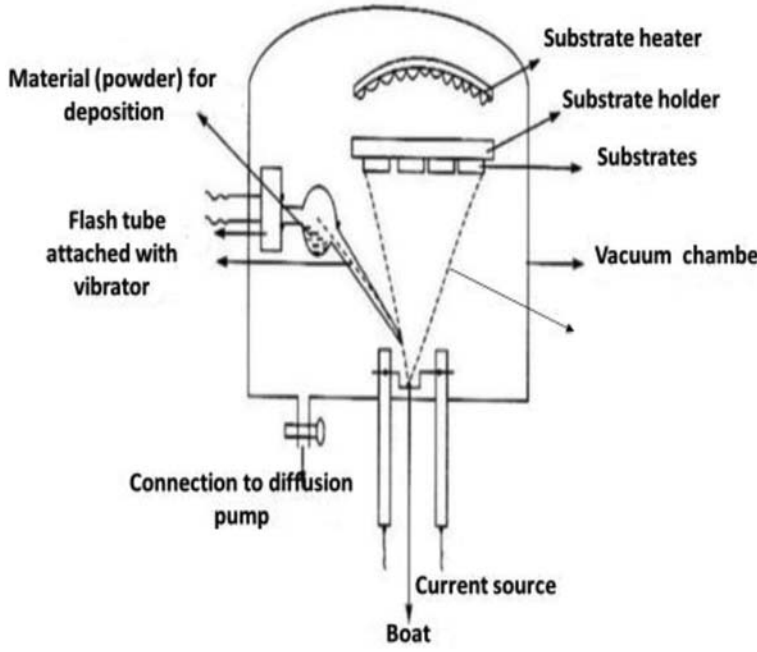

Figure 10.16 Schematic representation of flash evaporation.

10.3.2.9 Electron beam evaporation

Electron beam evaporation technique is one of the PVD techniques in which the electron beam given off by the hot tungsten filament is bombarded with the target under high vacuum. The surface of the target is melted by the electron beam and the atoms are evaporated. These atoms condense into solid thin film form on the substrates [59−61]. It is used to evaporate a wide range of materials. In this technique a stream of electrons is thermionically generated from the filament and is accelerated to attain high kinetic energy. These accelerated electrons are focused onto the surface of the evaporant material loaded in a water-cooled copper/graphite crucible. Usually, materials to be deposited are made into pellets/commercially available material slugs and are taken into water-cooled copper crucible with a carbon liner. Due to the incidence of the electron beam on the evaporant surface, which can be scanned over a limited area, the electrons lose their kinetic energy on the surface mostly as heat and instantaneous evaporation takes place from the surface of the material. Since a focused small area is only exposed, it avoids the decomposition of the starting material to some extent and the reactions with the crucible walls. As the material is in molten state only at the surface where the electron beam is focused and as the crucible is cooled, the evaporant material does not contaminate and the film composition will almost be the same as that of the starting material.

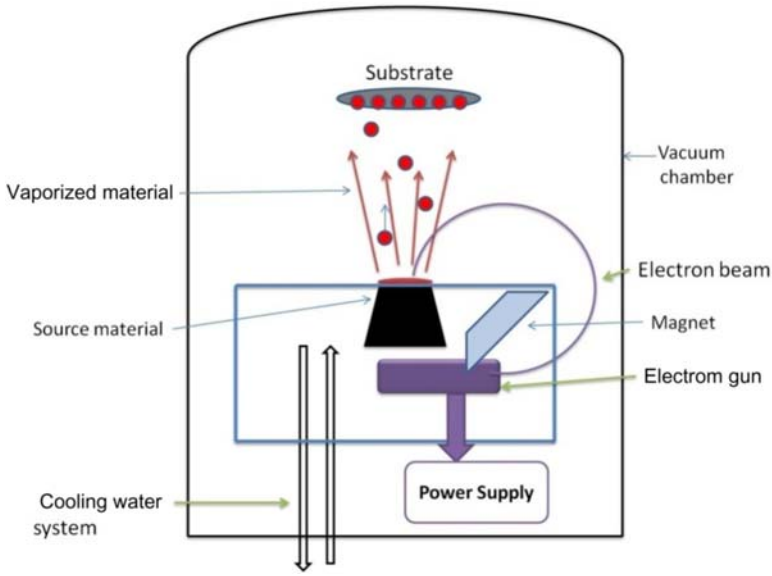

Figure 10.17 Schematic diagram of electron beam evaporation technique.

Temperatures exceeding 3000°C are obtainable and hence even materials with high melting points can be evaporated by this technique. The temperature is high at the surface where the beam is scanned, and the other part of the material remains cool. High deposition rates can be made possible by controlling the current and voltage of the electron beam. The typical electron beam evaporation system and its working mechanism are shown in Fig. 10.17.

10.3.2.10 Ion plating technique

Ion plating could be a PVD method that is typically referred to as ion power−assisted deposition or ion vapor deposition, which is one of the methods of vacuum deposition. Primarily, the bombardment process is used to clean the substrate surface and then to deposit film by atomic-sized energetic particles as shown in Fig. 10.18.

Throughout deposition the bombardment is employed, which has effect on the properties of the depositing film. To maintain atomically clean surface, it is vital that the bombardment should be continuous between the cleaning and deposition parts.

10.4 Conclusion

Metal oxides have a wide range of properties and are very promising materials for energy storage devices, gas sensors, memories, solid-state microbatteries, catalysts, transistors, electronic components, transducers, optoelectronic devices, membrane reactors, and bioapplications. TPCs act as barriers with respect to the degrading

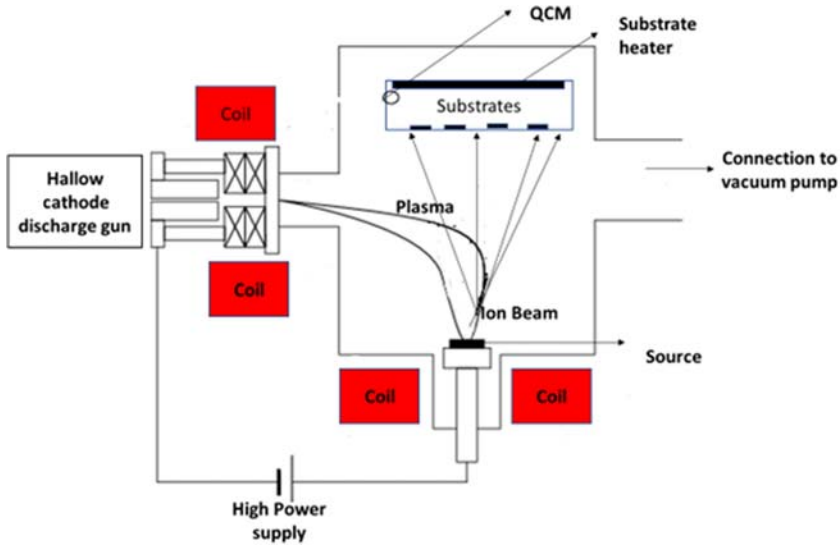

Figure 10.18 Process involved in ion plating.

harsh environments for the engines, photovoltaic panels, solar cells, biomedical coatings, gas turbines, industrial components, which are operated at higher temperatures and corrosive environments. Continuous improvements will be needed in this area to meet the challenges of enhancing the efficiency, lifetime, and cyclability of device components. Efforts are being made in identifying the new materials and compositions to enhance the performance by using different crystal structures and atomic level simulations. This chapter dealt various CVD and PVD methods used to deposit TPC on the oxide materials. The basic principle of the methods and relative merits are briefly discussed. The choice of the technique and deposition parameters depend largely on the component, structural stability of the overlayer, the operating conditions, and the ease of employing the specific technique. The reader should be familiar with all the techniques in order to exploit the best method for the required application.

References

[1] N. Tsuda, K. Nasu, A. Yanase, K. Siratori, Electronic Conduction in Oxides, 94, Springer Series in Solid-State Sciences, 1991.
[2] C.N.R. Rao, J. Gopalakrishnan, New Directions in Solid State Chemistry, Cambridge University Press, UK, 1997.
[3] D. Adler, in: N.B. Hanny (Ed.), Treatise on Solid State Chemistry, vol. 2, Plenum Press, New York, 1975.

[4] C.N.R. Rao, G.V. Subba Rao, Transitional metal oxides, crystal chemistry, phase transition and related aspects, in: NSRDS—NBS Monograph, vol, 49, National Bureau of Standards, Washington, DC, 1974.
[5] J.B. Goodenough, Prog. Solid State Chem. 5 (1971) 149.
[6] C.N.R. Rao, Solid State Chemistry", Marcel Dekker, New York, 1974.
[7] R.F. Bunshah, Deposition Technologies for Films and Coatings, Noyes Publications, New Jersey, 1982.
[8] J. George, Preparation of Thin Films, Marcel Dekker, New York, 1992.
[9] L.I. Maissel, R. Glang, Handbook of Thin Film Technology, Mc Graw-Hill, New York, 1970.
[10] K.L. Chopra, Thin Film Phenomena, McGraw-Hill, New York, 1969.
[11] D.R. Clarke, S.R. Phillpot, Thermal barrier coating materials, Mater. Today (2005) 22−29.
[12] P.K. Wright, A.G. Evans, Current opinion in solid state, Mater. Sci. 4 (3) (1999) 255−265.
[13] G.C. Righini, A. Chiappini, Glass optical waveguides: a review of fabrication techniques, Opt. Eng. 53 (7) (2014) 071819.
[14] A. Duran, Y. Castro, A. Conde, Handbook of Sol-Gel Science and Technology, Springer International Publishing, 2016, pp. 1−65.
[15] S. Zhang, J. Li, Inorganic−organic sol-gel hybrid coatings for corrosion protection of metals, J. Sol-Gel Sci. Technol. 54 (2010) 174−187.
[16] M.L. Zheludkevich, I. Miranda Salvado, M.G.S. Ferreira, J. Mater. Chem. 15 (2005) 5099−5111.
[17] J.M. Yeh, C.J. Weng, W.J. Liao, Y.W. Mau, Surf. Coat. Technol. 201 (3−4) (2006) 1788−1793.
[18] H. Zhang, R. Lamb, J. Lewis, J. Sci. Technol. Adv. Mater. 6 (2005) 236−239.
[19] M.L. Zheludkevich, S.K. Poznyak, et al., Active protection coatings with layered double hydroxide nano containers of corrosion inhibitor, Corros. Sci. 52 (2) (2010) 602−611.
[20] M. Guglielmi, Sol-gel coatings on metals, J. Sol-Gel Sci. Technol. 8 (1−3) (1997) 443−449.
[21] L.C. Klein, Sol-Gel Optics Processing and Applications, Springer, 1994.
[22] I.K. Igumenov, A.N. Aksenov, Thermal barrier coatings on gas turbine blades: chemical vapour deposition, Therm. Eng. 64 (12) (2017) 865−873.
[23] H. Xu, H. Guo, Thermal Barrier Coatings, Woodhead Pub Ltd, Oxford, 2011.
[24] D.A. Chubarov, P.V. Matvev, New ceramic materials for thermal protection coatings of gas turbine engines working blades, Aviats. Mater. Technol. 4 (2013) 43−46.
[25] P.T. Kolomytsev, High temperature protection coatings for nickel alloys, Moscow, Metallurgiya, 1991, pp. 58−59.
[26] L. Cheng, Y. Xu, L. Zhang, J. Mater. Sci. 37 (2002) 5339−5344.
[27] Y. Xu, L. Cheng, L. Zhang, J. Mater. Sci. 34 (1999) 6009−6014.
[28] T. Piqnera, H. Vincent, C. Vincent, Carbon 33 (1995) 455−467.
[29] J.D. Webster, M.E. Westwood, F.H. Hayes, J. Eur. Ceram. Soc. 18 (1998) 2345−2350.
[30] H.O. Pierson, Handbook of CVD: Principles, Technology and Applications, second ed., William Andrew Publishing, New York, 1999.
[31] Q.M. Liu, L.T. Zhang, J. Liu, J. Am. Ceram. Soc. 93 (2010) 3990−3992.
[32] Y.S. Liu, L.T. Zhang, L.F. Cheng, Corros. Sci. 51 (2009) 820−826.
[33] M. Kamruzzaman, T.R. Luna, J. Podder, M.G.M. Anowar, Semicond. Sci. Technol. 27 (3) (2012). 035017.

[34] B.L. Zou, Z.S. Khan, X.Z. Fan, Surf. Coat. Technol. 219 (2013) 101–108.
[35] B.L. Zou, Z.S. Khan, X.Z. Fan, Corros. Sci. 62 (2012) 192–200.
[36] Y.H. Junqiyao, D. Wang, H. Peng, H. Gua, S. Gong, Corros. Sci. 80 (2014) 37–45.
[37] V. Viswanathan, R. Filmatter, S. Patil, S. Deshpande, S. Seal, J. Am. Ceram. Soc. 90 (3) (2007) 870–877.
[38] M. Gell, E.H. Jordan, M. Teichloz, B.M. Cetegen, N.P. Padture, L. Xie, et al., J. Therm. Spray Technol. 17 (1) (2008) 124–135.
[39] F.D. Balacianu, R. Bartos, A.C. Nechifor, Organic–inorganic membrane materials, UPB Sci. Bull., Ser. B: Chem. Mater. Sci. 71 (3) (2009) 37–54.
[40] E.L. Corral, R.E. Loehman, J. Am. Chem. Soc. 91 (5) (2008) 1495–1502.
[41] P.C. Innocenzi, M. Guglielmi, M. Gobbin, P. Colombo, J. Eur. Ceram. Soc. 10 (6) (1992) 431–436.
[42] M. Menning, G. Jonschker, H.K. Schmidt, Proceedings of SPIE 1958, 1992.
[43] D. Ebert, B. Bhushan, ACS 28 (2012) 11391–11399.
[44] G.P. Thim, M.A.S. Diveria, et al., Sol-gel silica film preparation from aqueous solutions for corrosion protection, J. Non-Cryst. Solids 273 (1–3) (2000) 124–128.
[45] R. Zazpe, J. Prikryl, V. Gartnerova, K. Nechvilova, L. Benes, L. Strizik, et al., 2017. Atomic layer deposition Al_2O_3 coatings significantly improve thermal, chemical, and mechanical stability of anodic TiO_2 nanotube layers. Langmuir 33 (13), 2017, 3208–3216
[46] J. Prakash, H.C. Swart, G. Zhang, S. Sun, J. Mater. Chem. C 6 (2019).
[47] D. Sohrabi, B. Heidary, C.A. Randall, Langmuir 27 (2016) 245701.
[48] X.Q. Cao, R. Vassen, D. Stoever, J. Eur. Ceram. Soc. 24 (2004) 1–10.
[49] J. Raul, Martin-Palma, A. Lakhtakia, Engineered Biomimicry, Elsevier, 2013, pp. 383–398.
[50] J.M. Lackner, C. Stotter, W. Waldhanger, R. Ebner, W. Lanz, M. Beutl, Surf. Coat. Technol. 174-175 (2003) 402–407.
[51] A.K. Singh, S. Kaity, K. Singh, J. Thomas, T.R.G. Kutty, S. Sinha, Mater. Chem. Phys. 143 (2014) 1446–1451.
[52] M. Fejdys, K. Olszewska, S. Kaczmarczyk, G. Owczarek, Polish J. Chem. Technol. 18 (3) (2016) 50–58.
[53] X.Q. Tan, J.-Y. Liu, J.-R. Niu, J.Y. Liu, J.Y. Tian, Materials 11 (2018) 1953.
[54] M.S. Shariatdoust, H. Aghajani, J. Mater. Eng. Perform. (2018).
[55] J.Y.A. Calahorra, H.E.E. Ponce, J.A.C. Miramontes, F.A. Calderón, C. Gaona, E C S Meeting Abstracts, ECS-The Electrochemical Society, 2015.
[56] K. Mumtaz, J. Echigoya, T. Hirai, Y. Shindo, Mater. Sci. Eng., A 167 (1–2) (1993) 187–195.
[57] A.Y. Cho, J. Vac. Sci. Technol. 16 (1979) 275.
[58] K. Alavic, Encyclopedia of Materials: Science and Technology, Elsevier, 2001.
[59] C.A. Bishop, Vacuum Deposition Onto webs, Films and Foils, second ed., Elsevier, 2011.
[60] B.E. Paton, B.A. Movchan, Thin Solid Films 54 (1) (1978) 1–8.
[61] E.M. Oks, A. Tyunkov, Y. Yushkov, D.B. Zolotukhiv, Surf. Coat. Technol. 325 (2017) 1–6.

This page intentionally left blank

Metal oxide nanoparticles in biomedical applications

11

Sudtha Murthy[1], *Paul Effiong*[2] *and Chee Chin Fei*[3]
[1]Department of Chemistry, University of Malaya, Kuala Lumpur, Malaysia, [2]Faculty of Applied Sciences, UCSI University, Kuala Lumpur, Malaysia, [3]Nanotechnology and Catalysis Research Centre, University of Malaya, Kuala Lumpur, Malaysia

11.1 Introduction and overview of metal oxides in biomedical applications

Over the years, metal oxides have been studied in various applications [1]. Metal oxides derived from the early transition metals exhibited a remarkable variety of properties, including catalytic, electro-optic, dielectric, electromechanical, ferroelectric, and wave density charging behavior [2]. These properties enable their use in various reactions such as selective oxidation, dehydration, photocatalysis, and electrocatalysis. Due to their distinctive physicochemical properties, a good deal of research has also been directed toward utilizing metal oxide materials in biomedical applications [3]. It has been reported that certain metal oxides can interact with the surfaces of a carrier to develop oxides' monolayer structures for drug delivery [3]. Magnetic metal oxide nanoparticles (NPs) are of great interest in medical research because they can be manipulated with an external magnetic field [4]. In particular, superparamagnetic iron oxides have attracted huge interest in targeted therapeutics and diagnostics. The physicochemical properties of these metal oxide NPs are correlated to their size and shapes [3]. Some of them are biocompatible and chemically stable [5]. It was reported that certain metal oxide NPs can kill cancer cells at low dose and remain nontoxic to normal cells [6]. Recent discoveries have opened a new boundary for biomedical applications of metal oxide NPs in retinopathy, biological sensors, and cancer treatment [7].

11.2 Structural diversity and its relationship to the properties of the metal oxides

Metal oxides come in various shapes and sizes. These properties strongly correlate with their method of synthesis. Metal oxide NPs range in size from 1 to 100 nm (1 nm is equal to 10^{-9} m). Compared to their micro- or bulk-sized counterparts, metal oxide NPs have various distinct features [5]. These NPs can enter the cell membrane, internal cellular organelles, and may even cross the blood–brain barrier.

Metal Oxide Powder Technologies. DOI: https://doi.org/10.1016/B978-0-12-817505-7.00011-7

Metal oxide NPs can interact with proteins to form protein corona, where layers of proteins are wrapping the NPs. The formation of protein corona can influence the biodistribution and transport of the metal oxide NPs [3]. Metal oxide NPs with a diameter of less than 20 nm are more efficient to cross the cell membrane. Small-sized NPs can penetrate bacterial cells and release toxic metal ions by dissolution [3]. The key factors that contribute to the distinct properties of metal oxides are surface area and quantum effects. Metal oxide NPs have a greater surface area per unit mass compared to their bulk-sized counterparts. As the surface area increases, the properties of the metal oxides will be affected. Quantum effects involve the number of atoms within the metal oxides that are constantly in motion. An increase in surface area will lead to an increase in the surface atoms that are constantly in motion and eventually affect the optical, electrical, and magnetic properties of metal oxide NPs [8]. Taken together, these factors can improve the properties of metal oxides in terms of reactivity, strength, and electrical properties. Hence, they must be considered when creating metal oxide nanostructures and nanosystems with new properties and functions.

11.3 Important considerations and challenges for the use of metal oxides in biomedical applications

An important aspect for the safe and effective use of metal oxides in biomedical applications is toxicity. Some studies have shown that metal NPs are toxic to human. The toxicity is depended on the size and surface load of metal NPs [9]. It is necessary to identify any potential health risks associated with these metal oxide NPs. With regards to potential genotoxicity, it is important to investigate on the subtle cellular alterations in DNA (deoxyribonucleic acid) damage and oxidative stress on human tissues. The other important consideration for metal oxides being used for implants is their chemical inertness. Iron oxide (Fe_2O_3), zinc oxide (ZnO), titanium oxide (TiO_2) are the most commonly used metal oxides in biomedical applications. The NP of these metal oxides can be synthesized and modified with appropriate functional groups that allow them to bind with drugs, antibodies, and ligands of interest. The functionalization of metal oxides can be facilitated by non-covalent interactions (coordination or hydrogen bonding) between the ligands and the surface metal ions or hydroxyl groups [5]. Ideally, the metal oxide NPs should have the following features for biomedical applications: (1) chemically stable, (2) resistance to wear and scratch, (3) biocompatible, and (4) nontoxic. The stability of metal oxides is strongly correlated to the heat of formation of metal oxides [10,11]. A stable metal oxide does not easily dissociate to metal ion. Today the use of metal oxides has reached to an internationally recognized standard. For example, zirconium dioxide (zirconia, ZrO_2) biomaterials must be prepared in accordance with the international standard of reference ISO 13356 (zirconia). These international standards specify the requirements and corresponding test methods for biocompatible metal oxide materials for medical uses [1].

There are several challenges in the production of metal oxides, among those are difficulty in scale up and high cost of production. For metal oxides to be used in magnetic resonance imaging (MRI), it is difficult to increase the production yields while optimizing the magnetic properties, surface coating, mean hydrodynamic size, and aggregation state of these materials [12]. For metal oxide NPs to be used as drug carriers, it is a big challenge to determine their drug-loading capacity. This is because part of the drugs is released before reaching the target cells due to unstable interaction between the drug molecules and the metal oxide NPs [13]. The bioavailability and biocompatibility of metal oxides are important to avoid agglomeration in physiological condition and remain intact in the tissue for enough time to elicit a desired response. The metal oxides should be removed before stimulating undesired side effects in the body [14]. In order for the metal oxide NPs to be freely circulated in blood, it requires a well-tailored design of the surface coating and hydrodynamic size of the metal oxide NPs. Taken together, these considerations are important for creating a useful metal oxide material in biomedical applications [15].

11.4 General synthesis of metal oxides and highlight on the biological synthesis of metal oxides

Numerous manufacturing techniques are available for synthesizing metal oxides, that is, chemical, physical, and biology methods [16]. Chemical method is the recurrent synthesis pathway for metal oxides because the raw materials are commercially available. Examples of the chemical methods include mechanochemical process, surfactant precipitation, sol−gel method, solvo-thermal, hydrothermal, and emulsion methods. Chemical method is cost-effective and easier to scale up when compared to the biological method. It offers flexibility to control the size and shape of the metal oxide NPs [16]. Details of the chemical synthesis method are covered in Chapter 3, Synthesis and preparation of metal oxide powders. Chapter 9, Chemical processes of metal oxide powders, covers the physical synthesis methods of metal oxides.

Biological method has been considered as a green synthetic method because of its simplicity and environmental friendliness. Metal oxide NPs such as CuO, TiO_2, ZnO, and iron oxides have recently been biologically synthesized using bacteria, fungi, and plant. Some bacteria have the capability to synthesize metal oxide NPs via reduction process. For example, thermophilic bacteria showed the ability to reduce amorphous Fe (III)-oxyhydroxide to magnetic iron oxide NP [17]. A simple step to synthesize zinc oxide NPs was reported using bacterium, *Aeromonas hydrophila* [18]. X-ray diffraction confirmed the crystalline nature of the zinc oxide NPs. The morphology of the NP was found to be spherical with an average size of 57.72 nm [18]. Biosynthesis of titanium dioxide NPs has been reported by using *Bacillus subtilis*. The morphological characteristics of the titanium dioxide NPs were found to be spherical and oval, with their sizes ranging between 66 and 77 nm [19].

Bacteria are extraordinarily skilled engineers of metal oxide NPs. However, the biosynthetic process on how to produce metal oxides in nano size is poorly understood. The main reason is because the enzymes involved in this biosynthesis process are largely uncharacterized. A recent study revealed that the structure of a bacterial enzyme is responsible for the biosynthesis of manganese oxide NPs [20]. This structural information provides a better understanding of the biosynthesis of manganese oxides. Although biological synthesis is known to produce less toxic metal oxide NPs, it requires fastidious cell cultivation and hence is difficult in controlling the size, shape, and crystallinity [9].

Compared to bacteria, fungi can synthesize larger amounts of metal oxide NPs. This is because fungi have high intracellular metal absorption capacity and a large number of enzymes are produced per biomass unit [21]. TiO_2 NPs have been synthesized using fungal spores of *Aspergillus flavus* TFR7 [21]. Zinc oxide NPs have been synthesized using *Aspergillus terreus* [21]. Fungal spores of *Fusarium oxysporum* has been used for the synthesis of barium titanate ($BaTiO_3$) and bismuth oxide (Bi_2O_3) [21]. NPs produced by different fungal species have different sizes and shapes. However, the time required to produce metal oxide NPs by fungi is a major disadvantage compared to the chemical methods. The intracellular synthesis of fungi has also led to difficult downstream processing and often fails to develop a simple and cheap process [21].

The synthesis of metal oxide NPs using plant extract is an alternative to the chemical methods. Compared with the latter, the plant extract-mediated biosynthesis of metal oxides is more environmental friendly [11]. It helps to reduce the formation of toxic by-products and also contributes to the fine-tuning of the size of NPs. Extracts from *Camellia sinensis* (green tea) have been used to synthesize spherical- and irregular cluster−shaped iron oxide NPs [21]. Zinc oxide NPs have been synthesized using leaf extracts of *Coriandrum sativum*, *Calotropis gigantea*, *Acalypha indica*, *Hibiscus rosa-sinensis*, and *C. sinensis* [21]. Titanum oxide NPs have been synthesized using extracts of *Jatropha curcas* and *Eclipta prostrata* [21]. Copper oxide NPs have been produced by leaf extracts of *Malva sylvestris* and *Aloe barbadensis Miller* [21]. The carbohydrates, proteins, and phytochemicals present in plant extracts are considered to play an important role in the production of metal oxide NPs. However, other factors, such as the phytochemical concentration, metal salt concentration, pH, temperature, and reaction time, are also known to affect the rate of NP production, quantity, and quality [21].

11.5 Commonly used metal oxides in biomedical applications

11.5.1 Iron oxides

Iron oxide NPs represent one of the most important classes of inorganic materials. Superparamagnetic iron oxide NPs (SPIONs) have been the most extensively

studied inorganic materials for imaging, drug delivery, and hyperthermia therapy. They are nontoxic, biodegradable, biocompatible, and efficiently cleared from the human body via the iron metabolism pathways. Ferumoxytol (one of the Fe_3O_4 NPs) has been approved as an iron supplement by the Food and Drug Administration (FDA). Other iron oxide NPs have been used in preclinical and clinical settings such as contract agents for MRI and drug carriers. Heike et al. revealed the intrinsic therapeutic effect of iron oxide NPs on tumors [22]. Tumor cells treated with iron oxide NPs have a slower growth rate than that of control [23]. Iron oxide NPs have also been found to possess an intrinsic enzyme mimetic activity like that of natural peroxidases, which oxidize organic substrates [24].

Iron oxide NPs are classified according to their sizes. They can be superparamagnetic or ferromagnetic. The terms are referred to the magnetic properties of iron oxide NPs. Superparamagnetic iron oxides have strong magnetic response to externally applied magnetic field [23]. However, these iron oxide NPs will not aggregate when the external magnetic field is removed. For this reason, they are suitable for the imaging of tumors and metastases. Another feature of SPION is their ability to induce local heating in tumor regions. Magnetic hyperthermia is known as an alternative treatment for cancer. When subject to external magnetic field, the iron oxide NPs will generate heat that can damage and kill cancer cells. The localized hyperthermia can also trigger the release of a loaded drug. Iron oxide NPs have been increasingly investigated as chemotherapeutic drug delivery vehicles [16]. The potential of using iron oxide NPs as a drug delivery system depends on its ability to target specific locations in the body.

11.5.2 Zinc oxide

Zinc oxide (ZnO) is another type of metal oxide NPs that have shown promising outcomes and broad applications [25]. This is due to the unique properties of ZnO such as biocompatibility, high selectivity, and ease of synthesis. These properties are determined by their size, shape, composition, crystallinity, and morphology of ZnO [26]. The cytotoxicity of ZnO correlates with its biocompatibility in cells [25]. ZnO exhibits promising antiproliferative activity against A549 lung cancer cells in vitro [27]. The selectivity of ZnO NPs against cancerous cells can be improved by introducing a surface coating and minimizing the hydrodynamic size of ZnO [24].

ZnO has been listed as a safe material by the FDA. It is nontoxic and can be used as a food additive or preservative. ZnO NPs have been proven to possess good antimicrobial properties [28]. Ngoepe et al. reported that ZnO NPs were effective against both Gram-positive and Gram-negative bacteria [27]. The results showed that the efficacy of these ZnO NPs varies with the size and surface area of the NPs [28]. ZnO NPs also have excellent anticorrosion properties and may suitable for use in medical implants. Ananth et al. reported that ZnO is a suitable material for bone repair and regeneration [29]. When used in combination with manganese-substituted hydroxyapatite (Mn-HAp), the resulting Mn-HAp/ZnO bilayer coating on stainless steels (type 316L SS) is suitable for orthopedic applications.

In addition, the Mn-HAp/ZnO coating on 316L SS implants shows high cell attachment and proliferation. The porous structured layer of coating offers enhanced bioactivity due to surface roughness, which leads to increased surface energy [29].

11.5.3 Titanium oxide

Titanium oxide (titania) NPs have generated great interest due to its chemical stability and low toxicity. Titanium oxide NPs are not toxic in vitro and in vivo. Due to these properties, titania is suitable for use in medical implants. A special engineered titanium oxide NP with controlled porosity and composition is ideal for protein adsorption and improves tissue attachment of implants. Deposition of these titanium oxide NPs as a film on medical implants facilitates bonding of the implant to the surrounding tissue. The bone-bonding feature of titania is correlated to the existence of surface hydroxyl groups, which can be enhanced by incorporating doping agents such as Ca, Mg, and F into titania [30]. Titanium oxide NPs have been shown to possess promising antibacterial, antifungal, and anticancer activities. NPs of titanium dioxide have been incorporated into various polymer patches. These patches have been shown a good antibacterial activity against Gram-positive and Gram-negative bacteria [31]. Decoration of curcumin in titanium oxide NPs was effective in wound healing [32]. Interestingly, incorporation of titanium oxide and curcumin in polymer patches has shown a good antibacterial activity against Gram-positive and Gram-negative bacteria [32].

11.5.4 Other metal oxides used in biomedical applications

Cerium oxide (ceria) NPs have attracted much attention as a useful biomaterial because of their ability to selectively induce irradiated cancer cells death, while protecting the surrounding tissue from damage caused by irradiation. These metal oxide NPs selectively induce oxidative stress in irradiated cancer cells without affecting normal cells [33]. Zirconium dioxide (zirconia, ZrO_2) is another promising metal oxide for biomedical implant. Zirconia is inert under physiological conditions. NPs made of ZrO_2 have excellent wear resistant and hardness. ZrO_2 NPs are more stable than their bulk-sized counterparts [34]. These properties allow it to be used as implant material for dental prosthetic surgery and total knee replacement [35]. Recently, composites made of zirconia and alumina have been introduced into the market [35].

11.6 Biomedical application of metal oxides

The properties of metal oxides have attracted considerable interest in biomedical research. Examples of biomedical application of metal oxides are drug delivery, implant, theranostic, cancer therapy, antimicrobial, and wound healing.

11.6.1 Drug delivery and theranostic applications

Drug delivery systems are designed to deliver therapeutic agents to the target sites in human body. Cerium oxide, zinc oxide, and SPIONs have been used as a carrier to deliver doxorubicin (DOX), tamoxifen, quercetin, rhodium (II) citrate, gallic acid, etc. The drugs are loaded in a way that does not compromise the functionality of the drug and it can be unloaded from the metal oxides upon triggered by stimuli [36].

Theranostics is a new area of medicine that combines specific targeted therapy with diagnostic tests. Theranostics uses specific biomarkers in the human body to obtain diagnostic images and provide the patient with a therapeutic dose of radiation [37]. Current research trends are directed toward combining drug delivery systems with different imaging contrast agents for tumor imaging, and monitoring of the delivery and efficacy of therapeutics. Recent advances in nanomedicine technologies have made it possible for the development of a single agent with combined targeted therapeutics and diagnostic functionality. Zinc oxide NPs have been utilized for this purpose. A summary of theranostic application in cancer using zinc oxide NPs is shown in Table 11.1.

SPION is another popular theranostic agent. The application of SPION as a contrast agent for MRI has been approved by the FDA. The SPION−drug conjugate can be magnetically guided to the desired tissues by using external magnets. Active targeting strategy has been used by conjugating targeting ligands on the surface of metal oxide NPs. This strategy is more effective in killing cancer cells than drugs alone because the metal oxide−drug complexes are more efficiently targeted toward the cancer cells. A study has reported that DOX-loaded SPIONs were more efficiently taken up by DOX-resistant breast cancer cells (1 μM DOX-resistant MCF-7) compared with free drug, thereby increasing the efficacy of the drug [39]. This approach leads to reduced doses of medicines and lower side effects [39].

11.6.2 Cancer therapy

An interesting feature about SPIONs is their thermal property. SPION can be used to induce local heating in tumor regions when suitably activated by an external magnetic field. The localized hyperthermia (temperature above 40°C) can subsequently trigger the release of a loaded drug or to cause cancer cell death by temperature-induced apoptosis [38]. However, the drawback is difficult to guide the SPION to the target site due to the drag of blood flow. SPION targeting is more effective in the regions of slower blood velocity, particularly when the magnetic field source is close to the target site [38].

Titanium dioxide (TiO_2) NPs have been used to kill cancer cells [33]. TiO_2 NPs have been found to be engulfed into the cell membrane and cytoplasm of cancerous cells. When these NPs are exposed to ultraviolet (UV) light, they generated cytotoxic radical oxygen species (ROS) that induced apoptosis. A major challenge in this approach is the direct illumination of tissues by UV light. Vinardell and Mitjans, Shrestha et al. showed that TiO_2 NPs can be mixed with SPIONs and thus

Table 11.1 Application of ZnO nanoparticles (NPs) as theranostic agents in cancer [38].

Type of ZnO nanocarrier[a]	Drug[b]	Stimuli[c]	Type of cell/animal used[d]
ZnO QDs	DOX	–	MCF-7
ZnO QDs	DOX	pH	MCF-7R, MCF-7S
ZnO QDs	DOX	pH	MDA-MB-231, HeLa, NCI/ADR-RES, MES-SA/Dx5
ZnO QDs	DOX	pH, ultrasounds	–
FA Mg ZnO QDs	DOX	pH	HeLa
FA hollow ZnO NPs	Paclitaxel	pH	MCF-7, MDA-MB-231, nude mice
FA ZnO nanosheets	DOX	pH, heat	MDA-MB-231, HBL-100, mice
ZnO nanorod	–	UV radiation	SMMC-7721
Lanthanide–ZnO QDs	–	UV, X-ray, γ-ray radiation	HeLa, PC3
ZnO nanorod	DOX	UV radiation	SMMC-7721
ZnO QDs	Paclitaxel, cisplatin	UVA irradiation	HNSCC
MUC1 aptamer S2.2. ZnO QDs	DOX	UV radiation	MCF-7
Gd-polymer–ZnO QDs	DOX	pH	BxPC-3, tumor-bearing nude mice
ZnO nanorod	–	UV radiation	SMMC-7721

[a]ZnO QDs: Zinc oxide quantum dots; FA: folic acid; QDs: quantum dots; MUC1: membrane glycoprotein that is highly expressed in most breast cancers; Aptamer S2.2.: (5-COOH-GCA-GTT-GAT-CCT-TTG-GAT-ACC-CTGGTTTTT-FAM-3?); SiO_2: silica; NCs: nanocrystals; MABG: TiO_2@ZnO–GO: ZnO-coated mesoporous titanium oxide QDs containing graphene oxide; Fe_3O_4@ZnO@mGd_2O_3:Eu@P(NIPAm-*co*-MAA): iron oxide QDs coated with ZnO and mesoporous Gd_2O_3:Eu shells with a polymer poly[(*N*-isopropylacrylamide)-*co*-(methacrylic acid)] [P(NIPAm-*co*-MAA)] to gate the mesoporous; $K_8(RGD)_2$ cationic peptide containing 2 RGD sequences; β-CD-Fe_3O_4@ZnO: Er^{3+}, Yb^{3+}: β-cyclodextrins functionalized iron oxide QDs doped with Er^{3+} and Yb^{3+} coated with ZnO; ZnO MSNs: mesoporous silica NPs with ZnO QDs as cap of the pores; UCNPs@mSiO_2-ZnO: lanthanide-doped upconverting NPs with a mesoporous silica layer and ZnO QDs as gatekeeper; ZnO-pSiO_2-GSSG NPs: ZnO QDs as cups of oxidized glutathione (GSSG) amino-functionalized silica NPs; L-pSiO_2/Cys/ZnO NPs: lemon like silica NPs with cysteine and ZnO QDs cups; MCNs: mesoporous carbon nanoparticles.
[b]DOX: Doxorubicin; Cur: curcumin; VP-16: chemotherapeutic drug etoposide; CPT: camptothecin.
[c]UV: Ultraviolet.
[d]MCF-7: Human breast cancer cell; MCF-7S/MCF-7R: human breast cancer cell sensitive/resistant to doxorubicin; MDA-MB-231: epithelial, human breast cancer cell; HeLa: human epithelial cells from a fatal cervical carcinoma; NCI/ADR-RES: ovarian tumor cell; MES-SA/Dx5: multidrug-resistant human sarcoma cell; HBL-100: human, Caucasian, breast cancer cell; SMMC-7721: human hepatocarcinoma cell; PC3: human prostate cancer cell; HNSCC: head and neck squamous cell carcinoma; BxPC-3: human pancreatic cancer cell; HEK 293T: human embryonic kidney cells; Caco-2: human epithelial colorectal adenocarcinoma cell; HepG2: human liver cancer cell; A549: adenocarcinomic human alveolar basal epithelial cell.

be magnetically guided to the target sites [33]. TiO_2 NPs can remain in the body for a long time without imposing any toxicity [40].

Cerium oxide NPs have been shown as a valuable tool to supplement classical chemotherapeutics, such as DOX, and protect against DOX-induced cytotoxicity [33].

Cerium oxide NPs have been shown to protect cells from ROS-induced damage. It was hypothesized that the selective toxicity of cerium oxide NPs to cancer cells is due to their catalase mimetic activity in acidic environments (pH 4.3). Cerium oxide NPs can act as radio-sensitizing agents by means of an additional biological mechanism to control the response to DNA damage. In radiation therapy, cerium oxide can selectively induce the death of irradiated cancer cells, at the same time protecting the surrounding tissue from radiation-induced damage and oxidative stress. A recent study has compared the cytotoxic effect of cerium oxide NPs against cancerous and normal cells [33]. The result showed that cerium oxide NPs were cytotoxic to cancerous cells but not normal cells [33].

Cerium oxide can exist in two oxidation states: Ce^{3+} or Ce^{4+}, which may be interchanged under redox environment. Ce^{3+} ions are associated with oxygen vacancies. A reduction in particle size of cerium oxides results in the formation of Ce^{3+}. This property allows ceria to be used as an excellent free radical scavenge agent. They are nontoxic to the healthy cells. Cerium oxide NPs are also nongenotoxic. Due to its radio-sensitizing property, cerium oxide can control the response to DNA damage. The mode of action of cerium oxide is strongly dependent on the size and cell type. Besides that, in vivo studies with immunodeficient nude xenografted mice have shown a decrease in tumor weight and volume after treatment with cerium oxide [9].

11.6.3 Implants

Bacterial adhesion and multiplication in biomedical implant are traumatic for patients. Infected implants may lead to bone resorption and has to be removed. Research has been directed toward the application of antimicrobial coating on implants that act independently or synergistically with the administered antibiotic to limit bacterial infection. Factors such as biocompatibility, antiinfective efficiency, durability, and resistance to mechanical stress were considered for their suitability to be used in antibacterial coating. Titania is often used in biomedical implants. Implants coated with titania have an excellent biocompatible surface for cell attachment and proliferation. TiO_2 NPs with different sizes and shapes have been produced to serve for this purpose [41]. Alumina (Al_2O_3), ZnO, and CuO NPs have also been shown to be suitable coating material for the prevention of infection in medical implant [9]. Fig. 11.1 shows the most important antimicrobial bone implant properties.

11.6.4 Antibacterial treatment and wound healing

Metal oxide NPs have been shown to exhibit antimicrobial activity at low concentration. Vijaykumar et al. reported that ZnO nano-powders have a lower minimum inhibitory and bactericidal concentration compared to that of zinc acetate. The ZnO nano-powders are also effective against a panel of Gram-positive and Gram-negative bacteria [42]. Azam et al. investigated the antimicrobial activity of ZnO, CuO, and Fe_2O_3 NPs against various Gram-positive and Gram-negative bacteria [42].

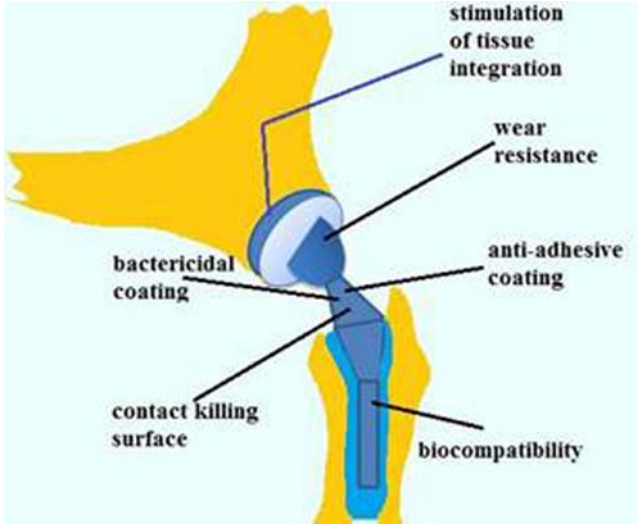

Figure 11.1 Multifunctional surfaces of an implant.
Adapted from: L.D. Duceac, S. Straticiuc, E. Hanganu, L. Stafie, G. Calin, S.L. Gavrilescu, Preventing bacterial infections using metal oxides nanocoatings on bone implant, IOP Conf. Ser. Mater. Sci. Eng. 209 (1) (2017).

They found that ZnO is more effective against Gram-positive bacterial strains than Gram-negative bacterial strains. The size of ZnO NPs greatly influences the efficacy of bacterial growth inhibition. A decrease in particle size increases the surface-to-volume ratio, which leads to the inhibition of bacterial growth. It was reported that the ZnO NPs facilitated the production of reactive oxygen species that kill bacteria [42].

Wound healing is a research area that aims to speed up the recovery of a wound and reduce the risk of infection. Zinc oxide NPs have been used in wound healing due to their excellent antibacterial and antifungal activities. Incorporation of ZnO NPs into wound dressing materials is found to improve the wound healing process. Studies have shown that ZnO NPs with size of less than 100 nm are more effective against bacteria. They are also less toxic to normal cells (MG-63, HDF) in vitro [43]. It was reported that leaching of Zn ions from the ZnO NPs facilitated keratinocytes migration and promoted epithelialization [41]. Enhanced antibacterial activity has been observed when ZnO NPs were introduced into hydrogel-based wound dressings. However, ZnO NPs may induce toxicity to human cells when the concentration exceeding 8 μg/mL [43].

Titanium oxide NPs have also been found to be effective in wound healing. When titanium oxide NPs were UV irradiated, the titanium ions were released and subsequently inhibited microbial proliferation and accelerated wound healing. In addition, the photocatalytic property of TiO_2 can lead to the formation of reactive oxygen species (ROS, i.e., superoxide anion and hydroxy radicals). These ROS

oxidizes the lipids and cell membrane of the bacteria. TiO_2 NPs could also induce DNA chain breakage [44]. However, dermal application of TiO_2 NP has been limited to the stratum corneum layer due to the weak penetration of UV light. Titanium is also known to cause skin irritation.

11.7 Toxicology of metal oxides

Recent studies on the toxicology of metal oxides have identified various mechanisms of toxicity, namely, oxidative stress, genotoxicity, cytotoxicity, and inflammation [45]. Factors that contribute to the toxicity of metal oxides are size, shapes, solubility, and exposure routes of the metal oxide NPs. The size and shape of SPION NPs have a different outcome in cellular toxicity (Fig. 11.2) [43]. SPIONs with size less than 100 nm can enter cells by receptor-mediated endocytosis while size less than 35 nm can pass the blood–brain barrier [43]. ZnO and TiO_2 NPs show varying degrees of cytotoxic effects that are not observed with their bulk-sized counterparts. Many metal oxide NPs can soluble within acidic compartment in the cell. The metal ions that are produced during the dissolution may destabilize phagolysosomes and cause inflammation. Therefore evaluation of in vivo toxicity of these metal oxide NPs is required prior to biomedical use. In addition, the biodistribution of these nanomaterials in the body should be identified.

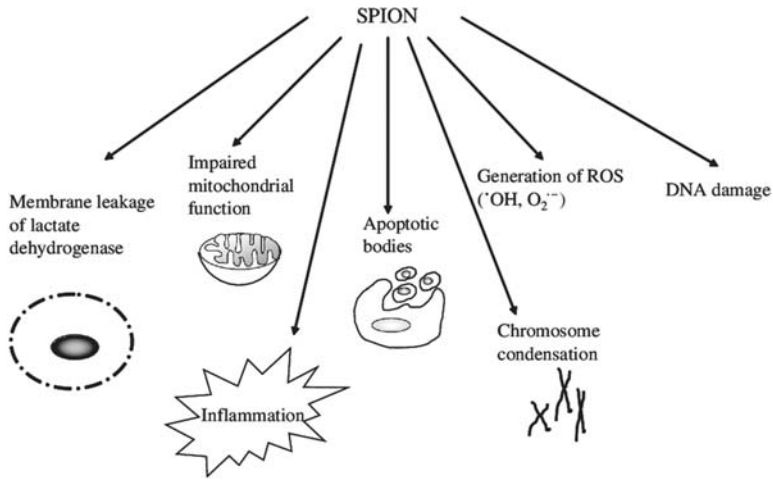

Figure 11.2 Cellular toxicity induced by SPION. *SPION*, Superparamagnetic iron oxide nanoparticle.
Adapted from: N. Singh, G.J.S. Jenkins, R. Asadi, S.H. Doak, Potential toxicity of superparamagnetic iron oxide nanoparticles (SPION), Nano Rev.1 (1) (2010) 5358 [46].

11.7.1 Oxidative stress

Oxidative stress is defined as an imbalance between the production of free radicals and antioxidants in the body. Free radicals are oxygen-containing molecules with an unpaired number of electrons. Reactions of the free radicals with other biomolecules trigger a long chain reaction in the body. This process is called oxidation and it can either be beneficial or harmful. As most of metal oxides are in nano size and have large surface area, their interactions with enzymes and proteins within the mammalian cells are closer. These metal oxide NPs can generate ROS, which may lead to the destruction of mitochondrion and cell death [41]. Prabhakar et al. [47] investigated the oxidative stress induced after oral treatment with high doses of Al_2O_3 NPs and bulk Al_2O_3 in Wistar rats. Both sizes of these nanomaterials induced significant oxidative stress in a dose-dependent manner.

Zinc oxide NPs have been shown to possess the ability to generate ROS upon UV irradiation [48]. The resulting reactive oxygen species will accumulate and finally lead to oxidative stress [49]. When the level of ROS increased, the cell membranes were damaged as a result of lipid peroxidation and protein denaturation. The damage of cell membranes may lead to cell death by necrosis and cause DNA alteration [50]. The presence of OH radical can cause single-stranded DNA breakage by forming 8-hydroxy-2-deoxyguanosine DNA adduct [49]. Fig. 11.3 shows a hypothetical cell death pathway induced by ZnO NPs. Despite the concern on the toxicity, there are commercial products (sunscreens and cosmetics) already in use that contain ZnO NPs [51].

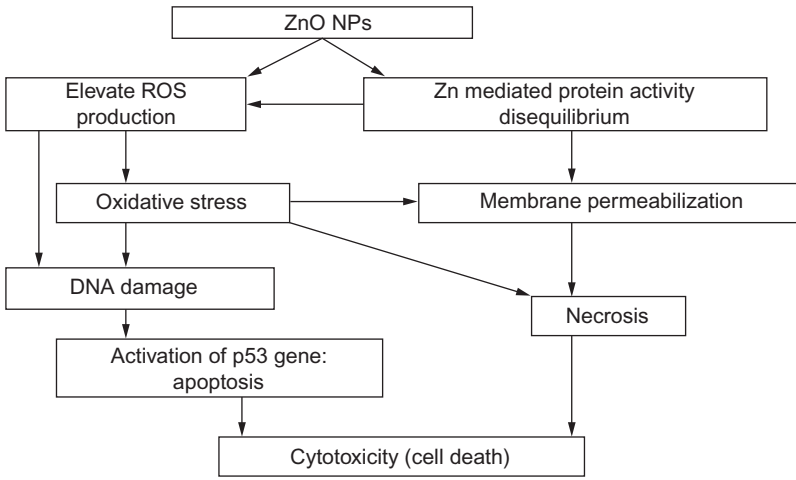

Figure 11.3 A hypothetical cell death pathway induced by ZnO nanoparticles. *ZnO*, Zinc oxide.
Adapted from: D.B Preetha Bhadra, S.M Biplab Dutta, Comparative Study of the Zno and Zno Coated with Sio_2 As Potential Antimicrobial and Anticancer Drugs. Bioscience Biotechnology Research Communications (Official Journal of Society for Science & Nature), 2019, volume 12.

11.7.2 Cytotoxicity

Like any other chemicals, metal oxide NPs are potentially toxic to human. The cytotoxicity of metal oxide NPs is often evaluated by treating them in mammalian cells. Evaluation of the cytotoxicity in animals is limited due to economical and ethical reasons. One of the major attributes of cytotoxicity is the produced by these metal oxide NPs. Fig. 11.4 illustrates a possible mechanism of action for cancer cell death induced by ZnO NPs. It is hypothesized that ZnO NPs are engulfed by the cell through pinocytosis and phagocytosis by endosomes and lysosomes. As the internal cellular pH decreases, the dissolution rate of ZnO NPs increases rapidly, leading to lysosome destabilization [52]. At low pH (pH 4.7), zinc ions are released and cascading zinc-dependent protein activity disequilibrium. At the same time, the ROS is released as a result of internalization of ZnO NPs into the cell. Elevation of ROS production leads to cell death [49].

Jeng and Swanson (2006) reported a cytotoxic study on different metal oxides. They found that Al_2O_3 was moderately toxic compared to Fe_3O_4 and TiO_2 when tested at 200 μg/mL [41]. Interestingly, CrO_3 displayed no toxicity at the tested

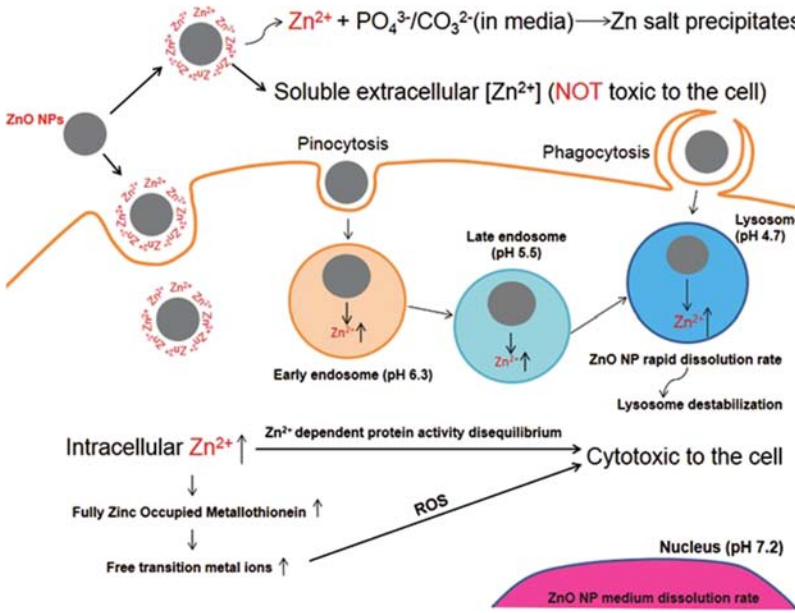

Figure 11.4 The mechanism of the cytotoxicity of ZnO NPs. *NP*, Nanoparticle; *ZnO*, zinc oxide.
Adapted from: Cenchao Shen, Simon A. James, Martin D. de Jonge, Terence W. Turney, Paul F. A. Wright, and Bryce N. Feltis, Relating Cytotoxicity, Zinc Ions, and Reactive Oxygen in ZnO Nanoparticle−Exposed Human Immune Cells, Toxicological Sciences, 136 (1) (2013) 120−130.

concentration. They suggested that mitochondrial dysfunction and cellular membrane damage are the reasons of cell death in this study [41].

11.7.3 Genotoxicity

Genotoxicity refers to the ability of a chemical agent to damage the genetic information within a cell, which may lead to cancer [53]. Chang et al. [54] reported that ZnO NP may bind to a protein and cause a major structural change of the resulting ZnO NP−bonded protein. Often, these materials in nano size are able to interact directly with the DNA [55]. The NPs can diffuse through the nuclear pore easily. They may get access to the nuclei when the nuclear membrane is dissolved during mitosis. The presence of metal oxide NPs in proximal perinuclear region may halt the cellular transcription and translation machinery. In addition, metal ions that are released after cellular internalization may cause cytoplasmic mRNA degradation by interacting with mRNA stabilizing proteins. The metal oxide NPs are also able to interact with cellular signal molecules that can lead to signaling cascade activation [54]. A study reported that CuO NPs caused DNA damage (single-strand breaks) and cell death [56]. Hanagata et al. [59] used DNA microarray to perform gene expression analysis in CuO NPs treated A549 cells. The results showed that CuO NPs upregulated the expression of 648 genes and downregulated the expression of 562 genes. Importantly, CuO NPs upregulated the genes involved in DNA damage and apoptosis (e.g., Hsp70, p53, Rad51, and MSH2). They also showed that CuO NPs (average size: 23 nm) induced dose-dependent (5−15 μg/mL) cytotoxicity, DNA damage (comet assay), and micronuclei induction in A549 cells [56]. DNA damage was observed in mice following a high dose exposure of TiO_2 NPs. Higher amount of 8-oxodG levels was found in liver compared with controls [57].

11.7.4 Inflammation

Inflammatory response occurs when tissues are injured by heat, bacterial infection, toxin, or other xenobiotics. Inflammatory response may also occur due to accumulation of ROS. Oxidative stress may induce inflammatory response by activating the nuclear factor-kappa B signaling pathway that controls the transcription of proinflammatory genes such as IL-1β, IL-8, and tumor necrosis factor-α as shown in Fig. 11.5 [58].

Huang et al. [58] reported that titanium oxide NPs can induce immune response. In their study, treatment of TiO_2 NP on the human autologous modular immune in vitro construct increased the level of proinflammatory cytokines that concurrently increase maturation and expression of costimulatory molecules on dendritic cells. The titanium oxide NPs are more capable of inducing proliferation of naive CD4-T cells in comparison with micrometer-sized (> 1 μm) TiO_2 [58]. Intratracheal instillation of rats with CuO NPs has resulted in severely cytotoxic inflammation and increased levels of inflammatory markers (i.e., lactate dehydrogenase). They compared the toxicity of CuO NPs as well as Cu ions in vitro and in vivo and found that CuO NPs caused eosinophilia, an effect not observed for the Cu ions.

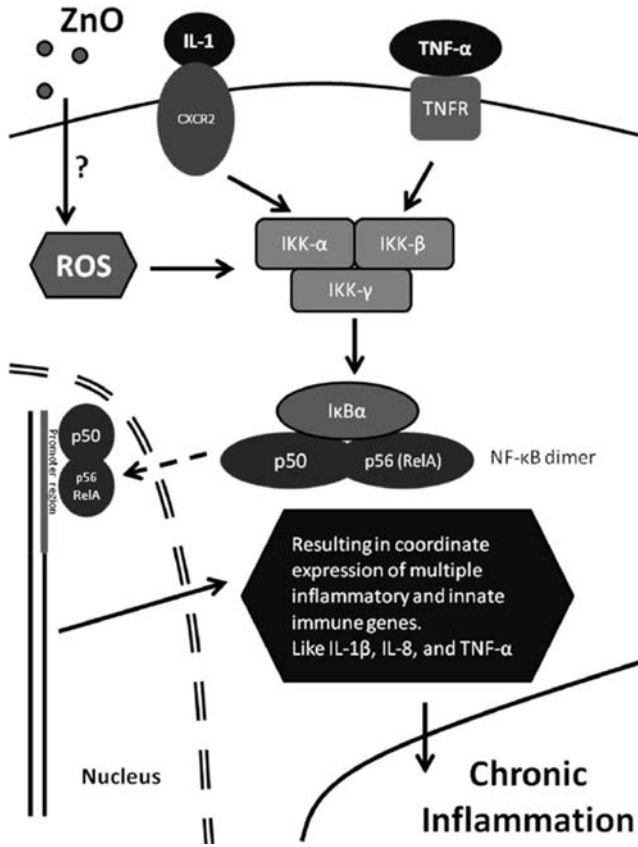

Figure 11.5 A model shows the simplified NF-κB signaling pathway that is activated by oxidative stress. Persistent activation leads to chronic inflammation. *NF-κB*, Nuclear factor-kappa B.
Adapted from: J. Yu, W. Zhang, S. Ghasaban, M. Atai, M. Imani, R.K. Matharu, et al., Enhanced bioactivity of ZnO nanoparticles—an antimicrobial study, (111) (2008) 0−7.

11.8 Conclusion

Due to their distinctive properties, metal oxide NPs are gaining extensive use in biomedical applications such as diagnostic agents, drug delivery, and medical implants. This chapter has described the recent applications of metal oxide NPs in biomedical fields and presented with examples. The distinctive properties of metal oxide NPs are derived from their nano size. Larger sizes of these metal oxides do not have such distinctive properties. Although the uses of metal oxide NPs have been well reported, studies of the toxicology and bioavailability of metal oxide NPs are still limited. Among all metal oxides, SPION has been found safe to be utilized by human. However, as particle size decreases, some metal oxides may display

increased toxicity compared to the same material in its bulk form. With respect to the production of metal oxide NPs, the biggest challenge remain is to modify these NPs to suit their biomedical applications by shape, size, and surface modification, while keeping them biocompatible and nontoxic. Nevertheless, there is a great potential for metal oxide NPs to be used widely in biomedical applications.

References

[1] A.M. Brezoiu, M. Deaconu, I. Nicu, E. Vasile, R.A. Mitran, C. Matei, et al., Heteroatom modified MCM-41-silica carriers for Lomefloxacin delivery systems, Microporous Mesoporous Mater. 275 (2019) 214−222.

[2] J.E. Goloboy, W.G. Klemperer, T.A. Marquart, G. Westwood, O.M. Yaghi, Complex oxides as molecular materials: structure and bonding in IDGH-valent early transition metal compounds, Polyoxometalate Mol. Sci. 98 (2003) 79−174.

[3] S. Laurent, S. Boutry, R.N. Muller, Metal oxide particles and their prospects for applications, Iron Oxide Nanoparticles for Biomedical Applications: Synthesis, Functionalization Application, 2018, pp. 3−42. Available from: <https://doi.org/10.1016/B978-0-08-101925-2.00001-2>.

[4] A. Khezerlou, M. Alizadeh-Sani, M. Azizi-Lalabadi, A. Ehsani, Nanoparticles and their antimicrobial properties against pathogens including bacteria, fungi, parasites and viruses, Microb. Pathog. 123 (2018) 505−526. Available from: <https://doi.org/10.1016/j.micpath.2018.08.008>.

[5] Y. Hou, H. Abdullah, D. Kuo, S. Leu, N.S. Gultom, C. Su, A comparison study of SiO_2/nano metal oxide composite sphere for antibacterial application, Composites, B: Eng. (2017). Available from: <https://doi.org/10.1016/j.compositesb.2017.09.021>.

[6] S. Gowri, K. Gopinath, A. Arumugam, Experimental and computational assessment of mycosynthesized CdO nanoparticles towards biomedical applications, J. Photochem. Photobiol., B Biol. 180 (2018) 166−174. Available from: <https://doi.org/10.1016/j.jphotobiol.2018.02.009>.

[7] L. He, Y. Su, J. Lanhong, S. Shi, Recent advances of cerium oxide nanoparticles in synthesis, luminescence and biomedical studies: a review, J. Rare Earths 33 (8) (2015) 791−799. The Chinese Society of Rare Earths. Available from: <https://doi.org/10.1016/S1002-0721(14)60486-5>.

[8] M. Aliofkhazraei, Handbook of Nanoparticles, Springer International Publishing, 2016.

[9] L.D. Duceac, S. Straticiuc, E. Hanganu, L. Stafie, G. Calin, S.L. Gavrilescu, Preventing bacterial infections using metal oxides nanocoatings on bone implant, IOP Conf. Ser. Mater. Sci. Eng. 209 (1) (2017).

[10] B. Shivaramakrishnan, B. Gurumurthy, A. Balasubramanian, Potential biomedical applications of metallic nanobiomaterials: a review, Int. J. Pharm. Sci. Res. 8 (3) (2017) 985−1000. Available from: <http://www.embase.com/search/results?subaction = viewrecord&from = export&id = L614652184%5Cnhttps://doi.org/10.13040/IJPSR.0975-8232.8(3).985-00>.

[11] S.M. Dizaj, F. Lotfipour, M. Barzegar-Jalali, M.H. Zarrintan, K. Adibkiab, Antimicrobial activity of the metals and metal oxide nanoparticles, Mater. Sci. Eng.: C. 44 (2014) 278−284.

[12] G. Cotin, S. Piant, D. Mertz, Iron Oxide Nanoparticles for Biomedical Applications: Synthesis, Functionalization, and Application, 2018, pp. 43−88. Available from: <https://doi.org/10.1016/B978-0-08-101925-2.00002-4>.
[13] S. Laurent, A. Roch, C. Robic, D. Forge, L. Vander Elst, R.N. Muller, et al., Magnetic iron oxide nanoparticles: synthesis, stabilization, vectorization, physicochemical characterizations, and biological applications, Chem. Rev. 110 (4) (2009) 2574.
[14] A.S. Teja, P. Koh, Synthesis, properties, and applications of magnetic iron oxide nanoparticles, Prog. Cryst. Growth Charact. Mater. 55 (1−2) (2009) 22−45.
[15] M. Arruebo, R. Fernández-Pacheco, M.R. Ibarra, J. Santamaría, Magnetic nanoparticles for drug delivery, Nano Today 2 (3) (2007) 22−32.
[16] C. NDong, J.A. Tate, W.C. Kett, J. Batra, E. Demidenko, L.D. Lewis, et al., Tumor cell targeting by iron oxide nanoparticles is dominated by different factors in vitro versus in vivo, PLoS One 10 (2) (2015) 1−18.
[17] S.V. Liu, J. Zhou, C. Zhang, D.R. Cole, T.J. Phelps, Thermophilic Fe(III)-reducing bacteria from the deep subsurface: the evolutionary implications, Science 277 (1997) 1106−1109.
[18] C. Jayaseelan, A.A. Rahuman, A.V. Kirthi, S. Marimuthu, T. Santhoshkumar, A. Bagavan, et al., Novel microbial route to synthesize ZnO nanoparticles using *Aeromonas hydrophila* and their activity against pathogenic bacteria and fungi, Spectrochim. Acta, A Mol. Biomol. Spectrosc. 90 (2012) 78−84.
[19] G. Elango, C. Jayaseelan, C. Kamaraj, S. Marimuthu, A.A. Rahuman, A.V. Kirthi, et al., Biosynthesis of titanium dioxide nanoparticles using bacterium *Bacillus subtilis*, Mater. Lett. 65 (17−18) (2011) 2745−2747.
[20] C.A. Romano, M. Zhou, Y. Song, V.H. Wysocki, A.C. Dohnalkova, L. Kovarik, et al., Biogenic manganese oxide nanoparticle formation by a multimeric multicopper oxidase Mnx, Nat. Commun. 8 (1) (2017) 1−8.
[21] J. Jeevanandam, Y.S. Chan, M.K. Danquah, Biosynthesis of metal and metal oxide nanoparticles, ChemBioEng Rev. 3 (2) (2016) 55−67.
[22] R. Spitler, S. Zanganeh, M. Mahmoudi, A. Shaw, J.S. Pajarinen, H. Nejadnik, et al., Iron oxide nanoparticles inhibit tumour growth by inducing pro-inflammatory macrophage polarization in tumour tissues, Nat. Nanotechnol. 11 (11) (2016) 986−994.
[23] R. Pulicharla, V.L. Pachapur, L.M.A. Dalila, S.K. Brar, M. Cledon, R.K. Das, et al., Biological synthesis of metallic nanoparticles: plants, animals and microbial aspects, Nanotechnol. Env. Eng. 2 (1) (2017).
[24] H. Mirzaei, M. Darroudi, Zinc oxide nanoparticles: biological synthesis and biomedical applications, Ceram. Int. 43 (1) (2017) 907−914. Available from: <https://doi.org/10.1016/j.ceramint.2016.10.051>.
[25] J.W. Rasmussen, E. Martinez, P. Louka, D.G. Wingett, Zinc oxide nanoparticles for selective destruction of tumor cells and potential for drug delivery applications, Expert Opin. Drug Delivery 7 (9) (2010) 1063−1077.
[26] A. Dhanalakshmi, A. Palanimurugan, B. Natarajan, Efficacy of saccharides biotemplate on structural, morphological, optical and antibacterial property of ZnO nanoparticles, Mater. Sci. Eng. C. 90 (2018) 95−103 (August 2017). Available from: <https://doi.org/10.1016/j.msec.2018.04.037>.
[27] M. Mathipa, N.M. Ngoepe, N. Mketo, N.C. Hintsho-Mbita, B. Ntsendwana, Z. Mbita, Biogenic synthesis of ZnO nanoparticles using *Monsonia burkeana* for use in photocatalytic, antibacterial and anticancer applications, Ceram. Int. 44 (14) (2018) 16999−17006. Available from: <https://doi.org/10.1016/j.ceramint.2018.06.142>.

[28] P. Judith, P. Espitia, Zinc Oxide Nanoparticles: Synthesis, Antimicrobial Activity and Food Packaging Applications, Food Bioprocess Technol 5 (2012) 1447–1464.
[29] K.P. Ananth, J. Sun, J. Bai, An innovative approach to manganese-substituted hydroxyapatite coating on zinc oxide–coated 316L SS for implant application, Int. J. Mol. Sci. 19 (8) (2018).
[30] M. Geetha, A.K. Singh, R. Asokamani, A.K. Gogia, Ti based biomaterials, the ultimate choice for orthopaedic implants—a review, Prog. Mater. Sci. 54 (3) (2009) 397–425.
[31] P. Taylor, H.A. Jeng, J. Swanson, Toxicity of Metal Oxide Nanoparticles in Mammalian Cells, Journal of Environmental Science and Health, Part A: Toxic/Hazardous Substances and Environmental Engineering, 41 (12) (2006) 2699–2711.
[32] R.T. Selvi, A.P.S. Prasanna, R. Niranjan, M. Kaushik, T. Devasena, J. Kumar, et al., Metal oxide curcumin incorporated polymer patches for wound healing, Appl. Surf. Sci. 449 (2018) 603–609. Available from: <https://doi.org/10.1016/j.apsusc.2018.01.143>.
[33] M. Vinardell, M. Mitjans, Antitumor activities of metal oxide nanoparticles, Nanomaterials 5 (2) (2015) 1004–1021.
[34] S.A. Corr, Metal oxide nanoparticles, SPR Nanosci. 3 (2016) 31–56.
[35] G. Renganathan, N. Tanneru, S.L. Madurai, Orthopedical and biomedical applications of titanium and zirconium metals, Fundamental Biomaterials: Metals, Elsevier Ltd., 2018, pp. 211–242. Available from: <https://doi.org/10.1016/B978-0-08-102205-4.00010-6>.
[36] R. Langer, New methods of drug delivery, Science 249 (4976) (1990) 1527–1533.
[37] Theranosticscomau, Cancer treatment Theranostics Australia. 2017. Available from: <http://theranostics.com.au/what-is-theranostics/> (accessed 28.08.19).
[38] A. Sharma, A.K. Goyal, G. Rath, Recent advances in metal nanoparticles in cancer therapy, J. Drug Target. 26 (8) (2018) 617–632. Available from: <https://doi.org/10.1080/1061186X.2017.1400553>.
[39] X.-Y. Zi, F. Chen, Y. Wang, X.-H. Pan, Y.-P. Hu, H.-X. Zhang, et al., Cuprous oxide nanoparticles inhibit the growth and metastasis of melanoma by targeting mitochondria, Cell Death Dis. 4 (8) (2013) e783.
[40] A. Sarkar, M. Ghosh, P.C. Sil, Nanotoxicity: oxidative stress mediated toxicity of metal and metal oxide nanoparticles, J. Nanosci. Nanotechnol. 14 (1) (2014) 730–743.
[41] P. Taylor, H.A. Jeng, J. Swanson, Toxicity of Metal Oxide Nanoparticles in Mammalian Cells, J Environ Sci Health A Tox Hazard Subst Environ Eng. 2012, pp. 37–41.
[42] A. Azam, A.S. Ahmed, M. Oves, et al., Antimicrobial activity of metal oxide nanoparticles against Gram-positive and Gram-negative bacteria: a comparative study, Int. J. Nanomed. 7 (2012) 6003–6009.
[43] A. Mohandas, S. Deepthi, R. Biswas, R. Jayakumar, Chitosan based metallic nanocomposite scaffolds as antimicrobial wound dressings, Bioact. Mater. 3 (3) (2018) 267–277. Available from: <https://doi.org/10.1016/j.bioactmat.2017.11.003>.
[44] S.L. Lee, H. Nur, S. Parham, D.H.B. Wicaksono, S. Bagherbaigi, Antimicrobial treatment of different metal oxide nanoparticles: a critical review, J. Chin. Chem. Soc. 63 (4) (2016) 385–393.
[45] K. Girigoswami, Toxicity of metal oxide nanoparticles, Adv. Exp. Med. Biol. 1048 (2018) 99–122.
[46] N. Singh, G.J.S. Jenkins, R. Asadi, S.H. Doak, Potential toxicity of superparamagnetic iron oxide nanoparticles (SPION), Nano Rev. 1 (1) (2010) 5358.

[47] P.V. Prabhakar, U.A. Reddy, S.P. Singh, A. Balasubramanyam, M.F. Rahman, S. Indu Kumari, M. Mahboob, Oxidative stress induced by aluminum oxide nanomaterials after acute oral treatment in Wistar rats, J Appl Toxicol 32 (2012) 436–445.
[48] P.K. Mishra, H. Mishra, A. Ekielski, Zinc oxide nanoparticles: a promising nanomaterial for biomedical applications, Drug Discov. Today 6446 (17) (2017). Available from: <https://doi.org/10.1016/j.drudis.2017.08.006>.
[49] G. Bisht, S. Rayamajhi, ZnO nanoparticles: a promising anticancer agent, Nanobiomedicine 3 (9) (2016).
[50] N. Padmavathy, R. Vijayaraghavan, Enhanced bioactivity of ZnO nanoparticles - An antimicrobial study, Sci Technol Adv Mater 9 (3) (2008).
[51] D.B. Preetha Bhadra, S.M. Biplab Dutta, Comparative Study of the Zno and Zno Coated with Sio2 As Potential Antimicrobial and Anticancer Drugs. Bioscience Biotechnology Research Communications (Official Journal of Society for Science – Nature), (2019) volume 12.
[52] Cenchao Shen, Simon A. James, Martin D. de Jonge, Terence W. Turney, Paul F. A. Wright, Bryce N. Feltis, Relating Cytotoxicity, Zinc Ions, and Reactive Oxygen in ZnO Nanoparticle–Exposed Human Immune Cells. Toxicological Sciences, 136 (1) (2013) pp. 120–130.
[53] C. Pellevoisin, C. Bouez, J. Cotovio, Cosmetic industry requirements regarding skin models for cosmetic testing, Skin Tissue Model, Elsevier Inc., 2017, pp. 3–37. Available from: <https://doi.org/10.1016/B978-0-12-810545-0.00001-2>.
[54] Y.N. Chang, M. Zhang, L. Xia, J. Zhang, G. Xing, The toxic effects and mechanisms of CuO and ZnO nanoparticles, Materials (Basel) 5 (12) (2012) 2850–2871.
[55] S. Karthik, P. Siva, K. Shanmugam, R. Suriyaprabha, *Acalypha indica*–mediated green synthesis of ZnO nanostructures under differential thermal treatment: effect on textile coating, hydrophobicity, UV resistance, and antibacterial activity, Adv. Powder Technol. 28 (12) (2017) 3184–3194. The Society of Powder Technology Japan. Available from: <https://doi.org/10.1016/j.apt.2017.09.033>.
[56] M. Ahamed, M.J. Akhtar, H.A. Alhadlaq, S.A. Alrokayan, Assessment of the lung toxicity of copper oxide nanoparticles: current status, Nanomedicine 10 (15) (2015) 2365–2377.
[57] B. Trouiller, R. Reliene, A. Westbrook, P. Solaimani, R.H. Schiestl, Titanium dioxide nanoparticles induce DNA damage and genetic instability in vivo in mice, Cancer Res. 69 (2009) 8784–8789.
[58] Y.W. Huang, C.H. Wu, R.S. Aronstam, Toxicity of transition metal oxide nanoparticles: recent insights from in vitro studies, Materials (Basel) 3 (10) (2010) 4842–4859.
[59] N. Hanagata, F. Zhuang, S. Connolly, J. Li, N. Ogawa, M. Xu, Molecular responses of human lung epithelial cells to the toxicity of copper oxide nanoparticles inferred from whole genome expression analysis, ACS Nano 5 (12) (2011) 9326–9338.

This page intentionally left blank

Metal oxides powder technology in energy technologies

12

Amjed Saleh Mahmood[1], *Riyadh A. Al-Samarai*[1] *and Y. Al-Douri*[2,3,4]
[1]Electromechanical Engineering Department, College of Engineering, University of Samarra, Samarra, Iraq, [2]University Research Center, Cihan University Sulaimaniya, Sulaymaniyah, Iraq, [3]Nanotechnology and Catalysis Research Center (NANOCAT), University of Malaya, Kuala Lumpur, Malaysia, [4]Department of Mechatronics Engineering, Faculty of Engineering and Natural Sciences, Bahcesehir University, Besiktas, Turkey

12.1 Introduction: importance of energy technologies in our life

The energy system tries to meet people's needs and requirements for different facilities such as transportation, cooking, lighting, making of comfortable indoor environment, refrigerated storage, communication, security, education, accommodation, and health sectors. Humans are only interested in energy facilities, not in energy. In recent years, technological advances in energy have significantly contributed to our everyday lives and procedures. All living organisms need solar energy for their growth. Energy is the primary source of life, but at night, organisms and humans use alternatives to solar energy. Most of the machines can operate by using energy, and the best example is fuel-powered cars. Electricity is used daily to operate various machines for heating, cooling, lighting, and others. Energy is generally divided into two parts: renewable and nonrenewable; and the majority of energy used in our daily lives come from fossil fuels such as oil, coal, and natural gas [1]. Uranium is another nonrenewable source used in nuclear power plants. The use of these natural resources causes them to run out of land. In addition, the use of such fuels is harmful to plants and animals [2] due to fuel emissions such as carbon monoxide and sulfur dioxide, which can contribute to acid rain and global warming. Renewable energy sources can be used repeatedly, which include solar, wind, geothermal, biomass, and hydropower. They produce much less pollution, but it is believed that oil will remain one of the most important sources of energy and resources [3]. Important is to balance power generation with demand because electrical energy cannot be stored and that constant balance has significant financial and operational costs. Although it is not possible to store energy in the form of electricity, it can be converted to another form, which can be saved. The stored energy can then be converted into electricity, and there is a wide range of ways in which energy can be saved. These include chemical energy (battery), kinetic energy (flywheel or compressed air), potential gravitational energy

Metal Oxide Powder Technologies. DOI: https://doi.org/10.1016/B978-0-12-817505-7.00012-9

(hydroelectric pump), and energy in the form of electric capacitors and magnetic fields [4]. From an electrical system perspective, energy storage methods act as loads during energy storage (e.g., while charging the battery) and power sources, when power is returned to the system (e.g., during battery discharge). Advances in storage space technology and the need for electric current allow energy storage to be an essential component of the future electric power system [5]. Some companies have a growing interest in energy storage for several things:

- The need to respond quickly to the increase in demand for electric power.
- The need to integrate renewable energy sources into the energy system [6–9].
- The need to invest in demand-driven energy distribution and distribution systems.
- The need to provide critical network support services for an efficient and reliable operating network. Increased demand for high-quality and reliable power supplies due to increased use of power supply systems, information, communication, and electronic devices are highly sensitive to changing energy intake [10].

12.2 Fuel cells and metal oxides powder technology

Demand for clean energy in the world is increasing as a result of technological advances, especially clean energy and low cost. This progress has been paralleled with the development of materials science and technology to meet the performance requirements of new energy modular systems [11]. Fuel cells are highly efficient, flexible, and efficient energy production devices. These unique characteristics have been fundamentally differentiated from the traditional thermal cells of fuel cells for power generation and thus have been the focus of world attention over the past few decades. In this book, the summary, features, application, and design of solid oxide fuel cells, SOFCs, are reviewed briefly. It can generate electricity more efficiently than conventional pair drive. This application undoubtedly became a catalyst for the pursuit of fuel cells as highly efficient potential energy devices in the 20th century [12–15]. If the 19th century was the era of curious fuel cells, the 20th century was, of course, the era of fuel cells under intensive research and development and marketing efforts. The conceptual SOFC was probably first introduced in 1937 by Swiss scientists, Bauer and Hans of ceramics, using zirconia as an electrolyte, Fe_3O_4 as a cathode, and C as a clear anode, when the problem of the instability of electronic materials and the propagation of the gas phase were prevailing [16,17]. However, the most focused and systematic research on SOFC began after the pioneering work of the German scientist, Karl Wagner, in 1943, who first realized the presence of oxygen vacancies in mixed oxides such as drug $ZrOO_2$ and attributed the observed electrical conductivity at high temperatures to the movement of these oxygen vacancies. In 1957, Kiukkola and Wagner He published another research paper describing thermodynamic research cells with a focus on solid electrolytes, which laid the theoretical foundations of SOFC solid-state photochemistry. A few years later, two scientists, Joseph Weissbar and Roswell Rocca, of Westinghouse Electric in 1961 reported a solid-state device in the first year based on a measurement of oxygen concentration in the gas phase at the concentration of cells 12, which subsequently patented the

"solid fuel cell electrolyte." Released in 1962, based on these initial efforts, a group of Westinghouse engineers developed and tested the first "up-and-pin" tubular stack from 1962 to 1963. This development eventually became one of the main components of the supported SOFC—electronically and less tubular developed by Westinghouse/Siemens. For the same time, there were also developments in the special electrode materials for SOFC. Notable progress has been observed in the development of cathode materials. It began with noble metals such as platinum and the transition to the psychedelic In_2O_3 [14] and finally settled on modern stainless $LaMnO_3$ [18–20].

Evolution of cathode materials occurred clearly due to capacity requirement, namely, the ability to effectively activate the oxygen crimped process. Unique electrical and catalytic properties, which have rare earth transition metal oxides of a perovskite cathode, are better to satisfy the requirement [21–23]. However, the requirement to balance the thermal expansion between the cathode and electrolyte narrowed the practical application of cathode materials for alloy $LaMnO_3$ SOFC based on ZrO_2-electrolyte. Another significant material developed in 1969 was doped perovskite $LaCrO_3$ that was stable in oxidizing and decreasing atmospheres [15]. It was directly found and used as interconnects in SOFC [24,25].

12.3 Applications of SOFC

Based on the unique pros mentioned above, the significant SOFC distributed application techniques, stationary power generation [26]. According to the capacity of the SOFC generator, it might be divided into the four categories:

- *Housing*. SOFC is manufactured to supply a power to houses with a rate 1–10 kW. Hot water, house heating, and cooling can also be provided as a byproduct. Net efficiency is expected to be more than 35%.
- *Commercial*. SOFC is aimed at supplying power to small factories or a hospital. Nominal power usually ranges from 100 to 1000 kW. Quality of energy can also be delivered as a byproduct. Net efficiency is expected to be more than 45% [27,28].
- *Industrial growth*. SOFC generators can be directed to supply larger industrial unit or a small community with a power of 2–10 MW. Net efficiency is expected to be more than 48%.
- *The largest system*. SOFC generator has a nominal capacity of 100 MW. In such a technique, generating electricity is the ultimate aim. Thus, the system is a hybrid design SOFC choice. Natural gas and coal gas obtained can be used as fuel. Efficiency is expected to be more than 60% [29–31].

12.4 Solar cells and metal oxides powder technology

In recent years, the sun has gone from the major residential tablets in backpacks and pockets, allowing anyone to have their own source of energy generated regardless of where they are contributing to the stability and individual freedom at all times. Sunny window, concentrating mirror panel, which dissolves in water, printed

panels, spray on solar energy, solar roll, and a variety of portable solar chargers of various sizes and destinations are only a small coverage in the field of intelligent and innovative ideas that are changing the global energy landscape [31−33].

The conversion of sunlight into clean energy without the negative byproducts from traditional sources, solar energy is the technology of our present and our future, making the world post-fossil fuels possible. Solar energy is inexhaustible, safe and saves money in the long run; it produces little or no waste to diversify our energy supply. Providing personal energy independently, it gives the average person the freedom of hope and dependence on external sources. Using the unlimited possibilities of a stable and constant source of energy ensures the reliability and convenience of the modern lifestyle demands. When used at home or stored in batteries or solar power recharge stations for later use, it serves our need to be constantly connected [33−37].

12.5 Metal oxides powder technology

Gas sensors based on metal oxides are currently one of the most experimental sensing groups [38]. It has attracted a lot of attention in the field of gas sensing due to low cost, weather conditions, flexibility in production, ease of use, and a large number of gases detected/possible applications. A variation in the conductivity of gas sensor materials specifies that the reaction can be carried out by evaluating the container, work, mass, or optical properties of the reaction energy emitted by the gas/solid reaction [39]. After a review of the metal oxide gas sensors, this section focuses on the conduct of metric oxide semiconductor gas sensors (particularly, conductive surface metal oxide). Many researchers have shown a reverse reaction with the gas surface. Materials are the superior behavior of semiconductor metal oxide gas sensors [40]. The reaction may depend on many factors, including internal and external factors, such as surface area, the properties of natural base materials, surface additives, microscopic structure of sensitive layers, humidity, and temperature [41−43]. As one of the key factors of gas sensors, attention sensitivity draws more and more efforts to improve the sensitivity of gas sensors. There is no standard definition of gas sensor sensitivity at this time. Typically, sensitivity (S), R/R_g for gas reduction, or R_g/R_a for oxidizing gases can be determined, where R_a is the gas-resistant reference gas (usually air) and R_g is the resistance of the reference gas containing the gases target. Both R_a and R_g have a great relationship with the surface of the reaction (s). Although there are many opinions in this area, to our knowledge, there were no special reviews of factors influencing allergies [44−50]. For factors related to the properties of gas-sensitive metal oxides, detect the metal oxide gas sensor in the sensor mechanism. The basic mechanisms that cause the reactions gas are still unknown, and it is a controversial issue among researchers, but they actually absorb electrons of capture molecules on the tapes and the curvature of these charged molecules responsible for the change in conductivity. Negative charge trapped in these types of oxygen produces the upward curvature of the tape, thus reducing the conductivity compared to laying the flat tape. The field of electronically depleted space charge layers, the thickness of which is the field of

length of the bending area [51,52]. The reaction of these forms of oxygen is reduced while reducing gases or competitive adsorption and replacing absorbed oxygen molecules and others can reverse the bending areas, resulting in an increase in conductivity. O− is believed to dominate the operating temperature of 300°C−450°C [53], which is the operating temperature, for most metal oxide gas sensors. A structural model and a conductive tape mechanism is a reference gas containing carbon dioxide and oxidized and released electron oxide compounds from bulk materials when exposed to a gas with or without it if the carbon dioxide sensor along with the reduction in the thickness of the space deck layer decreases [54]. Furthermore, the Schottky barrier between the granules is reduced, and it will be easy for electrons to make different layers of the sensor bead. Chapin et al. of Bell Labs found monocrystalline silicon solar cells that were invented and proven to be 6% effective. Then the researchers brought silicon solar cell efficiency to 15%. The timing was lucky, because Sputnik was launched in 1957 and the solar panels are quite easy to maintain—they work to provide remote electrical energy. Currently, silicon solar cells are utilized to operate the space station. In this regard, the higher the percentage of paint alloys, the lower the transition temperature [54]. Moreover, Wang et al. [55] reported that costimulants of tungsten VO_2 (magnesium) and magnesium (Mg) could offer a synergistic effect through which the temperature of the transformations and light transmittance of the film VO_2 could be developed. It should be noted that, as single crystals, the lattice of VO_2 cannot withstand the resulting stress in phase shift and crack after only some passing cycle. The compound was prepared as a thin film applied to the selected substrate, VO_2. The film may be more fleeting and will be more efficient for smart window applications. Progress in the development of thermal VO_2 thermal coating has recently been examined by researchers [56−62]. Different aspects of material development were considered, including VO_2 manufacturing process films, strategies to improve chromium thermal properties, and future trends. From the perspective of the manufacturing process, the various methods can be used for the preparation of VO_2 thermo-chromic glass coatings, including slush−gel [63], sputtering deposition, and chemical vapor deposition [64].

12.6 Supercapacitor and metal oxides powder technology

Metal oxides are an alternative to materials used in the manufacture of supercapacitors electrode, because it has high specific capacity and low resistance, which makes it simpler to build supercapacitors with high energy and power. Usually, used metal oxides are nickel oxide (NiO), manganese oxide (MnO_2), ruthenium dioxide (RuO_2), and iridium oxide (IrO_2) [65−68]. Low cost of production and use of a softer electrolyte make them an actual alternative to nickel oxide that is a promising electrode material for supercapacitors due to its environmental friendliness, easy for synthesis, and low cost. Among the advantages, electrochemical

schemes include reliability, precision, simplicity, low cost, and versatility. Using electrochemical nickel hydroxide strategy has been changed to using nickel oxide. It results in producing an ultrahigh specific capacity of 1478 F/g in aqueous 1 M KOH electrolyte solution [59–61]. Composite electrodes integrate carbon-based materials with any of metal oxides or conductive polymer materials that, in turn, present both a physicochemical mechanism of charge storage together in one electrode [62,63]. Activated carbon has effective characteristics such as good electrical properties, high surface area, and reasonable price used in this experiment. Three different metals such as oxides of nickel (Ni), cobalt (Co), and manganese (Mn) which are used to observe the combination that can produce the highest specific capacitance. An alternating current was used as an anode and combinations of two metal oxides as a cathode. Degree of inversion was adjusted by a factor of 0.2 to see the effect it will have on performance [64–66].

The operating principle of the supercapacitor, regarding the storage and distribution of ions, is arriving from the electrolyte to the surface area of the electrodes of energy. On the basis of the energy storage mechanism, supercapacitors are subdivided into three classes: electrochemical double layer, hybrid super, and pseudo capacitors [67–69].

12.7 Industrial emissions and metal oxides powder technology

Industrial emissions become significant with the fast development processes such as the production of a metal nozzle. Rick et al. [68] stated that sales had risen for materials by 49% in 2013. Different studies examined the aspects of environmental influence on steel powder processes. Sintering processes and newspapers manufacturing energy constitute about 90% of quantity products manufactured with black powder [70]. Three decades later, the effectiveness of sintering and energy consumption of press by water and atomization evaluated was evaluated [70]. Compared to other processes, powder metallurgy, printing, and sintering, it has been characterized with respect to its energy and materials efficiency. Additive manufacturing, the only process in addition to the press and sintering that impact the environment, has been studied in the literature. Huang et al. [71] examined the impact on the environment due to additive production of the full life cycle of the metal aircraft components and came to the conclusion that if it is used to the full potential emissions from civil aviation in the United States, it can be reduced by approximately 6%. Additive manufacturing allows more freedom compared to conventional design process, accommodating further optimization of components. The process is highly energy intensive [72]. The GHG emissions can be reduced most effectively by the use of this machine at its full capacity and can be turned off when not in use [73]. The environmental effect on additives production has been considered higher by researchers than any other powder metallurgy process [74,75].

12.8 Conclusion

In this chapter, research progress on energy uses of metal oxides powder technology was introduced separately by reviewing a reasonable number of peer-reviewed papers. Topics covered include materials that were manufactured by metal oxides powder technology and their uses in different kinds of energy such as fuel cells, solar cells, and supercapacitor. In addition, developments of different materials with improved performance of energy producers have been discussed in this chapter. It concludes that the development of new materials improves the overall efficiency in order to meet the increasing energy demands.

References

[1] U.S. Energy Information Administration (EIA), Updated Capital Cost Estimates for Electricity Generation Plants, 2010.
[2] EPRI; U.S. Department of Energy, EPRI-DOE Handbook of Energy Storage for Transmission & Distribution Applications, EPRI; U.S. Department of Energy, Palo Alto, CA ,Washington, DC, 2003.
[3] P. Agrawal, A. Nourai, L. Markel, R. Fioravanti, P. Gordon, N. Tong, et al., Characterization and Assessment of Novel Bulk Storage Technologies, Sandia National Laboratories, Albuquerque, NM, 2011.
[4] M.C. Grubelich, S.J. Bauer, P.W. Cooper, Potential Hazards of Compressed Air Energy Storage in Depleted Natural Gas Reservoirs, Sandia National Laboratories, Albuquerque, NM, 2011.
[5] R.H. Schulte, J. Nicholas Critelli, K. Holst, G. Huff, ", Lessons From Iowa: Development of a 270 Megawatt Compressed Air Energy Storage Project in Midwest Independent System Operator, Sandia National Laboratories, Albuquerque, NM, 2012.
[6] L. Pérez-Lombard, J. Ortiz, C. Pout, A review on buildings energy consumption information, Energy Build. 40 (2008) 394–398.
[7] H. Miyazaki, N. Kusumoto, S. Sasaki, N. Sakamoto, N. Wakiya, H. Suzuki, Thermochromic tungsten doped VO_2-SiO_2 nano-particle synthesized by chemical solution deposition technique, J. Ceram. Soc. Jpn. 117 (2009) 970–972.
[8] H. Miyazaki, K. Yoshida, S. Sasaki, N. Sakamoto, N. Wakiya, H. Suzuki, et al., Fabrication of transition temperature controlled W-doped VO_2 nano particles by aqueous solution, J. Ceram. Soc. Jpn. 119 (2011) 522–524.
[9] N. Wang, S. Liu, X.T. Zeng, S. Magdassi, Y. Long, Mg/W-codoped vanadium dioxide thin films with enhanced visible transmittance and low phase transition temperature, J. Mater. Chem. C 3 (2015) 6771–6777.
[10] S. Wang, M. Liu, L. Kong, Y. Long, X. Jiang, Recent progress in VO_2 smart coatings: Strategies to improve the thermochromics properties, Prog. Mater. Sci. 81 (2016) 1–54.
[11] W. Burkhardt, T. Christmann, B.K. Meyer, W. Niessner, D. Schalch, A. Scharmann, W- and F-doped VO_2 films studied by photoelectron spectrometry, Thin Solid Films 345 (1999) 229–235.

[12] D. Barreca, L.E. Depero, E. Franzato, G.A. Rizzi, L. Sangaletti, E. Tondello, et al., Vanadyl precursors used to modify the properties of vanadium oxide thin films obtained by chemical vapor deposition, J. Electrochem. Soc. 146 (1999) 551–558.
[13] F. Guinneton, L. Sauques, J.C. Valmalette, F. Cros, J.R. Gavarri, Optimized infrared switching properties in thermochromic vanadium dioxide thin films: role of deposition process and microstructure, Thin Solid Films 446 (2004) 287–295.
[14] L.T. Kang, Y.F. Gao, H.J. Luo, A novel solution process for the synthesis of VO_2 thin films with excellent thermochromic properties, ACS Appl. Mater. Interfaces 1 (2009) 2211–2218.
[15] S.S. Kalagi, D.S. Dalavi, R.C. Pawar, N.L. Tarwal, S.S. Mali, P.S. Patil, Polymer assisted deposition of electrochromic tungsten oxide thin films, J. Alloys Compd. 493 (2010) 335–339.
[16] Z. Peng, W. Jiang, H. Liu, Synthesis and electrical properties of tungsten-doped vanadium dioxide nanopowders by thermolysis, J. Phys. Chem. C 111 (2007) 1119–1122.
[17] Sandia National Laboratories, DOE energy storage database. [Online]. Available from: <http://www.energystorageexchange.org/projects>, 2012 (accessed December 2012).
[18] D. Rastler, Electric energy storage technology options for the electric enterprise: overview of status, application value, and U.S. activities, in: Smart Grid: A 360 View of Battery Storage, Atlanta, 2011.
[19] D.W. Wang, F. Li, J. Zhao, W. Ren, Z.G. Chen, J. Tan, et al., ACS Nano 3 (2009) 1745.
[20] M. Mastragostino, C. Arbizzani, F. Soavi, Solid State Ionics 148 (2002) 493.
[21] Q. Cheng, J. Tang, N. Shinya, L.C. Qin, J. Power Sources 241 (2013) 423.
[22] J. Li, H. Xie, Y. Li, J. Liu, Z. Li, J. Power Sources 196 (2011) 10775.
[23] X. Feng, R. Li, Z. Yan, X. Liu, R. Chen, Y. Ma, et al., IEEE 11 (2012) 1080.
[24] M. Vangari, T. Pryor, L. Jiang, J. Energy Eng. 139 (2013) 72.
[25] Y. Chen, X. Zhang, H. Zhang, X. Sun, D. Zhang, Y. Ma, RSC Adv. 2 (2012) 7747.
[26] F. Zhang, J. Tang, N. Shinya, L.C. Qin, Chem. Phys. Lett. 584 (2013) 124.
[27] Q. Cheng, J. Tang, J. Ma, H. Zhang, N. Shinya, L.-C. Qin, Carbon 49 (2011) 2917.
[28] L. Holzer, B. Iwanschitz, Th. Hocker, L. Keller, O. Pecgo, G. Sartoris, Ph. Gasser, B. Muench, J. Power Sources 242 (2013) 179–94.
[29] M. Mandal, D. Ghosh, S.S. Kalra, C.K. Das, Int. J. Latest Res. Sci. Tech. 3 (2014) 65.
[30] Z.S. Iro, C. Subramani, H.Y. Hafeez, Indian J. Sci. Technol. 9 (2016) 1.
[31] Y. Li, M.V. Zijll, S. Chiang, N. Pan, J. Power Sources 196 (2011) 6003.
[32] P. Sharma, T.S. Bhatti, Energy Convers. Manage. 51 (2010) 2901.
[33] F.W. De Souza Lucas, A. Zakutayev, Research update: Emerging chalcostibite absorbers for thin-film solar cells. APL Mater. 6 084501, 2018.
[34] G. Yu, L. Hu, N. Liu, H. Wang, M. Vosgueritchian, Y. Yang, et al., Nano Lett. 11 (2011) 4438.
[35] Y. Zhu, S. Murali, M.D. Stoller, K.J. Ganesh, W. Cai, P.J. Ferreira, et al., Science 332 (2011) 1537.
[36] J. Yang, F. Zhang, H. Lu, X. Hong, H. Jiang, Y. Wu, et al., Angew. Chem. Int. Ed. 54 (2015) 10889–10893.
[37] Y. Ban, Z. Li, Y. Li, Y. Peng, H. Jin, W. Jiao, et al., Angew. Chem. Int. Ed. 54 (2015) 15483–15487.
[38] L. Fan, P.F. Liu, X. Yan, L. Gu, Z.Z. Yang, H.G. Yang, et al., Nat. Commun. 7 (2016) 10667.
[39] K.P. Kuhl, T. Hatsukade, E.R. Cave, D.N. Abram, J. Kibsgaard, T.F. Jaramillo, J. Am. Chem. Soc. 136 (2014) 14107–14113.
[40] S. Back, J. Lim, N.-Y. Kim, Y.-H. Kim, Y. Jung, Chem. Sci. 8 (2017) 1090.

[41] Q. Lu, J. Rosen, Y. Zhou, G.S. Hutchings, Y.C. Kimmel, J.G. Chen, et al., Nat. Commun. 5 (2014) 3242.
[42] M. Ma, B.J. Trzesniewski, J. Xie, W.A. Smith, Angew. Chem. Int. Ed. 55 (2016) 9748–9752.
[43] M. Dunwell, Q. Lu, J.M. Heyes, J. Rosen, J.G. Chen, Y. Yan, et al., J. Am. Chem. Soc. 139 (2017) 3774–3783.
[44] V. Kruzhanov, V. Arnhold, Energy consumption in powder metallurgical manufacturing, Powder Metall. 55 (1) (2012) 14–21.
[45] J. Faludi, M. Baumers, I. Maskery, R. Hague, Environmental impacts of selective laser melting: do printer, powder, or power dominate, J. Ind. Ecol. 21 (2015) S144–S156.
[46] J.M. Cullen, J.M. Allwood, M.D. Bambach, Mapping the global flow of steel: from steelmaking to end-use goods, Environ. Sci. Technol. 46 (24) (2012) 13048–13055.
[47] Hoganas, Hoganas Handbook for Sintered Components, 2013. J.J. Dunkley, D. Aderhold, D. Millington-Smith, A.J. Yule, Atomization for Metal Powders—Notes to Accompany a Short Course, 2016.
[48] R.M. German, Powder Metallurgy and Particulate Materials Processing: The Processes, Materials, Products, Properties and Applications, Metal Powder Industries Federation, 2005. ISBN 9780976205715.
[49] J.J. Dunkley, Hot gas atomisation-economic and engineering aspects, Adv. Powder Metall. Part. Mater. 1 (2005) 2.
[50] Eurostat, Energy statistics—prices of natural gas and electricity. <http://ec.europa.eu/eurostat/web/energy/data/database>, 2015 (accessed 10.10.17).
[51] European Powder Metallurgy Association, EPMA key powder metallurgy figures 2012. <https://www.epma.com/558-epma-key-figures-2012/>, 2012 (accessed 19.05.17).
[52] F.J. Esper, Pulvermetallurgie: Das Flexible Und Fortschrittliche Verfahren Für Wirtschaftliche Und Zuverlässige Bauteile; Mit 15 Tabellen, Kontakt & Studium, Expert-Verlag, 1996. ISBN 9783816913214.
[53] J.B. Marean, Compressed Air Energy Storage Engineering and Technical Study, New York State Energy Research and Development Authority, Albany, NY, 2009.
[54] ASTM International, ASTM F3184-16—Standard Specification for Additive Manufacturing Stainless Steel Alloy (UNS s31603) With Powder Bed Fusion, Standard, 2016.
[55] S. Wang, M. Liu, L. Kong, Y. Long, X. Jiang, Recent progress in VO_2 smart coatings: Strategies to improve the thermochromics properties, Prog. Mater. Sci. 81 (2016) 1–54.
[56] Y. Tang, Y. Zhou, T. Hoff, M. Garon, Y.F. Zhao, Elastic modulus of 316 stainless steel lattice structure fabricated via binder jetting process, Mater. Sci. Technol. 32 (7) (2016) 648–656.
[57] S.M. Thompson, L. Bian, N. Shamsaei, A. Yadollahi, An overview of direct laser deposition for additive manufacturing; part I: transport phenomena, modeling and diagnostics, Addit. Manuf. 8 (2015) 36–62.
[58] B. Brunekreef, B. Forsberg, Epidemiological evidence of effects of coarse airborne particles on health, Eur. Respir. J. 26 (2) (2005) 309–318.
[59] W. Shifeng, L. Shuai, W. Qingsong, C. Yan, Z. Sheng, S. Yusheng, Effect of molten pool boundaries on the mechanical properties of selective laser melting parts, J. Mater. Process. Technol. 214 (11) (2014) 2660–2667.
[60] K. Kellens, E. Yasa, W. Dewulf, J. Duflou, Environmental Assessment of Selective Laser Melting and Selective Laser Sintering, Going Green-CARE INNOVATION 2010: From Legal Compliance to Energy-Efficient Products and Services, 2010.

[61] M. Baumers, C. Tuck, R. Hague, I. Ashcroft, R. Wildman, A comparative study of metallic additive manufacturing power consumption, in: Solid Freeform Fabrication Symposium Proceeding, the University of Texas at Austin, TX, USA, 2010, pp. 278−288.
[62] M. Baumers, C. Tuck, R. Wildman, I. Ashcroft, E. Rosamond, R. Hague, Transparency built-in, J. Ind. Ecol. 17 (3) (2013) 418−431.
[63] S.M. Kaufman, Energy consumption in the manufacture of precision metal parts from iron powder, in: Technical report, SAE Technical Paper, 1980.
[64] V. Kruzhanov, V. Arnhold, Energy consumption in iron powder production: annealing of water atomized powder, in: Proceedings of the World PM2016 Congress & Exhibition, European Powder Metallurgy Association, 2016.
[65] EPRI Center for Materials Production, Ind. Segment Profile Sic. 33991 (2000).
[66] E. Ernst, Energy balance of a belt sinter furnace, Powder Metall. 56 (2) (2013) 96−101.
[67] G. Zapf, K. Dalal, Raw material and energy conservation in production of sintered PM parts, Powder Metall. 26 (4) (1983) 207−216.
[68] C.-J. Rick, M. Engholm, K. Beskow, Increased stainless steel melt shop yield by improved converter tap weight management, in: The 6Th European Oxygen Steelmaking Conference, 2011.
[69] A.J. Yule, J.J. Dunkley, Atomization of Melts for Powder Production and Spray Deposition, Oxford University Press, USA, 1994.
[70] ASM International, ASM Handbook: Metalworking and Bulk Forming, vol. 14A, ASM Handbook ASM International, 1991. Number v. 11; v. 14. ISBN 9780871707086.
[71] R. Huang, M. Riddle, D. Graziano, J. Warren, S. Das, S. Nimbalkar, et al., Energy and emissions saving potential of additive manufacturing: the case of lightweight aircraft components, J. Cleaner Prod. 135 (2015) 1559−1570.
[72] R. Brindle, PM2 Industry Vision and Technology Roadmap, 2001.
[73] A. Leatham, Spray forming: alloys, products and markets, Met. Powder Rep. 54 (5) (1999) 28−37.
[74] R.J. Fruehan, O. Fortini, H.W. Paxton, R. Brindle, Theoretical Minimum Energies to Produce Steel, Report to the US Department of Energy, Office of Industrial Technologies, Washington, DC, 2000.
[75] M. Noro, R.M. Lazzarin, Energy audit experiences in foundries, Int. J. Energy Environ. Eng. 7 (2016) 409−423.

Metal oxides in electronics

13

Ali Abu Odeh[1] *and Y. Al-Douri*[2,3,4]
[1]Khawarizmi International College, Al Ain, United Arab Emirates, [2]University Research Center, Cihan University Sulaimaniya, Sulaimaniya, Iraq, [3]Nanotechnology and Catalysis Research Center (NANOCAT), University of Malaya, Kuala Lumpur, Malaysia, [4]Department of Mechatronics Engineering, Faculty of Engineering and Natural Sciences, Bahcesehir University, Istanbul, Turkey

13.1 Introduction

The strength of metal oxides (MOs) lies in the diversity of optical and electronic properties that determine the alignment of energy levels and thus dictate the performance of electronic devices. The majority of MO materials are considered to be semiconductors, and they are divided into two types, n-type materials such as tin oxide (SnO_2), indium oxide (In_2O_3), zinc oxide (ZnO), and titanium dioxide (TiO_2), on the other hand, p-type materials such as nickel oxide (NiO) and copper oxide (CuO). The charge carriers of these types are electrons for the first and holes for the second. The combination of different MO materials leads to forming nanojunctions such as n−p, n−n, and p−p junctions. The way the materials are combined together originates from different structures and thus different properties that have to be studied independently. These heterojunctions can be formed according to one of these nomenclatures: (1) a simple mixture of two or more compounds, the result is not controlled and randomly distributed, and it is identified by a dash between the different compounds. For example, "CuO−SnO_2" represents a mixture of CuO and SnO_2. (2) The base material on which is added by a second material on the top, this is identified by the "at" sign "@." For example, "SnO_2@PdO" could represent SnO_2 nanowires coated by PdO nanoparticles deposited by any method. (3) Define a clear partition between two or more compounds; a forward slash is inserted between compounds names. For example, "NiO/TiO_2" means a layer of TiO_2 is deposited over NiO layer [1]. Nanomaterials (NMs) are engineered materials to take advantage of the extraordinary chemical, physical, and electrical properties at this tiny size. NMs are defined as materials that have a grain size less than 100 nm and their surface-area-to-volume ratio is larger than their bulk. They are classified into three main categories: organic, inorganic, and hybrid NMs. Below the three categories are a broad range of materials such as graphene, carbon nanotubes, nanoparticles, nanofibers, nanocomposites, nanowires, nanorods, MOs, nanometals, and quantum dots. MOs have very different electrical properties from metals,

Metal Oxide Powder Technologies. DOI: https://doi.org/10.1016/B978-0-12-817505-7.00013-0

semiconductors, and insulators and are used in many different areas such as battery supercapacitor hybrid devices [2], sensors [3], superconductors [4], solar cell [5], and water treatment [6]. Many types of MOs have been used in different applications such as SnO_2 [7], TiO_2 [8], In_2O_3 [9], WO_3 [10], ZnO [11], Fe_2O_3 [12], zinc−tin oxide (ZTO) [13], AZO [14], MgZO [15], GaZO [16], InHfZO [17], and InSiZO [18]. The use of mixed oxides and noble metals has been investigated in many research papers to improve the selectivity and stability of the chemical reactions in biosensors [19]. Furthermore, these techniques enabled the researchers to concentrate on the materials that have the smallest crystallite size to make sure that their properties will remain stable during high temperature and long operations, which is crucial for effective chemical sensing in biosensing [20]. Fig. 13.1 shows the frequent attempts that took place in the 60 and 70 seconds to develop SnO_2 and ZnO semiconductor channel layers until the development of the amorphous indium−gallium−zinc oxide InGaZnO (a-IGZO) as channel layers for thin-film transistors (TFTs) in 2004 [21]. Many fabrication methods have been used to fabricate MO-based electronic devices whereas the structure and the morphology of oxide materials play an important role in deciding the type of the method. Among these, solution-based techniques have been used for their simplicity and effectiveness [22], electrodeposition [23], chemical precipitation [24], microwave synthesis (MS) [25], sol−gel (SG) [26], solvothermal synthesis [27], hydrothermal synthesis [28], and chemical bath deposition [29]. Before we start researching various electronic applications and devices, we should briefly highlight the field of optoelectronics. It is considered to be the merging of optics and electronics fields, and it is one of the most exciting and dynamic fields that researchers are working hard to develop new ways to increase the efficiency of these devices. Optoelectronics consists of two categories, the first is light sources such as light-emitting diodes (LEDs) and lasers, whereas the second is the light detectors such as photodetectors (PDs), photoconductors, and photovoltaic. This chapter is organized as

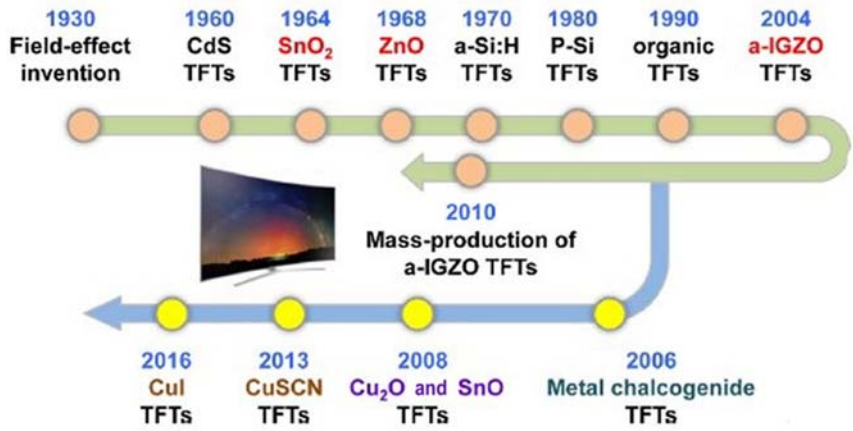

Figure 13.1 Timeline of thin-film transistors [21].

follows: Section 13.2 is devoted to shedding the light on the design consideration and multiple building configurations of TFTs and metal−oxide−semiconductor (MOS) field-effect transistor (MOSFET). Different properties, including the electrical, have been characterized, and different MOs have been identified for use in transistors. In Section 13.3, different types of diodes such as LEDs and Schottky diodes have been highlighted by using different MOs. In Section 13.4 the theory that lies behind PDs has been discussed along with some studies in this area. In Section 13.5, perspectives and conclusions on the future of MO-based electronics have been offered.

13.2 Transistors

Since the introduction of a-IGZO in transparent flexible TFT in 2004, the use of MO in TFTs has pulled in a lot of consideration due to their excellent properties such as low off current, low process temperature, high mobility of carriers, and high transparency in the visible region. It is worth mentioning that the low temperature of the synthesizing process enables the use of flexible substrates within oxide-based TFTs such as papers and polyethylene terephthalate (PET). Flexible electronics that based on flexible oxide−based TFTs can be used in many applications as shown in Fig. 13.2 [30]. TFT devices can be fabricated using many configurations, the first type of TFT structures is the bottom gate (BG) as shown in Fig. 13.3A [31] and Fig. 13.3B [32], whereas the second type of architecture is the top gate (TG) (Fig. 13.3C and D) [33]. The difference between the first and the second is whether the gate electrode is deposited before or after the active layer (semiconductor). BG and TG can be coplanar or staggered depending on how source/drain and semiconductor/dielectric are facing each

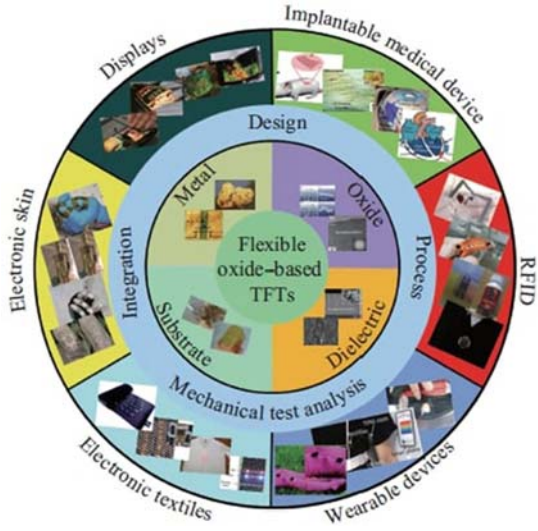

Figure 13.2 Applications of flexible oxide−based TFTs [30]. *TFTs*, Thin-film transistors.

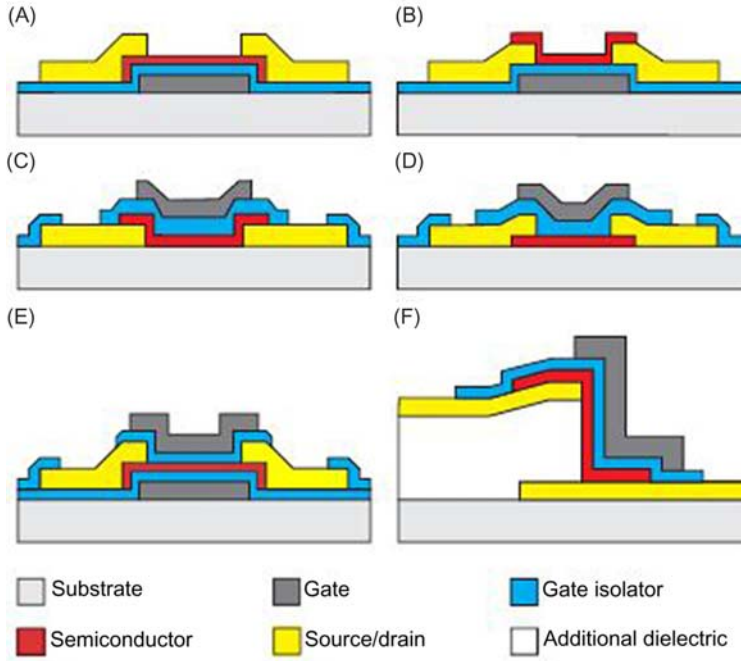

Figure 13.3 TFT device architectures: (A) BG staggered TFT, (B) BG coplanar TFT, (C) TG staggered TFT, (D) TG coplanar TFT, (E) DG TFT, and (F) VTFT [35]. *BG*, Bottom gate; *DG*, double gate; *TFT*, thin-film transistor; *TG*, top gate; *VTFT*, vertical thin-film transistor.

other. Another structure called double gate [34] is used to control a larger area of semiconductor channel by using an extra gate as shown in Fig. 13.3E. Finally, the alternative to the planar structure is the vertical TFTs as depicted in Fig. 13.3F [35]. TFTs are electronic devices with three terminals that can work as a switch or signal amplification. As depicted in Fig. 13.4, TFTs basically consist of three main parts: the first is a semiconductor material that acts as a channel for moving the accumulated charges such as electrons and holes, the second is a dielectric material between gate electrode and semiconductor to establish a capacitive coupling between them, and the third is a metallic source and drain electrodes to inject and extract the charge carriers. The flow of charges between the source and drain can be controlled by using the gate bias that leads to forming polarization in dielectric [36]. Oxide semiconductors are promising candidates for TFT applications due to their optical transparency in the visible range. Also, channel layers made by them exhibit superior electrical properties such as low subthreshold swing, high mobility of field effect, and uniformity of large area [37]. On the other hand, Lee et al. [38] have fabricated photochemically activated and thermally annealed IGZO-TFTs under light illumination that generates small photoinduced current and persistent photoconductivity (PPC) behavior due to the energy

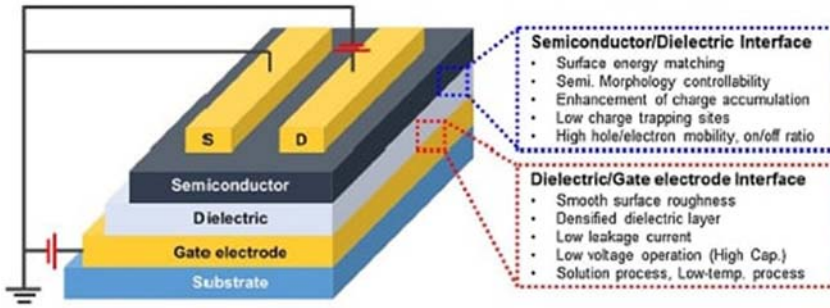

Figure 13.4 A schematic of TFT with the bottom-gate and top-contact configuration. Both interfaces are discussed in the dotted boxes [36]. *TFT*, Thin-film transistor.

barrier of the oxygen vacancies. IGZO-TFTs can be used in active-matrix backplanes and photosensors applications. Unfortunately, MOSs have a serious drawback that is related to their response to the light such as the PPC that refers to continuous high conductivity even after stopping the light illumination. Also, IGZO-TFTs have been fabricated and examined by Ruan et al. [39] using physical vapor deposition and low temperature. Multilayer stacks of $SiO_2/TiO_2/HfO_2$ are deposited to form a high-κ gate multilayer. IGZO interfacial layer between the MO channel and the multilayer stack is important for tuning the performance of the TFT. Many electrical parameters have been explored in the TFT, and field-effect mobility was about 37.8 cm^2/Vs and on/off current of 7×10^7 for the low gate leakage current. IGZO-TFTs can be used in an active-matrix display. Many MOSs are used as a dielectric layer, such as Al_2O_3, SiO_2, HfO_2, and ZrO_2, and have been used as surface passivation and gate insulator in heterostructure FETs. SiO_2 has a low-κ whereas HfO_2 and Al_2O_3 express a moderate to high-κ dielectric, and this will lead to lower the swing of the gate voltage and deactivation of tunneling effects and keep the gate capacitance high due to the increased thickness of MO [40]. The $C-V$ characteristics of ultrathin-body (UTB) of FETs using bulk Si and silicon-on-insulator substrates have been analyzed by a simulation package. Different parameters are considered to be important for the performance of the MOSFETs such as dimensions, electrical permittivity, gate dielectric, and channel thickness. Drain and source junctions are controlling the gate capacitance in a way that will prevent $C-V$ curve to have symmetry around the inversion voltage. $C-V$ curves in UTB MOSFET are looking different from similar curves found in conventional ones [41]. Al_2O_3, In_2O_3, and InZnO thin films have been fabricated by Xu et al. [42] using an aqueous solution–based technique. Thermal, structural, optical, morphological, and electrical properties have been examined at different annealing temperatures, 200°C and 250°C. At operation voltage of 4 V the mobilities were 2.04 and 36.69 $cm^2/V/s$, respectively. A silicon cantilever sensor based on n-type MOS (nMOS) transistor has been presented by Wang et al. [43]. The sensor is along (1 0 0) crystal orientation of the silicon, and it is using the transistor to sense the deflection of the cantilever that resulted by the chemisorption-based surface stress. The chemical

functionalized gold film was deposited at the bottom surface of cantilevers to analyze the reaction process and to differentiate surface stress between different intermolecular interactions. The schematic drawing of the cantilever sensor based on the nMOS transistor is presented in Fig. 13.5. Oertel et al. [44] have developed TFT by using low cost and nontoxic materials in the development process of MO. Indium−zinc oxide (IZO) with an (In)/(Zn) ratio of 3:1 precursors was used, and the deposition of ultrathin and high mobility semiconductor thin films was achieved by spray pyrolysis. $I-V$ measurements show a saturation mobility of 14.1 ± 1.1 $cm^2/V/s$ and an on−off current ratio of 10^6 at a drain voltage of 40 V. MOSs have been used widely in TFTs as an active channel for using in flat panel displays due to the low cost of processing and fabrication compared to polycrystalline silicon (Si). A number of MOSs have been studied in the literature such as zinc oxide (ZnO), indium oxide (In_2O_3), and IZO to improve the device's performance or to lower the cost of fabrication and processing. The preparation of MOS films by using solution based costs less than vacuum-based deposition techniques despite the need for a high-temperature annealing that used in solution-based technique. Using annealing for the fabrication of MOS, TFTs become a challenge due to using flexible substrates. The possibility of melting substrates in annealing inspires researchers to introduce some changes to the traditional solution-based techniques such as using preformed nanocrystals into precursor solution or using photo annealing method or doping additional elements or using combustion processing. Researchers are split into two groups in developing the electrical properties of TFTs, one is using polycrystalline structure and the other is using amorphous structure [32]. Zhang et al. [45] have developed TFT using ZTO as an active layer and SiO_2 as

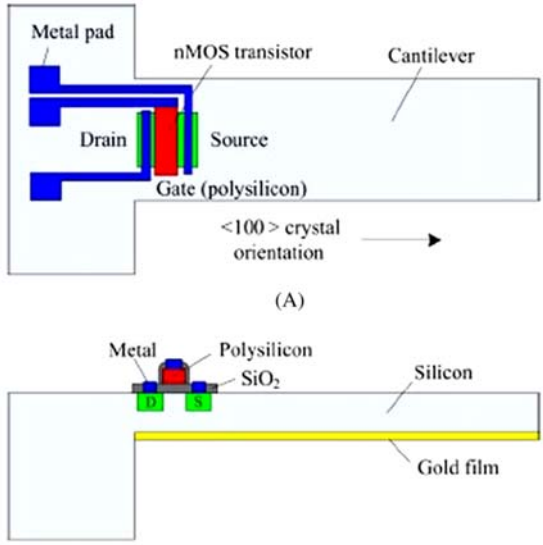

Figure 13.5 Schematic drawing of the cantilever sensor based on nMOS transistor: (A) top view and (B) cross-sectional view [43]. *nMOS*, n-Type metal−oxide−semiconductor.

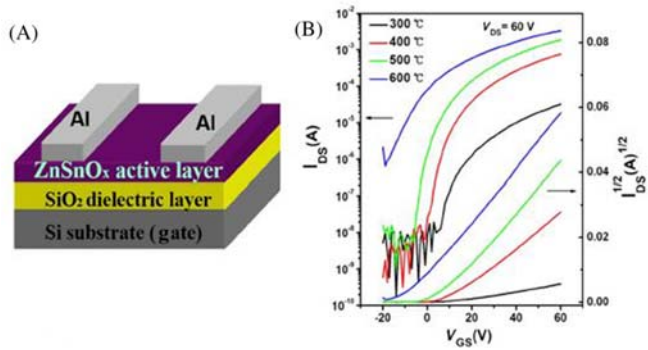

Figure 13.6 (A) The schematic structure of ZTO TFT. (B) The output curves of ZTO TFTs annealed at different temperatures: 300°C, 400°C, 500°C, and 600°C. [45]. *TFT*, Thin-film transistor; *ZTO*, zinc−tin oxide.

a dielectric layer as shown in Fig. 13.6A. ZTO solution has been deposited on Si/SiO_2 substrate using spin-coating technique followed by thermally evaporating Al source and drain electrodes. TFT device annealed at 300°C shows a saturation current of 97 μA at when gate-source voltage and drain-source voltage equal to +60 V, whereas it increases to 2.34 mA at an annealing temperature of 600°C as depicted in Fig. 13.6B. It is worth understanding that the drain to source current increases as the annealing temperature rises. ZnO-based MOSFET has been fabricated by Lin and Lee [46]. ZnO film has been deposited on a sapphire substrate using vapor cooling condensation system. The output is a very small gate leakage current of 24 nA resulted from applying a reverse voltage of −6 V. The saturation drain−source current (IDSS) and the maximum extrinsic transconductance (gm) were 5.64 mA/mm and 1.31 mS/mm, respectively.

13.3 Diodes

Semiconductor diodes are used extensively in electronics as mixers, rectifiers, and detectors of signals. The metal−insulator−semiconductor (MIS) diodes are called MIS tunnel diodes, and they are used in the thin insulator film to allow the tunneling of carriers in one bias condition [47]. Satoh et al. [48] have developed two different MO bilayer thin films that are stacked within an organic photodiode (OPD) as shown in Fig. 13.7. The first layer is aluminum oxide (Al_2O_3) that acts as a protective layer and it is deposited by using atomic layer deposition, whereas the second layer is silicon oxynitride (SiON) that acts as another protective layer to enhance the chemical and mechanical stability and it is deposited by using plasma-enhanced chemical vapor deposition. The advantage of the OPD device is the stability that reaching 85% relative humidity at 85°C and for a duration of 1000 hour

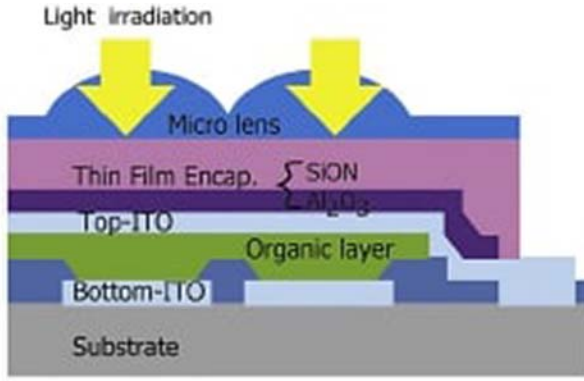

Figure 13.7 A schematic drawing of OPD device comprising the bilayer thin film between the microlens and the top electrode [48]. *OPD*, Organic photodiode.

without any degradation in the performance. Another p−n heterojunction diode has been fabricated using the dip-coating method, n-type transparent cadmium stannate (Cd_2SnO_4) was used as a conducting film deposited on a glass substrate with a thickness of 380 nm. On the other hand, several layers of p-type cupric oxide (CuO) were deposited on the transparent conducting films using the dip-coating method by Martínez-Saucedo et al. [49], and the thickness (τ) was about 49−270 nm. The samples have been exposed to thermal annealing treatment (RTA) in vacuum at a temperature ranging between 300°C and 450°C for 10 minutes to lower the CuO phase into the cuprous oxide (Cu_2O) phase. Silver paste on Cd_2SnO_4 and ohmic contacts made from a graphite probe on the copper oxide layer has been used to conduct current−voltage measurements. A rectifying behavior increases with increasing τ, and thus this behavior reaches the best with a sample thickness of 270 nm of Cu_2O and TA of 425°C. Also, saturation current density was 3.2×10^{-5} A/cm^2 and turn-on voltage is 1.1 V. MOS diodes are used as charge-coupled devices, voltage-dependent capacitors, and PDs. A simple bipolar energy transport model with nonconstant lattice temperature for a MOS diode has been introduced by Jüngel et al. [50]. Numerical analysis for the MOS diode shows that the $C-V$ characteristics are affected by the boundary temperature. Perovskite LEDs (PLEDs) attract the attention of the researchers for their potential use in the next-generation displays due to their extraordinary color purity, broad color tenability, tight emission bandwidth, and solution processability. Four inorganic layers are solution processed and used for building PLEDs, electron transport layer (ETL) that consists of cesium-doped aluminum zinc oxide nanoparticles (AZO:Cs), emissive layer that consists of triple cation lead halide perovskites, hole transport layer (HTL) that consists of copper sulfide gallium tin oxide (CuSGaSnO), and hole injection layer (HIL) that consists of tungsten trioxide nanoparticles (WO_3). Green-based PLEDs was the best whereas their efficiency exceeds 70 cd/A and 80 lm/W and the maximum luminance values exceed 50,000 cd/m^2. These achievements are

due to the use of CuSGaSnO as HTL and AZO:Cs as ETL [51]. Solution processed of molybdenum oxide (sMoOx) has been synthesized by Zheng et al. [52] using a layer of hole injection to prepare a quantum dot LEDs (QLEDs). The used method was low cost and simple and, also, the used materials are nontoxic. The maximum current efficiency of 5.46 cd/A was achieved by QLED compared to the conventional PEDOT:PSS devices. Under multiple mechanical bending of 5 mm curvature radius, the device has outstanding flexibility. Also, the introduction of sMoOx HIL to the diode helps to improve the stability of QLEDs, which is considered as a promising for future lightings and displays applications. A Pd/HfO_2/GaN MOS Schottky diode has been developed by Chen et al. [53] to sense different concentrations of hydrogen. The $I-V$ characteristics of the studied Pd/HfO_2/GaN MOS-type sensor compared to Pd/GaN MS-type device without using HfO_2 thin film at 300K are shown in Fig. 13.8. A similar $I-V$ characteristics have been found under forward voltage; however, under applied reverse voltages, MOS Schottky diode showed apparently a lower leakage current than the compared MS diode. This improved performance is caused by the enhanced Schottky barrier height due to the insertion of the HfO_2 dielectric layer between the Pd and GaN layer. It is worth mentioning that hafnium oxide (HfO_2) is used widely in the fabrication process of different electronic devices due to its larger dielectric constant and wider bandgap [54]. It is worth mentioning that some researchers investigate the effect of changing the concentration of some elements on the optical, structural, morphological, and electrical properties of the diodes as done by Rana et al. [55]. ZnO thin films were deposited on fluorine-doped tin oxide and soda-lime glass substrates using SG spin-coating technique. Cu thin films were deposited on ZnO by the sputtering technique through a shadow mask. The highest saturation current was obtained 8.67×10^{-4} A for 0.5 M thin-film sample at 5 V bias voltage. This result indicates that the

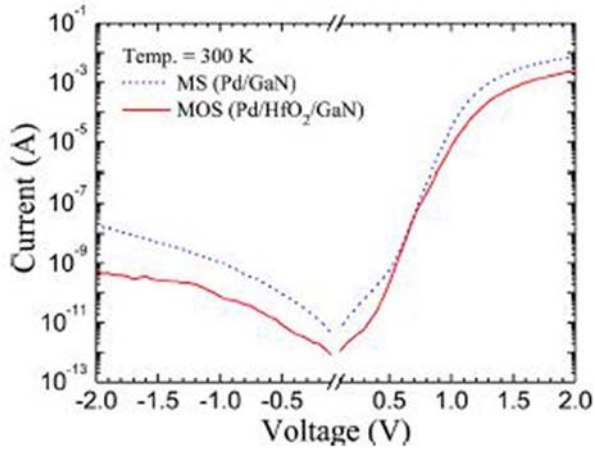

Figure 13.8 $I-V$ characteristics of Pd/HfO_2/GaN MOS-type and Pd/GaN MS-type devices. [53]. *MOS*, Metal−oxide−semiconductor; *MS*, microwave synthesis.

electrical properties of the Cu/ZnO Schottky diodes can be tuned by molar concentrations.

13.4 Photodetectors

Optoelectronics devices such as PDs are working on photoelectric effect principles [56]. They consist of an active layer that is surrounded by two electrodes, the active layer is a light-sensitive material that absorbs illuminating photon energy and generates electrons movement. These carriers are collected by the contact electrodes to provide light-induced current flow to the external circuit. A flexible and transparent PD based on Ag_xO/TiO_2/indium−tin oxide (ITO) layers deposited on a PET substrate has been fabricated and characterized by Abbas et al. [57]. Under UV illumination, it showed a high responsivity (323 mA/W) and detectivity (4.2×10^8 Jones). Also, a noise equivalent power of 2.3×10^{-9} W/Hz$^{1/2}$ is obtained, which confirmed its capability to detect light at nW level. Two PDs, Cu_4O_3/ZnO/ITO and NiO/Cu_4O_3/ZnO/ITO, have been prepared by Kim et al. [58] from p-type Cu_4O_3 that deposited on n-type ZnO to construct a rectifying junction at the interface, the ITO layer was acting as an electron transporting layer. UV and visible radiations were absorbed by both devices, and this leads to lower the transmittance within a given wavelength range. The reverse saturation current, as well as the recombination loss, increased due to the missing proper channel for hole movement. NiO/Cu_4O_3/ZnO/ITO PD boosts the photocurrent within a short time of 33 ms and then gets relaxed by 89 ms when the PD exposed to light. It is worth mentioning that the fast response of paramelaconite (Cu_4O_3)−based PDs is very useful for their operation. A perovskite-based MOS PDs have been developed by Wang et al. [59] by depositing a thin layer of Au on the top of perovskite film as the source and drain electrodes and Al as the BG electrode. The dark current was in a pA Scale with over than 1014 Jones detectivity under the illumination of 2 mW/cm^2. The ultralow dark and light switch current ensures the low consumption output as well as the wide operating voltage range. Fig. 13.9A illustrates the structure of the MOS PDs, the simplified structure is Au/ perovskite/SiO_2/Si/Al. On the other hand, Fig. 13.9B shows the

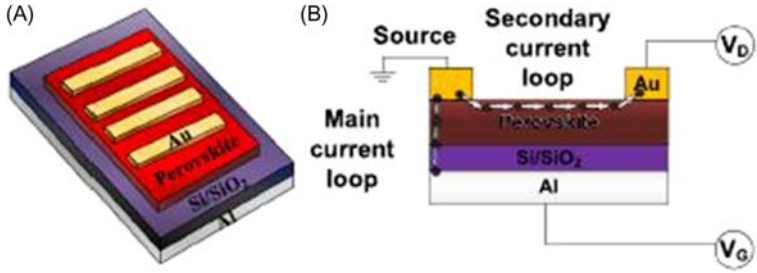

Figure 13.9 Perovskite-based MOS photodetector (A) schematic (B) electrical model [59]. *MOS*, Metal−oxide−semiconductor.

source electrode, drain voltage, and gate voltage with arrows as symbolic of two current loops. The main current loop is from source to the gate. Yang et al. [60] have synthesized a PD by depositing multiple thicknesses of hexagonal $YMnO_3$ (h-YMO) films on yttria-stabilized zirconia substrates using pulsed laser deposition (PLD). Al-doped ZnO (AZO) top electrodes were deposited on the YMO films using PLD through a shadow mask. Fig. 13.10A depicts the schematic diagram of the UV PD. Fig. 13.10B and C shows the current−voltage ($I-V$) curves for dark and light illumination, respectively, at a voltage range between -4 and $+4$ V. In the dark condition, current has a value of $\sim$10 pA for most of the thicknesses; however, it was significantly enhanced with the light condition that reached $\sim$300 pA. Fig. 13.10D reveals the time-resolved photoresponses of all PDs with applying a voltage of $+4$ V and 365 nm illumination light. When the UV light is on, the resulted current will rise rapidly and it will keep high as long as the PD is exposed to the UV light. On the other hand, when the UV light is off, the current will go down rapidly and constantly as long as the light is off. The resulted on and off currents are called Ion and Ioff. NiO/ZnO/ITO/PET transparent heterojunction ultraviolet PD has been developed by Patel and Kim [61] with a high visible-range transparent (74.8%) that is extremely sensitive to detect the tiny UV light density of

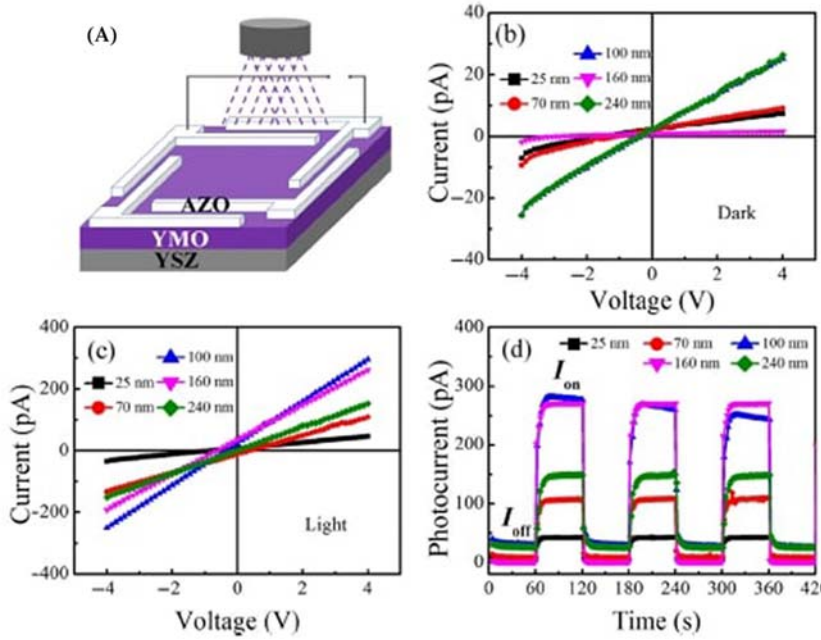

Figure 13.10 (A) Schematic of UV photodetector based on AZO/YMO/YSZ structure. The current−voltage ($I-V$) characteristics under (B) dark (C) light (D) time-resolved photocurrent using applied voltage of 4 V and 365 nm UV light illumination [60]. *YSZ*, Yttria-stabilized zirconia.

10 mW/cm^2 with the ultrafast photoresponse time (19 ms) and high photoresponse ratio of 1944.

Conclusion

MOs have been investigated widely as the key component in different electronic and optoelectronic devices. A clear understanding of optical, structural, electrical, and morphological properties of MOs provides a path for the growth of new MOs with characteristics that can be adjusted to meet the efficiency requirements of different applications. In this chapter, we present a comprehensive review of the synthesis, analysis, characterization, and applications of MO nanostructures. Careful attention has been paid to the aspects important to the development of electronic and optoelectronic devices: (1) types of MOs (i.e., bandgap and type of conductivity), (2) the combination of different MOs to form heterostructures with different morphologies and dimensions to be used more effectively in different electronic devices, and (3) the fabrication techniques (substrate type, deposition methods temperature, layer structure, etc.). This means combining advanced substrates, that is, PET [10] with suitable device architectures [35] to develop a broad range of electronic devices. The main part of the chapter has described the currently available approaches for fabricating and developing TFTs, FETs, LEDs, Schottky diodes, and PDs. Also, novel structures have been discussed such as adding an interfacial layer between the high-κ stack and MO channel [39] to enhance the on/off current and field-effect mobility. In this chapter the fabrication and characterization of flexible LED and Schottky diodes have been demonstrated, whereas a novel heterojunction diode with a high rectification was discussed [49]. In the end, photoresponses along with other electrical properties for an optoelectronic device such as PD were discussed and elaborated. Even though there is still work to be accomplished at the moment, the pace of growth that this sector has experienced in recent years allows us to predict that technology based on MOSs will play a main part in the electronic scenario of tomorrow.

References

[1] D. Zappa, V. Galstyan, N. Kaur, H.M.M. Munasinghe Arachchige, O. Sisman, E. Comini, Metal oxide—based heterostructures for gas sensors'—a review, Anal. Chim. Acta 1039 (2018) 1−23.

[2] Y. Huang, L. Lin, Efficient battery supercapacitor hybrid devices with quaternary metal oxide electrodes based on nickel and cobalt, J. Energy Storage 25 (2019) 100826.

[3] D. Chen, et al., Controlled synthesis of mesoporous zinc oxide containing oxygen vacancies in low annealing temperature for photoelectrochemical biosensor, Ceram. Int., 45, 2019, pp. 0−1.

[4] Y. Slimani, M.A. Almessiere, E. Hannachi, F.O. Al-qwairi, A. Manikandan, A. Baykal, AC susceptibility, DC magnetization and superconducting properties of tungsten oxide nanowires added YBa_2Cu_3Oy, Ceram. Int. 45 (2019) 0−1.
[5] N. Neugebohrn, K. Gehrke, K. Brucke, M. Götz, M. Vehse, Multifunctional metal oxide electrodes: colour for thin film solar cells, Thin Solid Films 685 (2019) 131−135.
[6] V. De Oliveira, S. Neto, T.M. Freire, G.D. Saraiva, Water Treatment Devices Based on Zero-Valent Metal and Metal Oxide Nanomaterials, 2019.
[7] O. Korostynska, A. Arshak, K. Arshak, D. Morris, Investigation into real-time pressure sensing properties of SnO_2, TiO_2, and TiO_2/ZnO thick films with interdigitated electrodes, Mater. Sci. Eng. B Solid-State Mater. Adv. Technol. 176 (16) (2011) 1297−1300.
[8] Y. Wang, X. Huang, H. Li, L. Guo, Sensitive impedimetric DNA biosensor based on (Nb,V) codoped TiO_2 for breast cancer susceptible gene detection, Mater. Sci. Eng. C 77 (2017) 867−873.
[9] F.N. Tuzluca, Y.O. Yesilbag, M. Ertugrul, Synthesis of In_2O_3 nanostructures with different morphologies as potential supercapacitor electrode materials, Appl. Surf. Sci. 427 (2018) 956−964.
[10] S. Li, et al., Design and preparation of the WO_3 hollow spheres@PANI conducting films for room temperature flexible NH_3 sensing device, Sens. Actuators, B: Chem. 289 (2019) 252−259.
[11] K.S. Lee, J. Shim, M. Park, H.Y. Kim, D.I. Son, Transparent nanofiber textiles with intercalated ZnO@graphene QD LEDs for wearable electronics, Composites, B: Eng. 130 (2017) 70−75.
[12] P. Zhao, N. Wang, W. Hu, S. Komarneni, Anode electrodeposition of 3D mesoporous Fe_2O_3 nanosheets on carbon fabric for flexible solid-state asymmetric supercapacitor, Ceram. Int. 45 (8) (2019) 10420−10428.
[13] S.-M. Lee, H.-W. Koo, T.-W. Kim, H.-K. Kim, Asymmetric ITO/Ag/ZTO and ZTO/Ag/ITO anodes prepared by roll-to-roll sputtering for flexible organic light-emitting diodes, Surf. Coat. Technol. 343 (2018) 115−120.
[14] S. Boscarino, et al., Ion irradiation of AZO thin films for flexible electronics, Nucl. Instrum. Methods Phys. Res., Sect. B: Beam Interact. Mater. At. 392 (2017) 14−20.
[15] Z. Zhong, H. Kang, Z. Lu, H. Long, J. Gu, Structure and optoelectrical properties of transparent conductive MGZO films deposited by magnetron sputtering, Optoelectron. Lett. 14 (1) (2018) 25−29.
[16] J.-H. Shin, D.-K. Shin, H. Lee, J.-Y. Lee, N.-I. Cho, S.-J. Lee, *Characteristics* of gallium and aluminum co-doped ZnO (GAZO) transparent thin films deposited by using the PLD process, J. Korean Phys. Soc. 55 (2009).
[17] H.-S. Kim, J.-S. Park, The performance and negative bias illumination stability of Hf-In-Zn-O thin film transistors on sputtering conditions, J. Electroceram. 32 (2) (2014) 220−223.
[18] J.Y. Choi, et al., Effect of Si on the energy band gap modulation and performance of silicon indium zinc oxide thin-film transistors, Sci. Rep. 7 (1) (2017) 15392.
[19] A.A. Odeh, et al., A needle-like Cu_2CdSnS_4 alloy nanostructure-based integrated electrochemical biosensor for detecting the DNA of dengue serotype 2, Microchim. Acta 184 (2017).
[20] E. Comini, One- and Two-Dimensional Metal Oxide Nanostructures for Chemical Sensing, Woodhead Publishing Limited, 2013.
[21] A. Liu, H. Zhu, Y.Y. Noh, Solution-processed inorganic p-channel transistors: recent advances and perspectives, Mater. Sci. Eng. R. Rep. 135 (2019) 85−100.

[22] H.F.X. Xia, Y. Zhang, D. Chao, C. Guan, Y. Zhang, L. Li, X. Ge, I. Bacho, J. Tu, Solution synthesis of metal oxides for electrochemical energy storage applications, R. Soc. Chem. 6 (10) (2014) 5008−5048.
[23] H. Chu, L. Jiang, Z. Song, Y. Xu, S. Zhao, C. Xiong, Repair of concrete crack by pulse electro-deposition technique, Constr. Build. Mater. 148 (2017) 241−248.
[24] Q. Chen, Y. Yao, X. Li, J. Lu, J. Zhou, Z. Huang, Comparison of heavy metal removals from aqueous solutions by chemical precipitation and characteristics of precipitates, J. Water Process. Eng. 26 (2018) 289−300.
[25] K. Schiørring, et al., Microwave synthesis of metal nanocatalysts for the electrochemical oxidation of small biomolecules, Curr. Opin. Electrochem. 4 (1) (2017) 124−132.
[26] M.G.S. Rao, et al., Low-temperature sol-gel $ZrHfO_2$-PMMA hybrid dielectric thin-films for metal oxide TFTs, J. Non-Cryst. Solids 502 (2018) 152−158.
[27] A. Maho, et al., Solar energy materials and solar cells solvothermally-synthesized tin-doped indium oxide plasmonic nanocrystals spray-deposited onto glass as near-infrared electrochromic films, Sol. Energy Mater. Sol. Cells 200 (2019) 110014.
[28] A. Kubiak, K. Siwi, J. Goscianska, A. Dobrowolska, Hydrothermal-assisted synthesis of highly crystalline titania-copper oxide binary systems with enhanced antibacterial properties, Mater. Sci. Eng. C. 104 (2019) 109839.
[29] M. Martínez-gil, M.I. Pintor-monroy, M. Cota-leal, D. Cabrera-german, A. Garzon-fontecha, Influence of annealing temperature on nickel oxide thin films grown by chemical bath deposition, Mater. Sci. Semicond. Process. 72 (2017) 37−45.
[30] Y. He, X. Wang, Y. Gao, Y. Hou, Q. Wan, Oxide-based thin film transistors for flexible electronics, J. Semicond. 39 (1) (2018).
[31] J.-H. Yang, C.-Y. Hwang, J.H. Choi, J.-E. Pi, H.-O. Kim, C.-S. Hwang, Origin of the dry etch damage in the short-channel oxide thin-film transistors for high resolution display application, Thin Solid Films 674 (2019) 71−75.
[32] S.Y. Han, M.C. Nguyen, A.H.T. Nguyen, J.W. Choi, J.Y. Kim, R. Choi, Effect of Li-doping on low temperature solution-processed indium−zinc oxide thin film transistors, Thin Solid. Films 641 (2017) 19−23.
[33] Y. Lin, P. Cheng, K. Huang, H. Lin, Atomic layer deposition of sub-10nm high-K gate dielectrics on top-gated MoS_2 transistors without surface functionalization, Appl. Surf. Sci. 443 (2018) 421−428.
[34] N. Dang, C. Shih, Oxide thickness-dependent effects of source doping profile on the performance of single- and double-gate tunnel field-effect transistors, Superlattices Microstruct. 102 (2017) 284−299.
[35] C. Vogt, et al., Metal oxide semiconductor thin-film transistors for flexible electronics, Appl. Phys. Rev. 3 (2) (2016) 021303.
[36] S. Park, C. Kim, W. Lee, S. Sung, M. Yoon, Sol-gel metal oxide dielectrics for all-solution-processed electronics, Mater. Sci. Eng. R. 114 (2017) 1−22.
[37] Y.C. Kim, S.J. Lee, I.K. Oh, S. Seo, H. Kim, J.M. Myoung, Bending stability of flexible amorphous IGZO thin film transistors with transparent IZO/Ag/IZO oxide−metal−oxide electrodes, J. Alloys Compd. 688 (2016) 1108−1114.
[38] M. Lee, K.T. Kim, M. Lee, S.K. Park, Y.H. Kim, A study on the persistent photoconductance and transient photo-response characteristics of photochemically activated and thermally annealed indium-gallium-zinc-oxide thin-film transistors, Thin Solid Films 660 (2018) 749−753.
[39] D. Ruan, et al., Effect of interfacial layer on device performance of metal oxide thin-film transistor with a multilayer high-k gate stack, Thin Solid Films 660 (2018) 578−584.

[40] Š. Haščík, et al., Characterization of interface states in AlGaN/GaN metal-oxide-semiconductor heterostructure field-effect transistors with HfO_2 gate dielectric grown by atomic layer deposition, Appl. Surf. Sci. 461 (2018) 255–259.
[41] E. Yu, S. Cho, B.G. Park, An accurate simulation study on capacitance-voltage characteristics of metal-oxide-semiconductor field-effect transistors in novel structures, Physica B: Condens. Matter 521 (2017) 305–311.
[42] W. Xu, et al., Fully solution-processed metal oxide thin-film transistors via a low-temperature aqueous route, Ceram. Int. 43 (8) (2017) 6130–6137.
[43] J. Wang, B. Feng, W. Wu, Y. Huang, Chemisorption sensing and analysis using silicon cantilever sensor based on n-type metal-oxide-semiconductor transistor, Microelectron. Eng. 88 (6) (2011) 1019–1023.
[44] E. Teuber, A.J. Bauer, M.P.M. Jank, S. Oertel, L. Frey, High-mobility metal-oxide thin-film transistors by spray deposition of environmentally friendly precursors, Thin Solid Films 553 (2013) 114–117.
[45] Q. Zhang, G. Xia, L. Li, W. Xia, H. Gong, S. Wang, High-performance zinc-tin-oxide thin film transistors based on environment friendly solution process, Curr. Appl. Phys. 19 (2) (2019) 174–181.
[46] T.S. Lin, C.T. Lee, Homostructured ZnO-based metal-oxide-semiconductor field-effect transistors deposited at low temperature by vapor cooling condensation system, Appl. Surf. Sci. 354 (2015) 71–73.
[47] M.A. Dominguez, J.A. Luna-Lopez, S. Ceron, Low-temperature ultrasonic spray deposited aluminum doped zinc oxide film and its application in flexible metal-insulator-semiconductor diodes, Thin Solid Films 645 (2018) 278–281.
[48] R.-i Satoh, et al., Bi-layered metal-oxide thin films processed at low-temperature for the encapsulation of highly stable organic photo-diode, Org. Electron. Phys. Mater. Appl. 41 (2017) 259–265.
[49] J. Márquez-Marín, O. Zelaya-Ángel, R. Castanedo-Pérez, G. Martínez-Saucedo, G. Torres-Delgado, Cuprous oxide/cadmium stannate heterojunction diodes obtained by dip-coating method, J. Alloys Compd. 774 (2018) 153–159.
[50] A. Jüngel, R. Pinnau, E. Röhrig, Analysis of a bipolar energy-transport model for a metal-oxide-semiconductor diode, J. Math. Anal. Appl. 378 (2) (2011) 764–774.
[51] A.G. Macedo, A.E.X. Gavim, M.A.M. Teridi, F.K. Schneider, W.J. da Silva, A.R.B.M. Yusoff, High-efficiency, solution-processable, multilayer triple cation perovskite light-emitting diodes with copper sulfide–gallium–tin oxide hole transport layer and aluminum-zinc oxide–doped cesium electron injection layer, Mater. Today Chem. 10 (2018) 104–111.
[52] C. Zheng, F. Li, Q. Zeng, H. Hu, T. Guo, Aqueous solution-processed molybdenum oxide as an efficient hole injection layer for flexible quantum dot light emitting diodes, Thin Solid Films 669 (2019) 387–391.
[53] H.I. Chen, et al., Hydrogen sensing performance of a Pd/HfO_2/GaN metal-oxide-semiconductor (MOS) Schottky diode, Sens. Actuators, B: Chem. 262 (2018) 852–859.
[54] C.H. Chang, K.W. Lin, H.H. Lu, R.C. Liu, W.C. Liu, Hydrogen sensing performance of a Pd/HfO_2/GaOx/GaN based metal-oxide-semiconductor type Schottky diode, Int. J. Hydrog. Energy 43 (42) (2018) 19816–19824.
[55] V.S. Rana, J.K. Rajput, T.K. Pathak, L.P. Purohit, Cu sputtered Cu/ZnO Schottky diodes on fluorine doped tin oxide substrate for optoelectronic applications, Thin Solid Films 679 (2019) 79–85.

[56] M. Patel, D. Ban, A. Ray, J. Kim, Transparent all-oxide photovoltaics and broadband high-speed energy-efficient optoelectronics, Sol. Energy Mater. Sol. Cell 194 (2019) 148−158.
[57] S. Abbas, M. Kumar, J. Kim, All metal oxide-based transparent and flexible photodetector, Mater. Sci. Semicond. Process. 88 (2018) 86−92.
[58] H.S. Kim, M.D. Kumar, W.H. Park, M. Patel, J. Kim, Cu_4O_3-based all metal oxides for transparent photodetectors, Sens. Actuators, A: Phys. 253 (2017) 35−40.
[59] Y. Wang, Y. Zhang, T. Pang, K. Sun, Z. Hu, Y. Zhu, Organolead halide perovskite-based metal-oxide-semiconductor structure photodetectors achieving ultrahigh detectivity, Sol. Energy 183 (2019) 226−233.
[60] S.B. Yang, et al., Hexagonal $YMnO_3$ films as promising ultraviolet photodetectors, Ceram. Int. 45 (3) (2019) 3239−3243.
[61] M. Patel, J. Kim, Transparent NiO/ZnO heterojunction for ultra-performing zero-bias ultraviolet photodetector on plastic substrate, J. Alloys Compd. 729 (2017) 796−801.

Metal oxide powder technologies in catalysis

14

Yanet Rodriguez Herrero and Aman Ullah
Department of Agricultural, Food & Nutritional Science, University of Alberta, Edmonton, AB, Canada

14.1 Introduction

Catalysts are materials that accelerate chemical processes, theoretically without consuming themselves. Metal oxides combine an oxide anion with a cation of single metal or metalloid element, displaying a wide range of physical and chemical properties that make them attractive to be used as heterogeneous catalyst, either as active phase or as support [1]. They are common in nature or can be readily synthesized from commercially available minerals. Their applications have been extensively developed since the mid-20th century in the chemical, environmental, and petroleum industries [2]. Metal oxides are used as catalysts in selective oxidation, acid−base, hydrogenation, polymerization, and redox processes [3]. Active sites, in general, employ transition and noble group metals, attributing their activity to the outer electron configuration, where the partially filled d-shell plays a major role in the catalytic transformation [4].

On the other hand, there is a synergistic effect between the active phase and the support [5], which influences the catalyst essential functions as activity, selectivity, and catalyst life. Supports such as zeolites, metal oxides, and many forms of carbon (activated carbon, carbon nanotubes, and quantum dots) are used to increase surface area, particles dispersion and protect active catalyst from carbon deposition and thermal deactivation [6].

The purpose of this chapter is to highlight the role of the metal oxides in important technological processes that have led to development of the society. Even though, industrial processes are already in place, there is always room for improvement of the activity and selectivity of the catalytic system by systematic studies of catalyst surface structures, synthesis methods, and operation conditions.

In this chapter, we will look at the structure of the catalysts, followed by some of the most used methods to synthesis the metal oxides that are used in the industry. The chapter will conclude with some metal oxides that are used in the industry and some of the challenges that these catalytic systems currently face. The active site of most of the catalysts is still in debate that will not be the focus of this chapter as a comprehensive review was recently published [7].

Metal Oxide Powder Technologies. DOI: https://doi.org/10.1016/B978-0-12-817505-7.00014-2

14.2 Supported metal oxides

Supported catalyst oxides are made of the combination of the active phase deposited on the surface on a solid support. The most common supports in industry applications are solid oxide supports such as alumina (Al_2O_3), silica (SiO_2), and titania (TiO_2). Oxide supports are often covered by hydroxyl groups that act as Brønsted acids or bases when in contact with water during impregnation step. These hydroxyl groups interact with catalytic precursors by proton exchanges, allowing the metal−support interaction such as electrostatic interactions, van der Waals, ion pairing, or even covalent bonding [8−12].

The advantage of using supported catalyst over pure metal oxides rests on the highly dispersion and stabilization that the supported layer contributes, leading to a more active and stable catalyst. A wide variety of inorganic supports such as metal oxides, zeolites, clays, and carbon materials find wide application in the immobilization of the active phase in many chemical, petrochemical, and environmental industries. Table 14.1 lists some significant industrial reactions catalyzed by supported metal oxides.

14.2.1 Catalyst molecular structure

Supported metal oxides are generally prepared by depositing metal oxides species on a second metal oxide followed by calcination. The calcined material contains supported metal oxide layers with several structures based on the synthetic method employed, metal−support molar ratio, specific surface area of the support, and chemical interactions between the support and active site layer. When the active site has a low metal−support molar ratio, the metal oxide is dispersed as monomeric species. When the metal−support molar ratio is increased, the monomeric species form oligomeric or polymeric species via metal−oxygen−metal linkages and ultimately to surface-bound (nano) crystalline metal oxide layer [3].

Many spectroscopy characterization techniques are employed to determine the molecular structure of the metal oxides, such as Raman [21−24], infrared (IR) absorption [23−26], UV/vis [24,27,28], solid-state nuclear magnetic resonance [29−31], and X-ray absorption [32−34]. These spectroscopy techniques allow studying the metal

Table 14.1 Some industrial applications of supported metal oxides.

Catalytic system	Application	Reference
$Cu-ZnO/Al_2O_3$	CO hydrogenation to methanol	[13]
WO_3/SiO_2	Alkene metathesis	[14]
$Pt-Sn/Al_2O_3$	Propane dehydrogenation to propylene	[15,16]
CrO_3/SiO_2	Ethylene polymerization	[17]
MoO_3/SiO_2	Antimicrobial drug tinidazole	[18]
$(V_2O_5 + WO_3)/TiO_2$	Selective catalytic reduction of NO_x using ammonia	[19]
$Ni/MgAl_2O_4$	Steam reforming to synthesis gas	[20]

oxides under different environmental conditions, mimicking the industrial conditions, and analyzing how the environment affects the catalytic species.

14.3 Synthesis methods of supported catalyst oxides

Synthetic routes are developed to attain a rational design of catalysts in order to control the catalytic activity of the surface, particle size, and surface area. The catalytic properties of the metal oxides greatly depend on the selection of the active phase and the support. The selection of the synthesis methods is important because it will influence the active sites dispersion, metal−support interaction, and surface area. In general, supported metal oxide catalysts are prepared by deposition of the active phase followed by activation, where the precursor is transformed to the active phase, depending on the reaction to catalyze. Different synthetic methods for the synthesis of supported metal oxides are presented in the following sections.

14.3.1 Impregnation method

In impregnation method a solution of the active metal precursor is introduced into the void space of the support with a subsequent drying. There are two major impregnation techniques: capillary or dry and diffusional or wet impregnation.

In capillary or dry impregnation the support material is initially dried [35] with a rapid filling of the pores. The volume of the pore of the support is generally equal to the volume of the solution containing the precursor, with no excess solution remaining after impregnation. One of the problems is to control heat release produced when the solid−gas interface is replaced by a solid−liquid interface. Another problem encountered is the capillary pressure created by entrapped air that causes the internal pores to collapse. In addition, the speed with which the pores are filled is limited by the entrapped air and its migration outside the grain.

In diffusional or wet impregnation the support is first filled by the solvent, usually water, without the precursor and followed by the mixing with the precursor solution. The concentration gradient between the precursor solution and the solvent inside the pores is the driven force to fill the voids. The diffusional impregnation takes longer than capillary impregnation.

After impregnation the prepared materials undergo drying to remove solvent from the support pores. The drying temperature will depend on the boiling point of the solvent and often can vary from 50°C to 250°C [36]. The metal oxide is finally obtained by calcination.

14.3.2 Precipitation/coprecipitation

Precipitation is the most frequently used synthesis method. It is employed to prepare very pure oxides that are further employed as catalysts or supports such as aluminum and silicon oxide.

Coprecipitation method involves the simultaneous precipitation of more than one metal precursor and support. The low solubility of the metal hydroxides favors the precipitation of their precursor salt solution. In practical applications, hydroxides are precipitated adding an alkaline precipitating agent to and acid solution that contained the metal precursor. Ammonia and sodium bicarbonate are the most used precipitating agents. The metal precursors are obtained from highly soluble inorganic salts such as nitrate, carbonates, and chlorides. Coprecipitation is very suitable for the synthesis of homogenous distribution of catalyst components or to control the stoichiometry in the catalyst. Problems encounter in these methods include the higher technological demands, the challenges to meet the quality of the precipitation process, and reproducibility of the precipitation when the process is interrupted.

14.3.3 Grafting

In grafting the active element is strongly attached to a functional group of the support by a covalent bond. Metal precursor is covalent attached to the hydroxyl group (s) of the support. In general, the precursors used are metal halides, oxyhalides, metal alkoxides, and organometallic complexes. There is only cover of the active metal up to a single monolayer allowing better control of the dispersion and the molecular structure of the catalyst. The oxide supports are thermally pretreated before undergoes grafting in order to remove any physisorbed water. Once the coordination metal is in contact with the support, a condensation reaction occurs between the precursor and the expose OH groups of the support. Then, the physisorbed metal complexes are removed from the material by washing with pure solvent or purging with inert gas. The process to eliminate the remaining ligands is performed by hydrolysis of the metal−ligand bond of the anchored complex or by decomposition under mild conditions.

14.3.4 Chemical vapor deposition

When grafting is performed using precursors vaporized in the gas phase is called chemical vapor deposition (CVD). There are many CVD processes reported for the formation of metal oxide catalyst such as thermal decomposition, hydrolysis, reduction, oxidation, and plasma-assisted methodology. CVD is a relatively simple and flexible technology for the synthesis of various catalytic materials. The metal carbonyls are used widely in the chemical industry for production of heterogeneous catalyst. CVD happens after heating to vaporize the precursors inside the CVD reactor. Another method uses an open reactor or flowing gas to direct interaction between the precursors and support at given temperature.

14.3.5 Sol−gel method

Sol−gel method is commonly used for the preparation of metal oxide catalysts at elevated temperatures by using metal alkoxide [37] or colloidal dispersion [38]

passing from solution state to a gel state before dehydration. Gel is generally formed by the dispersion of particles from 1 nm to 1 μm in a liquid forming a solid or a network or by the polymerization of molecules with a solid encapsulated a solvent [39]. The encapsulated solvent can be removed by evaporation or supercritical extraction.

A sol−gel method was used to prepare $Cu_xFe_{1-x}Al_2O_4$ spinels by dissolving the nitrate salts of copper, iron, and aluminum following by the addition of anhydrous citric acid as combustion agent and prevent the early hydrolysis of the salts. The resulting solution was kept mixing at 70°C overnight followed by a temperature increase to 250°C to achieved the citrate gel. Finally, the xerogel was burned, grounded, and calcined at 700°C for 20 hours. In this case the sol−gel method improved the stabilizing effect of $FeAl_2O_4$ phase through substitution of Cu at the Fe site of hercynite [40].

A sol−gel explosion-assisted technique was applied to rapid synthesize magnetic Fe_3O_4 nanoparticles with good dispersability [41]. At first, the metal oxide Fe_3O_4 nanoparticles were prepared using sol−gel technique. The ferric nitrate and citric acid were dissolved in water followed by the addition of ammonia to adjust the solution pH. This solution leads to the gel formation after heating and water evaporation. Then, picric acid was used during the reduction of the dry gel to control particle size and avoid agglomeration. In general, this technique can be used to synthesize any type of metal oxide from organic and/or inorganic precursors. The particle size and morphology of the particles can be controlled by drying and calcined conditions. The disadvantage of this method is the costly precursors and alkoxides.

14.3.6 Hydrothermal method

This synthesis method is based on crystallization techniques in aqueous solution using an autoclave at controlled pressure and temperature. The crystals are grown from a metal solution through oxo-hydroxide gels or sols [42]. The crystal size is control from agglomeration and aggregation using surfactant agent and controlling reaction conditions such as pH, temperature, pressure, reaction time, and molar concentration of the reactants.

14.3.7 Flame hydrolysis

Flame hydrolysis involves a reaction of a gaseous mixture of a precursor, hydrogen, and air or oxygen in a flame reactor at high temperature. This process produces oxides with high surface area at industrial scale. In general, the precursors used are metal chlorides, carbonyls, or volatile alcoholates applied in diluted aerosol form. Some examples include Al_2O_3 from $AlCl_3$ [43], Fe_2O_3 from $FeCl_3$ [44], and SiO_2 from $SiCl_4$ [45,46]. The particle size can be modeled by the flame temperature, residence time in the flame, precursor loading, and oxygen−hydrogen ratio.

14.4 Applications

14.4.1 Catalytic oxidation of methanol

Iron molybdate oxides are used for the oxidation of methanol to formaldehyde. Formaldehyde is the simplest and most active of the aldehydes. It is used in the synthesis of resins that are employed as adhesives in the production of plywood, particle board, and fiber board.

The oxidation of methanol is produced under excess air at 350°C−450°C. When the temperature is higher than 470°C, carbon monoxide, dimethyl ether, methyl formate, and formic acid are formed as by-products reducing the yield of formaldehyde.

$$CH_3OH + \frac{1}{2}O_2 \rightarrow CH_2O + H_2O \tag{14.1}$$

$$CH_2O + \frac{1}{2}O_2 \rightarrow CO + H_2O \tag{14.2}$$

$$CH_2O + 2CH_3OH \rightarrow CH_2(OCH_3)_2 + H_2O \tag{14.3}$$

$$CH_3OH + CH_3OH \rightarrow (CH_3)_2O + H_2O \tag{14.4}$$

$$CH_2O + \frac{1}{2}O_2 + CH_3OH \rightarrow HCOOCH_3 + H_2O \tag{14.5}$$

$$CH_2O + \frac{1}{2}O_2 \rightarrow CHOOH \tag{14.6}$$

The mixed catalyst comprises of 18−19 wt.% Fe_2O_3 and 81−82 wt.% MoO_3 using Cr or Co oxides as promoters [47]. The presence of iron(III) molybdate [$Fe_2(MoO_4)_3$] and MoO_3 has been confirmed at the surface and in the bulk by spectroscopic analysis [48−50], being the $Fe_2(MoO_4)_3$ confirmed as the active component of the catalyst. MoO_3 plays a role increasing the surface area per unit mass of catalyst, as a source of Mo replacement in $Fe_2(MoO_4)_3$. Fig. 14.1 shows the *lamellae* morphology when the Mo:Fe ratio is stoichiometric and sponge-like morphology when the Mo:Fe ratio corresponds to 3, which correspond to a higher surface area. The authors agree with previous study that stated that the formation of lamellae shape depends on Mo/Fe ratio, low pH, and long aging period. However, Soares disagreed with Sun-Kou et al. [51] in the cause of the surface area of the stoichiometry Mo/Fe ratio, attributing to thermal treatment exposure, the longer the treatment the higher the surface area.

The catalytic system Fe/Mo oxides are more resistant to catalyst poisons than the silver catalytic systems that are employed in the industry.

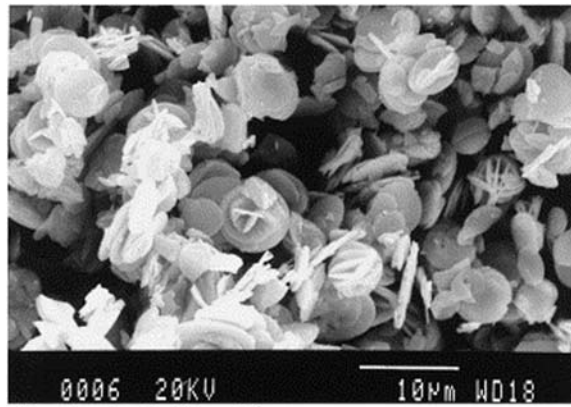

Atomic ratio Mo/Fe = 1.5

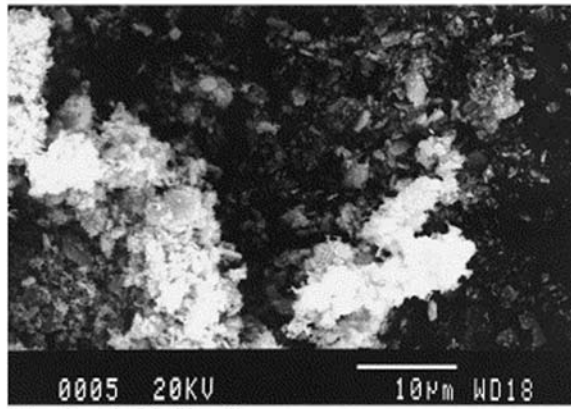

Atomic ratio Mo/Fe = 3

Figure 14.1 Scanning electron micrographs of Mo/Fe catalysts.
Source: Reproduced with permission from A.V. Soares, M.F. Portela, A. Kiennemann, L. Hilaire, J. Millet, Iron molybdate catalysts for methanol to formaldehyde oxidation: effects of Mo excess on catalytic behaviour, Appl. Catal. A: Gen. 206 (2001) 221−229. ©2001 Elsevier.

14.4.2 Selective catalytic reduction of NO_x

Selective catalytic reduction (SCR) refers to the reduction of nitrogen oxides (NO, NO_2, N_2O) with oxygen and a selective inorganic or organic reducing agent. Nitrogen oxides (NO_x) are produced as tail gas in the industrial synthesis of nitric acid or in the exhaust emissions from lean-burn or gasoline engines [52]. NO_x is a very harmful atmospheric pollutant, the principle origin of acid rain, and photochemical smog. The direct decomposition of NO_x to inert gases such as N_2 and O_2 remains an enormous challenge for many researchers.

SCR of NO_x with ammonia is a well-established process to reduce NO_x emissions of industrial and utility plants, industrial and municipal waste incinerators, and nitric acid plants. The emissions of these processes contain different NO/NO_2 ratios and space velocities; furthermore, SO_2 is part of the exhausted gases in the aforementioned processes except in the production of nitric acid. Vanadia supported on titania-based catalysts [19,53] can be generally used for any SCR-NH_3 previously mentioned. Other types of catalyst that show good activity in the nitric acid plants are the Cu-based oxides.

An approach to improve the catalyst that is already established in the industry is the temperature window in which the NO conversion is at maximum value, as the presence of ammonia, a side combustion reaction decrease the conversion temperature. Another factor to have in consideration is the selectivity in the conversion of NO with respect to ammonia, always present as a side reaction of ammonia combustion.

High vanadium loading has a positive impact in the catalytic activity, but it is required to maintained low to limit the oxidation of SO_2 to SO_3 which plugged due to ammonium sulfate or corrosion.

When ammonia is used nitrogen and water (Reactions 14.7−14.9) is produced. The commercialization of urea as selective reducing agent is still on development. When urea is used, carbon dioxide is produced along with nitrogen and water (Reaction 14.10)

$$4\,NO + 2NH_3 + O_2 \rightarrow 4\,N_2 + 6H_2O \tag{14.7}$$

$$2NO_2 + 4\,NH_3 + O_2 \rightarrow 3N_2 + 6\,H_2O \tag{14.8}$$

$$NO_2 + NO + 2NH_3 \rightarrow 2N_2 + 3H_2O \tag{14.9}$$

$$4NO + 2CH_4N_2O + O_3 \rightarrow 4N_2 + 2CO_2 + 4H_2O \tag{14.10}$$

In the case of mobile sources of NO_x for SCR-NH_3, V-TiO_2-based catalyst are used, as they are active in the presence of O_2, at very high space velocities, low reaction temperatures (120°C−200°C), and resistant to sulfur and phosphorus deactivation.

14.4.3 Catalytic hydrogenation of carbon monoxide

Carbon monoxide catalytic hydrogenation is the main route to produce methanol as a precursor of fuels, chemicals, and energy storage. The first set of the metal oxide used for this conversion is consisted of zinc oxide supported on chromium oxide. This system was stable for the sulfur and chlorine compounds contained in synthesis gas produced from coal in the early 1900s. After synthesis gas was produced with higher purity, zinc oxide/chromium oxide was substituted by copper oxide/zinc oxide supported on aluminum oxide with higher activity and selectivity at

lower temperature and pressure (50−100 bar and 200°C−270°C). Alternative metal oxide catalysts have been claimed such as Cu/Al alloys and noble metal combinations. Nevertheless, until today, none of the new noble catalytic systems published got industrial consideration for the synthesis gas conversion to methanol owing the considerably higher costs without improvements in the operational efficiency.

The following equations are used to describe the process:

$$CO + 2H_2 \rightleftarrows CH_3OH \tag{14.11}$$

$$CO_2 + 3H_2 \rightleftarrows CH_3OH + H_2O \tag{14.12}$$

$$CO_2 + H_2 \rightleftarrows CO + H_2O \tag{14.13}$$

The $Cu/ZnO/Al_2O_3$ catalyst system that is employed in the low-pressure methanol synthesis for CO hydrogenation is prepared by a coprecipitation method. A typical catalyst contains CuO 55 wt.%, ZnO 25 wt.%, and 8 wt.% Al_2O_3. Until this day, there is still debate on the nature of the carbon source for methanol—CO or CO_2 and the role of the synergistic effect of Cu−Zn.

Chinchen et al. report copper as the active catalyst with dual surface function with adsorbed oxygen and a surface available for hydrogen adsorption [54].

The role of zinc oxide has been exalted for increasing the catalyst surface area and neutralizing any copper poison as sulfur and chlorine that may be present in the feed. Another function of the zinc oxide has been associated to its basic property that neutralizes the alumina acidity that may dehydrate methanol to dimethyl ether [55]. Alumina and zinc oxide prevent the sintering of active copper.

The deactivation mechanism of the catalyst is more often by thermal deactivation than by poisoning as the desulfurization and halogenide processes are more developed. Thermal deactivation induces processes such as sintering and phase aggregation shortening the catalyst oxide life span. Sintering mechanisms are still under research. Some authors report that sintering takes place by the release of atomic or molecular species according to Hütting temperature [56]. Another studied using electron tomography and introducing local correlation between particles concluded that short interparticles distances contributed to a coalescence mechanism [57]. A more recent study [58] examined a systematic deactivation of three $Cu/ZnO/Al_2O_3$ catalysts aged under constant conditions and found that the presence of water significantly reduces the catalyst active surface area and specific activity. They labeled their samples CZA1−3 from higher to lower Cu:Zn ratio. CZA1 presented a higher catalytic activity attributed to the higher loading of Cu and the optimal distribution of Al^{3+} into the ZnO lattice generating oxygen defect sites and acting as an electronic promoter. The structure of CZA1 and CZA2 is represented by an intimate mixture of spherical ZnO and Cu nanoparticles (Fig. 14.2A and B). This leads to a very porous structure that is easily accessible for the gas atmosphere. The lower activity of the catalyst of catalyst with

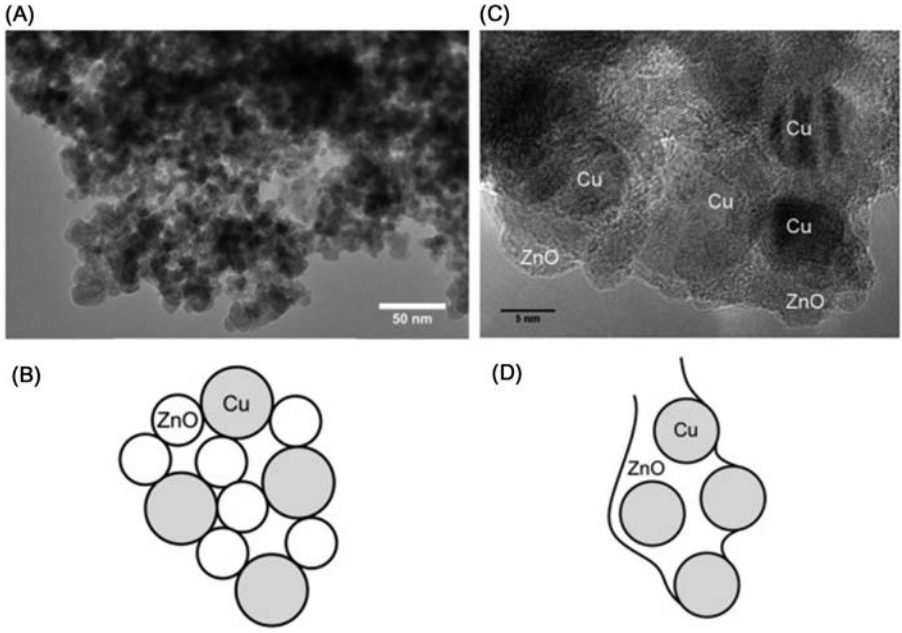

Figure 14.2 TEM images and exemplary representation of the microstructure of CZA1 and CZA2 (A and B) and CZA3 (C and D) [58].
Source: Reproduced with permission from M.T. Dunstan, D.M. Halat, M.L. Tate, I.R. Evans, C.P. Grey, Variable-temperature multinuclear solid-state NMR study of oxide ion dynamics in fluorite-type bismuth vanadate and phosphate solid electrolytes, Chem. Mater. 31 (2019). ©2015 Elsevier.

(CZA3) lower the copper loading is reported as a result of the catalyst microstructure from the ex-aurichalcite precursor phase. Cu surface is not accessible for the gas phase due to the strong fixation of the copper particles in the ZnO matrix (Fig. 14.2C and D).

14.4.4 Catalytic metathesis of olefins

Olefin metathesis involves the rearrangement of two olefins through unsaturated carbon−carbon bonds open up the opportunity to transform alkenes in new products. The general scheme of the reaction can be represented as [56]:

$$2RCH = CHR' \rightleftarrows RCH = CHR + R'CH = CHR' \tag{14.14}$$

This reaction finds wide commercial applications for the synthesis of new chemicals in petrochemical, polymers, and fine chemicals. That is the case for the

production of propene that is one of the most important olefins, as raw material of polypropylene, acrylonitrile, and acrylic acid products. Propene is commercially prepared by the metathesis reaction of ethane and 2-butene [14]:

$$CH_2 = CH_2 + CH_3CH_2 = CH_2CH_3 \rightleftarrows 2CH_3CH_2 = CH_2 \tag{14.15}$$

The metathesis reaction in commercial applications uses heterogeneous catalysts that are frequently prepared from a metal halide using organoaluminium or organotin compounds. They are preferred owing to the ease of catalyst recovery and separation. For the active site the most common catalyst are the one based on rhenium, molybdenum, or tungsten. For the support, oxides with high surface area are used such as alumina or silica−alumina. In the case of substitute olefins, they are active when promoted with trialkyltin or lead compound [59].

The most important industrial olefin metathesis technology employs heterogeneous supported metal oxide catalysts such as rhenium, molybdenum, and tungsten supported on Al_2O_3, SiO_2, and $SiO_2-Al_2O_3$ catalyst systems [60]. However, the effort and the research on the nature of the catalytic active site are still a question in the catalytic field.

The most important applications of olefin metathesis in the petrochemical field are the olefins conversion technology process (previously called the Phillips triolefin process) and the Shell higher olefins process (SHOP). The Phillips process in the reverse direction is established by ABB Lummus Global, Houston (United States) for the production of propene from ethylene and 2-butenes. Rhenium- and molybdenum-based catalysts are used. SHOP manufactures α-olefins as a raw material to produce detergents. The catalyst employs are supported molybdenum oxide on alumina catalysts.

WO_3/SiO_2 is a commonly used catalyst in the olefin metathesis due to its resistance to traces of oxygenate poisons in the feed, higher stability compared to Mo- and Re-based catalysts and simple removal of coke. The operational temperature of WO_3/SiO_2 is common above 400°C. The Lummus's "Comonomer Production Technology (CPT)" employs WO_3/SiO_2 for the production of 1-hexene from butenes [14].

The SHOP uses molybdenum-based catalysts supported on alumina [61]. MoO_3/Al_2O_3 is operational at temperatures of 100°C−200°C. Another set of catalyst reports in the olefin metathesis is Re_2O_7/Al_2O_3. It is attractive for being active at room temperature [62] and being tolerant to functional groups such as alkoxycarbonyl and alkoxy groups [63].

Generally, WO_3/SiO_2 catalysts are prepared by the deposition of W precursor on pretreated support by impregnation, drying, and calcination. A review in this method has shown inhomogeneity of the WO_3 deposition, pore plugging, and the buildup of inactive species [MoO_3 crystals and $Al_2(MoO_4)_3$], hence limiting the catalytic performance of catalysts synthesized [64]. A recent study [65] shows a WO_3-SiO_2 catalyst prepared by sol−gel method with high specific surface area between 490 and 570 m^2/g and supercalibrated micropores of 2 nm,

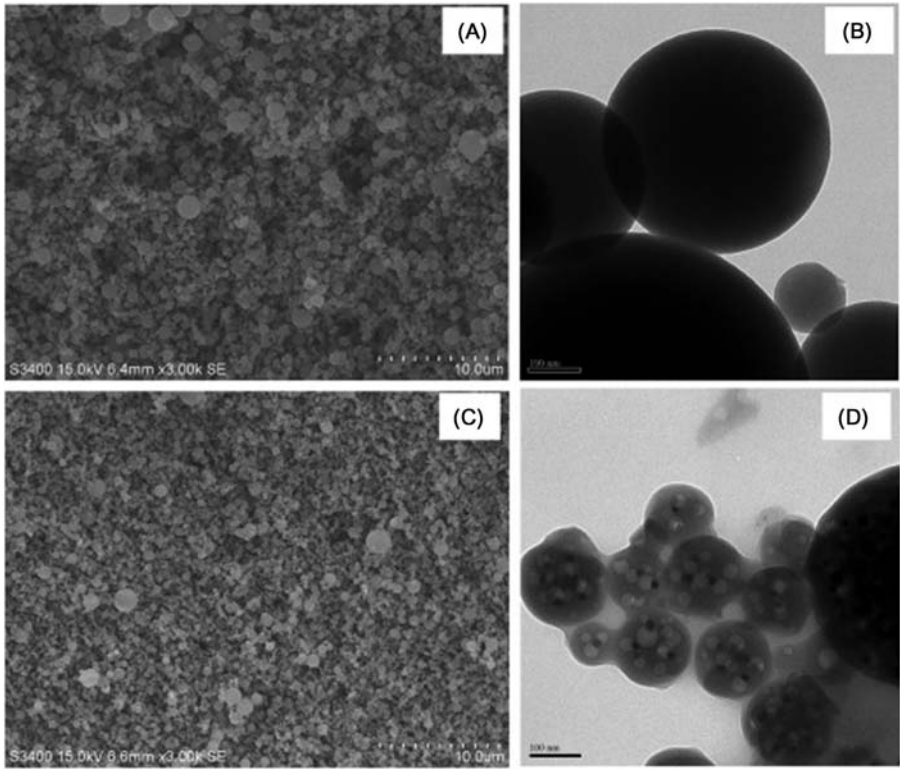

Figure 14.3 SEM (left) and TEM (right) micrographs obtained on (A and B) silica support and (C and D) 10WSi_850.
Source: Reproduced with permission from S. Maksasithorn, P. Praserthdam, K. Suriye, D.P. Debecker, Preparation of super-microporous WO_3-SiO_2 olefin metathesis catalysts by the aerosol-assisted sol−gel process, Microporous Mesoporous Mater. 213 (2015) 125−133. ©2015 Elsevier.

(Fig. 14.3). Spherical particles were generated with a nanosize ranging from 0.1 to 10 μm. When the nanoparticles were examined by TEM (Fig. 14.3B and C), nanopores were reveled in the core of the particles that facilitate diffusion through the pores.

14.4.5 Catalytic polymerization of olefins

Metal oxide catalyst plays an important role in the catalytic polymerization of olefins. Phillips catalyst has been recognized has one of the world's most important industrial catalysts for the last 50 years. Phillips catalyst, a chromium oxide supported on silica gel, is employed for the production of high-density polyethylene

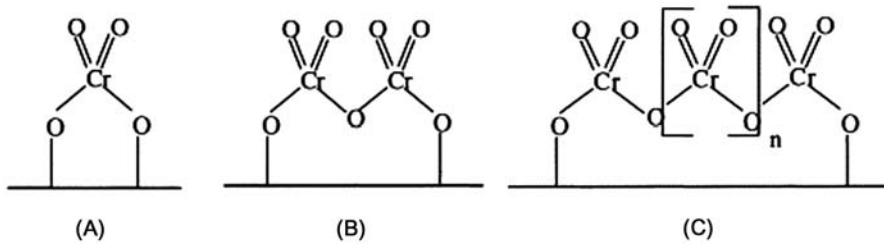

Figure 14.4 Plausible structures of surface-stabilized hexavalent chromate species [Cr(VI) $O_{x,surf}$] on silica surface of the Phillips CrO_x/SiO_2 catalyst ($n \geq 1$) (A) Chromate specie, (B) Dichromate specie, and (C) Cluster formation.
Source: Reproduced with permission from B. Liu, M. Terano, Investigation of the physicochemical state and aggregation mechanism of surface Cr species on a Phillips CrO_x/SiO_2 catalyst by XPS and EPMA, J. Mol. Catal. A: Chem. 172 (2001) 227−240 [67]. ©2001 Elsevier.

(HDPE), the most commonly used synthetic polymer. The Phillips catalyst dominates the market of some specific HDPE applications, for instance pipe, plastic blow molding, and geomembrane films.

Traditionally, Phillips catalyst is composed of hexavalent chromium ions highly dispersed on the surface of amorphous silica [66]. The catalyst is activated at temperatures higher than 600°C in an oxidizing atmosphere before performing any polymerization reaction. The activation requires to be finely controlled to avoid the Cr_2O_3 formation. During thermal activation, chromium oxidized to Cr(VI) that readily reacts with hydroxyl groups on the surface layer of the support (Fig. 14.4).

The activation procedure has a prevailing influence in the structure and composition of the prepared catalyst. The amount of hydroxyl groups available and the activity of the catalyst will influence the properties of the polymer-like molecular weight, polydispersity, melt index, and size of the chain [68]. For example, the more dehydrated the catalyst became the lower the molecular weight of the polymer produced. The support also plays an important role in the catalyst activity and modeling the properties of the polymer produced. For instance, adding titanium as a promoter has a tendency to enlarge the molecular weight (M_w) distribution, with the opposite effect adding silica with fluorine [69].

The support of preference in the olefin polymerization is silicon oxide that has a tendency to fracture during the growing chain of the polymer creating new active sites, promoting the ethylene polymerization [70] and bulk CrO_3 from decomposing even at temperatures higher than 1000°C [67]. Fig. 14.5 represents the SEM micrographs of chromium supported on silica aerogel. The silica particles retain a cubic form even after supporting the active metal with some wear off due to repetitive calcination steps [71].

Other supports that find application on the polymer industry are silica−alumina, silica−titania, aluminophosphates, aluminum sulfates, and various types of doped silicas.

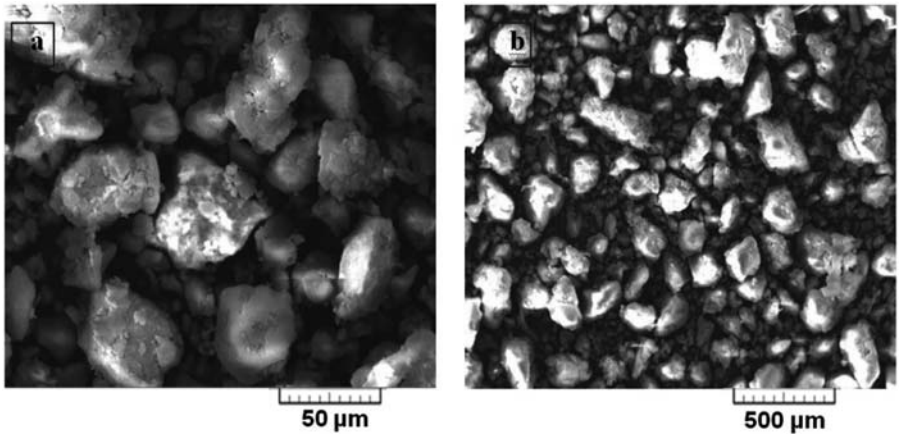

Figure 14.5 SEM micrographs of Cr/silica aerogel: (A) 50 and (B) 500 μm.
Source: Reproduced with permission from E. Ahmadi, Z. Mohamadnia, S. Rahimi, M.H. Armanmehr, M.H. Heydari, M. Razmjoo, Phillips catalysts synthesized over various silica supports: characterization and their catalytic evaluation in ethylene polymerization, Polyolefins J. 3 (2016) 23−36 [71].

Further improvements of the Phillips CrO_x/SiO_2 catalysts are desired for the industry to but still remained as a challenge. The polymerization mechanism and the active sits are still poorly understood, as the great majority of spectroscopic studies was conducted in model systems and undercontrol conditions different from industrial processes. Recently, new studies are starting to focus in situ research of Phillips catalyst mimicking industrial conditions employing techniques such as in situ diffuse reflectance IR Fourier transform spectroscopy [72−74] to name one, but more research is needed to fully understand the properties of the active chromium sites [75].

14.5 Summary

Powder oxides play an essential role in vital technological processes in the past and will continue in the future. At the same time, the understanding of the role of the metal oxide in the catalyzed reaction and the factors and mechanism of catalyst deactivation is essential knowledge to optimize the processes. In many cases the rapid development of the industrial process precedes the full understanding of the intrinsic of the reaction. The use of new characterization tools and the research focus on the understanding of processes will help to advance the knowledge of the metal powders as catalytic agents.

References

[1] D.W. Lee, B.R. Yoo, Advanced metal oxide (supported) catalysts: synthesis and applications, J. Ind. Eng. Chem. 20 (2014) 3947–3959.

[2] L. Lloyd, Handbook of Industrial Catalysts, Springer Science & Business Media, 2011.

[3] J.L.G. Fierro, Metal Oxides: Chemistry and Applications, CRC Press, 2005.

[4] A. Bogicevic, D. Jennison, Effect of oxide vacancies on metal island nucleation, Surf. Sci. 515 (2002) L481–L486.

[5] B. Delmon, Dynamic processes in active phase-support interactions, J. Mol. Catal. 59 (1990) 179–206.

[6] S. Campisi, C. Chan-Thaw, A. Villa, Understanding heteroatom-mediated metal–support interactions in functionalized carbons: a perspective review, Appl. Sci. 8 (2018) 1159.

[7] C. Copéret, F. Allouche, K.W. Chan, M.P. Conley, M.F. Delley, A. Fedorov, et al., Bridging the gap between industrial and well-defined supported catalysts, Angew. Chem. Int. Ed. 57 (2018) 6398–6440.

[8] S.J. Tauster, S.C. Fung, R.T. Baker, J.A. Horsley, Strong interactions in supported-metal catalysts, Science 211 (1981) 1121–1125.

[9] S. Tauster, S. Fung, R.L. Garten, Strong metal-support interactions. Group 8 noble metals supported on titanium dioxide, J. Am. Chem. Soc. 100 (1978) 170–175.

[10] S. Shaikhutdinov, Strong metal–support interaction and reactivity of ultrathin oxide films, Catal. Lett. 148 (2018) 2627–2635.

[11] J. Schumann, M. Eichelbaum, T. Lunkenbein, N. Thomas, M.C. Alvarez Galvan, R. Schlögl, et al., Promoting strong metal support interaction: doping ZnO for enhanced activity of Cu/ZnO: M (M = Al, Ga, Mg) catalysts, ACS Catal. 5 (2015) 3260–3270.

[12] J. Liu, Advanced electron microscopy of metal–support interactions in supported metal catalysts, ChemCatChem 3 (2011) 934–948.

[13] G.A. Olah, A. Goeppert, G.S. Prakash, Beyond Oil and Gas: The Methanol Economy, John Wiley & Sons, 2018.

[14] J. Mol, Industrial applications of olefin metathesis, J. Mol. Catal. A: Chem. 213 (2004) 39–45.

[15] S. Jackson, G. Kelly, G. Webb, Supported metal catalysts; preparation, characterisation, and function: Part VI. Hydrogenolysis of ethane, propane, *n*-butane and iso-butane over supported platinum catalysts, J. Catal. 176 (1998) 225–234.

[16] B.K. Vu, M.B. Song, I.Y. Ahn, Y. Suh, D.J. Suh, J.S. Kim, et al., Location and structure of coke generated over Pt–Sn/Al_2O_3 in propane dehydrogenation, J. Ind. Eng. Chem. 17 (2011) 71–76.

[17] M. McDaniel, Supported chromium catalysts for ethylene polymerization, Advances in Catalysis, Elsevier, 1985, pp. 47–98.

[18] J. Chandorkar, S. Umbarkar, C. Rode, V. Kotwal, M. Dongare, Synthesis of tinidazole by condensation–oxidation sequence using MoO_3/SiO_2 bifunctional catalyst, Catal. Commun. 8 (2007) 1550–1555.

[19] G. Busca, L. Lietti, G. Ramis, F. Berti, Chemical and mechanistic aspects of the selective catalytic reduction of NO_x by ammonia over oxide catalysts: a review, Appl. Catal. B: Environ. 18 (1998) 1–36.

[20] K. Aasberg-Petersen, I. Dybkjær, C. Ovesen, N. Schjødt, J. Sehested, S. Thomsen, Natural gas to synthesis gas−catalysts and catalytic processes, J. Nat. Gas Sci. Eng. 3 (2011) 423−459.
[21] S. Loridant, Raman spectroscopy of nanomaterials: applications to heterogeneous catalysis, Characterization of Nanomaterials, Elsevier, 2018, pp. 37−59.
[22] G. Deo, I.E. Wachs, Predicting molecular structures of surface metal oxide species on oxide supports under ambient conditions, J. Phys. Chem. 95 (1991) 5889−5895.
[23] J. Strunk, M.A. Bañares, I.E. Wachs, Vibrational spectroscopy of oxide overlayers, Top. Catal. 60 (2017) 1577−1617.
[24] D. Nitsche, C. Hess, Structure of isolated vanadia and titania: a deep UV Raman, UV−vis, and IR spectroscopic study, J. Phys. Chem. C 120 (2016) 1025−1037.
[25] F. Zaera, New advances in the use of infrared absorption spectroscopy for the characterization of heterogeneous catalytic reactions, Chem. Soc. Rev. 43 (2014) 7624−7663.
[26] B.L. Mojet, S.D. Ebbesen, L. Lefferts, Light at the interface: the potential of attenuated total reflection infrared spectroscopy for understanding heterogeneous catalysis in water, Chem. Soc. Rev. 39 (2010) 4643−4655.
[27] X. Gao, I.E. Wachs, Investigation of surface structures of supported vanadium oxide catalysts by UV−vis−NIR diffuse reflectance spectroscopy, J. Phys. Chem. B 104 (2000) 1261−1268.
[28] T. Fu, Y. Wang, A.M. Wernbacher, R. Schlögl, A. Trunschke, Single-site vanadyl species isolated within molybdenum oxide monolayers in propane oxidation, ACS Catal. 9 (2019).
[29] H. Eckert, I.E. Wachs, Solid-state vanadium-51 NMR structural studies on supported vanadium (V) oxide catalysts: vanadium oxide surface layers on alumina and titania supports, J. Phys. Chem. 93 (1989) 6796−6805.
[30] P.G. Kompio, A. Brückner, F. Hipler, O. Manoylova, G. Auer, G. Mestl, et al., V_2O_5-WO_3/TiO_2 catalysts under thermal stress: responses of structure and catalytic behavior in the selective catalytic reduction of NO by NH_3, Appl. Catal. B: Environ. 217 (2017) 365−377.
[31] M.T. Dunstan, D.M. Halat, M.L. Tate, I.R. Evans, C.P. Grey, Variable-temperature multinuclear solid-state NMR study of oxide ion dynamics in fluorite-type bismuth vanadate and phosphate solid electrolytes, Chem. Mater. 31 (2019).
[32] T. Tanaka, H. Yamashita, R. Tsuchitani, T. Funabiki, S. Yoshida, X-ray absorption (EXAFS/XANES) study of supported vanadium oxide catalysts. Structure of surface vanadium oxide species on silica and γ-alumina at a low level of vanadium loading, J. Chem. Soc., Faraday Trans. 1 84 (1988) 2987−2999.
[33] A.A. Guda, S.A. Guda, K.A. Lomachenko, M.A. Soldatov, I.A. Pankin, A.V. Soldatov, et al., Quantitative structural determination of active sites from in situ and operando XANES spectra: from standard ab initio simulations to chemometric and machine learning approaches, Catal. Today 336 (2018).
[34] M. Guerrero-Pérez, R. López-Medina, E. Rojas-Garcia, M. Bañares, XANES study of the dynamic states of V-based oxide catalysts under partial oxidation reaction conditions, Catal. Today 336 (2017).
[35] G. Ertl, H. Knözinger, J. Weitkamp, Preparation of Solid Catalysts, Wiley-VCH, Weinheim, New York, 1999.
[36] J. Regalbuto, Catalyst preparation, Sci. Eng. 1 (2007).

[37] S. McCaugherty, A.P. Grosvenor, Low-temperature synthesis of $CaZrTi_2O_7$ zirconolite-type materials using ceramic, coprecipitation, and sol−gel methods, J. Mater. Chem. C 7 (2019) 177−187.
[38] P. Sudarsanam, L. Katta, G. Thrimurthulu, B.M. Reddy, Vapor phase synthesis of cyclopentanone over nanostructured ceria−zirconia solid solution catalysts, J. Ind. Eng. Chem. 19 (2013) 1517−1524.
[39] S.S. Prasanna, K. Balaji, S. Pandey, S. Rana, Metal oxide based nanomaterials and their polymer nanocomposites, Nanomaterials and Polymer Nanocomposites, Elsevier, 2019, pp. 123−144.
[40] S. Maiti, D. Das, K. Pal, J. Llorca, L. Soler, S. Colussi, et al., Methanol steam reforming behavior of sol-gel synthesized nanodimensional $Cu_xFe_{1-x}Al_2O_4$ hercynites, Appl. Catal. A: Gen. 570 (2019) 73−83.
[41] P. Hu, T. Chang, W. Chen, J. Deng, S. Li, Y. Zuo, et al., Temperature effects on magnetic properties of Fe_3O_4 nanoparticles synthesized by the sol-gel explosion-assisted method, J. Alloys Compd. 773 (2019) 605−611.
[42] M. Titirici, M. Antonietti, A. Thomas, A generalized synthesis of metal oxide hollow spheres using a hydrothermal approach, Chem. Mater. 18 (2006) 3808−3812.
[43] R. Caillat, J. Cuer, J. Elston, F. Juillet, R. Pointud, M. Prettre, et al., Preparation of uniformly dispersed oxides in the hydrogen-oxygen flame, and some properties of these compounds, Bull. Soc. Chim. Fr. (1959) 152−156.
[44] P.G. Vergnon, H.B. Landouisi, Formation of ultrafine Fe_2O_3 aerosols from a flame supported reaction, Ind. Eng. Chem. Prod. Res. Dev. 19 (1980) 147−151.
[45] Z. Le-Tian, X. Wen-Fa, W. Yuan-Da, X. Hua, L. Ai-Wu, Z. Wei, et al., Thermal annealing of SiO_2 fabricated by flame hydrolysis deposition, Chin. Phys. Lett. 20 (2003) 1366.
[46] B. Hannebauer, F. Menzel, The combustion of $SiCl_4$ in hot O_2/H_2 flames, Z. Anorg. Allg. Chem. 629 (2003) 1485−1490.
[47] A.V. Soares, M.F. Portela, A. Kiennemann, L. Hilaire, J. Millet, Iron molybdate catalysts for methanol to formaldehyde oxidation: effects of Mo excess on catalytic behaviour, Appl. Catal. A: Gen. 206 (2001) 221−229.
[48] M.P. House, M.D. Shannon, M. Bowker, Surface segregation in iron molybdate catalysts, Catal. Lett. 122 (2008) 210−213.
[49] C. Brookes, M. Bowker, E.K. Gibson, D. Gianolio, K.M. Mohammed, S. Parry, et al., In situ spectroscopic investigations of MoO_x/Fe_2O_3 catalysts for the selective oxidation of methanol, Catal. Sci. Technol. 6 (2016) 722−730.
[50] M. Bowker, M. House, A. Alshehri, C. Brookes, E.K. Gibson, P.P. Wells, Selectivity determinants for dual function catalysts: applied to methanol selective oxidation on iron molybdate, Catal. Struct. React. 1 (2015) 95−100.
[51] M. Sun-Kou, S. Mendioroz, J. Fierro, J. Palacios, A. Guerrero-Ruiz, Influence of the preparation method on the behaviour of Fe-Mo catalysts for the oxidation of methanol, J. Mater. Sci. 30 (1995) 496−503.
[52] J.H. Baik, S.D. Yim, I. Nam, Y.S. Mok, J. Lee, B.K. Cho, et al., Control of NO_x emissions from diesel engine by selective catalytic reduction (SCR) with urea, Top. Catal. 30 (2004) 37−41.
[53] J. Schobing, V. Tschamber, J. Brilhac, A. Auclaire, Y. Hohl, Simultaneous soot combustion and NO_x reduction over a vanadia-based selective catalytic reduction catalyst, C.R. Chim. 21 (2018) 221−231.

[54] G. Chinchen, K. Mansfield, M. Spencer, The methanol synthesis: how does it work? Chemtech 20 (1990) 692−699.
[55] G.A. Olah, A. Goeppert, G.S. Prakash, Chemical recycling of carbon dioxide to methanol and dimethyl ether: from greenhouse gas to renewable, environmentally carbon neutral fuels and synthetic hydrocarbons, J. Org. Chem. 74 (2008) 487−498.
[56] G. Ertl, H. Knözinger, F. Schüth, J. Weitkamp, Online Handbook of Heterogeneous Catalysis, Wiley-VCH Verlag GmbH& Co, Germany, 2008.
[57] G. Prieto, J. Zečević, H. Friedrich, K.P. De Jong, P.E. De Jongh, Towards stable catalysts by controlling collective properties of supported metal nanoparticles, Nat. Mater. 12 (2013) 34.
[58] M.B. Fichtl, D. Schlereth, N. Jacobsen, I. Kasatkin, J. Schumann, M. Behrens, et al., Kinetics of deactivation on $Cu/ZnO/Al_2O_3$ methanol synthesis catalysts, Angew. Chem. 502 (2015) 262−270.
[59] J. Mol, Metathesis of functionalized acyclic olefins, J. Mol. Catal. 65 (1991) 145−162.
[60] S. Lwin, I.E. Wachs, Olefin metathesis by supported metal oxide catalysts, ACS Catal. 4 (2014) 2505−2520.
[61] K.J. Ivin, J.C. Mol, Olefin Metathesis and Metathesis Polymerization, Elsevier, 1997.
[62] S. Vorakitkanvasin, S.K.N. Ayudhya, K. Suriye, P. Praserthdam, J. Panpranot, Enhanced metathesis activity of low loading Re_2O_7/Al_2O_3 catalysts for propylene production by using aluminum nitrate as Al_2O_3 precursor, Appl. Catal. A: Gen. 517 (2016) 39−46.
[63] T. Oikawa, T. Ookoshi, T. Tanaka, T. Yamamoto, M. Onaka, A new heterogeneous olefin metathesis catalyst composed of rhenium oxide and mesoporous alumina, Microporous Mesoporous Mater. 74 (2004) 93−103.
[64] D.P. Debecker, M. Stoyanova, U. Rodemerck, E.M. Gaigneaux, Preparation of $MoO_3/SiO_2−Al_2O_3$ metathesis catalysts via wet impregnation with different Mo precursors, J. Mol. Catal. A: Chem. 340 (2011) 65−76.
[65] S. Maksasithorn, P. Praserthdam, K. Suriye, D.P. Debecker, Preparation of supermicroporous $WO_3−SiO_2$ olefin metathesis catalysts by the aerosol-assisted sol−gel process, Microporous Mesoporous Mater. 213 (2015) 125−133.
[66] M.P. McDaniel, The Phillips process for ethylene polymerization, in: G. Ertl, H. Knozinger, J. Weitkamp (Eds.), Handbook of Heterogeneous Catalysis, VCH-Wiley, Weinheim, Germany, 1997, pp. 2400−2405.
[67] B. Liu, M. Terano, Investigation of the physico-chemical state and aggregation mechanism of surface Cr species on a Phillips CrO_x/SiO_2 catalyst by XPS and EPMA, J. Mol. Catal. A: Chem. 172 (2001) 227−240.
[68] M. McDaniel, Manipulating polymerization chemistry of Cr/silica catalysts through calcination, Appl. Catal. A: Gen. 542 (2017) 392−410.
[69] M.P. McDaniel, A review of the Phillips supported chromium catalyst and its commercial use for ethylene polymerization, Advances in Catalysis, Elsevier, 2010, pp. 123−606.
[70] M.P. McDaniel, Fracturing silica-based catalysts during ethylene polymerization, J. Polym. Sci.: Polym. Chem. Ed. 19 (1981) 1967−1976.
[71] E. Ahmadi, Z. Mohamadnia, S. Rahimi, M.H. Armanmehr, M.H. Heydari, M. Razmjoo, Phillips catalysts synthesized over various silica supports: characterization and their catalytic evaluation in ethylene polymerization, Polyolefins J. 3 (2016) 23−36.

[72] D. Cicmil, J. Meeuwissen, A. Vantomme, B.M. Weckhuysen, Real-time analysis of a working triethylaluminium-modified Cr/Ti/SiO_2 ethylene polymerization catalyst with in situ infrared spectroscopy, ChemCatChem 8 (2016) 1937–1944.
[73] D. Cicmil, J. Meeuwissen, A. Vantomme, J. Wang, I.K. van Ravenhorst, H.E. van der Bij, et al., Polyethylene with reverse co-monomer incorporation: from an industrial serendipitous discovery to fundamental understanding, Angew. Chem. 127 (2015) 13265–13271.
[74] C. Barzan, A. Piovano, L. Braglia, G.A. Martino, C. Lamberti, S. Bordiga, et al., Ligands make the difference! Molecular insights into CrVI/SiO_2 Phillips catalyst during ethylene polymerization, J. Am. Chem. Soc. 139 (2017) 17064–17073.
[75] E. Groppo, G.A. Martino, A. Piovano, C. Barzan, The active sites in the Phillips catalysts: origins of a lively debate and a vision for the future, ACS Catal. 8 (2018) 10846–10863.

This page intentionally left blank

Metal oxide for heavy metal detection and removal

15

Nurhaswani Alias[1], Siti Azlina Rosli[1], Nurliyana Abu Hasan Sazalli[1], Haslinda Abdul Hamid[1,2], Sarasijah Arivalakan[1], Siti Nur Hanisah Umar[3], Beh Khi Khim[4], Bibi Nadia Taib[4], Yeoh Kar Keat[1], Khairunisak Abdul Razak[1], Yeoh Fei Yee[1], Zuhailawati Hussain[1], Elmi Abu Bakar[3], Noor Fazreena Kamaruddin[3], Asrulnizam Abd. Manaf[4], Naoki Uchiyama[5], Tan Wai Kian[6], Atsunori Matsuda[6], Go Kawamura[7], Kazuaki Sawada[7], Akihiko Matsumoto[8] and Zainovia Lockman[1]

[1]School of Materials and Mineral Resources, Universiti Sains Malaysia, George Town, Malaysia, [2]Faculty of Applied Sciences, Universiti Teknologi MARA, Permatang Pauh, Malaysia, [3]School of Aerospace Engineering, Universiti Sains Malaysia, George Town, Malaysia, [4]Collabrative Microelectronic Design Excellence Centre (CEDEC), Universiti Sains Malaysia, George Town, Malaysia, [5]Department of Mechanical Engineering, Toyohashi University of Technology, Toyohashi, Japan, [6]Center for International Education, Toyohashi University of Technology, Toyohashi, Japan, [7]Department of Electrical and Electronic Information Engineering, Toyohashi University of Technology, Toyohashi, Japan, [8]Department of Applied Chemistry and Life Science, Toyohashi University of Technology, Toyohashi, Japan

15.1 Introduction

The term "heavy metal" refers to metallic elements and metalloids having an atomic density greater than 5 g/cm^3. Lead (Pb), cadmium (Cd), zinc (Zn), mercury (Hg), arsenic (As), and chromium (Cr) are examples of heavy metals that are known to be extremely toxic even at low concentrations since they cannot be degraded or destroyed. Indeed, heavy metal ions can bioaccumulate in plants and animals when exposed to a polluted environment, especially in the aquatic environment [1]. The ions can also be transferred to humans through the consumption of these contaminated plants and animals, which can ultimately lead to bioaccumulation in humans [2]. Moreover, children are susceptible and are affected more by the toxicity of heavy metal ions compared to adults. The higher dose of heavy metal ions among children can lead to organ damage and can promote neurotoxicity, which may, in turn, cause behavioral disorders to eventuate (refer to Table 15.1). For example, the consumption of lead can lead to learning problems, impaired growth, and neuropsychological development in children.

Notwithstanding, some heavy metals such as Cr (hexavalent Cr) and Cd are carcinogenic [3]. Therefore by acknowledging the hazard posed by heavy metal ions,

Metal Oxide Powder Technologies. DOI: https://doi.org/10.1016/B978-0-12-817505-7.00015-4

Table 15.1 The list, sources, and guide line value of hazardous heavy metal [1,3].

Heavy metals	Limit value (mg/L)	Toxicity	Sources
As	0.01	Causes skin damage, cancer, neurobehavior sickness	Coloring agent in textile, wall paper, and toy-making industry
Cd	0.003	Kidney damage, cancer, and obstructive lung disease	Electroplating industry, battery
Cr	0.05	Diarrhea, skin and mucous membrane irritation, bronchopulmonary effects and systemic effects involving kidney, liver, gastrointestinal tract, and circulatory system	Electroplating, leather tanning, and textile industry
Cu	2	Liver damage, insomnia	Sewage effluent, fertilizers, and pesticide
Ni	0.07	Nausea, chronic asthma, and cancer	Electroplating, printing, silver refineries, battery-manufacturing industry
Zn	–	Depression, stomach cramps, nausea, and vomiting	Electroplating, smelting, and ore processing, as well as, acid mine drainage, effluents from chemical processes and discharge of untreated domestic sewage
Pb	2	Effect circulatory and nervous system, impaired growth in children, and induce learning disabilities	Plastic, paint, pipe, steel, lead–acid batteries, and gasoline
Hg	0.006	Rheumatoid arthritis, effect circulatory, and nervous system	Thermometer, electrical properties

it is crucial to investigate how to detect and remove heavy metal ions from the environment. Table 15.1 displays examples of the various sources of heavy metals pollution. As can be seen in the table, the primary source originates from industrial activities, possibly from those establishments that have inadequate or improper wastewater monitoring and treatment facilities. Monitoring can be achieved by providing portable sensors that can measure heavy metal concentrations in real time. Incorporating nanostructured metal oxide into such sensors can also lead to substantial improvement in the performance of the sensors, particularly regarding their sensitivity, selectivity, and detection capabilities. Portable sensors can also be used to measure the concentration of heavy metals in situ at the point of discharge. Hence,

heavy metals released into the environment can be appropriately monitored and controlled. In addition, biosensors, which also utilize metal oxide, can be used for more sensitive detection capabilities. In biosensors, small molecules, proteins, or enzymes can be integrated with metal oxide membrane or film to selectively bind with the heavy metal ions for detection. Accordingly, sensitive yet-portable instruments are indeed desirable for real-time measurement and continuous analysis, monitoring, and control of heavy metal ions in wastewater.

Removal, on the other hand, can also benefit from the use of metal oxide powders. Metal oxides are known to be suitable absorbent materials and some oxides can not only absorb but can also reduce certain heavy metal ions to their more benign counterparts. As for the former, clay-based material, this material has been used for decades to absorb heavy metal ions, whereas, for the latter, recent advances in nanostructured metal oxides have exposed possibilities of removing the extremely small concentrations of heavy metal ions from aqueous systems. This chapter begins by describing the distribution of heavy metal ions in Malaysia, followed by describing how oxide can be used to either detect or remove heavy metal ions from polluted industrial wastewater.

15.2 Distribution of heavy metal in Malaysia

Water is essential for all living organisms. A 95% of water used for consumption in Malaysia originates from inland river systems and hence keeping the river water clean is essential. In Malaysia, the Department of Environment Malaysia (DOE) is responsible for monitoring the water quality of rivers. Water quality is classified into three categories: clean, slightly polluted, and polluted. Rivers are further classified into Class I, II, III, IV, or V based on the water quality index (WQI) and the Interim National Water Quality Standards (NWQSs) for Malaysia. Class I represents the cleanest water and used for drinking water following treatment, while Class V is the worst (only suitable for navigation). The WQI is based on six main parameters; biochemical oxygen demand (BOD), chemical oxygen demand, ammoniacal nitrogen (NH_3N), pH, dissolved oxygen, and suspended solids (SS) [4]. According to the report published by the DOE in 2017, in Malaysia of 474 river systems, 216 (46%) were classified as clean rivers, 207 (43%) were slightly polluted, and 51 (11%) were polluted [5].

Table 15.2 displays the trace of heavy metal ions in the water collected in Peninsular Malaysia. As compared to the NWQS, heavy metals traced in the Jejawi and Juru Rivers exceeded the permissible levels (except for the zinc concentration). This observation is aligned with the annual report issued by the DOE [5], where both the Juru and Jejawi Rivers are labeled as heavily polluted rivers [5]. The source of pollutants may originate from nearby manufacturing industries such as electroplating, pulp and paper, textiles, and food facilities. The concentrations of As, Fe, Mn, and Ni found in the Kepayang River were considerable and, therefore,

Table 15.2 Heavy metal concentration in water collected in Peninsular Malaysia.

Location	Heavy metal concentration (mg/L)										Sources	Reference
	As	Cd	Cr	Cu	Fe	Hg	Mn	Ni	Pb	Zn		
Jejawi River, Penang	3.44	0.14	0.20	0.05	–	0.01	–	–	0.25	0.05	Rubber, pulp, paper, electroplating, and metal industrial	[6]
Juru River, Penang	3.38	0.17	0.12	0.05	–	0.02	–	–	0.31	0.09	Rubber, pulp, paper, electroplating, and metal industrial	[6]
Muda River, Penang	–	0.001	0.003	0.004	0.549	–	–	–	0.017	–	Industrial area	[7]
Jarak River, Penang	–	0.002	0.003	0.005	0.011	–	–	0.03	0.034	0.028	Industrial area	[7]
Kerian River, Penang	–	0.001	0.002	0.006	0.321	–	–	–	0.052	0.004	Industrial area	[7]
Kongsi River, Penang	–	0.001	0.002	0.005	0.018	–	–	–	0.007	0.002	Industrial area	[7]
Kepayang River, Perak	0.288	0.001	–	0.102	5.679	–	4.673	0.106	0.001	0.057	Tin mining	[8]
Selangor River, Selangor	0.0295	0.0004	0.0038	0.0094	1.734	–	0.093	0.0012	0.0039	0.0854	Industrial, tin-mining	[9]
Klang Valley, Selangor	0.056	0.012	–	–	–	–	0.281	–	0.006	–	Ex-mining	[10]
Klang River Basin, Selangor	0.076	0	0	0.0016	0.312	0	–	0.0022	0	0.0013	Household, industrial agriculture, and chemical discharges	[11]
Langat River Basin, Selangor	0.0035	0.0001	0.005	0.0035	0.264	0.002	–	0.0053	0.0002	0.0264	Household, industrial agriculture, and chemical discharges	[11]
Kuala Lipis, Pahang	–	–	–	0.0038	0.5183	–	0.2957	–	–	0.0053	Iron-mining	[12]
Bukit Ibam, Pahang	–	0.0013	–	0.011	0.0628	–	0.3715	–	0.005	0.1778	Ex-iron-mining	[12]
NWQS for Malaysia	0.05	0.01	0.05	0.02	1	0.001	0.1	0.05	0.05	5		[5]

NWQS, National Water Quality Standard.

this river has been reported as slightly polluted by the DOE [5]. This result could be due to the nearby mining industry [12,13].

Aside from water pollution, surface sediments have also become the main reservoir for hosting heavy metal pollutants [14]. The concentration of heavy metals found in sediment collected in Peninsular Malaysia is summarized in Table 15.3. As shown in the table, most contaminated sites of heavy metals are around mining areas such as in the Kepayang River region, Kuala Lipis, Bukit Ibam, and Pengerang. As mentioned earlier, humans can be exposed to heavy metal contamination through the consumption of contaminated water and/or aquatic foods. The latter is typically through the consumption of seafood; fish, mussels, and cockles [20,21]. Table 15.4 shows the concentration of heavy metals found in freshwater and marine fish muscles collected in Peninsular Malaysia. Among all, tilapia has been reported to have the highest accumulation of As (3.4 mg/kg), Cu (4.1 mg/kg), Zn (23.6 mg/kg), and Fe (100 mg/kg), whereas Mn (1.74 mg/kg) and Pb (12.44 mg/kg) are high in mackerel and Cd in yellow stripe scad (0.66 mg/kg). Notably, the red snapper has the highest Cr and Ni concentrations, with 4.205 and 1.587 mg/kg, respectively.

From the distribution of the heavy metal data in water, sediment, and fish (Tables 15.2–15.4) collected in Malaysia, it can be concluded that rather high concentration levels of heavy metal ions can be correlated to industrial activities near the area. Although the contamination is not as severe, given it falls within the permissible limit. However, as mentioned, heavy metal ions can bioaccumulate and hence monitoring and removing them entirely from the surrounding sources is essential.

15.3 Heavy metal detection

The most acceptable method in determining heavy metal concentrations in industrial wastewater is via “grab” sampling, followed by laboratory analysis. Several analytical techniques have been used for quantification purposes, as shown in Table 15.5 [28,29]. Although the listed instruments have the capability to detect heavy metals, the required analysis is often time-consuming, needs skilled and trained personnel, and is not suitable for on-site analysis. Moreover, there have been numerous attempts made to develop portable sensors for monitoring heavy metals from the point of discharge. For this purpose, electrochemical (EC) and biological sensors have gained significant interest and are the most promising for heavy metal detection. Both types of sensors often incorporate nanostructured metal oxides in the form of thin-film, nanoparticles, nanorods, or nanowires.

15.3.1 Electrochemical technique for detection of heavy metal

The EC technique for heavy metal removal is seen as one of the most preferred methods because of its high detection sensitivity, low-cost instrumentation, and its

Table 15.3 Heavy metal concentration in sediment collected in Peninsular Malaysia.

Location	Heavy metal concentration (mg/kg)									Sources	Reference
	As	Cd	Cr	Cu	Fe	Mn	Ni	Pb	Zn		
Juru	–	1.24	–	65.39	–	–	29.25	29.97	442.19	Industrial area	[15]
Langat River Estuary	–	–	13.80	–	–	–	42.13	20.12	22.34	Shipping, industrial effluent, agriculture, commercial activities	[16]
Segantang Garam, Kedah	–	1.25	–	34.79	–	–	13.11	27.78	60.83	Jetty, aquaculture, paddy field	[15]
Kepayang River	1038.1	0.48	7.4	94.48	14,526.73	289.34	19.91	149.34	39.78	Tin mining	[8]
Kuala Lipis	24	0.28	8.06	110	107,700	2359.23	2.93	56	105	Iron-mining	[12]
Bukit Ibam	287.38	0.04	4.935	1548.25	135,262.50	3756.13	3.91	731.13	1607	Ex-iron-mining	[12]
Bernam River	–	0.62	14.90	–	315	–	5.30	–	–	Agriculture, automobile	[17]
Puluh River, Klang	–	1.37	–	35.48	–	–	26.42	34.22	256.50	Jetty-receiving domestic waste. Industrial area	[15]
Bagan Lalang, Selangor	–	0.6	–	12.76	–	–	10.09	8.46	75.38	Recreation, agricultural	[15]
Sri Serdang Pond	–	0.42	–	24.73	36,633	–	3.70	22.75	24	Domestic waste	[18]

Lake Chini	–	1.68	6.22	11.16	–	–	–	–	53.01	Tourism, fishing	[19]
Langat River Basin	–	0.53	21.03	–	283	–	7.84	–	–	Industrial	[17]
Pengerang	2.49	0.11	6.49	15.73	22,824.24	124.4	–	34.14	20.54	Bauxite-mining	[13]
Tiga River, Johor	–	1.4	–	13.9	–	–	11.89	28.28	117.38	Jetty, agricultural, oil plantation	[15]
Minyak Beku, Johor	–	1.65	–	37.64	–	–	21.18	53.73	241.87	Jetty-receiving domestic waste, shipping	[15]
Canadian Council of Ministers of Environment (2001)	5.9	0.6	37.3	35.7	–	–	18	35	123		[12]

Table 15.4 Heavy metal concentration in freshwater and marine fish (muscle) in Peninsular Malaysia.

Fish species	Location	Heavy metal concentration (mg/kg) dry weight									Sources	Reference
		As	Cd	Cr	Cu	Fe	Mn	Ni	Pb	Zn		
Demersal fish												
Barramundi (*Lates calcarifer*: siakap)	Pulau Ketam	1.69	0.01	0.62	0.50	5.10	0.20	0.12	0.17	6.50	Fishery, tourism, Klang River	[22]
Red snapper (*Lutjanus campechanus*: merah)	Pulau Ketam	1.79	0.01	4.21	0.53	19.99	0.65	1.59	0.39	5.57		
Gray snapper (*Lutjanus griseus*)	Pulau Ketam	0.46	0.01	1.25	0.55	11.16	0.41	0.61	0.23	5.79		
Belanger's (*Johnius belangerii*: gelama panjang)	Kapar	–	0.06	–	0.66	–	0.54	–	–	18.27	Coal electric power station, agriculture industrialization, and urbanization	[23]
	Mersing	–	0.04	–	0.95	–	0.97	–	–	13.12	Ship and boat	
Pelagic fish												
Indo-Pacific tarpon (*Megalops cyprinoides*: bulan-bulan)	Simpang Empat, Pulau Pinang	–	0.004	0.22	0.07	3.13	0.003	0	0.23	1.35	Bukit Minyak industrial area	[24]

Torpedo scad (*Megalaspis cordyla*: cincaru)	Port Dickson	–	0.05	–	1.4	–	–	–	–	–	Tourism, shipping, oil tankers, refineries	[25]
	Terengganu coastal	–	0.31	–	1.16	66.72	1.36	–	0.02	10.42	Zn-galvanic industries, battery production	[26]
Mackerel (*Rastrelliger*: kembung)	Terengganu coastal	–	0.25	–	0.57	66.15	1.74	–	0.73	9.39	Zn-galvanic industries, battery production	
	Port Dickson	–	0.09	1.16	2.15	–	–	–	12.44	–	Tourism, shipping, oil tankers, refineries	[25]
Yellowstripe scad (*Selaroides leptolepis: pelata kuning*)	Terengganu coastal	–	0.66	–	0.68	61.05	0.87	–	0.14	11.28	Zn-galvanic industries, battery production	
	Port Dickson	–	0.07	2.34	2.46	–	–	–	10.18	–	Tourism, shipping, oil tankers, refineries	[25]
Fringescale sardinella (*Sardinella fimbriata*: tambansisik)	Port Dickson	–	0.1	1.42	3.21	–	–	–	8.34	–	Tourism, shipping, oil tankers, refineries	[25]
Freshwater												
Asian redtail catfish (*Hemibagrus nemurus*: baung)	Kelantan River basin	–	0.02	–	–	–	–	0.06	0.10	–	Chemical fertilizer, sand mining	[27]
	Kelantan River basin	–	0.03	–	–	–	–	0.09	0.06	–	Chemical fertilizer, sand mining	[27]
	Galas River, Kelantan	–	–	–	0.03	–	0.01	0.06	0.01	0.14		[20]

(*Continued*)

Table 15.4 (Continued)

Fish species	Location	Heavy metal concentration (mg/kg) dry weight									Sources	Reference
		As	Cd	Cr	Cu	Fe	Mn	Ni	Pb	Zn		
Catfish (*Clarias striatus*: keli)	Simpang Empat, Pulau Pinang	–	0.004	0.4	0.07	4.42	0.1	0.03	0.51	1.8	Bukit Minyak industrial area	[24]
	Langat River Basin	2.16	0.01	1.6	0.87	100	–	0.13	0.06	20.26	Household, industrial, and agricultural chemical discharges	[11]
	Kelantan River basin	–	0.01	–	–	–	–	0.06	0.08	–	Chemical fertilizer, sand mining	[27]
Silver Barb (*Barbonymus gonionotus*: lampam jawa)	Simpang Empat, Pulau Pinang	–	0.005	0.44	0.1	–	0.17	0.04	0.46	2.23	Bukit Minyak industrial area	[24]
	Kelantan River basin	–	0.05	–	–	–	–	0.06	0.07	–	Chemical fertilizer, sand mining	[27]
	Kelantan River basin	–	0.03	–	–	–	–	0.1	0.1	–	Chemical fertilizer, sand mining	[27]
	Galas River, Kelantan	–	–	–	0.02	–	0.01	0.07	0.01	0.31	–	[20]

Tilapia (*Oreochromis mossambicus*)	Simpang Empat, Pulau Pinang	–	0.004	0.6	0.2	24.34	0.83	0.01	0.72	2.9	Bukit Minyak industrial area	[24]
	Langat River Basin	0.8	0.01	1.42	0.73	100	–	0.1	0.05	5.8	Household, industrial, and agricultural chemical discharges	[11]
	Klang River Basin	3.4	0	0.2	4.1	41.6	–	0.12	0.4	23.6	Household, industrial, and agricultural chemical discharges	[11]
	Beranang Mining Pool, Kelantan	–	0.02	–	0.03	–	–	–	0.05	0.43	Mining	[20]
Bronze featherback (*Notopterus notopterus*: belida)	Simpang Empat, Pulau Pinang	–	0.004	0.6	0.08	6.35	0.3	0.08	0.5	2.63	Bukit Minyak industrial area	[24]
	Kelantan River basin	–	0.03	–	–	–	–	0.18	0.08	–	Chemical fertilizer, sand mining	[27]
Malaysian Food Act 1983		1	1	1	30	–	–	–	2	100		

Table 15.5 Comparison between the common heavy metal detection techniques.

Equipment	Description	Advantages	Disadvantages	Sample limitation
ICP-MS	• Combination of mass spectrometer with high temperature ICP source • ICP source transforms the elements' atoms in the sample into ions. These ions are detached and identified by the mass spectrometer • Measures an atom's mass by MS	• Wide elemental coverage with excellent sensitivity • Excellent low detection limit for most elements • Simple spectra • Isotopic analysis • Large linear dynamic working range	• Small linear range • Incapability to handle sample with high level of salt contain	• Samples must be diluted in acid before analysis to dissolve the element of interest
ICP-OES	• Uses an emission spectrum to identify and quantify the existing elements in the sample • The characteristic of constituent elements can be obviously recognized by the emission lines • Quantitation is based on measurement of excited atoms and ions at the wavelength features for the specific elements being measured	• Has higher tolerance for total dissolved solid than ICP-MS	• Relatively poor limit of detection • Many spectral interferences	• No isotope analysis

IC	• Technique of separation and determination of trace metals • Useful to measure concentration of cations and anions	• Can analyze nonmetals such as ion fluoride and chloride • Detects and analyzes multiple samples concurrently	• Causes lots of chemical waste, long run times, can be interferences from sample matrix	• Soil, sediment, and geological sample preparation is more complex
NAA	• During the reactions, the number of rapid gamma rays released from the sample is proportional to the amount of elements	• Nondestructive method for identifying and quantitating trace elements	• Expensive and required a nuclear reactor	• Cannot accomplish analysis on the certain elements such as carbon and oxygen
AAS	• Uses flame and furnace spectroscopy for trace metal analysis • Comprises the light absorption of elements concentration by a radiation source such as lamp • A monochromator is used to select only one wavelength elements of the determined element, while detector measures amount of elements absorption	• High selectivity and sensitivity • Low spectral interference • No sample preparation required	• Interference can occur from sample matrix • Can run only one element at a time	• Most AAS practices are more focused on liquid analysis than solids. This is because before it can be analyzed, the substance has to be vaporized

(*Continued*)

Table 15.5 (Continued)

Equipment	Description	Advantages	Disadvantages	Sample limitation
XRF	• X-rays as main excitation source frequently provided by X-ray tubes or radioisotope which initiated sample's elements emit secondary X-ray of wavelength properties • The elements in the sample are characterized by the emitted X-ray wavelength and the X-ray intensity provides the concentrations of elements	• One of the best elemental analysis in all kinds of samples such as liquid, solid, and loose powder • Minimal or no sample preparation	• Expensive because requires laboratory analysis for semiquantitative analysis	• No isotope analysis
AFS	• The spectroscopic process is based on the absorption by an atomic vapor of certain radiation wavelength with subsequent deactivation of the detector's excited atoms	• Low spectral interference • High selectivity	• Not all compounds fluorescence	• Contamination of sample can reduce the fluorescence and give incorrect result

AAS, Atomic Absorption Spectrometry; *AFS*, atomic fluorescence spectrometry; *IC*, ion chromatography; *ICP-MS*, inductively coupled plasma mass spectroscopy; *ICP-OES*, inductively coupled plasma optical emission spectrometry; *NAA*, neutron activation analysis; *XRF*, X-ray fluorescence spectrometry.

Table 15.6 Nanoparticle-modified electrodes with their limit of detection.

Modified electrode	Electrolyte	pH	Analyte	Limit of detection	Sensitivity (μA/μM)	Technique	Real sample	Reference
GO/$[Ru(bpy)_3]^{2+}$/Au	Citrate buffer	5.0	As(III)	2.30 nM	23.6	DPV	Cauvery river and tap water	[39]
			Cd(II)	2.80 nM	17.51			
			Hg(II)	1.60 nM	31.43			
			Pb(II)	1.41 nM	34.74			
Bi/Fe_2O_3 NPs/G/GCE	Acetate buffer	4.5	Cd(II)	0.08 μg/L	–	DPASV	Tap water	[36]
			Pb(II)	0.07 μg/L				
			Zn(II)	0.11 μg/L				
Fe_3O_4 NPs/TA/GCE	Acetate buffer	5.0	Cd(II)	0.2 μM	12.15	SWASV	Yamuna river water	[40]
			Hg(II)	0.3 μM	13.81			
			Pb(II)	0.04 μM	8.56			
SnO_2/rGO/GCE	NaAc/HAc buffer	5.0	Cd(II)	0.1015 nM	18.4	SWASV	–	[38]
			Cu(II)	0.2269 nM	14.98			
			Hg(II)	0.2789 nM	28.2			
			Pb(II)	0.1839 nM	18.6			
ZnO/rGO/GCE	NaAc/HAc buffer	5.0	Cd(II)	0.04 μM	–	SWASV	–	[37]
			Cu(II)	0.03 μM				
			Hg(II)	0.06 μM				
			Pb(II)	0.03 μM				
AuNPs/SPCE	Britton–Robinson buffer	7.0	Cu(II)	1.4 ng/L	3.52	SWASV	Tap water	[41]
			Pb(II)	2.1 ng/L	5.94			
Bi/MWCNT–EBP–NA/GCE	Acetate buffer	5.5	Cd(II)	0.06 μg/L	–	SWASV	Soil	[32]
			Pb(II)	0.08 μg/L				
BiNPs/ITO	Acetate buffer	4.5	Pb(II)	2.5 μg/L	–	DPASV	–	[33]
3D G/BiNPs film/GCE	NaAc/HAc buffer	5.0	Cd(II)	0.05 μg/L	–	SWASV	Lake and tap water	[34]
			Pb(II)	0.02 μg/L				

Au, gold; *Bi*, bismuth; *DPASV*, differential pulse anodic stripping voltammetry; *DPV*, differential pulse voltammetry; *EBP*, emeraldine base polyaniline; *G*, graphene; *GCE*, glassy carbon electrode; *GO*, graphene oxide; *ITO*, indium tin oxide; *MWCNT*, multiwalled carbon nanotube; *NA*, Nafion; *NaAc/HAc*, sodium acetate–acetic acid; *NPs*, nanoparticles; *rGO*, reduced graphene oxide; *SPCE*, screen printed carbon electrode; *SWASV*, square wave anodic stripping voltammetry; *TA*, terephthalic acid.

ability to accurately detect heavy metal ions [30]. Among the various EC techniques, the anodic stripping voltammetry (ASV) method is the most reported for heavy metal ions detection. This technique is performed in combination with pulse voltammetry (PV) techniques such as differential pulse ASV and square wave ASV (SWASV). Moreover, they are performed using three electrodes: a working electrode, a reference electrode, and a counter electrode. This method is carried out by supplying potential current and measuring the current produced at the working electrode. The working electrode plays a crucial role in the EC cell as the redox reaction occurs at the interface between the working electrode and the electrolyte (analyte ions). Therefore the selection of material for the working electrode is paramount for a redox reaction to occur.

Previously, mercury was used as the working electrode. Even though mercury has significant advantages concerning sensitivity, it is highly toxic. Hence, bismuth (Bi) was introduced by researchers to replace mercury given Bi is more environment-friendly and less toxic [31–34]. Electrodes made of gold and silver have also been investigated for their suitability as a sensor for heavy metal detection [35]. Recently, working electrodes have been modified with nanomaterials, especially metal oxide such as hematite (Fe_2O_3) [36], zinc oxide (ZnO) [37], and tin oxide (SnO_2) [38], in order to enhance the detection limit and selectivity of the electrode for heavy metal ion detection as shown in Table 15.6.

Fig. 15.1 displays an illustration in modifying a commercial working electrode with nanostructure materials such as nanoparticles and nanoflakes. These nanostructures enable fast electron transfer at the working electron that enhances both the sensitivity and specificity of detection. As shown in the table, the SWASV technique is the most widely used method for heavy metal detection, given it has a

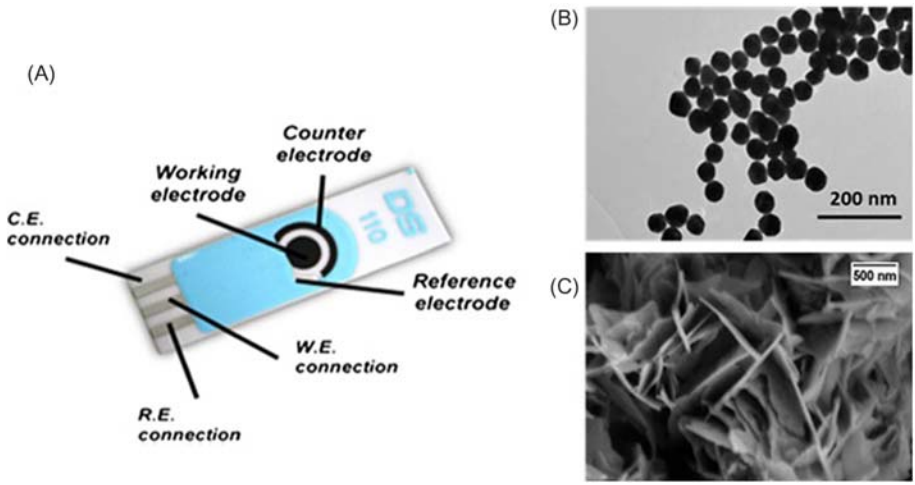

Figure 15.1 Typical electrochemical electrode: (A) commercial screen printed electrode by DropSens, (B) nanoparticles for working electrode modification, and (C) oxide nanoflakes for working electrode modification.

faster potential scan rate compared to differential PV [42]. As such, utilizing such sensors will allow for the detection of heavy metal ions in real-time situations as well the benefit of their portability, thereby enabling analysts to perform accurate measurements at any point of discharge.

15.3.2 Biosensor

Biosensors such as EC, optical, and electrical have also been developed for the detection of heavy metal ions in contaminated water [43]. Aptamer-based biosensors are fast becoming popular, given their precise detection capability and defined three-dimensional structures. Aptamers are oligonucleotide (ssDNA or ssRNA) or peptide molecules of size less than 25 kDa [44]. Moreover, they can detect specific target molecules with high affinity and specificity [45]. EC biosensors are of significant interest in the detection of heavy metal ions given their advantages; high sensitivity, rapid detection, miniature in size, easy to handle, and low cost [46]. EC biosensors are constructed using two or three electrodes as an EC cell, which can then transfer a biological event as an EC signal [47]. Typically, EC biosensors will generate a measurable current (amperometric/voltammetric detection); measurable potential or charge accumulation (potentiometric detection); measurable potential or charge accumulation (amperometric/voltammetric detection); measurable potential or charge accumulation (potentiometric detection); measurable conductive properties of a medium (conductometric detection) between the electrodes [46]; or a measurable impedance (impedimetric detection) [48]. The detection limit of a peptide aptamer−based EC sensor for heavy metal ions detection is shown in Table 15.7.

Furthermore, optical biosensors comprise sensors that can capture signals of ultraviolet (UV), visible, and infrared radiations from a chemical/biological/physical reaction or event and transform them into a different energy form. Optical biosensors are classified as colorimetric, fluorimetric, bioluminescence-based, chemiluminescence-based, and surface plasmon resonance-based sensors, based on the light source [59]. These optical biosensors are commonly used in heavy metal detection with the limit of detection (LOD) in the nanomolar range [60,61]. On the other hand, the ion sensitive field-effect transistor (FET) was created to measure ionic in-fluxes and ex-fluxes at nerve membranes [62]. FET biosensors are one of the electrical sensors and are easy to construct, given their compatibility with complementary metal-oxide semiconductor technology. However, only a few FET biosensors have been produced for heavy metal detection as most FET biosensors are used to detect protein, DNA, and viruses. In the detection of heavy metals, peptide aptamer−based single-walled carbon nanotube FETs have provided LOD in the picomolar range [63], and DNA aptamer−based graphene FET results in the nanomolar range [64]. Moreover, silicon nanowire FETs have recently attracted significant attention as a promising instrument in biosensor design due to their ultrasensitivity, selectivity, are label-free, and given their real-time detection capabilities [65]. However, FET biosensors have disadvantages, because the sensitivity is lost when samples have a high ionic concentration as it shortens the Debye length [66]. Consequently, several strategies have been proposed to address the limitation

Table 15.7 Peptide aptamer−based electrochemical sensor for heavy metal detection.

Modified electrode	Electrolyte	pH	Analyte	Redox active indicator	Limit of detection	Sensitivity	Technique	Real sample	Reference
Au(Fc-GSH)/Cd^{2+}	PBS buffer	7.0	Cd(II)	Fc	0.1 nM	–	CV	Water	[49]
Au/MPA−GSH/Cd^{2+}	Ammonium acetate and MES buffer	7.0 and 6.8	Cd(II)	–	5 nM	–	OSWV	Water	[50]
Au/MPA−HSQKVF/Cd^{2+}	Ammonium acetate and MES buffer	7.0 and 6.8	Cd(II)	–	0.9 nM	–	OSWV	Water	[51]
Au/MWCNT/dipeptide/Cd^{2+}	Borate buffer	3.0	Cd(II)	–	27.49 nM	6×10^{-6} A/ppm	CV	Waste water	[52]
Au/MPA−angiotensin/Pb^{2+} Au/TA−angiotensin/Pb^{2+}	Ammonium acetate buffer	7.0	Pb(II)	–	1 nM 1.9 nM	–	OSWV	Lake Bedford, Sydney Park, Australia	[51]
Au/PTAA/TNTLSNN/Pb^{2+}	Ammonium acetate buffer	3.5	Pb(II)	–	1 nM	–	CV, SWV	Han River, Seoul	[53]
Au/CTNTLSNNC (−S−S−)/Pb^{2+}	Ammonium acetate and MES buffer	3.5 and 6.8	Pb(II)	–	1 nM	–	SWV	Tap water	[54]
Au/MPA−HFHAHFAF/Hg^{2+}	Na_2SO_4 and MES buffer	7.0 and 5.5	Hg(II)	–	9.5 nM	5×10^{-7} A/μM	CV	Waste water	[55]
Au/MWCNT/dipeptide/Hg^{2+}	Acetate buffer	2.0	Hg(II)	–	0.9068 nM	8×10^{-7} A/ppm	CV	Waste water	[52]
Au/MT/Hg^{2+}	Tris buffer	7.4	Hg(II)	–	80 nM	–	CSDPV	–	[56]
Pt/CNTs/leucine/Nafion/As^{3+}	Citrate buffer	5.0	As(III)	–	1.67 nM	20.7 μA μM	CV	Waste water	[57]
Carbon/MT/As^{3+}	Tris buffer	7.4	As(III)	–	370 nM	–	CV, ASV	–	[58]

ASV, Anodic stripping voltammetry; *Au*, gold; *CSDPV*, cathodic stripping differential pulse voltammetry; *CTNTLSNNC*, Cys−Thr−Asn−Thr−Leu−Ser−Asn−Asn−Cys; *CV*, cyclic voltammetry; *Fc*, ferrocene; *Fc-GSH*, ferrocenyl glutathione; *HFHAHFAF*, His−Phe−His−Ala−His−Phe−Ala−Phe; *HSQKVF*, His-Ser-Gln-Lys-Val-Phe; *MES*, *N*-morpholino-ethanesulfonic acid; *MPA*, 3-mercaptopropionic acid; *MT*, metallothioneins; *MWCNT*, multiwalled carbon nanotube; *OSWV*, Osteryoung square wave voltammetry; *PBS*, phosphate buffered saline; *Pt*, platinum; *PTAA*, poly thiophene acetic acid; *SWV*, square wave voltammetry; *TA*, thioctic acid; *TNTLSNN*, heptapeptide; *Tris*, tris-hydroxymethyl-aminomethane.

of FETs in higher ionic strength solutions or to gain adequate sensitivity to enable detection by merely diluting the sample [67]. One alternative strategy has been proposed to explore different nanoelectronic configurations of the sensing elements and measurement modes. Utilizing memristive biosensor is one strategy.

Accordingly, the initial concept of the memristor was introduced in 1971 by Chua [68]. Following this theoretical prediction, many researchers have since explored the memristive biosensor. Moreover, there are several device configurations that can be employed with metal oxide as the resistive membrane. Among the metal oxides, titanium oxide (TiO_2) has been commonly employed due to its robustness and functional properties such as good memristance behavior. Nevertheless, several other transition metal oxides such as ZnO and tantalum (V) oxide have also been explored. A sketch of a typical memristor biosensor utilizing Pt/TiO_2/conducting glass [In SnO_2 (ITO)] configuration is shown in Fig. 15.2. This type of biosensor has a high potential to be used in heavy metal detection once the surface modification is undertaken whereby sensitive-to-heavy metal ions are incorporated into the TiO_2 layer.

Nonetheless, there have been numerous attempts to develop portable sensors for monitoring heavy metals in industrial wastewater. The development of metal oxide nanomaterials for small, portable sensor devices is advantageous for in situ analytical monitoring techniques with continuous analysis of industrial wastewaters. Likewise, the incorporation of metal oxide nanostructures into the sensors enhances

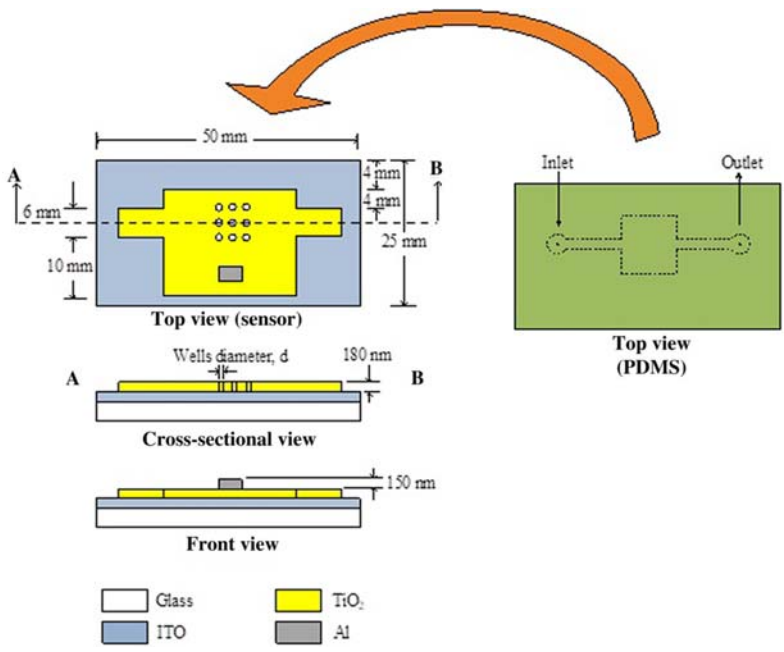

Figure 15.2 A proposed memristor biosensor structure for detection of metal ions.

the performance of the devices. Moreover, biomolecules have been integrated with a metal oxide to selectively bind heavy metals for molecular recognition probes.

15.4 Heavy metal ions removal

As mentioned earlier in this chapter, heavy metal pollution in wastewater is a significant issue that needs urgent attention in resolving. Without doubt, heavy metal pollutions from industrial wastewater can severely impact the water quality and are harmful to the environment and aquatic life but most importantly, the health of local communities. In the previous section, several metal oxide−based sensors have been suggested as probable portable devices to monitor heavy metal ions from the point of discharge in real-time situations. Frequently, in industrial facilities having wastewater laden with heavy metals needs to be subjected to treatment to ensure that the impurities are reduced to legal limits before discharging into the environment.

Generally, conventional water treatment processes consist of several steps. The initial step is the primary treatment, which is undertaken in order to separate solids and greases from the wastewater. Then, a biological treatment (secondary treatment) process is performed to eliminate the dissolved organic material. At this stage, BOD, total SS, and a small amount of nitrogen, phosphorus, and heavy metals are removed. Finally, the tertiary treatment process is conducted to further improve the quality of the effluent obtained from the primary and secondary treatment processes. At this stage the dissolved heavy metal ions are normally treated. The methods for the removal of heavy metal ions are listed in Table 15.8, highlighting the advantages and disadvantages of each technique. Powder oxide is often used as an adsorbent or photocatalyst. However, not all heavy metals can be removed via these processes and are often a mixture of techniques being used since the nature of wastewater is complex.

Metal oxides have surface properties that allow excellent ions absorption in an aqueous system. Further, some oxides have semiconducting properties enabling them to absorb and reduce heavy metal ions to their more benign counterparts. Metal oxides such as Fe_2O_3 or maghemite (Fe_3O_4) have been used as an adsorbent, whereas TiO_2 and zirconia oxide (ZrO_2) have been used as both adsorbent and photocatalyst where specific metal ions can be adsorbed and reduced on their surfaces under light irradiation [85−87]. More traditional oxides such as montmorillonite, bentonite, and kaolinite are also known to be effective adsorbent materials as discussed in the next section.

15.4.1 Adsorption method

The adsorption method is perceived as a flexible, simple, and easy method to employ compared to other technologies for heavy metal wastewater treatment [69,88]. Generally, there are two types of adsorption mechanisms: physical and

Table 15.8 Comparison between various methods for heavy metal treatment in wastewater.

Method	Advantage	Disadvantage	Reference
Adsorption	• Sorbent like clay is abundant • Low cost • Ease of condition for operating • Can be used to remove high concentration of heavy metal ions	• Low selectivity • Production of waste products • Limited tolerant for pH range • Performance depends on the type of adsorbent • Efficiency depends on production of waste products	[69]
Ion exchange	• High removal efficiency • Regeneration of the sorbent • Reduction of chemical or biological sludge	• Requires regeneration of ion exchange resin • High operating cost • Requires difference in affinity of ions in resin and ions to be removed	[70]
Chemical precipitation	• High concentration of heavy metal ions can be removed • Simple operation • Low capital cost	• Leads to further pollution due to large amount of chemicals usage in order to reduce metal ions to an acceptable limit for discharge • Mix metal is difficult to remove	[71]
Photocatalysis	• Near-complete heavy metal ions removal • Can use nanostructured metal oxide for higher reactivity and near-complete removal • Can also achieve 100% reduction/ removal efficient on certain nanostructured metal oxide surfaces or modified metal oxide surface (e.g., coupled with graphene)	• Only possible with minute/low concentration heavy metal ions • Not all heavy metal ions can be reduced; knowledge in thermodynamics is needed • Only as final polishing step • Requires light as to promote catalytic processes on the surface of the oxide	[72–74]

(*Continued*)

Table 15.8 (Continued)

	• Ease of operation	• pH-dependent process • Mix metal ions are also difficult to be treated	
Forward osmosis	• High efficiency in removing heavy metals • Low energy process • Low fouling rate • Satisfactory for pure water permeation	• Still in infancy stage • Requires higher flux rates • Prone to ineffective membranes and reverse solute leakage	[75–78]
Electroflotation	• Can operate efficiently for very dilute solutions • Popular for its adaptability and simplicity in design and operation • Low running costs	• Must be combined with electrocoagulation for higher removal efficiency	[79–81]
Electrocoagulation	• Simple and productive technology • Environment-friendly technique because it uses electrons as reagents which are clean	• Possibility of sludge generation • High chemical utilization	[79,82]
Membrane filtration	• High efficiency • Reuse of water, salts, and heat • Simple technique	• High operational cost due to membrane fouling • Generation of sludge • Depends on the size of the membrane	[83,84]
Electrochemical	• Fast process • Requires fewer chemicals in the system • Less sludge produced	• Large chemical investment • Expensive method • Chemical used can introduce another sort of pollution	[84]

chemical. Physical adsorption is a process in which binding of adsorbate on the adsorbent surface is caused by van der Waals forces of attraction. Here, the electronic structure of the atom or molecule is hardly disturbed upon physical adsorption. van der Waals forces originate from the interactions between induced, permanent, or transient electric dipoles. Although physical adsorption can only be observed in the low-temperature environments, and under appropriate conditions in

which gas-phase molecules form multilayer adsorption. Commercial adsorbents utilize physical adsorption for its surface binding.

Moreover, chemical adsorption involves a chemical reaction between the adsorbent and the adsorbate. The intense interaction between the adsorbate and the substrate surface creates new types of electronic bonds. The adsorbate can also form a monolayer that is utilized in catalytic operations. Three steps are involved during the adsorption process: (1) transport of the pollutant from the bulk solution to the sorbent surface, (2) adsorption on the active site of the particle surface, and (3) transport within the sorbent particle [2]. The efficiency of the adsorption method is notably influenced by the surface area, pore size distribution, functional group, and the polarity of the absorbent [88]. However, cost-effective natural adsorbent is usually preferred.

Notwithstanding, various types of adsorbents have been highlighted for the adsorption process in which they are used to remove selected heavy metals, as shown in Table 15.9. Many studies have been conducted investigating the removal of various heavy metal ions employing natural clays. Nevertheless, for comparison, cellulose, cellulose acetate, and activated carbon are included in the table.

15.4.2 Photocatalyst

Photocatalysis is a promising technique for a simple, clean, and effective treatment of organic pollutants and heavy metal ions. Photocatalysts are often used to oxidize or reduce hazardous pollutants. Examples of oxide semiconductor photocatalysts are TiO_2 [106−110], ZrO_2 [74,87], niobium pentoxide (Nb_2O_5) [111−113], and copper oxide (CuO) [114,115]. Moreover, oxide semiconductors have favorable electronic structures that are characterized by a filled valence band (VB) and an empty conduction band (CB) having excellent light absorption properties for electrons/holes generation on their surfaces [2]. When light energy [equivalent or greater than the semiconductor bandgap (E_g)] is illuminated on the oxide semiconductor, electron/hole pairs are formed in the CB and VB of the oxide, respectively. The reduction can occur when electrons are transferred from the CB to adsorb the heavy metal ions. The reduction process, however, must be accompanied by an oxidation process where holes in the valance band are expected to oxidize water (Fig. 15.3). Table 15.10 shows an example of metal oxide used for heavy metal removal from water/wastewater.

Nevertheless, not all metal ions can be reduced by oxide photocatalysts. Wahyuni et al. [123] investigated the capability of TiO_2 to remove Cu(II), Cd(II), Cr(VI), and Pb(II) under UV irradiation. Here, Cr(VI) was shown to be mostly removed (75%), followed by Cu(II) (45%), Pb(II) (40%), and Cd(II) (18%). Therefore this indicates that Cr(VI) can be reduced effectively but not Cd(II). The effective removal of Cr(VI) from contaminated solution was also investigated by Bashirom et al. [106] where almost 99.8% of Cr(VI) was removed within 120 minutes on nanostructure TiO_2. The removal of Cr(VI) is said to be via reduction to Cr (III) on the surface of the oxide. Unlike Cr(VI), Cr(III) is benign and can be easily removed via precipitation in the treated water [109]. In this case, it appears that the

Table 15.9 Adsorption rate of different materials on specific heavy metal.

Adsorbent	Adsorption rate (mg/g)					Reference
	Cu	Cd	Hg	Ni	Zn	
Cellulose acetate			258.75			[89]
Activated carbon			40.12			[90]
Modified cellulose		83.60				[91]
Zeolite	23.25	10.87			12.85	[92]
Ball clay		27.27				[93]
Montmorillonite		6.30				[94]
Montmorillonite					154.60	[95]
Kaolinite		41.84				[96]
Kaolinite	10.78					[97]
Kaolinite				2.10		[98]
Kaolinite					4.95	[99]
Bentonite		11.20				[94]
Bentonite				92.59		[100]
Bentonite					68.49	[101]
Cellulose − chitosan composite	65.80					[102]
Natural clay	44.84					[103]
Cellulose/ZrO_2				79.00		[104]
Chitosan					75.00	[105]

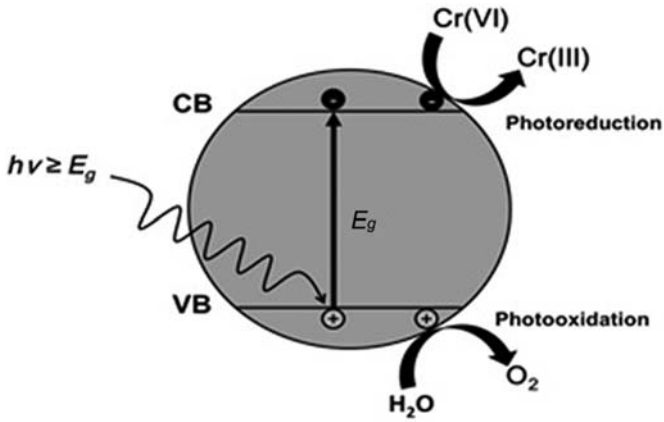

Figure 15.3 Schematic diagram of photocatalytic process.

reduction process on the oxide photocatalysts is pH-dependent [124]. The optimum photocatalytic performance of TiO_2 for Cr(VI) removal is at pH 2 [125], Cu(III) at pH 2−3.5 [123], and Hg(II) at pH 4−4.1 [126], which is related to the point-zero-charge of the oxide and thus causing the ability of the oxide to absorb the metal ions.

Table 15.10 Metal oxide for heavy metal removal from water/wastewater.

Type of metal oxide	Target metal	Light sources	Catalyst dosage (g/L)	C^0 (μg/L)	pH	Time (min)	Hole scavenger	Description	Reference
TiO_2	Zn(II), Cd(II), Pb (II), Ni(II)		0.01, 0.1, or 0.5	500	8	120	–	• Nanoparticles were able to simultaneously remove multiple metals (Zn, Cd, Pb, Ni, and Cu)	[116]
TiO_2 hollow sphere	Cr(VI)	UV	0.03	5	2.82–4.92	120	–	• Photoreduction of Cr(VI) at pH 2.82 is 96% for TiO_2 with a size of 450 nm	[117]
TiO_2	Cr(VI)	Sunlight	2	20	2.2	120	Tartaric acid	• Photoreduction of Cr(VI) is 100% in the presence of tartaric acid as scavenger compared to without scavenger (33% after 180 min)	[118]
Nb_2O_5/carbon fiber	Cr(VI)	UV	0.05	100		60	Oxalic acid	• Photoreduction of Cr(VI) is 99.9% and no significant decrease in photocatalytic performance after 10 repeated cycles	[119]
Nb_2O_5/CuO	Cr(VI)	UV and visible	0.01	50	6	210	–	• 10% CuO on Nb_2O_5 provided the best photoreduction activity, with 84% reduction of Cr (VI)	[114]
Nb_2O_5 nanorods	Cr(VI)	UV	0.1	100–150	2–12	50–60	Oxalate acid	• Photoreduction of Cr(VI) is 94.5% [Cr(VI) concentration of 100 ppm] and 90% [Cr(VI) concentration 150 ppm] after photoreaction for 50 and 60 min, respectively	[120]
rGO-modified ZnO nanorod	Cu(II) and Co(II) ions	Visible	20	100	2–10	180	–	• Adsorption efficiency Cu(II) increases from 9.7% to 96.9% and Co(II) increases from 11.7% to 90.1% with pH variation (2–10) • rGO	[121]
TiO_2/ ZnO–CaAlg	Cu(II)	UV	1	10–80	3–9	120	–	• Removal of Cu, ranging from 7.14 to 62.0 ppm (first cycle). Bare CaAlg was only able to remove 6.9–48 ppm of similar initial Cu concentrations • The highest removal of Cu(II) at 98.9%, which was obtained at pH ~ 7 • CaAlg	[122]

CaAlg, Calcium alginate; *rGO*, reduced graphene oxide; *UV*, ultraviolet.

Moreover, hole scavengers such as phenol, methanol, formic acid, salicylic acid, and citric acid are often added to enhance the photocatalytic reaction [127,128]. For instance, a study by Wang et al. [129] revealed the increase of the reduction rate for Cr(VI) in the presence of scavenger in the following order: citric acid ($0.02439\ \text{minute}^{-1}$) > salicylic acid ($0.01267\ \text{minute}^{-1}$) > phenol ($0.0087\ \text{minute}^{-1}$) > blank ($0.00598\ \text{minute}^{-1}$). The function of scavenger is to suppress charge recombination, thus leading to the improvement of the photo reduction.

15.5 Conclusion

Increasing heavy metal concentrations in water, soil, and aquatic life, as shown in this chapter, cause damage, not only to the environment but also to human health and animals. Therefore environmental regulations should be more stringent to improve the quality of treated effluent that has been discharged into the river systems in Malaysia from various industries. Heavy metal detection and wastewater treatment should be more focused on resolving these issues. Along with the development of heavy metal detection technologies, the concentration of heavy metals in the environment can be detected more readily, easier, conveniently, and efficiently. The EC method and using portable biosensors are the most common methods to detect heavy metals. However, it is important to note that some criteria used for detection such as high sensitivity, rapid detection, easy to handle, and affordability are usually highlighted as the most suitable methods. Most of these aspects also used for the selection of heavy metal treatment, since treatment performance and operational costs have become the primary factor in protecting the environment. Therefore all factors should be considered in order to determine the most suitable treatment to eliminate the majority of heavy metals in the environment.

15.6 Acknowledgments

Heavy Metal Mitigation project is supported by USM-Research University Grant for Toyohashi University of Technology, Japan-USM Collaboration; 1001/PBAHAN/870048, 1001/PBAHAN/870049, 1001/PCEDEC/870050, and 1001/PBAHAN/870051. On the other hand, author acknowledges the financial support of the USM Fellowship Scheme, Universiti Sains Malaysia.

References

[1] S. Mishra, R.N. Bharagava, N. More, A. Yadav, S. Zainith, S. Mani, et al., Heavy metal contamination: an alarming threat to environment and human health, in: R.C. Sobti, N. K. Arora, R. Kothari (Eds.), Environmental Biotechnology: For Sustainable Future, Springer, Singapore, 2019, pp. 103–125.

[2] M. Barakat, New trends in removing heavy metals from industrial wastewater, Arabian J. Chem. 4 (4) (2011) 361–377.
[3] P.B. Tchounwou, C.G. Yedjou, A.K. Patlolla, D.J. Sutton, Heavy metal toxicity and the environment, *Molecular, Clinical and Environmental Toxicology*, Springer, 2012, pp. 133–164.
[4] N.W. Chan, Managing urban rivers and water quality in Malaysia for sustainable water resources, Int. J. Water Resour. Dev. 28 (2) (2012) 343–354.
[5] DOE Malaysia, Environmental Quality Report 2017, 2017, p. 128.
[6] A.F.M. Alkarkhi, A. Ahmad, N. Ismail, A.M. Easa, Multivariate analysis of heavy metals concentrations in river estuary, Environ. Monit. Assess. 143 (2008) 179–186.
[7] M.S. Alsaffar, M. Suhaimi Jaafar, N. Ahmad Kabir, Evaluation of heavy metals in surface water of major rivers in Penang, Malaysia, Int. J. Environ. Sci. 6 (2016) 657–669.
[8] F.A. Affandi, M.Y. Ishak, Heavy metal concentrations in tin mine effluents in Kepayang River, Perak, Malaysia, J. Phys. Sci. 29 (2018) 81–86.
[9] F. Othman, M.S.U. Chowdhury, W.Z. Wan Jaafar, E.M.M. Faresh, S.M. Shirazi, Assessing risk and sources of heavy metals in a tropical river basin: a case study of the Selangor River, Malaysia, Pol. J. Environ. Stud. 27 (2018) 1659–1672.
[10] I.B. Koki, K.H. Low, H. Juahir, M. Abdul Zali, A. Azid, S.M. Zain, Consumption of water from ex-mining ponds in Klang Valley and Melaka, Malaysia: a health risk study, Chemosphere 195 (2018) 641–652.
[11] W.C. Poon, G. Herath, A. Sarker, T. Masuda, R. Kada, River and fish pollution in Malaysia: a green ergonomics perspective, Appl. Ergon. 57 (2016) 80–93.
[12] Z. Madzin, F.M. Kusin, F.M. Yusof, S.N. Muhammad, Assessment of water quality index and heavy metal contamination in active and abandoned iron ore mining sites in Pahang, Malaysia, MATEC Web Conf. 103 (2017) 05010.
[13] F.M. Kusin, N.N.M. Azani, S.N.M.S. Hasan, N.A. Sulong, Distribution of heavy metals and metalloid in surface sediments of heavily-mined area for bauxite ore in Pengerang, Malaysia and associated risk assessment, Catena 165 (2018) 454–464.
[14] S. Khodami, M. Surif, W.M. Wo, R. Daryanabard, Assessment of heavy metal pollution in surface sediments of the Bayan Lepas area, Penang, Malaysia, Mar. Pollut. Bull. 114 (2016) 615–622.
[15] T. R. i Buhari, A. Ismail, Heavy metals pollution and ecological risk assessment in surface sediments of west coast of Peninsular Malaysia, Int. J. Environ. Sci. Dev. 7 (2016) 750–756.
[16] N.F. Mokhtar, A.Z. Aris, S.M. Praveena, Preliminary study of heavy metal (Zn, Pb, Cr, Ni) contaminations in Langat River Estuary, Selangor, Procedia Environ. Sci. 30 (2015) 285–290.
[17] S.A. Kadhum, M.Y. Ishak, S.Z. Zulkifli, R. Hashim, Evaluation of the status and distributions of heavy metal pollution in surface sediments of the Langat River Basin in Selangor Malaysia, Mar. Pollut. Bull. 101 (2015) 391–396.
[18] C.K. Yap, A. Jusoh, W.J. Leong, A. Karami, G.H. Ong, Potential human health risk assessment of heavy metals via the consumption of tilapia *Oreochromis mossambicus* collected from contaminated and uncontaminated ponds, Environ. Monit. Assess. 187 (2015) 584.
[19] A.K. Ahmad, M. Shuhaimi-Othman, Heavy metal concentrations in sediments and fishes from Lake Chini, Pahang, Malaysia, J. Biol. Sci. 10 (2010) 93–100.
[20] Z.S. Baharom, M.Y. Ishak, Determination of heavy metal accumulation in fish species in Galas River, Kelantan and Beranang Mining Pool, Selangor, Procedia Environ. Sci. 30 (2015) 320–325.

[21] A.A. Idris, A.K. Ahmad, Concentration of selected heavy metals in water of the Juru River, Penang, Malaysia, Afr. J. Biotechnol. 11 (2012) 8234−8240.
[22] N. Nasyitah Sobihah, A. Ahmad Zaharin, M. Khairul Nizam, L. Ley Juen, K. Kyoung-Woong, Bioaccumulation of heavy metals in maricultured fish, *Lates calcarifer* (Barramundi), *Lutjanus campechanus* (red snapper) and *Lutjanus griseus* (grey snapper), Chemosphere 197 (2018) 318−324.
[23] F.H. Bashir, M.S. Othman, A.G. Mazlan, S.M. Rahim, K.D. Simon, Heavy metal concentration in fishes from the coastal waters of Kapar and Mersing, Malaysia, Turkish J. Fish. Aquat. Sci. 13 (2013) 8.
[24] W. Fadhullah, U. Sains, W. Fadhullah, Preliminary study of heavy metals pollution in freshwater fishes of Sungai Simpang Empat, Penang, J. Acad. 3 (2015) 48−65.
[25] S.M. Praveena, C.L.S. Lin, Assessment of heavy metal in self-caught saltwater fish from Port Dickson coastal water, Malaysia, Sains Malays. 44 (2015) 91−99.
[26] M.N.R. Rosli, S.B. Samat, M.S. Yasir, Analysis of heavy metal accumulation in fish at Terengganu coastal area, Malaysia, Sains Malays. 47 (2018) 1277−1283.
[27] R. Hashim, T.H. Song, N.Z.M. Muslim, T.P. Yen, Determination of heavy metal levels in fishes from the lower reach of the Kelantan River, Kelantan, Malaysia, Tropical Life Sci. Res. 25 (2014) 21−39.
[28] M.B. Gumpu, S. Sethuraman, U.M. Krishnan, J.B.B. Rayappan, A review on detection of heavy metal ions in water—an electrochemical approach, Sens. Actuators B: Chem. 213 (2015) 515−533.
[29] J. Sneddon, M.D. Vincent, ICP-OES and ICP-MS for the determination of metals: application to oysters, Anal. Lett. 41 (8) (2008) 1291−1303.
[30] O. Farghaly, R.A. Hameed, A.-A.H. Abu-Nawwas, Analytical application using modern electrochemical techniques, Int. J. Electrochem. Sci. 9 (1) (2014).
[31] S. Lee, S. Bong, J. Ha, M. Kwak, S.-K. Park, Y. Piao, Electrochemical deposition of bismuth on activated graphene-Nafion composite for anodic stripping voltammetric determination of trace heavy metals, Sens. Actuators B: Chem. 215 (2015) 62−69.
[32] G. Zhao, Y. Yin, H. Wang, G. Liu, Z. Wang, Sensitive stripping voltammetric determination of Cd(II) and Pb(II) by a Bi/multi-walled carbon nanotube-emeraldine base polyaniline-Nafion composite modified glassy carbon electrode, Electrochim. Acta 220 (2016) 267−275.
[33] K.A. Razak, T.J. Jian, Z.A. Zulkifli, N.M. Nor, N.S. Ridhuan, N.D. Zakaria, et al., Effect of hydrothermal reaction temperature on properties of bismuth nanoparticles and its properties as modified electrode for Pb sensors, J. Phys. Conf. Ser. 1082 (2018) 012077.
[34] L. Shi, Y. Li, X. Rong, Y. Wang, S. Ding, Facile fabrication of a novel 3D graphene framework/Bi nanoparticle film for ultrasensitive electrochemical assays of heavy metal ions, Anal. Chim. Acta 968 (2017) 21−29.
[35] Y. Bonfil, M. Brand, E. Kirowa-Eisner, Characteristics of subtractive anodic stripping voltammetry of Pb and Cd at silver and gold electrodes, Anal. Chim. Acta 464 (1) (2002) 99−114.
[36] S. Lee, J. Oh, D. Kim, Y. Piao, A sensitive electrochemical sensor using an iron oxide/graphene composite for the simultaneous detection of heavy metal ions, Talanta 160 (2016) 528−536.
[37] W. Liu, Preparation of a zinc oxide-reduced graphene oxide nanocomposite for the determination of cadmium(II), lead(II), copper(II), and mercury(II) in water, Int. J. Electrochem. Sci. 12 (2017) 5392−5403.

[38] W.J. Yi, Y. Li, G. Ran, H.Q. Luo, N.B. Li, Determination of cadmium(II) by square wave anodic stripping voltammetry using bismuth−antimony film electrode, Sens. Actuators B: Chem. 166−167 (2012) 544−548.
[39] M.B. Gumpu, M. Veerapandian, U.M. Krishnan, J.B.B. Rayappan, Simultaneous electrochemical detection of Cd(II), Pb(II), As(III) and Hg(II) ions using ruthenium(II)-textured graphene oxide nanocomposite, Talanta 162 (2017) 574−582.
[40] S. Deshmukh, G. Kandasamy, R.K. Upadhyay, G. Bhattacharya, D. Banerjee, D. Maity, et al., Terephthalic acid capped iron oxide nanoparticles for sensitive electrochemical detection of heavy metal ions in water, J. Electroanal. Chem. 788 (2017) 91−98.
[41] P. Kanyong, S. Rawlinson, J. Davis, Gold nanoparticle modified screen-printed carbon arrays for the simultaneous electrochemical analysis of lead and copper in tap water, Microchim. Acta 183 (8) (2016) 2361−2368.
[42] R.M. Town, H. Emons, J. Buffle, in: R. Cornelis, J. Caruso, H. Crews, K. Heumann (Eds.), Handbook of Elemental Speciation: Techniques and Methodology, John Wiley & Sons, Ltd, England, 2003, pp. 427−460.
[43] M. Li, H. Gou, I. Al-Ogaidi, N. Wu, Nanostructured Sensors for Detection of Heavy Metals: A Review, ACS Publications, 2013.
[44] G. Mayer, The chemical biology of aptamers, Angew. Chem. Int. Ed. 48 (15) (2009) 2672−2689.
[45] A.D. Ellington, J.W. Szostak, In vitro selection of RNA molecules that bind specific ligands, Nature 346 (6287) (1990) 818.
[46] A. Chaubey, B. Malhotra, Mediated biosensors, Biosens. Bioelectron. 17 (6-7) (2002) 441−456.
[47] Z. Zhu, H.S. Zhou, Nanoparticles (NPs) for biosensing applications: current aspects and prospects, The World Scientific Encyclopedia of Nanomedicine and Bioengineering I: Volume 1: Noble Metal Nanoparticles for Biomedical Applications, World Scientific, 2017, pp. 177−209.
[48] A. Guiseppi-Elie, L. Lingerfelt, Impedimetric detection of DNA hybridization: towards near-patient DNA diagnostics, *Immobilisation of DNA on Chips I*, Springer, 2005, pp. 161−186.
[49] L. Sun, Q. Zhao, J. Xiang, J. Shi, L. Wang, S. Hu, et al., Adsorption of NO and NH_3 over CuO/γ-Al_2O_3 catalyst by DRIFTS, J. Chem. Ind. Eng. Soc. China 2009 (2009) 444−449.
[50] E. Chow, D.B. Hibbert, J.J. Gooding, Voltammetric detection of cadmium ions at glutathione-modified gold electrodes, Analyst 130 (6) (2005) 831−837.
[51] E. Chow, D.B. Hibbert, J.J. Gooding, Electrochemical detection of lead ions via the covalent attachment of human angiotensin I to mercaptopropionic acid and thioctic acid self-assembled monolayers, Anal. Chim. Acta 543 (1−2) (2005) 167−176.
[52] N.A. Rahman, N.A. Yusof, N.A.M. Maamor, S.M.M. Noor, Development of electrochemical sensor for simultaneous determination of Cd(II) and Hg(II) ion by exploiting newly synthesized cyclic dipeptide, Int. J. Electrochem. Sci. 7 (1) (2012) 186−196.
[53] W. Su, M. Cho, J.-D. Nam, W.-S. Choe, Y. Lee, Highly sensitive electrochemical lead ion sensor harnessing peptide probe molecules on porous gold electrodes, Biosens. Bioelectron. 48 (2013) 263−269.
[54] M. Lin, M. Cho, W.S. Choe, Y. Lee, Electrochemical detection of lead ion based on a peptide modified electrode, Electroanalysis 28 (5) (2016) 998−1002.
[55] N. Daud, N.A. Yusof, T.W. Tee, Development of electrochemical sensor for detection of mercury by exploiting His-Phe-His-Ala-His-Phe-Ala-Phe modified electrode, Int. J. Electrochem. Sci. 6 (2011) 2798−2807.

[56] H. Ju, D. Leech, Electrochemical study of a metallothionein modified gold disk electrode and its action on Hg^{2+} cations, J. Electroanal. Chem. 484 (2) (2000) 150−156.
[57] N. Daud, N.A. Yusof, T.W. Tee, A.H. Abdullah, Electrochemical sensor for As(III) utilizing CNTs/leucine/Nafion modified electrode, Int. J. Electrochem. Sci. 7 (2012) 175−185.
[58] G. Irvine, S. Tan, M. Stillman, A simple metallothionein-based biosensor for enhanced detection of arsenic and mercury, Biosensors 7 (1) (2017) 14.
[59] R. Sharma, K. Ragavan, M. Thakur, K. Raghavarao, Recent advances in nanoparticle based aptasensors for food contaminants, Biosens. Bioelectron. 74 (2015) 612−627.
[60] Y. Luan, A. Lu, J. Chen, H. Fu, L. Xu, A label-free aptamer-based fluorescent assay for cadmium detection, Appl. Sci. 6 (12) (2016) 432.
[61] Y. Xiang, Y. Lu, DNA as sensors and imaging agents for metal ions, Inorg. Chem. 53 (4) (2013) 1925−1942.
[62] J. Wei, H. Yang, H. Sun, Z. Lin, S. Xia, A fully CMOS-integrated pH-ISFET interface circuit, in: 2005 Sixth International Conference on ASIC, IEEE, 2005, pp. 365−367.
[63] E.S. Forzani, X. Li, P. Zhang, N. Tao, R. Zhang, I. Amlani, et al., Tuning the chemical selectivity of SWNT-FETs for detection of heavy-metal ions, Small 2 (11) (2006) 1283−1291.
[64] C. Wang, X. Cui, Y. Li, H. Li, L. Huang, J. Bi, et al., A label-free and portable graphene FET aptasensor for children blood lead detection, Sci. Rep. 6 (2016) 21711.
[65] K.-I. Chen, B.-R. Li, Y.-T. Chen, Silicon nanowire field-effect transistor-based biosensors for biomedical diagnosis and cellular recording investigation, Nano Today 6 (2) (2011) 131−154.
[66] E. Stern, R. Wagner, F.J. Sigworth, R. Breaker, T.M. Fahmy, M.A. Reed, Importance of the Debye screening length on nanowire field effect transistor sensors, Nano Lett. 7 (11) (2007) 3405−3409.
[67] M.-K. Tsang, W. Ye, G. Wang, J. Li, M. Yang, J. Hao, Ultrasensitive detection of *Ebola virus* oligonucleotide based on upconversion nanoprobe/nanoporous membrane system, ACS Nano 10 (1) (2016) 598−605.
[68] L. Chua, Memristor-the missing circuit element, IEEE Trans. Circuit Theory 18 (5) (1971) 507−519.
[69] F. Budiman, T.W. Kian, K.A. Razak, A. Matsuda, Z. Lockman, The assessment of Cr (VI) removal by iron oxide nanosheets and nanowires synthesized by thermal oxidation of iron in water vapour, Procedia Chem. 19 (2016) 586−593.
[70] C. Balan, I. Volf, D. Bilba, Chromium(VI) removal from aqueous solutions by purolite base anion-exchange resins with gel structure, Chem. Ind. Chem. Eng. Q./CICEQ 19 (4) (2013) 615−628.
[71] A. Azimi, A. Azari, M. Rezakazemi, M. Ansarpour, Removal of heavy metals from industrial wastewaters: a review, ChemBioEng Rev. 4 (1) (2017) 37−59.
[72] C.E. Barrera-Díaz, V. Lugo-Lugo, B. Bilyeu, A review of chemical, electrochemical and biological methods for aqueous Cr(VI) reduction, J. Hazard. Mater. 223 (2012) 1−12.
[73] K. Gandha, J. Mohapatra, M.K. Hossain, K. Elkins, N. Poudyal, K. Rajeshwar, et al., Mesoporous iron oxide nanowires: synthesis, magnetic and photocatalytic properties, RSC Adv. 6 (93) (2016) 90537−90546.
[74] N. Bashirom, K.A. Razak, Z. Lockman, Synthesis of freestanding amorphous ZrO_2 nanotubes by anodization and their application in photoreduction of Cr(VI) under visible light, Surf. Coat. Technol. 320 (2017) 371−376.

[75] D.J. Johnson, W.A. Suwaileh, A.W. Mohammed, N. Hilal, Osmotic's potential: an overview of draw solutes for forward osmosis, Desalination 434 (2018) 100–120.
[76] P. Goh, A. Ismail, A review on inorganic membranes for desalination and wastewater treatment, Desalination 434 (2018) 60–80.
[77] Y. Cui, Q. Ge, X.-Y. Liu, T.-S. Chung, Novel forward osmosis process to effectively remove heavy metal ions, J. Membr. Sci. 467 (2014) 188–194.
[78] K. Lutchmiah, A. Verliefde, K. Roest, L.C. Rietveld, E. Cornelissen, Forward osmosis for application in wastewater treatment: a review, Water Res. 58 (2014) 179–197.
[79] V. Khandegar, A.K. Saroha, Electrocoagulation for the treatment of textile industry effluent—a review, J. Environ. Manage. 128 (2013) 949–963.
[80] S. Zodi, O. Potier, F. Lapicque, J.-P. Leclerc, Treatment of the textile wastewaters by electrocoagulation: effect of operating parameters on the sludge settling characteristics, Sep. Purif. Technol. 69 (1) (2009) 29–36.
[81] I. de Oliveira da Mota, J.A. de Castro, R. de Góes Casqueira, A.G. de Oliveira Junior, Study of electroflotation method for treatment of wastewater from washing soil contaminated by heavy metals, J. Mater. Res. Technol. 4 (2) (2015) 109–113.
[82] M.M. Emamjomeh, M. Sivakumar, Review of pollutants removed by electrocoagulation and electrocoagulation/flotation processes, J. Environ. Manage. 90 (5) (2009) 1663–1679.
[83] V. Madhavi, A.V.B. Reddy, K.G. Reddy, G. Madhavi, T. Prasad, An overview on research trends in remediation of chromium, Res. J. Recent. Sci. ISSN 2277 (2013) 2502.
[84] E. Kaprara, K. Simeonidis, A. Zouboulis, M. Mitrakas, Evaluation of current treatment technologies for Cr(VI) removal from water sources at sub-ppb levels, in: Proceedings of the 13th International Conference on Environmental Science and Technology, Athens, Greece, 2013, pp. 5–7.
[85] Z. Lockman, 1-Dimensional Metal Oxide Nanostructures: Growth, Properties, and Devices, CRC Press, 2018.
[86] F. Budiman, N. Bashirom, W.K. Tan, K.A. Razak, A. Matsuda, Z. Lockman, Rapid nanosheets and nanowires formation by thermal oxidation of iron in water vapour and their applications as Cr(VI) adsorbent, Appl. Surf. Sci. 380 (2016) 172–177.
[87] B. Nurulhuda, K. Tan Wai, K. Go, M. Atsunori, R. Khairunisak Abdul, L. Zainovia, Sunlight activated anodic freestanding ZrO_2 nanotube arrays for Cr(VI) photoreduction, Nanotechnology 29 (37) (2018) 375701.
[88] C.F. Carolin, P.S. Kumar, A. Saravanan, G.J. Joshiba, M. Naushad, Efficient techniques for the removal of toxic heavy metals from aquatic environment: a review, J. Environ. Chem. Eng. 5 (3) (2017) 2782–2799.
[89] S. Kumari, G.S. Chauhan, New cellulose–lysine Schiff-base-based sensor–adsorbent for mercury ions, ACS Appl. Mater. Interfaces 6 (8) (2014) 5908–5917.
[90] C. Huang, D. Blankenship, The removal of mercury(II) from dilute aqueous solution by activated carbon, Water Res. 18 (1) (1984) 37–46.
[91] J. Liu, T.-H. Xie, C. Deng, K.-F. Du, N. Zhang, J.-J. Yu, et al., Welan gum-modified cellulose bead as an effective adsorbent of heavy metal ions (Pb^{2+}, Cu^{2+}, and Cd^{2+}) in aqueous solution, Sep. Sci. Technol. 49 (7) (2014) 1096–1103.
[92] Y.S. Ok, J.E. Yang, Y.-S. Zhang, S.-J. Kim, D.-Y. Chung, Heavy metal adsorption by a formulated zeolite-Portland cement mixture, J. Hazard. Mater. 147 (1-2) (2007) 91–96.
[93] R.A.K. Rao, M. Kashifuddin, Adsorption studies of Cd(II) on ball clay: comparison with other natural clays, Arabian J. Chem. 9 (2016) S1233–S1241.

[94] S. Dal Bosco, R. Jimenez, C. Vignado, J. Fontana, B. Geraldo, F. Figueiredo, et al., Removal of Mn(II) and Cd(II) from wastewaters by natural and modified clays, Adsorption 12 (2) (2006) 133–146.
[95] L. de Pablo, M.L. Chávez, M. Abatal, Adsorption of heavy metals in acid to alkaline environments by montmorillonite and Ca-montmorillonite, Chem. Eng. J. 171 (3) (2011) 1276–1286.
[96] T. Sen, M. Sarali, Adsorption of cadmium metal ion (Cd^{2+}) from its aqueous solution by aluminium oxide and kaolin: a kinetic and equilibrium study, J. Environ. Res. Dev. 3 (1) (2008) 220–227.
[97] Ö. Yavuz, Y. Altunkaynak, F. Güzel, Removal of copper, nickel, cobalt and manganese from aqueous solution by kaolinite, Water Res. 37 (4) (2003) 948–952.
[98] S.S. Gupta, K.G. Bhattacharyya, Immobilization of Pb(II), Cd(II) and Ni(II) ions on kaolinite and montmorillonite surfaces from aqueous medium, J. Environ. Manage. 87 (1) (2008) 46–58.
[99] S. Shahmohammadi-Kalalagh, Isotherm and kinetic studies on adsorption of Pb, Zn and Cu by kaolinite, Caspian J. Environ. Sci. 9 (2) (2011) 243–255.
[100] B. Sathyanarayana, K. Seshaiah, Kinetics and equilibrium studies on the sorption of manganese(II) and nickel(II) onto kaolinite and bentonite, J. Chem.—N.Y. 8 (1) (2011) 373–385.
[101] T.K. Sen, D. Gomez, Adsorption of zinc (Zn^{2+}) from aqueous solution on natural bentonite, Desalination 267 (2-3) (2011) 286–294.
[102] P. Liu, H. Sehaqui, P. Tingaut, A. Wichser, K. Oksman, A.P. Mathew, Cellulose and chitin nanomaterials for capturing silver ions (Ag^{+}) from water via surface adsorption, Cellulose 21 (1) (2014) 449–461.
[103] Y. Sharma, Thermodynamics of removal of cadmium by adsorption on an indigenous clay, Chem. Eng. J. 145 (1) (2008) 64–68.
[104] H. Sokker, Y. Gad, S. Ismail, Synthesis of bifunctional cellulosic adsorbent by radiation induced graft polymerization of glycidyl methacrylate-*co*-methacrylic acids, J. Appl. Polym. Sci. 126 (S1) (2012) E54–E62.
[105] J.R. Evans, W.G. Davids, J.D. MacRae, A. Amirbahman, Kinetics of cadmium uptake by chitosan-based crab shells, Water Res. 36 (13) (2002) 3219–3226.
[106] N. Bashirom, M.A. Zulkifli, S. Subagja, T.W. Kian, A. Matsuda, Z. Lockman, Cr(VI) removal on visible light active TiO_2 nanotube arrays, in: AIP Conference Proceeding, 2018.
[107] M.A. Zulkifli, N. Bashirom, K.T. Wai, K. Go, M. Atsunori, Z. Lockman, Rapid TNTs formation in aged electrolyte and their applications as photocatalysts for Cr(VI) reduction under visible light, IEEE T. Nanotechnol. 17 (6) (2018) 1106–1110.
[108] Q. Wang, J. Shang, T. Zhu, F. Zhao, Efficient photoelectrocatalytic reduction of Cr (VI) using TiO_2 nanotube arrays as the photoanode and a large-area titanium mesh as the photocathode, J. Mol. Catal. A: Chem. 335 (1) (2011) 242–247.
[109] Q. Wu, J. Zhao, G. Qin, C. Wang, X. Tong, S. Xue, Photocatalytic reduction of Cr (VI) with TiO_2 film under visible light, Appl. Catal. B: Environ. 142–143 (2013) 142–148.
[110] J.K. Yang, S.M. Lee, M. Farrokhi, O. Giahi, M. Shirzad Siboni, Photocatalytic removal of Cr(VI) with illuminated TiO_2, Desalin. Water Treat. 46 (1-3) (2012) 375–380.
[111] F. Hashemzadeh, A. Gaffarinejad, R. Rahimi, Porous p-NiO/n-Nb_2O_5 nanocomposites prepared by an EISA route with enhanced photocatalytic activity in simultaneous Cr

(VI) reduction and methyl orange decolorization under visible light irradiation, J. Hazard. Mater. 286 (2015) 64−74.
[112] H.-Y. Lin, H.-C. Yang, W.-L. Wang, Synthesis of mesoporous Nb_2O_5 photocatalysts with Pt, Au, Cu and NiO cocatalyst for water splitting, Catal. Today 174 (1) (2011) 106−113.
[113] X. Liu, R. Zheng, R. Yuan, L. Peng, Y. Liu, J. Lin, Released defective Nb_2O_5 with optimized solar photocatalytic activity, ECS J. Solid State Sci. Technol. 6 (9) (2017) P665−P670.
[114] A.E. Nogueira, O.F. Lopes, A.B.S. Neto, C. Ribeiro, Enhanced Cr(VI) photoreduction in aqueous solution using Nb_2O_5/CuO heterostructures under UV and visible irradiation, Chem. Eng. J. 312 (2017) 220−227.
[115] X. Tian, Q. Wang, Q. Zhao, L. Qiu, X. Zhang, S. Gao, SILAR deposition of CuO nanosheets on the TiO_2 nanotube arrays for the high performance solar cells and photocatalysts, Sep. Purif. Technol. 209 (2019) 368−374.
[116] K.E. Engates, H.J. Shipley, Adsorption of Pb, Cd, Cu, Zn, and Ni to titanium dioxide nanoparticles: effect of particle size, solid concentration, and exhaustion, Environ. Sci. Pollut. Res. Int. 18 (3) (2011) 386−395.
[117] J. Cai, X. Wu, F. Zheng, S. Li, Y. Wu, Y. Lin, et al., Influence of TiO_2 hollow sphere size on its photo-reduction activity for toxic Cr(VI) removal, J. Colloid Interface Sci. 490 (2017) 37−45.
[118] R. Djellabi, F.M. Ghorab, S. Nouacer, A. Smara, O. Khireddine, Cr(VI) photocatalytic reduction under sunlight followed by Cr(III) extraction from TiO_2 surface, Mater. Lett. 176 (2016) 106−109.
[119] Y. Du, S. Zhang, J. Wang, J. Wu, H. Dai, Nb_2O_5 nanowires in-situ grown on carbon fiber: a high-efficiency material for the photocatalytic reduction of Cr(VI), J. Environ. Sci.—China 66 (2018) 358−367.
[120] Y. Du, X. Wang, J. Wu, C. Qi, Y. Li, Adsorption and photoreduction of Cr(VI) via diatomite modified by Nb_2O_5 nanorods, Particuology 40 (2018) 123−130.
[121] K.S. Ranjith, P. Manivel, R.T. Rajendrakumar, T. Uyar, Multifunctional ZnO nanorod-reduced graphene oxide hybrids nanocomposites for effective water remediation: effective sunlight driven degradation of organic dyes and rapid heavy metal adsorption, Chem. Eng. J. 325 (2017) 588−600.
[122] D. Kanakaraju, S. Ravichandar, Y.C. Lim, Combined effects of adsorption and photocatalysis by hybrid TiO_2/ZnO-calcium alginate beads for the removal of copper, J. Environ. Sci. 55 (2017) 214−223.
[123] E. Wahyuni, N. Aprilita, H. Hatimah, A. Wulandari, M. Mudasir, Removal of toxic metal ions in water by photocatalytic method, Am. Chem. Sci. J. 5 (2) (2015) 194−201.
[124] P. Chowdhury, A. Elkamel and A.K. Ray Photocatalytic processes for the removal of toxic metal ions, in: S.K. Sanjay (Ed.), Heavy Metals in Water: Presence, Removal and Safety, The Royal Society of Chemistry, 2015, pp. 25−43.
[125] T. Kanki, H. Yoneda, N. Sano, A. Toyoda, C. Nagai, Photocatalytic reduction and deposition of metallic ions in aqueous phase, Chem. Eng. J. 97 (1) (2004) 77−81.
[126] G. Lenzi, C. Fávero, L. Colpini, H. Bernabe, M. Baesso, S. Specchia, et al., Photocatalytic reduction of Hg(II) on TiO_2 and Ag/TiO_2 prepared by the sol−gel and impregnation methods, Desalination 270 (1-3) (2011) 241−247.
[127] N. Wang, L. Zhu, K. Deng, Y. She, Y. Yu, H. Tang, Visible light photocatalytic reduction of Cr(VI) on TiO_2 in situ modified with small molecular weight organic acids, Appl. Catal. B: Environ. 95 (3) (2010) 400−407.

[128] M.L. Vera, H.D. Traid, E.R. Henrikson, A.E. Ares, M.I. Litter, Heterogeneous photocatalytic Cr(VI) reduction with short and long nanotubular TiO_2 coatings prepared by anodic oxidation, Mater. Res. Bull. 97 (2018) 150−157.

[129] L. Wang, N. Wang, L. Zhu, H. Yu, H. Tang, Photocatalytic reduction of Cr(VI) over different TiO_2 photocatalysts and the effects of dissolved organic species, J. Hazard. Mater. 152 (1) (2008) 93−99.

Solution combustion synthesis of metal oxide nanoparticles for membrane technology

16

A. Jegatha Christy[1], *M. Umadevi*[2] *and Suresh Sagadevan*[3]
[1]Department of Physics, Jayaraj Annapackiam College for Women, Periyakulam, India,
[2]Department of Physics, Mother Teresa Women's University, Kodaikanal, India,
[3]Nanotechnology and Catalysis Research Centre, University of Malaya, Kuala Lumpur, Malaysia

16.1 Introduction

The emergence of infectious diseases, in general, poses a serious threat to public health worldwide, especially with the emergence of antibiotic-resistant bacterial strains. Generally, both Gram-positive and Gram-negative bacterial strains are thought to present a major public health problem. Over the years, antibiotics have been used to control infections resulting from both community and hospital environments [1−3]. Current advances in the field of nanobiotechnology, particularly the ability to prepare metal oxide nanomaterials of specific size and shape, are likely to lead to the development of new antibacterial agents. The functional activities of nanoparticles (NPs) are influenced largely by the particle size. Therefore NPs have received great attention due to their unique physical, chemical, and effective biological properties in various fields, including medicine. The properties of NPs can easily be altered by reducing or changing their size, especially when the manipulations are done at the nanometer scale [4−7]. The filtration devices such as microfiltration are successfully used in the separation and concentration of particulate suspensions or solutions, the recovery of low-molecular-weight substances and, in some instances, the recovery of macromolecules such as proteins [8]. Generally, microfiltration membranes can be classified into organic membranes that mainly made of polymeric compounds and inorganic membranes that contain ceramic or metallic materials. Inorganic microfiltration membranes can be operated at elevated temperatures, metal membranes are stable at temperatures ranging from 500°C to 800°C, and many ceramic membranes are usable at over 1000°C. The development of inorganic membranes for industrial applications enables the realization of high thermal capability, high chemical stability, and good cleaning ability by means of high pressure or backflushing, which cannot be implemented by polymer membranes [9]. Fabrication of inorganic membranes was studied by many investigators from different viewpoints [10]. The present study introduces a new approach for the manufacturing

Metal Oxide Powder Technologies. DOI: https://doi.org/10.1016/B978-0-12-817505-7.00016-6

of porous metallic membrane via reduction of metal oxides. The formation of metallic materials with small pores could be achieved in two ways: when small particles of metal oxides are used as starting materials (average particle size 300−500 nm), metallic materials with pores less than 100 nm can be produced. The second way to achieve metallic materials with very small pores comes from the mechanism of reduction reactions of metal oxides where the removal of oxygen during reduction will enhance the formation of additional small pores.

As an important p-type semiconductor, CuO has found many diverse applications such as gas sensors, catalysis, batteries, high-temperature superconductors, solar energy conversion, and field emission emitters. CuO is cheaper than silver, easily mixed with polymers, and relatively stable in terms of both chemical and physical properties. Highly ionic nanoparticulate metal oxides, such as CuO, may be particularly valuable antimicrobial agents as they can be prepared with extremely high surface areas and unusual crystal morphologies [5]. High purity and ultrafine nickel metal powder is a key component of many different materials that are used to manufacture a wide range of end-use products such as catalysts, magnetic devices, powder metallurgical components, and gas sensing. Although a multitude of water contaminants pose health threats, the utmost waterborne threat comes from pathogenic bacteria, viruses, and fungi. Traditional solutions to water disinfection such as chlorination and ozonation are faced with increasing barriers and complexities. They produce carcinogenic disinfection by-products (DBP) such as trihalomethanes, haloamides, halonitriles, and bromate and have become increasingly less effective to treat a rising number of resistant microorganisms. Unlike traditional disinfectants, nanomaterials are not strong oxidants and, hence, do not produce harmful DBP and have the potential to enhance conventional treatment methods. Nanotechnology has the potential to advance water and wastewater treatment by improving treatment efficiency. There are several classes of nanomaterials that are being evaluated as materials for water purification, which have a broad range of physicochemical properties that make them attractive for water purification. Nanomaterials can attack microbial cells through various antimicrobial mechanisms. The most common inorganic antimicrobial nanomaterials are AgNP, TiO_2, and ZnO, but the most widely used currently are AgNP NPs. These are used in a wide variety of microbial control applications such as disinfection of medical devices and home appliances, and water treatment [11]. ZnO NPs, being similar to TiO_2, also hold many outstanding properties: nano-ZnO particles can easily absorb hydrophilic hydroxyl groups (−OH) to become hydrophilic; ZnO at the nano level exhibits a higher surface area than that of nano-TiO_2 due to its crystallographic structure [12]; it exhibits an excellent antibacterial and antifungal characteristic, due to its valuable ultraviolet-resistant and photocatalytic properties [13]. It has low cost and is less toxic than any TiO_2 NPs, and ZnO NPs are processed easily than TiO_2 NPs. Few reports have been published, in which, Wang et al. prepared a new pervaporation membrane by the combination of ZnO particles and cellulose acetate [14]. In this investigation, it has been reported that ZnO particles at 4.01% (w/w) increased

the hydrophilicity of cellulose acetate, which improved both the permeation flux and separation factor of the methanol/methyl *tert*-butyl ether system.

One of the major limitations of membrane-based separations is fouling and polymeric membranes being hydrophobic in nature are more prone to fouling. Fouling is a deposition of various colloidal particles, macromolecules (polysaccharides, proteins), salts, etc. on the membrane surface and within pores thus impedes membrane performance, reduces flux, and results in high cost. Modification of polymeric membranes due to its tailoring ability with nanomaterials such as metal-based and carbon-based results in polymeric nanocomposite membranes with high antifouling characteristics. Nanomaterials impart high selectivity, permeability, hydrophilicity, thermal stability, mechanical strength, and antibacterial properties to polymeric membranes via blending, coating, etc. modification methods. Polymer−metal nanocomposite exhibits antifouling properties as shown in Fig. 16.1.

Ahmad et al. studied the antifouling properties of polyethersulfone (PES) membranes blended with different amounts of ZnO. The presence of highly volatile acetone contributed to the tight skin layer of the membrane, which shows remarkable antifouling ability with the highest flux recovery ratio (FRR) and negligible irreversible fouling. Although the antifouling ability of ZnO/acetone is moderate, it is still plausible to obtain good membranes using these two materials, which show a

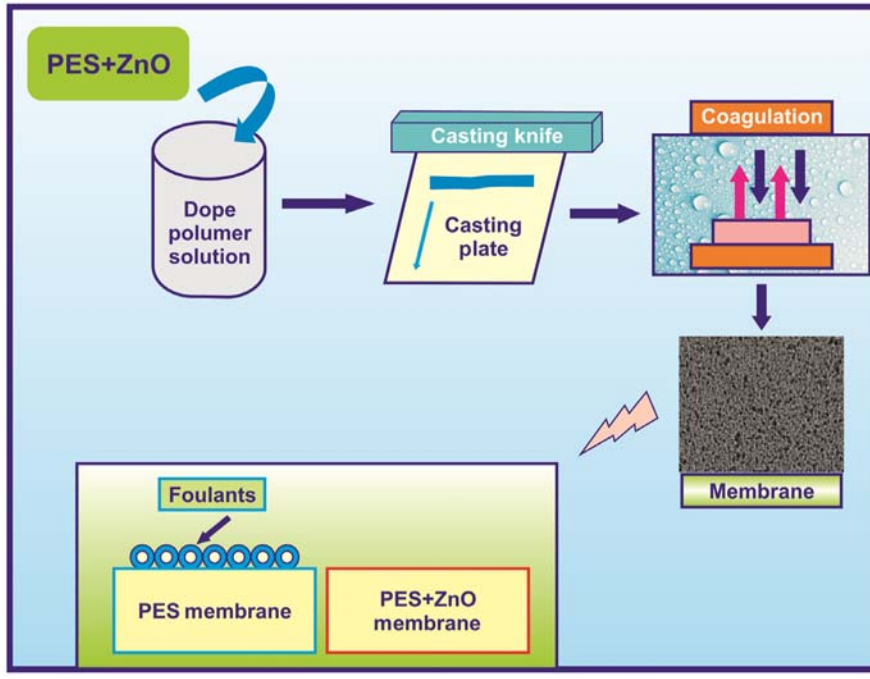

Figure 16.1 Schematic diagram of polymer−metal nanocomposite exhibiting antifouling properties.

remarkable fouling resistance [15]. Nasrollahi et al. prepared novel PES ultrafiltration membranes blended with different contents of the CuO/ZnO (CZN) nanocomposite. High hydrophilicity of ZnO NP made it an excellent choice to be incorporated with CuO NPs in order to improve the membrane properties as a nanofiller additive. When the content of CZN was 0.2 wt.%, the pure water flux growth of the blended membrane was about 32%. In addition, the cited blended membrane displayed a higher FRR (%) in the bovine serum albumin (BSA) fouling agent. BSA rejection was above 95% for all of the nanocomposite membranes [16].

As a versatile semiconductor material, ZnO is extensively used in shock resistance, sound installation, photosensitization, fluorescence, gas sensitization, and catalysis. ZnO is one of the best bactericides and photocatalysts. Though there are many methods for preparing NPs, combustion synthesis has evolved as a straightforward method. Recently, increasing attention has been paid to it for preparing NPs with tailored properties. In this method the formation of the NP is a result of the self-propagating exothermic redox reaction that occurs between an oxidizer (metal nitrate) and a reducing agent (various fuels). Once the combustion reaction is ignited, no additional heat source is required. The advantages of this method are its simplicity, short reaction time, and the environmental friendly nature of reaction by-products. The solution combustion technique also allows homogenous mixing in an aqueous solution of reactants at the molecular level yielding precise control over the stoichiometry of the final product. The present chapter describes that the copper oxide, nickel oxide, and zinc oxide NPs are synthesized by solution combustion method using glycine as fuel and their antimicrobial activity is studied extensively.

16.2 Experimental procedures

16.2.1 Introduction

Metal combustion has received renewed interest now and it is having the long-term potential for nanotechnology to allow for an unprecedented level of control over the structure of reactive/energetic materials on length scales from nanometers to meters [17]. Solution combustion synthesis (SCS) is a versatile, simple, rapid, and single-step process, which involves a self-sustained reaction inhomogeneous solution of different oxidizers (e.g., metal nitrates) and fuels (e.g., urea, glycine, citric acid, and hydrazides). Depending on the type of the precursors, as well as on the conditions used for the process organization, the SCS may occur as either volume or layer-by-layer propagating combustion modes [6]. The most important fact about SCS is that it is a short duration process and the various gases formed during the process inhibit particle size growth, which favors the formation of nano-sized powders [18]. The choice of fuel for SCS is the most important factor. The glycine and citric acid have been adopted for the synthesis of metal/metal oxide NPs because they are widely used for the synthesis of nanomaterials. Among known fuels,

glycine has demonstrated the versatility of combustion methods by the successful preparation of a large number of single-phase, well-crystallized, multicomponent oxides. Also, it is inexpensive and its combustion heat (−3.24 kcal/g) is more negative compared with urea (−2.98 kcal/g). When citric acid is employed in a combustion process, the heat released in combustion is more and as a result, the combustion enthalpy is more, which is responsible for the growth of the sample and complete combustion reaction with more crystalline phase takes place. The citric acid and glycine are considered to be ideal fuels because (1) they act as a good source of N, C, and H, which on combustion evolve N_2, CO_2, and H_2O gases, favoring the formation of NPs; (2) they form complexes with the metal ions facilitating homogenous mixing of the cations in solution; and (3) these fuels are water-soluble and good homogenization can be achieved in solution. A number of preparation methods and techniques have been examined for identifying the most reliable and cheapest method of producing nanomaterials. However, these methods require specific apparatus, vacuum conditions, and high-cost equipment, but the solution combustion method is an alternative quick process, low-cost method and prepared a large amount of nanopowders. A few publications described the fabrication of metal oxide semiconductor nanopowders by solution combustion method. However, it is a challenge to find an efficient and simple way, using a low-temperature and convenient method suitable for large-scale production of metal oxide semiconductor powders with particle size about several nanometers by using this method.

16.2.2 Preparation of metal oxides by solution combustion method

For the preparation of NPs the corresponding metal nitrate (oxidizer) was taken as a precursor and glycine or citric acid was used as fuel. The stoichiometric composition of the solution components (fuels and oxidizer) was calculated according to the principle of propellant chemistry, keeping the oxidizer (metal nitrate) to fuel (glycine or citric acid) ratio as unity. In the combustion reaction the molar ratio (Ψ) is defined as the ratio of fuel to metal nitrate and it corresponds to the situation of an "equivalent stoichiometric ratio," which implies that the oxygen content of metal nitrate can be completely oxidized or it can consume fuel exactly. As a result, metal or metal oxide product and gases of CO_2, H_2O, and N_2 can be formed directly from the reaction between the fuel and the oxidizer without the need of getting oxygen from outside. The solution was kept in the furnace at 300°C. With a large amount of fumes produced the combustion reaction was completed and the loose powder was formed, which was crushed and ground thoroughly. Schematic representation of the synthesis process is shown in Fig. 16.2.

16.2.3 Synthesis of CuO, NiO, and ZnO nanoparticles

For the preparation of NPs, metal nitrate [$Cu(NO_3)_2$, $Ni(NO_3)_2 \cdot 6H_2O$, $Zn(NO_3)_2 \cdot 6H_2O$] and fuel [glycine (CH_2NH_2COOH)] were taken as starting materials

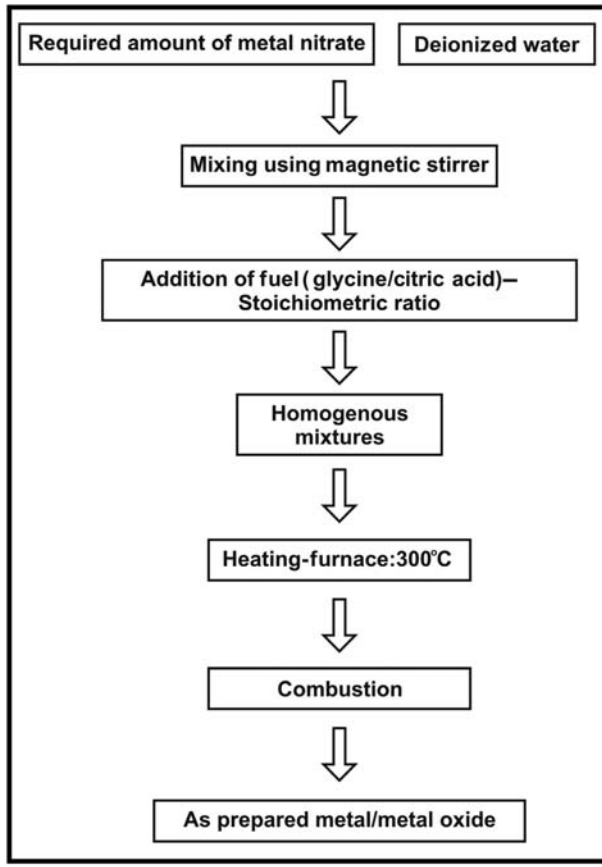

Figure 16.2 A schematic representation of the synthesis process.

(AR grade). The stoichiometric compositions of the solution components (fuels and oxidizer) were calculated according to the principle of propellant chemistry, keeping the oxidizer (metal nitrate) to fuel (glycine) ratio as unity [19]. A stoichiometric amount of metal nitrate was dissolved in deionized water and then fuel was added into it. The solution was kept in the furnace at 300°C. Initially, the solution is boiled and underwent dehydration followed by decomposition with the evolution of a large number of gases. After the solution reached the point of spontaneous combustion, burning began releasing heat. It vaporized the entire solution instantly and became loose powder. The normal atmosphere was maintained in the furnace without any inert gas. The atmospheric temperature outside the furnace was 22°C−25°C. Different combinations of fuels and their oxidant-to-fuel ratio were used to tailor the powder properties. Schematic representation of the synthesis of CuO/NiO/ZnO NPs by combustion method is shown in Fig. 16.3.

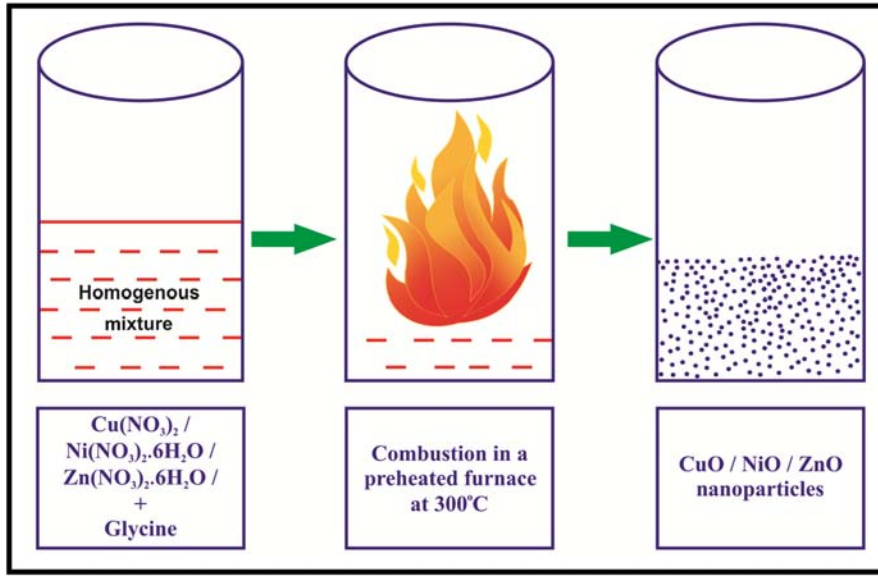

Figure 16.3 Schematic of synthesis of CuO/NiO/ZnO nanoparticles by combustion method.

16.2.4 Assay for antimicrobial activity of metal oxide nanoparticles against microorganisms

The antimicrobial activity of metal oxide NPs was evaluated against the 0.2 mL of fresh cultures. Each sample was inoculated into 5mL of sterile nutrient broth (HiMedia) and incubated for 3−5 hours to standardize the culture to McFarland standards (106 CFC/mL). Three replicates of respective microorganism were prepared by spreading 100 μL of the revived culture on Mueller−Hinton agar—HiMedia with the help of the spreader. The well was of 7 mm in diameter. Samples of 50 μL metal/metal oxide were added in one well and 50 μL of distilled water was used as a control. The Petri plates were kept at 37°C for 24 hours in an incubator for bacteria, during which its antibacterial activity was evidenced by the presence of a zone of inhibition (mm).

16.3 Result and discussion

16.3.1 Structural analysis

X-ray diffraction (XRD) is a popular technique for determining the phase purity of the materials. Small-angle scattering is useful for evaluating the average interparticle distance while the wide-angle diffraction is useful for refining the atomic structure of nanoclusters [20]. The width of the diffraction lines is closely related to the

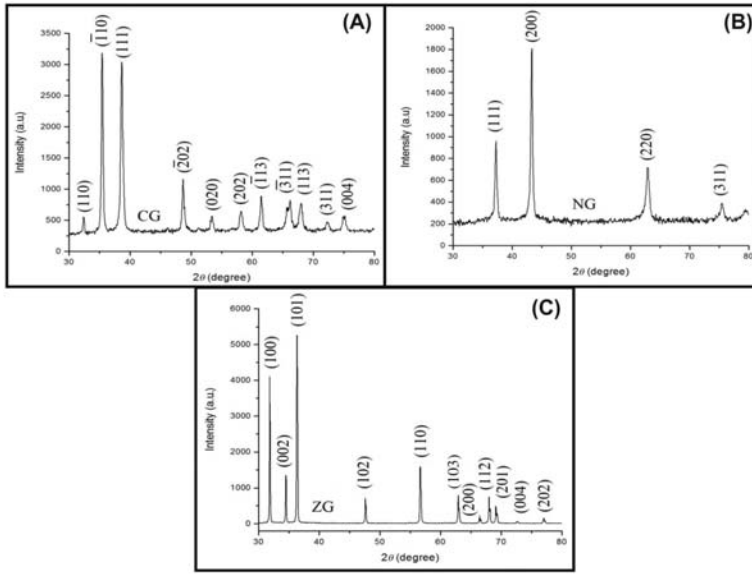

Figure 16.4 XRD pattern of (A) CuO NPs, (B) NiO NPs, and (C) ZnO NPs. *NP*, Nanoparticle; *XRD*, X-ray diffraction.

size distribution, defects, and strain in NPs. Fig. 16.4A shows the XRD pattern of the prepared glycine-assisted CuO NPs (CG). The diffraction peaks corresponding to (1 1 0), $(\bar{1}\ 1\ 0)$. (1 1 1), $(\bar{2}\ 0\ 2)$, (0 2 0), (2 0 2), $(\bar{1}\ 1\ 3)$, $(\bar{3}\ 1\ 1)$, (1 1 3), (3 1 1), and (0 0 4) planes were perfectly indexed to the monoclinic structure (ICDD 80-1916). Li et al. prepared synthesized open interconnected macroporous copper oxide films by using the gas bubble template-directed synthesis method. By this approach, hydrogen bubbles arising from the reduction of H^+ functioned as the dynamic template for copper electrodeposition. Copper was electrodeposited and grew within the interstitial spaces between the hydrogen bubbles, forming macroporous films on the gold substrate [21]. Fig. 16.4B shows the XRD patterns of NiO NPs. All peaks of glycine-assisted NiO (NG) NPs are labeled and can be indexed to face-centered cubic structure (ICDD 78-0429). All diffraction peaks corresponding to (1 1 1), (2 0 0), (2 2 0), and (3 1 1) planes were in good agreement with the typical face-centered cubic structure of pure NiO. Ran et al. prepared feasible, low-cost composite energy storage materials, which can be applied to prepare other high-performance hybrid materials using porous nickel oxide membrane by a phase-separation technique and nickel oxide membrane electrode by pressing the membranes between two foam nickels at 10 MPa for supercapacitor device. It was possible to put into practical applications in a flexible and wearable energy storage device [22]. Synthesized ZnO is commonly characterized using XRD. A good agreement between the obtained peaks and standard diffraction peaks corresponding to (1 1 0), (0 0 2), (1 0 1), (1 0 2), (1 1 0), (2 0 2), (1 0 3), (2 0 0), (1 1 2), (2 0 1), (0 0 4), and (2 0 2) diffraction planes, respectively, reveals the hexagonal structure

of ZnO according to ICDD 89-7102. Diffraction peaks related to impurities, which are not observed in XRD graph, confirm high purity. Moreover, diffraction peaks that are narrower and intensive imply good crystalline nature of the ZnO, and that broadening of the peaks at the bottom are indications that the crystallite sizes are small. A typical ZnO XRD graph is shown in Fig. 16.4C shows the XRD pattern of glycine-assisted ZnO NPs (ZG). The peaks observed are corresponding to (1 1 0), (0 0 2), (1 0 1), (1 0 2), (1 1 0), (2 0 2), (1 0 3), (2 0 0), (1 1 2), (2 0 1), (0 0 4), and (2 0 2) diffraction planes, respectively, of the hexagonal structure of ZnO (ICDD 89-7102).

16.3.2 Surface morphological studies

The field emission scanning electron microscope (FESEM) is a type of electron microscope capable of providing high-resolution, magnification, and depth of field images than optically attained. SEM images have a characteristic three-dimensional appearance and are useful for judging the surface structure of the sample. Fig. 16.5A shows the FESEM images of the CuO NPs. The prepared CG is of a flower-shaped structure consisting of dense CuO nanosheets (petals) with a typical thickness around 50 nm with the size of a single flower being 3.5 μm. The

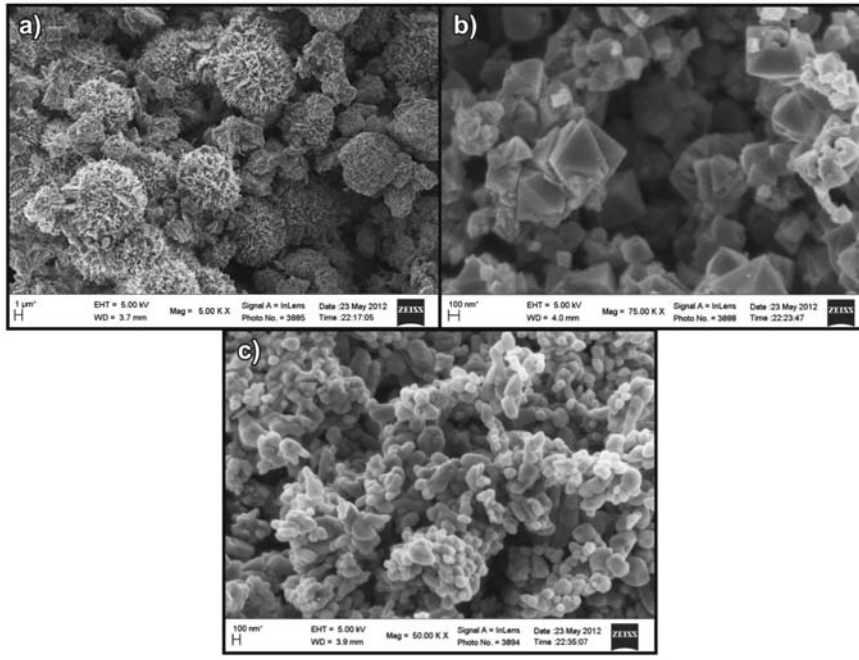

Figure 16.5 FESEM image of (A) CuO NPs, (B) NiO NPs, and (C) ZnO NPs. *FESEM*, Field emission scanning electron microscope; *NP*, nanoparticle.

nanosheets are connected together on the bases, rooted in one center, and assembled into the beautiful flower-like morphology. Fig. 16.5B shows the FESEM image of the prepared NiO. From the FESEM images, it is confirmed that NiO is having octahedral structures. This morphology is due to the inherent effect of organic fuels. The FESEM image of NiO shows that some of the octahedral particles are broken at the edges due to the escaping of gases during combustion [23]. Fig. 16.5C shows the FESEM image of the ZnO NPs. The prepared ZnO NPs have flake-like morphology. The ZnO morphology is affected by synthesis conditions such as precursor type, temperature, and pH. There are only a few studies on the effect of morphology on the antibacterial activity of ZnO NPs and there is no general agreement on the effect of particle shape.

16.3.3 Antimicrobial activity of floral CuO nanoparticles

In this study the antimicrobial activity of floral CuO NPs (CG) was tested against both Gram-positive (*Bacillus cereus* and *Staphylococcus aureus*) and Gram-negative bacteria (*Escherichia coli* and *Klebsiella pneumoniae*) and fungi (*Penicillium chrysogenum*). The CuO nanostructures showed antimicrobial activity against *B. cereus* (16 mm), *S. aureus* (16 mm), *E. coli* (20 mm), *K. pneumoniae* (18 mm), and *P. chrysogenum* (16 mm). While comparing the effect of floral nano CuO on microbial strains, the greatest inhibitory effect was recorded against *E. coli* strain. The prepared nano CuO was more toxic to *E. coli* and *K. pneumoniae.* For the Gram-positive bacteria the effect of CuO was less pronounced than Gram-negative bacteria. Fig. 16.6 shows the photographic image of an inhibition zone produced by CG against (1) *E. coli* and (2) *K. pneumoniae*. Table 16.1 shows the zone of inhibition of CuO NPs for various microorganisms. In the present study the antimicrobial activity shows that the Gram-positive bacterial strains are less

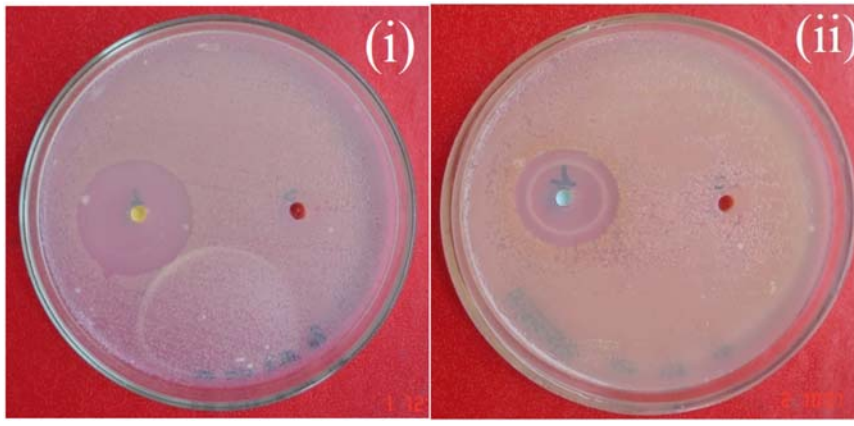

Figure 16.6 Photographic image of an inhibition zone produced by CG against (A) *Escherichia coli* and (B) *Klebsiella pneumoniae*.

Table 16.1 Zone of inhibition (mm) of CuO nanoparticles for various microorganisms.

Microorganism	Strain no	Zone of inhibition (mm)
Bacillus cereus	MTCC-4079	16
Staphylococcus aureus	MTCC-7443	16
Escherichia coli	MTCC-1721	17
Klebsiella pneumoniae	MTCC-4030	16.5
Penicillium chrysogenum	MTCC-5108	16

affected than Gram-negative. The variation in the sensitivity or resistance of both Gram-positive and -negative bacteria populations could be due to the differences in the cell structure, physiology, metabolism, or degree of contact of organisms with NPs. The overall charges of bacterial cells at biological pH values are negative due to the excess of carboxylic groups present in the lipoproteins on the bacterial surface, which, upon dissociation, makes the cell surface negative [24]. The opposite charges of bacteria and copper ions released from NPs are thought to cause adhesion and bioactivity due to electrostatic forces. Since peptidoglycans are negatively charged molecules, they bind Cu^{2+} ions released from copper NPs in the liquid growth medium. Being Gram-negative, the bacterium *E. coli* may allow more Cu^{2+} ions to reach the plasma membrane but is generally considered less susceptible to antibiotics and antibacterial agents than Gram-positive bacteria [25]. Finally, it can be concluded that Gram-negative bacterial strains are showing higher antimicrobial activity than Gram-positive because of their membrane structure.

The antibacterial properties of copper NPs are mainly attributed to adhesion with bacteria because of their opposite electric charges resulting in a reduction at the bacterial cell wall. Gram-positive and Gram-negative bacteria have differences in their membrane structure, the most distinctive of which is the thickness of the peptidoglycan layer. The lower efficacy of the Cu NPs against *S. aureus* and *B. cereus* may derive from the difference as a point of membrane structure [26]. For oxidized copper particles embedded in an inert, teflon-like matrix, Cioffi et al. demonstrated significant antimicrobial activity due to the release of ions [27]. Azam et al. discussed the antimicrobial activity of copper NPs are synthesized by the gel combustion method and they reported that the antibacterial activity is completely size-dependent and suggested that the release of copper ions is responsible for bacterial death [28]. Consequently, the bactericidal effects observed in this study might have been influenced by the release of Cu^{2+} ions in solution. From these results, it is believed that the binding of copper ions to the bacterial cell surface plays an important role in the bactericidal activity.

Azam et al. reported that the antimicrobial activity is size-dependent and the CuO NPs about 20 nm showed maximum activity for *E. coli* (20 mm). In the present case the nanosheets have the size of 50 nm and show 20 mm activity. This shows that the shape of the NPs also influences the antimicrobial activity. Pang et al. discussed that as the cuprous oxide crystals change from cubic to octahedral, the antibacterial activity changes from general bacteriostasis to high sensitivity

[29]. However, from the current study, it can be suggested that like the size of the NPs, the shape of the particles also influences the antimicrobial activity.

16.3.4 Antimicrobial activity of octahedral NiO nanoparticles

Antimicrobial activity of Ni NPs was tested against *K. pneumoniae*, *Pseudomonas aeruginosa*, *P. chrysogenum*, *Aspergillus niger*, and *Candida albicans*. In this study the prepared glycine-assisted octahedral NiO NPs (NG) exhibited high antimicrobial activity against *K. pneumoniae* (18 mm), *P. aeruginosa* (14 mm), *P. chrysogenum* (16 mm), *A. niger* (10 mm), and *C. albicans* (7 mm). Table 16.2 shows the zone of inhibition of nickel oxide NPs for various microorganisms. Fig. 16.7 shows the photographic image of an inhibition zone produced by NG against (1) *P. aeruginosa* and (2) *P. chrysogenum*. In the present case, Gram-positive strains are more active than Gram-negative strains. The results show that the antimicrobial activities of NiO NPs are less efficient (2%) against *E. coli* and *S. aureus*. The NiO at a dosage of 1 g/100 mL showed a significantly lower reduction of *E. coli.* NiO dosage of 5 g/100 mL showed a high reduction decreased after 4 hours of contact. This corresponds to the beginning of the log phase of the bacterial growth in the control bottles. There were no significant differences in the final antimicrobial activity of NiO supported on natural clintoptilolite after 24 hours of contact at both dosages. Singh et al. studied the antimicrobial activity of the Ni complexes with two new Schiff bases of 1,3-diphenyl-1H-pyrazole-4-carboxaldehyde (HL_1) and 4-amino-5-mercapto-3-methyl/H-1,2,4-triazole (HL_2) [24]. These Schiff bases were biologically active. The metal complexes were added to these Schiff bases and their antimicrobial activity was studied. The diameter of growth of inhibition zone of HL_1 and HL_2 for *P. aeruginosa* was around 15 mm. The NiO complexes added to these two Schiff bases showed the activity of around 16 mm, which exhibited that NiO complex does not influence the activity. The mycelial growth inhibition of HL_1 and HL_2 for *A. niger* was around 45 and 57 mm, respectively. The NiO complex added with the Schiff bases showed activity up to 48 and 45 mm, respectively. These observations show that the NiO complex itself was not having antimicrobial activity. Manikshete et al. investigated the ligand and metal (II) complexes and the antimicrobial activity also studied against *S. aureus*, *P. aeruginosa*, *A. niger*, and *C. albicans* [25]. The result showed that the antimicrobial activity was very feeble and they are mostly inactive. Chandra et al. synthesized the Ni (II) complexes with

Table 16.2 Zone of inhibition (mm) of NiO nanoparticles for various microorganisms.

Microorganism	Strain no	Zone of inhibition (mm)
Klebsiella pneumoniae	MTCC-4030	18
Pseudomonas aeruginosa	MTCC-2453	14
Aspergillus niger	MTCC-4325	10
Candida albicans	MTCC-1637	7
Penicillium chrysogenum	MTCC-5108	16

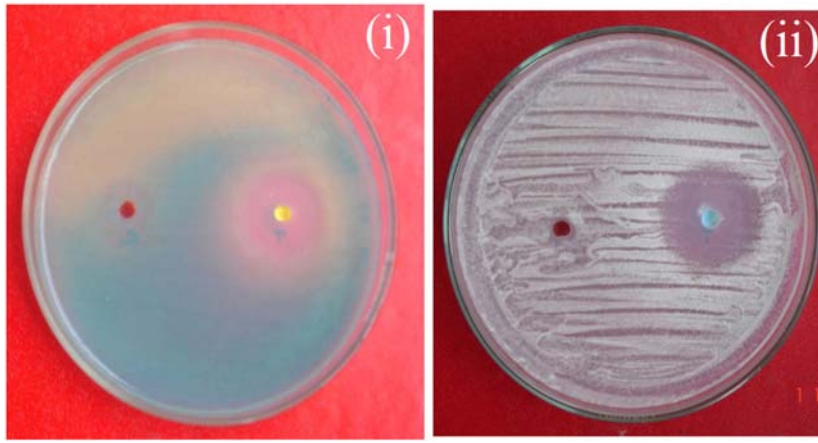

Figure 16.7 Photographic image of an inhibition zone produced by NG against (A) *Pseudomonas aeruginosa* and (B) *Penicillium chrysogenum*.

hexadentate macrocyclic ligand and studied its antimicrobial activity against two different species of bacteria *Bacillus subtilis* and *Xanthomonas campestris* and plant pathogenic fungi *Rhizoctonia solani* and *R. blast*. In both strains the antimicrobial strains do not show any activity [30].

In the present case the prepared octahedral NiO NPs show very high antimicrobial activity than the reported NiO NPs and its complexes. The prepared NiO NPs are more effective against Gram-positive bacterial strains than the Gram-negative strains. Gram-positive bacteria typically have one cytoplasmic membrane and thick wall composed of multilayers of peptidoglycan. On the other hand, Gram-negative bacteria have a more complex cell wall structure, with a layer of peptidoglycan between the outer membrane and cytoplasmic membrane. Thus the cell membrane of Gram-positive bacteria can be damaged more easily [31]. The high antimicrobial activity achieved can be explained under the factors of shape and crystal quality.

16.3.5 Antimicrobial activity of ZnO nanoflakes

In this study the prepared glycine-assisted ZnO nanoflakes (ZG) exhibited high antimicrobial activity against *K. pneumoniae* (18 mm), *P. aeruginosa* (11 mm), *P. chrysogenum* (16 mm), *A. niger* (9 mm), and *C. albicans* (11 mm). Table 16.3 shows the zone of inhibition of ZnO NPs for various microorganisms. Fig. 16.8 shows the photographic image of an inhibition zone produced by ZG against (1) *K. Pneumoniae* and (2) *P. aeruginosa*. Tam et al. investigated the antibacterial activity of ZnO nanorods prepared by hydrothermal method. They are not showing a prominent effect for lesser concentrations [12].

Moghaddam et al. biosynthesized ZnO NPs using a new strain of yeast (*Pichia kudriavzevii* GY1) and evaluated their anticancer activity in breast cancer MCF-7 cells. ZnO NPs have been observed to show powerful cytotoxicity against MCF-7

Table 16.3 Zone of inhibition (mm) of ZnO nanoparticles for various microorganisms.

Microorganism	Strain no	Zone of inhibition (mm)
Klebsiella pneumoniae	MTCC-4030	18
Pseudomonas aeruginosa	MTCC-2453	11
Aspergillus niger	MTCC-4325	9
Candida albicans	MTCC-1637	11
Penicillium chrysogenum	MTCC-5108	16

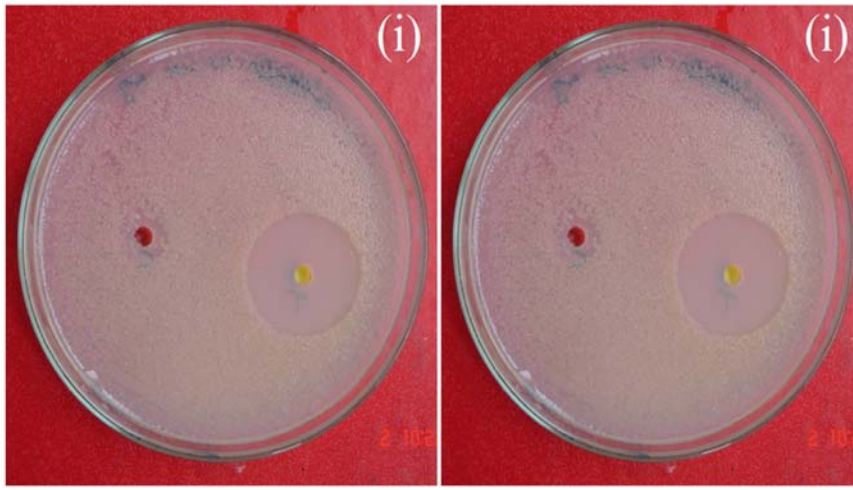

Figure 16.8 Photographic image of an inhibition zone produced by ZG against (A) *Klebsiella pneumoniae* and (B) *Pseudomonas aeruginosa*.

cells, which was associated with the occurrence of apoptosis, more than cell cycle arrest [32]. The antibacterial activity may involve the accumulation of ZnO NPs in the outer membrane or cytoplasm of bacterial cells and trigger Zn^{2+} release, which would cause bacterial cell membrane disintegration, membrane protein damage, and genomic instability, resulting in the death of bacterial cells. Many Gram-negative bacteria such as *E. coli*, *P. aeruginosa*, *Proteus vulgaris*, *Vibrio cholerae* and Gram-positive bacteria such as *S. aureus*, *B. subtilis*, and *Enterococcus faecalis* are also investigated [33]. Schematic illustration of antibacterial activity in ZnO NPs is shown in Fig. 16.9.

It showed that ZnO NPs with an average size of about 30 nm caused cell death by directly contacting with the phospholipid bilayer of the membrane, destroying the membrane integrity. The addition of radical scavengers such as mannitol, vitamin E, and glutathione could block the bactericidal action of ZnO NPs. Thus Zn^{2+} released from ZnO NPs suspensions was the apparent cause to antibacterial effect. Moreover, Ohira and Yamamoto also found the antibacterial (*E. coli* and *S. aureus*)

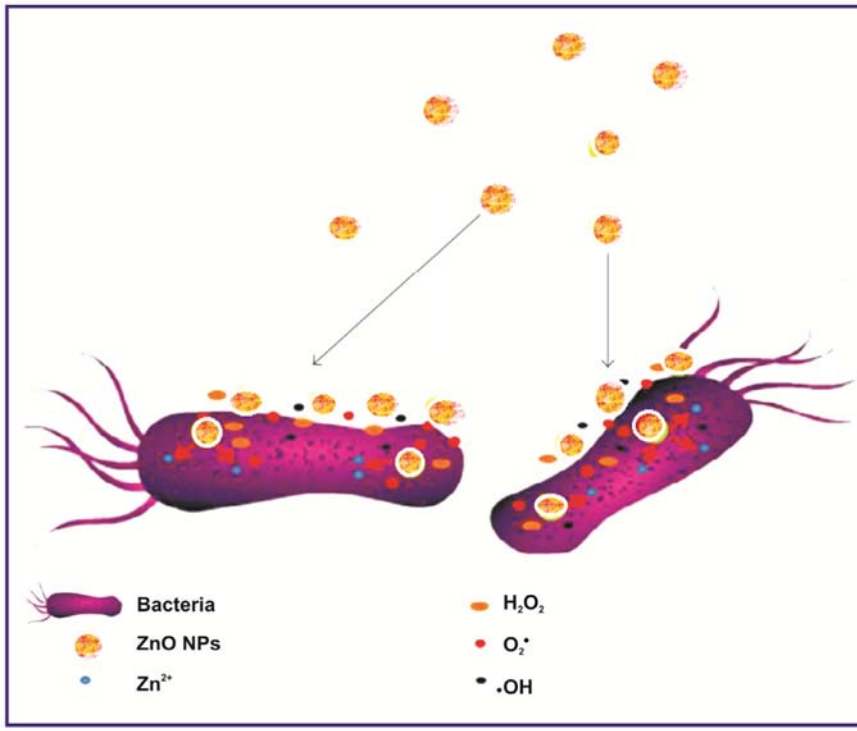

Figure 16.9 Schematic illustration of antibacterial activity in ZnO nanoparticle.

activity of ZnO NPs with small crystallite sizes was stronger than those with large crystallite sizes [34]. From ICP-AES measurement the amount of Zn^{2+} released from the small ZnO NPs was much higher than large ZnO powder sample and *E. coli* was more sensitive to Zn^{2+} than *S. aureus*. So, we can believe that eluted Zn^{2+} from ZnO NPs also take a key role in antibacterial action.

16.4 Conclusion

The CuO, NiO, and ZnO NPs were prepared by solution combustion method using glycine as fuel and their antimicrobial activities were studied. The XRD pattern analysis showed that floral- and rod-like CuO is having a monoclinic crystal structure. FESEM confirms the shape of floral CuO NPs. FESEM confirms the octahedral shape of NiO NPs and XRD showed that the prepared NiO NPs having fcc structure. XRD pattern confirms the hexagonal structure of ZnO nanoflakes. The FESEM images confirm the fine nanoflakes morphology. From the present study, it could be suggested that the antimicrobial activity of NPs does not only depend on size but also on the shape, uniformity, and crystalline nature. Further researches

have to be done in the synthesis of small-sized different-shaped NPs that could provide far better antimicrobial activity. The antibacterial activity of floral CuO NPs explained in terms of the shape of the NPs. In the octahedral NiO the shape and crystal quality determine the antimicrobial activity. Studying the antimicrobial activity of ZnO nanoflakes reveals that it provides a better antibacterial activity because of their shape. Comparing all the prepared metal oxide NPs, it can be concluded that the shape is playing a vital role than the size of the NPs. Further researches have to be done in the synthesis of small-sized different-shaped NPs that could provide far better antimicrobial activity.

Acknowledgment

The author Dr. A. Jegatha Christy is grateful to SERO/UGC for financial support.

References

[1] J.S. Kim, E. Kuk, K. Nam Yu, J. Kim, S.J. Park, H.J. Lee, et al., Nanomed. Nanotechnol. Biol. Med. 3 (2007) 95.
[2] M. Messaoud, F. Chadeau, C. Brunon, T. Ballet, L. Rappenne, F. Roussel, et al., J. Photochem. Photobiol., A 215 (2010) 147.
[3] J.R. Morones, J.L. Elechiguerra, A. Camacho, K. Holt, J.B. Kouri, J.T. Ramirez, et al., Nanotechnology 16 (2005) 2346.
[4] M. Singh, S. Singh, S. Prasada, I.S. Gambhir, Dig. J. Nanomater. Biostruct. 3 (2008) 115.
[5] H.-X. Zhang, U. Siegert, R. Liu, W.-B. Cai, Nanoscale Res. Lett. 4 (2009) 705.
[6] S.T. Aruna, A.S. Mukasyan, Curr. Opin. Solid State Mater. Sci. 12 (2008) 44.
[7] C.F. Bohren, D.F. Huffman, Absorption and Scattering of Light by Small Particles, Wiley, New York, 1983.
[8] A. Katiyar, L. Ji, P. Smirniotis, N.G. Pinto, Mesoporous molecular sieves for size selective separation of biomolecules, in: F.T. Atkin, Y.S. Linn (Eds.), Proceedings of 8th International Conference on Inorganic Membranes, 2004, pp. 63−66. 1-929612-67-2.
[9] L. Zaho, M. Bram, H.P. Buchkremer, D. Stover, Z. Li, J. Membr. Sci. 244 (2004) 107−115.
[10] D.W. Lee, S.J. Park, C.Y. Yu, S.K. Ihm, K.H. Lee, J. Membr. Sci. 302 (2007) 265−270.
[11] E.A.S. Dimapilis, C.-S. Hsu, R.M.O. Mendoza, M.-C. Lu, Sustain. Environ. Res. 28 (2018) 47−56.
[12] K.H. Tam, A.B. Djurisic, C.M.N. Chan, Y.Y. Xi, C.W. Tse, Y.H. Leung, et al., Thin Solid Films 516 (2008) 6167.
[13] M. Ali, M. Zafar, T. Jamil, M.T.Z. Butt, Desalination 270 (2011) 98.
[14] Y. Wang, Y. Liangrong, L. Guangsheng, D. Youyuan, Chem. Eng. J. 146 (2009) 6.
[15] A.L. Ahmad, J. Sugumaran, N.F. Shoparwe, Membranes 8 (2018) 131.
[16] N. Nasrollahi, V. Vatanpour, S. Aber, N. Mohammad Mahmoodi, Sep. Purif. Technol. 192 (2018) 369−382.

[17] R.A. Yetter, G.A. Risha, F.S. Steven, Proc. Combust. Inst. 32 (2009) 1819.
[18] A.S. Mukasyan, P. Epstein, P. Dinka, Proc. Combust. Inst. 31 (2007) 1789.
[19] P.K. Stoimenov, R.L. Klinger, G.L. Marchin, K.J. Klabunde, Langmuir 18 (2002) 6679.
[20] A.L. Koch, Am. Sci. 78 (1990) 327.
[21] Y. Li, W.-Z. Jia, Y.-Y. Song, X.-H. Xia, Chem. Mater. 19 (2007) 5758−5764.
[22] F. Ran, H. Yang, Y. Wu, X. Zhao, Y. Tan, Y. Liu, et al., J. Membr. Sci. 514 (2016) 366−375.
[23] S. Balta, A. Sotto, P. Luis, L. Benea, B. Van der Bruggen, J. Kim, J. Membr. Sci. 389 (2012) 155.
[24] K. Singh, Y. Kumar, P. Puri, M. Kumar, C. Sharma, Eur. J. Med. Chem. 52 (2012) 313.
[25] H. Manikshete, S.K. Sarsamkar, S.A. Deodware, V.N. Kamble, M.R. Asabe, Inorg. Chem. Commun. 14 (2011) 618.
[26] G. Tong, M. Yulong, G. Peng, X. Zirong, Vet. Microbiol. 105 (2005) 113.
[27] N. Cioffi, N. Ditaranto, L. Torsi, R.A. Picca, L. Sabbatini, A. Valentini, et al., Anal. Bioanal. Chem. 381 (2005) 607.
[28] A. Azam, A.S. Ahmed, M. Oves, M.S. Khan, A. Memic, Int. J. Nanomed. 7 (2012) 3527.
[29] H. Pang, F. Gao, Q. Lu, Chem. Commun. (Camb.) 7 (2009) 1076.
[30] S. Chandra, Ruchi, K. Qanungo, S.K. Sharma, Spectrochim. Acta A 94 (2012) 312.
[31] G. Fu, P.S. Vary, C.T. Lin, J. Phys. Chem. B 109 (2005) 8889.
[32] A.B. Moghaddam, M. Moniri, S. Azizi, et al., Genes 8 (2017) 281.
[33] Y. Jiang, L. Zhang, D. Wen, Y. Ding, Mater. Sci. Eng.: C. 69 (2016) 1361−1366.
[34] T. Ohira, O. Yamamoto, Chem. Eng. Sci. 68 (2012) 355−361.

This page intentionally left blank

Three-dimensional printing of ceramic powder technology

17

Waleed K. Ahmed[1] *and Y. Al-Douri*[2,3,4]
[1]ERU and Mechanical Engineering Department, College of Engineering, United Arab Emirates University, Al Ain, United Arab Emirates, [2]University Research Center, Cihan University Sulaimaniya, Sulaimaniya, Iraq, [3]Nanotechnology and Catalysis Research Center (NANOCAT), University of Malaya, Kuala Lumpur, Malaysia, [4]Department of Mechatronics Engineering, Faculty of Engineering and Natural Sciences, Bahcesehir University, Istanbul, Turkey

There are many applications and advantages of the current revolution of the additive manufacturing (AM) technology, or what is traditionally known as three-dimensional (3D) printing technology. This erupting technology has invaded our lives in different ways, providing a change to the traditional manufacturing techniques that have been used for many years. Moreover, the benefits of 3D printing (3DP) technology are not restricted within the industrial sector, but can also be used for innovative learning [1,2] as well as in failure experimentation [3], where the prototyping and the modeling developed trends helped a lot in the acceleration of the continuous of the inventions of different sectors [4]. One of the promising materials that scientists and researchers have tested and examined using 3DP technology is ceramic, since it has many advantages like corrosion resistance that make it very attractive in the medical sector, but unfortunately it has some of weak properties, like low tensile properties as well as the lack of toughness, that cause problems during and after the manufacturing process. The impact of the cracked microparticles has been studied intensively to investigate the negative impact on the mechanical properties [5–7], challenging scientists to overcome the weak properties of the ceramic to enable its use in 3DP technology. Nowadays, the 3DP technology has been extended to 4D printing, where it becomes possible to control the deformation and the response of the 3D printed parts within the macro- and nanolevels [8].

In this chapter, three main applications (medical, mechanical, and physical) of using ceramic in 3DP technology are presented and discussed.

17.1 Using three-dimensional printed ceramic for medical applications

AM, also known as 3DP, has emerged over the past three decades as a disruptive technology for rapid prototyping and manufacturing. Vat polymerization, powder

Metal Oxide Powder Technologies. DOI: https://doi.org/10.1016/B978-0-12-817505-7.00017-8

bed fusion, material extrusion, and binder jetting were distinct technologies of AM, which have been used in a wide variety of fields, including biomedical research and tissue engineering. The ability to print biocompatible, patient-specific geometries with controlled macro- and micropores, and to incorporate cells, drugs, and proteins has made 3D-printing ideal for orthopedic applications, such as bone grafting. The present section focuses on the uses of ceramics in 3DP technology for medical applications.

The good dispersity and flowability assuring the high density and uniform porous structure of β-tri-calcium phosphate (β-TCP) ceramics were addressed by Ben et al. [9]. β-TCP were used as biological ceramic materials and completely met the standard for bone tissue engineering. Monodispersed and spherical β-TCP granules for 3DP were prepared by spray drying with the surface modification of polyvinyl butyral (PVB). Modifier PVB attached to the particle surface to form the cross-linked network structure and keep them combined with each other into aggregates. The morphology, size, forming performance, and crushing behavior of granules as well as the microstructure and density of as-fabricated β-TCP ceramics were used to optimize the PVB contents. Promising results could be expected with PVB contents at 1.0 wt.% and the average particle size of granules was 37.36 mm. The modified granules exhibited excellent forming performance with monodispersed and spherical aggregates for 3DP. They could be completely crushed under 80 MPa without obvious intergranules voids. These granules with 1.0 wt.% PVB had defined strengths for ceramic forming. Huang and Bártolo [10] presented an extensive rheological characterization of polymer/ceramic blends commonly used for the fabrication of bone scaffolds through AM. The fabrication of optimized scaffolds for bone regeneration requires complex physical and biological requirements, which strongly depend on the processing conditions and the material morphological development during the fabrication process. Poly-ε-caprolactone (PCL)/hydroxyapatite (HA) and PCL/TCP blends with different ceramic contents (5, 10, and 20 wt.%) were prepared using melt blending and studied using rotational and oscillation rheological tests. Screw-assisted extrusion AM systems have been extensively used to produce bone scaffolds in a wide range of polymers and polymer/ceramic composites, as illustrated in Fig. 17.1.

Results showed that all samples present a shear-thinning behavior making them suitable for AM. All samples present a viscoelastic behavior with significantly higher viscous modulus than elastic modulus at low frequencies. Both moduli increase with the addition of ceramic particles. Their results also showed that PCL/HA samples present a higher elastic modulus than PCL/TCP. Roopavath et al. [11] presented materials and the design optimization of clinically approved HA using extrusion-based 3DP process. The effect of various printing parameters including print speed, extrusion pressure, accuracy, and infill density to produce defined porous structures was established using various techniques, as depicted in Fig. 17.2.

Scanning electron microscopy (SEM) and microcomputed tomography have been employed in particular to study internal and external accuracy. Mechanical testing was employed to study the effect of porosity on compressive properties of 3D printed structures. The study showed that the infill density and shrinkage of 3D

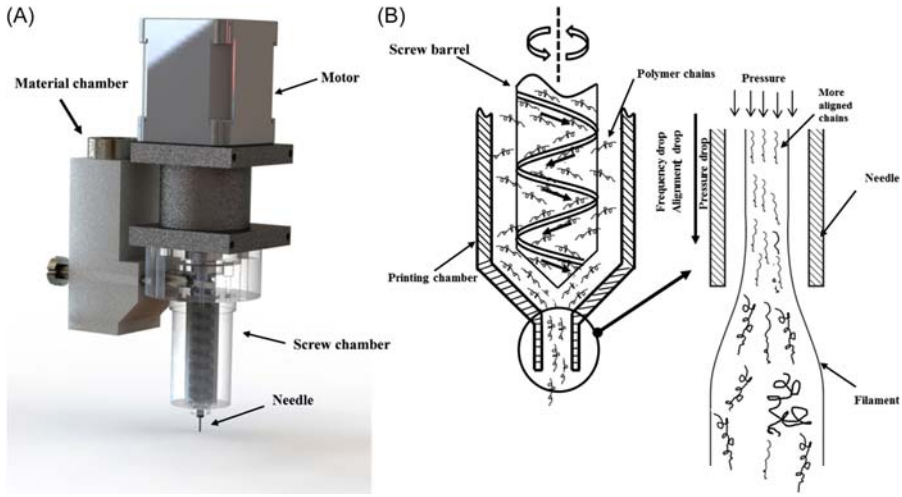

Figure 17.1 Diagram of (A) screw-assisted extrusion printhead (B) polymer printing process [10].

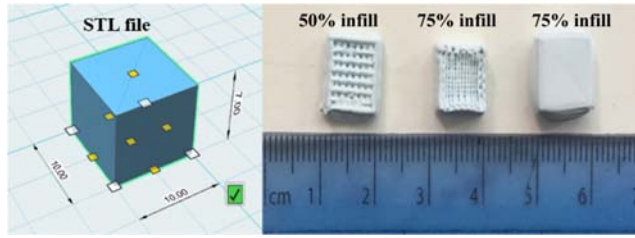

Figure 17.2 Images of STL file and 3D printed HA Cube scaffolds at different infill densities sintered at 1350°C [11]. *3D*, Three-dimensional; *HA*, hydroxyapatite.

printed HA scaffolds postsintering have a linear relationship. Porosity and mechanical strength of 3D printed scaffolds depend on the infill density of the designed CAD file. Tailoring infill density also helps in altering mechanical properties in a predictable manner. A case study on HA printing of a patient-specific bone graft demonstrated the ability of this material and technique to print complex porous structures created on CT-based anatomical bone models and preoperative 3D planning, providing further promise for custom implant development for complex bony designs. Yang et al. [12] focused on preparing diamond tools with orderly arranged abrasive particles for dental ceramics processing via 3DP to overcome such drawbacks of the existing methods of dental ceramics processing as weak bonding strength, short service life, and irregular diamond distribution in diamond tools. First, the CAD model of the dental diamond tool was constructed using 3D cartographic software, with level-scan path geometry information generated via hierarchical slicing, as presented in Fig. 17.3.

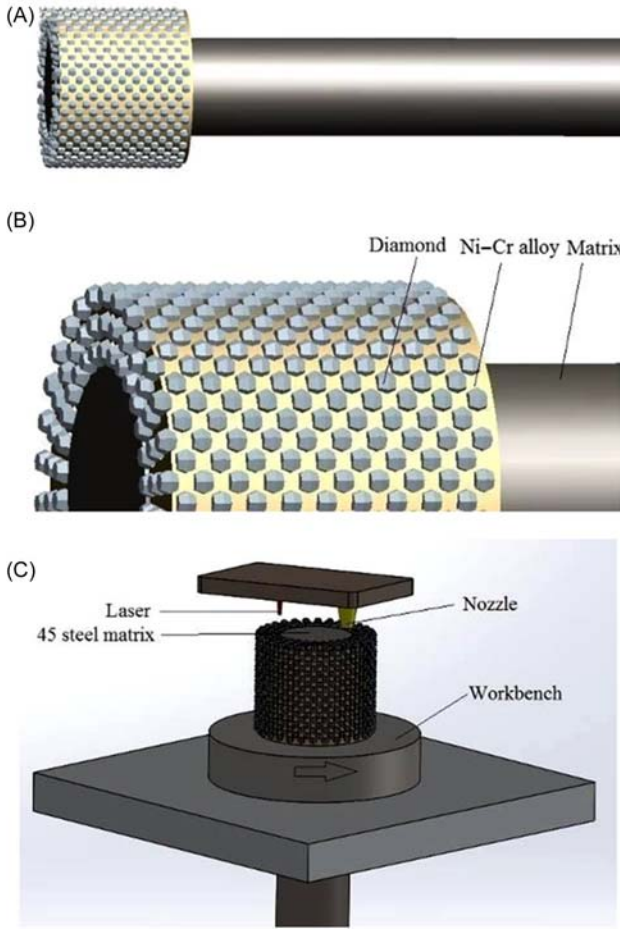

Figure 17.3 (A) Entity model of diamond tool. (B) Regular distribution of diamond abrasive particles. (C) Diamond tool with regularly distributed grains [12].

Then, using Ni−Cr alloy powder and diamond as raw materials, the dental ceramics processing diamond tool with orderly arranged diamond particles was prepared via a 3D printer. Next, an X-ray diffractometer, energy dispersive spectrometer, and scanning electron microscope were used to analyze the microstructure of the Ni−Cr alloy and diamond particle interfaces, resulting in the identification of their bonding mechanism. Finally, the diamond grinding wheel produced by 3DP was subjected to dental zirconia ceramics grinding performance tests. The results obtained confirm that diamond particles experience normal wear, while no abrasive falling off occurs on the 3D printed diamond tool surface. Trombetta et al. [13] performed a systematic review examining the fabrication of calcium phosphate (CaP) ceramics by 3DP, their biocompatibility in vitro, and their bone regenerative

potential in vivo, as well as their use in localized delivery of bioactive molecules or cells. Understanding the advantages and limitations of the different 3DP approaches, CaP materials, and bioactive additives through critical evaluation of in vitro and in vivo evidence of efficacy was essential for developing new classes of bone graft substitutes that can perform as well as autografts and allografts or even surpass the performance of these clinical standards. Hierarchical structures with tailored macro/microporosity architecture play an important role in bone tissue regeneration. In the 3DP process, the printing ink formulation will influence the ceramic macro- and microporous architectures. Fig. 17.4 illustrates major technologies used in 3DP of pure or composite CaP scaffolds for bone regeneration and drug delivery.

In the paper of Zhang et al. [14], HA powders of nanosized grains (NP) with diameters of 30−50 nm, air-jet milling powders (AP) with diameters of 10−30 μm, and spherical powder (SP) with diameters of 10−50 μm, were used as the initial printing materials in the printing ink formulations. The viscosity and the rheological behavior of printing inks were studied. The microstructure and morphology of the printed scaffold were observed and the mechanical properties of different types of scaffolds were tested, as given by Fig. 17.5.

The results showed that the initial printing materials would influence printing performance, both of the AP and SP inks may print porous scaffolds successfully. However, NP printing inks exhibited dramatic shrinkage and it was not suitable for 3DP of bioceramics. The printing ink formulation also has effects on the ceramic macro- and microporous architectures and mechanical properties. The maximum compressive strength of spherical powder scaffold (SPS) was 5.5, 3.2, and 0.9 MPa with porosities of 60%, 70%, and 80%, respectively. As the macroporosity decreases, the mechanical properties of the material would drop dramatically. With the same porosities, the compressive strength of air jet milling powder scaffold was slightly higher than that of the SPS specimens.

17.2 Application of three-dimensional printed ceramic in mechanics

AM is an innovative complex shaping technique with unlimited freedom and flexibility in fabrication. Though the majority of AM processes were focused in polymers, they were later extended to metals and very recently to ceramics. Conventional prototyping of ceramics, especially complex parts proceeds through several iterations of design and fabrication of dies, molds, fixtures, etc. which were cost-intensive and also time is taken to arrive at the final designs. Often the finished parts also need machining to achieve the microfeatures. 3DP of ceramics with its inherent advantages simplifies the above issues, especially for fabrication of prototypes leading to the selection of optimum designs in a very short time. Further, as the same infrastructure was based on the printing of ceramic shapes using software-generated virtual images it also results in lower cost. In this section, the 3DP

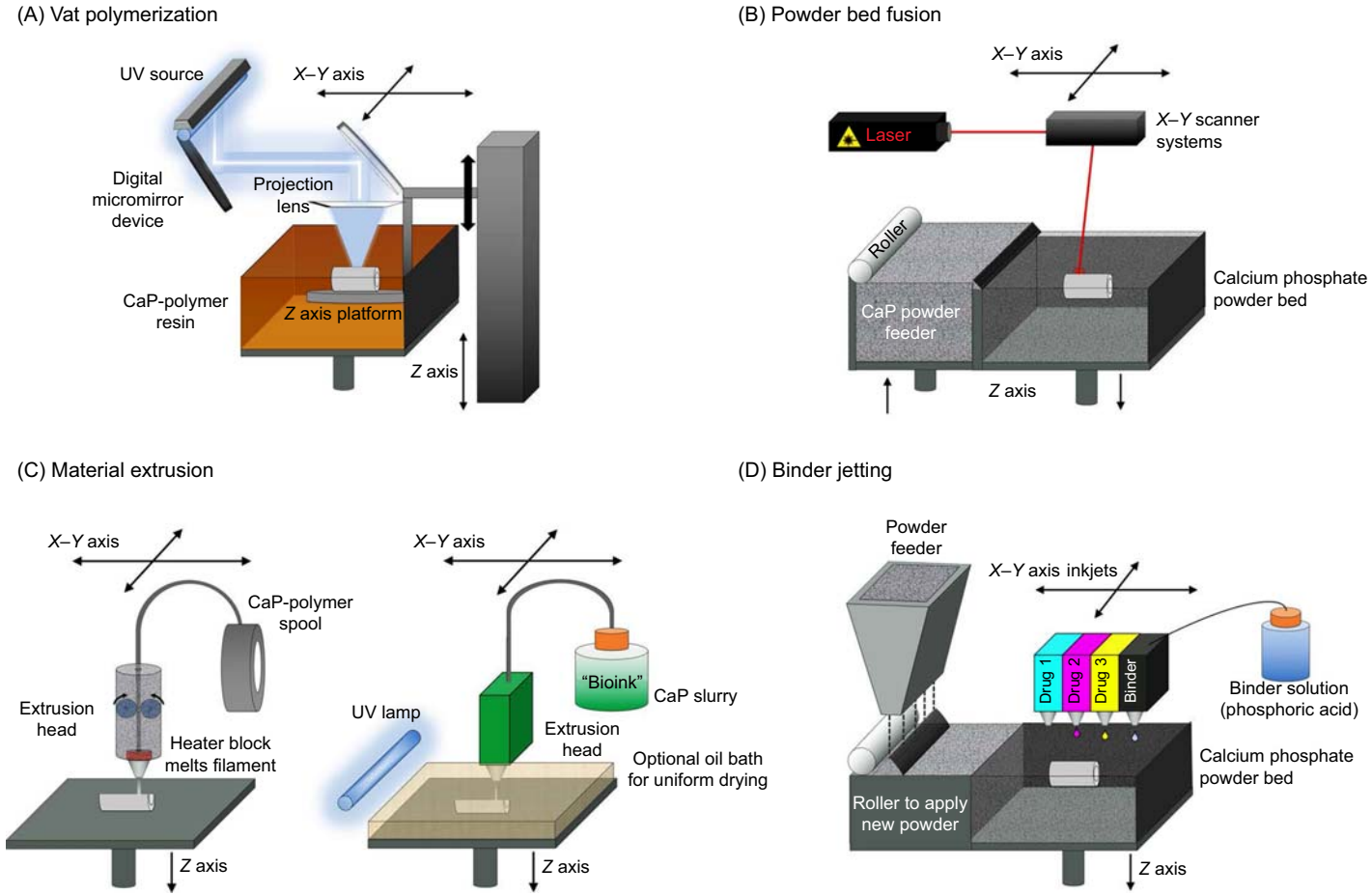

Figure 17.4 Schematic depiction of the major technologies used in 3D printing of pure or composite calcium phosphate scaffolds for bone regeneration and drug delivery [13]. (A) Vat Polymerization, (B) powder bed fusion, (C) material extrusion, and (D) binder jetting. *3D*, Three-dimensional.

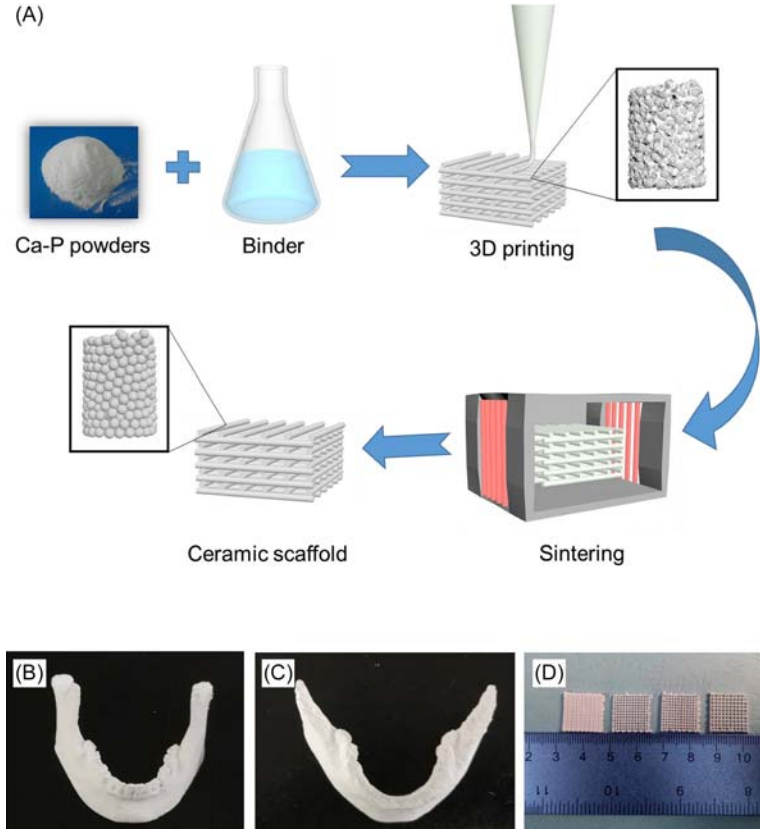

Figure 17.5 Porous bioceramics produced by inkjet 3D printing: effect of printing ink formulation on the ceramic macro- and microporous architectures control [14]. *3D*, Three-dimensional. (A) Vat Polymerization, (B) Powder bed fusion (C) Material extrusion (D) Binder jetting.

technology using ceramics is highlighted through the applications. Peng et al. [15] used Al_2O_3 ceramics parts that were printed by inkjet printing technology with different printed paths distributions, such as the spiral printed path, round trip straight printed path, and ladder lap printed path. The influence of inkjet-printed paths on sintering performance and thermal shock resistance of the Al_2O_3 green bodies was investigated. The sintering performance of the green sample with the ladder lap printed path was the highest among the three samples. The samples were built up from layers of ceramic ink. Sintered at 1550, its ;bulk density and porosity reached 3.73 g/cm^3 and 10.80%, respectively. In addition, the thermal shock resistance of the sample with the step print path reached 11 times. The results suggest that the optimization of the printed path provides an effective way to print 3D ceramics with good performances through 3D inkjet-printing technology. Mask projection stereolithography (MP-SL) can be used to fabricate complex ceramic parts layer by

layer through the photopolymerization of ceramic suspensions. The broadening or lateral overcure of the curing shape occurs because of light scattering effects. Achieving a better dimension and strength quality by adjusting light energy delivery in the boundary mask area has been insufficiently investigated thus far [16]. In his study, the conventional mask was segmented into the boundary and interior masks. The exposure time and power of the boundary mask (two pixels wide) were varied to investigate the effects of segmented exposure. The segmented exposure constrained the dimension errors to a width of within two pixels for a feature dimension of fewer than 1200 μm. It further smoothed the lateral surface of the green part to achieve Ra values of below 6 μm. Moreover, enhancing the boundary mask increased the flexural strength and Weibull modulus to 248 MPa and 11.1, respectively. The micro- and macrostructures of the fabricated parts before and after the thermal treatment are shown in Fig. 17.6.

The results indicate that segmented exposure can potentially be used in complex lattice ceramic structures. Monodispersed and spherical β-TCP granules for 3DP were prepared by spray drying with the surface modification of PVB [17]. Modifier PVB was attached to the particle surface to form the cross-linked network structure and keep them combined with each other into aggregates. The morphology, size, forming performance, and crushing behavior of granules, as well as the microstructure and density of as-fabricated β-TCP ceramics were used to optimize the PVB contents. Promising results could be expected that PVB contents were 1.0 wt.% and the average particle size of granules was 37.36 mm. The modified granules

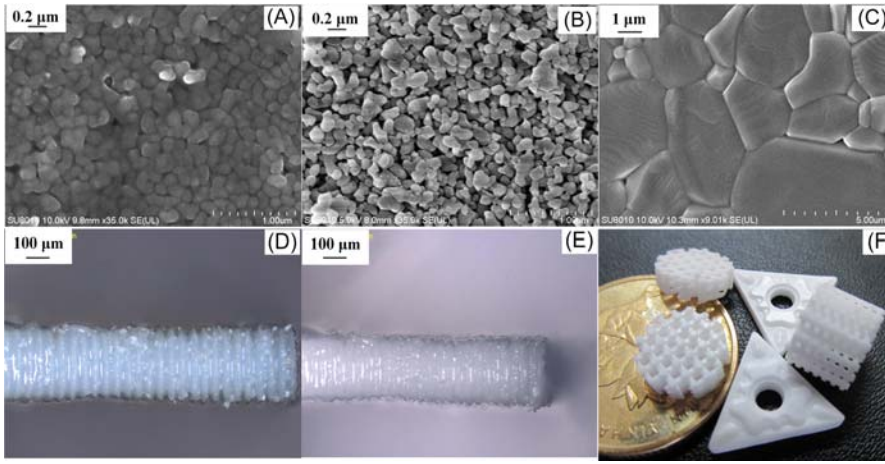

Figure 17.6 Micro- and macrostructures of the fabricated parts before and after the thermal treatment: (A) SEM image of the green part; (B) SEM image of the brown part after debinding at 525°C; (C) SEM image of the sintered part after sintering at 1650°C for 2 h; (D) optical image of the plate (green part, parameter A-1, plate number 1); (E) optical image of the plate (sintered part, parameter A-1, plate number 1); and (F) an indexable insert and a porous scaffold, used to demonstrate the capability of high precision fabrication [16]. *SEM*, Scanning electron microscopy.

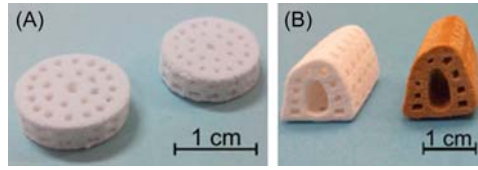

Figure 17.7 Picture of (A) cylinder scaffolds and (B) custom-made scaffolds [18].

exhibited excellent forming performance with monodispersed and spherical aggregates for 3DP. They could be completely crushed under 80 MPa without obvious intergranules void. These granules with 1.0 wt.% PVB had defined strengths for ceramic forming. The good dispersity and flowability assured the high density and uniform porous structure of β-TCP ceramics, which were used as biological ceramic materials and completely met the standard for bone tissue engineering. Particle size gradation was regarded as an effective method for overcoming the contradicting requirements in 3DP. Particle size gradation was optimized to obtain both acceptable flowability of the powder material and high-strength 3D printed glass−ceramic products [18]. As an inorganic material, glass−ceramic material possesses good bioactivity, osteoconductivity, chemical stability, and mechanical properties, and therefore it is regarded as a good candidate for bone scaffold (Fig. 17.7).

The effect of gradation on the printing process, sintering process, and performance of the 3D printed glass−ceramic products was investigated comprehensively. The glass−ceramic powders with three size ranges were mixed in certain proportions and applied to print parts. The result showed parts printed with powder mixed by 60 wt.% 45−100 μm and 40 wt.% 0−25 μm particles had a satisfactory density of 1.60 g/cm^3 and bending strength of 13.8 MPa. The flowability decreased with an increasing proportion of fine particles. Part density was determined by the powder bulk density in the powder bed as well as the shrinkage during sintering while the strength of part was found to be dependent on the sintering degree. Directionally solidified eutectic ceramics such as Al_2O_3/ZrO_2 were promising structural materials for applications in a harsh environment with an ultrahigh temperature. Liu et al. [19] adopted assistant heating laser 3DP and Al_2O_3/ZrO_2 eutectic samples were manufactured suppressing the formation of cracks. The setting of the equipment and the schematics of the experimental process of the laser 3DP are shown in Fig. 17.8. This consists of a PRC2000 continuous wave CO_2 laser, a four-axis numerical control working table, a powder feeder with a lateral nozzle, and a preheating system close-loop controlled by the thermal couple and the temperature controller (Shimaden, SRS13A).

The dependence of the average rod spacing (λav) on the scanning rate (V) follows a relation with $\lambda_{av}V^{0.5} = 1\,\mu m^{1.5}\,s^{-0.5}$. Typical eutectic microstructures, so-called complex regular, were analyzed with respect to their evolution with modulating the growth conditions. The formation mechanism of the solidification defect, shrinkage porosity, was discussed and the defect was found to be significantly suppressed by optimizing the solidification parameters. The maximum hardness and

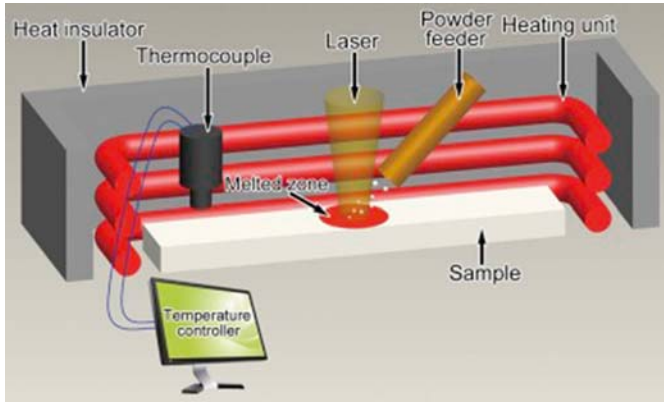

Figure 17.8 Schematic diagram of the equipment and the experimental process of the laser 3D printing [19]. *3D*, Three-dimensional.

fracture toughness were measured to be 16.7 GPa and 4.5 MPa $m^{1/2}$, respectively. The interplay between the propagation of cracks and the Al_2O_3/ZrO_2 interface was discussed. Biswas et al. [20], unlike the UV or visible curable resins generally used to 3D print the green ceramic parts, presented a new concept of thermally induced gelation of methylcellulose (MC) to retain the shape while printing of the parts. In this process, magnesium aluminate spinel paste formulated with 0.25% by weight of MC having optimized rheology was 3D printed simultaneously with exposure to the hot air flow close to the MC gelation temperature. Magnesium aluminate spinel test specimens were also shaped using generally practiced slip casting process for the sake of comparison, as the slip casting process was not adaptable to fabricate the parts' microfeatures by 3DP in the present study. The formed parts by both the techniques were pressure less sintered at 1650°C. 3D printed spinel specimens have shown comparable density, hardness, and flexural strength with respect to the slip cast specimens complemented by fractographic analysis. Maurath and Willenbacher presented [21] a novel processing route for manufacturing highly open-porous, hierarchically structured ceramics via direct ink writing (DIW). We manufactured cellular samples with overall porosities up to 88% that exhibit fully open-porous struts with porosities between 45% and 60% and pore sizes $\times 50$, $3 < 6$ m using capillary suspension-based inks. Fig. 17.9 shows the processing steps for manufacturing ceramic structures via filamentary-based DIW. The capillary suspensions were extruded through tapered nozzles (inner diameters of: 200, 250, 610 μm; Nordson EFD).

An innovative processing strategy enabled manufacturing of crack-free, undeformed, cellular ceramic samples. We printed hexagonal honeycomb structures that showed exceptionally high specific strength under compression load and significantly enlarged the strength-density range that was covered by sintered capillary suspensions, so far. Without loss of mechanical strength, the density of ceramic parts was decreased by about a factor of 2−3. Strength of in-plane and out-of-plane

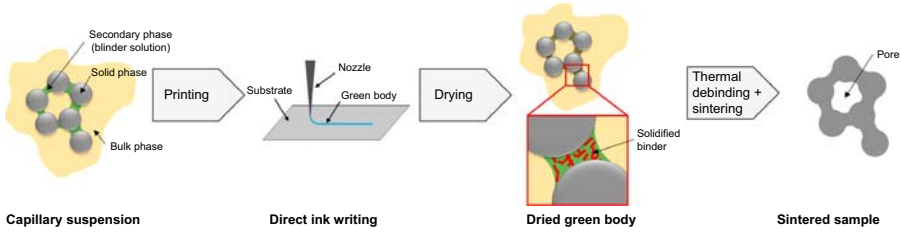

Figure 17.9 Flow sheet of the processing route for direct ink writing of capillary suspension based inks. The open-porous structure of the sintered filaments is based on the open-porous network of capillary suspensions that serve as precursor for the ceramic part [21].

loaded hexagonal honeycomb structures varies according to common scaling laws for cellular structures. The honeycombs were mechanically more efficient than bulk specimens from capillary suspensions since they show a distinctly lower sensitivity of strength on density. Zhu et al. [22] developed a novel method to fabricate carbon fiber reinforced SiC (Cf/SiC) composites by combining a 3DP and liquid silicon infiltration process. Green parts were first fabricated through 3DP from a starting phenolic resin-coated carbon fiber composite powder; then the green parts were subjected to vacuum resin infiltration and pyrolysis successively to generate carbon fiber/carbon (Cf/C) preforms; finally, the Cf/C preforms were infiltrated with liquid silicon to obtain Cf/SiC composites. The preparation process is schematically shown in Fig. 17.10.

The 3DP processing parameters show significant effects on the physical properties of the green parts and also the resultant Cf/C preforms, consequently greatly affecting the microstructures and mechanical performances of the final Cf/SiC composites. The overall linear shrinkage of the Cf/SiC composites was less than 3%, and the maximum density, flexural strength, and fracture toughness were 2.83 ± 0.03 g/cm^3, 249 ± 17.0 MPa, and 3.48 ± 0.24 MPa m$^{1/2}$, respectively. It demonstrates the capability of making near-net-shape Cf/SiC composite parts with complex structures. A stereolithography (SLA)-based method of 3DP was successfully used to fabricate a complex-shaped triangular zirconia cutting tool with a tool withdrawal groove and a honeycomb ceramic component [23]. A diagram of the working principles of digital light processing (DLP) is shown in Fig. 17.11.

The sintered bodies displayed significant shrinkage after sintering, with the maximum shrinkage being 35.26%. The X-ray powder diffraction pattern indicated that the crystalline phase of the parts was the t-ZrO_2 phase, while SEM characterization revealed that the sintered bodies were composed of densely packed submicron-grade grains, without any discernible pores. The density of the parts was measured as 97.14% via Archimedes' water displacement method, which was consistent with the results of SEM characterization. Additionally, the measured Vickers hardness and fracture toughness of the fabricated parts were 13.0597 GPa and 6.0380 MPa m$^{1/2}$, respectively. These values were close to the structural properties of common zirconia ceramics prepared by conventional approaches. Hence, a novel

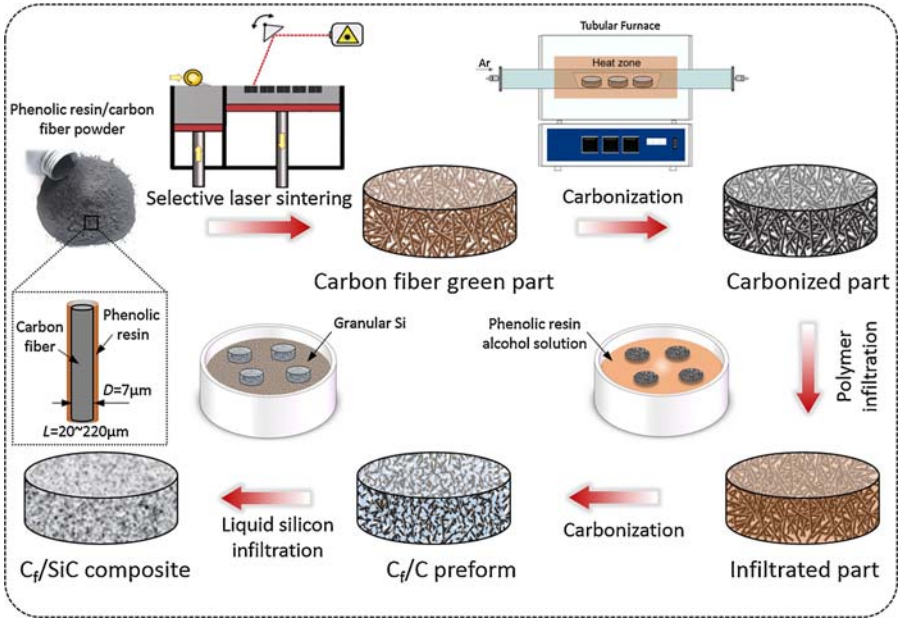

Figure 17.10 The schematic diagram of the procedure for fabricating Cf/SiC composite parts [22].

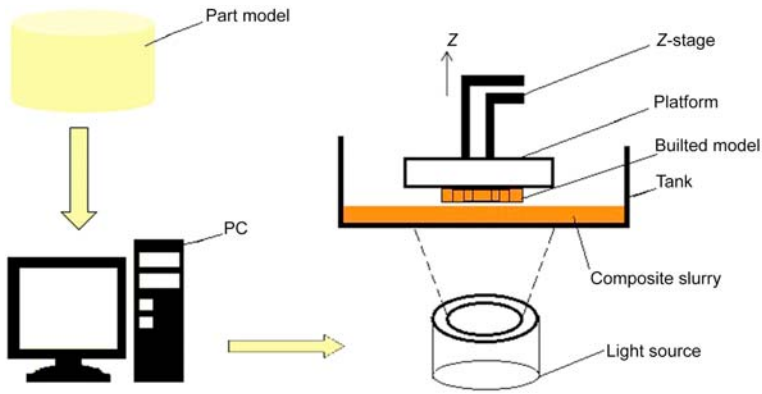

Figure 17.11 The working principles of DLP [23]. *DLP*, Digital light processing.

DLP- SLA-based 3DP process for the fabrication of complex and dense zirconia ceramic parts has been proposed in this work. Zhang and Yang [24] described two ceramic-forming technologies based on 3DP. One technology forms the product with 3DP indirectly, while the other technology forms the product directly with 3DP. The whole 3DP technique, including computer-aided design, 3DP of a model

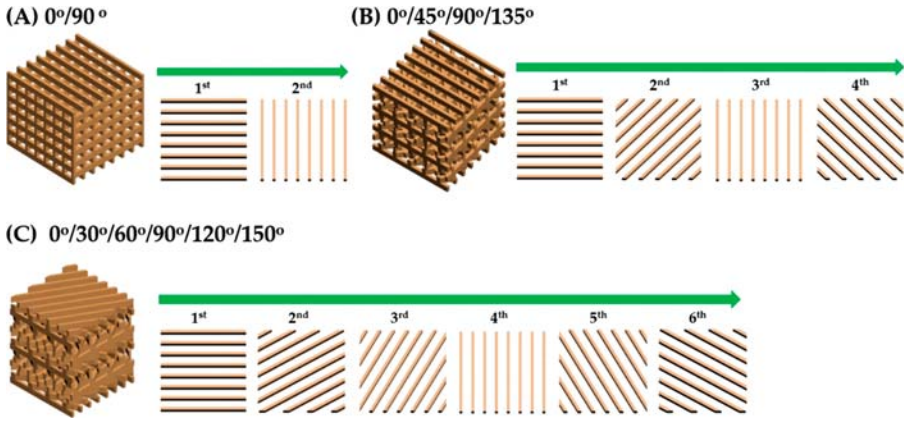

Figure 17.12 Schematic diagram showing the porous structures of various CaP scaffolds with different pore orientations with their top-down view of the repeating CaP frameworks [25]. *CaP*, Calcium phosphate.

with plastic laminate, molding with plaster, and slip casting, was shown to produce a pineapple cup. Compared with the traditional ceramic-forming technology, the new method was more efficient, and articles can be precisely made, especially for mass production of complicated designs. Lee et al. [25] demonstrated the usefulness of the lithography-based ceramic 3DP technique with a specifically designed top-down process for the production of porous CaP ceramic scaffolds with tailored pore orientations and mechanical properties. The processing parameters including the preparation of a photocurable CaP slurry with high solid loading ($j = 45$ vol.%), the exposure time for photocuring process, and the initial designs of the porous scaffolds were carefully controlled. Three types of porous CaP scaffolds with different pore orientations (i.e., 0_/90_, 0_/45_/90_/135_, and 0_/30_/60_/90_/120_/150_) were produced as a way to control mechanical properties of the scaffolds (Fig. 17.12). Each scaffold was composed of straight CaP frameworks arranged in a controlled, periodic pattern.

All the scaffolds exhibited a tightly controlled porous structure with straight CaP frameworks arranged in a periodic pattern while the porosity was kept constant. The porous CaP scaffold with a pore orientation of 0_/90_ demonstrated the highest compressive strength and modulus due to a number of CaP frameworks parallel to the loading direction. On the other hand, scaffolds with multiple pore orientations may exhibit more isotropic mechanical properties regardless of the loading directions. The porous CaP scaffolds exhibited an excellent in vitro apatite-forming ability in a simulated body fluid (SBF) solution. These findings suggest that porous CaP scaffolds with tailored pore orientations may provide tunable mechanical properties with good bone regeneration ability. With the development of information technology, 3DP technology, which was called the symbol of the third industrial revolution and characterized by digitalization,

artificial intelligence, and new materials application, has brought a revolutionary reform to the future product manufacture. On the basis of the application of 3DP technology to the ceramic product design, an introduction to the working principle of 3DP technology and the advantages of its application to the ceramic product design was made, and the influence of 3DP technology development on the ceramic product design was discussed from four aspects, including design ideas, design models, ceramics designers, and product development modes, finally together with a further analysis of the limitations as well as the prospects of the application of 3DP technology to the ceramic product design [26]. In situ HA/apatite−wollastonite glass−ceramic composite was fabricated by a 3DP technique and characterized [27]. It was found that the as-fabricated mean green strength of the composite was 1.27 MPa which was sufficient for general handling. After varying sintering temperatures (1050°C−1300°C) and times (1−10 hours), it was found that sintering at 1300°C for 3 hours gave the greatest flexural modulus and strength, 34.10 GPa and 76.82 MPa, respectively. This was associated with a decrease in porosity and an increase in densification ability of the composite resulting from liquid phase sintering. Bioactivity tested by soaking in SBF and in vitro toxicity studies showed that 3D printed HA/A−W glass ceramic composite was nontoxic and bioactive. A new CaP layer was observed on the surface of the composite after soaking in SBF for only 1 day while osteoblast cells were able to attach and attain normal morphology on the surface of the composite.

17.3 The three-dimensional printing technology in physics

AM is an innovative complex shaping technique with unlimited freedom and flexibility in fabrication. Though the majority of AM processes were focused on polymers, it was later extended to metals and very recently to ceramics. Conventional prototyping of ceramics, especially complex parts, proceeds through several iterations of design and fabrication of dies, molds, fixtures, etc. which were cost-intensive and also time is taken to arrive at the final designs. Often the finished parts also need machining to achieve the microfeatures. 3DP of ceramics with its inherent advantages simplifies the above issues, especially for fabrication of prototypes leading to the selection of optimum designs in a very short time. Further, as the same infrastructure is based on the printing of ceramic shapes using software-generated virtual images, it also results in lower cost. This section presents the role of physics in developing 3DP technology by focusing on the significant research done in this direction. Xing et al. [28] developed a high solid loading suspension of Al_2O_3 dispersed in a UV curable acrylic-based resin, suitable for SLA-3DP of microcomponents with complex shapes. Silane coupling agents KH550, KH560, and the stearic acid (SA) were investigated as the

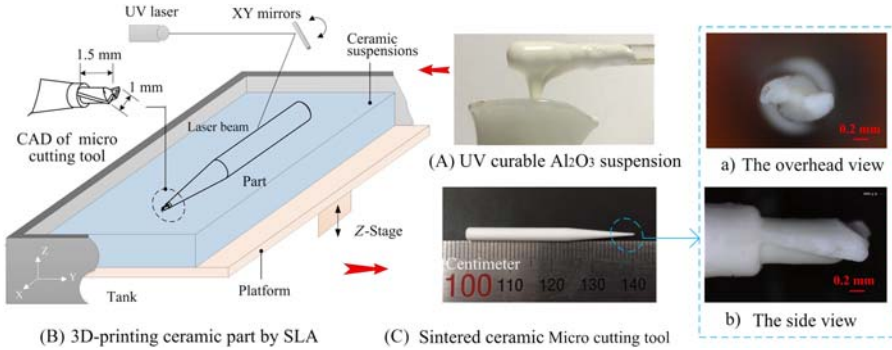

Figure 17.13 Schematic representing the fabrication process of Al_2O_3 microcomponents via SLA technology [28]. *SLA*, Stereolithography.

surfactants for Al_2O_3 particles, and the low viscosity acrylic monomers ACMO, HDDA, and NPG2PODA were used as the reactive diluents for Di-TMPTA-based premixed resins. Al_2O_3 ceramic microcomponent was manufactured using SLA technology and subsequent sintering, as shown in Fig. 17.13.

The modified Al_2O_3 powders exhibit different wettability with premixed resins to cause the different rheology behaviors among the formulated suspensions. The KH560-modified Al_2O_3 powders show the better wettability performance with NPG2PODA/Di-TMPTA-based solvents and their corresponding 75 wt.% Al_2O_3 suspensions (44.2 vol.% solid loading) with a viscosity <25,000 mPa s at 30 second^{-1} shear rate were successfully prepared. The further analyses approve that hydrophobic structures of KH560 molecules have been introduced on the surfaces of Al_2O_3 powders. This consequence results in the lowest sediment rate and contact angle between the KH560-modified Al_2O_3 powders and NPG2PODA/Di-TMPTA-based resins, which contributes to their better wettability performance. The optimum parameter of NPG2PODA concentration of prepared suspension was range from 50% to 70% in the premixed resin. Finally, Al_2O_3 ceramic microcomponent with 99.5% density was fabricated via an SLA process and subsequent sintering. Both the Al_2O_3 suspensions and sintered microcomponents exhibit good homogeneous microstructures, indicating an optimistic dispersal uniformity of KH560-modified Al_2O_3 particles in the premixed resins. Li et al. [29] developed a high solid loading suspension of Al_2O_3 dispersed in a UV-curable acrylic-based resin, suitable for SLA-3DP microcomponents with complex shapes. Silane coupling agents KH550, KH560, and SA were investigated as the surfactants for Al_2O_3 particles, and the low viscosity acrylic monomers ACMO, HDDA, and NPG2PODA were used as the reactive diluents for Di-TMPTA-based premixed resins. The modified Al_2O_3 powders exhibit different wettability with premixed resins to cause the different rheology behaviors among the formulated suspensions. The KH560-modified Al_2O_3 powders show the better wettability performance with NPG2PODA/Di-TMPTA-based solvents and their corresponding 75 wt.% Al_2O_3

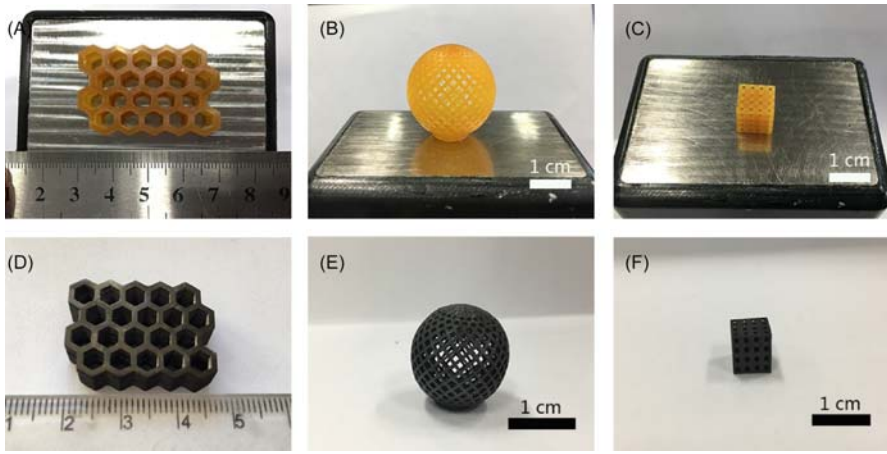

Figure 17.14 The pictures of (A−C) the printed green components and (D−F) the corresponding pyrolyzed SiBCN ceramic components [29].

suspensions (44.2 vol.% solid loading) with a viscosity <25,000 mPa s at 30 second^{-1} shear rate were successfully prepared. Several images of the SiBCN examples before and after pyrolysis were shown in Fig. 17.14. The printed green body had fine and complicated features, which could be well preserved after pyrolysis at 900°C without visible deformation due to the homogeneous shrinkage of the material.

The further analyses prove that hydrophobic structures of KH560 molecules have been introduced on the surfaces of Al_2O_3 powders. This consequence results in the lowest sediment rate and contact angle between the KH560-modified Al_2O_3 powders and NPG2PODA/Di-TMPTA-based resins, which contributes to their better wettability performance. The optimum parameter of NPG2PODA concentration of prepared suspension ranged from 50% to 70% in the premixed resin. Finally, Al_2O_3 ceramic microcomponent with 99.5% density was fabricated via an SLA process and subsequent sintering. Both the Al_2O_3 suspensions and sintered microcomponents exhibit good homogeneous microstructures, indicating an optimistic dispersal uniformity of KH560-modified Al_2O_3 particles in the premixed resins. For SLA 3DP applications, Al_2O_3 ceramic particles with a different coating thickness of silane coupling agent (VTES, vinyltriethoxysilane) were prepared by hydrolysis and condensation reactions [30]. Then, VTES-coated Al_2O_3 ceramic particles were dispersed in commercial photopolymers (3DK-A83B) based on interpenetrating network phenomena (Fig. 17.15).

The morphology and average coating thickness of VTES-coated Al_2O_3 ceramic particles were observed by field-emission (FE) transmission electron microscopy, and the particle size of VTES-coated Al_2O_3 ceramic particles was investigated by a laser scattering particle size distribution analyzer. The dispersion stability of the

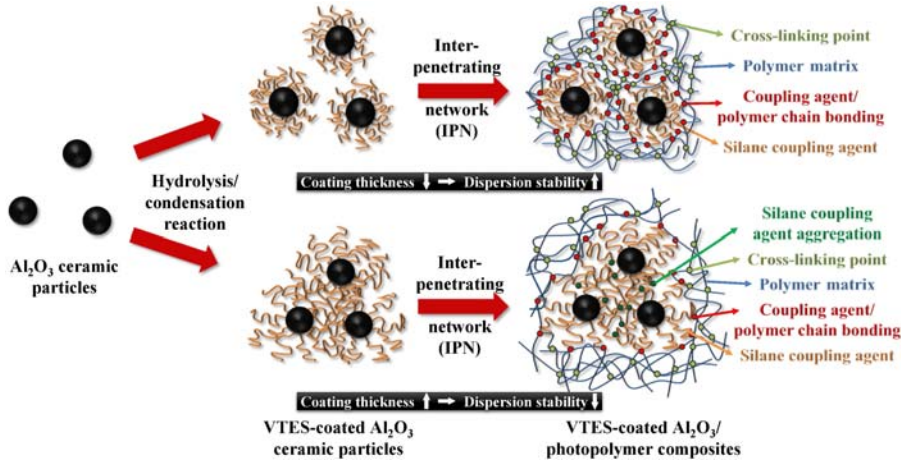

Figure 17.15 Schematic illustration of dispersion mechanism of ceramic particles according to coating thickness of silane coupling agents in photopolymer solution [30].

VTES-coated Al_2O_3/3DK-A83B composite solution with different VTES coating thicknesses and ceramic contents was investigated by Turbiscan and relaxation nuclear magnetic resonance, while the optimum coating conditions for VTES were also observed. In the case of Al_2O_3 ceramic particles with a similar VTES coating thickness, the dispersion stability was similar, even when the ceramic content increased. The cross-sectional images of 3D printed objects were observed by FE-SEM, and about 48% of volume shrinkage of the 3D printed objects was calculated after sintering. Park et al. [31] presented a new conversion process combined with a 3DP technique that has been developed for application in the fabrication of a ceramic core. The new process allows the provision of a sufficient amount of inorganic binder on the particle surface and at the interface between particles. Two types of polyvinyl alcohol (PVA) with a similar molecular structure, but with a large difference in decomposition temperature were used as an organic binder. A green body was prepared with two kinds of PVA using a 3D printer, which was heat-treated at 250°C to evaporate the PVA with the lower decomposition point. The heat-treated core samples were dipped into the inorganic precursor and then dried and heat-treated at 1000°C for the organic−inorganic conversion process. In the new conversion process, the formability of the core sample was controlled through the remaining organic compounds and the inorganic binder penetrating between particles and/or coated on the particle surface, and the firing strength was attributed to the glass phase generated by the inorganic precursor. The firing strength of the core prepared through the new process was improved because of the increase in the inorganic precursor that infiltrated the spaces/sites of the decomposed PVA, and it could be readily applied to the production of a core using 3DP techniques without further shrinkage in high-temperature heat treatment. Kunchala

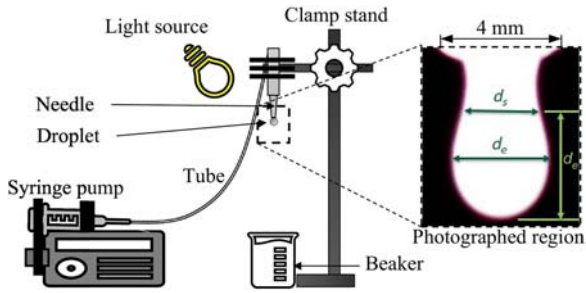

Figure 17.16 Schematic of pendant droplet test set up. Inset shows the image of a droplet captured during testing, showing the equatorial and selected-plane diameters [32].

and Kappagantula [32] examined the effects of nanoparticle densifiers added to printing liquid on the mechanical performance and manufacturability of ceramics made using binder jetting. "Green" alumina samples were synthesized with filler particles of average particle size 40 μm embedded with nanoparticles of the average size of 50 nm suspended in the printing liquid with varying concentration of 0−15 wt.%. Samples were characterized for density, porosity, compressive strength, and printing liquid penetration depth in the filler powder layer assessed using surface tension testing, as illustrated in Fig. 17.16.

Results showed that the presence of the nanoparticle had a marked effect on the physical and mechanical properties of the samples whose relative density (RD) increased by about 30%. Micro-CT imaging of the samples showed a decrease in interparticle pores with an addition of 15 wt.% alumina nanoparticles. Compressive strength improved by 743%, from 76 to 641 kPa as the densifier content was increased from 0 to 15 wt.%. The surface tension of the printing liquid decreased from 44 to 23 mN/m with increasing densifier concentration from 0 to 15 wt.%, indicating that the penetration depth of the printing liquid would decrease with increasing densifier content. Implications of this approach on high-density ceramic part printing efficiency were discussed in detail. Shao et al. [33] presented the 3D gel-printing (3DGP) process based on a water-based gelation system which was was used to prepare zirconia (ZrO_2) ceramic parts. 3DGP was a new printing method, which was based on a 2-hydroxyethyl methacrylate gelation system to produce complex shape parts, as depicted in Fig. 17.17.

The water-based ZrO_2 ceramic slurry with a solid volume fraction of 50 vol.% was prepared and its rheological property was characterized. The surface roughness was Ra 8.90 μm on the printed green sample and Ra 8.25 μm on the sample after sintered at 1520°C for 2 hours. The RD, the Vickers hardness, and the transverse rupture strength of the sintered sample were 97.6%, 14.4 GPa, and 450 MPa, respectively. Tian et al. [34] fabricated successfully $BN-SiO_2$ porous ceramics with high porosity using bottom-up DLP SLA and pressureless sintering. The phase composition, microstructure, compressive strength, dielectric properties, and porosity of the porous material were investigated. The results show that the skeleton of

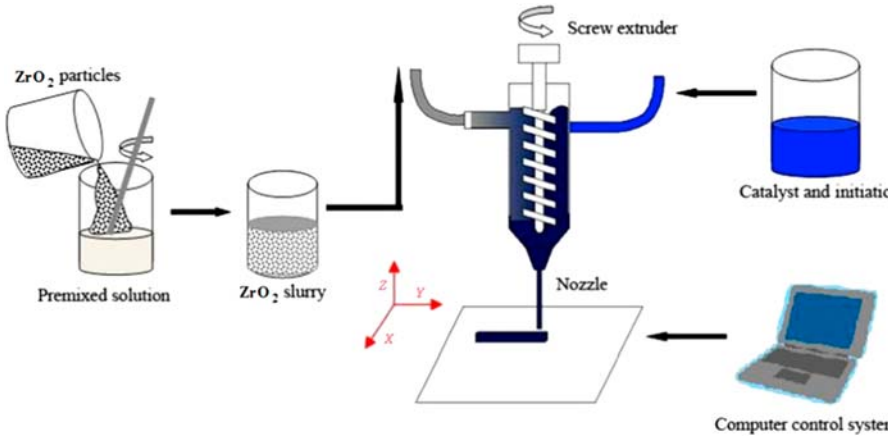

Figure 17.17 Schematic diagram of the 3DGP process for printing zirconia parts [25].
3DGP, Three-dimensional gel-printing.
From X.Y. Ren, H.P. Shao, T. Lin, H. Zheng, 3D gel-printing—an additive manufacturing method for producing complex shape parts, Mater. Des., 101 (2016), pp. 80-87, https://doi.org/10.1016/j.matdes.2016.03.152.

the porous material was composed of h-BN, and the silica was "coated" on the surface of the h-BN particles. The dielectric constant, dielectric loss, compressive strength, and porosity of the material were 1.41−1.45, 1.85×10^{-3}−1.93×10^{-3}, 11.2 MPa, 77.2%, respectively. These characteristics make the h-BN−SiO_2 porous ceramics useful in the wave transmitting field. The HA scaffolds doped with $MgSiO_3$ were prepared by 3DGP technology by He et al. [35]. The effect of $MgSiO_3$ in the scaffold characteristics has been studied, and the composite ceramic scaffold with higher strength was obtained. The viscosity of different $MgSiO_3$ weight percentages slurry decrease with the shear rate increases. When the solid loading was 50 vol.% and the shear rate was 100 $S-1$, the viscosity of the slurry decreased with the weight percent of $MgSiO_3$ increasing. The scaffold has interconnected internal structures and the sintered body has a pore size of about 350−620 μm. The porosity of the scaffolds with different weight percents of $MgSiO_3$ was kept at 65%, and the scaffold with 3% $MgSiO_3$ has the highest compressive strength of 93.15 MPa. As an increasing weight percent of $MgSiO_3$, the compressive strength of the scaffold gradually decreases and remains at 40 MPa eventually. The ceramic scaffold with 3% $MgSiO_3$ has better degradability than that of other weight percent of $MgSiO_3$. After soaking in Tris−HCl solution for 5 weeks, the weight loss of the scaffold reached 9.91%. Kim et al. [36] developed a simple and facile method to fabricate functional bulk barium titanate ($BaTiO_3$, BT) ceramics using the paste extrusion 3DP technique. The BT ceramic was a lead-free ferroelectric material widely used for various applications in sensors, energy storage, and harvesting. There were several traditional methods (e.g., tape casting) to

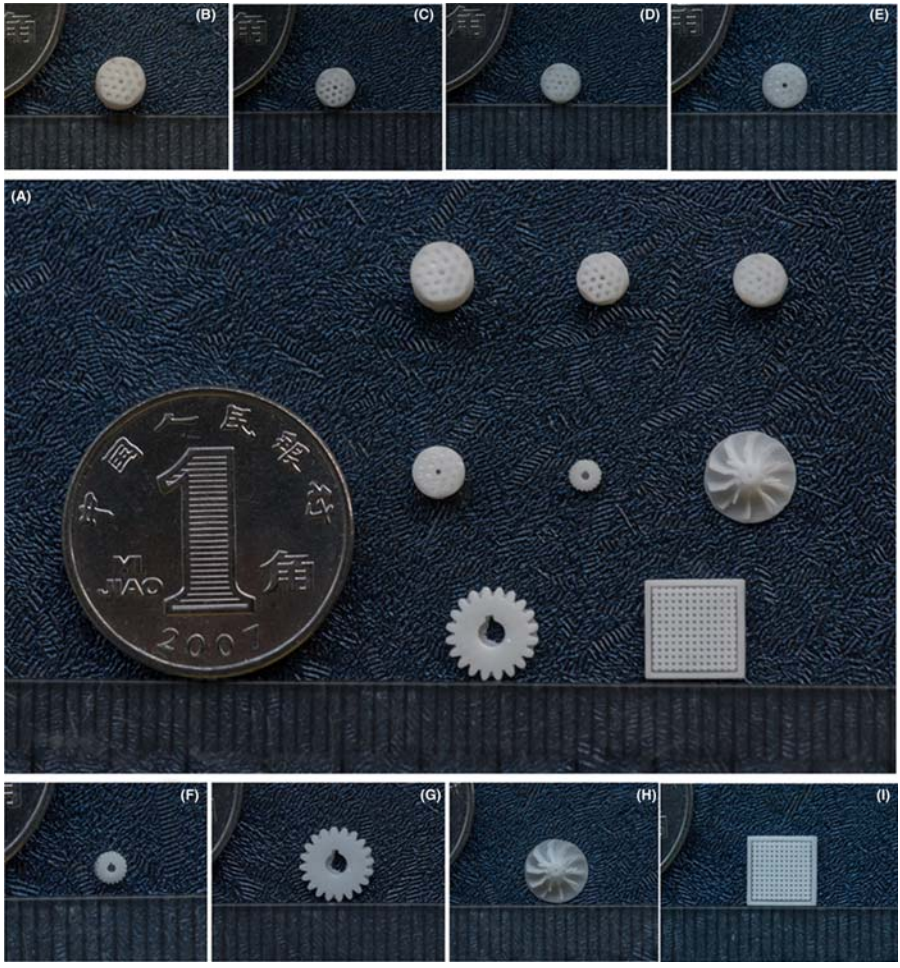

Figure 17.18 (A) Typical oxide ceramic microcomponents with high precision and high smoothness; (B−E) microcellulars with different diameters and helical pore structure; (F and G) microgears with different geometry and size; (H) a microturbine rotor; (I) a periodic columnar array with the diameter of the pillar $\sim 100-200\ \mu m$ [37].

process bulk BT ceramics but they have disadvantages, such as difficult handing without shape deformation, demolding, complex geometric shapes, expansive molds, etc. Fig. 17.18 shows each 3D printed sample at different binder ratios of 1:14, 1:10, and 1:8.8, which are BT vol.% of 20.50, 26.25, and 28.66, respectively.

In this research, the paste extrusion 3DP technique was utilized to overcome the traditional issues and develop printable ceramic suspensions containing BT ceramic powder, polyvinylidene fluoride (PVDF), *N*,*N*-dimethylformamide through a simple

mixing method and chemical formulation. This PVDF solution performed multiple roles of binder, plasticizer, and dispersant for excellent manufacturability while providing high volume percent and density of the final bulk ceramic. Based on empirical data, it was found that the maximum binder ratio with good viscosity and retention for desired geometry was 1:8.8, while the maximum BT content was 35.45 vol.% (77.01 wt.%) in order to achieve a maximum density of 3.93 g/cm^3 (65.3%) for 3D printed BT ceramic. Among different sintering temperatures, it was observed that the sintered BT ceramic at 1400°C had highest grain growth and tetragonality which affected high performing piezoelectric and dielectric properties, 200 pC/N and 4730 at 10^3 Hz, respectively. This paste extrusion 3DP technique and simple synthesis method for ceramic suspensions were expected to enable rapid massive production, customization, the design flexibility of the bulk piezoelectric and dielectric devices for next-generation technology. Liu et al. [37] successfully developed a unique 3DP approach based on mask−image−projection SLA to fabricate structural ceramics microcomponents with low cost and high efficiency. Ultradense submicron crystalline ceramics without fierce grain growth could be obtained via tailoring the sintering kinetics. The ZrO_2 ceramic microcomponents reached the highest RD of 99.7% with the average grain size of 0.52 μm upon sintering at 1550°C while the Al_2O_3 ceramic micro components reached its highest RD of 98.31% with the average grain size of 2.6 μm upon sintering at 1600°C. Oxide ceramics microcomponents of fully flexible design can be produced easily without visible defects via the method developed in this study, which demonstrates significant potential in the applications of microelectromechanical systems, microoptical electronics systems, and microoptoelectromechanical systems. The method developed in this study has addressed the problem successfully by healing the interlayer interface defects in the densification process via the sintering kinetic window and microstructure evolution. The current work provides a promising opportunity to fabricate structural ceramic microcomponents with complex shape, high precision, and high surface smoothness. Transformation of gypsum model fabricated by 3DP into HA by treating in ammonium phosphate solution was possible. However, 3DP powder supplied by the manufacturer contains unknown additives which may be questionable for biomaterials. Accordingly, pure plaster of Paris (POP) powder was used for fabrication in the present study [38]. For accurate fabrication, reduction of supplied binder ink to 80% of the standard amount for 3DP powder supplied by the manufacturer was found to be the optimal condition for POP fabrication. The transformation from POP to HA was done by immersing into 1 mol/L ammonium phosphate solution. However, preheating of the fabricated POP specimen at 200°C for 30 minutes to change from calcium sulfate dihydrate into calcium sulfate hemihydrate could accelerate the transformation into HA effectively. To increase compressive strength, HA transformed specimen was sintering at 1150°C for 3 hours. The compressive strength increased four times compared with a transformed HA specimen. However, the crystal structure was transformed to β-TCP due to the chemical reaction between the transformed HA and remained phosphate from ammonium phosphate solution at the sintering temperature. A sophisticated application of the

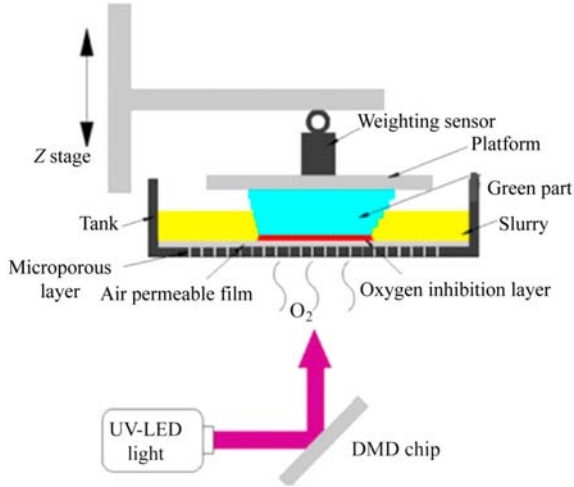

Figure 17.19 Bottom-up MP-SL equipment with an oxygen-controlled concentration tank and a separation-force measuring device [40]. *MP-SL*, Mask projection stereolithography.

present 3DP method to fabricate the freeform bio ceramic for the osseous defect was attempted, and jaw bone defect filling biomaterial of β-TCP and scaffold with microporous structures could be fabricated. The present 3DP method has the possibility to fabricate freeform bioceramic for osseous defect or scaffold. Al_2O_3 ceramics were printed by SLA from particles with different particle size distributions, which were the microsized Al_2O_3, nanosized Al_2O_3, and a mixture of both [39]. The influence of the particle size and the debinding method on the density and morphology of the sintered bodies were investigated. The density of the samples containing both microsized and nanosize alumina particles was highest among the three samples. Furthermore, the samples subjected to the vacuum debinding showed a higher density compared with the samples subjected to the traditional thermal debinding. The results suggest that the combination of a powder with a bimodal particle size distribution and the vacuum debinding process offers an effective way to print 3D ceramics with good performance through SLA. To fabricate ceramic components with a complex structure, the bottom-up MP-SL technique was employed (Fig. 17.19).

However, a fracture or a defect was normally found because of the large separation force formed between the newly cured layer and the bottom surface of the slurry tank. Hence, to overcome this issue, an oxygen-permeable layer was integrated into the conventional MP-SL system for printing a β-TCP ceramic slurry by Lian et al. [40]. The system was based on the fact that oxygen inhibits the photopolymerization process by consuming free radicals. The effects of the light exposure time and oxygen concentration on the curing depth and thickness of the oxygen-inhibition layer were investigated. Moreover, the separation forces were indirectly

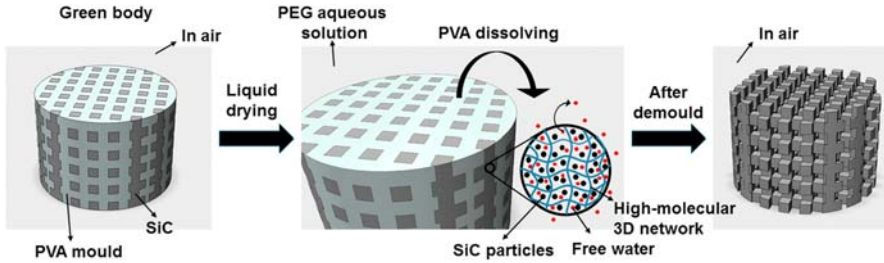

Figure 17.20 Liquid drying process of gelled silicon carbide green body. (For interpretation of the references to color in this figure legend, the reader is referred [42].)

determined using a weight sensor. The results show that the oxygen-inhibition layer helped in reducing the separation force by 60% compared to that wherein oxygen was not employed. The solid loading could be increased by up to 44 vol.% and the printable cross-sectional area by five times. In summary, the proposed oxygen-controlled bottom-up MP-SL technique helped in improving the ceramic printing efficiency and product quality. The possibility of obtaining complex structure SiC ceramic components by 3DP and gel casting was demonstrated [41]. Polyethylene glycol (PEG)was used to improve the surface quality of SiC specimen and sucrose was used as the carbon source. Effects of PEG and sucrose on the stability and rheological properties of SiC slurry were studied. The mechanism of inhibiting SiC surface exfoliation by PEG and the effect of different sucrose content on the properties and microstructure of SiC ceramic were investigated. The results showed that the addition with 1.0 wt.% PEG and 4.0 wt.% sucrose can improve the surface quality and sintered body properties of SiC ceramics. Therefore a complex structure SiC impeller, which had good surface quality and properties, was successfully fabricated. Silicon carbide reticulated porous ceramics with a regular shape were successfully prepared by combining 3DP, gel casting, and liquid drying [42]. A 3D reticulated structured PVA mold was first fabricated by 3DP, and then a slurry with a high-loading of SiC was gel cast into it. The PVA mold could be removed without any damage to form the gelled SiC structure by immersion in an aqueous solution, that is, by liquid drying, that is shown in Fig. 17.20 of the silicon carbide green body.

In the process the gelled parts were immersed into a concentrated PEG aqueous solution. After sintering, dense SiC ceramics with the reticulated structure were obtained. Zeta potentials, rheological properties, and gelling behaviors of the slurry were studied together with liquid drying technology and characteristics of the ceramics. The present method shows good potential for fabricating porous and/or complex-shaped high-quality ceramics, and could also be applied in various kinds of advanced ceramics. Revelo and Colorado [43] employed kaolinite clay from Colombia as a raw material for the AM of diverse samples using the DIW technique in which a filament of the printing material was extruded from a nozzle. DIW was a simple and inexpensive technology suitable for adaption to large-scale

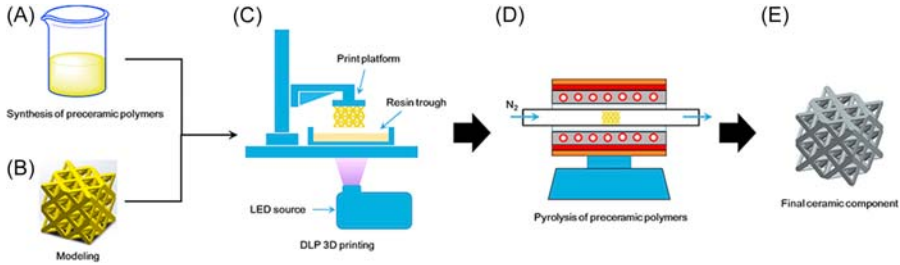

Figure 17.21 Additive manufacturing of polymer-derive ceramics. (A) Photocurable preceramic polymers were prepared by sol−gel method. (B) Octet truss structure was designed using CAD software. (C) The resin was exposed with LED light in a DLP 3D printer. (D) The resin model was heat treated with tube furnace in nitrogen atmosphere. (E) SiOC ceramic component with octet truss structure was obtained after pyrolysis [44]. *3D*, Three-dimensional; *DLP*, digital light processing.

production. Different samples fabricated from clays were manufactured with water to clay ratios (W/C) of between 0.65 and 0.69. Cylinders for compression tests were printed and tested after being cured for 1 day at room temperature and then exposed to 1100°C for 1 hour. Compression, thermal stability, density tests, and Weibull analysis were presented. SEM images showed no significant macro- or microdefects after manufacturing, and X-ray diffraction and Rietveld quantitative analysis revealed different phases. Rheological behavior and several process parameters were also shown. Multiple metals-doped polymer-derived SiOC ceramics with octet truss structure were prepared by employing a photosensitive methylsilsesquioxane as preceramic polymer through the sol−gel method and DLP 3DP [44]. The fabrication process of SiOC ceramic component with octet truss structure is shown in Fig. 17.21, including synthesis of preceramic polymers, modeling, DLP 3DP, and pyrolysis treatment.

The physical and chemical properties of the preceramic polymers and printed octet truss structure SiOC ceramics were investigated. Results show that the organosilicon preceramic polymers have outstanding photocuring properties and could transform into amorphous SiOC ceramics at 800°C−1200°C. It was illustrated that the excellent mechanical properties of SiOC ceramics with octet truss structure (after 3DP and pyrolysis) were attributed to the metal elements pinning in the amorphous matrix on the atomic level. Doping other metal elements such as Fe, Ni, Co, Pt, etc., was thought to bring promising properties for the lattice structure SiOC ceramics and potentially further expand its applications in the future. Biswas et al. [45], unlike the generally employed UV or visible curable resins used to 3D print the green ceramic parts, used a new concept of thermally induced gelation of MC to retain the shape while printing the parts. In this process, magnesium aluminate spinel paste formulated with 0.25% by weight of MC having optimized rheology was 3D printed and simultaneously exposed to the hot air flow close to the MC gelation temperature. Magnesium aluminate spinel test specimens were also shaped

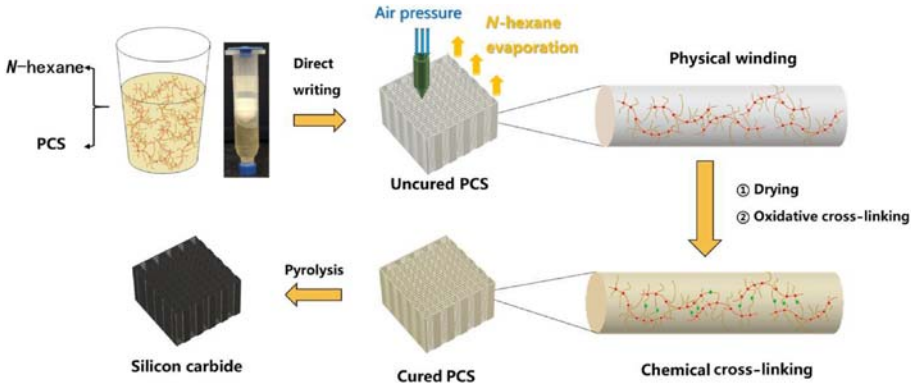

Figure 17.22 Schematic illustration of the fabrication process of SiC with 3D structure [47]. *3D*, Three-dimensional.

using the generally practiced slip casting process for the sake of comparison, as the slip casting process was not adaptable to fabricate the parts' microfeatures by 3DP in this study. The parts formed by both the techniques were pressureless sintered at 1650°C. 3D printed spinel specimens have shown comparable density, hardness, and flexural strength with respect to the slip cast specimens complemented by fractographic analysis. The 3DP of a ceramic core with nanoceramic suspension as a binder was performed to investigate a novel method for the fabrication of a complex-shaped ceramic core [46]. Green bodies were printed using CaO powder as a precursor material and nanozirconia-absolute ethyl alcohol solution suspension as a binder. The green bodies were sintered at 1300°C−1500°C for 2 hours. The effects of binder saturation level on the properties of the sintered bodies were investigated. Increasing the binder saturation level caused decreases in the linear shrinkage of the sintered bodies, but increases in hydration resistance and bending strength. The nanozirconia particles were deposited on the surfaces of the CaO particles and filled the pores of green bodies, and then formed a high melting temperature $CaZrO_3$ layer with the CaO at the surfaces of the CaO grains, which improved the hydration resistance of the CaO-based ceramic core parts. 3D structured SiC ceramics with varying feature sizes (100−400 μm) were achieved by DIW of polycarbosilane (PCS)/*n*-hexane solution [47], as shown in Fig. 17.22.

The rheological properties of the PCS solution and printing parameters were tailored for optimum writing behavior. The integrity and clear surface of the filaments indicated the printing ability to form the self-supporting features along with the rapid evaporation of the solvent. As-printed 3D structured PCS was processed by oxidative cross-linking and pyrolysis and converted to SiC ceramic. Although strong shrinkage occurred during the pyrolysis, SiC ceramic maintained the original 3D structure. Both proper viscoelasticity of printable solutions and the homogeneous shrinkage in the pyrolysis determine the integrity and feature characteristics of 3D structured SiC using DIW preceramic polymer. SiC-based ceramics with the

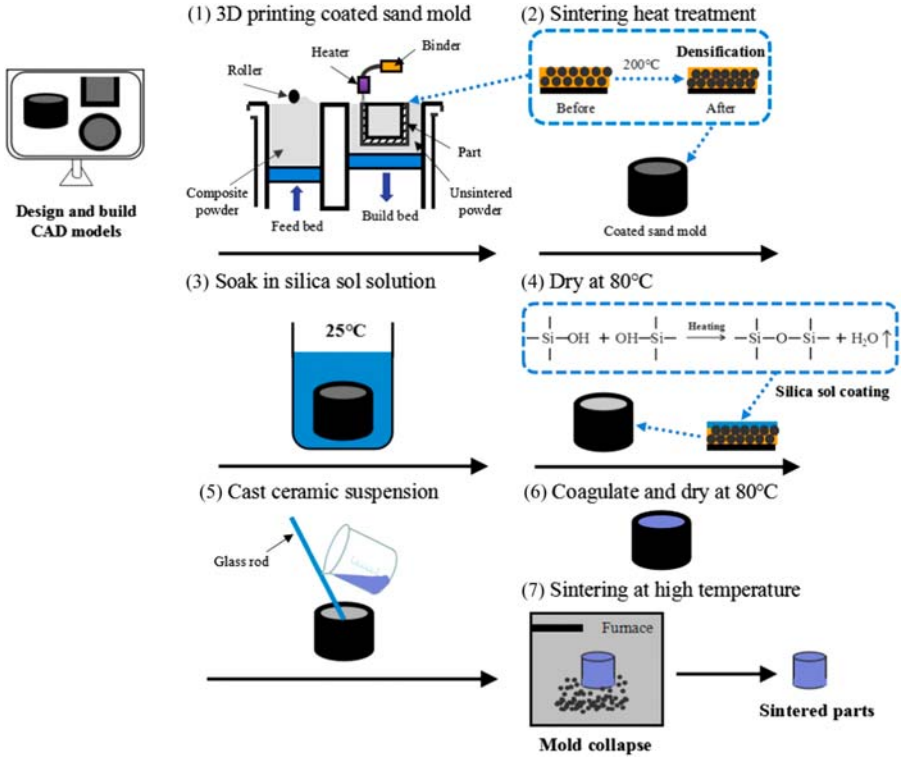

Figure 17.23 Schematic of the preparation of coated sand molds for fabricating porous fibrous alumina ceramics [50].

periodic structure were successfully fabricated by extrusion free-forming 3DP technology and liquid silicon infiltration process [48]. The ceramic slurries containing SiC, carbon black, and chopped carbon fiber were first prepared with the appropriate viscosity and rheological properties; they were formed by extrusion free-forming 3DP technology and densified by liquid silicon infiltration sintering successively, to acquire SiC ceramic composites components. The microstructure and morphology of green parts and sintered bodies were observed. Chopped carbon fibers were found to be distributed in SiC ceramic composites parts. The sintered bodies exhibited maximum flexural strength of 300 MPa and sintered linear shrinkage below 2%. The manufacturing method has demonstrated the big potential to fabricate ceramic components with personalized complex structure. A SLA-based AM technique has been used for the fabrication of advanced ceramics [49]. A customized 3D printer using a DLP projector as UV source has been built to fabricate green bodies from photosensitive resins loaded with 25−60 wt.% of alumina, 3- and 8-YSZ. The 3D printed bodies were then sintered in the 1200°C−1500°C and exhibited thermal stability. As expected, higher ceramic loadings rendered objects

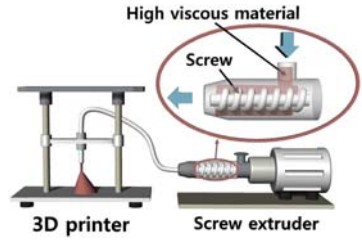

Figure 17.24 Diagram of STE and monkey-bar style 3D printer [51]. *3D*, Three-dimensional; *STE*, screw type extrusion.

with a higher density for a given sintering temperature. The limit of solid loading of the resin was approximately 60% and beyond that content, the extra ceramic appears as powder loosely adhered to the sintered objects. Photogrammetry was used to evaluate the accuracy of the 3DP process and highlighted a marked deviation between the CAD model and the resulting object, particularly in the top part of the specimens, possibly due to the use of volatile solvents which cause changes in the photoresist used. Nevertheless, that problem may be overcome by thermostatizing the printer vat and/or using solvents with higher boiling point. The results obtained suggest the potential application of low-cost DLP 3DP techniques to process ceramics for a number of applications including ceramic fuel cells, piezoelectrics, dental applications, etc. A novel forming method for preparing porous alumina ceramics using alumina fibers as raw materials by direct coagulation casting (DCC) combined with 3DP was proposed [50]. Fig. 17.23 shows the schematic of the preparation of coated sand molds for fabricating porous fibrous alumina ceramics.

Porous fibrous alumina ceramics were fabricated through temperature-induced coagulation of an aqueous-based DCC process using sodium tripolyphosphate (STPP) as a dispersant and adding K_2SO_4 as removable sintering additives. The sacrificial coated sand molds were fabricated by 3DP technology, followed by the infiltration of silica sol solution for the subsequent suspension casting. Stable alumina suspension of 40 vol.% solid loading was obtained by adding 2.0 wt.% STPP and 40 wt.% K_2SO_4. The controlled coagulation of the suspension could be realized after heating at 90°C for about 35 minutes. The ceramic sample sintered at 1450°C for 2 hours showed the highest compressive strength of 24.33 MPa with a porosity of 57.38%. All samples sintered at 1300°C−1450°C had uniform pore size distributions with an average pore size of 7.2 μm, which indicated the good structure stability when sintered at high temperature. Minimizing the variation of the discharging volume becomes a critical point to control the 3D printability of non-Newtonian ceramics and precise control of pressure, shear rates, and time-dependent viscosity become important factors. Taguchi method was used by Kim et al. [51] to obtain a constant linear-velocity by optimizing the printing parameters: A L9 orthogonal array, magnitude, signal-to-noise (S/N) ratio, and extent of

the impact of independent variables, which were water content in material (WC), revolutions per minute (RPM), and diameter of the nozzle tip (TIP). This data is employed to improve the 3D printability and linear-velocity of discharged ceramics. Bowls, pottery, and patterns of 2.5D and 3D structures have been successfully printed in various sizes with ceramic materials under optimal conditions. The Taguchi method optimizes the screw type extrusion process and provides 3DP data on precise control of ceramics as biomaterials, as shown in Fig. 17.24.

Ceramic parts possessing an ordered porosity were produced for the first time by powder-based 3DP of a preceramic polymer followed by pyrolysis in an inert atmosphere [52]. The main parameters involved in the process were investigated, and the precision of the printed and ceramized parts was assessed by means of SEM and microcomputed tomography. The influence of two different printing solvents was investigated and the use of a mixture of 1-hexanol and hexylacetate, in particular, allowed the production of parts with a RD of 80% both in the polymeric and in the ceramic state. The mixing of a cross-linking catalyst directly with the printing liquid greatly simplified the process, minimizing the necessity of preprocessing the starting powder. 3DP of a preceramic polymer not containing any inert or active fillers was proved to be a feasible, convenient, and precise process for the production of porous ceramic possessing a complex, ordered structure, such as stretch-dominated lattices. Scheithauer et al. [53] investigated the AM of ceramic-based functionally graded materials by the direct AM technology thermoplastic 3DP (T3DP). Zirconia components with varying microstructures were additively manufactured by using thermoplastic suspensions with different contents of pore-forming agents (PFA), which were cosintered defect-free. Different materials were investigated concerning their suitability as PFA for the T3DP process. Diverse zirconia-based suspensions were prepared and used for the AM of single and multimaterial test components. All of the samples were sintered defect-free, and in the end, we could realize a brick wall-like component consisting of dense ($<$1% porosity) and porous (approx. 5% porosity) zirconia areas to combine different properties in one component. T3DP opens the door to the AM of further ceramic-based 4D components, such as multicolor, multimaterial, or especially multifunctional components. In T3DP a high-filled ceramic suspension based on thermoplastic binder systems was used to produce dense ceramic components by AM [54]. Alumina (67 vol.%) and zirconia (45 vol.%) suspensions were prepared by ball milling at a temperature of about 100°C to adjust a low viscosity. After the preparation, the suspension solidified at cooling. For the sintered samples (alumina at 1600°C, zirconia at 1500°C), a density of about 99% and higher was obtained. FE-SEM studies of the samples' cross section showed a homogenous microstructure and a very good bond between the single printed layers.

Eventually, along with extensive research on the 3DP of polymers and metals, 3DP of ceramics is now the latest trend to come under the spotlight. The ability to fabricate ceramic components of arbitrarily complex shapes has been extremely challenging without 3DP. This review has focused on the latest advances in the 3DP of ceramics and presented the historical origins and evolution of each related

technique [55]. The main technical aspects, including feedstock properties, process control, posttreatments, and energy source−material interactions, were also discussed. The technical challenges and advice about how to address these were presented. Comparisons were made between the techniques to facilitate the selection of the best ones in practical use. In addition, representative applications of the 3DP of various types of ceramics were surveyed. Future directions were pointed out for the advancement of materials and forming a mechanism for the fabrication of high-performance ceramic components. Moreover, 3DP, alongside the rapidly advancing field of porous ceramics, is quickly expanding the horizon of what is going to be possible in the future. In this chapter, 3DP technology was evaluated for its compatibility with porous ceramic materials, due to its competitive process in terms of speed and specific tooling, especially for good quality fabrication. Hwa et al. [56] reviewed the capabilities of these new technology techniques for the fabrication of porous ceramic. The basic technology was the 3DP techniques, which were used to fabricate porous green ceramic parts that were later sintered. Different ceramic materials were evaluated and the classification of different powders according to their 3DP quality as well as material aspects was examined. The evaluation of the 3DP process in terms of the powders' physical properties such as particle size, flowability, and wettability were also discussed. The relationship between the different 3DP parameters and the final printing outcome were assessed.

17.4 Conclusion

The new 3DP revolution has tremendous advantages, but at the same time has real challenges that make the deployment of this promising technology slow, especially when dealing with ceramic, due to its unique properties. In this chapter, we have covered the most up-to-date methods that have been adopted in the 3DP technology to utilize ceramic as a printing material. Although the progress is slow, the potential in this direction is promising due to its numerous applications.

References

[1] W.K. Ahmed, I.M. Alhamad, 3D printing innovations in UAE: case study: Abu Dhabi summer challenge 2017, in: 2018 Advances in Science and Engineering Technology International Conferences (ASET), 2018, doi:10.1109/icaset.2018.8376924.

[2] I.M. Alhamad, et al., Boosting teaching experience in mechanical engineering courses using additive manufacturing technologies, in: 2019 Advances in Science and Engineering Technology International Conferences (ASET), 2019, doi:10.1109/icaset.2019.8714338.

[3] A. Aldarmaki, et al., Designing and developing innovative structural engineering failure experiment using additive manufacturing technology, in: 2019 Advances in Science and Engineering Technology International Conferences (ASET), 2019, doi:10.1109/icaset.2019.8714208.

[4] W. Ahmed, Toothpaste Cap With Dental Care Tools, Patent No US20190100363A1, <https://patents.google.com/patent/US20190100363A1/en>.
[5] W. Ahmed, W. Al-Rifaie, The impact of cracked microparticles on the mechanical and the fracture behavior of particulate composite, J. Nano- Electron. Phys. 7 (3) (2015). essuir.sumdu.edu.ua/handle/123456789/42891.
[6] W.K. Ahmed, H. Teng, Characterisation of fractured particulate reinforced composite, Int. J. Microstruct. Mater. Prop. 9 (2) (2014) 160. Available from: https://doi.org/10.1504/ijmmp.2014.066563.
[7] W. Ahmed, Y. Al-Douri, Failure of pre-cracked nano-composite, J. Nanostruct. Polym. Nanocompos. 9 (3) (2013) 59–66.
[8] W. Ahmed, Y. Al-Douri, Additive manufacturing technology for nanoscale applications: the revolution of 3D and 4D printing technology in nanoscale applications, in: Meeting on Nanotechnology: Principles and Applications, University of Malaya (UM), 2018.
[9] Y. Ben, et al., PVB modified spherical granules of β-TCP by spray drying for 3D ceramic printing, J. Alloy. Compd. 721 (2017) 312–319. Available from: https://doi.org/10.1016/j.jallcom.2017.06.022.
[10] B. Huang, P.J. Bártolo, Rheological characterization of polymer/ceramic blends for 3D printing of bone scaffolds, Polym. Test. 68 (2018) 365–378. Available from: https://doi.org/10.1016/j.polymertesting.2018.04.033.
[11] U.K. Roopavath, et al., Optimization of extrusion based ceramic 3D printing process for complex bony designs, Mater. Des. 162 (2019) 263–270. Available from: https://doi.org/10.1016/j.matdes.2018.11.054.
[12] Z. Yang, et al., 3D printing of diamond tools for dental ceramics processing, Adv. Eng. Mater. 20 (3) (2017) 1700747. Available from: https://doi.org/10.1002/adem.201700747.
[13] R. Trombetta, et al., 3D printing of calcium phosphate ceramics for bone tissue engineering and drug delivery, Ann. Biomed. Eng. 45 (1) (2016) 23–44. Available from: https://doi.org/10.1007/s10439-016-1678-3.
[14] B. Zhang, et al., Porous bioceramics produced by inkjet 3D printing: effect of printing ink formulation on the ceramic macro and micro porous architectures control, Compos. B Eng. 155 (2018) 112–121. Available from: https://doi.org/10.1016/j.compositesb.2018.08.047.
[15] Z. Peng, et al., Effect of print path process on sintering behavior and thermal shock resistance of Al_2O_3 ceramics fabricated by 3D inkjet-printing, Ceram. Int. 44 (14) (2018) 16766–16772. Available from: https://doi.org/10.1016/j.ceramint.2018.06.108.
[16] X. Wu, et al., Influence of boundary masks on dimensions and surface roughness using segmented exposure in ceramic 3D printing, Ceram. Int. 45 (3) (2019) 3687–3697. Available from: https://doi.org/10.1016/j.ceramint.2018.11.031.
[17] Y. Ben, et al., PVB modified spherical granules of β-TCP by spray drying for 3D ceramic printing, J. Alloy. Compd. 721 (2017) 312–319. Available from: https://doi.org/10.1016/j.jallcom.2017.06.022.
[18] C. Sun, et al., Effect of particle size gradation on the performance of glass-ceramic 3D printing process, Ceram. Int. 43 (1) (2017) 578–584. Available from: https://doi.org/10.1016/j.ceramint.2016.09.197.
[19] Z. Liu, et al., Microstructure and mechanical properties of Al_2O_3/ZrO_2 directionally solidified eutectic ceramic prepared by laser 3D printing, J. Mater. Sci. Technol. 32 (4) (2016) 320–325. Available from: https://doi.org/10.1016/j.jmst.2015.11.017.

[20] P. Biswas, et al., 3D extrusion printing of magnesium aluminate spinel ceramic parts using thermally induced gelation of methyl cellulose, J. Alloy. Compd. 770 (2019) 419–423. Available from: https://doi.org/10.1016/j.jallcom.2018.08.152.
[21] J. Maurath, N. Willenbacher, 3D printing of open-porous cellular ceramics with high specific strength, J. Eur. Ceram. Soc. 37 (15) (2017) 4833–4842. Available from: https://doi.org/10.1016/j.jeurceramsoc.2017.06.001.
[22] W. Zhu, et al., Fabrication and characterization of carbon fiber reinforced SiC ceramic matrix composites based on 3D printing technology, J. Eur. Ceram. Soc. 38 (14) (2018) 4604–4613. Available from: https://doi.org/10.1016/j.jeurceramsoc.2018.06.022.
[23] R. He, et al., Fabrication of complex-shaped zirconia ceramic parts via a DLP-stereolithography-based 3D printing method, Ceram. Int. 44 (3) (2018) 3412–3416. Available from: https://doi.org/10.1016/j.ceramint.2017.11.135.
[24] M. Zhang, L. Yang, Ceramic product forming technologies research based on 3D printing, IEEE Access 4 (2016) 9345–9349. Available from: https://doi.org/10.1109/access.2016.2642122.
[25] J.-B. Lee, et al., Porous calcium phosphate ceramic scaffolds with tailored pore orientations and mechanical properties using lithography-based ceramic 3D printing technique, Materials 11 (9) (2018) 1711. Available from: https://doi.org/10.3390/ma11091711.
[26] C. Dong, Ceramic product design based on 3D printing technology, Appl. Mech. Mater. 633–634 (2014) 351–354. Available from: https://doi.org/10.4028/www.scientific.net/amm.633-634.351.
[27] J. Suwanprateeb, et al., Mechanical and in vitro performance of apatite–wollastonite glass ceramic reinforced hydroxyapatite composite fabricated by 3D-printing, J. Mater. Sci. Mater. Med. 20 (6) (2009) 1281–1289. Available from: https://doi.org/10.1007/s10856-009-3697-1.
[28] H. Xing, et al., Preparation and characterization of UV curable Al_2O_3 suspensions applying for stereolithography 3D printing ceramic microcomponent, Powder Technol. 338 (2018) 153–161. Available from: https://doi.org/10.1016/j.powtec.2018.07.023.
[29] S. Li, et al., The fabrication of SiBCN ceramic components from preceramic polymers by digital light processing (DLP) 3D printing technology, J. Eur. Ceram. Soc. 38 (14) (2018) 4597–4603. Available from: https://doi.org/10.1016/j.jeurceramsoc.2018.06.046.
[30] S.Y. Song, et al., Improvement of dispersion stability and 3D-printing characteristics of ceramics in photopolymers by controlling the coating thickness of silane coupling agents, Mater. Chem. Phys. 216 (2018) 446–453. Available from: https://doi.org/10.1016/j.matchemphys.2018.06.023.
[31] H.-Y. Park, et al., New conversion process for fabricating a ceramic core by a 3D printing technique, Surf. Coat. Technol. 332 (2017) 527–532. Available from: https://doi.org/10.1016/j.surfcoat.2017.07.034.
[32] P. Kunchala, K. Kappagantula, 3D printing high density ceramics using binder jetting with nanoparticle densifiers, Mater. Des. 155 (2018) 443–450. Available from: https://doi.org/10.1016/j.matdes.2018.06.009.
[33] H. Shao, et al., 3D gel-printing of zirconia ceramic parts, Ceram. Int. 43 (16) (2017) 13938–13942. Available from: https://doi.org/10.1016/j.ceramint.2017.07.124.
[34] Z. Tian, et al., Fabrication and properties of a high porosity h-BN–SiO_2 ceramics fabricated by stereolithography-based 3D printing, Mater. Lett. 236 (2019) 144–147. Available from: https://doi.org/10.1016/j.matlet.2018.10.058.

[35] J. He, et al., Effect of magnesium silicate on 3D gel-printing of hydroxyapatite ceramic composite scaffold, Int. J. Appl. Ceram. Technol. 16 (2) (2018) 494−502. Available from: https://doi.org/10.1111/ijac.13133.
[36] H. Kim, et al., Fabrication of bulk piezoelectric and dielectric $BaTiO_3$ ceramics using paste extrusion 3D printing technique, J. Am. Ceram. Soc. (2018). Available from: https://doi.org/10.1111/jace.16242.
[37] W. Liu, et al., 3D printing of dense structural ceramic microcomponents with low cost: tailoring the sintering kinetics and the microstructure evolution, J. Am. Ceram. Soc. 102 (5) (2018) 2257−2262. Available from: https://doi.org/10.1111/jace.16241.
[38] R. Lowmunkong, et al., Fabrication of freeform bone-filling calcium phosphate ceramics by gypsum 3D printing method, J. Biomed. Mater. Res. B Appl. Biomater. 90B (2) (2009) 531−539. Available from: https://doi.org/10.1002/jbm.b.31314.
[39] H. Wu, et al., Effect of the particle size and the debinding process on the density of alumina ceramics fabricated by 3D printing based on stereolithography, Ceram. Int. 42 (15) (2016) 17290−17294. Available from: https://doi.org/10.1016/j.ceramint.2016.08.024.
[40] Q. Lian, et al., Oxygen-controlled bottom-up mask-projection stereolithography for ceramic 3D printing, Ceram. Int. 43 (17) (2017) 14956−14961. Available from: https://doi.org/10.1016/j.ceramint.2017.08.014.
[41] F. Chen, et al., Fabrication of complicated silicon carbide ceramic components using combined 3D printing with gelcasting, Ceram. Int. 44 (1) (2018) 254−260. Available from: https://doi.org/10.1016/j.ceramint.2017.09.166.
[42] T. Tu, G. Jiang, SiC reticulated porous ceramics by 3D printing, gelcasting and liquid drying, Ceram. Int. 44 (3) (2018) 3400−3405. Available from: https://doi.org/10.1016/j.ceramint.2017.11.133.
[43] C.F. Revelo, H.A. Colorado, 3D printing of kaolinite clay ceramics using the direct ink writing (DIW) technique, Ceram. Int. 44 (5) (2018) 5673−5682. Available from: https://doi.org/10.1016/j.ceramint.2017.12.219.
[44] Y. Fu, et al., Multiple metals doped polymer-derived SiOC ceramics for 3D printing, Ceram. Int. 44 (10) (2018) 11030−11038. Available from: https://doi.org/10.1016/j.ceramint.2018.03.075.
[45] P. Biswas, et al., 3D extrusion printing of magnesium aluminate spinel ceramic parts using thermally induced gelation of methyl cellulose, J. Alloy. Compd. 770 (2019) 419−423. Available from: https://doi.org/10.1016/j.jallcom.2018.08.152.
[46] H. Zhao, et al., 3D printing of CaO-based ceramic core using nanozirconia suspension as a binder, J. Eur. Ceram. Soc. 37 (15) (2017) 5119−5125. Available from: https://doi.org/10.1016/j.jeurceramsoc.2017.06.050.
[47] H. Chen, et al., 3D printing of SiC ceramic: direct ink writing with a solution of preceramic polymers, J. Eur. Ceram. Soc. 38 (16) (2018) 5294−5300. Available from: https://doi.org/10.1016/j.jeurceramsoc.2018.08.009.
[48] H. Zhang, et al., The preparation of SiC-based ceramics by one novel strategy combined 3D printing technology and liquid silicon infiltration process, Ceram. Int. (2019). Available from: https://doi.org/10.1016/j.ceramint.2019.02.154.
[49] G. Varghese, et al., Fabrication and characterisation of ceramics via low-cost DLP 3D printing, Bol. Soc. Esp. Cerám. Vidr. 57 (1) (2018) 9−18. Available from: https://doi.org/10.1016/j.bsecv.2017.09.004.
[50] A.-N. Chen, et al., Fabrication of porous fibrous alumina ceramics by direct coagulation casting combined with 3D printing, Ceram. Int. 44 (5) (2018) 4845−4852. Available from: https://doi.org/10.1016/j.ceramint.2017.12.073.

[51] N.P. Kim, et al., Optimization of 3D printing parameters of screw type extrusion (STE) for ceramics using the Taguchi method, Ceram. Int. 45 (2) (2019) 2351−2360. Available from: https://doi.org/10.1016/j.ceramint.2018.10.152.
[52] A. Zocca, et al., SiOC ceramics with ordered porosity by 3D-printing of a preceramic polymer, J. Mater. Res. 28 (17) (2013) 2243−2252. Available from: https://doi.org/10.1557/jmr.2013.129.
[53] U. Scheithauer, et al., Ceramic-based 4D components: additive manufacturing (AM) of ceramic-based functionally graded materials (FGM) by thermoplastic 3D printing (T3DP), Materials 10 (12) (2017) 1368. Available from: https://doi.org/10.3390/ma10121368.
[54] U. Scheithauer, et al., Thermoplastic 3D printing—an additive manufacturing method for producing dense ceramics, Int. J. Appl. Ceram. Technol. 12 (1) (2014) 26−31. Available from: https://doi.org/10.1111/ijac.12306.
[55] Z. Chen, et al., 3D printing of ceramics: a review, J. Eur. Ceram. Soc. 39 (4) (2019) 661−687.
[56] L.C. Hwa, et al., Recent advances in 3D printing of porous ceramics: a review, Curr. Opin. Solid State 21 (2017).

This page intentionally left blank

Metal oxides powder technology in dielectric materials

18

Yasmin Abdul Wahab[1], Sharifah Fatmadiana[2], Muhammad Nihal Naseer[3], Mohd Rafie Johan[1], Nor Aliya Hamizi[1], Suresh Sagadevan[1], Omid Akbarzadeh[1], Zaira Zaman Chowdhury[1], Thennarasan Sabapathy[4] and Y. Al Douri[1,5,6]

[1]Nanotechnology & Catalysis Research Centre, Deputy Vice Chancellor (Research & Innovation) Office, University of Malaya, Kuala Lumpur, Malaysia, [2]Department of Electrical Engineering, Faculty of Engineering, University of Malaya, Kuala Lumpur, Malaysia, [3]Department of Mechanical Engineering, National University of Sciences and Technology, Islamabad, Pakistan, [4]Bioelectromagnetics Research Group, School of Computer and Communication Engineering, Universiti Malaysia Perlis (UniMAP), Kampus Pauh Putra, Arau, Malaysia, [5]University Research Center, Cihan University of Sulaimaniya, Sulaymaniyah, Iraq, [6]Department of Mechatronics Engineering, Faculty of Engineering and Natural Sciences, Bahcesehir University, Istanbul, Turkey

18.1 Introduction

Metal oxide powder technology represents a growing asset in numerous areas of physics materials science and chemistry especially with their heightened mechanical, electronic, and surface properties compared with their bulk counterparts. These nanomaterials are being multifaceted and can be utilized in various applications, for example, ecological remediation, therapeutic innovation, cosmetics, and to meet energy and water deficiencies with their applications projected to increase.

Metal oxide powder have unique properties to form a large diversify of oxide compounds that allow for numerous applications and uses in industry and consumer products. These inaugurate vast structural geometries with an electronic structure to perform different characters (conductive, semiconductive, or insulative).

In internet of things and other innovative technological applications, these nanomaterials find their utilization microelectronic circuits' fabrication, piezoelectric devices, fuel cells, anticorrosive coatings, and as catalysts. Increasing energy demands and forecasted water scarcity threats have also stimulated the research of these nanostructured metal oxides. Past two decades are the witnessed to renewed importance of nanostructured metal oxides (such as ZnO) because they depict best photocatalytic efficiency [1]. Moreover, nanostructured titanium metal oxides are used to optimize method of photodegradation efficiency in ultraviolet and visible regions of light [2]. In nut shell, time has proved nanostructured metal oxides very crucial for every field of study due to its versatile applications, spanning over all industries.

Metal Oxide Powder Technologies. DOI: https://doi.org/10.1016/B978-0-12-817505-7.00018-X

Molecule estimate size is relied upon to impact three significant gatherings of essential characteristics of any material. The first contains the basic qualities of structural properties, specifically the lattice symmetry and cell parameters [3]. The bulk oxides are generally vigorous and stable frameworks with well-characterized crystallographic structural behavior. Be that as it may, the growth significance of surface free energy and stress with diminishing molecule size changes the thermodynamic stability corresponding with size, and it can instigate the alteration of cell parameters as well as auxiliary changes [4,5]. At the uttermost the nanoparticle can disappear due to interactions between its surrounding environment and a high surface free vitality/energy [6]. The necessity of having low surface free energy of a nanoparticle is significant in order to manifest mechanical and structural ability. Of note, diminishing the size of particle and surface area manages an exponential increment in surface area relative to the volume that subsequently results in surface functioning on itself and to its adjacent milieu. So as to show mechanical or basic dependability, a nanoparticle must exhibit a low surface free vitality. In the consequence of this requirement, stages that have a low steadiness in mass materials can turn out to be truly steady in nanomaterial. This auxiliary marvel has been identified in TiO_2, Al_2O_3, ZnO, SnO_2, and CuO or other oxides [5−7].

Nanostructured metal oxides have been utilized in every field from energy harvesting, to photocatalysis. Over the regime of last few years, these nanostructured metal oxides are undergoing a paradigm shift with respect to their utilizations and applications as huge scientific literature [1,8] growth is observed in improving and efficiently utilizing dielectric properties of powered metal oxides. The aim of this chapter is to further broaden the knowledge of nanostructured metal oxides with respect to their dielectric properties. To achieve mentioned goal, this chapter will briefly explain the fundamental aspects of dielectric properties and applications of metal oxides powder technologies as dielectrics. This chapter will review the technicalities and the findings of state-of-the-art theory to describe in detail the dielectric properties and innovative technical applications of nanostructured metal oxides.

18.2 Dielectric materials: properties and behaviors

18.2.1 Dielectric materials

A material described by low electric conductivity, high value of specific resistance, and negative value of Temp. Coefficient of Resistance is known as a dielectric material. This material exhibits the phenomena of *polarization* when subjected to electric potential (V/m). When electric potential is applied charges do not show mobility through whole dielectric as seen in the case of conductors, but they only have a paradigm shift about its mean position that results in polarization. This polarization subsequently results in displacement of positive charges toward applied field and negative charges opposite to positive ones. This arrangement responds as an internal electric field that diminished the overall effect of external field in

dielectric. Dielectrics are also characterized by their relative permittivity constant ε_r. This constant is also known as dielectric constant.

Dielectric materials have high insulation resistance that depends on operating temperature, moisture content, dielectric material, and applied potential. With mentioned characteristics, these dielectrics find a range of applications in electric devices such as capacitors, SONAR appliances, and strain gauge. A daily life example of this material is insulation (usually mica and ceramic) between the plates of capacitor.

18.2.2 Types of dielectric materials

Being extensively used material in electrical appliances, it can be commonly found in all three physical states, that is, solid, gas, and liquid as described in Table 18.1.

18.2.3 Dielectric fundamentals

Dielectric materials are characterized by following significant properties.

- *Resistivity*: Restively is a material property defined as inverse of resistance. It is denoted by ρ (rho) and measured in SI unit of ohm-meter. It can also be called as specific resistance of dielectric.
- *Permittivity*: The hindrance offered by dielectric to subjected potential or field in presence a specific medium is called permittivity of dielectric. It is denoted by ε and measured in the unit of farad/meter. It can also be defined as measurement of the stored energy inside the sample in the applied electric field. Its value can be calculated as

$$\varepsilon = \frac{Ct}{\varepsilon_0 A}$$

Table 18.1 Common dielectric materials.

Material	Solid	Liquid	Gas
Description	• Inorganic materials • Plastic films • Flexible insulating sleeves • Rigid fibrous reinforced laminates • Resins, varnishes, and silicones • Pressure sensitive and vulcanized adhesive types • Mica products • Textile materials • Elastomers-EPR, polymeric thermoplastics	• Hydro carbon • Mineral oils • Silicon fluids • Synthetic esters	• Nitrogen • Sulfur hexafluoride • Hydrogen • Carbon dioxide

EPR, Ethylene propylene rubber.
Courtesy: M. Bolotinha, Insulating and dielectric materials—types, properties & applications, Electr. Technol. (2019). [Online]. Available: https://www.electricaltechnology.org/2018/03/insulating-and-dielectric-materials.html#types-of-dielectric-materials (accessed 25.06.19) [9].

where C is the capacitance (measured in Farad), t is the thickness of pelletized powder (measured in meter), ε_0 is the permittivity of free space (8.854×10^{-12} m^{-3}/kg/s^4/A^{21}), and A is the area of the dielectric.

- *Relative permittivity*: It is defined as the ratio of dielectric permittivity to the permittivity of vacuum.
- *Dielectric strength*: It is one of important properties of dielectric. It is defined as the extent of dielectric material which it can confront electric stress prior to fracture. It is measured in kV/mm.
- *Dielectric loss*: It is a vital factor that play important role in material selection for a dielectric. It can be defined as the ratio of dielectric power loss to total transmitted power. It is also known as *electrical dissipation factor* and denoted by "tan δ." In the case of an ideal insulator only I_C (capacitive current) passes, but in the case of real ones due to impurity I_R (resistive current) also occurs. The relation of both is described in Fig. 18.1.

Optimum operating temperature of a dielectric material is also of primary importance. It is a common observation that a dielectric material deteriorates swiftly if operating temperature is high. The deterioration point at which designed performance

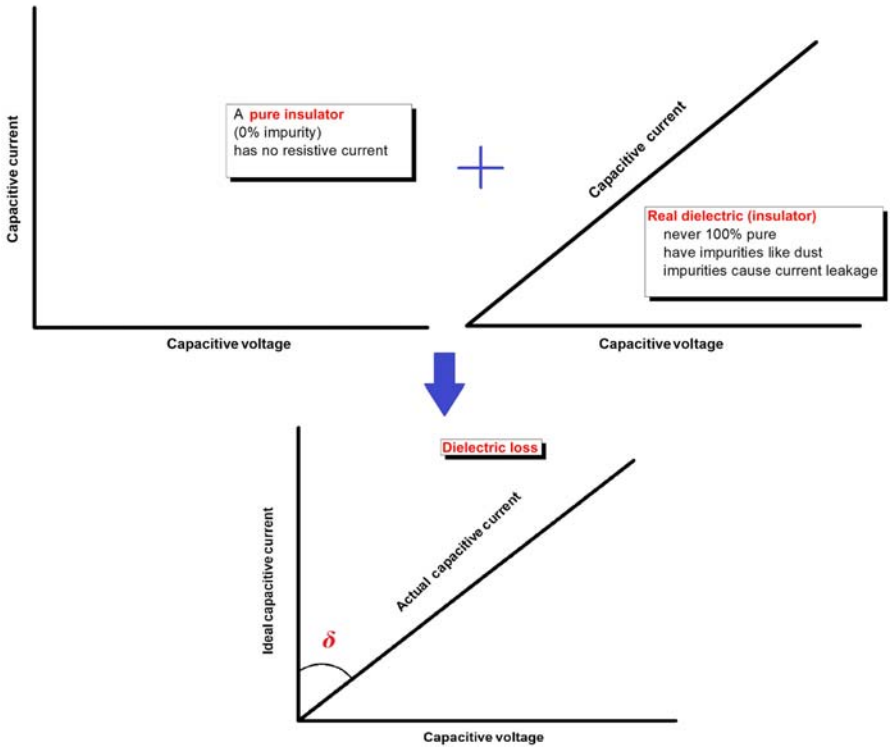

Figure 18.1 Schematic of dielectric loss and actual capacitive currents of an insulator.

of insulation is diminished is called *ageing*. The ageing phenomenon is highly affected by following parameters:

- Chemical composition of dielectric
- Subjected thermal stresses
- Exposure to mechanical stress
- Operating environment

It is very important to mention that dielectric materials may confront the phenomena of ageing prior to their specified timeline. *This is* called premature ageing. Some important main causes of premature ageing are as following:

- presence of contaminants (Cu)
- presence of excessive water content
- over heating
- excessive potential

Along with the abovementioned defects, there may be electromigration and stress migration defects as seen in the case of Cu. These defects create Cu voids [10] that alter the characteristic of Cu wafers. If theses wafers are utilized in synthesis of nano-CuO, it will drastically affect the dielectric properties. To get rid of these defects, recent studies are conducted [10,11] that elaborates the detection and reduction of these defects efficiently.

All abovementioned parameters and phenomena define the lifetime of a dielectric. They must be taken into account during the material selection for a dielectric. The applicability of metal oxide powder technology in electrical devices as dielectric can be determined by measuring mentioned dielectric properties of the material for a variation of temperatures and frequency.

18.3 Metal oxide powder in dielectric materials

18.3.1 ZnO, TiO_2, and other metal oxides

Zinc oxide (ZnO) powder is a widely used compound in many household, electrical, and industrial products. Though naturally occurring in the mineral zincite, most production originates from anthropogenic sources. Nano-sized ZnO (nano-ZnO) can be produced by the grinding of bulk ZnO, where it takes on a wurtzite crystalline structure that can then be utilized for a number of applications. Nano-ZnO power can be prepared by various methods. Some of them are as follows:

- polyol medium hydrolysis method
- gas condensation method
- polymeric precursor method
- pyrolysis (aerosol spray) method
- hydrothermal method
- sol−gel method
- solid state microwave decomposition method

All abovementioned methods are conventional methods as they require a high rate of energy consumption that makes it uneconomical. Most sustainable and economical method for ZnO powder synthesis is precipitation method [12]. Nano-ZnO serves as n-type semiconductor due to its wide-bandwidth (~3.37 eV) [13]. Based on electric, thermal, and chemical stability, piezoelectric and superconductive properties, nano-ZnO has many applications in devices such as piezoelectric cells [14], cholesterol and glucose biosensing [15], solar cells [16], and photovoltaic transducers [17]. When in a powder form, nano-ZnO can be mixed into foods, paints, pigments, and adhesives [18], medical disinfection, and environmental remediation [19]. Due to UV−Vis luminescence and UV blocking properties, nano-ZnO is used in personal care products, such as sunscreens and cosmetics [18,20]. Production of nano-ZnO and other metal oxides have been found to be popular for cosmetic applications with an estimated 1000 t/year during 2005−10 [21] (Table18.2).

Titanium dioxide powder/nanomaterials, also known for photocatalytic properties serves as a useful nanomaterial in industry today. Nano-TiO_2 and bulk TiO_2 have both been studied based on their roles as photocatalysts. Nano-TiO_2, the more chemically reactive of the two, can serve in both oxidative and reductive processes in the removal of organic and inorganic compounds in wastewater. One study has shown nano-TiO_2 to play a successful role in the adsorption of heavy metals (Cu, Cd, Ni, Pd, and Zn) from spiked San Antonio tap water samples [23]. In addition, nano-TiO_2 can be used in the metal ions removal and nonbiodegradable organics [24] and total organic carbon degradation using UV light [25] from synthetic wastewater. Nano-TiO_2 is included in many consumer products due to its ability to absorb UV radiation and is widely used in sunscreens, cosmetics, and self-cleaning coatings for antimicrobial properties [26]. Nano-TiO_2 can also be found in pharmaceuticals, pigments, food additives, and solar cells [27,28]. Nano-TiO_2 is

Table 18.2 Applications of metal oxide nanomaterials.

Sr. no.	Nanomaterials	Application
1.	Nano-TiO_2	Sunscreens, cosmetics, self-cleaning coatings, pharmaceuticals, pigments, food additives, and solar cells
2.	Nano-ZnO	Food additives, paints, pigments, adhesives Medical disinfection, environmental remediation Sunscreens and cosmetics
3.	Nano-FeO_x	Wastewater treatment and bioremediation
4.	Nano-MnO	Wastewater treatment
5.	Nano-Al_2O_3	Water-resistant coating and gas-discharge lamps
6.	Nano-CeO_2	Televisions, glass mirrors, ophthalmic lenses Fuel additives
7.	Nano-CuO_x	Antimicrobial studies, solar cells, catalysts, and sensors

Courtesy: J.E. Cañas-Carrell, S. Li, A.M. Parra, B. Shrestha, Metal oxide nanomaterials: health and environmental effects, in: Health and Environmental Safety of Nanomaterials, Elsevier, 2014, pp. 200−221 [22].

synthesized by the method of sol−gel technique, reactive plasma synthesis and hydrolysis, and peptization of titanium isopropoxide solution.

Other metal oxides powder additional metal oxide nanomaterials have been of interest due to their unique properties. Aside from nano-ZnO and nano-TiO_2, nano-ferric oxides (nano-FeO_x) are one of the most widely used nanomaterials in industry. Stemming from the ubiquitous source of iron, nano-FeO_x compounds have been used in wastewater treatment and bioremediation of toxic metal contaminated sites with little risk of secondary contamination [29]. Other metal oxide nanomaterials, such as nano-magnesium oxide (nano-MgO_x), can be used in heavy metal adsorption in wastewater treatment. Nano-MgO_x has been used as an absorbent for catatonic and ionic compounds such as phosphates [30] and arsenates [31] in natural waters. Nanoaluminum oxide (nano-Al_2O_3) particles are used as a wear-resistant coating for tools and gas discharge lamps due to their inert properties [32]. Known also for UV-blocking and catalytic properties, cerium dioxide (nano-CeO_2) nanoparticles are used in commercial uses such as polishing agents for television tubes, glass mirrors, and ophthalmic lenses [33]. Nano-CeO_2 can also serve as a fuel additive, resulting in decreased emissions [34]. Lastly, copper oxide nanoparticles (nano-CuO_x), which are known for their semiconductive, catalytic, and electronic properties, are used in applications such as antimicrobials [35] and solar cells, catalysts, and gas and liquid sensors [36].

18.3.2 Dielectric materials: ferroelectric and application

One of the dielectric materials is ferroelectrics, and this section will discuss about its properties, types, and applications.

18.3.2.1 Ferroelectric materials

The type of dielectric materials that exhibits a value of more than 2000 for relative permittivity is classified as ferroelectric materials. This type of material is in line with ferromagnetic character, that is, all domains get aligned in single direction along the subjected field's direction.

This aligning property of ferroelectric materials leads to extensive spontaneous polarization. Along with polarization, piezometric effect is also observed in these materials. As mentioned in Table 18.3, these materials also have ferroelectric Curie temperature. It is defined as critical temperature at which structural and behavior amendments are noted. A list of few ferroelectric crystals along with their respective Curie temperatures is shown in Table 18.3.

18.3.2.2 Examples and applications

Some industrially important ferroelectrics are Rochelle salt, $SrTiO_3$, KH_2AsO_4, lead zirconate ($PbZrO_3$), lithium niobate ($LiNbO_3$), and lithium tantalate ($LiTaO_3$). Usually this type of material is utilized in electro-optic materials, sonar devices, strain gauges, microphones and miniature capacitors, and many other applications.

Table 18.3 Properties of some ferroelectrics.

Material	Spontaneous polarization (C/m^2)	Ferroelectric Curie temperature, T_{fe} (°C)
KH_2PO_4	0.05	− 148
$BaTiO_3$	0.25	122
$KNbO_3$	0.30	437
$PbTiO_3$	0.50	492

Courtesy: K.M. Gupta, N. Gupta, Advanced Electrical and Electronics Materials, John Wiley & Sons, Inc., Hoboken, NJ, 2015 [37].

18.3.3 Dielectric properties of metal oxides powder dispersions in paraffin oil

This chapter contributes to the review of metal oxides powder dispersed in paraffin oil, an organic liquid with insulation character. This chapter also covers the phenomena of nanofluids polarization that is a consequence of nanoparticle inclusions in paraffin oil.

Those fluid that are characterized by the suspensions of metal oxides nanoparticles (few tens of nanometers) and dispersion of metal oxide powders with extent of 5% w/v in the liquid matrix are known as nanofluids. The relative permittivity and loss tangent of paraffin oil and nanofluid is observed in the range of 20 Hz to 1 MHz [38].

The outcomes execution was noteworthy to both grain size and explicit compound. As far as the case of nanoparticles are concerned, dielectric character is dominated by grain surface polarization that was initially induced by adsorbed water. But this impact has been counteracted by the expansion of titania nanoparticles layers. This is achieved due to unique properties of titanium (Ti) and ferric oxide, as their dielectric constants get increased accompanying normal frequencies. Simultaneously, at high frequency, cupric and cuprous oxides show a relaxation mechanism. That also contributes to get mentioned results. Finally, nanomaterial's surface show a tremendous increment in electronic density.

Recently, a comparison study was conducted between nano-filled insulators and microfilled insulators. The findings of the study concluded that nano-filled materials behave in glamorously different way from that of microfilled. These results worked as an attractive finding for scientists and led to the further studies [39]. Consequently, nanodielectrics (nano-filled solid insulators) were discovered [40]. Later on, research revealed the fact that recently invented nanodielectrics accompanied by nanofluids can work as a two-phase system, matrix as one phase and dispersed nanoparticles as other. To have conduction and permittivity as the property of nanofluid, the materials preferred for nanofluid inclusion were metals, metal oxides (e.g., Al_2O_3, CuO, ZnO), and nitrides (AlN). To exhibit magnetic behaviors, some magnetic oxides such as Fe_3O_4 can also be used [41].

Nanoscaled oil have superior properties compared to that of pure oils. Nanofluids have a different dielectric strength than pure oils. This dielectric

strength can be easily modified in the case of nanofluids but it is quite difficult to change in the case of pure fluids. This makes nanofluid superiors. In nanofluids, dispersion of metal nanoparticles attributes an increment in the breakdown voltage of oil. This increment consequences as capturing of fast stream electron. These formed negative charges have high thermal conductivity than its surrounding. Hence, an overall increment in cooling takes place as a result [42]. This is the property of nanofluids that attracted the focus for its applications in OFEE [43]. In OFEE, these nanofluids find a vast range of application covering:

- simulate impurity effects
- control collective response of dielectric liquid
- mitigate adverse effects of ageing
- reduction in polarization

The main focus of this work is to review the polarization of organic liquid (paraffin oil) on addition of dispersed micro- and nanoparticles. To study this effect, various oxides are used starting from the one that were previously used. The observations reveal the fact that all oxides show unique effect because in this case of grain size is transformed from microscale to nano scale and surface/volume ratio is increased.

18.3.3.1 Aluminum

Aluminum oxides in the form of nano powder behave as hygroscopic and a reactive metal that contribute as an increment of water content in oil. This hydration/dehydration attributes to change in permittivity.

18.3.3.2 Iron and Cu

The oxides of these metals are semiconductors. Presence of these impurities in oil results in high acidity of oil. These impurities are usually induced by electrochemical corrosion of respective metal.

18.3.3.3 Titanium

The addition of titanium dioxide results in high energy storage, low friction, and wear resistance [3,4].

18.4 Review of metal oxides powder technologies in dielectric materials

18.4.1 Introduction: metal oxides powder as dielectric materials

Dielectrics are extensively used in current electronic and electrical industries, particularly in capacitors, insulation, sensors, actuators, transistors, electro-optical devices, and in microelectromechanical structures.

Metal oxides powder technology as dielectric materials has opened up a promising field in material science and engineering. By having high specific capacitance and conductivity, these materials are suitable for electrode fabrication focused on high-energy and high-power supercapacitors [44]. Metal oxides technology are widely applied in catalysis [45,46], thermochemical energy storage [47], magnetic and optical data storages [48], sensors, and ferrofluids. Metal oxides powders are attractive due to its high charge capacity, better dielectric response, as well as high stability.

There are numerous such materials that are used for dielectric and conductive fabrication, for example, RuO_2 [49], IrO_2 [50], MnO_2 [51], NiO [52], Co_2O_3 [53], SnO_2 [54], V_2O_5 [55], and MO_x [56]. The most studied ones are ruthenium and manganese oxides [57].

18.4.2 Properties of the metal oxide powders as dielectric materials

As all solid very materials are sensitive to applied potential, different significant properties such as optimum operational temperature, frequency range, permittivity constant, and loss coefficient can be calculated easily. These calculated results are very helpful to get familiar with structural changes and defects. For instance, dielectric behaviors and electric transportation properties of nano materials are observed to be different than its bulk even different from microscaled materials too. This is due to increase in interfacial atoms or ions and sinking of large amount of defects at or near the grain boundaries [58].

There have been several works scrutinizing on measuring the efficiency of the metal oxide powder technology, particularly as dielectric materials. For instance, dependence of dielectric behavior of a material and ac conductivity of the ZnO/CdO nanoparticles on temperature (300K−403K) and frequency (1 kHz to 10 MHz,) was studied [59] in which the dielectric permittivity was evaluated from the observed values of capacitance in the mentioned range. It was observed in this study that the dielectric constant is inversely proportional to the frequency due to space charge polarization and rotation direction polarization. Due to the conduction of free charges at the interfaces of composites in heterogeneous dielectric materials and dielectric relaxation caused by segmental movement [60,61], the dielectric constant will vary as a function of frequency attributed to the space charges polarization. At varying frequencies the energies of the dipoles at respective sides of the potential barrier will be charged in which the dipoles parallel to the field will have lower potential energy as compared to the dipoles which are antiparallel to the field. The dipoles will then oscillate at a resonance frequency about its equilibrium position.

A recent study in the mixtures of metal and dielectric powders through plasma-chemical processes under high power gyrotron's discharge had been carried out [62] in looking at new perspectives to the preparation of nanostructured materials with controlled composition and structure, which further enable the determination

of yield and performance of the powdered dielectric materials. A recent study of nanoparticles revealed the fact that a nanocomposite with following properties

- low dielectric loss,
- high permittivity, and
- low dependence on temperature

can be utilized as small-scaled capacitor that has high energy storage ability and extensive voltage rating [63].

Another recent study on powdered metal oxide composites for dielectric applications was done [64] in which a fine powder prepared from periwinkle shells was observed for its use as filler polymer composites in enabling polymeric insulation in high voltage application. Different metal microcomposite powders, of high thermal conductivity, such as CaO, Al_2O_3, SiO_2, FeO_2, TiO_2, and Mn_2O_3, were produced from that powder. The work had demonstrated that the dielectric constant of the pelletized powder lies in the range of metal oxide ceramics and is directly dependent on the temperature, while the loss tangent decreases with temperature. It was also reported that the charge transport in these materials is due to the migration of negative oxygen ions via crystal and the electrons "hopping" from donor to donor.

In determining the energy distribution of the electron traps in metal oxides powder, a study was conducted [65] through reversed double-beam photoacoustic spectroscopy. The work had developed a method of determining energy resolved distribution of electron traps and conduction band bottom position to reflect surface structure and bulk structure respectively.

18.5 Conclusion

This work reviews the sustainability and applicability of most versatile and emerging nano material, nano metal oxides, for their utilization as dielectrics in various equipment ranging from capacitor to novel electronic devices. An overview of numerous metal oxides (RuO_2, Al_2O_3, IrO_2, TiO_2, MnO_2, Co_2O_3, SnO_3, and V_2O_5) as dielectric materials in solid and liquid phase is provided. Results obtained from different recent studies are combined and compared to elect superior nano metal oxide for its dielectric applications. The unique classes of dielectrics, ferromagnetic, and liquid (paraffin) are also covered along with diversity of effects they exhibit on addition of nano metal oxides. Different factors such as frequency range, operating temperature, and loss coefficient that determine the applicability of nanometal oxide dielectric materials are also discussed to define the lifetime of dielectric. A set of ideal properties that promises a high energy storage nano metal oxide dielectric is also mentioned in this study.

References

[1] L.-H. Xu, D.S. Patil, J. Yang, J. Xiao, Metal oxide nanostructures: synthesis, properties, and applications, J. Nanotechnol. 2015 (2015) 1–2.

[2] M.M. Mahlambi, A.K. Mishra, S.B. Mishra, R.W. Krause, B.B. Mamba, A.M. Raichur, TiO_2 nanocatalysts supported on a hybrid carbon-covered alumina support: comparison between visible light and UV light degradation of rhodamine B, J. Nanotechnol. 2015 (2015) 1–8.
[3] P. Ayyub, V.R. Palkar, S. Chattopadhyay, M. Multani, Effect of crystal size reduction on lattice symmetry and cooperative properties, Phys. Rev. B 51 (1995).
[4] J.M. McHale, A. Auroux, A.J. Perrotta, A. Navrotsky, Surface energies and thermodynamic phase stability in nanocrystalline aluminas, Science 277 (1997).
[5] H. Zhang, J.F. Banfield, Size dependence of the kinetic rate constant for phase transformation in TiO_2 nanoparticles, Chem. Mater. 17 (2005).
[6] V.M. Samsonov, N.Y. Sdobnyakov, A.N. Bazulev, On thermodynamic stability conditions for nanosized particles, Surf. Sci. 532–535 (2003).
[7] Z. Lou, Q. Chen, Y. Zhang, W. Wang, Y. Qian, Diamond formation by reduction of carbon dioxide at low temperatures, J. Am. Chem. Soc. 125 (31) (2003) 9302–9303.
[8] J. Zhuang, et al., Solution-processed rare-earth oxide thin films for alternative gate dielectric application, ACS Appl. Mater. Interfaces 8 (45) (2016) 31128–31135.
[9] M. Bolotinha, Insulating and dielectric materials—types, properties & applications, Electr. Technol. (2019) [Online]. Available:. Available from: https://www.electricaltechnology.org/2018/03/insulating-and-dielectric-materials.html#types-of-dielectric-materials [Accessed: 25-Jun-2019].
[10] Y.A. Wahab, A.F. Ahmad, Z. Awang, Comparison of missing metal defect formation on He in-situ and furnace annealed electroplated copper films, in: SCOReD 2006—Proceedings of 2006 4th Student Conference on Research and Development "Towards Enhancing Research Excellence in the Region," 2006.
[11] Y. Abdul Wahab, A.F. Ahmad, H. Hussin, N. Soin, Reduction of annealed-induced wafer defects in dual-damascene copper interconnects, Microelectron. Reliab. 52 (2012).
[12] Z.M. Dang, L.Z. Fan, S.J. Zhao, C.W. Nan, Preparation of nanosized ZnO and dielectric properties of composites filled with nanosized ZnO, Mater. Sci. Eng. B: Solid-State Mater. Adv. Technol. 99 (2003).
[13] S.B. Khan, M. Faisal, M.M. Rahman, A. Jamal, Low-temperature growth of ZnO nanoparticles: photocatalyst and acetone sensor, Talanta 85 (2) (2011) 943–949.
[14] S.C. Minne, S.R. Manalis, C.F. Quate, Parallel atomic force microscopy using cantilevers with integrated piezoresistive sensors and integrated piezoelectric actuators, Appl. Phys. Lett. 67 (26) (1995) 3918–3920.
[15] A. Umar, M.M. Rahman, M. Vaseem, Y.-B. Hahn, Ultra-sensitive cholesterol biosensor based on low-temperature grown ZnO nanoparticles, Electrochem. Commun. 11 (1) (2009) 118–121.
[16] K. Keis, E. Magnusson, H. Lindström, S.-E. Lindquist, A. Hagfeldt, A 5% efficient photoelectrochemical solar cell based on nanostructured ZnO electrodes, Sol. Energy Mater. Sol. Cells 73 (1) (2002) 51–58.
[17] P.M. Martin, M.S. Good, J.W. Johnston, G.J. Posakony, L.J. Bond, S.L. Crawford, Piezoelectric films for 100-MHz ultrasonic transducers, Thin Solid Films 379 (1–2) (2000) 253–258.
[18] M.A. Morris, R.S. Walsh IV, Zinc oxide photoactive material, U.S. Patent No. 6,063,849, 2000.
[19] P. Thurian, G. Kaczmarczyk, H. Siegle, R. Heitz, A. Hoffmann, I. Broser, et al., Local vibrational modes of 3d elements in wurtzite type ZnO and GaN crystals, Mater. Sci. Forum (1995) 196–201.

[20] N.M. Franklin, N.J. Rogers, S.C. Apte, G.E. Batley, G.E. Gadd, P.S. Casey, Comparative toxicity of nanoparticulate ZnO, bulk ZnO, and $ZnCl_2$ to a freshwater microalga (*Pseudokirchneriella subcapitata*): the importance of particle solubility, Environ. Sci. Technol. 41 (24) (2007) 8484–8490.
[21] M.J. Pitkethly, Nanomaterials – the driving force, Mater. Today 7 (12) (2004) 20–29.
[22] J.E. Cañas-Carrell, S. Li, A.M. Parra, B. Shrestha, Metal oxide nanomaterials: health and environmental effects, Health and Environmental Safety of Nanomaterials, Elsevier, 2014, pp. 200–221.
[23] K.E. Engates, H.J. Shipley, Adsorption of Pb, Cd, Cu, Zn, and Ni to titanium dioxide nanoparticles: effect of particle size, solid concentration, and exhaustion, Environ. Sci. Pollut. Res. 18 (3) (2011) 386–395.
[24] K. Kabra, R. Chaudhary, R.L. Sawhney, Treatment of hazardous organic and inorganic compounds through aqueous-phase photocatalysis: a review, Ind. Eng. Chem. Res. 43 (24) (2004) 7683–7696.
[25] N. Chitose, S. Ueta, S. Seino, T.A. Yamamoto, Radiolysis of aqueous phenol solutions with nanoparticles. 1. Phenol degradation and TOC removal in solutions containing TiO_2 induced by UV, γ-ray and electron beams, Chemosphere 50 (8) (2003) 1007–1013.
[26] K. Das, S.N. Sharma, M. Kumar, S.K. De, Morphology dependent luminescence properties of co doped TiO_2 nanostructures, J. Phys. Chem. C. 113 (33) (2009) 14783–14792.
[27] Y. Ju-Nam, J.R. Lead, Manufactured nanoparticles: an overview of their chemistry, interactions and potential environmental implications, Sci. Total Environ. 400 (1–3) (2008) 396–414.
[28] K. Sugibayashi, H. Todo, E. Kimura, Safety evaluation of titanium dioxide nanoparticles by their absorption and elimination profiles, J. Toxicol. Sci. 33 (3) (2008) 293–298.
[29] E.A. Deliyanni, N.K. Lazaridis, E.N. Peleka, K.A. Matis, Metals removal from aqueous solution by iron-based bonding agents, Environ. Sci. Pollut. Res. 11 (1) (2004) 18–21.
[30] M. Kawashima, Phosphate adsorption onto hydrous manganese(IV) oxide in the presence of divalent cations, Water Res. 20 (4) (1986) 471–475.
[31] T. Takamatsu, M. Kawashima, M. Koyama, The role of Mn^{2+}-rich hydrous manganese oxide in the accumulation of arsenic in lake sediments, Water Res. 19 (8) (1985) 1029–1032.
[32] J. Njuguna, K. Pielichowski, H. Zhu, Health and environmental safety of nanomaterials, Polymer Nancomposites and Other Materials Containing Nanoparticles (2014, Elsevier).
[33] K. Reinhardt, H. Winkler, Cerium mischmetal, cerium alloys, and cerium compounds, Ullmann's Encyclopedia of Industrial Chemistry, Wiley-VCH Verlag GmbH & Co. KGaA, Weinheim, Germany, 2000.
[34] J. Seo, J. Jang, S. Park, C. Kim, B. Park, J. Cheon, Two-dimensional SnS_2 nanoplates with extraordinary high discharge capacity for lithium ion batteries, Adv. Mater. 20 (22) (2008) 4269–4273.
[35] A. Esteban-Cubillo, C. Pecharromán, E. Aguilar, J. Santarén, J.S. Moya, Antibacterial activity of copper monodispersed nanoparticles into sepiolite, J. Mater. Sci. 41 (16) (2006) 5208–5212.
[36] G. Filipič, U. Cvelbar, Copper oxide nanowires: a review of growth, Nanotechnology 23 (19) (2012) 194001.

[37] K.M. Gupta, N. Gupta, Advanced Electrical and Electronics Materials, John Wiley & Sons, Inc, Hoboken, NJ, 2015.
[38] J.A. Mergos, M.D. Athanassopoulou, T.G. Argyropoulos, C.T. Dervos, Dielectric properties of nanopowder dispersions in paraffin oil, IEEE Trans. Dielectr. Electr. Insul. 19 (2012).
[39] H. Gleiter, Nanostructured materials: state of the art and perspectives, Nanostruct. Mater. 6 (1995).
[40] M. Valden, X. Lai, D.W. Goodman, Onset of catalytic activity of gold clusters on titania with the appearance of nonmetallic properties, Science 281 (1998).
[41] J.A. Rodriguez, et al., Activation of gold on titania: adsorption and reaction of SO_2 on Au/TiO_2 (110), J. Am. Chem. Soc. 124 (18) (2002) 5242−5250.
[42] J.M. Vohs, The surface science of metal oxides. By V. E. Henrich and P. A. Cox, Cambridge University Press, Cambridge, U.K., 1994, 464 pp. hardcover $99.95; paperback $39.95, AIChE J. 44 (2) (1998) 502−503.
[43] M. Bäumer, H.J. Freund, Metal deposits on well-ordered oxide films, Prog. Surf. Sci. 61 (1999).
[44] P. Sharma, T.S. Bhatti, A review on electrochemical double-layer capacitors, Energy Convers. Manage. 51 (2010).
[45] E.J. Grootendorst, Y. Verbeek, V. Ponec, The role of the Mars and van Krevelen mechanism in the selective oxidation of nitrosobenzene and the deoxygenation of nitrobenzene on oxidic catalysts, J. Catal. 157 (2) (1995) 706−712.
[46] E.R. Stobbe, B.A. De Boer, J.W. Geus, The reduction and oxidation behaviour of manganese oxides, Catal. Today 47 (1999).
[47] T. Block, M. Schmücker, Metal oxides for thermochemical energy storage: a comparison of several metal oxide systems, Sol. Energy 126 (2016).
[48] S.P. Gubin, Y.I. Spichkin, G.Y. Yurkov, A.M. Tishin, Nanomaterial for high-density magnetic data storage, Russ. J. Inorg. Chem. 47 (Suppl. 1) (2002) S32−S67.
[49] Y.R. Ahn, M.Y. Song, S.M. Jo, C.R. Park, D.Y. Kim, Electrochemical capacitors based on electrodeposited ruthenium oxide on nanofibre substrates, Nanotechnology 17 (2006).
[50] C.C. Hu, Y.H. Huang, K.H. Chang, Annealing effects on the physicochemical characteristics of hydrous ruthenium and ruthenium-iridium oxides for electrochemical supercapacitors, J. Power Sources 108 (2002).
[51] J. Yan, T. Wei, J. Cheng, Z. Fan, M. Zhang, Preparation and electrochemical properties of lamellar MnO_2 for supercapacitors, Mater. Res. Bull. 45 (2010).
[52] U.M. Patil, R.R. Salunkhe, K.V. Gurav, C.D. Lokhande, Chemically deposited nanocrystalline NiO thin films for supercapacitor application, Appl. Surf. Sci. 255 (2008).
[53] S.G. Kandalkar, J.L. Gunjakar, C.D. Lokhande, Preparation of cobalt oxide thin films and its use in supercapacitor application, Appl. Surf. Sci. 254 (2008).
[54] N. Miura, S. Oonishi, K. Rajendra Prasad, Indium tin oxide/carbon composite electrode material for electrochemical supercapacitors, Electrochem. Solid-State Lett. 7 (8) (2004) A247.
[55] C.C. Hu, C.M. Huang, K.H. Chang, Anodic deposition of porous vanadium oxide network with high power characteristics for pseudocapacitors, J. Power Sources 185 (2008).
[56] S. Park, C.H. Kim, W.J. Lee, S. Sung, M.H. Yoon, Sol-gel metal oxide dielectrics for all-solution-processed electronics, Mater. Sci. Eng. R: Rep. 114 (2017).
[57] G. Wang, L. Zhang, J. Zhang, A review of electrode materials for electrochemical supercapacitors, Chem. Soc. Rev. 41 (2012).

[58] N.J. Tharayil, S. Sagar, R. Raveendran, A.V. Vaidyan, Dielectric studies of nanocrystalline nickel−cobalt oxide, Physica B: Condens. Matter 399 (1) (2007) 1−8.
[59] P.P. Sharmila, R.M. Sebastain, S. Sagar, E.M. Mohammed, N.J. Tharayil, Dielectric properties and conductivity of (ZnO/CdO) mixed oxide nanocomposite, Ferroelectrics 474 (1) (2015) 144−155.
[60] Ra.S.G. Boyd, Polymer Dynamics and Relaxation, Cambridge University Press, 2007.
[61] A. Patsidis, G.C. Psarras, Dielectric behaviour and functionality of polymer matrix − ceramic $BaTiO_3$ composites, Express Polym. Lett. 2 (10) (2008) 718−726.
[62] N.S. Akhmadullina, et al., Plasma-chemical processes under high-power gyrotron's discharge in the mixtures of metal and dielectric powders, Chem. Phys. 516 (2019).
[63] Z. Li, et al., In situ catalytic encapsulation of core-shell nanoparticles having variable shell thickness: dielectric and energy storage properties of high-permittivity metal oxide nanocomposites, Chem. Mater. 22 (2010).
[64] A.A. Abdelmalik, A. Sadiq, Thermal and electrical characterization of composite metal oxides particles from periwinkle shell for dielectric application, SN Appl. Sci. 1 (4) (2019) 373.
[65] A. Nitta, M. Takase, M. Takashima, N. Murakami, B. Ohtani, A fingerprint of metal-oxide powders: energy-resolved distribution of electron traps, Chem. Commun. 52 (81) (2016) 12096−12099.

This page intentionally left blank

Index

Note: Page numbers followed by "*f*" and "*t*" refer to figures and tables, respectively.

Metal Oxides Series

Metal Oxide Powder Technologies

Fundamentals, Processing Methods and Applications

Edited by
Yarub Al-Douri

A comprehensive look combining theoretical and experimental approaches to metal oxide powders development and evaluation, including a review of key applications.

Metal Oxide Powder Technologies: Fundamentals, Processing Methods, and Applications reviews the fundamentals, processing methods, and applications of this key materials system. The topics addressed are comprehensive including both chemical and physical properties, synthesis, preparation, both accepted and novel processing methods, modeling, and simulation.

The book provides fundamental information on key properties that impact performance such as particle size and crystal structure, followed by methods to measure, analyze, and evaluate metal oxide powders and particles. Finally, important applications are covered including biomedical, energy, electronics, and materials applications.

This book is suitable for those working in the disciplines of materials science, chemistry, and physics.

Key Features

- Provides a comprehensive overview of key topics both on the theoretical side and the experimental
- Discusses important properties that impact metal oxide performance, processing methods both novel and accepted, and important applications
- Reviews the most relevant applications such as biomedical, energy, electronics and materials applications

About the Editor

Dr. Yarub Al-Douri is a Professor of Nanotechnology at the University of Malaya in Malaysia, a Visiting Professor at Cihan University Sulaimaniya, Iraq, and an Adjunct Professor at Bahcesehir University, Istanbul, Turkey. He is the Editor-in-Chief of *Experimental and Theoretical NANOTECHNOLOGY* and the Editor-in-Chief of the *World Journal of Nano Science and Engineering*.

ISBN 978-0-12-817505-7

9 780128 175057

ELSEVIER elsevier.com/books-and-journals